Fast-dynamic response and failure of masonry structures of non-standard geometry subjected to blast loads

Filippo Masi

THESE DE DOCTORAT DE

L'ÉCOLE CENTRALE DE NANTES

ECOLE DOCTORALE N° 602
Sciences pour l'Ingénieur
Spécialité : Mécanique des solides, des matériaux des structures et des surfaces

Par
Filippo MASI

Fast-dynamic response and failure of masonry structures of non-standard geometry subjected to blast loads

Thèse présentée et soutenue à l'École Centrale de Nantes, le 14 Décembre 2020
Unité de recherche : Institut de Recherche en Génie Civil et Mécanique (GeM)

Rapporteurs avant soutenance :

Maurizio Brocato	Professeur, ENSA Paris-Malaquais
José Lemos	Directeur de recherche, Laboratorio Nacional de Engenharia Civil, Portugal

Composition du Jury :

Président :	Laurent Stainier	Professeur des universités, École Centrale de Nantes
Examinateurs :	Félix Darve	Professeur des universités, Grenoble INP
	Katrin Beyer	Professeur associé, École Polytechnique Fédérale de Lausanne, Suisse
Dir. de thèse :	Ioannis Stefanou	Professeur des universités, École Centrale de Nantes
Co-dir. de thèse :	Paolo Vannucci	Professeur des universités, Université de Versailles et Saint-Quentin

Whenever a theory appears to you
as the only possible one, take this as a sign
that you have neither understood the theory
nor the problem which it was intended to solve.

Karl Popper *Objective Knowledge : An Evolutionary Approach.*

Remerciements – Aknowledgements

Le présent manuscrit représente la tentative de regrouper plusieurs années de travail au sein du laboratoire Navier de l'ENPC et du laboratoire GeM de l'ECN. Il est la résultante, pierre après pierre, *joint* après *joint*, d'interactions avec de nombreuses personnes. Certaines de ces personnes m'ont entouré, soutenu et conseillé dans cette aventure et j'aimerais les remercier ici de la façon la plus exhaustive possible.

C'est une histoire qui a commencé en l'an 2016 avec un stage dans le cadre du projet « Cathédrales Durables » (CNRS, *Attentats-Recherche*), sous la direction de Paolo Vannucci et Ioannis Stefanou. C'est grâce à eux, ainsi qu'au support de Paolo Mariano, que j'ai pu cultiver ma passion pour le monde de la recherche et plus spécifiquement pour la mécanique. Cela a conduit, un an plus tard, au commencement d'une thèse sous la direction de Ioannis Stefanou et Paolo Vannucci, dans le cadre d'une CIFRE, en partenariat avec Ingérop.
Je remercie profondément Ioannis Stefanou : merci pour ton aide, pour tout le temps que tu m'as accordé et pour nos discussions diverses et variées sur la mécanique et la philosophie. Je remercie vivement Paolo Vannucci : merci pour tes nombreux conseils, ton aide précieuse et ton regard critique. Merci également à Victor Maffi-Berthier, qui a permis la concrétisation de cette aventure : merci pour tes suggestions et ton soutien tout au long de ces trois années.

Je voudrais ensuite remercier ceux qui ont permis à cette aventure de se terminer : le Jury. It was a great honor to have them (*virtually*) present for my defense and that they agreed to be associated with this thesis. First of all, I would like to thank the two reviewers, who have accepted the heavy work of reading and commenting my thesis : José Lemos and Maurizio Brocato. Thank you for your interest in this work and the numerous thought-provoking remarks. Je remercie Laurent Stainier d'avoir présidé ce jury avec bienveillance et pour nos nombreux échanges stimulants. Merci à Félix Darve pour ses questions et son regard attentif et critique. I would like to thank Katrin Beyer for her interesting and stimulating questions and remarks.
Then, I would like to thank Matthew DeJong. Despite the impossibility to join the defense and, for me, to come in Berkeley, due to the peculiar situation of this last year, I thank him for his interest to this work and I hope we will have the chance to continue discussing.

Je tiens aussi à remercier sincèrement les personnes qui ont partagé mon quotidien au laboratoire, dans les jours de pluie comme dans ceux ensoleillés, de l'équipe MSA à l'équipe MEO, en passant par Ingérop : Timos, Chadi, Leila, Charlotte, Baptiste, Benjamin, Nicolas, Eki, Florian, Paul, Nihal, Nadine, Ingrid, Philippe, Vianney, Léo, Nick, Philipp, Hadrien, Sabine, Julien, Koliann, Marie-Francoise, Axelle, Sophie, Pierre, Cyril, Frédéric, Alex, Georgios, Pravin, Andrianna, Kexin, Aliénor, Quentin, Constantinos, Anne-Laure, Nicolas, Panos, Katia, Elisa, Mahsa, Mustapha, Nicolas (les deux !), Pierre, Sandy, Veronique, Binh, Charles, Carlos, Jiabin, Ramzi, Sophie et Félix.

Je terminerai par remercier tous mes amis et ma famille pour leur soutien inconditionnel et tous les moments mémorables que nous avons partagé : Asia (et ses carottes), Nadine, Laetitia (et les innombrables *quadrilles* sur le dancefloor), Stefano, Beatrice, Giovanna, Mathéo, Mona-Lise, Timothée, Nicoletta, Mario, Matilde, Giacomo, Maria, Lisa, et Luana. Enfin, je ne pourrai jamais assez remercier mes parents : (mamma) Laura et (babbo) Roberto. Merci de m'avoir toujours soutenu, c'est aussi grâce à vous deux que je me retrouve ici ! *Last, but not least*, je remercie la personne qui m'a le plus aidé dans le sprint final et qui a dû faire preuve de beaucoup de patiente et résilience : Christophe.

Abstract

Masonry structures are often characterized by non-standard geometries, consisting of arches, vaults, and domes. This is also the case for historical and monumental structures, which are often primary targets of accidental and deliberate explosions. The main goal of this work is to shed light on the dynamic behavior and failure modes of monolithic and non-standard, curvilinear masonry geometries subjected to blast loading. This is, first, accomplished through simplified analytical tools and advanced numerical simulations relying on the Discrete Element Method (DEM). Then, a simplified macroscopic modeling approach, using the Finite Element Method (FEM), is presented as an engineering tool to be used in the investigation of complex, large masonry buildings, such as monuments.

In particular, new analytical, closed-form solutions for the rocking response and the overturning domain of slender, monolithic structures are derived and validated against existing experiments and detailed numerical simulations. Rocking mechanism is found to be predominant over sliding, up-lifting, and direct damage modes.

DEM is used to investigate the response of non-standard masonry structures, e.g. arches and vaults, and the influence of various mechanical parameters (e.g. dilatancy angle, tensile strength and cohesion of the masonry joints, and building blocks size). The approach allows considering the detailed mechanical and geometrical characteristics of masonry, as well as the inherent coupling between the in- and out-of-plane motion.

Relying on DEM numerical results, we develop a macroscopic FEM modeling approach, based on simplified upscaling techniques and the smeared cracking model, to make preliminary predictions of the structural response of masonry assets at large scale. The proposed, simplified model assumes isotropic behavior and allows taking into account the strain softening phenomenon.

With the aim of developing more accurate and detailed material models of the aforementioned simplified approach, a new class of Artificial Neural Networks (ANNs) is also proposed as a robust, thermodynamics-based, tool to derive constitutive models, at the material point level, in the framework of physics-based multiscale analyses. Thermodynamics-based Artificial Neural Networks (TANNs) are applied—and their superiority with the respect to classical ANNs approaches is proved—for the case of materials displaying softening behavior.

Finally, we propose new scaling laws for the response of masonry structures subjected to explosions. Our aim is to design future experimental, reduced-scale experiments, which are of paramount importance to further improve current understanding and corroborate the proposed models. Indeed, at present, experimental tests of masonry structures subjected to explosions are limited, compared to tests under different dynamic conditions, such as earthquakes.

Keywords : • Masonry • Blast loads • Fast-dynamics • Discrete Element Method • Finite Element Method • Artificial Neural Networks • Scaling laws.

Résumé

Les bâtiments en maçonnerie ont souvent une géométrie non-standard, caractérisée par des arcs, des voûtes et des dômes. C'est également le cas des structures appartenantes au patrimoine bâti historique, qui sont souvent des cibles symboliques et privilégiées des actions violentes, telles que des explosions. L'objectif principal de ce travail est de mettre en lumière le comportement dynamique et les modes de ruine des structures maçonnées avec soit un comportement monolithique soit une géométrie non-standard, vis-à-vis d'explosions. Ceci est d'abord accompli grâce à des outils analytiques simplifiés et à des simulations numériques détaillées reposant sur la Méthode aux Éléments Discrets (ED). Ensuite, une approche de modélisation macroscopique simplifiée, utilisant la Méthode aux Éléments Finis (EF), est introduite comme un outil d'ingénieur pour étudier de grands bâtiments en maçonnerie, tels que des monuments.

En particulier, de nouvelles solutions analytiques pour la réponse en basculement des structures élancées et monolithiques sont dérivées et validées par rapport à des expériences existantes et à des simulations numériques détaillées. Le mécanisme de basculement est prédominant par rapport aux modes de glissement, de soulèvement et d'endommagement direct.

La Méthode aux ED est utilisée pour étudier la réponse des structures maçonnées non-standard, telles que des arcs et des voûtes, et l'influence de divers paramètres mécaniques (angle de dilatance, résistance à la traction et cohésion des joints, ainsi que la taille des blocs). L'approche permet de considérer les caractéristiques mécaniques et géométriques détaillées de la maçonnerie, ainsi que le couplage inhérent entre les mouvements dans et hors le plan.

En nous appuyant sur les résultats numériques ED, nous développons une approche de modélisation aux EF macroscopique, basée sur des techniques simplifiées de upscaling et un modèle de fissuration étalé, afin de prédire la réponse d'éléments structuraux en maçonnerie à grande échelle. Le modèle proposé prévoit un comportement isotrope et permet de prendre en compte le phénomène d'adoucissement, qui affecte fortement la réponse du matériau.

Dans le but de développer des modèles de matériaux plus précis et détaillés de l'approche mentionnée ci-dessus, une nouvelle classe de réseaux de neurones artificiels (ANNs) est également proposée comme un outil robuste, basé sur la thermodynamique, pour dériver des modèles constitutifs, au niveau du point matériel, dans le cadre d'analyses physiques multi-échelle. Les réseaux de neurones artificiels basés sur la thermodynamique (TANNs) sont appliqués − et leur supériorité par rapport aux approches ANNs classiques est prouvée − pour le cas des matériaux présentant un comportement d'adoucissement.

Enfin, nous proposons de nouvelles lois de similitude pour la réponse des structures en maçonnerie soumises à des explosions. Notre objectif est de concevoir de futurs essais expérimentaux à échelle réduite, qui sont d'une importance capitale pour améliorer la connaissance actuelle et corroborer les modèles proposés. En effet, à l'heure actuelle, les essais expérimentaux de structures de maçonnerie soumises à des explosions sont limités, par rapport aux essais sous différentes conditions dynamiques, telles que p. ex. les chargements sismiques.

Mots-clés : • Maçonnerie • Explosions • Dynamique rapide • Méthode aux Éléments Discrets • Méthode aux Éléments Finis • Réseaux de neurones artificiels • Lois de similitude.

Cathedral of St. Peter and St. Paul in Nantes (France), 18 July 2020 (Filippo Masi).

Contents

Introduction

In this Thesis we investigate the dynamic response and failure of brick and stone masonry structures, of *non-standard* geometry, subjected to the fast-dynamic excitations arising from an explosion. The term *non-standard* geometry refers here to assets being composed of arches, vaults, domes, and any other structural element that is substantially different from planar walls. The class of non-standard geometry masonry structures includes, but it is not limited to, historical buildings, monuments, and halls. Such kind of structures have been repeatedly exposed to accidental or deliberate blasts, e.g. the Parthenon in Athens (Greece) in 1687, the Monumental Arch of Palmyra (Syria) in 2015, the recent blast in Beirut (Lebanon), on 4 August 2020, or the destruction of the Ghazanchetsots Cathedral (Azerbaijan), on 10 October 2020.
In the last decades, increasing scientific interest has being shown on the blast response and potential damage of masonry structures, via experiments and modeling. Attention has been mostly focused on regular geometries, i.e., flat walls (Gabrielsen et al., 1975; Keys and Clubley, 2017; Li et al., 2017; Michaloudis and Gebbeken, 2019; Wei and Stewart, 2010; Rafsanjani et al., 2015; Silva et al., 2017; Wang et al., 2009; Pereira et al., 2015). The research activity for non-standard structures and related load-carrying members under blast actions is very limited (compared to tests under other dynamic conditions, such as earthquakes). The experimental testing of structures subjected to blast loads is particularly challenging, due to the cost, environmental hazards, and safety risks that have to be considered in designing and executing experimental tests (Draganić et al., 2018). Complexity further increases when dealing with masonry structures due to their highly nonlinear behavior, complex cracking and failure modes.

Masonry, composed of blocks assembled with a specific texture and interacting through joints, exhibits distinct directional properties. Masonry joints typically act as planes with reduced strength (weak planes) whose orientation strongly affects the overall mechanical response of the structure (Page, 1981, 1983; Van der Pluijm, 1999). Masonry displays strain softening behavior, i.e., progressive loss of stiffness at the post-peak, which governs the ultimate load-capacity of the material (Van der Pluijm, 1999). The mechanical response may also depend on the loading rates (Asprone et al., 2009; Chen et al., 2014; Jin et al., 2017; Pereira and Lourenço, 2017), among other factors which are explored in this Thesis.
Several approaches exist to model the response and collapse of masonry structures, depending on the type of construction, the loading conditions, the desired accuracy and the corresponding computational cost. When subjected to blast loading, the dynamic response additionally depends on the intensity of the explosion, the stand-off distance, the degree of confinement of the building, as well as the geometry of the structure impinged by the blast waves. In the case of large structures, far-field blast scenarios are of particular

interest.
Typical collapse modes involve coupled in-plane and out-of-plane deformations, especially in the case of non-standard geometries. Models that are able to account for that coupling usually rely on a meso-scale description of the material, where both blocks and joints are modeled, and are usually discrete in nature, e.g. the Discrete Element Method. Nevertheless, their computational cost is such that meso-scale modeling approaches are limited to investigations of single load-carrying elements. When entire buildings, or portions of them, are the object of the investigation, macro-scale models are usually adopted, which rely, in most instances, on the theory of continuum mechanics and are frequently solved using the Finite Element Method. Macro-modeling relies on the basic assumption that the masonry material is a (quasi-)periodic repetition of a characteristic elementary pattern, whose properties can be upscaled and assigned to material points in a continuum representation (Bakhvalov and Panasenko, 1989; Lourenço et al., 2007).
Under some circumstances, monolithic behavior (involving rigid-body motion, such as rocking and sliding) may also be displayed by masonry structures subjected to explosions. This is due to the very short characteristic time of blast waves compared to the characteristic time of the structure, i.e., milliseconds versus seconds. Under such circumstances, simplified modeling strategies may be considered.

In this Thesis we extend the current understanding of the dynamic mechanical response and collapse modes of non-standard masonry structures subjected to blast loading. This is accomplished by:

(a) Studying the response and failure modes of monolithic structures, including rocking, sliding, up-lifting, and direct damage mechanisms;

(b) Investigating the failure modes and the overall strength of typical elements in standard and non-standard geometry masonry buildings, namely walls, circular and pointed arches, and barrel and cross vaults.

We adopt analytical and numerical models, after validation against existing experimental data and detailed numerical simulations. The latter account for the fluid-structure interactions in a blast scenario. Non-standard geometry assets are studied using the Discrete Element Method, and the influence of several mechanical parameters is assessed. In particular, we investigate the role of the strength of the masonry joints, the (non-) associativity of the sliding behavior, and the building blocks size. The present studies shed light on the collapse modes of these types of structures, for which the experimental literature is extremely limited.

Relying on the above mentioned investigations, we develop modeling approaches/strategies to study the behavior of existing buildings and to design new ones. In particular:

(c) We develop a Finite Element macroscopic modeling approach based on a simplified upscaling procedure, accounting for the post-peak, softening behavior. Our approach aims at providing safe estimations of the overall structural resistance of non-standard masonry structures to be used as an engineering tool for intervention/ restoration/ reinforcement on/of existing non-standard buildings and the design of modern ones;

(d) We propose a computational Machine Learning framework to provide more accurate and detailed material models, introducing a new class of Artificial Neural Networks based on the principles of thermodynamics. Preliminary results for elasto-plastic materials displaying softening are given.

The proposed macro-model is based on the smeared cracking model (Hillerborg et al., 1976) and allows us to mimic, through macroscopic parameters, the meso-scale behavior, which in turn depends on micro-mechanical parameters, such as the building blocks dimensions, the elastic parameters of the constituents (blocks and joints), the material strength and the softening behavior, among others. The model is corroborated against existing experimental tests and the aforementioned detailed Discrete Element simulations. Its advantages and limitations are presented and discussed.
In view of a more detailed material description, we propose the substitution of the macroscopic constitutive law by Artificial Neural Networks. We present preliminary results using Thermodynamics-based Neural Networks, which are able to predict the material laws by enforcing the laws of thermodynamics. This opens new perspectives in multiscale modeling.

Experimental campaigns are a major issue and a necessary step to further validate our results and draw appropriate protective strategies for masonry buildings, ancient and modern ones. For this purpose, we set the basis for designing new experimental tests for validating/falsifying the derived models and theoretical assumptions on the base of reduced-scale models. With the aim of performing laboratory tests, we develop

(e) New scaling laws for the dynamic response of masonry structures and blast actions.

The scaling procedure is validated against detailed numerical simulations. In particular, we demonstrate their applicability to masonry elements with applications to multi-drums columns.

The present manuscript is organized into three Parts. Part I gives a detailed introduction to the subject. The current state of knowledge in blast excitations (Chapter 1) and the mechanical behavior of the masonry material (Chapter 2) are briefly summarized. The dynamic response and failure modes of structures under dynamic and fast-dynamic loading conditions are described by reviewing the current literature. Several modeling techniques, based on a micro-, meso-, or macro-level approach, are further presented and discussed as tools to investigate such phenomena. In these Chapters we highlight the main modeling assumptions that were made in this study.
In Part II, we model the behavior and overall resistance to blasts of non-standard masonry elements via several methods (analytical, in Chapter 3, and numerical, in Chapter 4). The obtained results are used to develop a macroscopic modeling technique described in Chapter 5. The possibility for computational enhancement by Machine Learning methods for the constitutive modeling is presented in Chapter 6.
Finally, Part III focuses attention on the design of future laboratory reduced-scale experiments by providing new scaling laws for the blast loading and the dynamic, structural response.

Part I

Blast loads and failure modes of masonry structures

Chapter 1

Blast loads

Abstract. *Explosions are associated with sudden energy release that produces large quantities of expanding gases and shock waves. Shock waves originating from explosion events are known as blast waves.*
Here we present a brief description of the characteristic features of blast waves and the generated pressure loads to structures. Particular attention is focused on how such kind of loads can be modeled, either through empirical, simplified approaches or physics-based models.
We finally compare both models through a representative case-study. In the case of non-standard geometry structures, empirical models give overall safe estimations of the blast actions. Despite some limitations, when studying the response of typical load-carrying structural elements, such as walls, vaults, arches, etc., empirical models allow to have reliable and conservative estimates of the loading.

Contents

1.1 Introduction

Blast waves arise in rapid releases of energy from a concentrated source, e.g., the detonation of high-explosives or pressurized gas mixtures. High-explosives are detonating explosive materials, such as trinitrotoluene (TNT) and dynamite, characterized by extremely rapid decomposition and development of high pressures [1]. In the detonation process of high-explosives, detonation waves develop inside the explosive material and rapidly release energy in the form of high-pressure accompanying high-temperature gases (detonation products). Since these gases are at very high temperatures and pressures, they expand and initiate a pressure wave into the surrounding medium. If certain conditions are met, the pressure wave develops into a supersonic blast (or shock) wave.
Blast waves are characterized by the very rapid increase of all the physical quantities of the ambient gas, i.e., the incident overpressure, the density, the particle velocity, and the temperature. Here, we use the term overpressure to denote a differential pressure, relative to ambient one, P_0. Behind the shock front, these quantities gradually decrease. Following Dewey (2016), we briefly recall the following definitions:

- the incident overpressure, P_s, is associated with free air pressure waves that have not yet interacted with any obstacle. It does not include any component due to the translational movement of the gas. The incident overpressure is usually measured by transducers that are flush mounted in a surface that is parallel to the flow (see Pape et al., 2010; Dewey, 2016).

- the dynamic pressure is the pressure due to the gas flow behind the pressure front. It is defined as $q = \frac{1}{2}\rho_s u_s^2$ with ρ_s the air density and u_s the particle velocity. The dynamic pressure is responsible of aerodynamic forces, such as lift and drag [2].

Typical time-history and spatial evolution of physical quantities such as the incident overpressure, P_s, are represented in Figure 1.1.

At a distance R from the explosive charge, the incident overpressure increases, with a strong discontinuity, to a peak P_{so}, at the shock wave arrival time, t_A. For $t > t_A$ the overpressure rapidly decreases, with an almost exponential rate, until time $t_A + t_o$, the end of the so-called *positive phase*. After $t_A + t_o$, the overpressure takes negative values and it asymptotically approaches to the initial value (ambient pressure), with time. This phase is called *negative phase*. During the negative phase, the decrease of the pressure is lower, in absolute value, than the peak pressure of the positive phase, while its duration is always much longer. Secondary and tertiary shocks can also develop (beside the primary peak P_{so}). This is the result of the repeated over-expansion, subsequent implosion, and re-expansion of the detonation products.

With reference to Figure 1.1a, the impulse of the positive phase is computed as

$$i_s = \int_{t_A}^{t_A+t_o} P_s(t)\, dt, \tag{1.1}$$

1. High-explosives distinguish from deflagrating (or low-) explosives, such as black and smokeless powders, which involve fast burning and produce relatively low pressures.

2. Lift and drag are forces exerted on an object by a flowing fluid. Lift is the force acting perpendicularly to the flow direction and drag the one acting in the direction parallel to the flow.

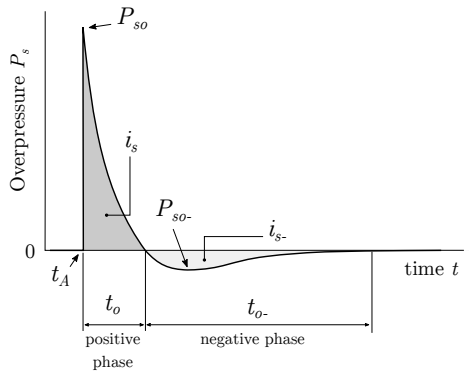

(a) time-history.

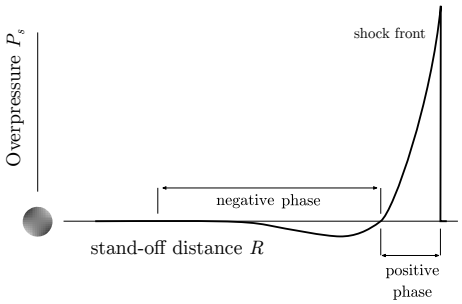

(b) spatial evolution.

Figure 1.1 – Time-history at a fixed point in space, at distance R from the explosive source (a) and spatial evolution in term of the stand-off distance R (b) of the incident overpressure in a free-field blast wave.

and the negative phase impulse as

$$i_{s-} = \int_{t_A+t_o}^{t_A+t_o+t_{o-}} P_s(t)\, dt. \tag{1.2}$$

1.1.1 Classification of explosions

Explosions, and blast loads, can be distinguished into two main groups based on the confinement of the explosive charge: confined (or internal) and unconfined (external) explosions (from the classification in USACE, 2008), see Figure 1.2.

(a) Internal explosions. Explosions occurring inside a structure, in which each surface is subjected to shock waves due to the reflections of multiple surfaces. Depending on the loading density $W/V-$i.e. the ratio between the charge weight (W) and the free volume of the structure $(V)-$ an internal explosion may be fully vented, partially vented/confined or fully confined (USACE, 2008; Feldgun et al., 2016), see Figure 1.2.

(1) Fully vented explosion. An explosion occurring within or immediately adjacent to a barrier or cubicle-like structure with one or more surfaces open to the atmosphere. The initial shock wave and the products of detonation are totally vented to the atmosphere and propagate away from the structure.

(2) Partially confined explosion. An explosion produced within a barrier or cubicle type structure with limited size openings. The initial shock wave and the products of detonation are vented to the atmosphere, after a finite period of time. The confinement of the detonation products, which consist of the accumulation of high temperatures and gaseous products, results in a quasi-static pressure which has a longer duration in comparison to that of the shock wave (see Fig. 1.1a).

(3) Fully confined explosion. An explosion associated with either total or near total containment by a barrier structure. Internal blast loads consist of unvented shock loads and long duration quasi-static pressure depending on the degree of confinement.

(b) External explosions. External or unconfined explosions can be classified into three different categories in function of the relative position and angle of the explosive source and the structure subjected to the blast.

(1) Free-air burst. An explosion occurring in free air, where the blast waves propagate spherically outwards and impinges directly onto the structure, without prior interaction with other obstacles or the ground.

(2) Air burst. An explosion occurring in air, in which the blast waves propagate spherically outwards and impinge onto the structure, after having interacted first with the ground.

(3) Surface burst. An explosion occurring almost at ground surface, the blast waves immediately interact locally with the ground and they next propagate hemispherically outwards and impinge onto the structure.

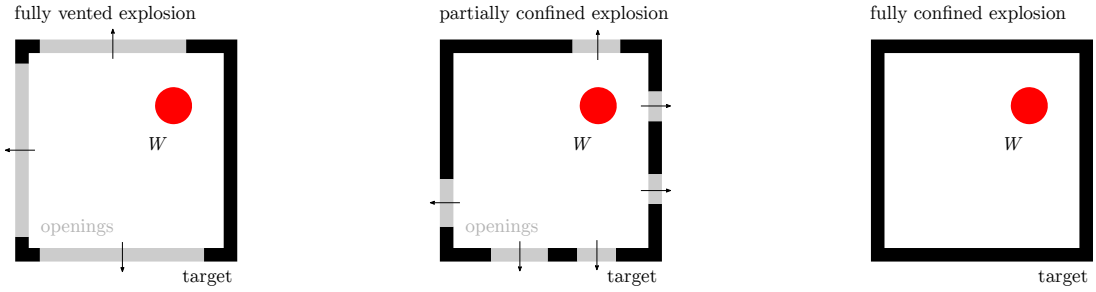

(a) fully vented, partially confined, and fully confined explosion.

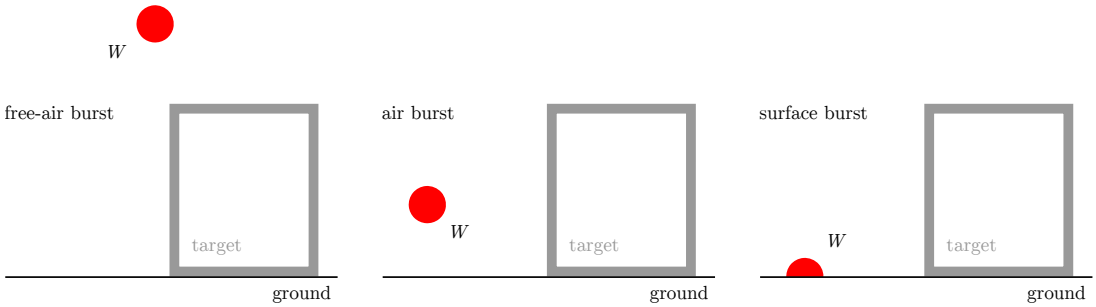

(b) free-air, air, and surface burst.

Figure 1.2 – Classification of explosions: (a) internal and (b) external/unconfined explosions.

1.1.2 TNT equivalence

Different kind of high-explosives, e.g. TNT, Composition B, Composition C4, or Ammonium-Nitrate-Fuel-Oil (ANFO), produce similar blast waves, but with different properties. As a result, the blast wave properties are often quoted in terms of the equivalent energy yield of TNT, used as reference explosive. To assess the effects of a blast produced by another explosive, we use the concept of TNT equivalence. The TNT equivalence factor, $E_{q_{TNT}}$, is defined as the ratio between W and W_e where W and W_e are the charge mass of TNT and the actual explosive, that yields the same blast effects. Namely, $E_{q_{TNT}} = W/W_e$. The TNT equivalent mass is a basic quantity for estimating the blast parameters generated from the detonation of various explosives, see Table 1.1. TNT equivalence factors can be determined by theoretical, experimental tests, and numerical methods. Different approaches exist for the determination of the TNT equivalence [3], either based on the equivalence in term of released energy, overpressure, or impulse. For more details, we refer to Sochet (2010) and Xiao et al. (2020).

Table 1.1 – TNT equivalence factors of high explosives derived from empirical formulae in the far field range, see paragraph 1.1.3, from (USACE, 2008; Xiao et al., 2020).

Explosive	$E_{q_{TNT}}$
Composition A3	1.213
Composition B	1.134
Composition C4	1.224
PBX-9404	1.250
Pentolite	1.078
ANFO	0.80

1.1.3 Scaling laws

Scaling of blast wave properties is a common practice used to generalize blast data from explosives and to predict the properties of blast waves from large-scale explosions based on tests at a much smaller scale. The most common scaling law is the one formulated independently by Hopkinson (1915) and Cranz (1925). It states that two explosives, of similar geometry and of the same explosive material, with TNT equivalent weight W and $\widetilde{W}$, detonated in the same atmosphere, produce self-similar blast waves at distances R and $\widetilde{R}$, respectively, if they have the same scaled distance Z, namely

$$Z = \widetilde{Z}, \quad \text{with } Z = \frac{R}{\sqrt[3]{W}}, \quad \widetilde{Z} = \frac{\widetilde{R}}{\sqrt[3]{\widetilde{W}}}. \tag{1.3}$$

3. We shall record the work of Rigby et al. (2020) and Diaz (2020), who investigated the TNT equivalent of the (series of) explosions occurred in the port of Beirut, Lebanon, caused by the detonation of approximately 2.75 kt of ammonium nitrate. In both studies, videos and audio recordings were used, in addition to empirical interpolations (Taylor, 1950; Kingery and Bulmash, 1984) of the blast parameters, to determine the TNT equivalence. Rigby et al. (2020) and Diaz (2020) estimated a TNT equivalent weight equal to $0.50 \div 1.12$ kt and $0.95 \div 1.05$ kt, respectively.

Figure 1.3 shows the Hopkinson-Cranz scaling law for a real scale and reduced scale explosions. Further modifications to the Hopkinson-Cranz similarity laws were introduced by Sachs (1944) to predict the effects of detonations at different ambient conditions. We shall see, in Chapter 7, that different scaling laws can also be derived.

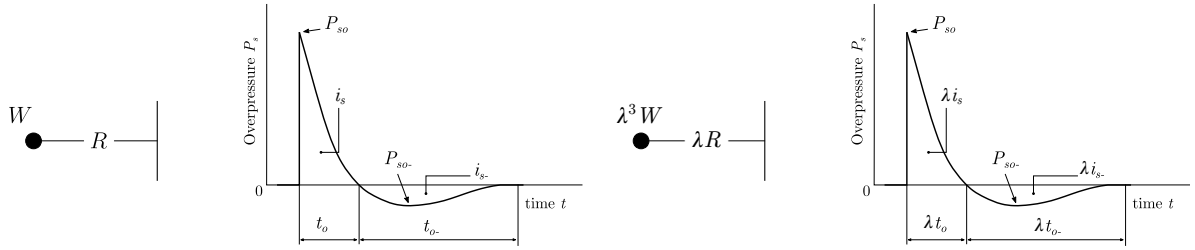

(a) real scale. (b) small scale.

Figure 1.3 – Hopkinson-Cranz scaling law: (a) overpressure time-history for a TNT explosive weight W at a stand-off distance R and reduced scale (geometric factor λ) overpressure time-history for a TNT explosive weight $\lambda^3 W$ at a stand-off distance λR .

1.1.4 Effects on structures

The large increases of incident and dynamic pressures in a blast wave are the physical characteristics that produce most of the damage to structures and injure people. This was the case in the recent series of explosions in the port of Beirut, see Figures 1.4 and 1.5.

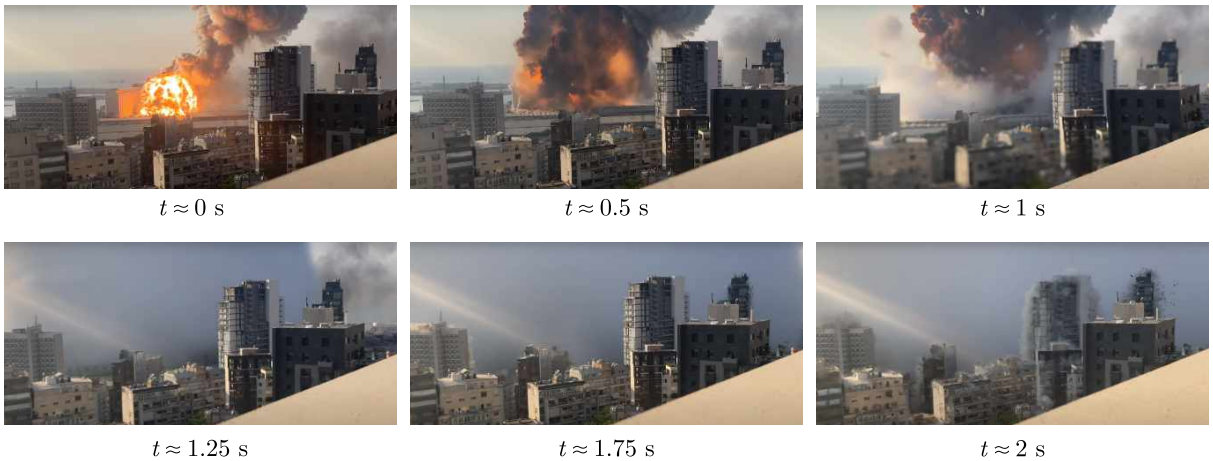

$t \approx 0$ s $t \approx 0.5$ s $t \approx 1$ s

$t \approx 1.25$ s $t \approx 1.75$ s $t \approx 2$ s

Figure 1.4 – Footage of the blast at the port of Beirut (Lebanon) on August 4 2020. Image downloaded from Newsflare.

When the leading edge of a blast wave strikes a target, whose surface forms a certain angle of incidence with respect to the direction of the shock, it is reflected and a high pressure is exerted on the surface. This pressure is called the *reflected pressure*, P_r. As

Figure 1.5 – A masonry building completely destroyed by the blast in Beirut (Lebanon). Photo credit: Mohamed Azakir, Reuters.

the shock diffracts [4] around the obstacle, a rarefaction wave [5] is produced at the edge of the structure and moves in to relieve the reflected pressure.
The reflected overpressure acting on a surface can be far greater than the incident overpressure, depending on the angle of incidence. The same holds for the reflected impulse, denoted as i_{ro}, with respect to the incident impulse, i_s Eq. (1.1). The angle of incidence denotes the angle formed between the normal of the impinged surface and the direction of the shock wave. From experimental evidence (Karlos and Solomos, 2013), the ratio of the reflected pressure over the incident one varies between 1 (for an angle equal to 90°) and approximately 12 (for a perpendicular shock, i.e., an angle equal to 0°), depending on the scaled distance Z, see Figure 1.6.

More general, the pressure loads acting a structure due to an explosion mainly depend on the stand-off distance, R, the explosive quantity, W, and the geometry of the structure. For obstacle and structures with non-standard geometry, shock waves can be reflected multiple times and give rise to complex fluid-structure interaction phenomena, such as focalization. These phenomena can be significant, especially in internal explosions (Masi et al., 2018b).

Beside the effects of overpressure, explosions can produce thermal loading, energized projectiles (e.g. fragments, debris), ground shocks, and cratering. Projectiles, ground shocks, and cratering may be the source of additional damage to structures and human injury. These secondary effects will not be discussed further in this Chapter (for more, we refer to USACE, 2008). Thermal effects can be significant in explosions where a fireball—that is, a volume of radiating hot gas—occurs (see Fig. 1.4). Thermal effects primarily consists of radiant heat transfer from the fireball and convective heating of structures in the proximity of the explosion. In a non-nuclear explosions, involving e.g.

4. The term diffraction represents various phenomena occurring when a wave encounters an obstacle and bends around the corners of the obstacle.

5. A rarefaction wave, like a shock wave, separates moving and stationary material/medium, but it causes the expansion of the material to a lower density, see (Davis, 1998).

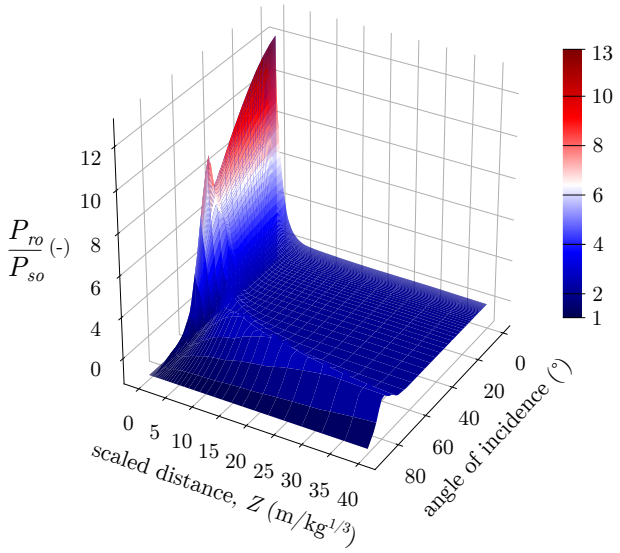

Figure 1.6 – Ratio of the reflected pressure peak, P_{ro}, over the incident pressure peak, P_{so}, as function of the incidence angle and the stand-off distance.

TNT, RDX, C4 or ammonium-nitrate-fuel-oil (ANFO) (Sochet, 2010), the convective and radiant heating effects are not as important as the air blast (mechanical loading), see Pape et al. (2010).
In the following, we shall assume that the thermal effects are negligible, so that a pure mechanical treatment of the loading conditions is appropriate.

1.2 Blast waves and Rankine-Hugoniot relations

Rankine (1870) and Hugoniot (1887, 1889) independently developed a set of equations which describe the relationships between the physical properties in two possible states of a moving compressible gas where mass, momentum and energy are conserved. The two states are divided by a contact surface, i.e., a shock front. In their original form, these equations describe the relationships of a supersonic gas passing into a subsonic state, through a stationary shock. For blast wave applications, the equations are transformed to describe the physical properties of the gas behind a shock moving into a stationary ambient atmosphere. The gas is considered as an ideal gas with total pressure given by

$$P = (\gamma - 1)\,\rho \mathsf{e}, \tag{1.4}$$

where γ is the ratio of the specific heat at constant pressure to the specific heat at constant volume, ρ the density, and e the specific internal energy.
The Rankine-Hugoniot (RH) relationships are often used for calibrating gauges and pressure transducers in blast wave measurements. Indeed, if appropriate values of the ratio of the specific heats γ are used, the thermodynamic framework on which such equations rely allows high degree of validity in real cases (see Dewey, 2016; Needham, 2018).

Consider a shock moving at velocity U through an ambient atmosphere at rest. Figure 1.7 shows the two states are that of the ambient gas (state 0) and that immediately behind the shock (state SO). Contrarily to the steady shock assumed in the RH equations, in reality the quantity of state SO (such as the pressure, the density and the fluid velocity) rapidly decay in both time and traveled distance. However, RH equations are a very powerful tool which allows to compute all the parameters of a blast wave from knowing the ambient conditions ahead the shock front and one of the parameters immediately behind it.

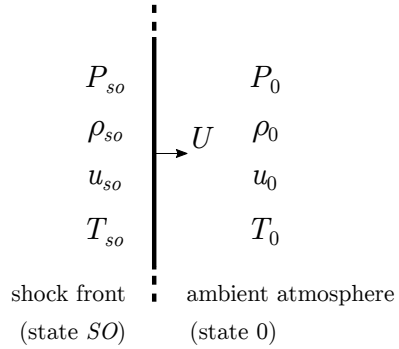

Figure 1.7 – Configuration of a shock moving with speed U into a stationary gas in state 0. The gas behind the shock is in state SO. P, ρ, T and u are the incident (over)pressure, density, temperature, and particle speed, respectively.

We denote the incident overpressure P_{so} as the main descriptor of the shock front. We recall that the overpressure is defined as the pressure at the shock front minus the ambient pressure, P_0. From this, we can derive several other parameters (Needham, 2018):

– The *density* at the shock front, ρ_{so}, which is function of the ratio of the specific heats, γ, the ambient pressure, P_0, and the ambient density, ρ_0

$$\frac{\rho_{so}}{\rho_0} = \frac{2\gamma + (\gamma+1)\,\frac{P_{so}}{P_0}}{2\gamma + (\gamma-1)\,\frac{P_{so}}{P_0}}. \tag{1.5}$$

For air at pressure below 2 MPa, a value of γ of 1.4 can be used with about 99% accuracy (Needham, 2018). The above relationship thus becomes

$$\left.\frac{\rho_{so}}{\rho_0}\right|_{\gamma=1.4} = \frac{7 + 6\frac{P_{so}}{P_0}}{7 + \frac{P_{so}}{P_0}}. \tag{1.6}$$

– The *shock velocity* magnitude, which can be expressed as

$$U = a_0\sqrt{1 + \frac{(\gamma+1)P_{so}}{2\gamma P_0}}, \tag{1.7}$$

where a_0 is the ambient sound speed, which can be calculated as $a_0 = \sqrt{\gamma\left(\frac{P_0+P_{so}}{\rho_s}\right)}$. For $\gamma = 1.4$,

$$U\big|_{\gamma=1.4} = a_0\sqrt{1+\frac{6P_{so}}{7P_0}}. \tag{1.8}$$

– The *fluid velocity magnitude* at the shock front, which is function of a_0, P_0, and P_{so},

$$u_{so} = \frac{P_{so}}{\gamma P_0}\frac{a_0}{\sqrt{1+\frac{(\gamma+1)P_{so}}{2\gamma P_0}}}. \tag{1.9}$$

For $\gamma = 1.4$, it simplifies to

$$u_{so}\big|_{\gamma=1.4} = \frac{5P_{so}}{7P_0}\frac{a_0}{\sqrt{1+\frac{6P_{so}}{7P_0}}}. \tag{1.10}$$

– The *temperature of the gas* at shock front, which is

$$\frac{T_{so}}{T_0} = \left(1+\frac{P_{so}}{P_0}\right)\left(\frac{2\gamma+(\gamma-1)\frac{P_{so}}{P_0}}{2\gamma+(\gamma+1)\frac{P_{so}}{P_0}}\right), \tag{1.11}$$

which, for $\gamma = 1.4$, becomes

$$\left.\frac{T_{so}}{T_0}\right|_{\gamma=1.4} = \left(1+\frac{P_{so}}{P_0}\right)\left(\frac{7+\frac{P_{so}}{P_0}}{7+6\frac{P_{so}}{P_0}}\right). \tag{1.12}$$

– The *magnitude of the dynamic pressure* at the shock front, which is

$$q_{so} = \frac{1}{2}\rho_{so}u_{so}^2 = \frac{P_{so}^2}{2\gamma P_0+(\gamma-1)P_{so}}, \tag{1.13}$$

and for $\gamma = 1.4$

$$q_{so}\big|_{\gamma=1.4} = \frac{5}{2}\frac{P_{so}^2}{7P_0+P_{so}}. \tag{1.14}$$

– The *reflected overpressure* at the shock front, when a shock wave strikes a solid surface and the velocity vector is perpendicular to that surface, which is

$$P_{ro} = 2P_{so}+(\gamma+1)q_{so}. \tag{1.15}$$

We can clearly see from Eq. (1.15) that the reflected overpressure involves both the incident and the dynamic (over-)pressures, see Figure 1.8. The increase in intensity of the overpressure due to the striking of the shock wave on a rigid surface is equal to two times the incident overpressure, at least, and it may even be greater, depending on the value of γ and q_{so}. For $\gamma = 1.4$, P_{ro} is

$$P_{ro} = 2P_{so}\frac{7+4\frac{P_{so}}{P_0}}{7+\frac{P_{so}}{P_0}}. \tag{1.16}$$

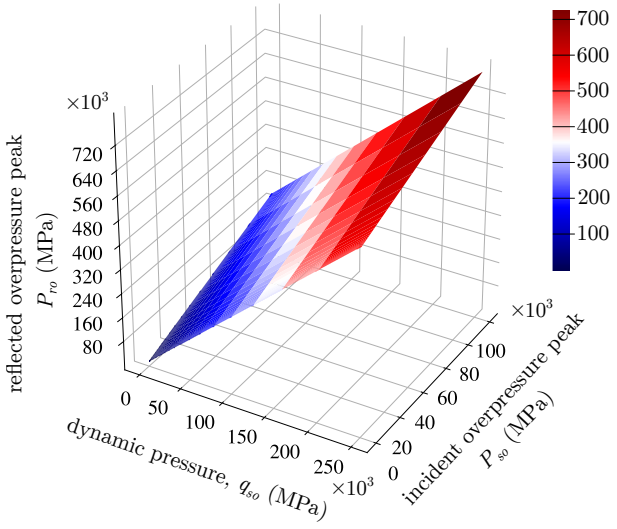

Figure 1.8 – Reflected overpressure peak, P_{ro}, at varying of the incident overpressure peak, P_{so}, and the dynamic pressure, q_{so}, according to Eq. (1.15).

1.3 Detonation waves

During the detonation of an explosive material, detonation waves, similarly to blast waves develop. Detonations can be distinguished in two types, ideal and non-ideal ones. Ideal detonation theories are useful tools in understanding the phenomenology of the detonation process, in a simplified manner.
An ideal detonation refers to a one-dimensional problem of propagation of a detonation wave, which consists of a shock wave, a reaction zone, and a rarefaction wave. The wave moves through a material (the explosive) in which all of the energy is released immediately behind the front and where no further chemical reactions take place (Needham, 2018). Moreover any transport effect, such as heat conduction, radiation, diffusion and viscosity, is neglected.

Among ideal detonation models, Chapman (1899)-Jouguet (1905) conditions are a restatement of the RH relations with the addition of energy at the shock front. In this frame, the propagation velocity of the detonation front is set equal to the sum of the sound speed and the material speed of the gas immediately behind the detonation front. For more, we refer to Needham (2018). From the conservation of mass, momentum and energy, similar expressions to those reported in Section 1.2 can be obtained. Nevertheless, the detonation productions cannot be simply described as ideal gases (as for air in RH relationships). Several equations of state exist (see e.g. Needham, 2018), to account for the evolution of the properties of detonation products at varying conditions. This is the case, for instance, of the Jones-Wilkins-Lee equation of state (Jones and Miller, 1948; Wilkins et al., 1965; Lee et al., 1968). The equation has the form:

$$P = (\gamma - 1)\,\rho \mathsf{e}_0 + A\left(1 - \frac{\omega\ \rho}{R_1\rho_0}\right)\exp\left(-R_1\frac{\rho_0}{\rho}\right) + B\left(1 - \frac{\omega\ \rho}{R_2\rho_0}\right)\exp\left(-R_2\frac{\rho_0}{\rho}\right), \quad (1.17)$$

where A, B, R_1, R_2, and ω are parameters depending upon the explosive, along with

ρ_0, the initial density of the explosive; ρ is the density of the detonation products and e_0 the internal energy density released by the detonation of the explosive. All values (A, B, R_1, R_2, ω,
rho_0, e_0) are selected to fit experimental results on a cylinder expansion test. Three different contributions determine the pressure state of the detonation productions: (1) the first exponential term accounts for high-pressure regime and high density of the detonation products; (2) the second represents the intermediate pressure range; (3) the last term is the constitutive equation of an ideal gas and defines the behavior at low pressure or large expansion.

1.4 Air-blast parameters

Air-blast parameters, such as the reflected peak overpressure, P_{ro}, and impulse, i_{ro}, shock-front arrival times, t_A, are typically estimated using the compilation of experiments documented in Kingery and Bulmash (1984). The blast parameters concern free-air bursts and hemispherical surface bursts of TNT (USACE, 1990). Kingery and Bulmash (1984) collected and compiled the data from several references on experimental data, see Figure 1.9. The authors proposed best-fit expressions of the blast parameters, known as Kingery-Bulmash (KB) interpolations, as function of the scaled distance Z. The KB curves provide an accurate representation of the blast load parameters in the frame of moderate to far field scenarios, i.e., for scaled distances $Z \geq 0.4$ m/kg$^{1/3}$ (see Browning et al., 2013; Karlos and Solomos, 2013; Shin et al., 2015). In the near field, $Z < 0.1$ m/kg$^{1/3}$, KB interpolations are found to significantly underestimate peak overpressure and impulse values. Notice, that in the following cases and for all investigations in this Thesis (cf. Chapters 3-7), we always consider explosion scenarios involving moderate to far field blasts. Figure 1.10 shows the KB data for hemispherical surface burst, according to Karlos and Solomos (2013).

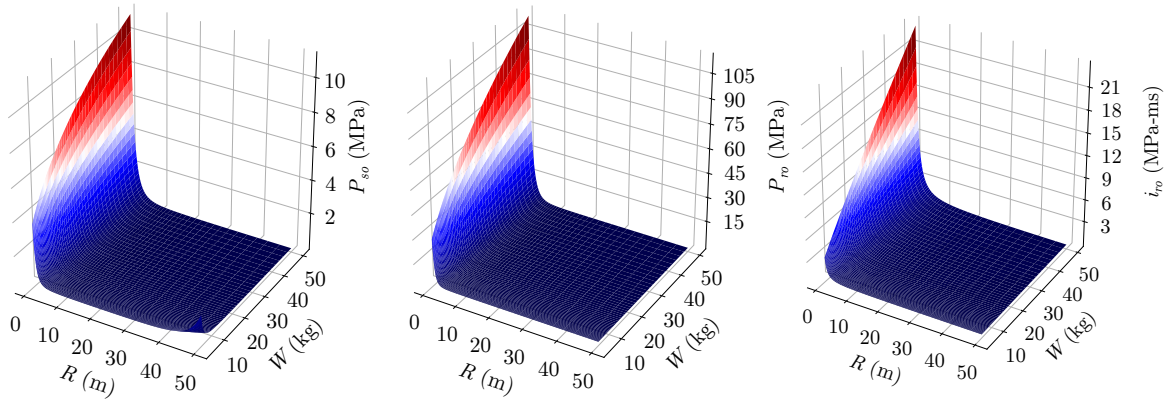

(a) incident overpressure peak. (b) reflected overpressure peak. (c) reflected impulse peak.

Figure 1.9 – Incident overpressure peak (a), reflected overpressure peak (b), and reflected impulse peak (c) for the positive phase of a hemispherical blast, according to Kingery and Bulmash (1984) and Karlos and Solomos (2013).

Beside KB interpolations, other best-fits exist in the literature, e.g. (Swisdak Jr,

1994). In a previous study, we derive new, (more) precise best-fitting expressions for both the positive and negative phase parameters (Vannucci et al., 2017a; Masi et al., 2019a), which are reported in detail in Appendix A.

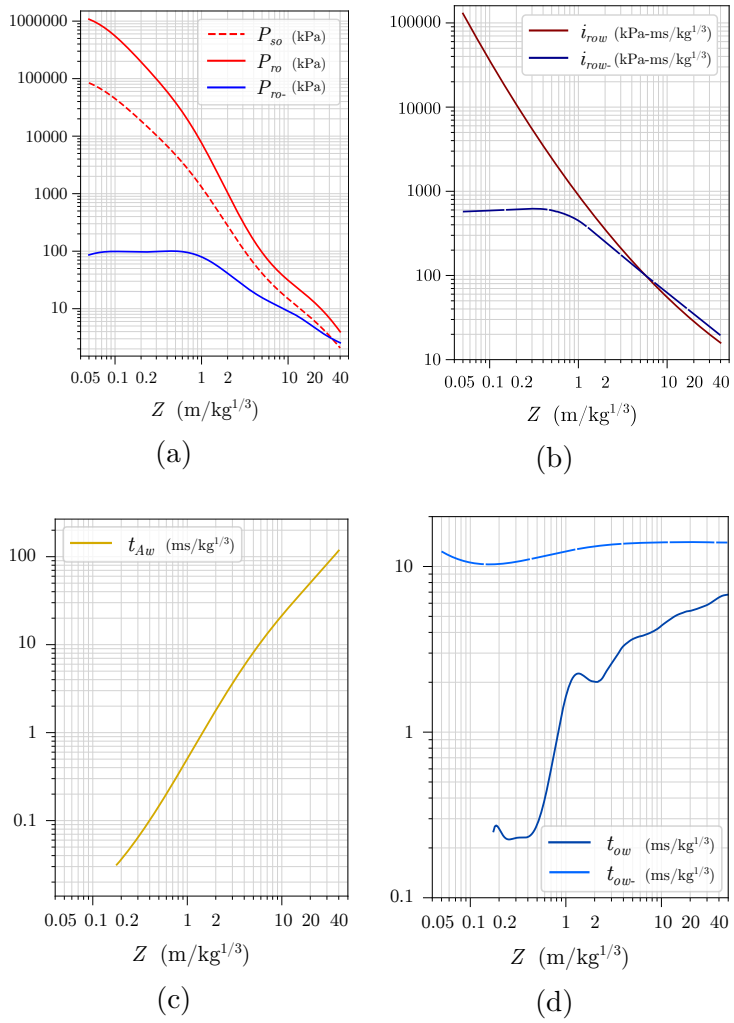

Figure 1.10 – Blast parameters for a hemispherical blast, according to Kingery and Bulmash (1984) and Karlos and Solomos (2013): (a) incident and reflected overpressure peak, (b) scaled reflected impulse, $i_{row} = i_{ro}/W^{1/3}$ and $i_{row-} = i_{ro-}/W^{1/3}$, (c) scaled arrival time, $t_{Aw} = t_A/W^{1/3}$, and (d) positive and negative phase duration, $t_{ow} = t_o/W^{1/3}$ and $t_{ow-} = t_{o-}/W^{1/3}$.

1.5 Modeling blast loads

The simulation of a blast can be performed by using different approaches (Remennikov, 2003; Dewey, 2016), i.e., empirical or physics-based ones. These models are presented below.

1.5.1 Empirical models

Empirical models rely on best-fit interpolations of experimental results. Frequently they are based on the Kingery and Bulmash (1984) interpolations, which allow to determine the blast parameters and pressure loading from the knowledge of the TNT equivalent explosive weight, W, and the Hopkinson-Cranz scaled distance, $Z = R/\sqrt[3]{W}$. Based on these parameters, we can determine all the necessary quantities characterizing the blast waves. More specifically, we can estimate the arrival time of the shock wave, t_A, the overpressure peak, P_{ro}, the positive phase duration, t_o, negative phase duration, t_{o-}, the underpressure peak (i.e., negative overpressure), P_{ro-}, and the reflected positive and negative impulses, i_{ro} and i_{ro-}.
The time history is then expressed mathematically using appropriate models for both the positive phase and the negative phase or simplified linear approximations.

1.5.1.1 Positive phase

The time evolution of the positive phase of the reflected pressure is modeled with the well established *modified Friedlander equation* (Friedlander, 1946),

$$P_{r+}(t) = P_{ro}\left(1 - \frac{t - t_A}{t_o}\right)\exp\left(-d\frac{t - t_A}{t_o}\right), \qquad \text{for } t_A < t < t_A + t_o \tag{1.18}$$

where d is the exponential decay coefficient. The impulse i_{ro} associated to the positive phase reads

$$i_{ro} = \int_{t_A}^{t_o} P_{r+}\, dt = \left[e^{-d} + d - 1\right]\frac{P_{ro}\, t_o}{d^2}, \tag{1.19}$$

The above equation allows to determine the exponential decay coefficient, d, by equating it with the best-fit interpolation of i_{ro} from experiments (see Appendix A).

1.5.1.2 Negative phase

The negative phase is here modeled with the so-called cubic approximation (Granström, 1956), namely

$$P_{r-}(t) = P_{ro-}\left(\frac{27}{4}\frac{t - t_o}{t_{o-}}\right)\left(1 - \frac{t - t_o}{t_{o-}}\right)^2, \qquad \text{for } t_A + t_o < t < t_A + t_o + t_{o-} \tag{1.20}$$

Accordingly, the negative reflected impulse i_{r-} can be evaluated as

$$i_{r-} = \int_{t_o}^{t_o + t_{o-}} P_{r-}\, dt = \frac{9P_{ro-}}{16}t_{o-}, \tag{1.21}$$

which is computed from the best-fit interpolations of t_{o-} and P_{ro-} (see again Appendix A).

It is worth noting that Friedlander equation captures very well the positive phase of the reflected pressure as compared to extensive experimental data (Needham, 2018). However, for the negative phase of the reflected pressure there is not a universal, established best-fit expression. This is mostly due by the lack of sufficient experimental data (Bogosian et al., 2002), from which the extraction of the negative phase blast parameters (such as the underpressure peak and impulse) is not trivial. Here we follow the work of Granström (1956) and we use the cubic approximation, which gives a reasonable agreement with experimental evidence. For a complete review of empirical modeling of the negative phase, we refer to the work of Rigby et al. (2014).

1.5.1.3 Simplified linear approximation

A simplified modeling approach of the blast loading consists in using a piece-wise linear function, as is the approach of Krauthammer and Altenberg (2000). The positive phase is approximated as a linearly decaying triangular pulse, with the linear load duration, $\hat{t}_o$, set such that the impulse given by the triangular load matches that given by the empirical method, and namely

$$\hat{t}_o = 2\frac{i_{ro}}{P_{ro}}. \tag{1.22}$$

The linear approximation of the negative phase begins at t_o, rather than $\hat{t}_o$, giving a period of zero pressure between the linear positive and negative phases. This approach is also recommended in USACE (2008), with the following piece-wise expression

$$\hat{P}_r(t) = \begin{cases} P_{ro}\left(1 - \dfrac{t}{t_o}\right) & \text{for } t \leq \bar{t}_o, \\ 0 & \text{for } \bar{t}_o \leq t \leq t_o, \\ -P_{ro-}\left(\dfrac{t - t_o}{0.25\ \hat{t}_{o-}}\right) & \text{for } t_o \leq t \leq t_l, \\ -P_{ro-}\left(1 - \dfrac{t - t_l}{0.75\ \hat{t}_{o-}}\right) & \text{for } t_l \leq t \leq t_o + \hat{t}_{o-}, \end{cases} \tag{1.23}$$

with $t_l = t_o + 0.25\ \hat{t}_{o-}$. In Chapter 7, we use such a simplified linear approximation to model blast loads in the frame of scaling laws.

Figure 1.11 displays the comparison of the time-history of the linear approximation with the Friedlander and cubic phase models, for a scaled distance $Z = 4$ m/kg$^{1/3}$.

1.5.1.4 Numerical computation

Relying on the above models, different numerical procedures exist to compute the blast loads on structures. One of the most often adopted method is based on the work of Hyde (1991)−that is the ConWep approach. This approach is implemented in several commercial Finite Element codes, such as ABAQUS (ABAQUS, 2018). ConWep model is able to accurately predict the blast loads for simple geometries, but it neglects multiple phenomena, such as the Mach stem (Vannucci et al., 2017a) and the diffraction of shock waves (stemming from the finite-size of the target), also known as clearing effects (Rigby,

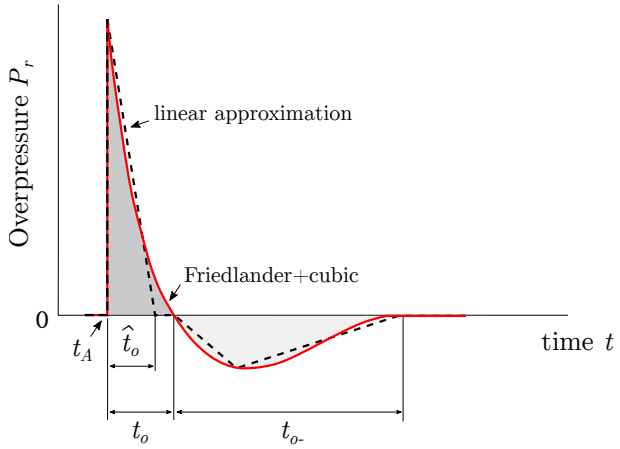

Figure 1.11 – Friedlander and cubic negative phase compared with the first-order approximation of the time evolution of the overpressure due to an explosion acting on a target, for a scaled distance $Z = 4$ m/kg$^{1/3}$.

2014).
In a previous study, we proposed a more detailed numerical approach (Vannucci et al., 2017a) to account for Mach stem and incidence angle effects, see Figure 1.6.

In both cases (ConWep or the approach in Vannucci et al. (2017a)), blast load calculations through empirical models are here computed through an external library written in C++ language (Masi et al., 2020a). This allows the integration of the library in several existing codes. The calculations account for the effects of surface rotation of targets, change of the incident angle, variation of the relative distance between explosive and target, and the deformability of the latter. At each time step, the history of the blast overpressure $P_r(t)$ is thus computed according to the detonation time and point, the actual position and the angle of incidence of the elements used to discretized the target.

1.5.2 Physics-based models

Physics-based, numerical approaches allow a rather detailed description of the main features of the blast phenomenon with, of course, an increased calculation cost. They are based on the definition of two domains: the explosive charge and the surrounding air. Through fluid dynamic numerical simulations, detonation, propagation of shock waves and their interaction with deformable structures can be efficiently modeled with either a Coupled Eulerian-Langrangian (CEL) scheme or an Arbitrary Lagragian Eulerian (ALE) approach (ABAQUS, 2018; Masi et al., 2018a). CEL analyses allow Eulerian and Lagrangian bodies within the same model to interact and are typically used to model the interactions between a solid body (Lagrangian representation) and a fluid material (Eulerian). ALE adaptive meshing techniques combine features of Lagrangian and Eulerian analysis within the same part mesh.
In both cases, a multi-material definition is used (Benson, 1992). The Eulerian body is split into multiple materials−the explosive source, the propagating medium, air, and void

(volume occupied by the Lagrangian body). As material flows through the Eulerian mesh, they are tracked through the definition of the volume fraction, i.e., the percentage of the element volume occupied by a certain material, see Figure 1.12. The interaction between Eulerian and Lagrangian (structures) bodies is defined through a contact interaction based on a penalty algorithm (Benson and Okazawa, 2004).

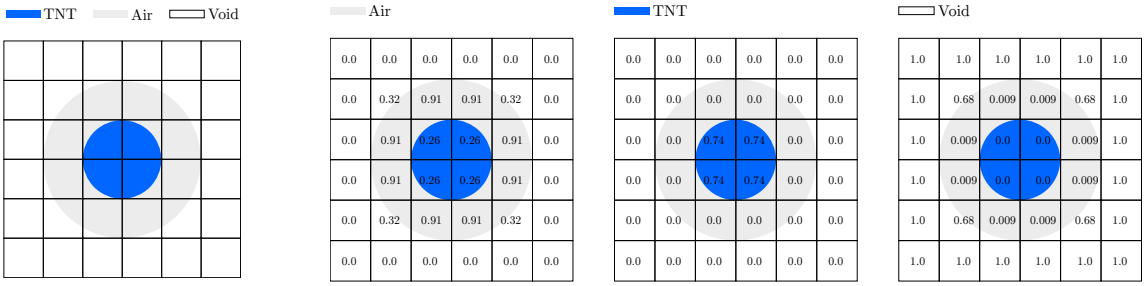

(a) Eulerian part, consists of TNT, air, and void materials.

(b) volume fraction of air material.

(c) volume fraction of TNT material.

(d) volume fraction of void material.

Figure 1.12 – Eulerian body representation in CEL analyses, using a multi-material formulation.

Air is commonly considered as an ideal gas (cf. Section 1.2). Explosive is usually modeled with the empirical JWL equation of state (Jones, Wilkins, and Lee Jones and Miller, 1948; Wilkins et al., 1965; Lee et al., 1968).
An alternative, simplified model for generating the blast wave is the so-called *balloon analogue* (Brode, 1955). This approach replaces the solid explosive charge with an energetically equivalent sphere of compressed air, resulting in reduced calculation cost compared to the JWL. Moreover, this approach has been proved to be in good agreement with experimental tests and numerical analyses (Larcher and Casadei, 2010; Blanc et al., 2018; Legrand et al., 2020).

In physics-based methods, both the charge and the fluid domain, through which blast waves propagate, need to be finely discretized. Consequently, the computational cost is very high and many times prohibitive. Nevertheless, such models can account for reflection, diffraction and interaction of multiple shock waves. Depending upon the geometry of the structure, the concentration of the reflected waves can create local effects that can be greater than the original shock wave, see Figure 1.13. This is the case of non-standard geometry that are usually met in historical buildings and monuments (e.g. the Pantheon Masi et al., 2018b). In the following, we give an example.

1.6 Explosions inside a structure of non-standard geometry. A case-study

The problem of evaluating the effects of an explosion inside a monumental-like structure is here addressed through a simplified case-study. In particular, we aim at comparing the loading estimation of empirical models (surface blasts) with those obtained performing simulations with a detailed numerical, physics-based model, based on the balloon analogue (see paragraph 1.5.2). In a previous study (Vannucci et al., 2017a), we showed that

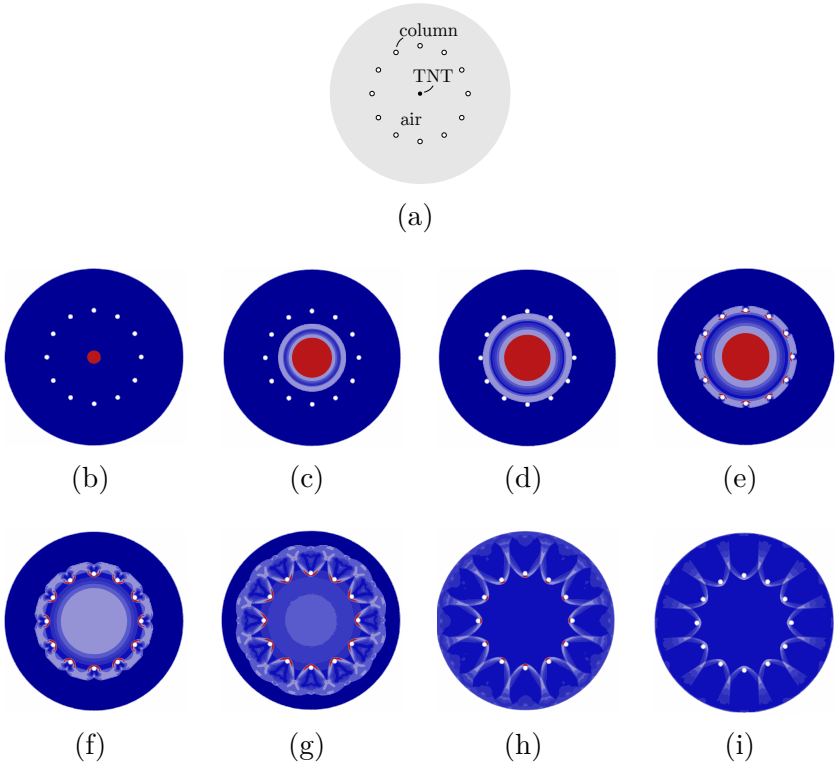

Figure 1.13 – Example of CEL (two-dimensional) analysis. The simplified model consists of an explosive source, at the center of a circular colonnade (solid structure, Lagragian), (a). Figures (b)-(i) represent the evolution of the pressure field (red means high pressure, while blue represents the atmospheric value). ABAQUS commercial software (ABAQUS, 2018) is used to perform the numerical simulation.

except for certain localized regions, empirical models give safe estimations of the blast loads arising from an internal explosion in a vaulted hall.
Herein a more detailed geometrical model is considered, as shown in Figure 1.14. We opt for a representative monumental geometry, whose resemblance to real buildings is purely coincidental. We use a scaled model of the structure, with height and width equal to ≈ 1 m and ≈ 1.4 m, respectively. We model the surface burst of 4 g of TNT equivalent explosive weight. The numerical simulations are two-dimensional [6]. Due to the high computational cost, only half of the model is considered (symmetric boundary conditions are applied along the axis of symmetry). Upon mesh converge analyses, the selected mesh discretization involves elements with characteristic size equal to 1.5 mm. The structure is assumed to behave as an infinitely rigid body.
The simulation is performed using a 24-cores workstation. The analysis took around 240 hours (≈ 10 days).

Figure 1.15 displays the evolution of the pressure field inside the structure at different

6. Detailed three-dimensional results for a real structure have been performed in previous works (Vannucci et al., 2017b; Masi et al., 2018b).

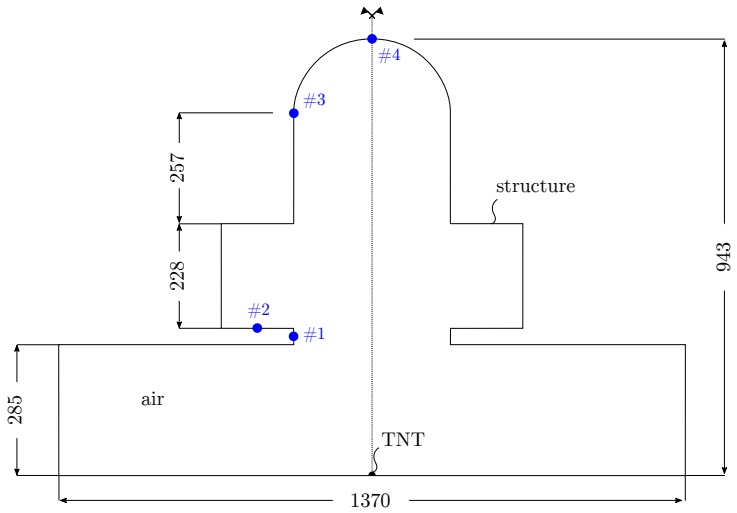

Figure 1.14 – Geometric model representative of a monumental structure, in reduced scale, subjected to the explosion of 4 g of TNT equivalent explosive weight. Dimensions are in millimeters. Four gauge points are used to monitor the evolution of the pressure.

time points. Focalization phenomena, in the proximity of the vault, are clearly visible. We compare in Figure 1.16 the numerically measured pressure loading with the empirical estimations obtained with ConWep, at various points of the structures (cf. Fig. 1.14). We observe that overall the empirical model is found to overestimate the numerical results, at least as far it concerns the positive phase. This allows for safe estimates, when using simplified, empirical models (as also discussed in Rigby, 2014). In particular, at the gauge point #1, where important clearing effects take place, the numerical simulation predicts an ovepressure peak that is 54% the value computed with the empirical model. For point #4, at the vault's key, the numerical simulations give an overpressure peak 4 times higher than the empirical value. Focalization of blast waves, within this region, is not a surprising result. The phenomenon is very similar to what observed by Rayleigh. (1910, 1914) for acoustic waves in the study of the whispering galleries. The vault, with its shape, behaves like a concave, i.e., converging, mirror for the shock waves, which has the tendency to collect the blast pressure. For a comprehensive discussion of the results, we refer to our previous work Vannucci et al. (2017a) and Masi et al. (2018b). The above results suggest that, when dealing with non-standard geometry structures, particular attention has to be paid. Safety factors for the prediction of the empirical blast calculations should be used when important focalization phenomena are expected. This is the case, for instance, in the work presented in Chapter 5.
Regarding the negative phase, it is worth noticing that ConWep predictions of the negative phase at points #1-4 are unsatisfactory. This is primarily due to the multiple diffraction phenomena that take place at the edges of the structure. Locally, the shock wave is reflected into an expansion wave, which is responsible of an amplified negative phase, with respect to the empirical model. Nevertheless, we shall mention that the negative phase may have significant effects on the structural response only in the case of light

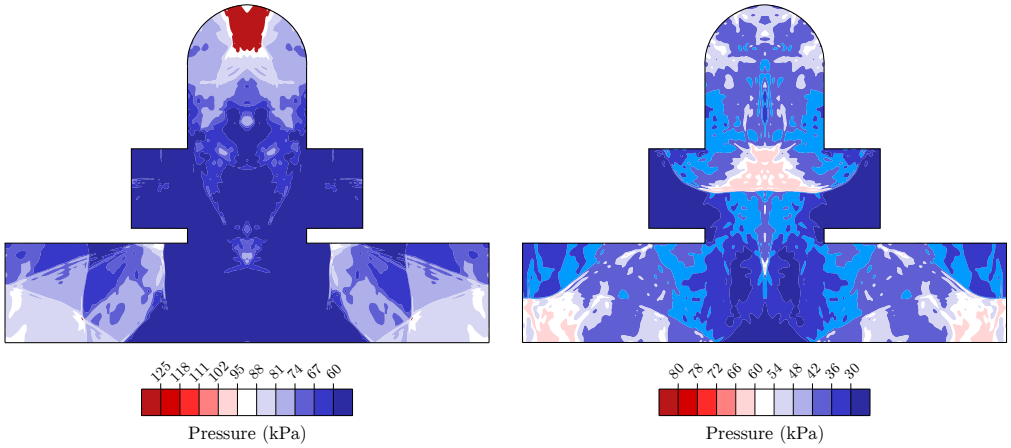

(a) 5 ms after denotation. (b) 10 ms after detonation.

Figure 1.15 – Evolution of the overpressure field inside the structure at two different time points.

targets, such as glass panels (Krauthammer and Altenberg, 2000; Rigby et al., 2014). The structures investigated in this work and in the following Chapters are, instead, heavy and characterized by large masses. This is why the difference of the negative phase between the empirical model and the numerical calculations can be neglected.

The above analyses and our work in Vannucci et al. (2017a) suggest that, for simulations of the response of non-standard geometry structures to explosions, empirical models give overall safe estimations of the blast actions, at least for the case of surface blasts. Therefore, when analyzing the response of typical load-carrying structural elements, such as walls, vaults, arches, etc., empirical models usually allow to have safe estimates of the loading. Nevertheless, when focalizing phenomena, as in the case of vaulted halls, empirical estimations can be far away from the (numerical, detailed) reality. Hence, appropriate corrections need to be considered. This is important for applications focusing on the assessment of the strength of existing buildings, the design of reinforcements or of new structures.

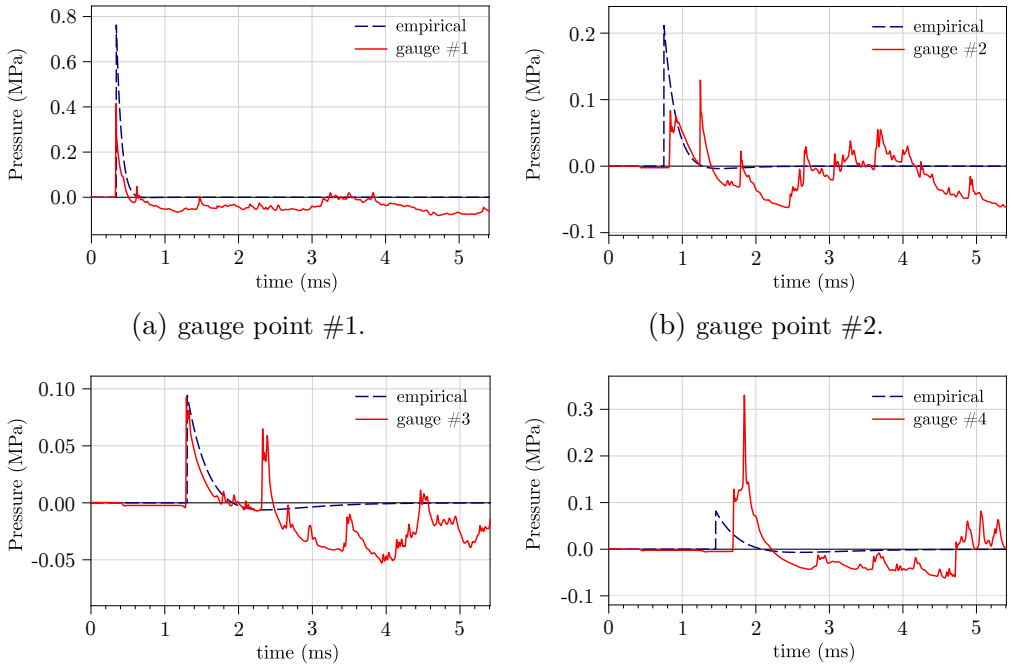

(a) gauge point #1.

(b) gauge point #2.

(c) gauge point #3.

(d) gauge point #4.

Figure 1.16 – Evolution of the overpressure loading at various gauge points (in Figure 1.14).

Chapter 2

Response of masonry structures to blast loading and modeling strategies

Abstract. *Masonry is a heterogeneous material, whose mechanical behavior is governed by the mechanical behavior of its constituents (units and joints), and displays softening behavior (progressive loss of stiffness, once the onset of failure has been reached). We give a brief introduction of the mechanical behavior of the masonry material, through review of existing experimental works. The response at both low- and high strain-rates is discussed. The enhancement of the material properties of masonry, under dynamic loading, still remains an open subject. Nevertheless, the increase of the material strength due to high strain-rates is limited and approximately equal to 2. Neglecting these dynamic effects and any viscoelastic effect allows to have safe estimates of the material strength, which is desirable especially in safety and design criteria and investigations.*
Attention is then focused on the in-plane and out-of plane response of masonry structures and the failure modes due to blast loading. The recent research activity on the response to explosions of standard, regular structures (such as wall) opposes to the very limited investigations on non-standard structures (i.e., arches, vaults, etc.).
Finally, a review of the different modeling techniques of masonry structures is detailed. This comprehends micro-, meso-, and macroscopic modeling strategies, either based on Finite Element Method or Discrete Element Method. The advantages of multiscale approaches and their possible enhancement through Machine Learning methods are addressed.

Contents

2.1 Introduction

Masonry is a heterogeneous material composed of assembled blocks, interacting through interfaces (joints), where mortar might be present or not (dry joints). Masonry shows a large variety in geometry and arrangement of units and characteristics of the components, see Fig. 2.1. Units can be bricks, ashlars, adobes, stones, and others. Mortar can be clay, chalk, lime/cement based mortar, or other. In dry masonry joints, mortar is not used and the resistance to mechanical loads is assured through interlocking and friction. Whilst the large variety of masonry assemblages, the overall mechanical behavior of masonry shows several recurrent features. We briefly present an overview of the salient characteristics of the mechanical behavior of masonry. In particular, the key quasi-static and fast-dynamic characteristics of the material are presented and discussed. We denote here with quasi-static material behavior the material response under static or quasi-static loading (such as gravitational acceleration), for which the material strain-rates assume values smaller than $\approx 1\ s^{-1}$. Fast-dynamic excitations refer instead to dynamic loads, such as earthquakes, explosions, and impacts, originating strain-rates much higher than in the quasi-static case.
We further present the failure modes of masonry material and structures. In the frame of preserving existing masonry structures and designing new ones, we define herein structural failure as the limit state where the structure loses its load carrying capacity. Structural failure is caused by combinations of failure modes of the material(s) comprising a structure. In the frame of masonry, we denote material failure as the limit state where the masonry material is no longer able to withstand/resist against external forces. Material failure of masonry is caused by fracture and/or excessive plastic deformations of its constituents and/or the bond between them (Davis and Selvadurai, 2005; Gdoutos, 2020).

2.2 Mechanical behavior at low strain-rates

The mechanical behavior of masonry is substantially governed by the mechanical behavior of its constituents (units and joints), their interaction/bond, and their arrangement in space. Experimental campaigns provide extensive information (Page, 1981, 1983; Dhanasekar et al., 1985; Hoffinann and Schubert, 1994; Rots, 1997; Schubert, 1988; Van der Pluijm, 1999; Lawrence et al., 2008). From a phenomenological point of view, masonry can be regarded as a composite material with an overall anisotropic behavior, i.e., its mechanical properties (such as the stiffness or the strength) depend on the direction along which they are measured (Vannucci, 2018).

The different elastic mechanical properties of the constituents, as well as their spatial arrangement, govern the elastic response of the material.
Like most of geomaterials, masonry constituents have higher values of strength in the compressive behavior, rather than in the tensile one. For instance, Schubert (1988) reported ratios between the tensile and compressive strength ranging from 0.03 to 0.10, for clay, calcium-silicate, and concrete units. The inelastic response is mainly dictated by the masonry joints, which are usually characterized by smaller values of the mechanical strength with respect to the units. Joints typically act as weak planes, and the structural

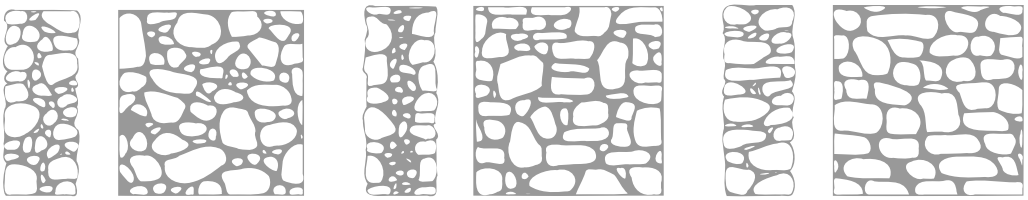

(a) irregular stone masonry, with erratic and irregular stone units.

(b) uncut stone masonry.

(c) cut stone masonry.

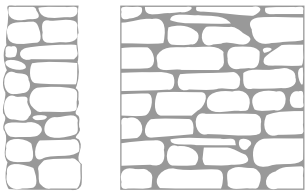

(d) soft stone regular masonry.

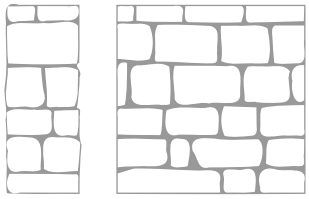

(e) regular squared block masonry with mortar joints.

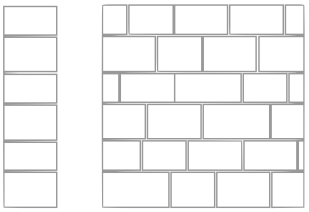

(f) regular dry-joint ashlar masonry.

Figure 2.1 – Stone masonry typologies: sketches of typical patterns and cross-sections, according to (MIT, 2009).

response is strongly dependent on their orientation. Figure 2.2 displays the strength of solid clay units, under different bi-axial stress configurations, as obtained in Page (1981, 1983).
Van der Pluijm (1999) extensively investigated the mechanical behavior of units and joints in tension, and combined compression and shear. Usually, the bond between the mortar and the blocks is extremely weak, with a cohesive-frictional response in shear and a cohesive response in tension (null cohesion in case of dry stone masonry) (Hendry, 1998). Rots (1997) and Van der Pluijm (1997) showed that the tensile strength of a masonry joint is generally in the range of $0.2 \div 3.0$ MPa, with the strength largely depending on the class of mortar used. Van der Pluijm (1997) further reported that the bond area between mortar and bricks can be highly irregular due to shrinkage, see Figure 2.3. The net bond area is found to be just approximately 35% of the cross-sectional area, asymmetric and typically restricted to the central part of the specimen. The strength of masonry joints is hence affected by the net bond area (due to the highly non-uniform stress distribution), and it value can drop to 10% of the strength of the gross joint area (Burnett et al., 2007).

Under combined normal and shear stress, masonry shear strength increases with the confining compression stress, because of its frictional behavior, see Figure 2.4. The Coulomb friction angle, φ, typically ranges from 35° to 50° (Van der Pluijm, 1999; Stefanou et al., 2011a). Moreover, masonry joints usually display non-associative behavior. (Non-)associativeness of the sliding behavior (Davis and Selvadurai, 2005) is quantified through the dilatancy angle ψ, which measures the volume change of the mortar, upon

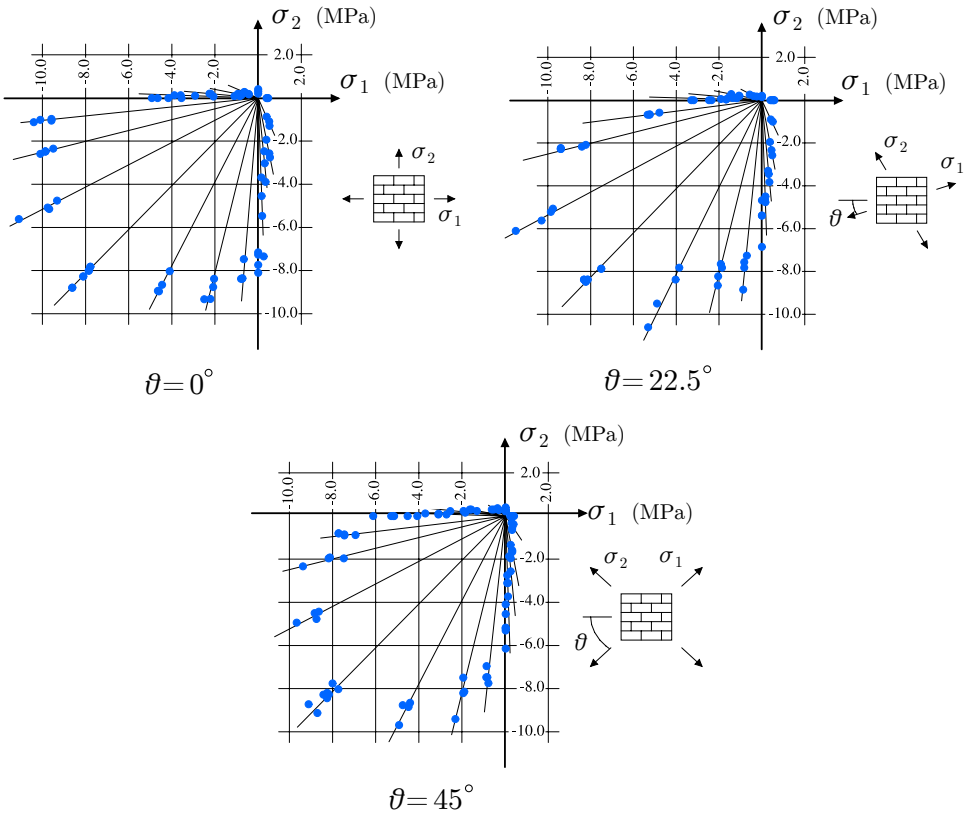

Figure 2.2 – Bi-axial strength of solid clay units masonry (Page, 1981, 1983).

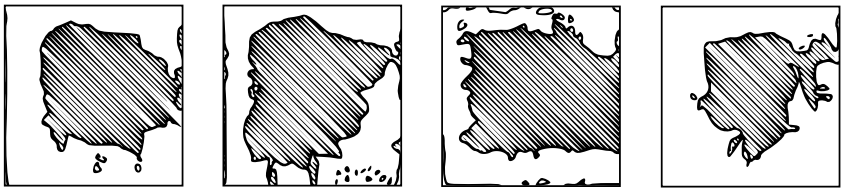

Figure 2.3 – Net bond surface of a masonry joint (Van der Pluijm, 1997).

shearing. Namely

$$\psi = \arctan \frac{\delta_n}{\delta_t}, \tag{2.1}$$

with δ_n and δ_t the inelastic normal and tangential displacements at the interface. An associative behavior indicates $\varphi = \psi$. Non-associativity is used to denote a dilatancy angle smaller than the friction angle. The dilatancy angle usually depends on the level of the confining stress and amount of slippage, but usually it takes very small values for masonry (Van der Pluijm, 1997; Lourenço and Ramos, 2004).

The inelastic response of the masonry constituents is characterized by plastic deformations and damage. In particular, one of the most relevant characteristic features is strain softening. Softening consists of a degradation of the mechanical stiffness, under a continuous

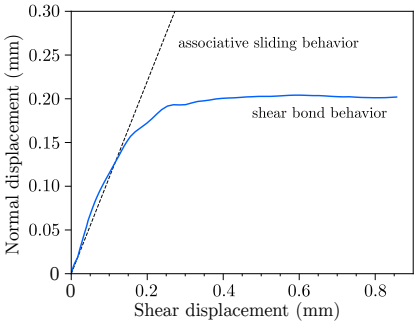

(a) sliding behavior of masonry interfaces.

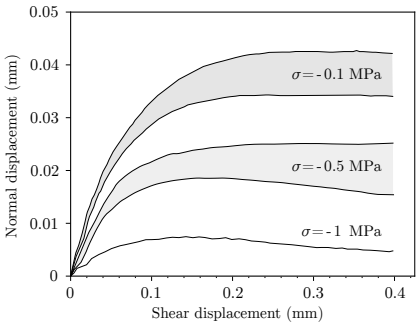

(b) influence of the confining stress.

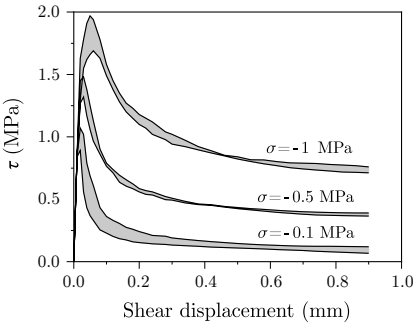

(c) stress-displacement diagram.

Figure 2.4 – Associative sliding behavior versus typical shear bond behavior of the joints (a) (Van der Pluijm, 1999), inelastic displacement normal to the joint upon inelastic shear of masonry (b) (Van der Pluijm, 1992), and stress-displacement diagram (c) for different normal stress levels (shaded areas indicate the envelope of multiple tests) (Van der Pluijm, 1999). Negative stress represents compression.

increase of deformation (see Figure 2.5). Such a characteristic persists also for high loading rates of the masonry (Ross et al., 1989; Ožbolt et al., 2014). Softening is a salient feature of geomaterials, such as brick, mortar, stone or concrete, which fail due to a process of progressive internal crack growth Hillerborg (1985); Van der Pluijm (1997); Lourenço (PhD Thesis, 1997). The softening behavior is influenced by the material heterogeneity, e.g. presence of different phases and material defects (such as flaws, voids, microcracks). As the material is loaded, existing microcracks grow and new ones form. At the onset of the peak load, crack growth and formation phenomena accelerate and macrocracks form. The macrocracks growth is unstable[1]. This results in softening and strain localization into narrow zones of increased deformation. Softening affects the inelastic tensile, shear, and compressive behaviors. Figure 2.5 shows a schematic representation of the stress-displacement diagrams of masonry in uni-axial tension (Fig. 2.5a), uni-axial compression (Fig. 2.5b) and pure shear (Fig. 2.5c). f_t equals the tensile

1. Instability refers here to a process growing without bonds. In the case of unstable macrocracks, we denote their growth unstable to indicate the fact that, even if the external loads acting on body are removed, the process of growth continues.

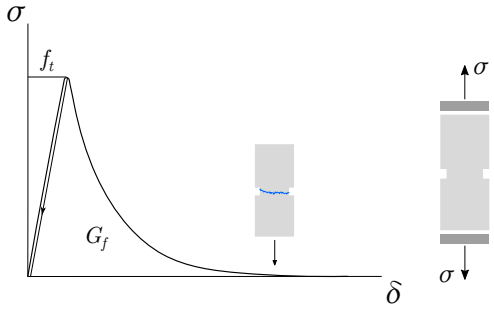

(a) behavior of a quasi-brittle material under uni-axial tensile loading.

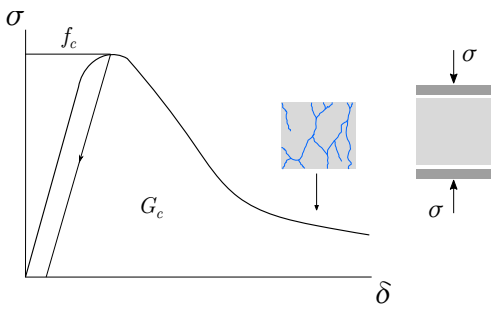

(b) behavior of a quasi-brittle material under uni-axial compressive loading.

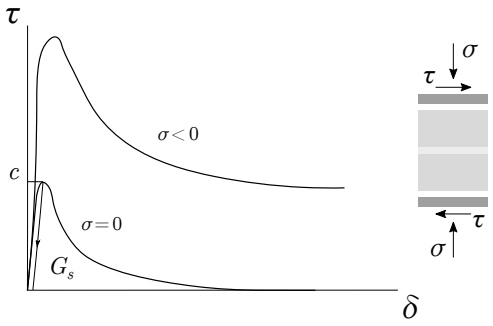

(c) behavior of masonry under shear, depending on the confining stress.

Figure 2.5 – Softening behavior of geomaterials: (a) uni-axial tension, (b) uni-axial compression, and (c) pure shear. Negative stress represents compression.

strength, f_c equals the compressive strength, and c the cohesion. The integral beneath the stress-displacement curve represents the fracture energy, denoted by G_f, G_c, and G_s for tension, compression, and shear, respectively. The fracture energy is the energy needed for unit of crack propagation during the period from crack initiation to the strain localization within a narrow zone (Hillerborg, 1985; Xu et al., 2006).

2.3 Mechanical behavior at high strain-rates

Extensive experimental research showed that the loading rate influences the resistance of geomaterials (strength), the elastic (tangent) modulus, and the peak strain, mainly due to the finite growth rate of micro-cracks (Freund, 1972a,b) and the viscosity of the material (Weerheijm, 1992). Concrete, for instance, when subjected to dynamic loading conditions, exhibits a *dynamic increase* of the strength, among other material properties, as strain-rates approach 1 s^{-1} (Ross et al., 1989; Ožbolt et al., 2014). Some designing criteria and models, e.g. (USACE, 2008; CEB-FIP (Comité Euro-International du Beton Fédération International de la Précontrainte), 2010), account for the dynamic increase of the properties of concrete and steel construction materials.
Nevertheless, in comparison with concrete, only limited amount of data and studies exist for masonry material constituents, e.g., bricks, stones, mortar. Recent studies report that strain-rate effects can be considerable also for masonry constituents. Asprone et al. (2009)

investigated, using a Hopkinson bar apparatus, the dynamic tensile strength increase of classical porous natural stones from the Naples area (Italy). Neapolitan yellow tuff exhibited dynamic tensile strength increasing with strain-rate, up to about three times its quasi-static value, in the case of very high strain-rates (50 s^{-1}). The strain-rate effects are usually quantified in terms of the dynamic increase factor−that is, the ratio of a material property, measured for a certain value of strain-rates, over its quasi-static value. Chen et al. (2014) analyzed the high strain-rate behavior of cement mortar at varying of the water-to-cement ratio, through the split-Hopkinson pressure bar technique, and reported dynamic increase factors (DIF) of tensile strength varying from 1.2 to 2.7 for rates ranges from 1 to 12 s^{-1}. Jin et al. (2017), based on splitting tests of Brazilian discs, reported DIF of tensile strength of cement-sand mortar varying from 2 (at 60 s^{-1}) to 3 (at 200 s^{-1}). Hao and Tarasov (2008) investigated the compressive strength of solid clay bricks and mortar mixed with cement, lime and sand, using a tri-axial static-dynamic testing machine and reported dynamic increase factors (at 150 s^{-1}), of 2.3, 1.12, and 1.95 for the compressive strength, strain at peak strength, and modulus of elasticity, respectively. Pereira and Lourenço (2017) investigated the dynamic enhancement of compressive strength of clay bricks and mortar, using a drop-weight impact machine. Dynamic increase factors ranging from 1 to 2.3 for the bricks strength were reported, for strain-rates between 4 to 176 s^{-1}. Mortar compressive strength DIF was found varying from 1 to 4.38, for strain-rates ranging between 7 and 193 s^{-1}.

Notice that the quantification of the dynamic enhancement of materials, exhibited at high strain-rates, is affected by large variance of the experimental results, as the above references show, see Figure 2.6. The characterization of such effects as a material characteristic per se is hence difficult. This is hold also true when considering the dependency on the strain-rates of the elastic behavior, i.e., viscoelastic behavior. Indeed, differently from concrete (cf. CEB-FIP (Comité Euro-International du Beton Fédération International de la Précontrainte), 2010), the viscoelastic behavior of masonry constituents is difficult to characterize and quantify, due to the limited and only partial amount of experimental tests (see, among others, Harsh et al., 1990; Hao and Tarasov, 2008).

Moreover, the above cited experimental works involved testing of the solely constituents of the masonry, i.e., bricks, stone, and mortar. Very few experimental studies exist for characterizing the dynamic behavior of masonry, as a composite and heterogeneous material. For instance, Pereira and Lourenço (2017) studied the compressive strength enhancement at high rate loading for masonry of solid clay bricks and mortar. Dynamic increase factors for the strength, Young's modulus, strain at peak strength, and fracture energy were characterized for strain-rates ranging between 2 to 54 s^{-1}. The compressive strength DIF was reported to vary between 1 and 2.09. Burnett et al. (2007) studied the tensile behavior of masonry under dynamic loading, through a specially designed split-Hopkinson pressure bar. Burnett et al. (2007) reported mean peak failure stresses for specimens subjected to dynamic (approximately 1 s^{-1}) and quasi-static tensile load equal to 1.56 MPa and 0.51 MPa. The measured DIF equals 3.1.

It is worth noticing that the authors performed numerical simulations of the test set-up, in order to investigate the possible influence of any non-uniformity of the brick-mortar bonding, as reported by Van der Pluijm (1997) (see Figure 2.3). The simulations

confirmed that the apparent dynamic strength enhancement effect is likely to be at least partly caused by the inherent variability of the unit-mortar bond, and may not be a genuine material characteristic per se. Furthermore, a specific characterization for different types of masonry materials, with variable unit-mortar bonding area, and their behavior under fast-dynamic excitations remain to be determined.

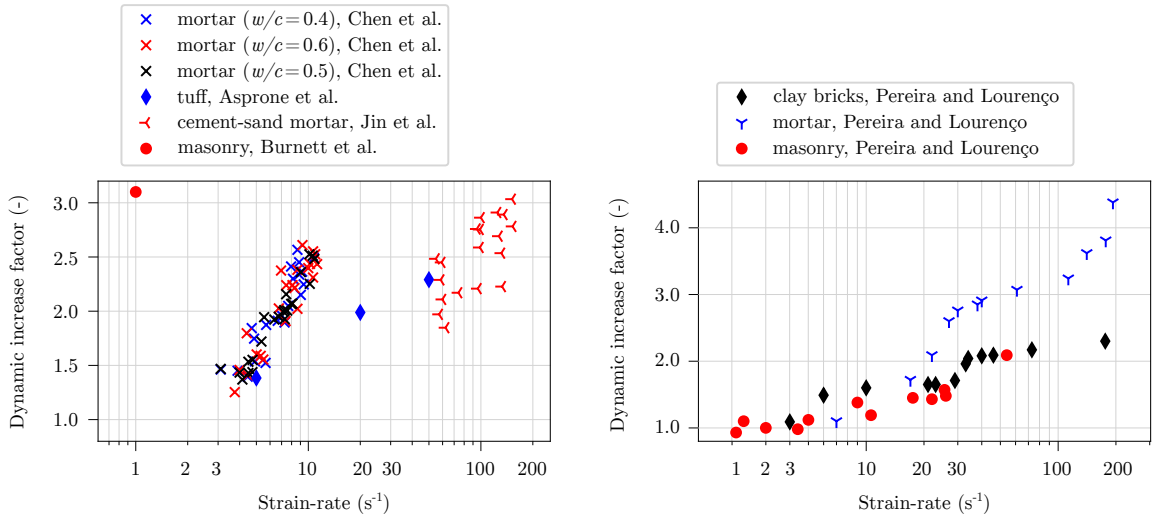

(a) tensile strength. (b) compressive strength.

Figure 2.6 – Collection of dynamic increase factor for tensile strength (a) and compressive strength (b) of mortar, bricks, stone, and masonry. From (Asprone et al., 2009; Chen et al., 2014; Jin et al., 2017; Pereira and Lourenço, 2017; Burnett et al., 2007).

It is worth noticing that the dynamic enhancement of the material properties of masonry and the viscoelastic behavior still remain open research subjects and further investigations are needed to clarify, at best, the dynamic effects and quantify their influence on the mechanical response of masonry structures. Nevertheless, we would like to note that overall the increase of tensile and compressive strength of masonry varies approximately between 1 and 2.3 (only few studies reported higher values) (Gebbeken et al., 2012), cf. Figure 2.6.

As far it concerns the increase at high strain-rates of the elastic (secant) modulus, an appropriate characterization of such effects needs still to be identified. Indeed, Harsh et al. (1990); Hao and Tarasov (2008); Pereira and Lourenço (2017) found, among others, that the increase of the material stiffness at high strain-rates is proportional and similar to the increase of the material strength. Differently, Zhou and Chen (2013); Xiong et al. reported the lack of strain-rate effects on the elastic modulus (see Fig. 2.7).

Considering the aforementioned experimental evidences, we emhasize that, if dynamic effects on the material strength, elastic (tangent) modulus, and peak strain are to be neglected, the resulting estimations will be on the safety side. More specifically, setting DIF = 1 allows to have safe estimates of the masonry resistance against fast-dynamic loading. This is justified and desirable (up to a certain extent) especially in safety and design criteria and investigations. Moreover, given the various uncertainties of the

properties of the masonry constituents and of the construction procedures, followed in practice, being on the safety side is strongly justified. Notice that technical guidelines for the design of masonry structures, such as European Committee for Standardization (2010), consider an overall safety factor between 2 and 3. Consequently, underestimating the resistance of our material by a factor of 2 is acceptable for design purposes. This holds true also in the evaluation of the mechanical performance of historical and/or monumental structures, where the properties of the built materials are hard to acquire. Neglecting the dynamic increase of the strength of the masonry allows a safer design of interventions. Moreover, as presented and discussed in Chapter 4, the strain-rates developed during a blast scenario, computed by our analyses, are overall below 2 s^{-1}, which further justifies the simplifying assumption of assuming DIF = 1.

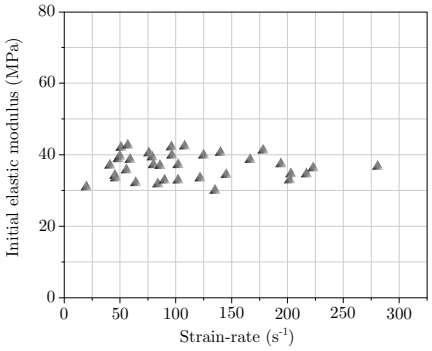

(a) initial elastic modulus versus strain-rate for cement mortar, from Zhou and Chen (2013).

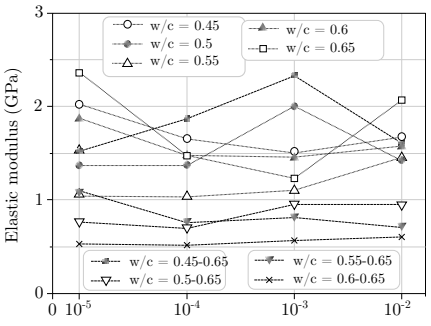

(b) elastic (tangent) modulus versus strain-rate for cement mortar at various water/cement ratios, from Xiong et al..

Figure 2.7 – Collection of the elastic modulus of cement mortar for different values of the strain-rate. From (Zhou and Chen, 2013; Xiong et al.).

2.4 Masonry failure modes

We can distinguish failure modes at the scale of the constituents of the masonry (joints and units), i.e., material failure modes, from structural failure modes, also known as failure mechanisms, which involve larger scales.

2.4.1 Material failure modes

Masonry failure strongly depends on the state of stress, the loading and boundary conditions (Roca et al., 2010; DeJong, 2009; Petry and Beyer, 2015b). We recall here that we define material failure as the loss of ability to withstand external forces by the material. Failure stems from the initiation and propagation of macrocracks and plastic deformations (Davis and Selvadurai, 2005; Gdoutos, 2020). When mortar has smaller mechanical resistance than units, as it typically happens, failure is often induced by the joints, who act as weak planes. Four material failure modes can be identified: (a) failure of the masonry units, (b) of the mortar, (c) of the brick-mortar interface, and (d) of

all the above. Figure 2.8 shows schematic representations of the material failure modes. Brick-mortar interface tensile failure (Fig. 2.8a) and shear (Fig. 2.8b) are characterized by the failure of the bond between brick and mortar. The last three depicted failure modes (Fig.s 2.8c-2.8e) are combined failure mechanisms involving bricks, mortar, and brick-mortar interfaces.

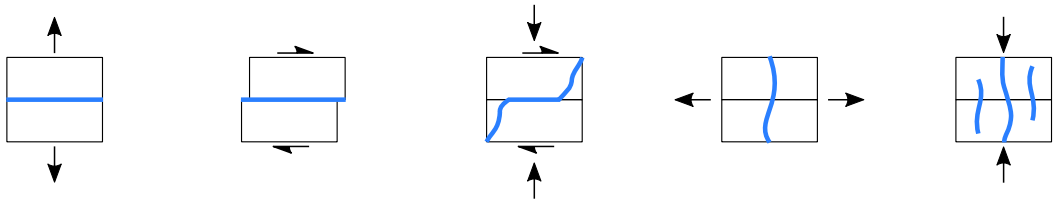

(a) interface tensile cracking. (b) interface shear. (c) unit diagonal tension crack. (d) unit tensile. (e) unit compression.

Figure 2.8 – Schematic local failure modes. Modes (a-c) are dominated by interface failure, while modes (d,c) strongly depend on the mechanical properties of the masonry units.

2.4.2 Structural failure modes

Structural failure modes can be distinguished into in-plane [2] failure mechanisms and out-of-plane [3] ones. However, depending on the loading, masonry structures usually experience combinations of in-plane and out-of-plane deformation regimes. This holds true especially for non-standard geometry masonry structures.

2.4.2.1 In-plane structural failure modes

Basic in-plane structural failure modes are presented in Figure 2.9. According to the classification in (Lishak et al., 2012), we can distinguish the following scenarios:

(a) Partition into columns. Failure under uni-axial compression normal to the horizontal (bed) joints as a result of the formation of cracks passing through the masonry units and vertical (head) joints or only through masonry units.

(b) Partition into layers of one or several masonry rows. Failure under uni-axial compression parallel to the bed as a result of the crack formations along horizontal (bed) joints.

(c) Splitting parallel to the external surfaces of the masonry. Failure under bi-axial compression normal to and parallel to the bed.

(d) Breakage along a bed joint.

(e) Breakage along a toothing crack. Failure under tension that is applied parallel to the bed as a result of sliding along the bed joints and breakage of head joints.

2. In-plane refers here to failure and/or loads acting on the geometrical plane where masonry units are arranged.

3. Out-plane refers here to failure and/or loads acting on geometrical planes perpendicular to the in-plane.

(f) Vertical breakage through masonry elements. Failure under tension that is applied parallel to the bed as a result of the formation of a crack that crosses the masonry units and head joints of the masonry.

(g) Splitting along a stepped crack with shear along the bed. Failure with shear and compression acting normal to the bed.

(h) Shearing along the bed. Failure due to shear along the contact surface of the horizontal mortar joint and the masonry units or along a crack inside this joint.

(i) Splitting along an inclined crack. Failure under shear and compression due to the formation of an inclined crack that crosses the masonry units.

Combinations of the above failure modes are also possible.

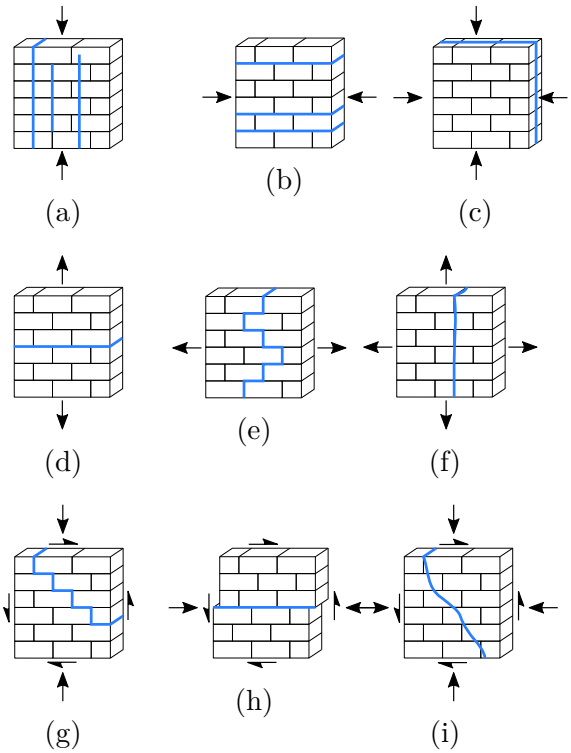

Figure 2.9 – Main in-plane failure modes, from (Lishak et al., 2012). (a) Partition into columns. (b) Partition into layers of one or several masonry rows. (c) Splitting parallel to the external surfaces of the masonry. (d) Break along a bed joint. (e) Break along a tooting crack. (f) Vertical break through masonry elements. (g) Splitting along a stepped crack with shear along the bed. (h) Shear along the bed. (i) Splitting along an inclined crack.

2.4.2.2 Out-of-plane structural failure modes

Out-of-plane failure modes/mechanisms consist of structures undergoing flexure (bending). Figure 2.10 displays schematic representations of the out-of-plane failure of flat masonry walls. Depending on the boundary conditions, flat masonry walls can be classified into

one-way and two-way spanning walls (McKenzie, 2001). One-way spanning walls are supported (simply supported or clamped) on at least one edge, either vertical or horizontal (see Fig.s 2.10b and 2.10a). The wall, subjected to out-of-plane loading, undergoes uni-axial bending which results in propagation of cracks parallel to the axis of bending. Two-way spanning walls are, instead, supported on at least one vertical edge and one horizontal edge. Such structures undergo bi-axial bending and usually exhibit combinations of vertical, horizontal, and diagonal cracks (see Fig. 2.10c).

In all cases, failure mechanisms are accompanied by combinations of material failure modes. For instance, in the case of one-way spanning walls supported at one edge, interface shear and tensile failure modes co-exist. Crushing of interfaces and units, interface shear and tensile failure usually characterize the mechanism of a one-way spanning wall supported at two edges. In the case of two-way spanning walls, the stress state involves combinations of several material failure modes strongly depending on the orientation of the interfaces (masonry pattern) and the mechanical parameters of the constituents (units and mortar).

Gilbert et al. (2002) investigated the out-of-plane response of free-standing un-reinforced [4] masonry walls subjected to impacts. Figure 2.11 displays some of the observed failure modes. A number of characteristic out-of-plane sliding failure modes was reported by the authors. Whole-wall rocking (cf. Figure 2.10a) was reported in the case of all walls tested without lateral supports. Whilst the reported structural failure modes strongly depend on the impact location, the local failure modes overall observed involved masonry joints, see Figure 2.11.

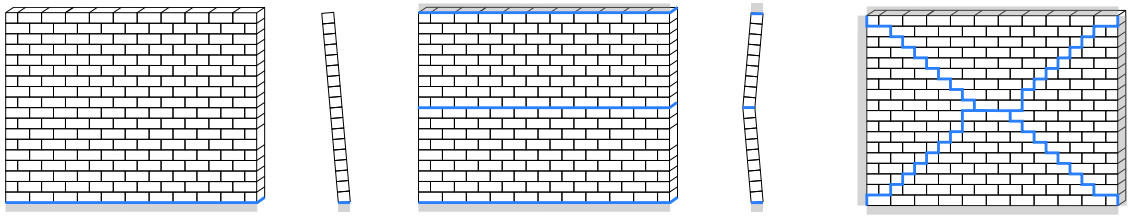

(a) one-way spanning wall (one edge).

(b) one-way spanning wall (two edges).

(c) two-way spanning wall.

Figure 2.10 – Out-of-plane failure mechanisms of a masonry wall. One-way spanning wall supported on (a) two edges and (b) one edge. (c) Two-way spanning wall.

2.4.2.3 Structural failure modes of non-standard geometry masonry structures

When considering masonry structure with non-standard geometry, such as arches, vaults, domes, the identification of failure mechanisms is usually more complex than the case of simple, flat walls. In particular, the geometry and stereotomy, i.e., the spatial arrangement of masonry units and the particular shape of the structure, are predominant parameters (Block et al., 2006; DeJong, 2009; Shapiro, 2012; Fantin et al., 2019). Hence, a general classification of structural failure mechanisms of curved geometry structures is

4. Unreinforced masonry is any type of masonry that is not braced by reinforcing material, such as rebars.

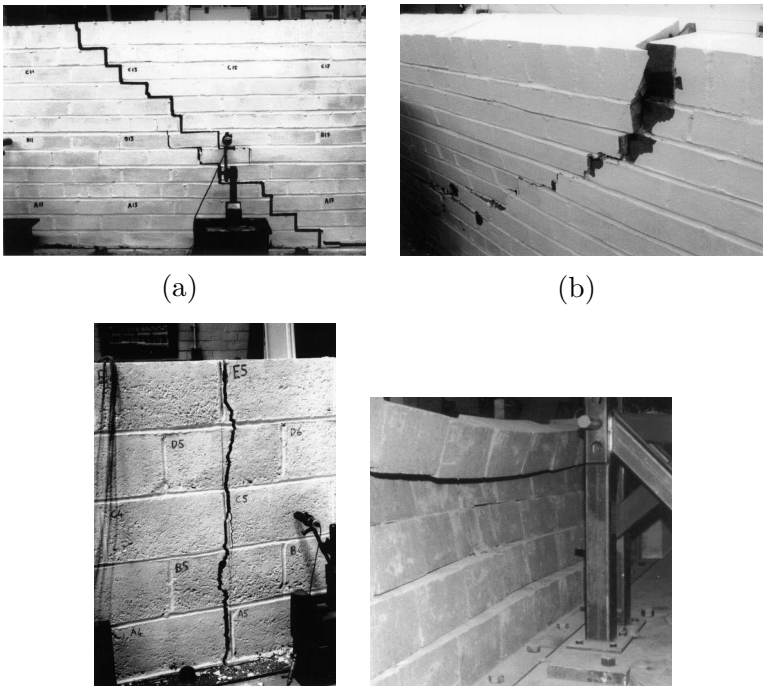

Figure 2.11 – Some structural failure modes of masonry subjected to impacts. Credit: Gilbert et al. (2002).

not trivial. Typical reported masonry arches structural failure modes involve formation of hinges, sliding, crushing, and to a lesser extent cracking (Brocato et al., 2001; Shapiro, 2012; Sarhosis et al., 2016c), see Figure 2.12. Hinging mechanisms involve the formation of hinges, due a local tensile failure of masonry joints under flexural stress configurations and consequent opening. Shapiro (2012) investigated, through reduced-scale experiments, the response of barrel and groin vaults [5] subjected to different combination of loads (such as spreading of the supports, concentrated loads, and horizontal acceleration through tilting). Figure 2.13 shows the collapse mechanism of a barrel vault on spreading supports. Formation of hinges results in structural failure.
Quinonez et al. (2010) investigated collapse mechanisms of masonry domes on spreading supports, see Figure 2.14. The authors reported hinging as predominant failure mode and sliding to a lesser extent. Rossi et al. (2016) investigated the seismic response of masonry cross vaults subjected to static differential displacements at the abutments, see Figure 2.15. They reported sliding and hinging as the predominant failure modes. Rossi et al. (2017) investigated the structural behavior of a pavilion vault on spreading supports by means of experimental tests on a printed scale model. Typical failure modes involved formation of hinging mechanisms and shearing, see Figure 2.16.

5. A barrel vault is an architectural element formed by the extrusion of an arch. A groin or cross vault consists of the intersection of two barrel vaults.

2.4. Masonry failure modes

In the case of non-standard geometry masonry structures, the effects of dynamic loading conditions received smaller interest from the scientific community. Nevertheless, several (historical) examples exist showing the vulnerability of such kind of structures to earthquake loading and impacts (Roca et al., 2019), see Figure 2.17. We record, for instance, the work of DeJong et al. (2008) who focused attention on the dynamic (rocking) response of masonry arches subjected to several earthquake loading time histories, see Figure 2.18.

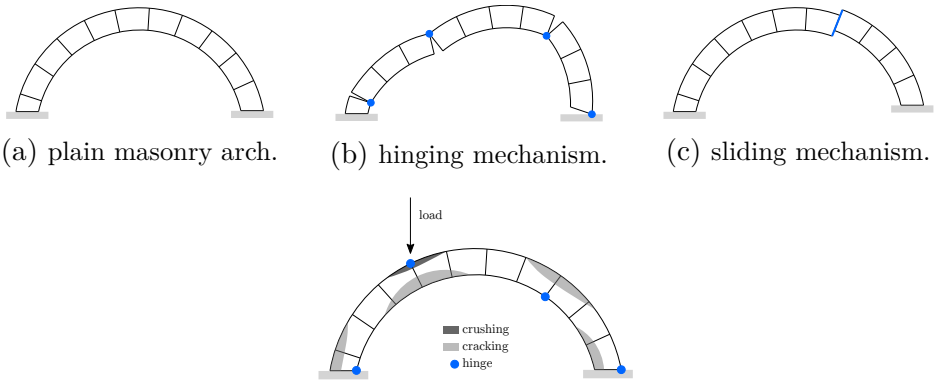

(a) plain masonry arch. (b) hinging mechanism. (c) sliding mechanism.

(d) combined mechanisms for a masonry arch bridge (from Sarhosis et al., 2016c).

Figure 2.12 – Some typical structural failure mechanisms in plain arches under vertical loading and self-weight.

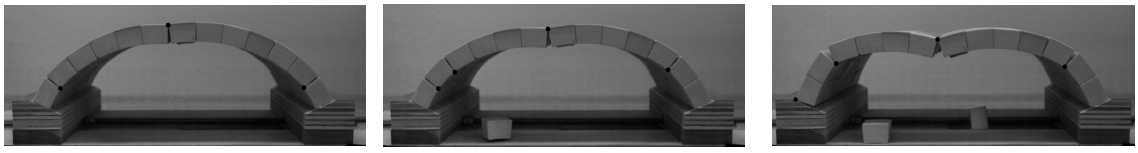

(a) (b) (c)

Figure 2.13 – Collapse mechanism of a masonry dome on spreading supports. Credit: Shapiro (2012).

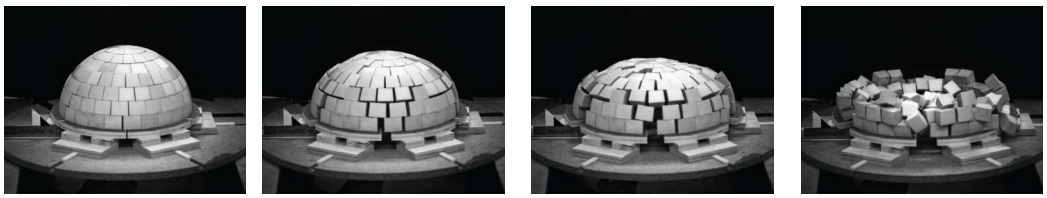

(a) (b) (c) (d)

Figure 2.14 – Structural failure mode of a masonry dome on spreading supports (a-d). Credit: Quinonez et al. (2010).

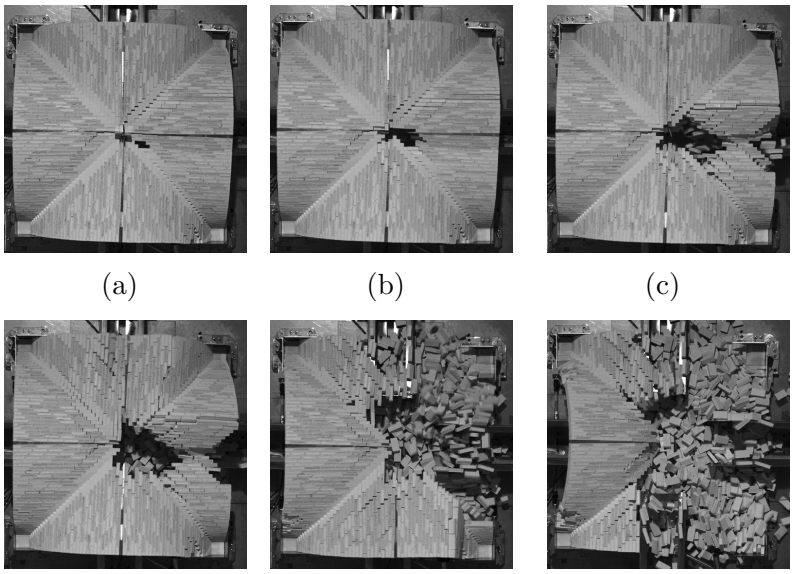

(a) (b) (c)

(d) (e) (f)

Figure 2.15 – Evolution of the structural failure mode of a masonry cross vault subjected to differential horizontal displacements of the abutments. Credit: Rossi et al. (2016).

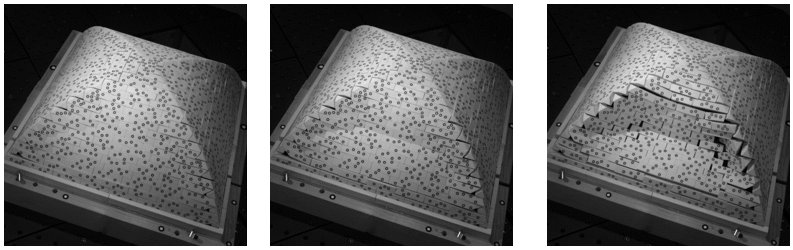

(a) (b) (c)

Figure 2.16 – Collapse mechanism of a masonry pavilion vault on spreading supports. Credit: Rossi et al. (2017).

(a) (b) (c)

Figure 2.17 – Structural failure modes of vaulted masonry structures subjected to earthquake loading (a, b) and impacts (c): (a) vault of the Basilica di San Francesco after the 26 September 1997 earthquake, (credit: Del Prete et al., 1998), (b) remains of the Carmo Convent damaged by the Lisbon earthquake in 1755, (photo credit: Chris Adams), and (c) ruins of the main vault of Notre Dame, Paris, after having pierced by the (collapse of the) spire (Lesté-Lasserre, 2020).

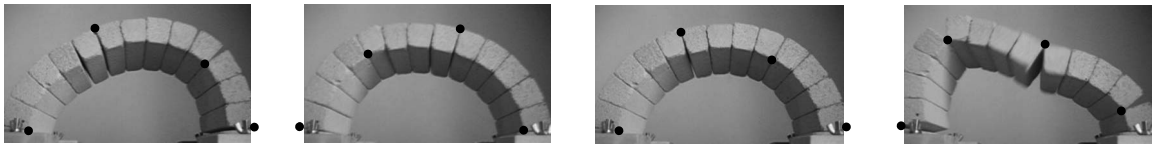

(a) (b) (c) (d)

Figure 2.18 – The four consecutive mechanisms of a masonry arch subjected to the El Centro earthquake acceleration record (a-d). Credit: DeJong et al. (2008).

2.4.2.4 Failure modes due to blast loading

Structural failure modes of masonry structures subjected to explosions usually involve out-of-plane response. This is particularly true for planar geometries, such as walls.
The analysis of the blast loads effects on masonry structures received some attention in the last two decades, although limited to simple flat walls.
It is worth noticing that, under far-field and medium-field explosions, the most common reported local failure mechanism involves masonry joints, representing weak planes. We record, for instance, the work of Varma et al. (1997), who performed tests on several masonry panels of different thickness, under near- and far-field explosions. Gabrielsen et al. (1975) experimentally investigated the response to blast loading of full-scale un-reinforced masonry walls with and without development of arching actions. Arching actions occur in a wall, butted against rigid supports, undergoing flexion along an out-of-plane direction. The strength increase of one-way arching masonry walls comes from arising of (beneficial) compressive membrane stresses in the out-of-plane response. Abou-Zeid et al. (2011) studied the response of one-way arching walls made of hollow concrete bricks under several explosive weights, in a far-field scenario. Some reported failure modes are shown in Figure 2.19. Most damage occurs at the joints interfaces, under sliding and spalling mechanisms. Whilst the arching actions developed within the wall (high compressive in-plane stresses), failure of bricks was reported to be negligible.

(a) test set-up. (b) sliding. (c) spalling.

Figure 2.19 – Structural failure modes of one-way arching masonry wall subjected to blast loads. Credit: Abou-Zeid et al. (2011).

Keys and Clubley (Keys and Clubley, 2017) investigated masonry debris distribution and failure patterns of masonry walls when subjected to long duration blast loading (typically exceeding 100 milliseconds). Figures 2.20 and 2.21 displays the mechanical response of different flat masonry structures under vented explosions and post-test observations of the failure modes. Similarly to what reported by Gilbert et al. (2002) for impact loading, propagation of cracks was found to occur almost exclusively along the bed joints and damage within the body of individual bricks was negligible.

Li et al. (2017) investigated through experimental and numerical studies the response of un-reinforced clay brick masonry walls subjected to vented gas explosions. The results showed that boundary conditions and wall thickness have great influence on the performance of masonry walls. More recently, Michaloudis and Gebbeken (2019) analyzed the response of un-reinforced masonry walls constrained to rigid supports and subjected to far-field and contact explosions. In the case of far-field explosions, global collapse was induced by the failure at the interfaces between blocks. Damage of bricks was negligible, see Figure

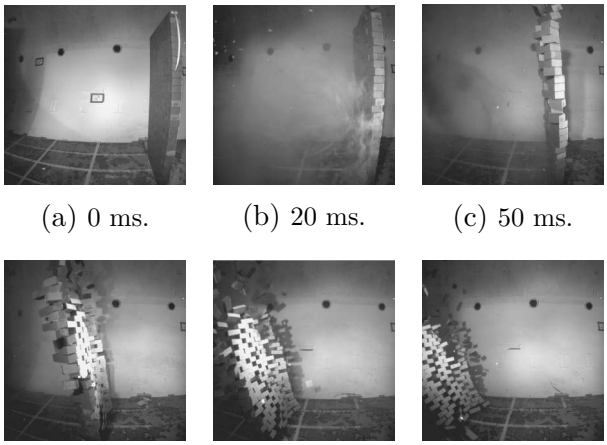

(a) 0 ms. (b) 20 ms. (c) 50 ms.

(d) 100 ms. (e) 150 ms. (f) 200 ms.

Figure 2.20 – Side perspective of the response to a long-duration blast of a masonry structure (MW1). Credit: Keys and Clubley (2017).

2.22. For contact detonations, the same authors reported strain-rate as high as 100 s^{-1}, for which the dynamic enhancement may be higher than 1 (DIF $\approx$ 2). Differently from far- and medium-field explosions, in this case failure within the volume of the bricks occurred, leading debris to travel at high velocities.

It is worth emphasizing that a similar research experimental activity is not reported for masonry structures with curved geometry or, in general, non-standard geometry, such as arches, vaults, domes, etc. Indeed, neither experimental nor numerical investigations of the response to explosions of such architectural elements exist. Except, some real cases such the blast of the Parthenon in 1687, see Figure 2.23, or the destructions at Palmyra in 2015 and 2016, see Figure 2.24.

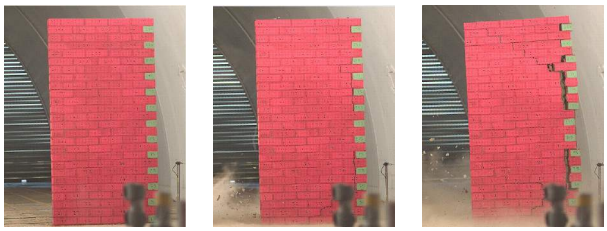

(a) 0 ms. (b) 20 ms. (c) 50 ms.

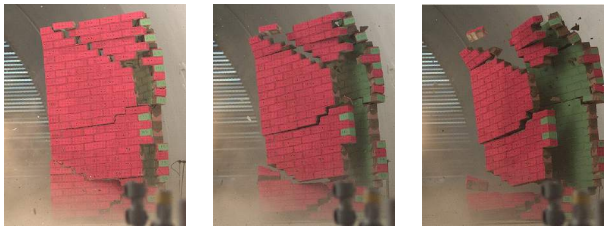

(d) 100 ms. (e) 150 ms. (f) 200 ms.

Figure 2.21 – Side perspective of the response to a long-duration blast of a masonry structure (BWL2B). Credit: Keys and Clubley (2017).

(a) test set-up. (b) breaching.

Figure 2.22 – Masonry subjected to a far-field blast event. Credit: Michaloudis and Gebbeken (2019).

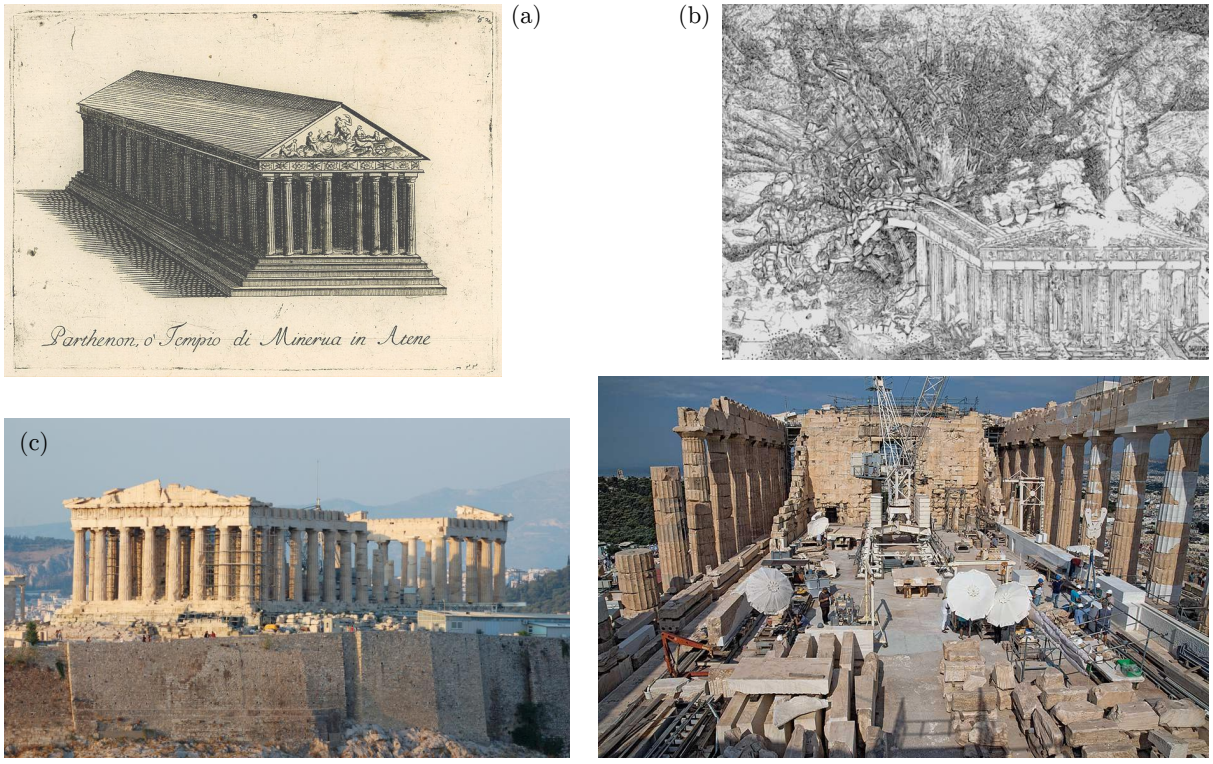

Figure 2.23 – Parthenon in Athens (Greece). Before the destructions (a), credit: V. Coronelli - Republic of Venice, 1688. The explosion of the temple in 1687 (b), from http://hdl.handle.net/11174/241. Actual configuration (c) and (d), image downloaded from www.greece-is.com/how-to-restore-the-parthenon.

(a) Temple of Bel. (b) Monumental Arch.

Figure 2.24 – Destructions at Palmyra in 2015 and 2016: the rests of (a) the Temple of Bel and (b) the monumental arch. Photo credit: thinkglobalheritage.wordpress.com.

2.5 Modeling strategies

Several numerical techniques have been developed to investigate and predict the behavior of masonry structures. Over the last 50 years, the scientific community has demonstrated great interest in the development of detailed numerical approaches and tools. We refer to Sacco (2014); DAltri et al. (2019) for a complete review.
Among the several existing approaches, the selection of one method depends, first, on the structure under investigation and the loading conditions. Second, on the level of desired accuracy, the financial and time resources to be invested, as well as, the knowledge of the material properties and available experimental data of the system under study (Sarhosis and Lemos, 2018). Indeed, different kind of methods may lead to different results, depending on the accuracy and adequacy of the approach. The modeling approach selected should, in principle, provide the desired information about the response of the structure, within an acceptable degree of accuracy and with least cost/time.
By taking into account the heterogeneity of the masonry regarded as a composite material composed by units and interfaces, three different scales can be identified: micro-, meso-, and macro-scale, see Figure 2.25.

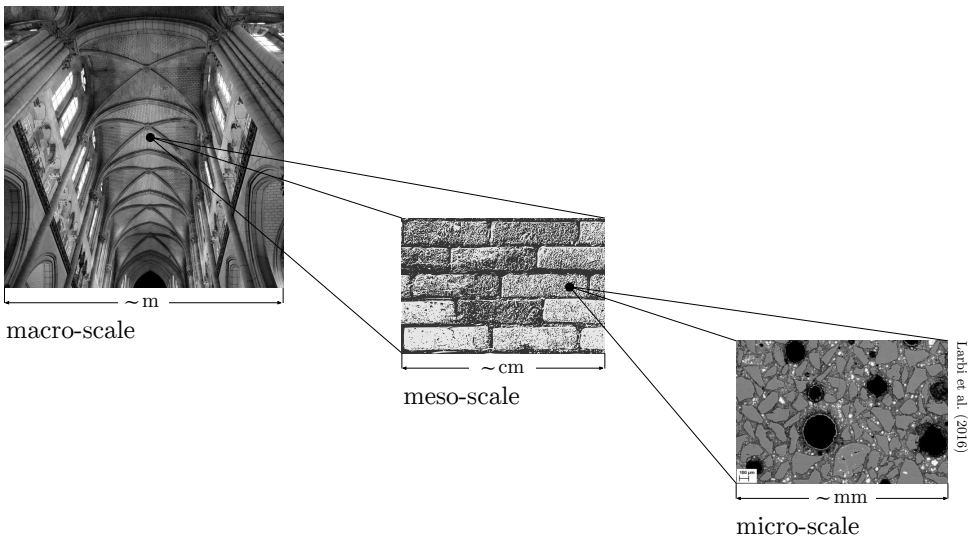

Figure 2.25 – Response of masonry structures: from a macro-scale description to the micro-scale one (from Larbi et al., 2016).

A micro-scale description is here denoted as a description involving characteristic length scales of the order of micrometers (see Figure 2.25). Geomaterials, such as rock, concrete, mortar, etc., are heterogeneous and, at the micro-scale (grain scale), are characterized by the presence of different aggregates, void, micro-cracks, different additives, etc. These features characterize the micro-scale of the masonry components, units and interfaces, and influence the stress distribution and the initiation and propagation of cracks.
We define here as micro-modeling strategies those describing the mechanics of the micro-structure, taking into account the heterogeneity of masonry units and interfaces.

The characterization of the masonry behavior at larger length scales, of the order of some centimeters, passes through what we define here as a meso-scale description. Masonry is here regarded as an assemblage of units, interacting through interfaces (dry or mortared). At this level, the information pertaining the heterogeneity of the masonry components is lost and masonry is described as a homogeneous equivalent material. This scale coincides with the scale of the so-called *Representative Elementary Volume* (REV).

Finally, we define a macro-scale description when dealing with masonry structures (see Fig. 2.25). The characteristic length of this scale is of the order of meters and describes the whole structure. Based on a hierarchical bottom-up approach, the mechanical resistance of a masonry structure will depend on the meso-scale, which in turn will accordingly depend on the micro-scale. Of course, the loading conditions, the structural geometry and the boundary conditions may render the role of meso- and micro-scales more or less important for the description of the overall dynamic behavior of a structure. Incorporating only the necessary information and complexity of the micro- and meso-scales is an important factor in successful modeling of masonry structures at the macro-scale.

We shall notice that, the scientific community of masonry acknowledges a different distinction of length scales, compared to that detailed above. In this case, the scale here defined as meso-scale is usually denoted as the micro-one (Lourenço, PhD Thesis, 1997).

2.5.1 Micro-, meso-, and macroscopic modeling

The selection of a particular modeling approach strongly depends on the characteristic scale at which the investigated phenomena take place.
Micro-models are employed to investigate the behavior of the masonry components (units or mortar), but not their interactions, see e.g. (Tengattini et al., 2014; Stamati et al., 2019; Collins-Craft et al., 2020). More detailed material descriptions can be achieved with atomistic, nano-scale modeling, where very few constitutive assumptions are made. For instance, we record the work of Pellenq et al. (2009), who derived an atomistic level structural model of cement hydrates. Micro-modeling strategies require enormous computational time, that soon becomes unaffordable when passing to a meso-scale description of the material. Furthermore, detailed information about the material micro-structure is needed, which is not always available.

Macro-models, typically based on the Finite Element Method (FEM), regard the masonry material as a homogeneous isotropic or anisotropic continuum, either following a classical Cauchy continuum formulation (Pelà et al., 2013; Stefanou et al., 2015a; Petracca et al., 2017) or relying on micromorphic continua (Stefanou et al., 2008; Godio et al., 2017), in which masonry units and mortar joints are smeared out (Lourenço, PhD Thesis, 1997; Lourenço et al., 1998; Pelà et al., 2013; Rafsanjani et al., 2015). The formulation of macroscopic constitutive laws is still a challenging task (Pelà et al., 2013; Stefanou et al., 2015a; Godio et al., 2017). A large spectrum of constitutive models have been proposed in the literature, based on observations and experimental testing.

This is usually achieved either through heuristic approaches and assumptions or through asymptotic approximations and averaging (e.g. Lloberas Valls et al., 2019; Nitka et al., 2011; Feyel, 2003; Bakhvalov and Panasenko, 1989; Cecchi and Sab, 2002). The history and the state of a material is commonly taken into account through ad hoc enrichment of simpler constitutive laws and extensive calibration. For a complete review on the existing upscaling approaches [6] in the frame of masonry structures, we refer to Lourenço et al. (2007). The recent trend of Machine Learning based constitutive models seems offering promising solutions to the definition of appropriate, detailed material models, see Plevris and Asteris (2014); Mishra et al. (2019); Friaa et al. (2020) and paragraph 2.5.3. Macroscopic approaches present some intrinsic difficulties mainly related to the identification of the mechanical parameters of the equivalent continuum and the definition of realistic phenomenological failure criteria (e.g. the definition of yield surfaces). Moreover, they do not allow the modeling of discontinuities between different blocks of the masonry. Nevertheless, macro-models are still a suitable option for the numerical analysis of large and complex structures due to their limited computational cost.

Meso-models, accounting for the discontinuous nature of the masonry, may be preferred to macro-models, although their calculation cost can be prohibitive to study large structures. Meso-models characterize each masonry component with different constitutive laws and are often used in the analysis of single structural members (e.g., walls). Meso-modeling approaches can be distinguished into two categories, see Figure 2.26. The first class of meso-models consist in accounting for the discretization of units, mortars, and the interfaces between them (Raffa et al., 2013; Petracca, 2016; Sarhosis and Lemos, 2018; D'Altri et al., 2018). In this case, a complete description of the masonry material failure modes (cf. Fig. 2.8) is obtained. The second class of meso-scale approaches (also known as simplified meso-scale models) consists in modeling masonry units as blocks (either rigid or deformable), interacting through contact interfaces. Mortar joints and unit-mortar interfaces are lumped into a single zero-thickness interface, while the units are slightly expanded in size, to keep the geometry unchanged (Lotfi and Shing, 1994; Giambanco et al., 2001; Van Mele et al., 2012; Drougkas et al., 2014; Godio et al., 2018; DAltri et al., 2019). In the framework of simplified meso-models, the Discrete Element Method (DEM) is usually preferred (e.g. Sarhosis et al., 2016b; Lemos, 2007b; Godio et al., 2018), to FEM. Discrete approaches account for several mechanical parameters (at the meso-scale level), allow to simulate the progressive failure of masonry and capture with fidelity the post-peak, softening, dynamic behavior of a masonry structure with bricks undergoing large displacements and rotations (Godio et al., 2018; Lemos, 2007b; Itasca Consulting Group, Inc., 2018).

It is worth noticing that the above mentioned classification of modeling techniques, based on the characteristic length scales (i.e., micro-, meso-, and macro-models), does not allow to include several other modeling strategies (Roca et al., 2010), which do not

6. Upscaling approaches are used to replace the micro- and/or the meso-structure of a material with an equivalent homogeneous material.

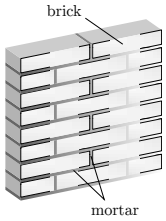

(a) representative scheme.

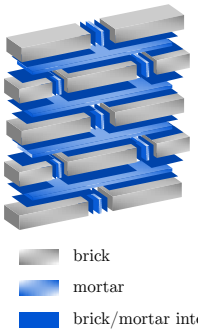

(b) meso-scale model.

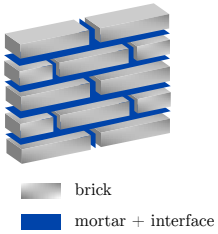

(c) simplified meso-scale model.

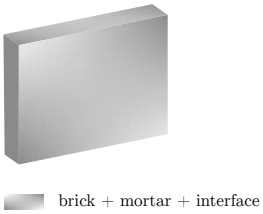

(d) macro-scale model: continuum.

Figure 2.26 – Modeling approaches for masonry according to a meso-scale description, (b) and (c), and a macro-scale one (d).

fit a particular class in the above classification.
We record, without being exhaustive, modeling approaches, based on deformable or rigid models, to analyze the activation and the evolution of failure mechanisms in masonry structures, see (Peña et al., 2007; DeJong et al., 2008; Penna et al., 2014; Alessandri et al., 2015; Pantò et al., 2016; Baraldi and Cecchi, 2017; Silva et al., 2017). Such approaches have been applied both at the macroscopic and mesoscopic scales. We refer, for instance, to the structural failure modes of rocking and overturning (Zhang and Makris, 2001; Voyagaki et al., 2013; Dimitrakopoulos and DeJong, 2012; Peña et al., 2007; Konstantinidis and Makris, 2010), who attracted significant scientific research, mostly in the domain of earthquake engineering (construction of bridges, seismic isolation, masonry structures, historical monuments, etc.).

Different from the above simplified methods, limit analysis can also be used for estimating the vulnerability masonry structures, based on prescribed failure modes (Del Piero, 1998; Como, 2013; D'Ayala and Speranza, 2003; Cascini et al., 2018) under quasi-static

loading conditions. The evaluation of the load factor corresponding to the activation of a failure mode is carried out through the application of the limit analysis theorems (lower- and, more often, upper-bound theorems) (Davis and Selvadurai, 2005; Portioli et al., 2014; Cascini et al., 2018). A known problem of limit analysis is the overestimation of the strength (loading factor) when non-associative (Radenkovic, 1962; Salençon, 1974) or strain-softening (Davis and Selvadurai, 2005; Kramer et al., 1996) materials are considered. Masonry is such a material, especially under shearing. Therefore the results of such analyses have to be considered with caution (see also Godio et al., 2018; Masi et al., 2019b, 2020a).
Software tools based on rigid block modeling for limit analysis are also available (Orduña, 2004). In particular, we refer to LiABlock_3D (Cascini et al., 2018), which is a novel software tool for the limit equilibrium analysis of three-dimensional masonry structures subjected to live loads and settlements, where the non-associativity of the frictional behavior of joints have been tackled using cone programming (Portioli et al., 2014).
Finally, we record Thrust Line Analysis (TLA) (Block, 2009), a graphical method for calculating the equilibrium configurations of masonry systems, where joints are assumed to have zero tensile strength (no-tension material, Heyman, 1995). In these approaches, equilibrium is visualized using a line of thrust. This is a theoretical line, which represents the path of the resultants of the compressive forces through the masonry structure. In the frame of no-tension materials, equilibrium under some applied loads, is met if a line of thrust that lies entirely within the masonry section can be found. The concept was first formulated in (Moseley, 1853; Milankovitch, 1907; Ochsendorf, 2002; Block, 2009).

2.5.2 Multiscale modeling

The main goal of a multiscale technique is to capture the effect of the micro-/meso-scale constituents and their interactions at the macro-scale behavior and provide a bottom-up detailed simulation of masonry structures. Following the classification suggested by Remacle et al. (2012), multiscale modeling techniques can be distinguished into hierarchical and concurrent. By defining the characteristic length of the macro-scale with ℓ and the length associated to the micro with ℓ^*, hierarchical techniques, also known as computational asymptotic homogenization models (Nguyen et al., 2011), assume separation of the two scales, i.e., $\ell >> \ell^*$. Concurrent methods take into account the coupling between the different scales, i.e., $\ell = \ell^*$, see Figure 2.27.
In hierarchical multiscale modeling approaches, the coupling between the two scales is made via numerical asymptotic homogenization of a characteristic elementary pattern, or representative elementary volume (REV), for the micro-scale, which provides a constitutive law to the macro-scale. An appropriate selection of REV is based on the representativeness of the micro-structure, which is then used to derive an up-scaled response. Well known examples are the FE^2 (Feyel, 2003; Eijnden et al., 2016; Lloberas Valls et al., 2019) (coupling of the micro- and macro-scales using FEM) and FEM×DEM (coupling of DEM at micro-scale with FEM at macro-scale) approaches (Nitka et al., 2011; Guo and Zhao, 2014; Claramunt, 2016; Liu et al., 2017; Argilaga et al., 2018).
Differently from upscaling techniques, in multi-scale modeling, the macroscopic constitutive behavior does not exist a priori, but it is built upon recursive downscaling (the macro-

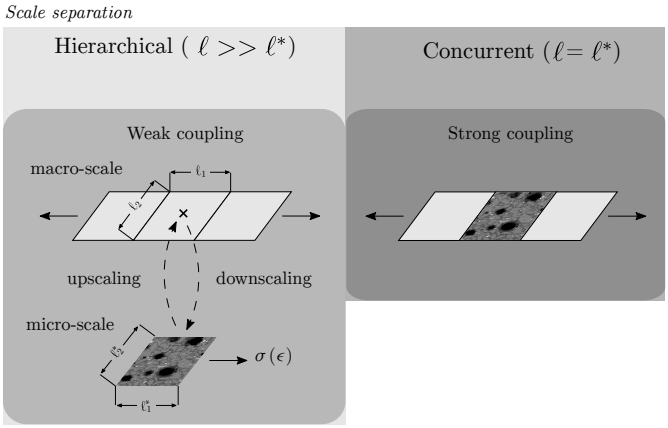

Figure 2.27 – Classification of multiscale modeling techniques, on the basis of the scale separation, according to Remacle et al. (2012).

scale to the micro-scale) and upscaling (the micro-structure information to the macro-scale) (Geers et al., 2010). If the behavior of the micro-scale, REV, has been previously determined through resolution of the auxiliary boundary value problem of the REV with combinations of loads and boundary conditions, then the connection between the two scales is said to be offline. Alternatively, we say it is on-the-fly (online), which means that, during the execution of the numerical simulations, the downscaling is used to solve the auxiliary boundary value problem on the micro-structure, whose solution is then upscaled, at each increment.
Hierarchical multiscale techniques extract a simplified microscopic behavior which is then assumed for each material point, at the macroscopic scale. They may fail in describing the failure of non-linear heterogeneous material, involving mechanisms at different length scales (such as propagation of cracks, strain localization, etc.), see (Feyel, 2003). To overcome such limitations, regularization techniques, such as viscous regularization or micromorphic continua regularization, accounting for various characteristic length and time scales, that the classical Cauchy continuum fails to represent (Geers et al., 2003; Nguyen et al., 2011; Rezakhani and Cusatis, 2016; Stefanou and Gerolymatou, 2019).

In contrast with hierarchical modeling, concurrent multiscale techniques solve the micro- and macro-scale simultaneously (Nuggehally et al., 2007; Lloberas-Valls et al., 2012; Remacle et al., 2012). The coupling is realized through enforcement of global equilibrium and displacement compatibility. The micro-structural scale is adaptively inserted and resolved on the structural model. Such techniques do not suffer from the shortcomings above mentioned, when accounting for softening and strain localization phenomena.

Multiscale techniques offer a high level definition of microscopic effects, described at the macro-scale. However, they are characterized by high computational costs, so that it is difficult to perform numerical simulations at large scales. However, with the increase of computational power, it is nowadays possible to foresee detailed multiscale

simulations that can account for realistic physics and explore stress paths and non-linear phenomena, which are experimentally inaccessible or hard to access. Multiscale methods offer great capabilities in detailed modeling of the micro-structural behaviors. Despite the fact that, in multiscale modeling, the constitutive laws of the micro-structure are not a priori identified, some constitutive assumptions are always necessary. But these latter are at a smaller scale, where the material properties are measurable and probably easier to identify. This scale is for instance the scale of the micro-structure of a material (e.g. the scale of sand grains, crystals, alloys' grains, composites' fibers, masonry bricks' etc. including their topological configuration). Nevertheless, multiscale models have currently a tremendous calculation cost, which is impossible to afford in large-scale, non-linear, incremental simulations (e.g. Finite Elements) that are usually needed in applications (cf. (Rattez et al., 2018a,b; Collins-Craft et al., 2020; Lloberas Valls et al., 2019; Nitka et al., 2011; Eijnden et al., 2016; Feyel, 2003)). A promising solution to this issue seems to be Machine Learning, and in particular artificial neural networks (Oishi and Yagawa, 2017).

2.5.3 Computational enhancement by Machine Learning

Machine Learning (ML) and, in particular, Artificial Neural Networks (ANNs) are promising solutions for (1) the derivation of detailed material constitutive models, that can be used at the macro-scale (or at the meso-scale, depending on the investigated phenomena), and (2) reducing the calculation cost of multiscale techniques. ML can be used for analyzing vast amounts of real, experimental or numerical data at a variety of length and time scales allowing to capture a wide range of mechanical properties and phenomena.

We refer to the pioneer work of Ghaboussi et al. (1991) but also, without being exhaustive, to Lefik and Schrefler (2003); Ghaboussi and Sidarta (1998); Jung and Ghaboussi (2006); Heider et al. (2020); Settgast et al. (2019); Ghavamian and Simone (2019); Liu and Wu (2019); Lu et al. (2019); Xu et al. (2020); Huang et al. (2020); Mozaffar et al. (2019); Frankel et al. (2019); Liu and Wu (2019); Gajek et al. (2020). The main idea in these works is to appropriately train ANNs on experimental or numerical material data, and predict the material response at the material point level, independently of the observed characteristic length investigated. In this sense ANNs can be seen as rich interpolation spaces, able to represent complex material behavior. Successful applications to the masonry material can be found in (Plevris and Asteris, 2014; Mishra et al., 2019; Friaa et al., 2020).
As far it concerns multiscale models based on machine learning, we refer to (Wang et al., 2020; Peng et al., 2020; Rocha et al., 2020). In particular, Peng et al. (2020) discussed extensively the state-of-the-art of combining machine learning and multiscale modeling, identifying applications and opportunities, and addressing potential challenges and limitations. Rocha et al. (2020) recently proposed and applied on-the-fly construction of surrogate models based on probabilistic ML, in the framework of concurrent multiscale FE simulations.
Nevertheless, it is worth noticing that, until now, ANNs for constitutive modeling are

mainly used as a 'black-box' mathematical operator, which once trained on available data-sets, does not embody the basic laws of thermodynamics. As a result, vast amount of high quality data (e.g. with reduced noise and free of outliers) are needed to enable ANNs to identify and learn the underlying thermodynamic laws. Moreover, nothing guarantees that the predictions of trained ANNs will be thermodynamically consistent, especially for unseen data.

Novel data- and physics-driven methods allow to integrate information based on physics laws and conservation principles in the derivation of material constitutive models. Among others, we record Physics-Informed Neural Networks (PINNs) (Raissi et al., 2019) and data-driven computing (Kirchdoerfer and Ortiz, 2016).

Physics-Informed Neural Networks (PINNs) (Raissi et al., 2019) are ANNs used to solve nonlinear partial differential equations, by prescribing a priori given laws of physics. In data-driven computing, the auxiliary boundary value problem of the REV (micro-scale) is solved directly from experimental material data (measurements), bypassing the empirical material modeling step, involving the calibration of constitutive parameters Kirchdoerfer and Ortiz (2016); Ibañez et al. (2017); Kirchdoerfer and Ortiz (2018); Ibanez et al. (2018); Eggersmann et al. (2019); Reese et al. (2019); Carrara et al. (2020). While data-driven computing can be extremely powerful in many applications Eggersmann et al. (2019); Carrara et al. (2020), the first class of methods above-mentioned (ANNs and PINNs) can be advantageous when modeling complex and abstract constitutive behaviors, which are not a priori known. Moreover, they can be used even if the auxialiary boundary value problem does not have a unique solution due to important non-linearities and bifurcation phenomena (e.g. loss of uniqueness, strain localization at the length of interest, multi-physics, runway instabilities etc.).

Inspired by the framework proposed by PINNs, we present and discuss in detail applications on constitutive modeling through Thermodynamics-based Artificial Neural Networks, in Chapter 6. Thermodynamics-based Artificial Neural Networks (TANNs) are novel ANNs whose architecture is directly encoded on the two basic laws of thermodynamics. This assures thermodynamically consistent and more accurate predictions, with respect to standard ANNs.

Part II

Modeling the response of masonry structures to blast loads

Chapter 3

Modeling rocking and overturning

Abstract. *Masonry structures subjected to blast loads may display a monolithic behavior, under some circumstances. To this purpose, we investigate herein the dynamic rigid body response and failure modes of monolithic masonry structures, modeled as inverted pendulum structures. We model blast actions using established empirical models and best-fit interpolations of existing experimental tests. We target pure rocking response mechanisms, which represent the predominant failure mode of monolithic masonry structures. Inspired by previous works in the frame of earthquake engineering, we derive new analytical, closed-form solutions for the rocking response and the overturning domain of slender blocks due to explosions. The analytical findings and assumptions are validated through existing experimental tests and detailed three-dimensional numerical simulations, which consider the full interaction between the blast waves and the structure.*
Direct damage due to the high tensile stresses is also investigated and computed for different target geometries. For the dimensions and explosive quantities herein considered, we show that unilateral rocking response and overturning are predominant mechanisms compared to sliding, up-lifting, and direct damage.
Finally, we develop design charts to be used as a straightforward decision making tool for determining the critical stand-off distance between the explosive source and the target in order to prevent overturning.

Contents

3.1 Introduction

The response and failure modes of masonry structures subjected to blast loads usually involves combinations of in-plane and out-of-plane deformations (cf. Chapter 2). Depending on the boundary conditions and structural geometry, a monolithic behavior can occur (see e.g. Fig.s 2.10 and 2.11). In this case, investigating the rigid body response (rocking, overturning, etc.) allows to highlight the predominant characteristics of a monolithic failure mode. Herein, we investigate the rocking and overturning failure mechanisms of masonry structures, modeled as inverted pendulum structures. The results can be applied to masonry structures, under low confining (compressive) stresses, such as one-spanning walls.

Our modeling approach is analytical and focuses on providing closed form solutions. The most important physics of the problem are considered in order to describe the dominant features of the rocking motion due to blast waves. This is accomplished through adequate modeling assumptions, which allow the mathematical treatment of the system and the identification of the dominant parameters that pilot the dynamic behavior and failure. Failure is defined here as the limit state where overturning (toppling) happens.

The modeling of inverted pendulum structures involves several difficulties. In particular, the inherent non-linearity and the unilateral contact conditions at the base of the inverted pendulum (rocking) make the dynamics of the system much different from the classical single- or multi-degree-of-freedom harmonic oscillators (Makris and Konstantinidis, 2003). Therefore, special treatment is needed.

The problem of rocking attracts significant scientific research, mostly in the domain of earthquake engineering (construction of bridges, seismic isolation, masonry structures, historical monuments, etc.). We refer, for instance, to the seminal works of Omori (1900, 1902) and especially to the investigations of Housner (1963), who was the first to study the response of a rigid, free-standing block subjected to constant and square pulse seismic (ground) accelerations. Zhang and Makris (2001) investigated the overturning of a rigid block under trigonometric pulses and, more recently, Voyagaki et al. (2013) studied rocking for time-symmetrical pulses of various shapes. In the same framework, Dimitrakopoulos and DeJong (2012) provided useful insight on the dynamic response of a rocking block under finite-duration actions, revisiting the subject via the identification of self-similarity laws both for slender and non-slender blocks. The rocking response of structures has been also studied experimentally (e.g. Peña et al., 2007; Konstantinidis and Makris, 2010; Bachmann et al., 2018). Peña et al. (2007) investigated through shaking table tests the rocking response under free vibration, harmonic and random motions of the base and compared the test results with analytical and numerical approaches.

Interest has been also shown in the effects of blast induced ground shocks (Merkle et al., 1993; Hao and Zhou, 2012). Hao and Zhou (2012) investigated the response of a rigid block under vertical and horizontal ground shocks. Explosion induced ground shocks are generally characterized by higher frequency content, larger amplitude, and shorter period with respect to earthquake motion. If the peak vertical ground acceleration due

to blast induced ground shocks is substantially higher than the gravitational one, unanchored rigid structures may fly into the air (uplifting). However, we record that in relatively far-field explosions the contribution of ground shocks is generally negligible with respect to the air-blast shock, see e.g. (Scherbatiuk, 2010; Scherbatiuk et al., 2008; Scherbatiuk and Rattanawangcharoen, 2008), where uplifting due to vertical ground accelerations is unlikely.

Our developments are based on the existing knowledge and theory of inverted pendulum structures subjected to earthquake loading and extend them to non-symmetrical pulses provoked by blast waves. We model blast actions using well-established empirical models accounting for both the positive and the negative phase of the blast pressure (see Sect. 1.5.1). Moment balance equations and overturning conditions are presented and used to determine the critical (minimum) stand-off distance between the source and the target to prevent toppling. This is accomplished by deriving new analytical, closed-form solutions, which lead to the identification of the central and dominant dimensionless parameters that govern the dynamical behavior of the system. These dimensional parameters improve and extend the current understanding of rocking due to blasts (cf. Merkle et al., 1993; Hao and Zhou, 2012; Scherbatiuk, 2010; Scherbatiuk et al., 2008; Scherbatiuk and Rattanawangcharoen, 2008; Custard and Thayer, 1970; Baker et al., 1975; Soper, 1967) and lead to fundamental insights for design. Moreover, they can be helpful to conceive in-scale experimental tests focusing on overturning of (slender) blocks under the loading rates under study (see Chapter 7). Notice that performing blast experiments either in reduced (Soper, 1967) or in full scale (Scherbatiuk, 2010) presents many difficulties, due to the nature of the loading action (e.g. need of specialized personnel, risks, measuring devices, repeatability, uncertainties etc.).

Contrary to earthquake actions, the excitation due to explosions presents additional complexity. This is not only because of the ultra-high rates involved−the characteristic time of a blast is of several milliseconds instead of $\approx 1 \div 10$ s for earthquakes−but also due to several phenomena related to wave propagation and fluid-structure interaction (e.g. diffraction, rarefaction, reflections, damage etc.), see Chapter 1. The effect of these phenomena on our modeling assumptions is extensively discussed in this Chapter. More specifically, the predictions of our analytical model are compared to detailed numerical analyses that consider the above mentioned phenomena, a combined sliding/rocking behavior, and the possibility of uplifting (flight mode). The numerical analyses are three-dimensional, they use the well-established balloon analogue (Blanc et al., 2018) for modeling the explosive source and they are based on a Coupled Eulerian-Langrangian (CEL) scheme for modeling the propagation of shock waves and their interaction with the rocking block (cf. Chapter 1). It is worth emphasizing that a complete three-dimensional fluid-structure interaction of shock waves with all sides of the block is considered in order to assess the validity of our modeling assumptions and simplifications. Finally, the results of our analytical model are confirmed by comparisons with existing experimental results (Soper, 1967; Scherbatiuk, 2010).

Besides failure due to overturning, direct material damage due to the development of important tensile stresses arising from the impinging blast waves can play also a crucial

role. Detailed numerical Finite Element simulations are used to investigate the critical stand-off distance related to material damage.

For the dimensions and explosive weights considered herein, both direct material damage and rocking are found to be predominant response mechanisms to blast loads (contrary to sliding and up-lifting). Overturning is found to be predominant for targets with regular geometry.

Beside masonry, direct engineering applications of the present study can be found in several domains. For instance, our analyses can be used for protecting un-anchored equipment and museum (slender) artifacts from overturning (e.g. statues), securing historical buildings made of monolithic columns from collapse (e.g. classical Greek and Roman temples, see Stefanou et al., 2011b; Casapulla et al., 2017) and for designing barriers and blast walls to protect existing buildings, assets and humans. Finally, our analysis could be used for conceiving energy absorbing systems based on rocking.

The Chapter is structured as follows. In Section 3.2 we present the main assumptions of our modeling approach regarding the dynamics of the system and the considered blast actions. Our simplifying assumptions cover a broad spectrum of loading cases. In Section 3.3 we derive analytical solutions for the non-linear rocking motion and the overturning domain, by considering only the positive phase of the blast action. Then, in Section 3.4 we assess the influence of the negative phase, which has a significant stabilizing effect as far as it concerns toppling. Detailed charts for the critical stand-off distance (i.e., the minimum distance to avoid targets overturning) are presented as a result of the analytical model. Finally, in Section 3.5 we investigate the accuracy and the validity of the main assumptions of our model through detailed numerical simulations and the limited experimental results that were retrieved from the literature.

3.2 Statement of the problem

The problem of a rigid block resting on a horizontal plane is studied based on the following assumptions (Fig. 3.1):

i. A rectangular slender, rigid block is assumed with a uniformly distributed mass m. The dimensions of the block are $2b \times 2h \times 2w$ and the radial distance from the rocking pivot point O to the center of gravity is $r = h/\cos\alpha$, where α is the slenderness angle.

ii. The contact with the horizontal plane is assumed punctual at point O (no contact moment). Contact is considered to be unilateral. The angle of friction, φ, is assumed to be sufficiently large to prevent sliding.

iii. The pressure load due to the explosion is exclusively applied on the front surface S (incident surface, see Fig. 3.1) and the blast wave is assumed to impinge all points of S at the same time (simultaneously) and with the same magnitude (uniformly). We consider the resulting load to act always horizontally and at the block's center of mass as the loading pulse duration is extremely short (i.e., small inclination angle within the duration of the loading). Diffraction phenomena are neglected. The effects of induced ground shocks are also omitted (Hao and Zhou, 2012; Scherbatiuk

and Rattanawangcharoen, 2008).

These simplifying assumptions are helpful for reducing the complexity of the problem and for deriving analytical, closed-form solutions. Their adequacy is explored in Section 3.5, where it is shown that the analytical solution represents quite well the dynamic behavior of the system and the overturning condition. In particular, it is shown that the minimum distance that has to be assured between the explosive source and the target, such that toppling is avoided, is in good agreement and on the safety side with the one determined by the full numerical model and experimental results presented in Section 3.5.

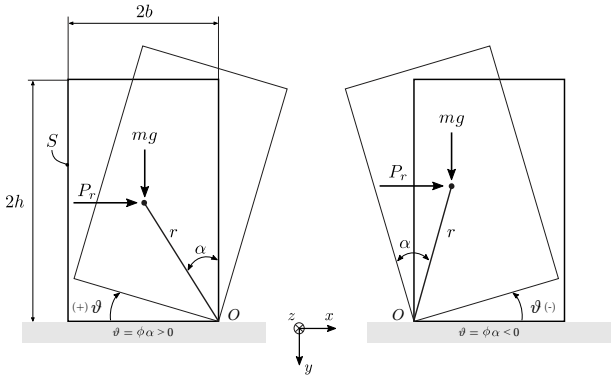

Figure 3.1 – Configuration considered for the rocking problem: a rectangular slender, rigid block resting on a horizontal plane with uniformly distributed mass, subjected to uniform pressure load due to an explosion.

3.2.1 Rocking motion

Depending on the characteristics of the excitation and the properties of the friction angle, the rigid block can either slide, rock, or both. As far as it concerns the response mechanisms of pure rocking and sliding, the corresponding initiation conditions can be found from rotational and transnational equilibria, respectively.

– *Rocking initiation.* Rocking initiates if the moment due to blast actions exceeds the restoring moment due to gravity. The initiation condition reads

$$\frac{S}{mg} P_{ro} \geq \tan \alpha, \tag{3.1}$$

where P_{ro} is the overpressure peak acting on block's front surface S (see below), and g is the gravitational acceleration.

– *Sliding initiation.* Sliding initiates when

$$\frac{S}{mg} P_{ro} \geq \tan \varphi. \tag{3.2}$$

For relatively slender blocks, i.e. $\alpha \leq 20°$, which are of interest here, and for an angle of friction $\varphi \approx 30°$−typical value for marble to marble interfaces, see for instance Papadopoulos et al. (1998)−, rocking initiation is critical.

3.3 Rocking response to an explosion

First we solely account for the positive phase using the empirical relation of Friedlander (cf. Chapter 1 and paragraph 1.5.1.1). The negative phase is expected to have a stabilizing effect on the rocking response and, therefore, its influence is studied separately in the next section. In all cases, the explosive source is considered to be (very) close to the ground (surface burst).

3.3.1 Equation of motion

The moment balance around the rocking pivot point gives the equation of motion

$$\begin{cases} \mathscr{I}_o\ddot{\theta} + mgr\sin(\alpha-\theta) = SrP_r\cos(\alpha-\theta), & \theta(t) > 0, \\ \mathscr{I}_o\ddot{\theta} + mgr\sin(-\alpha-\theta) = SrP_r\cos(-\alpha-\theta), & \theta(t) < 0, \end{cases} \tag{3.3}$$

where $\mathscr{I}_o = (4/3)mr^2$ is the moment of inertia with respect to the pivot point, $\theta = \theta(t)$ is the inclination angle, and $P_r = P_{r+}(t)$ is the loading which is given by the Friedlander equation (1.18) as mentioned above. Introducing the frequency parameter q, and the load parameter, s, the above equations can be rearranged into

$$\frac{\ddot{\theta}}{q^2} = -\sin\left[\alpha\,\mathrm{sgn}\left(\theta\right) - \theta\right] + \frac{s^2}{q^2}P_{ro}\,p\cos\left[\alpha\,\mathrm{sgn}\left(\theta\right) - \theta\right], \tag{3.4}$$

where $\mathrm{sgn}(\cdot)$ denotes the signum function and

$$\begin{aligned} q &= \sqrt{\frac{mgr}{\mathscr{I}_o}} = \sqrt{\frac{3g}{4r}}, \\ s &= \sqrt{\frac{Sr}{\mathscr{I}_o}} = \frac{1}{2}\sqrt{\frac{3}{2b\rho r}}, \\ p &= \frac{P_r}{P_{ro}}, \end{aligned} \tag{3.5}$$

with ρ the material density.

3.3.1.1 Dimensionless form of governing equations

Using the dimensionless angle of rotation $\phi = \theta/\alpha$ and the normalized time $\tau = qt$ we obtain

$$\ddot{\phi} = -\frac{1}{\alpha}\sin\left[\alpha\left(\mathrm{sgn}\left(\phi\right) - \phi\right)\right] + \chi\,p\,\cos\left[\alpha\left(\mathrm{sgn}\left(\phi\right) - \phi\right)\right], \tag{3.6}$$

where χ represents the normalized rocking moment, i.e., the ratio between the moment due to the blast load and the restoring moment due to gravity, p_+ the normalized Friedlander time-history, and τ_o the ratio between the characteristic time of the load and the time parameter, T, related to the response of the rigid block:

$$\begin{aligned} \chi &= \frac{s^2}{q^2}\frac{P_{ro}}{\alpha} = \frac{1}{2\rho bg}\frac{P_{ro}}{\alpha}, \\ p_+ &= \left[\left(1-\frac{\tau}{\tau_o}\right)\left(1-\mathscr{H}[\tau-\tau_o]\right)\right]e^{-d\frac{\tau}{\tau_o}}, \\ \tau_o &= qt_o = \frac{t_o}{T}. \end{aligned} \tag{3.7}$$

3.3.1.2 Analytical solution for slender blocks

For tall, slender blocks, angles θ and α are small and the equation of motion (3.6) can be linearized using the first-order approximations $\sin(\cdot) \cong \cdot$ and $\cos(\cdot) \cong 1$

$$\ddot{\phi} = \phi + \chi\, p_+ - \mathrm{sgn}(\phi). \tag{3.8}$$

Notice that under this normalization the rocking initiation condition, Eq. (3.1), simply reads $\chi \geq 1$.

As the load is acting always on the same direction (positive), a unilateral response mechanism is expected. Here we focus on overturning, thus we restrict expression (3.8) to positive angles only,

$$\ddot{\phi} = \phi + \chi\, p_+ - 1. \tag{3.9}$$

Initially the block is at rest ($\dot{\phi}(0) = 0$, $\phi(0) = 0$). Equation (3.9) admits a close form solution, whose complete mathematical expression is given in Appendix B.
Notice that the characteristic time parameter, T, of blocks of centimetric scale or larger,

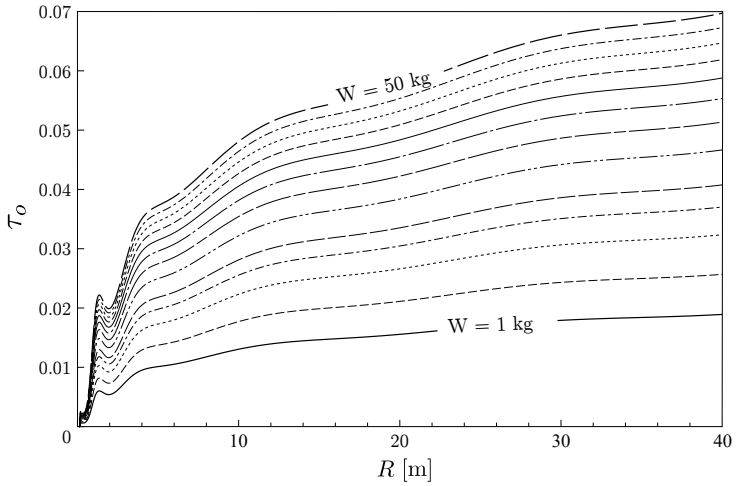

Figure 3.2 – Normalized time, $\tau_o = t_o/T$ in function of the stand-off distance, R, for different explosive quantities, W, in equivalent TNT weight. The ratio between the characteristic time of the blast load, t_o, and the time parameter, T, related to the dynamic, rocking, response of the rigid block is small for blocks of centrimetric scale or larger.

is much higher than the characteristic time of blast loads t_o and, therefore, $\tau_o << 1$. Figure 3.2 shows τ_o with respect to the explosive weight, W, and the stand-off distance, R. For instance, if we consider $h = 1$ m, 1 kg of TNT and a stand-off distance $R = 10$ m, $\tau_o \approx 0.01$, i.e., the positive phase duration, t_o, is two orders of magnitude smaller than T. Indeed, a $\tau \approx 1$ for the same values of W and R would actually correspond to a block with a height of ≈ 0.33 mm, which is too small for the applications that we focus on in the current Thesis.

3.3.2 Overturning domain

For unilateral excitations, overturning happens when the rocking angle $\theta \geq \alpha$ or, equivalently, when $\phi \geq 1$. The overturning condition can be found by equating the total work done by the blast load to the difference in potential energy between positions $\theta = \alpha$ and $\theta = 0$ (see also Housner, 1963):

$$\int_0^{\infty} rSP_{ro}\, p\, \dot{\theta} \cos\left(\alpha - \theta\right)\, dt \geq mgr(1 - \cos\alpha). \tag{3.10}$$

Noticing that $p\,(t \geq t_o) = 0$ and rearranging the inequality in terms of the non-dimensional rocking angle and normalized time, one obtains

$$\alpha r SP_{ro} \int_0^{\tau_o} p_+ \dot{\phi} \cos\left[\alpha(1-\phi)\right]\, d\tau \geq mgr(1 - \cos\alpha). \tag{3.11}$$

Applying further the mean-value theorem, Eq. (3.11) becomes

$$\begin{aligned} &\frac{\alpha^2 \cos\left[\alpha(1-\tilde{\phi})\right]}{1-\cos\alpha}\, I\chi \geq 1, \\ &I = \int_0^{\tau_o} p_+\, \dot{\phi}\, d\tau, \end{aligned} \tag{3.12}$$

where $0 < \tilde{\phi} \leq 1$.

For slender blocks, the power series expansion at the first order gives $\frac{\alpha^2 \cos\left[\alpha(1-\tilde{\phi})\right]}{1-\cos\alpha} \cong 2$, hence the overturning condition simply becomes

$$2I\chi \geq 1, \tag{3.13}$$

The left-hand side term in inequality (3.13) represents the non-dimensional overturning moment.

Figure 3.3 shows the dimensionless rocking and overturning moments as functions of the stand-off distance, R, for an explosion of 1 kg of TNT. The rocking moment, χ, expresses the condition for rocking initiation ($\chi \geq 1$), while the overturning moment the condition for overturning ($2I\chi \geq 1$). We observe that the minimum stand-off distance to avoid overturning is 0.6 m. For $R \geq 35$ m, rocking is not initiated at all.

It is worth comparing the overturning condition from the linearized equations of motion with the one from the non-linear ones. Taking the ratio between the non-dimensional overturning moments in expression (3.12) and (3.13) and further considering angles $\alpha \leq 20°$, we obtain

$$\frac{\text{non-linear overturning condition}}{\text{linear overturning condition}} = 1 - \frac{1}{2}\left[\alpha\left(1-\tilde{\phi}\right)\right]^2 \leq 1. \tag{3.14}$$

Therefore, the linearized overturning condition is a lower bound of the *exact* one. The ratio is usually higher than 0.95 for blocks with $\alpha \leq 20°$ and does not drop under 0.80 for $\alpha < 40°$ (see also Voyagaki et al., 2013).

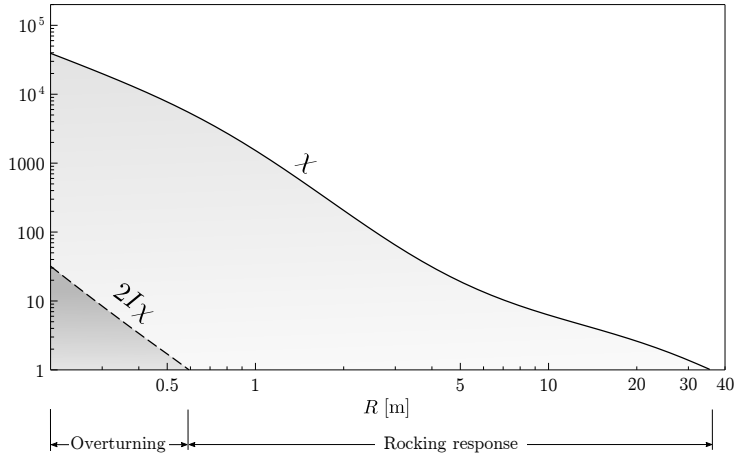

Figure 3.3 – Rocking initiation and overturning conditions for a block with $h = 1$ m, $\rho = 2000$ kg/m^3, and $\alpha = 20°$, subjected to $W = 1$ kg at various stand-off distances, R. The rocking moment, χ, expresses the condition for rocking initiation ($\chi \geq 1$), while the overturning moment the condition for overturning ($2I\chi \geq 1$).

3.3.3 Minimum stand-off distance

Using the overturning condition ($2I\chi = 1$) we can determine the minimum required distance between the explosive source and the target, $R^\sharp$, in order to avoid toppling. Figure 3.4 shows the contours of the critical distance $R^\sharp$ for different slenderness angles, block heights, densities, and explosive quantities.

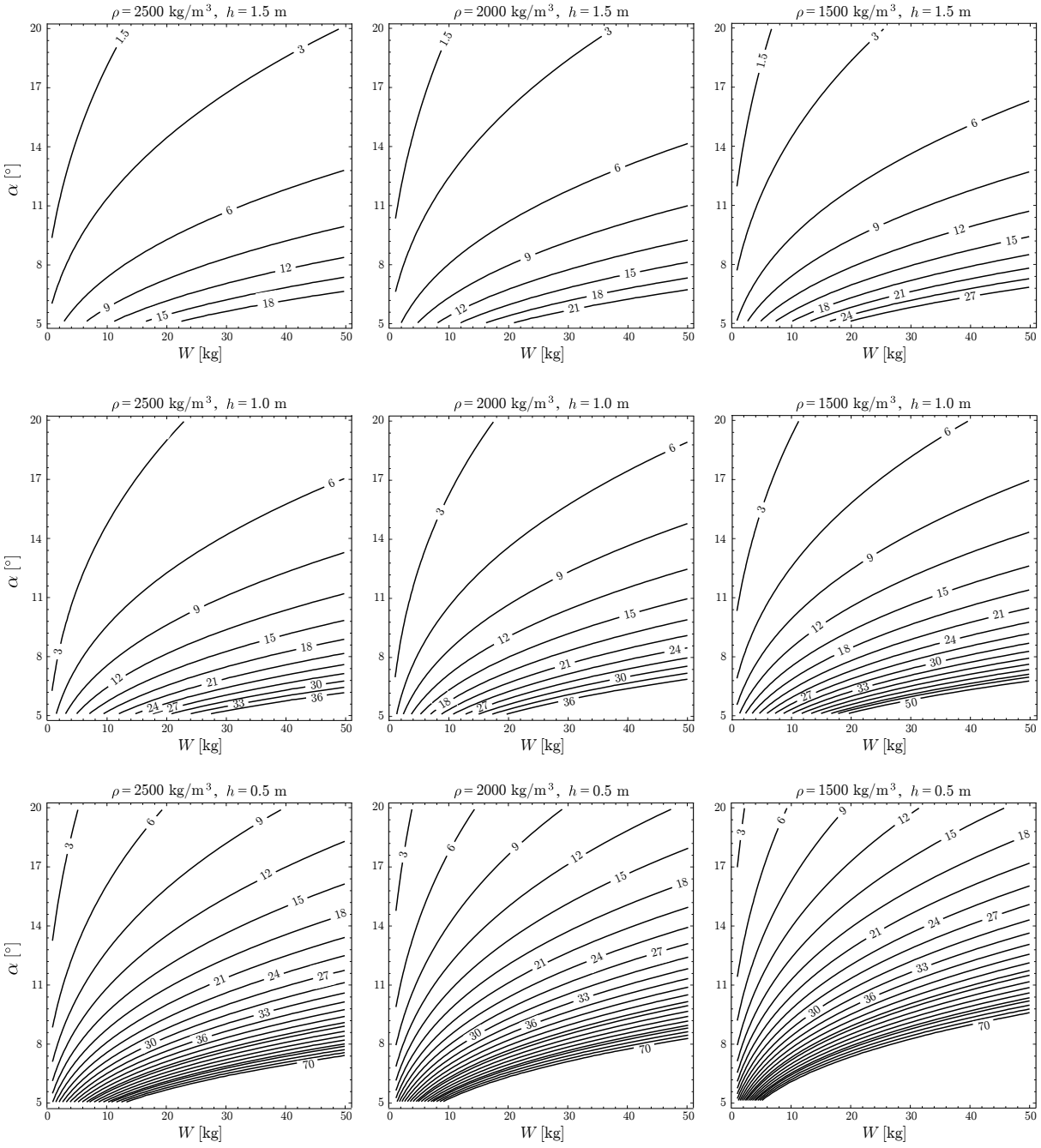

Figure 3.4 – Contours of the critical stand-off distance, i.e., the minimum required distance between the explosive source and the rigid target, $R^\sharp$, in order to avoid toppling. For $\rho = 2500$ (left column), 2000 (center column), 1500 kg/m^3 (right column), heights $h = 1.5$ (top row), 1.0 (center row), 0.5 m (bottom row), $R^\sharp$ is plotted as a function of the explosive quantity, W, and slenderness, α.

3.4 Influence of the negative phase

In this Section we explore the influence of the negative phase on the response mechanisms and the overturning criterion. We represent the positive phase with Friedlander equation, as above, but in this case the negative phase is also considered (cf. Chapter 1 and paragraph 1.5.1.2).

Equations (3.6) and (3.9) become respectively

$$\ddot{\phi} = -\frac{1}{\alpha}\tan\left[\alpha\left(\operatorname{sgn}(\phi) - \phi\right)\right] + \chi\, p_+ - \bar{\chi}\, p_-, \tag{3.15}$$

and

$$\ddot{\phi} = \phi + \chi\, p_+ - \bar{\chi}\, p_- - \operatorname{sgn}(\phi). \tag{3.16}$$

$\bar{\chi}$ is the dimensionless blast stabilizing moment, i.e., a negative pressure component, which has a restoring role, p_- the normalized negative time-history, and τ_{o-} the ratio between the characteristic time of the negative phase and the time parameter of the rigid block:

$$\begin{aligned}
&\bar{\chi} = \frac{s^2}{q^2}\frac{P_{ro-}}{\alpha},\\
&p_- = \left(\frac{27}{4}\frac{\tau-\tau_o}{\tau_{o-}}\right)\left(1-\frac{\tau-\tau_o}{\tau_{o-}}\right)^2\Big(\mathscr{H}[\tau-\tau_o] - \mathscr{H}[\tau-(\tau_o+\tau_{o-})]\Big),\\
&\tau_{o-} = q t_{o-} = \frac{t_{o-}}{T}.
\end{aligned} \tag{3.17}$$

Equation (3.16) admits a closed-form solution under the assumption of small slenderness angles. The solutions ϕ, $\dot{\phi}$ are given in Appendix B.

The negative phase plays a significant role on the response mechanism. In Figure 3.5 we present the angular displacement and velocity as solutions of Eq.s (3.8) and (3.16). Perfectly plastic impact is considered. The plots display the response due to a 10 kg TNT explosive charge at varying stand-off distance and for a block with $\alpha = 15°$, $\rho = 2000$ kg/m^3 and $h = 1$ m. The negative phase clearly limits the amplitude of the rocking angle since the suction, negative component of the blast load acts as a restoring moment, see Eq. (3.15).

Figures 3.6 and 3.7 depict the trajectories $(\phi, \dot{\phi})$ in the phase space. The phase portraits highlight the pulse nature of blast loads. Notice that the duration of the positive phase, t_o, is extremely short and in some cases it may be replaced by an instantaneous increment of the angular velocity $\dot{\phi}$ at $\phi = 0$, as suggested in Scherbatiuk (2010).
Figure 3.7 shows the important role of the negative phase, which decreases the angular velocity $\dot{\phi}$ and stabilizes the system. Contrary to the positive phase, the negative one can be hardly simplified by a jump discontinuity of $\dot{\phi}$.

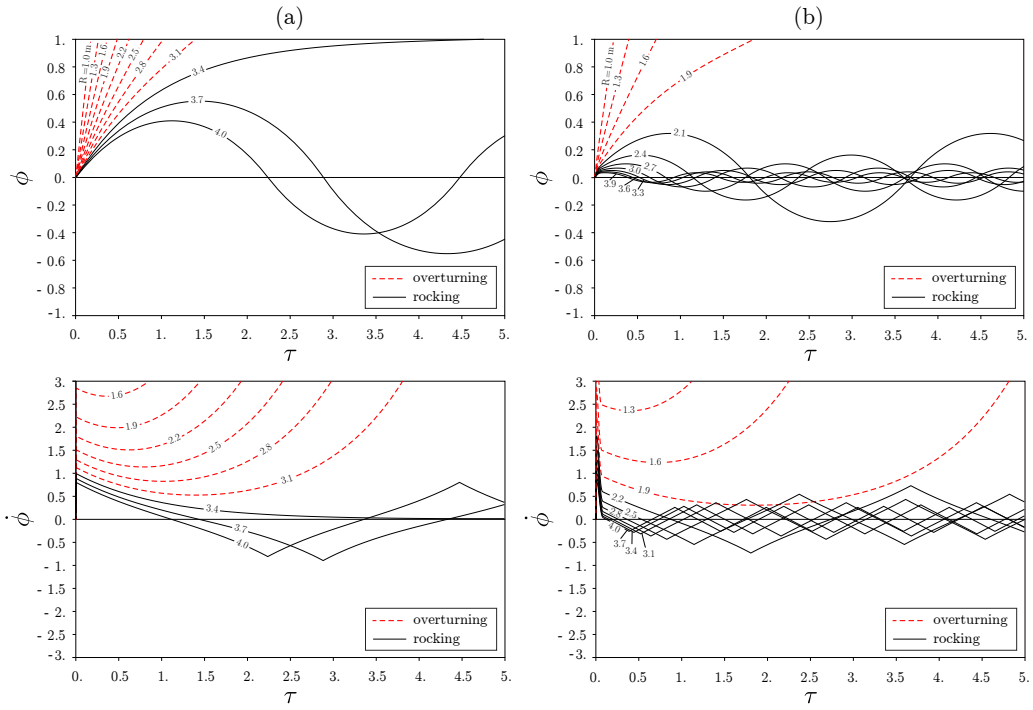

Figure 3.5 – Normalized inclination angle, ϕ, and angular velocity, $\dot{\phi}$, of the rocking block considering (a) only the positive phase of the blast wave, Eq. (3.8), and (b) accounting for both positive and negative blast phases, Eq. (3.16). The plots refer to a TNT explosive weight $W = 10$ kg and a rigid target with $\alpha = 15°$, $h = 1$ m, $\rho = 2000$ kg/m^3, for stand-off distances $R \in [1, 4]$ m. Red dashed curves indicate overturning.

3.4.1 Overturning domain and minimum stand-off distance

The overturning condition can be written taking advantage of Eq. (3.10) and updating the work done by the external loads in order to consider the negative phase, as follows

$$\frac{\alpha^2 \cos\left[\alpha(1-\tilde{\phi})\right]}{1-\cos\alpha}\left(I\chi - \bar{I}\bar{\chi}\right) \geq 1, \tag{3.18}$$

where

$$I = \int_0^{\tau_o} p_+ \,\dot{\phi}\, d\tau \quad \text{and} \quad \bar{I} = \int_{\tau_o}^{\tau_o+\tau_{o_-}} p_- \,\dot{\phi}\, d\tau, \tag{3.19}$$

For slender blocks, equation (3.19) is simplified to

$$2\left(I\chi - \bar{I}\bar{\chi}\right) \geq 1. \tag{3.20}$$

The required minimum distance between an explosive source W and a block in order to avoid toppling, is here denoted with $R^\natural$ and is retrieved by setting $(2\left(I\chi + \bar{I}\bar{\chi}\right) = 1)$. In Figure 3.8 we present the contours of the critical stand-off distance $R^\natural$, for different values of ρ, h, W and α. It should be emphasized that the negative phase *de novo* engenders a considerable stabilizing effect.

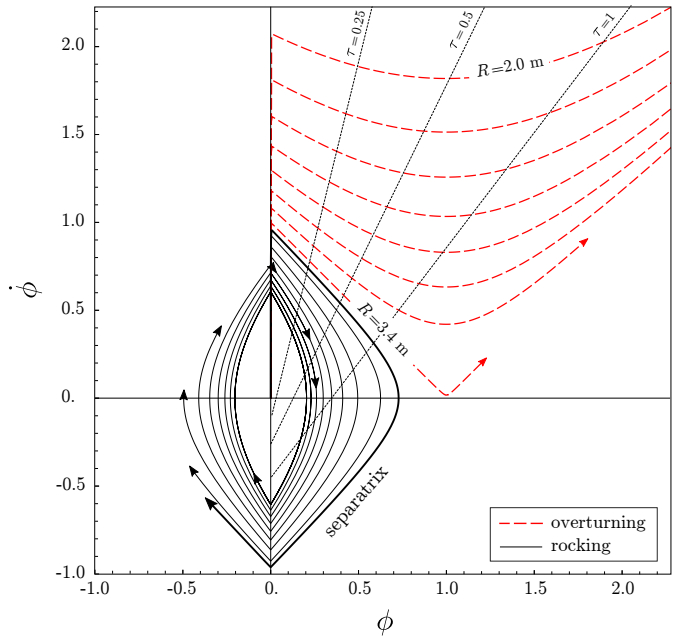

Figure 3.6 – Phase space $(\phi, \dot{\phi})$ considering only the blast positive phase. In this plot, the TNT explosive weight is $W = 10$ kg and the rigid target has $\alpha = 15°$, $h = 1$ m, $\rho = 2000$ kg/m^3. Different values of the stand-off distance are considered, $R \in [2, 5]$ m. Red dashed curves correspond to overturning. Dotted lines represent contours of the dimensionless time, τ_o.

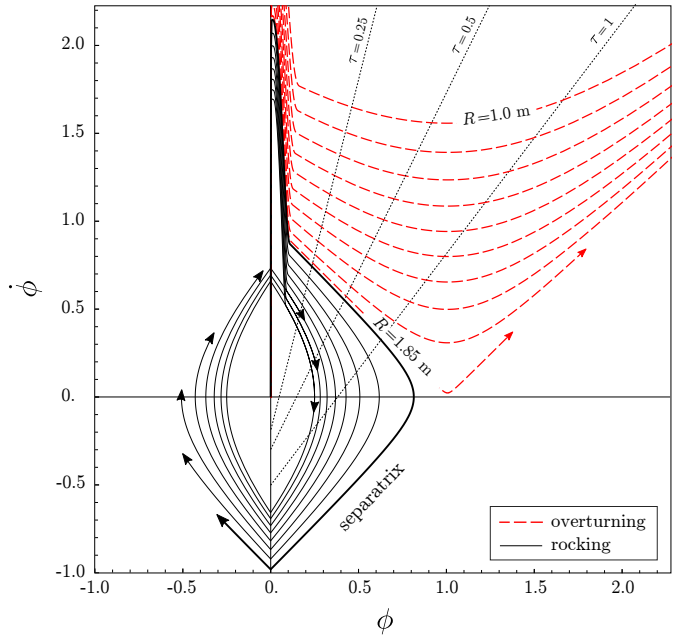

Figure 3.7 – Phase space $(\phi, \dot{\phi})$ considering both the blast positive and negative phase, see Eq. (3.16). The TNT explosive weight is $W = 10$ kg and the rigid target has $\alpha = 15°$, $h = 1$ m, $\rho = 2000$ kg/m^3. Different values of the stand-off distance are considered, $R \in [1.5, 2.3]$ m. Red dashed curves correspond to overturning. Dotted lines represent contours of the dimensionless time, τ_o.

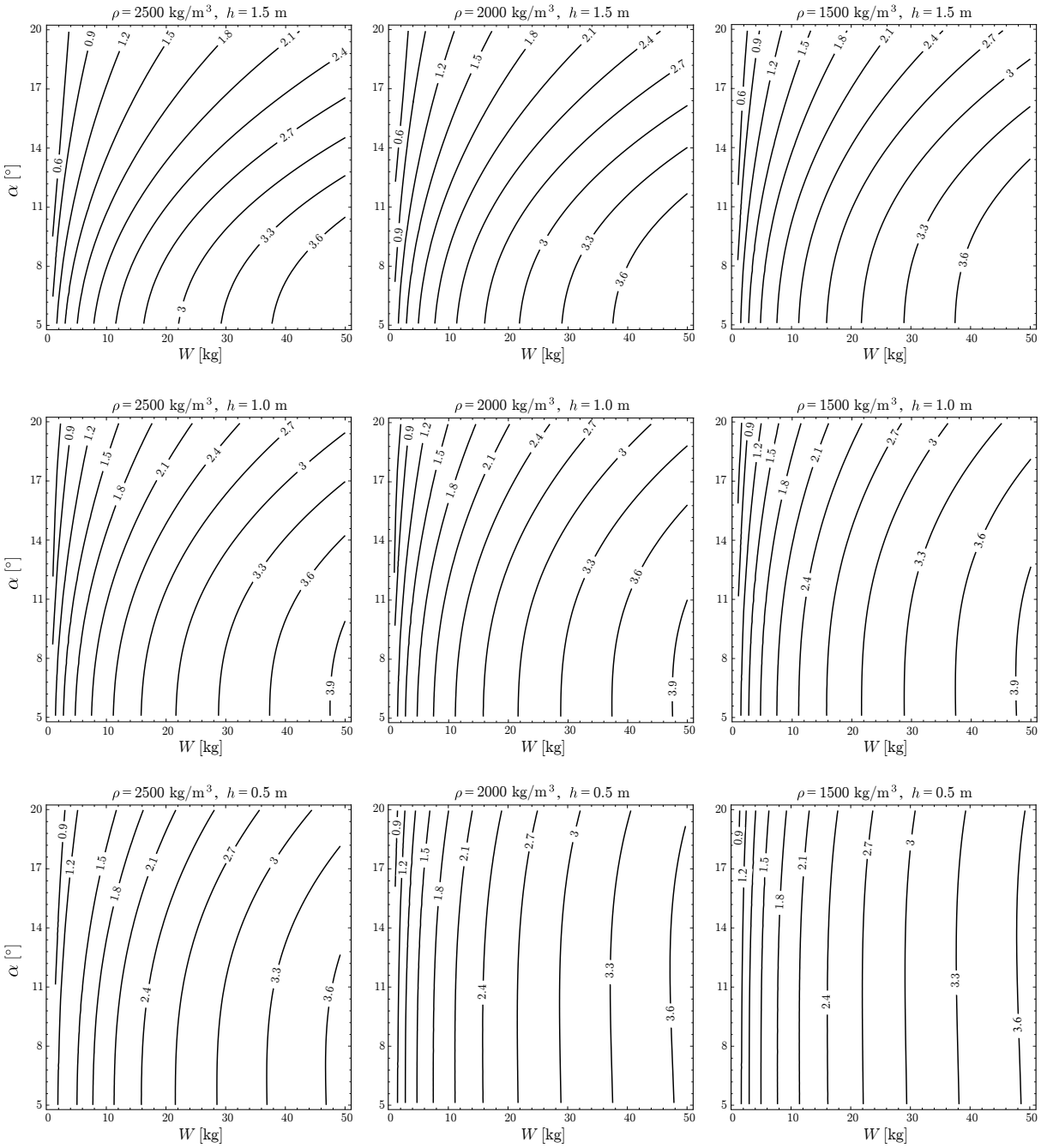

Figure 3.8 – Contours of the critical stand-off distance, i.e., the minimum required distance between the explosive source and the rigid target, $R^{\natural}$, in order to avoid toppling. The effect of both positive and negative phases of the blast wave is considered. For $\rho = 2500$ (left column), 2000 (center column), 1500 kg/m^3 (right column), heights $h = 1.5$ (top row), 1.0 (center row), 0.5 m (bottom row), $R^{\natural}$ is plotted as a function of the explosive quantity, W, and slenderness, α. The negative phase has a significant stabilizing effect (see also Fig. 3.4).

3.5 Validation of the overturning domain

The analytical approach presented in the previous Sections allowed to determine the minimum stand-off distance to prevent toppling. The calculations lead to closed-form solutions, which are useful for identifying the main factors that influence the dynamic response of the system under explosive loads. However, the aforementioned approach is based on some simplifying assumptions (see Sect. 3.2), whose validity is explored in the present Section.

Of interest here is the minimum stand-off distance, which is a central design quantity for protective measures. This quantity is first validated through numerical analyses that introduce more physics into the blast wave loading, its interaction with the rocking block, and the full dynamic response of the system. Next, the predictions of our analytical model are validated through available experimental results.

First we explore the validity of assumptions (i) and (ii) of Section 3.2. In other words, we quantify a) the linearization of the equations of motion (see also paragraph 3.3.2), and b) the effect of combined sliding, rocking, and uplift (flight mode). We consider Coulomb friction at the interface of the block with the rigid base, with an angle of friction equal to $\varphi = 35°$, which is common for many geomaterials (concrete, marble, stone etc.). Blast loads are applied as in Section 3.4, relying on the best-fit interpolations in Appendix A. ABAQUS commercial software is used for the computations. A *hard* contact formulation is used, i.e., no penetration is allowed at the contact of the rocking block with the base (ABAQUS, 2018). The rigid base is fixed and the rigid block is free to translate along $y-$ and $x-$axes, rotate around z, and uplift, see Figure 3.1.

It should be mentioned that our analyses are made only for rigid blocks. In the case of deformable ones, where significant dissipation is expected due to, for instance, deformability and damage, our model might underestimate the resistance of the system to overturning that allow to be on the safety side.

Next, we focus on assumption (iii) which concerns the simplifications related to the blast loads and their approximation by empirical models. In particular, we investigate the effects due to the interaction between blast waves and the rocking block. The analyses are performed again using ABAQUS FE software. The same modeling approach is used for the interaction of the block and the base as before. The results of this comparison are presented in paragraph 3.5.2, *Comparison C2*.

Finally, we validate our model with existing experimental tests of quasi-rigid (stiff) (Soper, 1967) and deformable targets (Scherbatiuk, 2010) subjected to explosions. Both the overturning domain and the rocking response are compared with large-scale tests. This comparison allows us to explore the validity of our assumptions in general and, in particular, to assess the effects of explosion induced ground motions (Scherbatiuk and Rattanawangcharoen, 2008; Hao and Zhou, 2012), which the above mentioned numerical model does not account for. In accordance with (Scherbatiuk and Rattanawangcharoen, 2008), the aforementioned ground motions were found to have negligible effects. The results are presented in paragraph 3.5.3, *Comparison C3*.

3.5. Validation of the overturning domain

3.5.1 Comparison C1

We investigate the minimum stand-off distance ($R^{\natural}_{num}$) for several combinations of slenderness angles and explosive weights. Figure 3.9 depicts the response of the rigid block, while Table 3.1 displays the comparison between the threshold range ($R^{\natural}$), derived in Section 3.4, and the one obtained from the numerical simulations ($R^{\natural}_{num}$). Finally, in Figure 3.10 we present the ratio $R^{\natural}_{num}/R^{\natural}$ as function of W.

The numerical analyses show that rocking and sliding happen together. However, for slender structures sliding is limited and rocking prevails. This justifies the no-sliding assumption. For blocks of high slenderness, sliding becomes even smaller and practically only rocking is observed. For blocks of lower slenderness, sliding has a more important effect and becomes more pronounced for increasing explosive weights. In the worst case studied here ($W = 50$ kg and $\alpha = 20°$) the analytical approximation overestimates the minimum stand-off distance by approximately 25%. This is due to the the fact that by increasing W, the duration of the positive phase increases (see Fig.s 3.2) enhancing sliding and frictional energy dissipation (toppling is less favorable due to low slenderness). Consequently, our analytical estimation provides a close upper bound for the critical distance and, therefore, can be safely used for the design of protective measures.

Table 3.1 – Comparison of the overturning domain between the analytical solution, $R^{\natural}$, and the numerical one, $R^{\natural}_{num}$. The rocking block has $h = 1$ m, $\rho = 2000$ kg/m^3, and variable slenderness angle α. Different weights of TNT, W, are considered. Good agreement is found, being always on the safety side.

		$\alpha = 20°$			$\alpha = 15°$			$\alpha = 10°$		
W	(kg)	10	20	50	10	20	50	10	20	50
t_o	(ms)	1.292	1.744	2.422	2.499	2.991	3.507	3.728	3.873	4.01
$R^{\natural}$	(m)	1.51	2.10	3.18	1.88	2.53	3.67	2.21	2.84	3.93
$R^{\natural}_{num}$	(m)	1.40	1.75	2.40	1.85	2.35	3.15	2.20	2.80	3.15
$\frac{R^{\natural}_{num}}{R^{\natural}}$		0.9283	0.8373	0.7547	0.9831	0.9282	0.8580	0.9965	0.9919	0.9899

3.5.2 Comparison C2

We account for three-dimensional fluid-structure interactions (FSI) with a CEL approach (cf. Chapter 1): the balloon analogue models the explosive source and air is assumed as an ideal gas. The material parameters for the constitutive laws of the balloon are those detailed in Blanc et al. (2018) (p. 645, model #6). Figure 3.11 displays the geometry of the whole domain. We impose symmetry along the $x - y$ plane and non-reflecting boundary conditions at the other faces. To ensure mesh convergence, the Eulerian domain is discretized with 8-node linear hexahedral elements of approximately $10 \times 10 \times 10$ mm^3 size. The solid block is discretized with rigid (non-deformable) elements which have the same size with the Eulerian mesh elements in order to assure a proper description of the fluid-structure interaction (mesh compatibility). For more details, we refer to (Masi et al., 2018b).

The numerical analyses account for diffraction and rarefaction phenomena, multiple

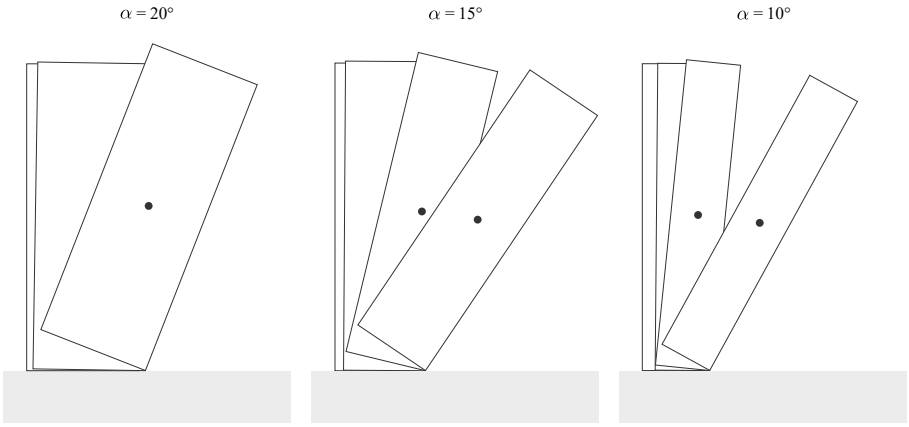

Figure 3.9 – Response mechanism as computed by numerical simulations considering an empirical model for blast actions and allowing for sliding, rocking and uplift. The explosive quantity considered is $W = 10$ kg. The rocking block has $h = 1$ m, $\rho = 2000$ kg/m^3 and slenderness angle α equal to 20° (left), 15° (center) and 10° (right). Overturning is observed with limited sliding.

reflections, no-normal incident angle of the blast waves with all the faces of the rocking block, and the three-dimensionality of the shock front. For example, due to diffraction, a rarefaction wave is developed when the shock front arrives at the boundaries of the impinged surface, while the diffracted wave continues to propagate on the rear surface. These effects result in an overall reduction of the blast impulse with respect to the analytical model. Nevertheless, this reduction is small.

The detailed numerical analyses showed limited uplifting even for combinations of stand-off distance and explosive weight close to the critical ones. Therefore, the hypothesis of neglecting uplifting (flight modes) is justified and pertinent.

Despite the aforementioned phenomena that our simplified approach neglects, a remarkably good agreement of the numerical results with the analytical model is found. Table 3.2 presents the critical distance, as obtained from the numerical simulations, $R^{\natural}_{FSI}$, for slenderness $\alpha = 15°$ and $W = 10$, 20, 50 kg. In Figure 3.12, we plot the ratio $R^{\natural}_{FSI}/R^{\natural}$ as function of W and we compare it with the one of C1 ($R^{\natural}_{num}/R^{\natural}$). An opposite trend is observed for increasing W. More specifically, the error of the simplified model is higher for small values of W and lower for large W. This difference is attributed to the aforementioned complex phenomena and depends on the geometry of the rocking object (cf. statues). Nevertheless, our simplified solution gives a safe estimate for the critical stand-off distance (upper bond) that it is close to the one derived from the detailed analysis. This means that the most important physics of the system are incorporated in our model and justifies the assumptions made in Section 3.2.

3.5.3 Comparison C3

We investigate the reliability of the analytical model in predicting the rocking response and overturning of targets on the basis of the experimental tests conducted by Soper (1967) and Scherbatiuk (2010).

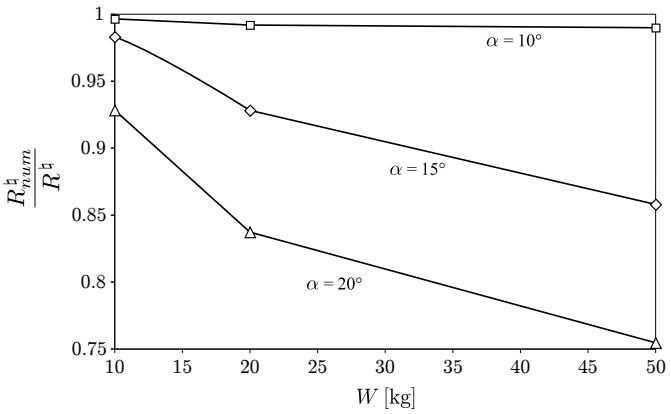

Figure 3.10 – Ratio of the numerical overturning domain, $R^{\natural}_{num}$, and the analytical one, $R^{\natural}$, (cf. Tab. 3.1). The rocking block has $h = 1$ m, $\rho = 2000$ kg/m^3 and variable slenderness angle α. Good agreement is found between the analytical model and the detailed numerical one. In the worst case study, the analytical model overestimates the minimum stand-off distance by approximately 25% (safety side).

Table 3.2 – Comparison of the overturning domain between the analytical solution, $R^{\natural}$, and the numerical one, $R^{\natural}_{FSI}$. The rocking block has $h = 1$ m, $\rho = 2000$ kg/m^3, and slenderness angle $\alpha = 15°$. Different weights of TNT, W, are considered. Again, good agreement is found, justifying the simplifying assumptions of the analytical model, which gives close upper bound estimates for the critical stand-off distance.

		$\alpha = 15°$		
W	(kg)	10	20	50
$R^{\natural}$	(m)	1.88	2.53	3.67
$R^{\natural}_{num}$	(m)	1.50	2.25	3.35
$\frac{R^{\natural}_{num}}{R^{\natural}}$		0.7978	0.8893	0.9128

3.5.3.1 Soper's experimental tests

Soper Baker et al. (see also 1991) conducted tests of a prototype ten-wheel van subjected to the detonation of 226.8 kg (500 lb) TNT equivalent charge at a distance equal to 10.7 m (35 ft). Soper further examined a scaled model in which the geometry of the specimen, as well as the stand-off distance, were reduced by a factor of 20, requiring the invariance of the scaled distance Z. Notice that in Chapter 7 we propose novel scaling laws, substantially differing from those used in Baker et al. (1991). Table 3.3 presents the overall dimensions of the targets. Subscripts p and m refer to the prototype and the scaled model, respectively.

In both tests, the target showed a combined sliding/rocking response and overturned. However, no information is available about the time evolution of the rocking response in

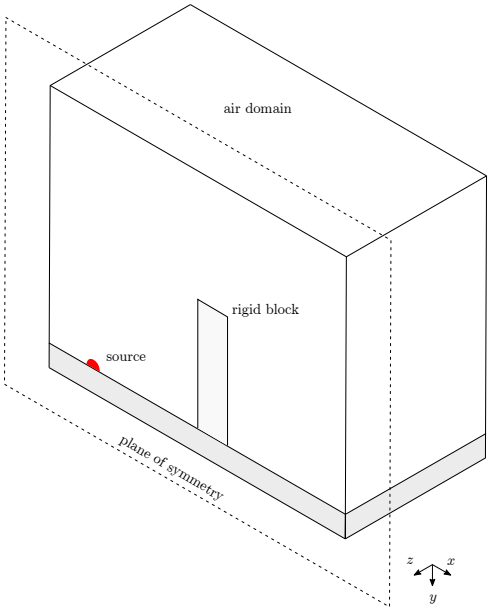

Figure 3.11 – Geometrical domain used in the Finite Element numerical simulations, which consider three-dimensional Fluid-Structure Interaction between the target (in gray) and the blast waves originated by the detonation of the explosive source (in red).

the experiments.

To compare our model, we consider a homogeneous rigid block with overall dimensions equal to those of the experiment (see Tab. 3.3) and same weight, imposing an equivalent density for the different widths (here denoted with subscripts f and b for front and back width, respectively). It is with no doubt that this is a strong simplification as a) we neglect the vehicle's suspensions and b) we consider the geometric center instead of the center of mass of the van, which is lower due to the presence of the engine, the car shaft and the chassis. The latter assumption is justified by the fact that even though a lower center of mass results in a decrease of the slenderness, the applied overturning moment due to the blast loading is higher (surface S remains unchanged, see Fig. 3.1), which counterbalances the effect of the lower mass center (see Tab. 3.3).

The analytical model predicts for the prototype a critical stand-off distance $R^{\natural}_{fp} = 11.82$ m, considering the block's width equal to the van's front width, and $R^{\natural}_{bp} = 11.85$ m, for the back width.

For the scaled model, we obtain $R^{\natural}_{fm} = 1.072$ m and $R^{\natural}_{bm} = 1.073$ m, leading to overturning as in the experimental tests.

3.5.3.2 Scherbatiuk's experimental tests

Scherbatiuk (2010) investigated experimentally the response under explosive loads of free-standing soil-filled containers, see Figure 3.13. He also developed two models for studying the rocking behavior of the aforementioned soil-filled containers. The first one is a rocking rigid-body model, where the blast loading is considered only through an initial angular velocity applied at the block, while the second, called *rigid-body hybrid*

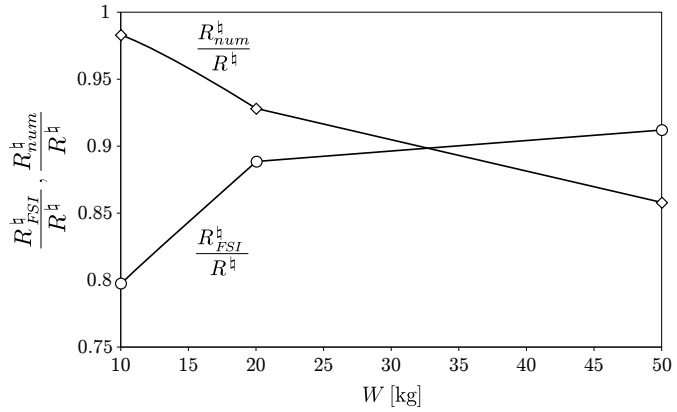

Figure 3.12 – Ratio of the numerical overturning domains, $R^{\natural}_{num}$ and $R^{\natural}_{FSI}$, and the analytical one, $R^{\natural}$, for a rocking block with $h = 1$ m, $\rho = 2000$ kg/m^3, and slenderness $\alpha = 15°$. Different weights of TNT, W, are considered and good agreement is found. The analytical solution provides safe estimates, with a maximum difference of 20%

model, goes further by accounting for the local deformation of the block at its pivot point. Both rigid and hybrid models were developed for non-slender structures (non-linearization of the equation of motion) and they were integrated numerically in order to assess overturning. The numerical results were compared then with full-scale experiments. Here we refer only to trials 1, 4, and 6 (see Scherbatiuk, 2010), as the rest were for blocks with high slenderness angles ($\alpha \approx 58°$), whose study exceeds the scope of the present work.

(a) (b)

Figure 3.13 – Free-standing soil-filled containers from Scherbatiuk (2010): (a) experimental set-up and (b) overturning of the target.

In Table 3.4 we compare the predictions of our model with the ones from Scherbatiuk (2010) and the experimental results as far it concerns overturning. We recall that our model does not account for the deformability of the blocks tested and, therefore, it ignores the energy dissipation due to damage at the incident surface and the deformation of the block at the pivot point. Therefore, we expect to overestimate the overturning domain, which results in a safety factor for applications and design. Moreover, our analytical model is valid only for slender blocks (i.e., $\alpha \lessapprox 20°$), while the targets in trials 1, 4, and 6 have a slenderness angle $\alpha = 31.61°$. This means that our predictions underestimate

Table 3.3 – Geometric parameters, explosive, and stand-off distance for the prototype and scaled model in (Soper, 1967), and corresponding parameters for the analytical model. Subscripts p and m refer to the prototype and the model test, respectively. Subscript f indicates that the rectangular rigid model has a width equal to the front width of the van, and subscript b to the back. Good agreement is found regarding overturning.

Experimental test							
Prototype				Scaled model			
Front width	1.77	m	$W_p = 226.8$ kg	*Front width*	88.39	mm	$W_m = 28.35$ g
Back width	2.16	m	$R_p = 10.7$ m	*Back width*	108.2	mm	$R_m = 535$ mm
Length	5.85	m		*Length*	293.37	mm	
Height	2.93	m		*Height*	146.56	mm	
Weight	5443	kg		*Weight*	28.35	g	
Overturning : Y				Overturning : Y			
Analytical model							
Prototype				Scaled model			
$2b_{fp} = 1.77$ m			$W_p = 226.8$ kg	$2b_{fm} = 88.39$ mm			$W_m = 28.35$ g
$2b_{bp} = 2.16$ m			$R_p = 10.7$ m	$2b_{bm} = 108.2$ mm			$R_m = 535$ mm
$2h_p = 2.93$ m				$2h_m = 146.56$ mm			
$\rho_{fp} = 179.80$ kg/m^3				$\rho_{fm} = 179.80$ kg/m^3			
$\rho_{bp} = 7.46$ g/m^3				$\rho_{bm} = 6.09$ kg/m^3			
Overturning : Y				Overturning: Y			

the resistance to overturn, see Eq. (3.14), being again on the safety side. This is clearly shown in the comparison for trial 1, see Tab. 3.4. However, if the linearization assumption is neglected and the non-linear equations of motion (3.6) are numerically integrated we do not have overturning in trial 1 and we predict a maximum rotation angle $\theta_{\max} = 17.7°$ which is very close to the experimental results and closer than the prediction of Scherbatiuk hybrid model.

For trials 4 and 6, we present in Figure 3.14 the evolution of the horizontal block displacements as reported in (Scherbatiuk, 2010). The response of the experimental system is bounded by the linearized system (upped bound) and the non-linear one (lower bound).

Despite the complex physics involved (fluid-structure interaction phenomena, induced ground shocks vibration, etc.), the deformability of targets, and a combined rocking/sliding response of soil-filled containers subjected to explosions, our predictions exhibit good agreement with the experiment reality, on the safety side. They always provide a close upper bound of the critical stand-off distance for overturning.

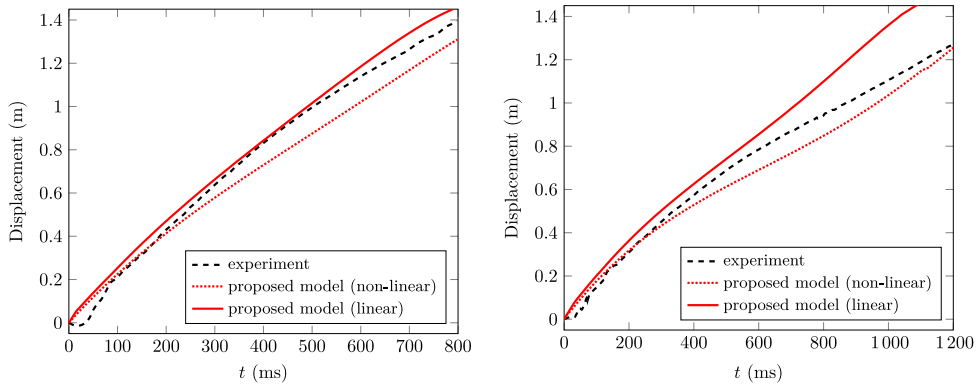

Figure 3.14 – Comparison between the experimental results for trials 4 (left) and 6 (right) and the proposed analytical model in terms of the horizontal displacement of a point located at 1.50 m above the ground and on the rear face of the container. Both the linearized and non-linearized versions of the model, with respect to slenderness, are presented. The experimental response is closely bounded by the linearized system (upper bound) and the non-linear one (lower bound).

Table 3.4 – Comparison between experimental tests (Scherbatiuk, 2010), the rocking block models proposed by Scherbatiuk and our model. Targets dimensions are $1.2 \times 1.95 \times 3.9$ m ($2b \times 2h \times$ depth). $\theta_{\max}$ represents the maximum rotation angle. Compared to previous analyses, our approach shows closer agreement regarding overturning and maximum inclination angle with the experimental results.

Trial	Blast impulse	Overturning (Y/N)				
		Experiment	Scherbatiuk models Scherbatiuk (2010)		Proposed models	
			Rigid body model	Hybrid model	Analytical	Non-linear
1	$i_r = 4.096$ MPa.ms	N ($\theta_{\max} = 15°$)	N ($\theta_{\max} = 13°$)	N ($\theta_{\max} = 20°$)	Y –	N ($\theta_{\max} = 17.7°$)
4	$i_r = 4.184$ MPa.ms	Y	Y	Y	Y	Y
6	$i_r = 3.391$ MPa.ms	Y	N	Y	Y	Y

3.6 Damage due to blast loading

Once the analytical model for rocking and overturning has been validated against detailed numerical simulations and existing experimental tests, we address the issue of damage due to blast loading of monolithic structures. Monolithic structures may be directly damaged due to the development of important tensile stresses, as the shock wave impinges the target. In such scenarios, strain-rate effects may influence the structural response. Moreover, we neglect the presence of masonry interfaces and other heterogeneities that can act as weak planes. As we shall see in Appendix B, this study stems from the investigation of the resistance of museum artifacts to explosions. Nevertheless, assuming monolithic rectangular structures, the results here derived can be considered also valid for masonry structures, once the rocking segment of the masonry (see Fig.s 2.10 and 2.11) has been formed.
In order to investigate the material response to blast waves, we consider first the following simplified case. A target, with infinite height and square cross-section $A = 0.5 \times 0.5$ m^2, is subjected to an explosion with $R = 1$ m and $W = 10$ kg. To this purpose, a Finite Element model is used assuming the material behavior as linearly elastic, with Young modulus $E = 40$ GPa and Poisson's ratio $\nu = 0.15$. The pressure load is computed using the empirical interpolations from Kingery and Bulmash (1984) and applied using ConWep model Hyde (1991), see Chapter 1. Figure 3.15 presents, at cross-section A, the normalized stress $\varsigma = \sigma_t / P_{ro}$, with σ_t the maximum principal stress and P_{ro} the overpressure peak. At time $t = 0$, the shock wave impinges the front surface (bottom boundary of section A). A wave propagates through the material locally compressing it, with amplitude approximately equal to the overpressure peak, P_{ro}, (cf. Meyers, 1994). Due to refraction phenomena at the free boundaries, the wave is reflected and causes high fluctuations of stress and strain (Meyers, 1994; Vales et al., 1996; Gu et al., 2016). The further localization of stress waves results in tensile stresses higher in value than the initial compression stress (see Fig. 3.15: for $t >$170, $\varsigma > 1$). The high loading rate of the blast wave gives rise to volumetric (tensile) strain-rates [1] as high as 500 s^{-1}.

Following the experimental results of (Wong et al., 2014), for marble, and the numerical investigations by Wei and Hao (2009), we consider an overall tensile strength, in quasi-static loading conditions, equal to 6.9 MPa, which reaches a value of 50 MPa at $\dot{\varepsilon} = 18$ s^{-1}, as experimentally observed in (Wong et al., 2014).

In the aforementioned case, strain-rates are much higher than 18 s^{-1}. We hence assume a constant tensile strength $f_t = 50$ MPa. The material constitutive law is accordingly modified: in tension, a linear elastic behavior is assumed until the maximum principal stress reaches the tensile strength. A subsequent tensile softening is considered in terms of the nonlinear brittle cracking model (ABAQUS, 2018; Hillerborg et al., 1976). Finite elements undergoing complete loss of strength (computed at the integration points) are assigned zero mass and removed from the mesh. In compression, the behavior is

1. The high values of the strain-rates is justified by the assumption of a monolithic behavior of the target, in contrast with the experimental findings discussed in Chapter 2.

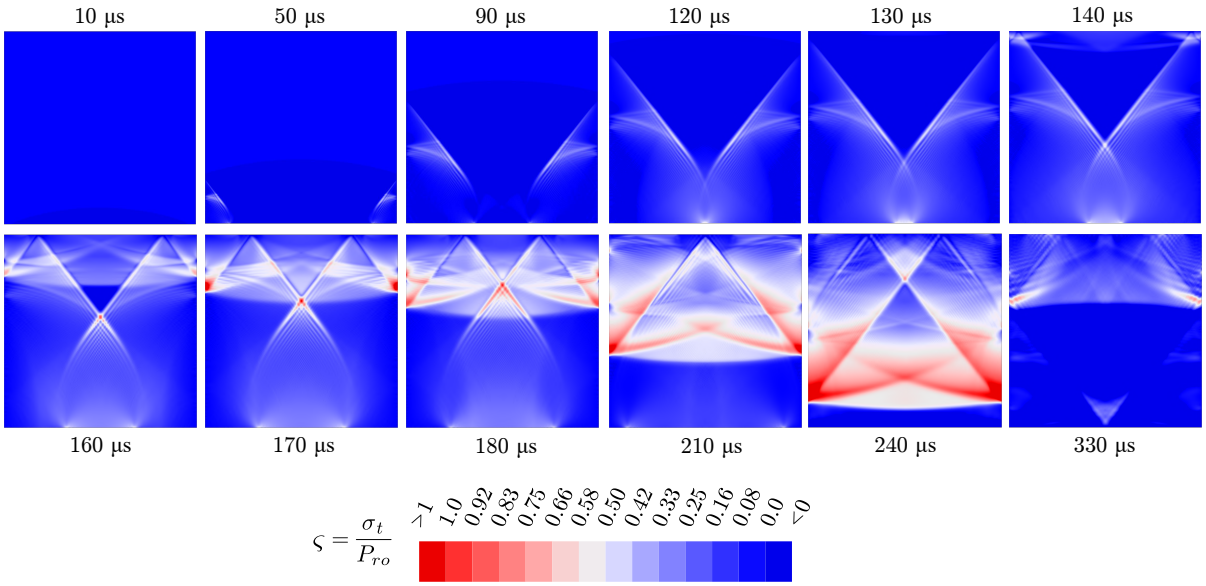

Figure 3.15 – Time evolution of the dimensionless stress $\varsigma = \sigma_t/P_{ro}$ through the cross-section $A = 0.5 \times 0.5$ m^2 of a target due to an explosion ($R = 1$ m, $W = 20$ kg). The time origin is at the shock wave arrival on the free bottom boundary. The initial longitudinal wave is refracted at the free boundaries. The released waves interact continuously and cause stress concentrations. The material is assumed to be linear elastic.

assumed to be linearly elastic due to the small values compression stresses, compared to the material strength, involved in the case at hand. Notice that we do not account for the dynamic increase of the modulus of elasticity. The results are displayed in Figure 3.16.

3.6.1 Critical stand-off distance for material failure

The tensile stress, σ_t, originating by refraction phenomena and localization is, without loss of generality, a multiple of the overpressure peak P_{ro}, namely $\sigma_t = \varsigma P_{ro}$. The focalization of stress waves gives rise to tensile stresses higher than the blast pressure, i.e., $\varsigma > 1$. In general, the value of ς depends on the material, the geometry of target, the stand-off distance, and the explosive weight.

Damage of a target due to blast loading is assumed to happen if the tensile stress exceeds the material strength (Galileo-Rankine criterion), namely if

$$\frac{\Gamma}{\varsigma} \leq 1 \qquad \text{with} \qquad \Gamma = \frac{f_t}{P_{ro}}. \tag{3.21}$$

The tensile strength f_t and consequently the dimensionless parameter Γ are functions of the strain-rate $\dot{\varepsilon}$. In the short time period, after the blast wave arrival (see Fig.s 3.15, 3.16), this strain-rate dependency is negligible, due to the high strain-rates involved, $\dot{\varepsilon} > 18$ s^{-1}, i.e. $\Gamma = \Gamma_{crit} = \Gamma|_{\dot{\varepsilon} \geq 18\ \mathrm{s}^{-1}}$. Accordingly, Figure 3.17 displays the values of Γ_{crit} ($\dot{\varepsilon} = 18$ s^{-1}, $f_t = 50$ MPa) for rectangular blocks of several dimensions subjected to different explosive weights. The phenomenon of localization of tensile stresses gains

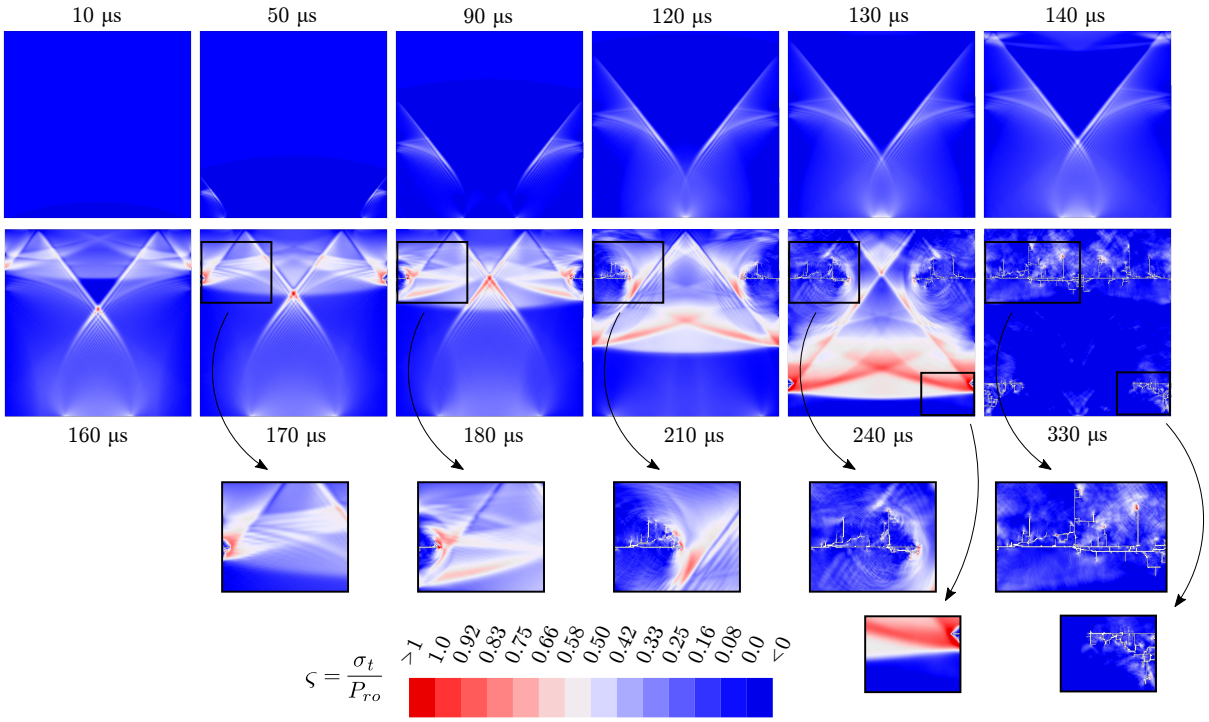

Figure 3.16 – Time evolution of the dimensionless stress $\varsigma = \sigma_t / P_{ro}$ through the cross-section $A = 0.5 \times 0.5$ m^2 of a target due to an explosion ($R = 1$ m, $W = 20$ kg). The time origin is at the shock wave arrival on the free bottom boundary. The initial longitudinal wave is refracted at the free boundaries. The released waves interact continuously and cause stress concentrations. Stresses exceeding the material strength results in damage (as shown in zoomed views).

importance for slender blocks and small cross-sections.
Table 3.5 compares for each block the critical stand-off distance to avoid material failure, R^*_{dam} , and overturning, R^*. For the dimensions and explosive weights here explored, toppling prevails. In other words, overturning is the most critical failure condition.
This stands only for the relatively short time period following the arrival of the shock wave, when the loading rates are sufficiently high to assume $f_t = 50$ MPa. If a smaller strain-rate is assumed a priori (and considered constant during the numerical simulations), the corresponding tensile strength decreases and the critical stand-off distance associated to material damage increases. Nevertheless, the dimensionless ratio Γ is only slightly dependent on the strain-rate. Consider, for instance, a block with $A = 0.25 \times 0.25$ m^2 subjected to an explosive weight $W = 10$ kg, we obtain the following values

$$\Gamma_{crit} = \Gamma|_{\dot{\varepsilon} \geq 18\ \text{s}^{-1}} = 2.15, \qquad \Gamma|_{\dot{\varepsilon}=1\ \text{s}^{-1}} = 2.02, \qquad \Gamma|_{\dot{\varepsilon} \leq 10^{-4}\ \text{s}^{-1}} = 2.40.$$

The corresponding critical stand-off distances to avoid material failure are

$$R^*_{\text{dam}}|_{\dot{\varepsilon} \geq 18\ \text{s}^{-1}} = 1.4\ \text{m} \qquad R^*_{\text{dam}}|_{\dot{\varepsilon}=1\ \text{s}^{-1}} = 2.3\ \text{m}, \qquad R^*_{\text{dam}}|_{\dot{\varepsilon} \leq 10^{-4}\ \text{s}^{-1}} = 3.1\ \text{m},$$

while $R^* = 2.27$ m (overturning).

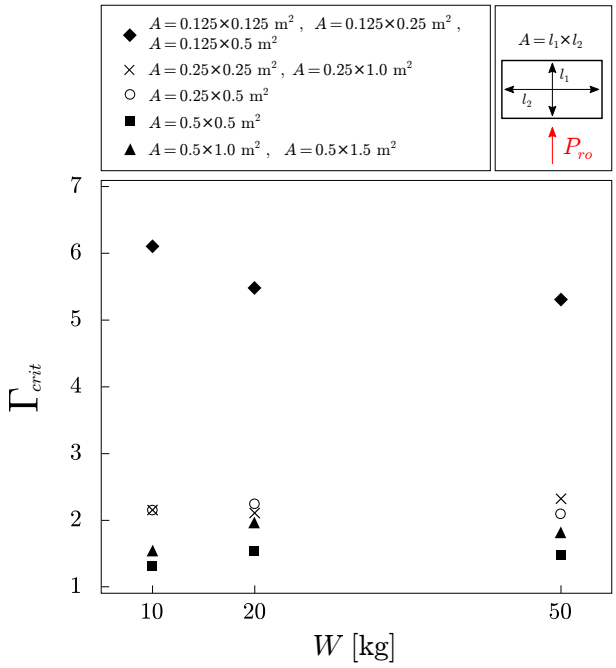

Figure 3.17 – $\Gamma_{crit} = \Gamma|_{\dot{\varepsilon} \geq 18\ \mathrm{s}^{-1}}$, i.e., $f_t = 50$ MPa, as function of the explosive weight for rectangular blocks with height $2h = 2$ m, different cross-sections $A = l_1 \times l_2$ and width $2b = l_1$.

Summarizing, blast loads induce two different types of response of a target (prevailing on other ones): rocking (overturning) and damage due to tensile stresses. For the case of simple rectangular blocks, overturning is usually predominant. We stress that, however, it is not possible to derive analytical expressions for the material failure condition, as the response is function of the particular geometry of the target and the highly non-linear material behavior at varying of the strain-rate. Each case requires ad-hoc investigations to asses the vulnerability to damage. A detailed example is given in Appendix B, in the framework of preservation of museum artifacts against explosions.

3.7 Additional remarks

We investigated the dynamics of monolithic structures, modeled as inverted pendulum systems, under fast-dynamic excitations arising from an explosion. We aim at understanding the predominant parameters governing the rigid body-like failure modes of masonry structures. The purpose of our analysis is to derive reliable decision making tools in the design of protective devices to preserve the historical heritage, secure buildings and humans.

First, by virtue of a simplified expression of blast actions and based on established empirical models, we derived the equations of motion for the rocking of inverted pendulum structures and analytical solutions for slender ones. In particular, it was found that the response is fully described by three non-dimensional parameters: the dimensionless rocking moment, χ, i.e., the ratio between the moment due to the blast load and the

Table 3.5 – Comparison of the critical stand-off distance to avoid material failure, R^*_{dam} , and overturning, R^* for blocks of different cross-sections $A = l_1 \times l_2$, width $2b = l_1$, and height $2h = 2$ m. Overturning represents the most critical failure condition.

	$W = 10$ kg		$W = 20$ kg		$W = 50$ kg	
Cross-section A (m^2)	R^*_{dam} (m)	R^* (m)	R^*_{dam} (m)	R^* (m)	R^*_{dam} (m)	R^* (m)
0.125×0.125 0.125×0.25 0.125×0.5	2.15	2.32	2.6	2.92	3.45	3.96
0.25×0.25 0.25×1.0	1.4	2.27	1.75	2.89	2.5	3.95
0.25×0.5	1.4	2.27	1.8	2.89	2.4	3.95
0.5×0.5	1.1	1.76	1.5	2.40	2.05	3.53
0.5×1.0 0.5×1.5	1.56	1.76	1.99	2.40	2.88	3.53

restoring moment due to gravity; the dimensionless load duration τ_o; and d, the exponential decay coefficient used to model the decrease in time of the pressure resulting from an explosion.
We derived then the overturning condition relying on an energy approach and we recovered the overturning strength in terms of the minimum distance (critical stand-off distance) that has to be assured between the explosive source and the target, such that toppling is avoided.

The stabilizing effect of the negative phase was investigated in order to provide more realistic estimations. In a similar manner, we derived a closed-form solution for the motion that depends on two additional dimensionless parameters. These are the dimensionless blast stabilizing moment $\bar{\chi}$ and the dimensionless negative phase duration τ_{o-}. It is shown that the negative phase has a non-negligible impact and has to be taken into account.

Finally, the adequacy of the assumptions made to derive the analytical solutions of the rocking response and overturning domain of inverted pendulum structures was investigated through two set of numerical simulations and existing experimental tests.
The numerical solutions allowed to assess the effect of sliding and of the complex loading due to an explosion as well as the validity of the linearization of the system. A good agreement was found. As expected, the analytical solution is exact for slender structures. For higher slenderness angles, α, the analytical computations overestimate to a small extent the critical distance, which from the design of point view favors safety.
Fluid Structure Interaction simulations, performed with the well-established balloon analogue model, allowed to account for more complex behaviors (e.g. diffraction, rarefaction, multiple reflections, no-normal incidence, three-dimensional shock front, uplifting etc.). Again the estimations of the analytical model remain close to the numerical results and

on the safety side. This means that the dominant features of the dynamic system are described by our analytical model.
The comparison of the proposed model with existing experimental tests of different target typologies showed good agreement and eventually validated our modeling assumptions.

Finally, direct material damage due to the development of tensile stresses within the body of the targets impinged by the shock wave was investigated. By means of detailed numerical simulations, we found that failure due to overturning prevails on material damage for targets of relatively regular geometry. In other words, the critical stand-off distance to prevent toppling is usually larger than the one to avoid direct material failure.

Based on our model, the critical stand-off distance can be easily calculated. Herein, we presented it in the form of design charts, which can be helpful in applications. For instance they can be used in museums, for determining the minimum perimeter around statues of high historical and aesthetic value or, in the frame of protection of existing buildings and assets, for the construction and positioning of blast wall and barriers. The presented model can be used as well for devising energy absorbing systems based on rocking. Our work can be extended in the future for studying systems with multiple degrees-of-freedom as it is done for instance in (Psycharis et al., 2013) and (Makris and Vassiliou, 2013a). Finally, the analytical derivations of the overturning domain can also be used in the design of experiments involving prototypes in reduced scale, as it will further discussed in Chapter 7.

Masonry structures, deending on the boundary conditions and structural geometry, may display rigid body failure modes as we investigated in this Chapter (rocking, overturning, see Fig.s 2.10 and 2.11). However, in most of the cases, non-standard geometry masonry structures fail under combined in-plane and out-of-plane deformation regimes. In these cases, the simplified approach here proposed is not appropriate. More detailed modeling strategies are required to accurately predict and analyze the dynamic response and failure modes of such kind of structures. We present detailed Discrete Element numerical simulations in the next Chapter.

Chapter 4

Meso-scale modeling of masonry structures subjected to blast loads

Abstract. *Masonry structures are often characterized by complex, non-planar geometries. This is especially the case for historical and monumental structures. Here we investigate the dynamic behavior and failure modes of non-standard, curvilinear masonry geometries, such as arches and vaults, subjected to blast loading.*
We use the Discrete Element Method (DEM) for modeling the dynamic structural response to explosions, at the meso-scale description. The approach allows considering the detailed mechanical and geometrical characteristics of masonry, as well as the inherent coupling between the in- and out-of-plane motion.
The proposed modeling approach is validated with existing experimental tests in the case of planar masonry geometries, walls, subjected to far-field explosions. The DEM model is found to satisfactorily capture the dynamic response of the system and the form of failure within the body of the masonry structure.
Then the response of emblematic non-standard masonry elements is investigated. The influence of various micro-mechanical parameters, such as the dilatancy angle, the tensile strength and the cohesion of the masonry joints on the overall dynamic structural response of the system is explored. The effect of the size of the building blocks is also studied.

Contents

4.1 Introduction

The analysis of masonry structures and their behavior attracts significant scientific research, mostly due to the fact that the vast majority of historical buildings and a considerable part of modern constructions are indeed made of masonry. Until now, attention was mainly focused on the mechanical behavior of masonry under quasi-static and seismic loads using experimental, numerical, and/or theoretical means (see Chapter 2 and e.g. Van der Pluijm, 1999; Lourenço, PhD Thesis, 1997; Stefanou et al., 2015b, 2011a; Godio et al., 2017, 2018; Cascini et al., 2018; Bui et al., 2019; Lemos, 2019).

In the existing, public (non-confidential), available literature, neither experimental nor numerical investigations of the response to explosions of typical structural elements of non-standard architectural assets, see also Section 2.4. To this purpose, we use the Discrete Element (DE) Method approach to analyze the blast loading response of typical elements of standard and non-standard masonry structures. In particular, we evaluate the dynamic response and strength of planar arches, barrel and cross vaults.

The main goal of this Chapter is to extend the existing knowledge on the behavior of planar masonry structures subjected to explosions to the aforementioned non-standard, arched ones. We consider herein ancient and modern masonry with bricks interacting through joints (mortared or dry). The strength of the joints is assumed lower than the strength of the masonry units (≈ 1 order of magnitude). This is a common assumption and results in enhanced weakness and structural vulnerability at the interfaces (see Chapter 2 and Van der Pluijm, 1999; Petry and Beyer, 2014, 2015b; Stefanou et al., 2015b; Godio et al., 2018; Roca et al., 2019).

The adopted Discrete Element (DE) model enables us to access the salient features of the system keeping at minimum the modeling assumptions. Consequently, important parameters, such as the dilatancy angle, the strength of the joints, and the building blocks size, are considered and their influence on the overall dynamic behavior of the system is discussed. The DE methodology is detailed in Section 4.2. Blast loads are computed using a dynamic library which accounts for the effect of surface rotation of building blocks as well as the evolution in time of their relative distance with respect to the impinging blast wave, as discussed in paragraph 1.5.1.4. In Section 4.3, the model is validated with the available experimental results in (Michaloudis and Gebbeken, 2019). Section 4.4 presents numerical investigations of the strength of masonry arches against explosions, assessing the influence of the slenderness ratio and the overall structural dimensions. Several configurations are investigated: semi-circular, segmented, and pointed arches. We investigate in Section 4.5 the response of a barrel vault and the influence of the meso-mechanical and geometric parameters on the response of a curvilinear masonry structure to surface blasts. Finally, in Section 4.6, we study the response of a cross vault to a centered explosion. The influence of the strength of the masonry joints and the building blocks size effects are further considered.

4.2 Discrete Element Model and main modeling assumptions

Herein we rely on the Discrete Element Method to investigate the behavior of masonry structures. The approach allows to directly model several mechanical parameters (at the meso-scale), such as the geometry of the building blocks and the constitutive behavior of the interfaces and of the blocks, without introducing strong, simplifying assumptions (cf. Cecchi and Sab, 2002; Stefanou et al., 2015b; Godio et al., 2017). A discrete approach further allows to simulate the progressive failure of masonry and capture with fidelity the post-peak, softening, dynamic behavior of a masonry structure with bricks undergoing large displacements and rotations (Godio et al., 2018; Bui et al., 2019; Lemos, 2019; Masi et al., 2019b).
DEM simulations are carried out using 3DEC software (Itasca Consulting Group, Inc., 2018). A central finite differences scheme is used for integrating in time the equations of motion of each block. A soft-contact algorithm is used to model the interactions between neighboring blocks through interfaces/joints, which are discretized into triangular sub-contact zones (Molecular Dynamic approach, Cundall and Strack, 1979). Notice that, as detailed in Chapter 2, we neglect strain-rate dynamic effects of both masonry units and joints (safety side).

We model the masonry bricks as deformable blocks interacting through zero thickness contact interfaces, and subdivided into finite-difference meshes of tetrahedral elements. Accounting for blocks deformability increases considerably the calculation time, compared to simulations using infinitely rigid ones. The pertinence of the simplifying assumption of rigid blocks is discussed in Appendix C, where it is shown that rigid blocks models may be affected by numerical artifacts (denoted as *rotational interlocking*).

Finally, for all simulations involving blast loading, no damping, neither at the material level nor artificially in the analyses, is considered to avoid any attenuation of high-frequency modes of response.

4.2.1 Constitutive behavior of masonry joints

4.2.1.1 Elastic behavior

The elastic behavior of the interfaces is defined through the following stress-displacement relationship:

$$\begin{pmatrix} t_n \\ t_t \end{pmatrix} = \begin{pmatrix} k_n & 0 \\ 0 & k_t \end{pmatrix} \begin{pmatrix} u_n \\ u_t \end{pmatrix}, \qquad \text{or} \qquad \boldsymbol{t} = \boldsymbol{k^{el}}\, \boldsymbol{u}, \tag{4.1}$$

where $\boldsymbol{t}$ and $\boldsymbol{u}$ are the vectors collecting the normal, t_n, and tangential, t_t, forces per joint's unit area and the joint normal, u_n, and tangential, u_t, displacement, respectively. The elastic stiffness matrix $\boldsymbol{k^{el}}$ collects the normal and tangential stiffness: k_n and k_t, respectively.
Normal and tangential stiffness are computed from the properties of the masonry components and the soft-contact assumption. For a deformable block model, the elastic parameters read:

$$k_n = \frac{E_m}{h_m} \qquad \text{and} \qquad k_t = \frac{G_m}{h_m}, \tag{4.2}$$

where E_m and G_m represent the Young's and shear moduli of mortar, respectively, and h_m is the thickness of the masonry joints (for more details, we refer to Masi et al., 2019b). The lumping estimation (4.2), usually adopted in the existing literature (cf. Godio et al., 2018; Malomo et al., 2019), is based on in-plane loading of planar structures (Sarhosis et al., 2016b). Expression (4.2) is considered for both head and bed joints.

4.2.1.2 Plastic and softening behavior

In the absence of more detailed experimental data regarding the behavior and the resistance of masonry joints, the Coulomb criterion seems to be a reasonable choice. Several experimental observations (e.g. Van der Pluijm, 1999; Lourenço and Ramos, 2004; Vélez et al., 2014) justify its use up to moderate compression.

The maximum shear (tangential) force per joint's unit area t_t is limited by the Coulomb failure surface:

$$f_1 = t_t - c - t_n \tan\varphi \leq 0, \tag{4.3}$$

where c is the cohesion of the interface, φ the friction angle. Compression is here considered negative. In shear/tensional regime a tension cut-off is often used as shown in Figure 4.1. In other words, the maximum normal force per joint's unit area t_n is limited by the tensile strength according to:

$$f_2 = t_n - f_t \leq 0, \tag{4.4}$$

where f_t is the tensile strength of the interface. The normal force F_n and shear force F_t vectors at the sub-contacts (i.e., discretized zones of the interfaces) are

$$F_t = A_j t_t \quad \text{and} \quad F_n = A_j t_n, \tag{4.5}$$

where A_j is the sub-contact area, which is updated at each time increment (for more, we refer to Itasca Consulting Group, Inc. (2018)).
We stress that the strength of the masonry joints is retrieved from static characterization of the material. The dynamic increase due to strain-rate effects is not taken into account to be on the safety side, as we consider masonry structures with weak joints (see Section 2.3). The built-in constitutive law presently implemented in 3DEC does not account for joint compressive failure. Although solutions to overcome such issue have been implemented in the existing literature (see e.g. Malomo et al. (2019)), as it follows, an infinite compressive strength of the masonry joints is assumed. This hypothesis is a posteriori verified by monitoring the compressive stresses in the numerical computations.

The two inequalities (4.3, 4.4) define the elastic domain of masonry joints. These surfaces can evolve and contract under combined shear and normal plastic deformation in order to take into account various micro-mechanisms related to progressive softening of the joints. As observed in experimental results on interfaces, a softening behavior, as depicted in Figure 4.1, is observed. Accordingly, maximum tensile strength, cohesion, friction angle, and dilatancy, ψ, can evolve from their initial values c; f_t; φ; ψ to some smaller residual values c_{res}; $f_{t_{res}}$; φ_{res}; ψ_{res}, to account for material damage. All these values can be determined by experimental tests on interfaces. Notice that, at the onset of

the tensile strength, blocks separation is allowed (Itasca Consulting Group, Inc., 2018). Regarding the plastic flow rule, this is given by the following potentials:

$$g_1 = t_t - t_n \tan\psi, \tag{4.6}$$

$$g_2 = t_n. \tag{4.7}$$

If $\psi = \varphi$ we say that the plastic flow rule is associative (normality condition), otherwise ($\psi < \varphi$) the material obeys a non-associative plastic flow rule. In both cases, the following

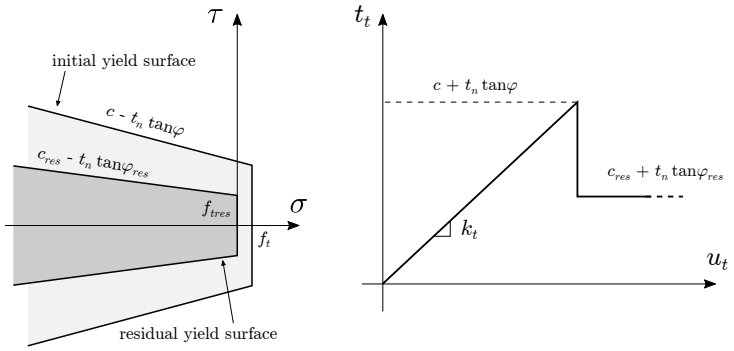

Figure 4.1 – Initial and residual strength surfaces (left) and tangential stress-displacement relationship (right) used for modeling joints behavior.

general relation between the rate of change of forces and the rate of change of total displacements stands:

$$\dot{\boldsymbol{t}} = \boldsymbol{k^{pl}}\dot{\boldsymbol{u}}, \tag{4.8}$$

with $\boldsymbol{k^{pl}}$ the plasticity matrix[1],

$$\boldsymbol{k^{pl}} = \frac{k_n}{\kappa + \tan\varphi\tan\psi}\begin{pmatrix}\tan\varphi\tan\psi & -\kappa\tan\psi\\ -\kappa\tan\varphi & \kappa^2\end{pmatrix},$$

where $\kappa = k_n/k_t$, and $\dot{\boldsymbol{t}}$ and $\dot{\boldsymbol{u}}$ represent the rate of change of the forces and of the total displacement vectors, $\boldsymbol{t}$ and $\boldsymbol{u}$, respectively.

4.2.2 Constitutive behavior of masonry blocks

Blocks are assumed to follow an elastic, isotropic material behavior. In the DE model, joints have zero thickness, which is not the case in real masonry. For this purpose, the elastic parameters of the blocks have to be modified in order to account for the finite thickness of the joints (Masi et al., 2019b). Namely, the Young's and shear moduli of the discrete elements become:

$$E_b^* = E_b\left(1 + \frac{h_m}{h_b}\right) \qquad \text{and} \qquad G_b^* = G_b\left(1 + \frac{h_m}{h_b}\right), \tag{4.9}$$

with E_b and G_m being the Young's and shear moduli of the masonry bricks, respectively; h_b is the height of the masonry bricks; h_m is the mortar joints' thickness. Notice that the

1. For the case of a perfectly plastic behavior of the masonry interfaces.

difference between the elastic parameters, E_b and G_m, and the corrected ones, E_b^* and G_m^*, is very small ($\approx 5 \div 10$ %) and in general negligible, for typical masonry. However, this difference can be important when comparing with experimental data.

We further assume infinite tensile and compressive strength for the blocks. This may be a strong assumption in the case of near-field explosions and especially in contact detonations, see e.g. (Michaloudis and Gebbeken, 2019). Nevertheless, experimental evidence shows that damage is generally negligible within the body of masonry bricks in moderate to far field explosions (i.e., scaled distance $Z > 1$ m/kg$^{1/3}$). In these conditions, the collapse of the masonry structure is governed by failure at the interfaces (Abou-Zeid et al., 2011; Keys and Clubley, 2017; Michaloudis and Gebbeken, 2019).
In each computation, strain-rates inside the bricks are monitored to verify that the related dynamic strength of the material is such that failure does not occur. This was true for all simulations presented in this Chapter.

4.3 Validation of the Discrete Element model

The proposed numerical model is herein compared and validated with existing experimental tests. Among the experiments available in the literature, we select one of the most well-documented (Michaloudis and Gebbeken, 2019). Notice that performing blast experiments in either reduced- or full-scale presents many difficulties, due to the nature of the loading action, which may result in large uncertainties of the recorded results.

Michaloudis and Gebbeken (2019) analyzed the response of unreinforced masonry walls subjected to far-field and contact explosions through experimental and numerical investigations. Among four tests, two involved masonry walls, which were subjected to the explosion of $W_1 = 810$ kg and $W_2 = 1150$ kg of TNT at $R = 37$ m from the targets, in the free-field (no confined explosions). No surfaces of reflection stand between the explosive material and the target. Due to the large stand-off distance, the blast wave impinges almost uniformly and simultaneously the entire target, without any other reflection taking place. Nevertheless, no information is given concerning the evolution of the blast pressure in the experimental tests. The brickwork consists of a running bond pattern with bricks of nominal dimensions $a \times b \times w = 80 \times 240 \times 120$ mm, see Figure 4.2. The boundaries of the walls are constrained, through mortar interfaces, to stiff fixed supports.

In Test 1 ($W_1 = 810$ kg, $R = 37$ m), the observed maximum outward and inward deflection at the center of the wall are 77 mm and 37 mm, respectively. In Test 2 ($W_2 = 1150$ kg, $R = 37$ m), a breach at the center of the wall originates mainly due to joints failure. Failure within the body of individual bricks is not observed or is negligible (Michaloudis and Gebbeken, 2019). The maximum dimensions of the breach are equal to 4 bricks along the length of the wall and to 13 bricks along the height (see Fig. 4.5).

In the numerical Discrete Element (DE) model, a constant thickness of the mortar $h_m = 10$ mm is assumed, in the lack of more detailed information for the walls. Table 4.1 presents the material parameters of the numerical model, which have been selected from the literature, see e.g. Stefanou et al. (2015b); Wild et al. (1997); Petry and Beyer (2015b). We recall that subscript res identifies the residual (post-softening) value of the

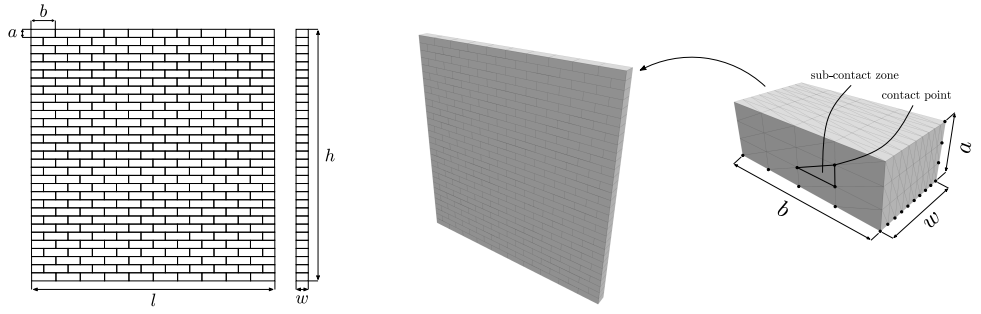

geometric model DE model

Figure 4.2 – Geometric (left) and DE model (right) for test 1 and 2 in (Michaloudis and Gebbeken, 2019). The masonry wall has thickness $w = 120$ mm, bricks have nominal size $a \times b \times w = 80 \times 240 \times 120$ mm.

parameters (see Fig. 4.1). We emphasize that the material parameters considered are retrieved from a quasi-static characterization of the material.
All the nodes of the edges of the surfaces at the boundaries are pinned. The blocks can thus only deform (no rotation is allowed). Blast loads are computed and applied using the dynamic library presented in paragraph 1.5.1.4.

From convergence analyses for contact and finite difference discretization (see Çakt et al. (2016); Godio et al. (2018); Masi et al. (2019b)), we find that at least 10 contact points along the wall's thickness (w in Fig. 4.2) are required to accurately modeling the out-of-plane deflection of the structure, otherwise important numerical artifacts (errors) may appear. The finite difference mesh for deformable blocks is selected from mesh convergence analyses, see Fig 4.2 (cf. Masi et al., 2019b).

Table 4.1 – Material parameters of the numerical DE model.

Blocks properties			Joints properties					
density	(kg/m^3)	2470	k_n	(GPa/m)	50	c	(kPa)	500
E_b^*	(MPa)	5220	k_t	(GPa/m)	20.83	f_t	(kPa)	100
G_b^*	(MPa)	2170				c_{res}, $f_{t_{res}}$	(kPa)	0
						φ	(°)	30
						ψ	(°)	0

4.3.1 Numerical results

We compare in Table 4.2 the numerical results obtained with the DE model and the test data (Michaloudis and Gebbeken, 2019) for Test 1 ($W_1 = 810$ kg, $R = 37$ m). The discrete approach predicts outward and inward deflections in agreement with the results in Michaloudis and Gebbeken (2019); the relative error is within 3.24% the experimental values. It has to be emphasized that typical values for masonry properties were used in the DE model and no fitting was performed. We present in Figure 4.3 the time evolution of the numerically measured deflection at the center of the wall. In the free-oscillating

response, the system gradually dissipates energy as a result of the slip along interfaces, until equilibrium. A permanent outward deflection of approximately 7.1 mm at the center is predicted by the model. No evidence is given in Michaloudis and Gebbeken (2019) concerning the permanent displacements. Therefore we cannot compare this effect due to plastic shear deformation of the joints.

Table 4.2 – Maximum outward and inward deflection at the center of the wall for Test 1. Comparison between the observed values and the numerical predictions with the DE model.

Maximum deflection	Experiment	DEM
Outward (mm)	77.0	78.2
Inward (mm)	37.0	38.2

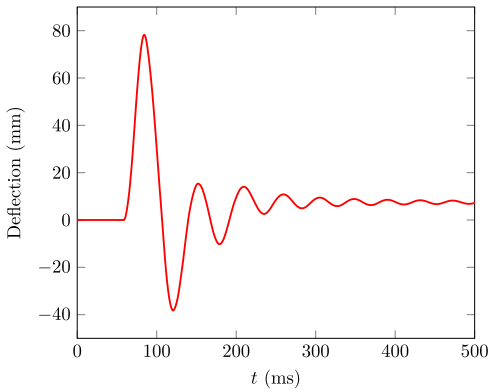

Figure 4.3 – Time evolution of the deflection at the center of the wall from the numerical DE simulations of Test 1 ($W_1 = 810$ kg, $R = 37$ m).

For Test 2 ($W_2 = 1150$ kg, $R = 37$ m), we present in Figure 4.4 the out-of-plane response and the consequent formation of the breach from the numerical simulations. Figure 4.5 and Table 4.3 compare the breach dimensions of the numerical simulations with the experimental evidence. The DE model is found to capture the form of failure and the location of the breach. Nevertheless, a small difference in the number of the bricks that are removed from the wall is observable. This may be due to the fact that (*i*) the complex fluid-structure interaction phenomena can take place during the explosion (and which are not considered in these simulations); (*ii*) in the test, some bricks involved in the breach, even being few, break, which is not considered herein, and (*iii*) head joints in the tested wall have lower strength than the bed joints, due to the lack of the beneficial effect of gravity and construction habits (Petry and Beyer, 2014, 2015a).

It is worth noticing that the numerical simulations show that the high loading rate effects on the material strength (see Sect. 2.3) are almost negligible for the structure

under study. Indeed, in all of the computations, strain rates are lower than 2 s^{-1}, hence the beneficial effects of high loading rates on the strength of the materials are limited.

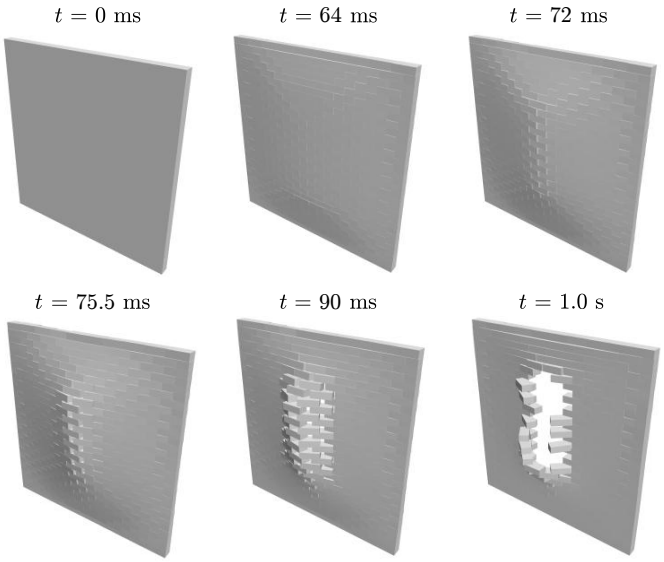

Figure 4.4 – Response of the DE model for Test 2 ($W_2 = 1150$ kg, $R = 37$ m).

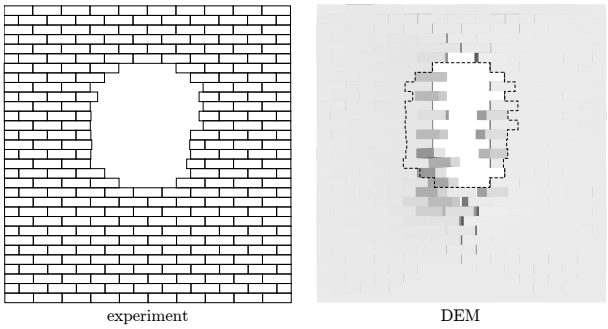

Figure 4.5 – Comparison between the experiment (left) and the numerical DEM results (right) for Test 2 ($W_2 = 1150$ kg, $R = 37$ m). The experimental breach extension is schematically represented by the black dashed line.

4.3.2 Influence of the (non-)associativity of the sliding behavior of masonry joints

In the above calculations, a non-dilatant sliding behavior was assumed for the interfaces, and namely $\psi = 0°$, as usually displayed by masonry joints (Lourenço and Ramos, 2004). We investigate herein the effect of an associative behavior of the interfaces, i.e., when $\psi = 35°$, on the response of the wall for both tests (1 and 2). All material parameters, except dilatancy, are kept the same as in Table 4.1. Figure 4.6 displays the time evolution of the deflection at the center of the wall for dilatant and non-dilatant joints. The

Table 4.3 – Comparison of the breach dimension (height×width in terms of number of involved bricks) from the numerical results (DEM) and the experimental test.

Breach	Experiment	DEM
Dimensions	13×4	14×2
No. involved bricks	40	22

associative case shows reduced out-of-plane response and increased strength, see also Godio et al. (2018).

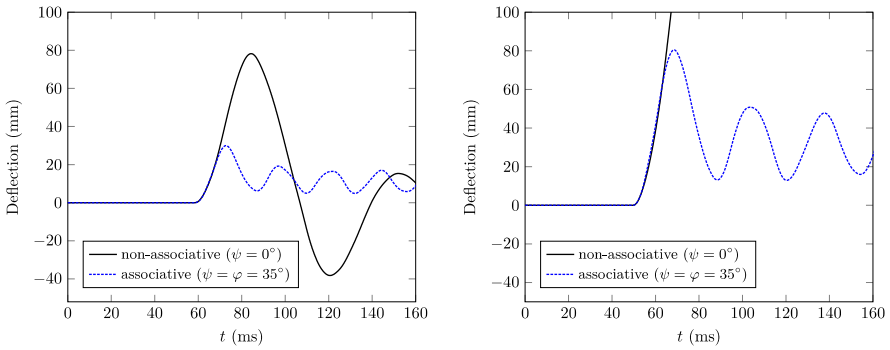

(a) test 1. (b) test 2.

Figure 4.6 – Influence of the dilatant behavior of masonry joints in terms of the deflection at the center of the wall for Test 1 ($W_1 = 810$ kg, $R = 37$ m) (a) and Test 2 ($W_2 = 1150$ kg, $R = 37$ m) (b).

In Test 1, the maximum deflection is 22.9 mm, namely 3.4 times smaller the one obtained with $\psi = 0°$ (i.e. 78.2 mm). The maximum and minimum principal stress within masonry bricks are respectively 4 and 15 times larger than the values obtained with zero dilatancy. In Test 2, associativity of the interfaces results in a structure able to withstand the blast loading of 1150 kg of TNT. In this case, the maximum deflection is 80.5 mm, which is comparable to the results obtained with a non-dilatant behavior, but under an explosive charge 340 kg smaller, i.e., 810 kg (Test 1). This difference in resistance and deformation is quite significant. As a result, limit analyses that are based on the assumption of associativity should carefully examined. Moreover, the increase of one order of magnitude on the internal principal stresses can lead to different failure modes when the non-dilatant behavior of masonry joints is not considered. This aspect is also very important in modeling (Fantin et al., 2019).

4.4 Study of the resistance of planar arches against explosions

Once the proposed model has been validated on the base of existing experimental data, we perform numerical simulations to investigate the response of planar arches subjected to blast loads. DEM simulations are used to investigate the classical issue of finding the minimum thickness required for equilibrium of a semi-circular masonry arch, subjected to its own weight, and extend it to blast loading. The limit equilibrium state of masonry

arches under self-weight has been extensively studied by the scientific and engineering community through the last two centuries (Heyman, 1982; Moseley, 1853; Milankovitch, 1907; Alexakis and Makris, 2013; Forgács et al., 2017; Brocato, 2016, 2020). Here, we aim at finding the critical explosive weight, i.e., the minimum explosive quantity to avoid collapse of a masonry arch subjected to a centered surface blast and gravitational acceleration, see Figure 4.7. We consider deformable masonry blocks with density equal to 2000 kg/m^3, Young modulus $E_b = 10$ GPa and Poisson ratio $\nu = 0.2$. Joints are modeled assuming $E_m = 1$ GPa, $\nu = 0.2$, angle of friction $\varphi = 35°$, zero dilatancy angle, cohesion $c = 500$ kPa, and tensile strength $f_t = 100$ kPa. The thickness of the mortar is 10 mm. The planar arch has depth equal to the mean radius, r, and displacements are constrained to be within the plane $x - y$. Blast loads are applied relying on the empirical model of ConWep (see Sect. 1.5.1.4), both negative and positive phases are considered. Discretization is selected upon mesh converge analyses. In the following simulations, gravity is first applied to the structure. The quasi-static equilibrium solution is used as the initial state for the simulation of the blast response, where no damping is used. Two set of parametric simulations are performed for semi-circular arches. First, the influence on the strength to blasts of the arch slenderness is investigated. Second, size effects are considered. It is worth mentioning that, due to blast loads, sliding, rocking, and internal wave propagation are expected to occur. These dynamic phenomena are important and they cannot be simply neglected. Therefore, simple limit equilibrium approaches can hardly provide information about the dynamic failure of this kind of structures (see also Chapter 3 and DeJong et al., 2008)
Finally, we aim at quantifying the influence of the type of arch and point source location in terms of the critical explosive quantity. This is accomplished for several type of arches: semi-circular, segmental, drop and equilateral pointed, see Figure 4.8.

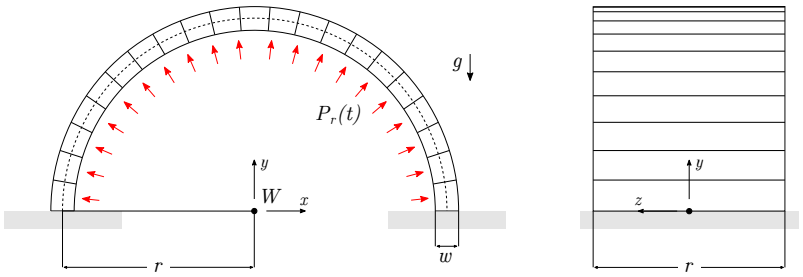

Figure 4.7 – Geometric model of the semi-circular masonry arch subjected to blast loads arising from W of TNT equivalent and self-weight ($g = 9.81$ gravitational acceleration). Displacement are constrained to be within the plane $x - y$.

4.4.1 Influence of the slenderness ratio

We investigate the critical explosive quantity as a function of the slenderness ratio. By setting the arch thickness $w = 0.2$ m, the slenderness ratio $\eta = w/r$, with r the mean radius, is varied between 0.108 and 0.216, see Figure 4.10c. In every case, the number of blocks within the masonry arch is maintained constant and equal to 21. The critical explosive quantity, W^*, is defined as the maximum TNT explosive weight such that the

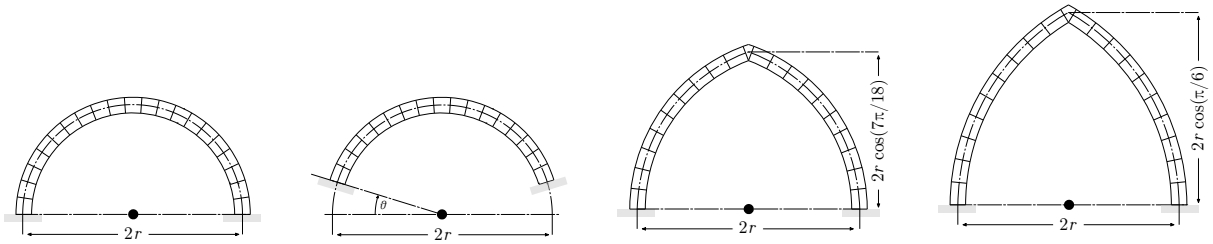

Figure 4.8 – Parametric study on the influence of the type of arch. From left to right: semi-circular arch, segmental arch ($\theta \approx \pi/10$), drop point arch, and equilateral pointed arch.

masonry arch does not collapse (i.e., returns to a stable equilibrium after the end of the blast action). Table 4.4 shows the investigated values of the mean radius r (cf. Fig. 4.7) and the slenderness η, as well as the critical weights, obtained with the numerical simulations. Figure 4.13 displays the normalized explosive weight and overpressure peak, and scaled distance for the considered cases.

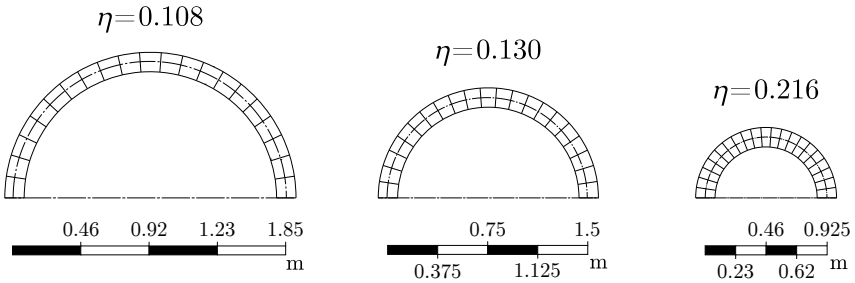

Figure 4.9 – Configurations for different slenderness ratios, η.

Table 4.4 – Critical explosive weight at varying of the slenderness ratio of a semi-circular arch, with thickness $w = 0.2$ m.

Mean radius r (m)	Slenderness ratio $\eta = w/r$ (-)	Critical TNT weight W^* (g)
1.85	0.108	0
1.65	0.120	55.5
1.57	0.127	300
1.53	0.130	1000
1.50	0.133	1500
1.37	0.146	1100
1.26	0.158	801
0.92	0.216	302

It is worth noticing that the case for $\eta = 0.108$ corresponds to the minimum slenderness ratio for (static) equilibrium, under gravity (i.e., $W^* = 0$ kg). This numerical value agrees with that derived by Milankovitch (1907)−that is, $\eta = 0.107478$.
In all cases, the collapse mechanism due to the critical explosive quantity consists of

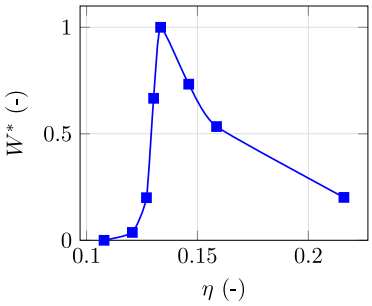

(a) normalized critical explosive weight, W^*, as function of the slenderness ratio, η.

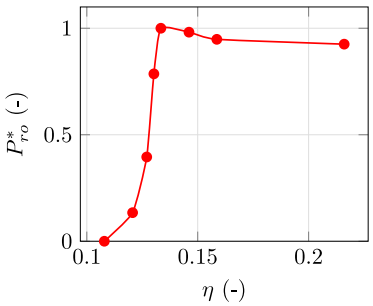

(b) normalized overpressure peak, P^*_{ro}, as function of the slenderness ratio, η.

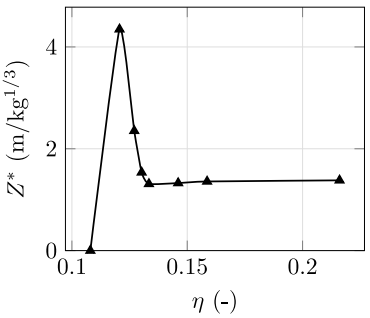

(c) scaled distance, Z^*, as function of the slenderness ratio, η.

Figure 4.10 – Critical explosive weight, overpressure peak, and scaled distance, at varying of the slenderness ratio of a semi-circular arch, with thickness $w = 0.20$ m.

combined sliding and tensile failure of the joints, which eventually results in hinging. Figure 4.11 shows a schematic representation of the mechanical response. First, the high pressure causes the masonry blocks to move outward, approximately along the radial direction. Then, self-weight acts as a stabilizing force, pushing the blocks downward, along the vertical direction. If the relative displacement developed between the masonry blocks is small enough, the arch will find eventually a new equilibrium configuration. If it is not, a hinging mechanism will take place and the arch will undergo collapse (Fig. 4.11).

Examining Figure 4.13, we can notice that, for very slender arches (small η), for which the equilibrium under gravity is critical, a small quantity of explosive is enough to destabilize the system. At increasing the slenderness ratio, the critical explosive weight increases up to $\eta = 0.133$ ($W^* = 1500$ g), then it decreases (see Fig. 4.10a). It is worth recalling that, as the arch thickness, w, is maintained constant, a reduction of η results in a reduction of the mean radius, r (see Fig. 4.9). That is, the stand-off distance decreases at higher η. Nevertheless, if one computes the overpressure peak associated to the critical explosive weight, P^*_{ro}, we can notice that for $\eta \geq 0.133$ the critical overpressure peak is approximately constant. The same holds for the critical scaled distance, Z^*, see Fig. 4.10c. Therefore, the numerical results show an optimal slenderness ratio equal to $\eta = 0.133$ for which the arch is the most resistant to centered surface blasts.

4.4.2 Size effects

We investigate the influence of the size effects in the strength of semi-circular masonry arches. We select one of the above considered cases, i.e., slenderness angle $\eta = 0.133$, and different (uniform) geometric scaling are applied to the geometry of the arch. In particular, we define the scaling λ as the ratio of the characteristic length of the scaled geometry with respect to that of the model with $\eta = 0.133$. Table 4.5 shows the scaling ratios herein investigated, while Figure 4.12 depicts some of the corresponding geometric

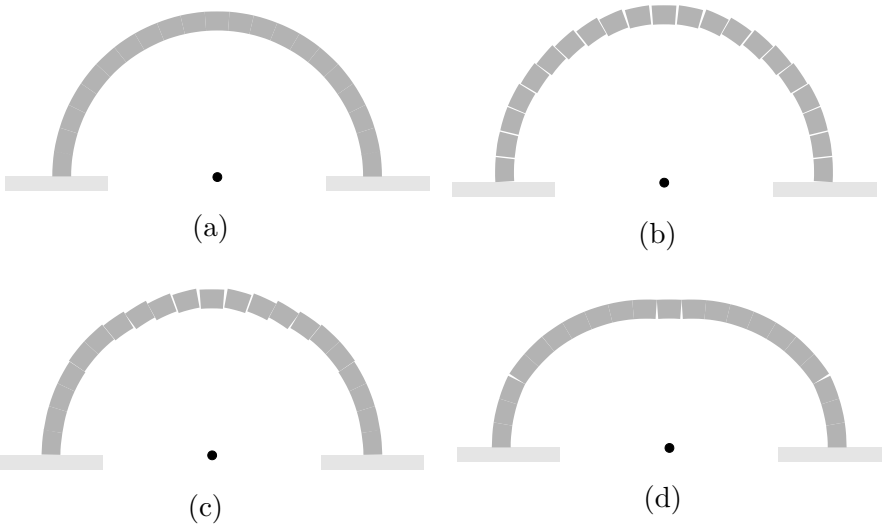

Figure 4.11 – Schematic representation, at successive times (a-d), of the failure mode of a semi-circular arch subjected to the critical quantity of explosive and self-weight.

models.
Through numerical simulations, we compute the critical explosive quantity for each scaling λ. Figure 4.13 shows the results. As the dimensions of the arch increase, the critical explosive weight increases, as well. Indeed, for larger λ, the stand-off distance increases, hence much higher quantity of explosive are needed for collapse. Nevertheless, as noticed in paragraph 4.4.1, the stand-off distance, as function of the scaling factor, remains approximately constant.

Table 4.5 – Critical explosive weight at varying of the dimensions (constant slenderness ratio) of a semi-circular arch, with $\eta = 0.133$.

Mean radius r (m)	Scaling factor λ (-)	Critical TNT weigth W^* (kg)
0.075	0.05	1.5×10^{-4}
0.75	0.5	0.146
1.5	1	1.5
3	2	12.5
6	4	97
15	10	1515

The critical explosive weight of semi-circular arches, i.e., the strength against blast loads, seems to be strongly dependent of the two parameters herein considered, i.e., the size and the slenderness ratio. They further suggest that the overpressure peak, or (equivalently) the scaled distance, is a significant design parameter. Indeed, except for very slender arches, the overall structural resistance seems to be directly identified by the value of the scaled distance, for the cases here investigated.

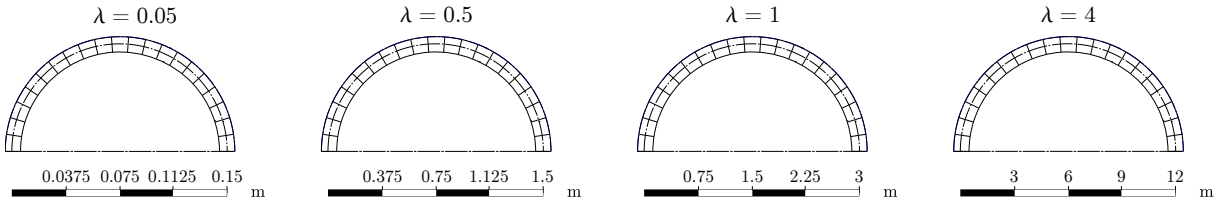

Figure 4.12 – Configurations for different scaling factors, λ.

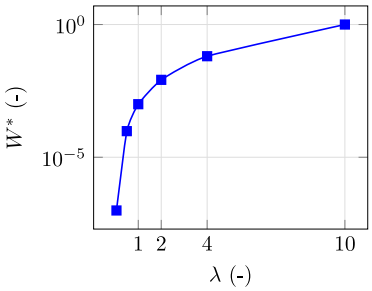

(a) normalized critical explosive weight, W^*, as function of the slenderness ratio, λ.

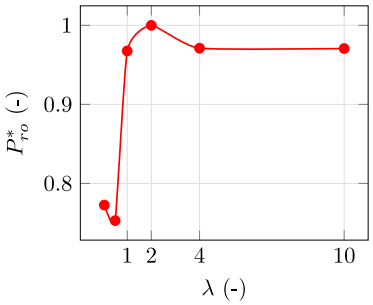

(b) normalized overpressure peak, P^*_{ro}, as function of the slenderness ratio, λ.

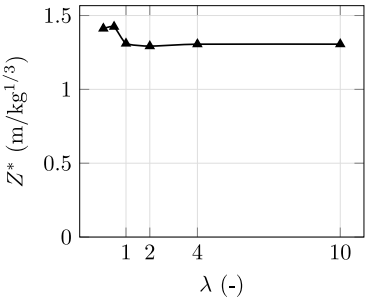

(c) scaled distance, Z^*, as function of the slenderness ratio, λ.

Figure 4.13 – Critical explosive weight, overpressure peak, and scaled distance, at varying of the dimensions (scaling factor, λ) of a semi-circular arch, with slenderness ratio $\eta = 0.133$.

4.4.3 Influence of the type of the arch

We investigate here the resistance to explosions of different types of arches, and namely: semi-circular, segmental, drop and equilateral pointed, see Figure 4.8. We select the following dimensions: $r = 1.5$, $w = 0.2$, thus slenderness ratio $\eta = 0.133$. Furthermore, different locations for the explosive source are investigated, see Figure 4.14.

Figure 4.15 and Table 4.6 show the critical explosive quantities obtained for each type of arch and for the four selected locations of the explosive.
We observe that significant changes of the resistance exist for centered or de-centered explosive locations. For de-centered locations (Fig. 4.15b) the critical explosive weight is approximately one order of magnitude smaller than the one for centered explosions. The reason lies on the modification of the pressure load (its distribution over the structure). For de-centered detonation points, the predominant failure mechanism involves important frictional/sliding at the joints. For centered explosions, the collapse mechanism is the same with the semi-circular arch.

It is worth mentioning that the resistance to blast is generally influenced by the arch configuration (circular, pointed, etc.) to a limited extent. The strength of a segmented arch is found to be larger than that of a semi-circular arch, as the formation of an hinging mechanism to cause structural collapse requires larger relative displacements between the masonry blocks, see (Forgács et al., 2017). Figure 4.16 displays the dynamic response of

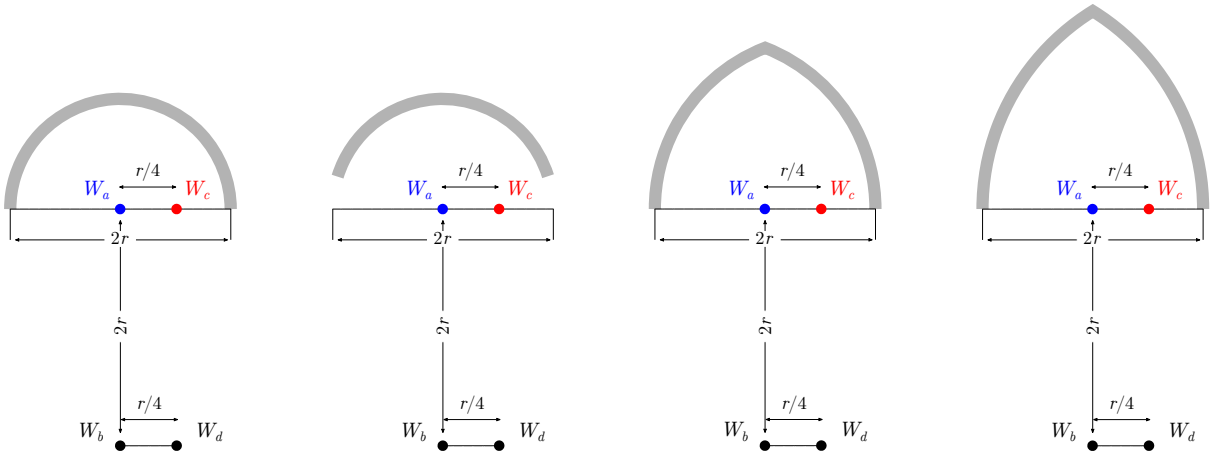

Figure 4.14 – Type of arches and configurations for different source locations.

Table 4.6 – Critical explosive weight for different typologies of arches and different source locations (see Fig. 4.14).

Source location	Critical TNT weight W^* (kg)			
	Semi-circular	Segmented	Drop pointed	Equilateral pointed
W_a	1.5	1.7	1.7	1.8
W_b	1.5	1.7	1.7	1.9
W_c	0.01	0.3	0.005	0.05
W_d	0.01	0.3	0.005	0.1

a segmented arch to a centered explosion. After the outward movement due to the blast pressure, self-weight allows to reach a new equilibrium position.
For pointed arches, the resistance is higher than the simple case of a semi-circular arch, mainly due to the fact that the upper part of the structure is at higher stand-off distances, with respect to the blocks at its base.
It is worth pointing and noticing that, for the source locations and arch typologies considered, the semi-circular arch is found to be the most vulnerable to blast loads. This is why, in the numerical investigations that follow, Section 4.5, a semi-circular barrel vault has been selected. This element is expected to be the most vulnerable geometry, compared to pointed (barrel) vaults and segmented ones.

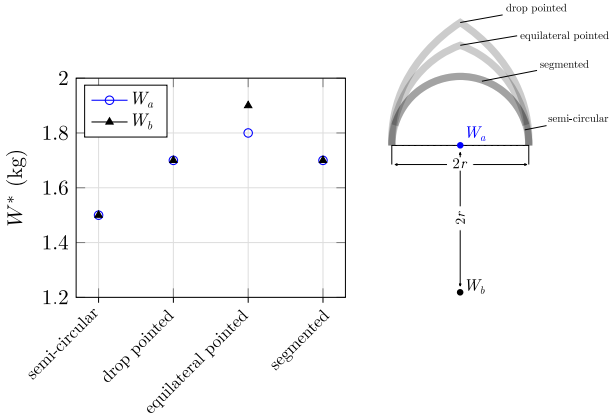

(a) critical explosive weight, W^*, for position W_a and W_b (explosive source located at the center of the arch). W_b case would correspond to an arch used for roofing of a building.

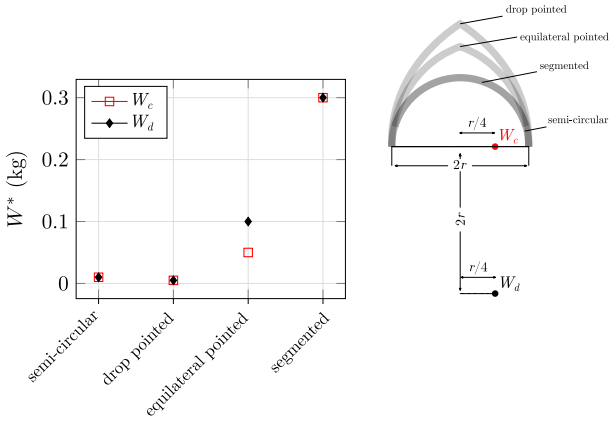

(b) critical explosive weight, W^*, for position W_c and W_d (explosive source located at $r/4$ from the center of the arch.

Figure 4.15 – Critical explosive weight for different typologies of arches and different source locations.

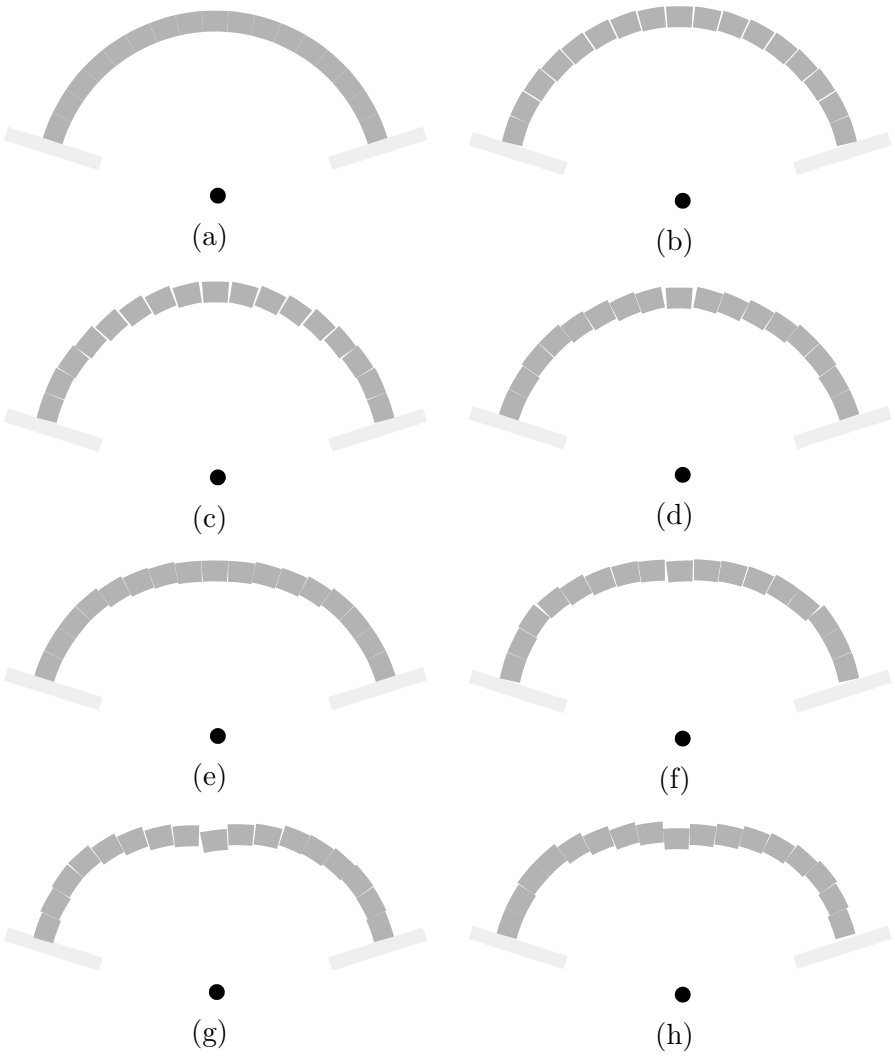

Figure 4.16 – Evolution of the dynamic response of a segmented arch subjected to a centered explosion, W_a (Fig. 4.14).

4.5 Dynamic behavior of a barrel vault subjected to blast loading

We investigate the response of an arched masonry structure, namely of a barrel vault (see Fig. 4.17), subjected to a centered blast. DEM simulations are used here to understand the influence of various micro-mechanical parameters, such as the dilatancy and the building blocks size, on the dynamic response of the system. The dynamic behavior of the structure is expected to be different from the one of the (semi-circular) arch studid in the previous Section due to its three-dimensional character and the provided confinement.

4.5.1 Geometric model and discretization

The geometric model of the considered configuration is presented in Figure 4.17. The masonry bricks have size $a \times b \times w = 250 \times 296 \times 200$ mm. The thickness of the mortar is 10 mm. The vault has inner diameter $d_i = 2800$ mm, thickness w (outer diameter $d_e = 3200$ mm), and length $l = 3060$ mm. The longitudinal length of the structure has been selected to be large enough compared to the characteristic lengths associated to the blast wave and the hemispherical shock front.
The base ($y = 0$) and the edges ($z = 0$ and $z = l$) of the structure are assumed to be connected with fixed supports through contact interfaces (whose mechanical properties are assumed to be identical to the masonry joints). The supports have length $l_s = 150$ mm and thickness w. The fixed supports can represent various physical situations. For instance, they may designate the presence of rigid arched ribs or rigid walls at the lateral extremities of the vault. In addition, they could be used to approximate, to a certain degree, a vault, whose longitudinal length is much bigger than its diameter. The latter situation can be justified only for hemispherical loads centered in the middle of the vault, as it is the case in this study at the beginning of the loading, which coincides with the maximum pressure.

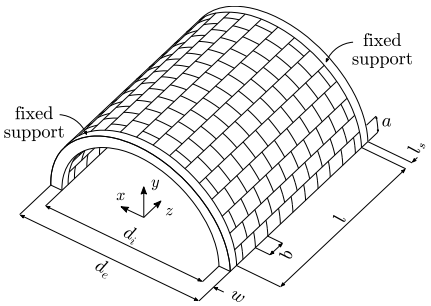

Figure 4.17 – Geometric model of the masonry barrel vault under investigation. Bricks have size $a \times b \times w = 250 \times 296 \times 200$ mm. The vault has inner diameter $d_i = 2800$ mm, thickness w (outer diameter $d_e = 3200$ mm), and depth $l = 3060$.

The contact discretization for the DE model is studied through two sets of analyses, which are fundamental for assuring reliable numerical results. First, in a quasi-static elastic calculation, the central layer of blocks is subjected to a constant and uniform pressure equal to 100 kPa acting on the inner faces. Mass damping is considered in this

phase in order to dissipate oscillations and reach equilibrium fast. This first calculation allows to determine the fineness of the discretization of contacts along the circumferential and radial directions for each block (mesh convergence analysis). Second, the structure is subjected to the pressure of a surface blast $W = 10$ kg located at the ground ($y = 0$) and at the center ($z = l/2$). No damping is considered in this phase. The deflection of different points at the vault's key is monitored to investigate the influence of the contact discretization along the longitudinal direction (z axis). On the basis of this mesh convergence analysis, the selected discretization consists of tetrahedrons of average characteristic length equal to 35 mm, with $13 \times 6 \times 10$ contacts points along dimensions $a \times b \times w$, see Figure 4.18. We recall that mesh convergence analyses are central for avoiding numerical errors (cf. Section 4.3)
We present in Figure 4.19 the deformed shape, along the longitudinal direction, for the selected discretization, obtained at the equilibrium, under a static pressure of 100 kPa.

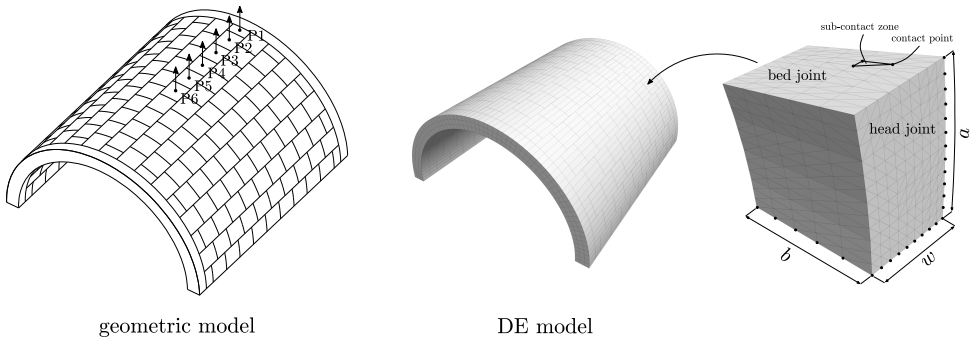

Figure 4.18 – Geometric model of the masonry barrel vault (left), with highlighted monitoring points used in the following simulations, and Discrete Element model with contact discretization and finite difference mesh of the blocks (right).

Once the appropriate discretization is selected, we proceed with the study of the behavior of the barrel vault under explosive loads. In the first step, gravity is applied to the structure to reproduce the stress state within the vault under self-weight. The quasi-static equilibrium solution is used as the initial state for the simulation of the response to a surface blast due to a TNT explosive weight $W = 10$ kg, located at the center ($y = 0$, $z = l/2$). The considered blast scenario corresponds to a moderate-field explosion. The best-fit interpolations used (Kingery and Bulmash, 1984) allow to be on the safety side (cf. Section 1.4). The elastic parameters for blocks and joints are presented in Table 4.7. In paragraph 4.5.2 we investigate the influence of the associativity of the sliding behavior of masonry joints and the combined effects of friction and dilatancy angles in paragraph 4.5.3. Different values of cohesion and tensile strength of the interfaces and their dependency on the structural strength of the system are explored in paragraph 4.5.4. Finally paragraph 4.5.5 examines the role that the size of the building blocks plays in the dynamic response.

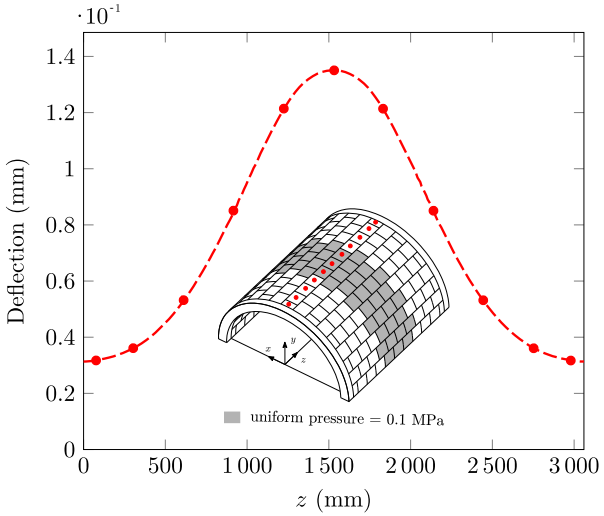

Figure 4.19 – Deformed shape, along the longitudinal direction, at the key's vault under a constant pressure of 100 kPa applied to the region highlighted in grey. The circles represent the blocks' centroids. An elastic behavior is assumed for the masonry joints.

Table 4.7 – Material parameters used in the numerical simulations of the masonry barrel vault.

Blocks properties			Joints properties		
density	(kg/m^3)	2000	k_n	(GPa/m)	100.0
E_b^*	(GPa)	14.5	k_t	(GPa/m)	41.7
G_b^*	(GPa)	6.0			

4.5.2 The effect of associative or non-associative friction

The influence of the associativity of the masonry joints behavior is studied, assuming zero cohesion and zero tensile strength for the joints. A constant angle of friction for both the head and bed joints is considered (cf. 4.18), namely $\varphi^b = \varphi^h = 35°$ (superscripts b and h refer to bed and head joints, respectively).

Figure 4.20 presents the time response in terms of the deflection at different points located at the vault's key (with reference to Fig. 4.18), assuming an associative sliding behavior, i.e., equal friction and dilatancy angles, $\varphi^h = \varphi^b = \psi^b = \psi^h = 35°$. The time history of the loading is presented, for the same locations, in Figure 4.21 and Table 4.8.

The blast overpressure, acting on the inner face of the vault, causes an initial outward slip ($\approx$ 1 mm) of the masonry blocks. The elements at the boundaries partially rotate around the rigid supports, while the longitudinal layers of blocks begin to deflect in the outward direction (see Fig. 4.22). Nevertheless, the relative confinement of the vault (due to the presence of the fixed supports and the dilatant behavior of interfaces) results in a limited in-plane response. Membrane compressive forces develop in the plane of the vault, along the longitudinal direction, giving rise to so-called *arching actions*. The resulting

response of the structure is similar to the one of an arching wall (between supports that restrain the outward movement) subjected to out-of-plane loads (Gabrielsen et al., 1975). Each layer of bricks along the longitudinal axis develops compressive arching actions (see Fig. 4.22), while the in-plane response is limited.

The presence of traveling bending and longitudinal compressive/tensile waves, which are further reflected at the boundaries of the structure, makes the displacements of the masonry blocks (cf. Fig. 4.20) to oscillate and move outward. This is a direct consequence of the aforementioned arching mechanism. The concurrent dilatant behavior of the masonry interfaces, which increases the membrane compressive forces, the geometry of the structure, and the presence of infinitely rigid supports oblige the structure to find a new equilibrium point towards positive (outward) deflections.

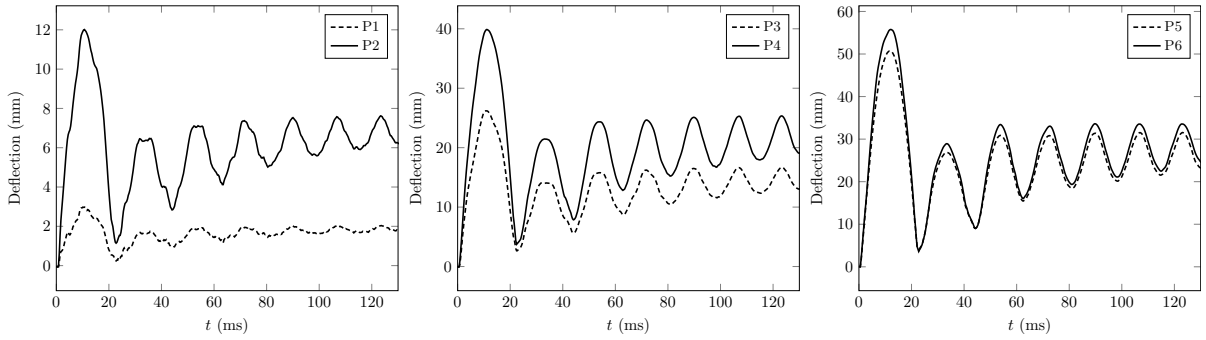

Figure 4.20 – Response of a barrel vault subjected to 10 kg of TNT in terms of the deflection of different points located at the vault's key. The results are for $\varphi^h = \varphi^b = 35°$, $\psi^b = \psi^h = 35°$, $f_t = c = 0$ MPa.

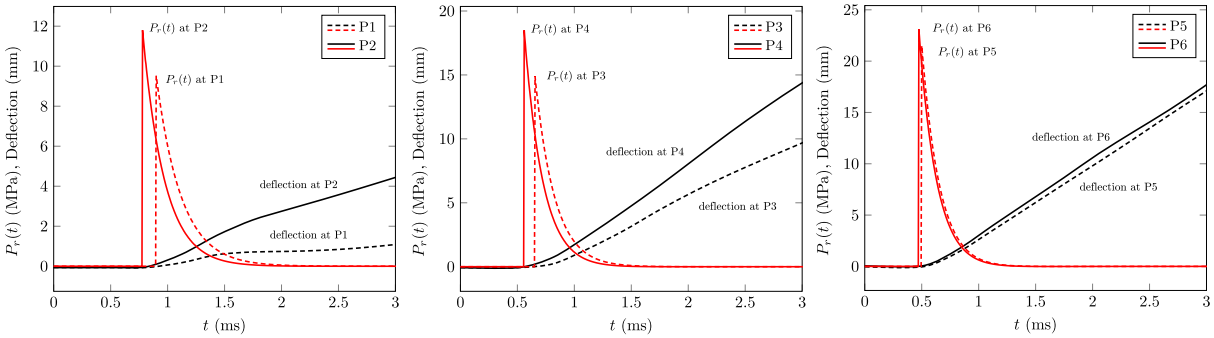

Figure 4.21 – Overpressure profiles due to 10 kg of TNT at the vault's key, see Fig. 4.20.

When a non-associative behavior with zero dilatancy is considered, the deflection of the structure is found to increase, as a result of the reduced membrane compressive stress (zero dilatancy) that reduce the apparent friction between the blocks in the longitudinal direction (z axis). Consequently, the arching mechanism is reduced as well. This is presented in Figure 4.23, where we show the displacement history measured at the vault's key for the case of associative and non-associative (with zero dilatancy) sliding behavior. The maximum deflection measured in the associative case is found to be 14% smaller than the one obtained with a non-dilatant sliding behavior, as presented in Table 4.9.

Table 4.8 – Overpressure peak, P_{ro}, underpressure peak, P_{ro-}, arrival time of the shock wave, t_A, positive phase duration, t_o, and negative phase duration, t_{o-}, due to 10 kg of TNT predicted by the model at different points located at the vault's key (refer to Fig. 4.18).

location	P_{ro} (MPa)	$P_{ro\_}$ (kPa)	t_A (ms)	t_o (ms)	$t_{o\_}$ (ms)
P6	23.08	-8.40	0.48	0.97	1.52
P5	21.54	-4.93	0.50	1.05	1.41
P4	18.48	-1.27	0.56	1.24	1.13
P3	14.87	-0.14	0.65	1.63	0.61
P2	11.77	-0.01	0.78	2.28	0.34
P1	9.52	0.0	0.91	2.98	0.0

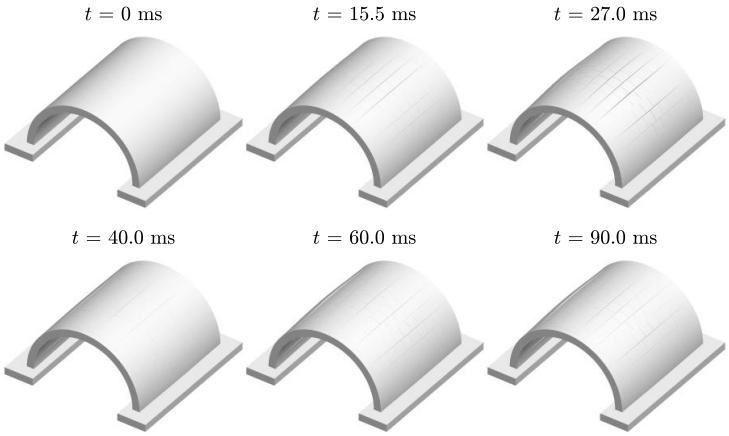

Figure 4.22 – Evolution of response of a barrel vault subjected to 10 kg of TNT and formation of the arching mechanism. The results refer to $\varphi^h = \varphi^b = 35°$, $\psi^b = \psi^h = 35°$, $f_t = c = 0$ MPa.

As also showed in paragraph 4.3.2, joints showing zero dilatancy reduce considerably the stress in masonry (see also Godio et al., 2018). In this case, a non-associative sliding behavior ($\psi^b = \psi^h = 0°$) results in a reduction of approximately 85% of both normal and shear stress at the joints and 50% of the maximum principal stress within the masonry blocks.

Differently from the above case, the outward oscillations of the blocks, due to the presence of internal stress waves, reflected at the boundaries, does not result in increased compressive membrane forces, because of to the lack of dilatancy. The deflection at the vault's key displays a second peak which is much higher, when compared with the associative case, due to the fact that the apparent frictional resistance at the edges is lower compared to the associative one. This counter-intuitive result is due to the presence of elastic waves in the structure which lead to the progressive development of additional frictional slip in the case of the non-associative case, which is more prone to frictional

slip. These waves are trapped in the structure due to the rigid supports that reflect them and are progressively dissipated through frictional slip.

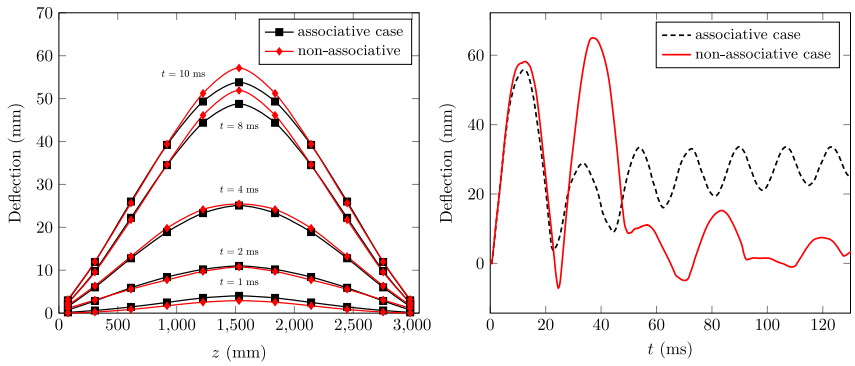

Figure 4.23 – Response of a barrel vault subjected to 10 kg of TNT in terms of the deformed shape at vault's key (left) and deflection at point P6 (right) for a dilatant behavior of the masonry joints and assuming a non-associative sliding behavior ($\psi^b = \psi^h = 0°$). The results are for $\varphi^h = \varphi^b = 35°$, $f_t = c = 0$ MPa. The blast parameters are those shown in Table 4.8.

Table 4.9 – Dilatancy ψ^b and friction angle φ^h considered in the parametric study and related maximum deflection observed in the masonry vault. The results refer to $\varphi^b = 35°$, $\psi^h = 0°$, and $f_t = c = 0$ MPa.

sliding behavior	$\varphi^b = \varphi^h$ (°)	$\psi^b = \psi^h$ (°)	Maximum deflection (mm)
associative	35	35	55.80
non-associative	35	0	65.04

4.5.3 Friction angle and dilatancy effect for non-associative friction

The effects of a non-associative behavior, with varying dilatancy, and of the friction angle of the joints are explored. For the bed joints, we consider a constant angle of friction, i.e., $\varphi^b = 35°$, while the dilatancy angle varies between 0° and 35°. At the interfaces representing the head joints, the influence of different values of the friction angle, φ^h, (and zero dilatancy) is explored. The choice originates from the fact that the head joints are usually much weaker than the bed joints in masonry structures. This is mainly due to the lack of gravity during the construction process. This stands also for the bed joints whose lying plane makes an angle less than 90° with the direction of applied gravity. Nevertheless, we neglect this latter condition herein. Table 4.10 presents the considered values of the dilatancy and of the friction angle, as well as the maximum deflection numerically measured within the structure, in each case.

Table 4.10 – Dilatancy ψ^b and friction angle φ^h considered in the parametric study and related maximum deflection observed in the masonry vault. The results refer to $\varphi^b = 35°$, $\psi^h = 0°$, and $f_t = c = 0$ MPa.

ψ^b (°)	φ^h (°)	Maximum deflection (mm)	ψ^b (°)	φ^h (°)	Maximum deflection (mm)
0	35	65.04	2	10	86.71
	20	63.45		5	> 200
	15	66.24		0	> 200
	10	86.86			
	5	> 200			
	0	> 200			
5	10	86.66	10	10	86.57
	5	> 200		5	> 200
	0	> 200		0	> 200

For different values of the friction angle, φ^h, arching actions still develop, but to a gradually reduced extent, see Fig. 4.24. As expected, the smaller the friction angle is, the larger the slip observed between adjacent blocks becomes. This is clearly visible at the supports, point P1 (Fig. 4.24). In fact, low angle of friction prevents the formation of membrane compressive stress, hence of an effective and beneficial arching mechanism. This is shown in Figure 4.25 which depicts the response of the structure for $\varphi^h = 10°$, $\varphi^b = 35°$, and $\psi^b = \psi^h = 0°$.

Table 4.10 and Figure 4.27 present the maximum deflection observed in the masonry vault for different angles of friction, φ^h, and dilatancy, ψ^b. In these simulations, numerical collapse is considered when a maximum deflection equal to 200 mm, i.e., the thickness of the vault, is developed. The response of the system is found to depend only on the friction angle, while the effect of bed joints dilatancy angle on the maximum deflection is negligible.

Figure 4.26 displays the time-evolution of the out-of-plane displacement in function of the dilatancy angle of the bed joints, ψ^b, and for constant friction angles $\varphi^b = 35°$ and $\varphi^h = 10°$. We clearly notice that the first-peak deflection does not depend on the value of the joints dilatancy. Nevertheless, the dynamic response, i.e., the evolution in time of the deflection, is influenced by the dilatant behavior of the joints, but only slightly. In particular, an increase of the post-peak deflection is observed for higher dilatancy. Indeed, the larger the dilatancy of the interfaces is, the higher the transmitted compressive thrust is and the lower the sliding becomes.

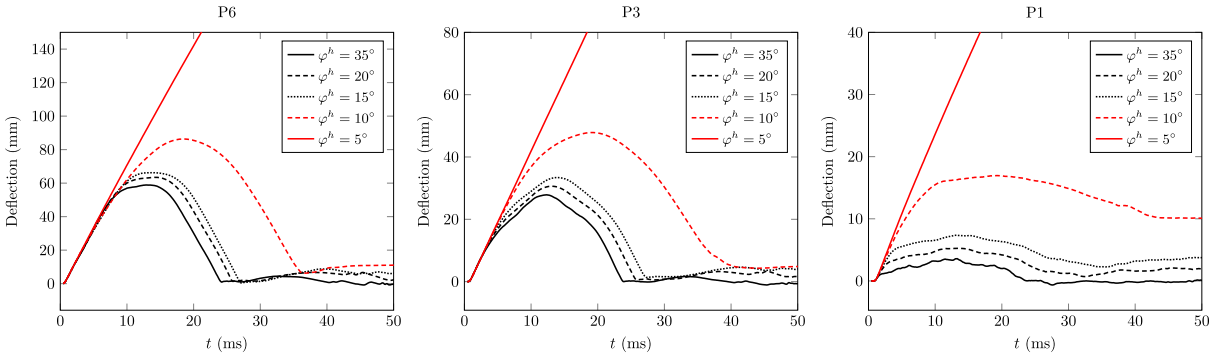

Figure 4.24 – Influence of the head joints angle of friction, φ^h, on the dynamic response of a barrel vault subjected to 10 kg of TNT in terms of the deflection of different points (P6, P3, and P1 cf. Fig. 4.18). The results refer to $\varphi^b = 35°$, $\psi^b = \psi^h = 0°$, and $f_t = c = 0$ MPa.

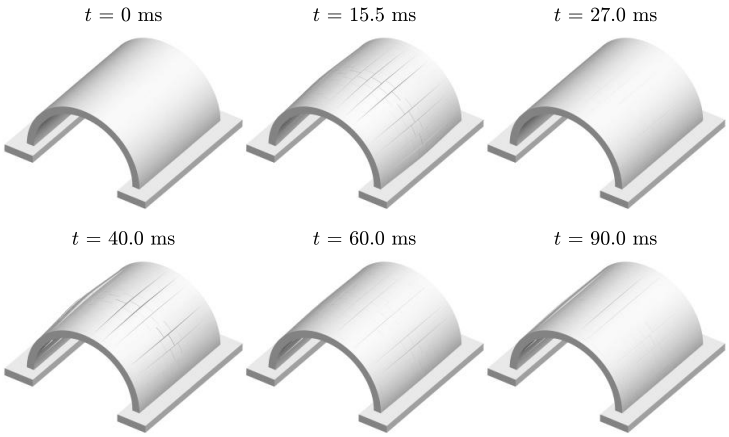

Figure 4.25 – Evolution of response of a barrel vault subjected to 10 kg of TNT. The results are for $\varphi^b = \varphi^h = 35°$, $\psi^b = \psi^h = 0°$, and $f_t = c = 0$ MPa.

4.5.4 Cohesion and tensile strength effect

The effect of the cohesion and tensile strength of the bed joints is herein investigated considering $\varphi^b = 35°$ and $\varphi^h = 10° - 5°$, and zero dilatancy $\psi^b = \psi^h = 0°$. The case with $\varphi^h = 10°$ is selected in order to investigate the effects on the dynamic response. Indeed, for the same value of the friction angle and zero cohesion and tensile strength, the vault does not undergo collapse (cf. Tab. 7). The influence of the two strength parameters on the failure mode and collapse capacity of the structure is instead investigated for $\varphi^h = 5°$ (collapse for $f_t = c = 0$ MPa, cf. Tab. 7). The selected combinations of values for cohesion and tensile strength are presented in Table 4.11. Once the onset of tensile and/or shear failure is reached, the residual values of cohesion and tensile strength are imposed to be zero (see Fig. 4.1). Zero cohesion and zero tensile strength are assumed for the head joints.

Figure 4.28 shows the response of the system for $\varphi^h = 10°$ and a wide range of the

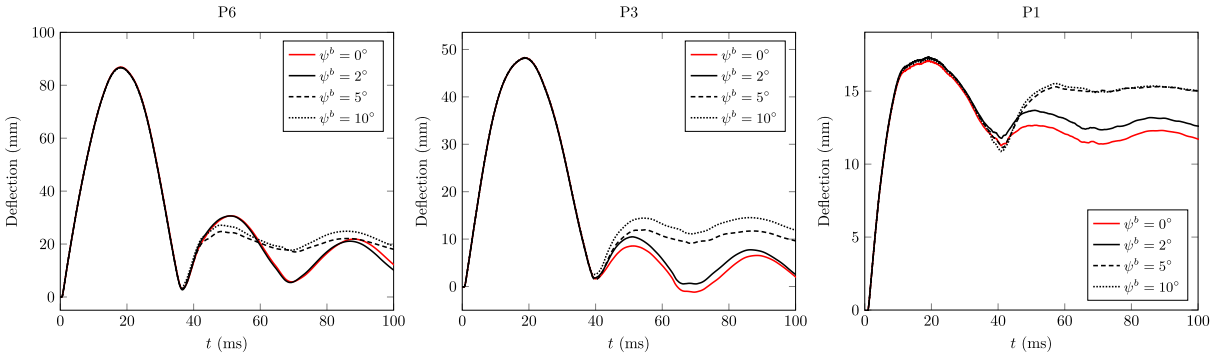

Figure 4.26 – Influence of the bed joints dilatancy, ψ^b, on the dynamic response of a barrel vault subjected to 10 kg of TNT in terms of the deflection of different points (P6, P3, and P1 cf. Fig. 4.18). The results refer to $\varphi^b = 35°$, $\varphi^h = 10°$, $\psi^h = 0°$, and $f_t = c = 0$ MPa.

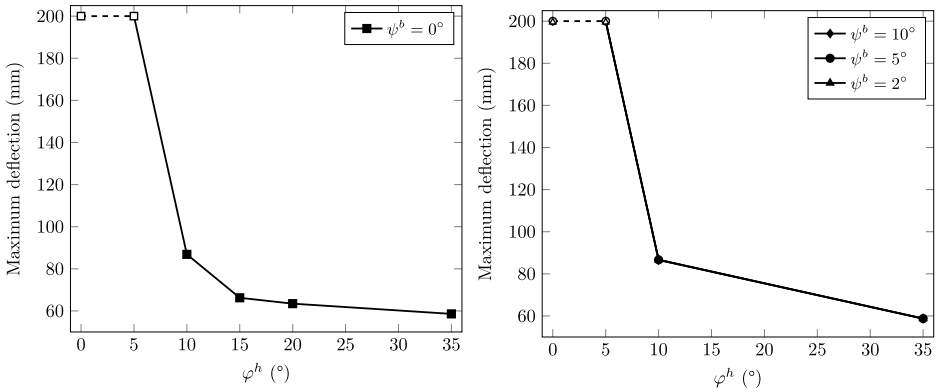

Figure 4.27 – Maximum deflection observed in the masonry vault at varying of φ^h and ψ^b ($\varphi^b = 35°$, $\psi^h = 0°$, $f_t = c = 0$ MPa).

value of the strength parameters. We observe that both cohesion and tensile strength do not influence the first-peak response of the structure. Only the post-peak response slightly depends on the two parameters, due to the increased/reduced amount of the number of joints that underwent softening. This holds true since the dynamic response is strongly influenced by the relative slip that takes place at the head joints along the longitudinal direction (z axis), for which zero cohesion and tensile strength are always assumed.

In the case of $\varphi^h = 5°$, the system's failure mode and collapse capacity are found to be independent from the value of tensile strength and cohesion, see Table 4.11.

4.5.5 Building blocks size effect

The size of the building blocks can influence the compression and the shear strength of the structure, as well as its stiffness and inertia (Petry and Beyer, 2014; Godio et al., 2018; Masi et al., 2019a). Several are the reasons of the scale effects of the building blocks. Among those, the number of joints in the structure is usually the leading parameter that

Table 4.11 – Cohesion c and tensile strength f_t considered in the parametric study and related maximum deflection observed in the masonry vault for $\varphi^b = 35°$, $\psi^b = \psi^h = 0°$. The residual values are kept constant $c_{res} = f_{t\,res} = 0$ MPa.

f_t (MPa)	c (MPa)	Maximum deflection $\varphi^h = 5°$ (mm)	$\varphi^h = 10°$ (mm)
0	0	> 200	86.86
	0.1	> 200	86.57
	0.5	> 200	86.55
0.1	0.5	> 200	86.29
0.5	1.5	> 200	86.29
1.5	3.0	> 200	86.29

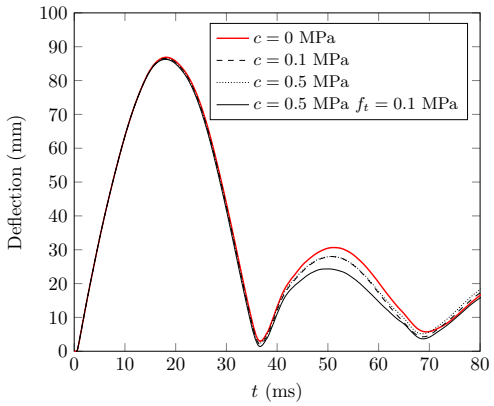

Figure 4.28 – Time evolution of the deflection at the center of the vault's key for different combinations of cohesion and tensile strength of the interfaces.

influences the dynamic response, energy dissipation (mainly due to friction), and overall strength.
We present herein numerical analyses to asses the building blocks size effect, for some sets of material parameters used in paragraphs 4.5.2 and 4.5.3. In particular, we investigate the behavior of the vault using blocks that are half and twice their original size, assuming constant overall thickness $w = 200$ mm (see Fig. 4.29) and mortar height $h_m = 10$ mm.

Table 4.12 and Figure 4.30 present the maximum deflection that was reported within the vault for different values of the dilatancy and friction angles and highlight the importance of the horizontal joints.
The system with half the blocks size displays an increase in the overall outward deflection of the structure due to the larger number of interfaces in the system. It is worth noticing that the mortar thickness is assumed to be the same in each model, thus the normal and tangential stiffness, k_n and k_t, are kept the same between the models, cf. Eq. (4.2).

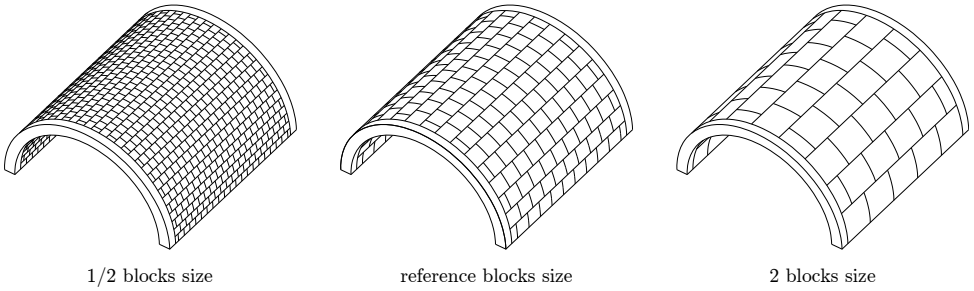

Figure 4.29 – The building blocks size effect is investigated using blocks that are half and twice their original size, assuming constant overall thickness $w = 200$ mm and mortar height $h_m = 10$ mm.

Therefore, the larger number of masonry joints results in a decrease of the overall flexural stiffness of the structure.
Similarly to what observed in paragraph 4.5.2, masonry joints with zero dilatancy result in an enhanced out-of-plane response also for blocks that are half the reference size (the maximum deflection is 9% larger than the one related to the associative case). Moreover, the zero dilatancy joints display reduced internal compressive stress (90% of compressive stress and 92% of shear stress) with respect to the associative case.

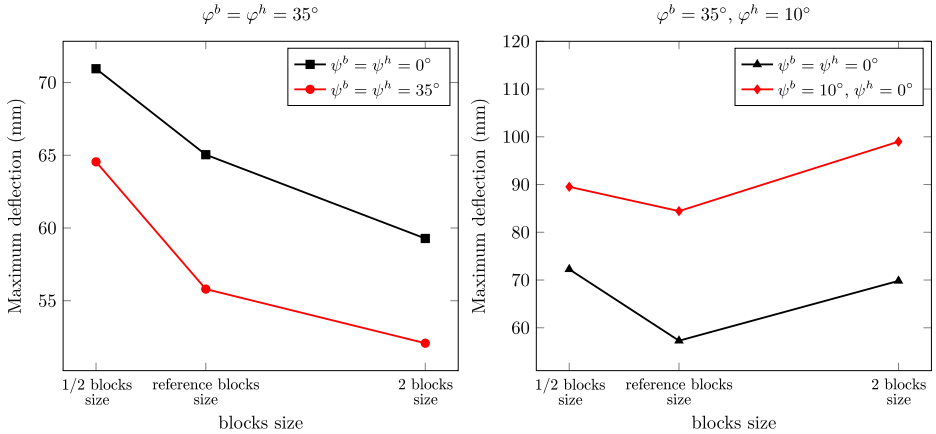

Figure 4.30 – Comparison of the maximum deflection observed in the masonry vault for different size of the building blocks, with $\varphi^b = \varphi^h = 35°$ (left) and $\varphi^b = 35°$, $\varphi^h = 10°$ (right). The results are for $f_t = c = 0$ MPa.

The model with twice the blocks size displays smaller out-of-plane displacements and reduced bending, if compared to the reference blocks size, for the case $\varphi^b = \varphi^h = 35°$. The reason lies on the same consideration made for the half blocks size: larger blocks result in higher flexural stiffness. Figure 4.31 displays the dynamic response for different building blocks sizes assuming (a) an associative sliding behavior and (b) zero dilatancy masonry joints. Also in the case of double blocks size, the non-associative sliding behavior corresponds to increased out-of-plane displacements (the maximum deflection is found to be 12% larger than the associative case) and reduced stress in the masonry (namely,

the compressive stresses are reduced to 96% of the ones corresponding to an associative behavior, while the shear stress to 95%.

For $\varphi^b = 35°$ and $\varphi^h = 10°$ (see Tab. 9), we find that the model with double blocks size

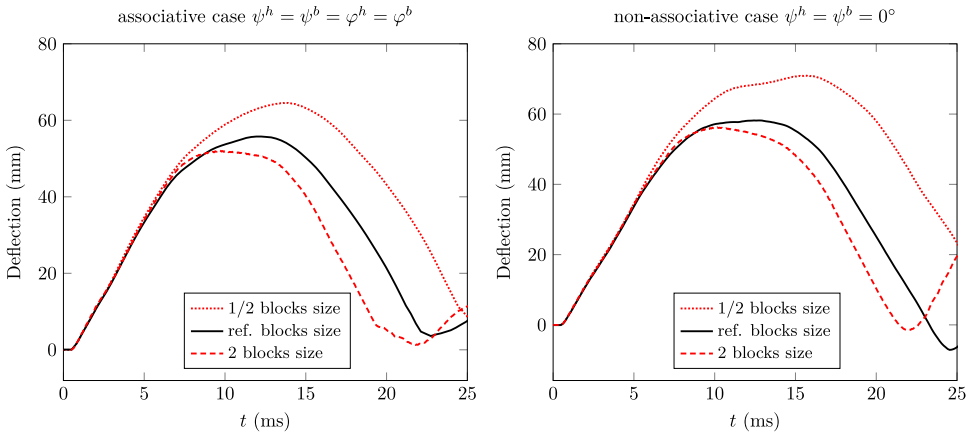

Figure 4.31 – Comparison of the response of the masonry vault in terms of deflection at the center of the vault's key (right, P6, cf. 4.17) for different size of the building blocks. The results are for $\varphi^b = \varphi^h = 35°$ and $f_t = c = 0$ MPa.

displays larger deflections, with respect to the reference size. Indeed, an increase in the blocks dimensions results in a decrease of the number of masonry joints, which further gives smaller overall plastic dissipation, namely friction work, and larger relative slip. In particular, the total friction work with double blocks size is approximately 50% smaller than the one corresponding to the model with half blocks size, see Fig. 4.32.

Table 4.12 – Building blocks size effect on the maximum deflection observed within the structure. The results refer to $f_t = c = 0$ MPa.

φ^b	φ^h	ψ^b	ψ^h	Maximum deflection		
				1/2 bocks size	reference blocks size	2 blocks size
(°)	(°)	(°)	(°)	(mm)	(mm)	(mm)
35	35	35	35	64.55	55.80	52.08
		0	0	70.95	65.04	59.29
35	10	10	0	121.95	53.62	71.51
		0	0	126.97	86.86	71.55

Notice that classical continuum descriptions of masonry do not account for internal lengths, like the size of the blocks, and one has to opt to higher-order continuum theories, such as the Cosserat continuum (Cosserat and Cosserat, 1909; Masiani and Trovalusci, 1996; Brocato and Capriz, 2001; Stefanou et al., 2008; Godio et al., 2017) or higher (Germain, 1973b,a; Brocato, 1994; Mariano, 2000).

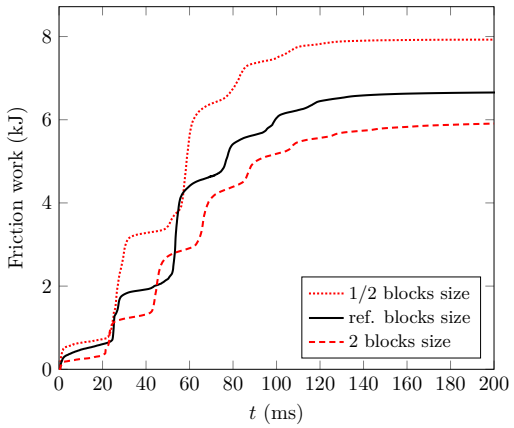

Figure 4.32 – Time-history of joints friction work for different blocks size. The results are for $\varphi^b = \varphi^h = 35°$, $\psi^b = \psi^h = 0°$, and $f_t = c = 0$ MPa.

4.6 Dynamic behavior of a cross vault subjected to blast loading

Similar to the case of the barrel vault, we investigate the response of a cross vault, subjected to a centered blast.

The geometric model is inspired by the cross vaults in *College des Bernardins*, Paris

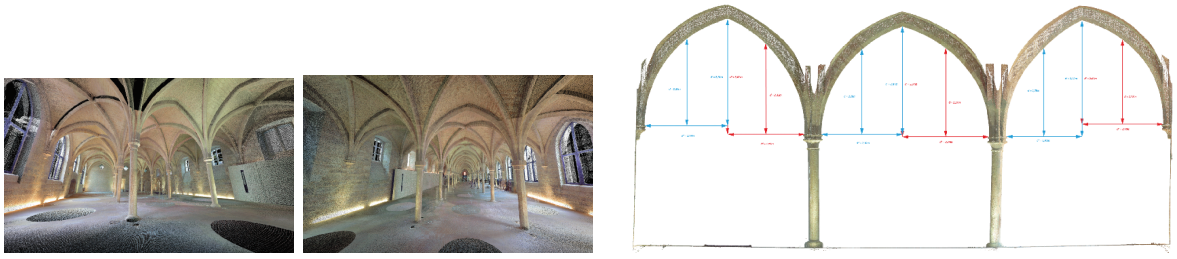

(a) (b)

Figure 4.33 – Laser scanning by Plemo 3D of the *College des Bernardins*, Paris (France): (a) general view, (b) cross section and typical dimensions.

(France), see Figure 4.33. The model is created relying on a computer-aided design (CAD) software, see Figure 4.34. Nevertheless, due to the complexity of discretizing the CAD model in 3DEC, we use a simplified geometric model, shown in Figure 4.35, built from the intersection of two pointed vaults. Indeed, 3DEC allows an appropriate discretization only of ruled surfaces, which is not the case for the masonry skin of the vault in Figure 4.34.

Figure 4.35 depicts the geometric model and DE discretization. The vault has span of approximately 5 m and height equal to 2.84 m. The masonry skin is 200 mm thick. The diagonal ribs have height equal to approximately 400 mm and thickness equal to 250 mm. The height and thickness of the lateral ribs are 320 and 120 mm, respectively.
Due to the high computational cost, only a quarter of the vault is simulated. This hypothesis holds true only for symmetric structures subjected to symmetric loading.

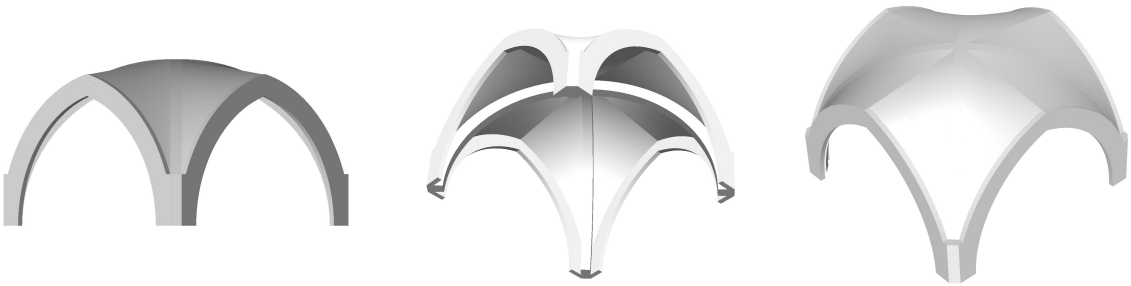

Figure 4.34 – Computer-aided design model of the cross vault in *College des Bernardins*, Paris (France).

The base of the cross vault is assumed to be fixed, see Figure 4.36, to allow the modeling

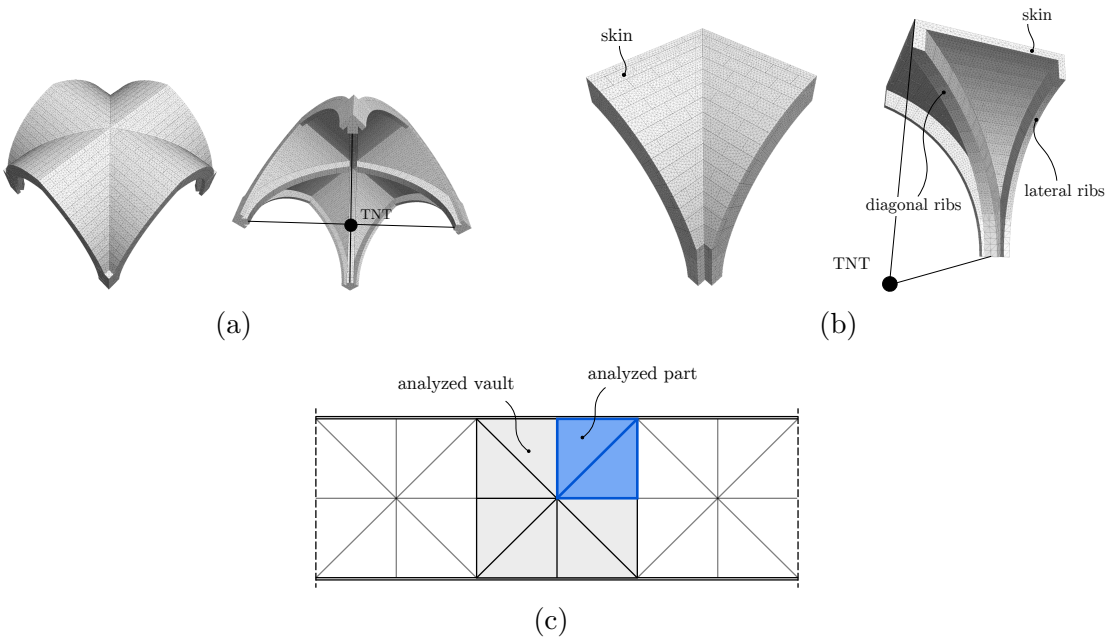

Figure 4.35 – Geometric and DE model of the cross-vault: (a) complete, (b) quarter (numerical simulations), and (c) schematic representation of the structure. The span is approximately 5 m, and the height is 2.84 m.

of the failure structural mechanism due to explosions, and avoiding displacements of the supports. Boundary conditions to impose symmetry are also considered, see Figure 4.36. The material parameters are shown in Table 4.13. Mortar joints have zero dilatancy frictional behavior and thickness equal to 10 mm. Different values of tensile strength and cohesion of joints are tested.

As in the case of the barrel vault, the following analyses consist of two steps. First, gravity is applied to the model to recreate the stress state, then, the blast loading of several quantities of TNT equivalent weights is applied. No damping is used in the second phase. The vertical displacement of several points is monitored during the analyses, see Figure 4.36c.

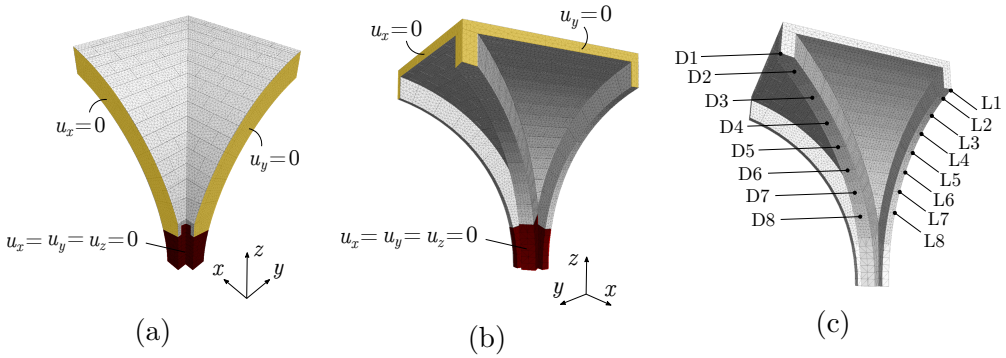

Figure 4.36 – Boundary conditions of the analyzed part (a, b) and monitored points (c).

Table 4.13 – Material parameters used in the numerical simulations of the masonry cross vault. Cohesion and tensile strength of the joints are $0 \div 10$ MPa and $0 - 1$ MPa, respectively.

Blocks properties			Joints properties		
density	(kg/m^3)	2000	k_n	(GPa/m)	100.0
E_b	(GPa)	10.5	k_t	(GPa/m)	41.7
G_b	(GPa)	4.4	φ	(°)	35
			ψ	(°)	0

4.6.1 Response at varying of the explosive quantity

The effects of different explosive quantities is here investigated. Zero joint tensile strength and cohesion are assumed. The model is subjected to 10, 15, 18, and 20 kg of TNT equivalent, located as shown in Figure 4.35.
Figure 4.37 displays the (vertical) displacements of some points (cf. Fig. 4.36) at the diagonal and lateral ribs. The structure is found to resist to explosive quantities equal and smaller than 15 kg. At 18 kg, the numerical results show structural failure of the masonry skin, see Figure 4.38. Nevertheless, the ribs are found to resist. Under the load of 20 kg, the global structural collapse is recorded. The time-history of the displacements, in Figure 4.37, certainly display the complexity of the structural response. A strong coupling between the out-of-plane and in-plane response characterizes the mechanical behavior. Moreover, the response of the masonry skin highly differs from that one of the ribs. For clarity, we refer to Figure 4.38, where the dynamic response under 18 kg is displayed [2].
In the very first moments, after the detonation, the blast pressure pushes in the upward direction (positive z, cf. Fig. 4.36) the ribs and the skin. The latter, made of bricks of smaller dimensions, undergoes larger displacements. Then, the effect of gravity make the

2. We stress that the blocks constituting the masonry skin located at the axes of symmetry are constrained, due to the symmetrical boundary conditions, to remain on the initial plane, no out-of-plane deformations are allowed.

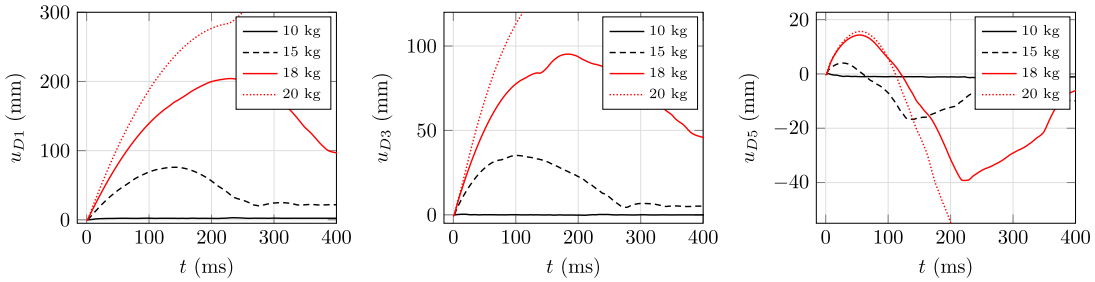

(a) diagonal ribs

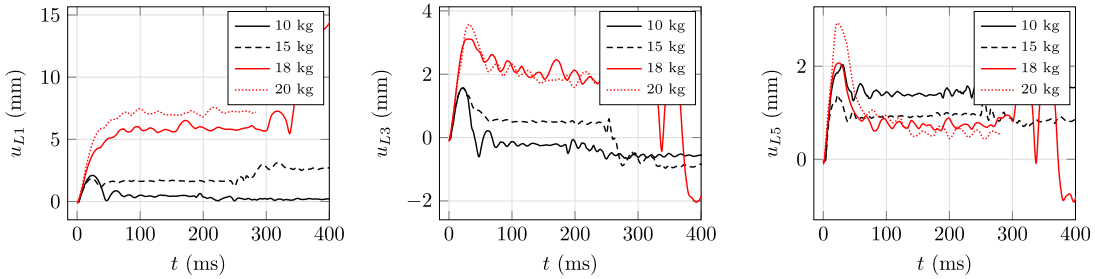

(b) lateral ribs

Figure 4.37 – Dynamic response of a cross vault subjected to 18 kg.

structure to move downward, in the search of a possible (new) equilibrium configuration. This is, for instance, the case with 10 and 15 kg. When 18 kg of TNT are used (cf. Fig. 4.38), the bricks composing the skin, as they are moving downward, fail in finding a new equilibrium shape, on the deformed ribs. For a quantity equal to 20 kg, the ribs collapse, as well.

It is worth noticing that the blast wave does not impinges simultaneously and with the same intensity all the points of the structure. In particular, the hemispherical wave impinges first the upper part of the diagonal ribs, then it further propagates to the skin and the lateral ribs. We shall recall that the empirical model for blast actions used in these simulations might lead to results which are different from the real scenario, due to the omission of complex focalization and clearing effects that may happen (cf. Chapter 1).

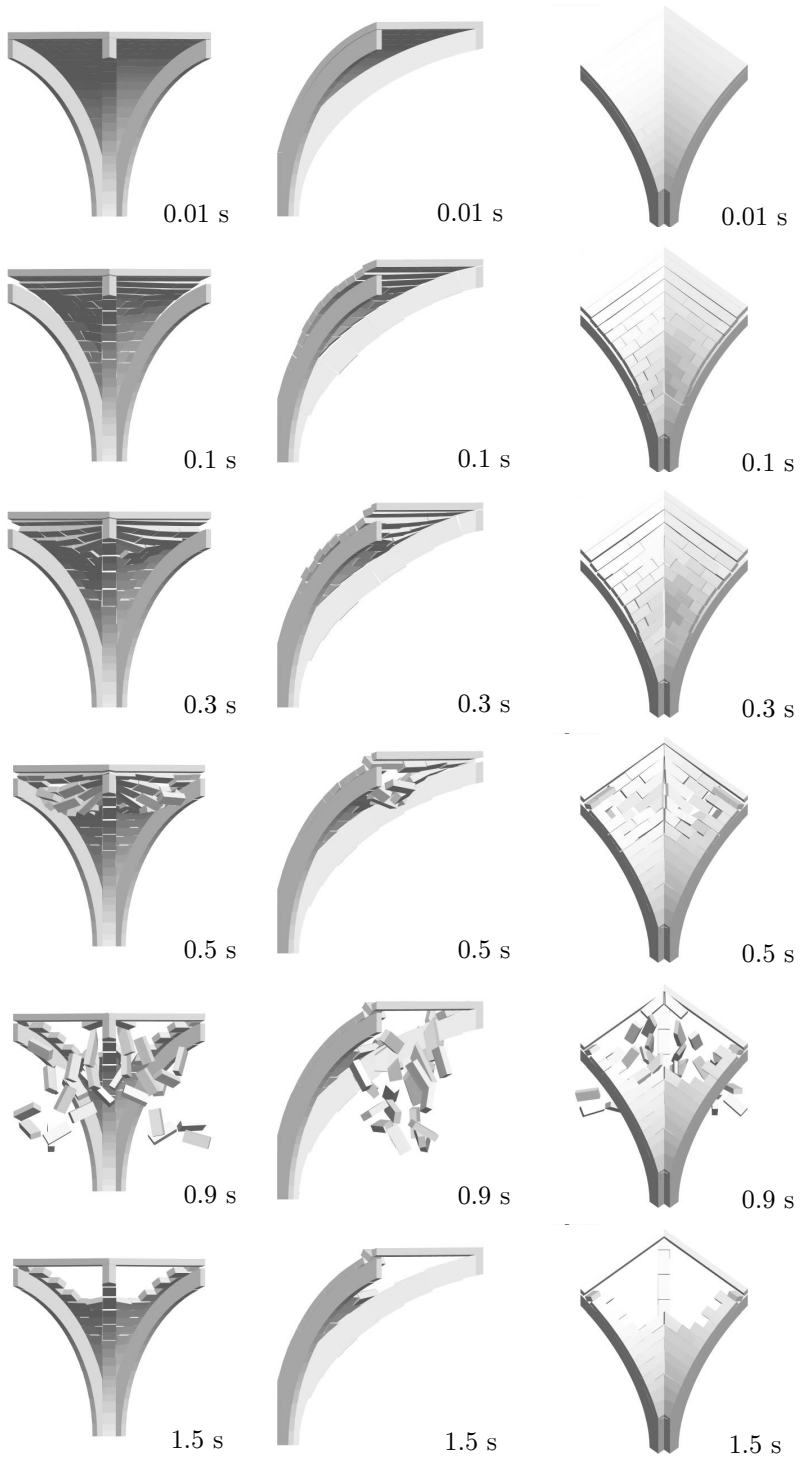

Figure 4.38 – Dynamic response of a cross vault subjected to 18 kg. Detonation happens at 0 s.

4.6.2 Influence of the tensile strength and cohesion of the interfaces

Similarly to the barrel vault (paragraph 4.5.4), we study the influence of the masonry joints strength (both bed and head joints of the ribs and of the skin), for a single loading case: 18 kg. We display in Figure 4.39 the vertical displacements at different locations of the diagonal rib. For this particular geometry, tensile strength and cohesion are found to

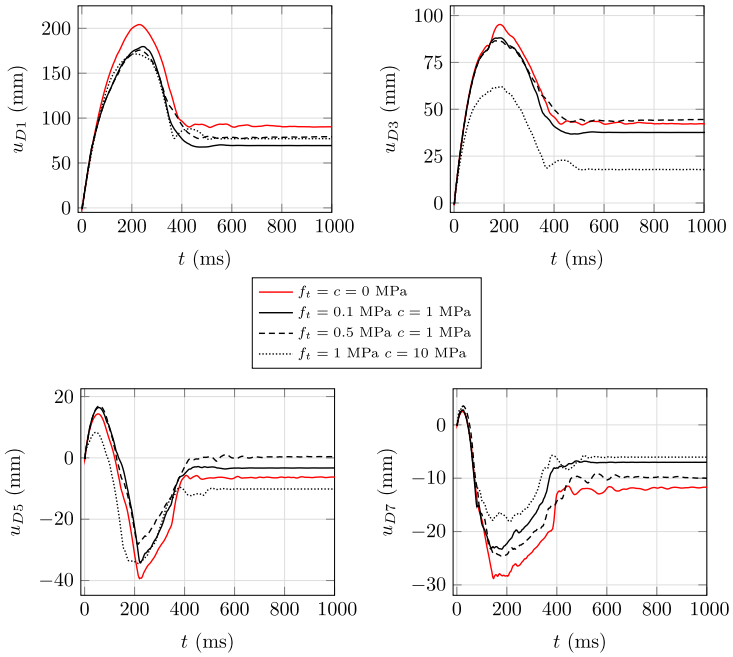

Figure 4.39 – Dynamic response of a cross vault subjected to 18 kg.

affect the structural response. Major differences, in terms of displacements, exist between the case with zero tensile strength and those with non-null strength. This holds true for the peak values and the permanent displacement ($t = 1500$ ms). Nevertheless, we can notice that, even for extremely large strength values ($f_t = 1$ MPa and $c = 10$ MPa, which are not realistic for the structures here investigated), global structural mechanism still remains the same, as the one depicted in Fig. 4.38.

4.6.3 Building blocks size effects

We present numerical analyses to asses the building blocks size effect, for zero joint tensile strength and cohesion, and two different explosive quantities (10 and 18 kg). As previously done for the barrel vault (see paragraph 4.5.5), we investigate the behavior of the vault using blocks that are approximately half and twice their original size, assuming constant overall thickness and mortar height, see Figure 4.40.

Figures 4.41 and 4.42 display the vertical displacement recorded at the keystone of the vault, the friction work, and joints strain energies, for 10 and 18 kg, respectively. The system with half the blocks size displays an increase in the overall outward deflection for both loading scenarios due to the larger number of interfaces in the system. As mentioned in paragraph 4.5.5, the smaller the blocks are, the larger the number of masonry joints is, hence a decrease of the overall flexural stiffness, with respect to the reference size, is

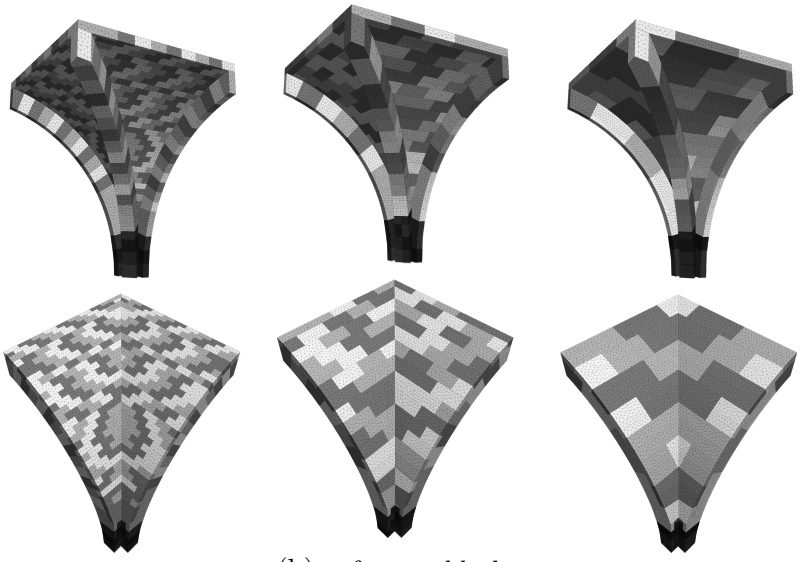

(a) 1/2 blocks size. (b) reference blocks size. (c) 2 blocks size.

Figure 4.40 – DE models using blocks that are half (a) and twice (b) the reference size (b).

observed.
Considering blocks with double size results in a reduction of the out-of-plane displacements, instead. This is due to the relative increase of the flexural stiffness of the model. It is worth noticing that as the blocks size reduces, the friction work and joints strain energy increases. The above results agree with those found for a barrel vault.
We shall notice that the response mechanism is independent of the dimensions of the blocks. Moreover, for the case of 18 kg, structural failure of the skin is observed in all cases. This is clearly shown by Figures 4.38 4.43 and 4.44.

4.7 Additional remarks

The dynamic behavior of masonry structures subjected to blast actions was studied here. For this purpose, a numerical model based on the DEM was presented and validated on the basis of recent existing, detailed experimental tests involving planar geometries subjected to far-field explosions. The essential features of the mechanical response and failure modes were captured by the numerical model.

Once the numerical model was validated, it was used to assess the response of various curvilinear masonry elements, namely arches and barrel and cross vaults.
For the case of two-dimensional arches, we investigated the resistance and failure modes of different types of arches (semi-circular, segmented, and pointed ones). In particular, we assessed the influence of the slenderness ratio, η, and the size of the system. For the quantities of explosive and material parameters considered, we found that the most vulnerable architectural asset is the semi-circular arch. For this reason, we further investigated the response of a barrel vault, i.e. a semi-circular vault, to a centered surface

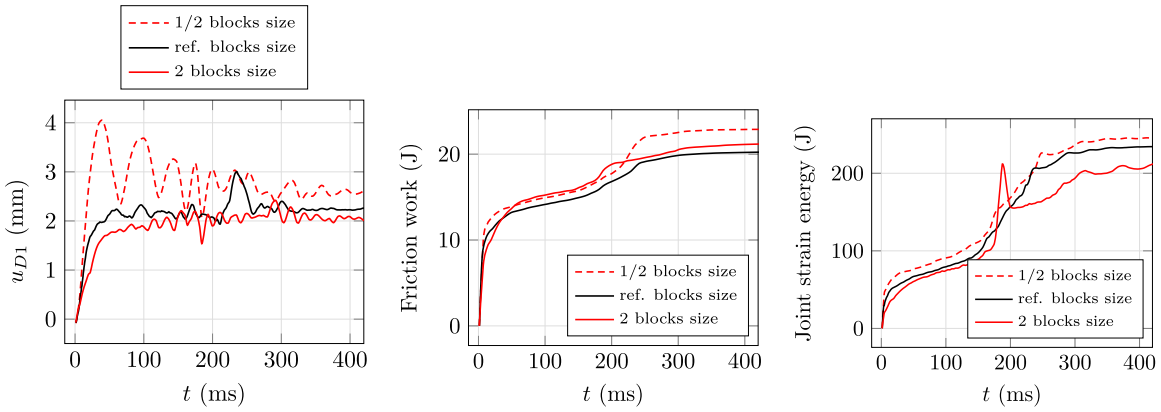

(a) vertical displacement. (b) friction work. (c) joints strain energy.

Figure 4.41 – Building blocks size effect for 10 kg: (a) vertical displacement of the keystone, (b) friction work, (c) joints strain energy.

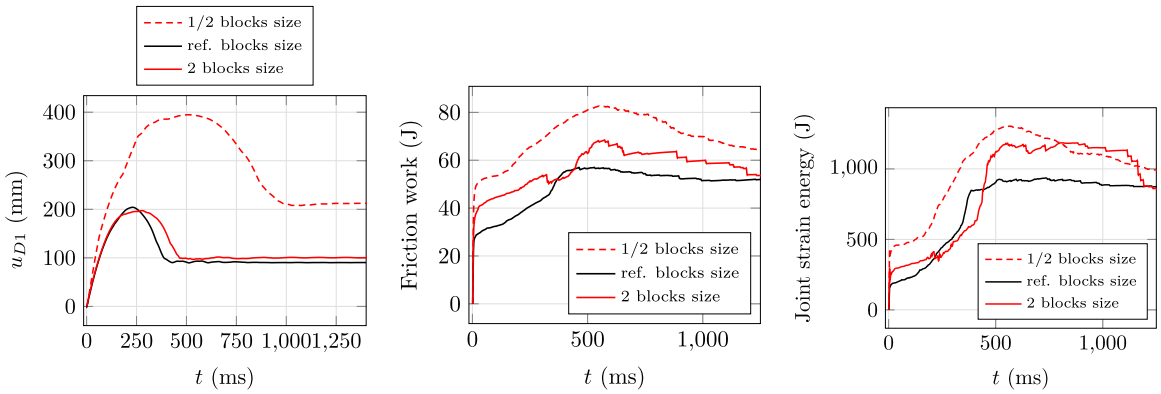

(a) vertical displacement. (b) friction work. (c) joints strain energy.

Figure 4.42 – Building blocks size effect for 18 kg: (a) vertical displacement of the keystone, (b) friction work, (c) joints strain energy.

blast. We examined the influence of micro-mechanical parameters such as the joints' dilatancy and friction angle, the cohesion and tensile strength of the mortar joints, as well as the size of the building blocks. Typical values or range of values for masonry were considered for the above mentioned parameters.
For the numerical examples that were investigated, it was shown that the response of a barrel vault restrained to fixed supports is similar to that of a planar wall subjected to out-of-plane loads, confined to supports that prevent outward movement. Under the action of blast loads, membrane compressive forces develop and the longitudinal layers of bricks bend, giving rise to an arching mechanism.
Masonry joints with zero dilatancy (non-associative plastic behavior) lead to reduced membrane forces, hence to an increase in out-of-plane deflections of the structure (14% larger with respect to the associative case). Moreover, we showed that zero dilatancy of joints decreases the stress in the masonry ($\approx$ 85% within the interfaces and $\approx$ 50%

within the blocks). This is not a surprising result but its quantification through our analyses shows the importance of non-associativity in the investigation, modeling, and design of masonry structures. This limits the application of conventional analysis tools of plasticity theory, such as limit analysis. Therefore dilatancy is related to two competing mechanisms, one that enhances failure due to sliding at the joints, when dilatancy is low, and another that enhances brick failure when dilatancy is high. These competing effects give the possibility to design mortars providing optimal dilatancy for a given structural system.
As far it concerns the effect of the size of the blocks, it was found that in general the larger the blocks are, the higher the strength of the masonry becomes, see also (Masi et al., 2019a; Godio et al., 2018; Petry and Beyer, 2014).
Finally, the case of a cross vault subjected to an explosion was also simulated. As for the barrel vault, the influence of the strength of the masonry joints and the building blocks size effects were assessed, leading to the same qualitative results as for as it concerns the dynamic response and dissipation mechanisms.

The numerical simulations showed that the high loading strain-rate effects on the material strength are almost negligible for the structure under study. Indeed, in all of the computations, strain-rates were found to be lower than 2 s^{-1}, hence the beneficial effects of high loading rates on the strength of the materials are limited (see also Chapter 2). Moreover, the above mentioned negligible influence of cohesion and tensile strength on the dynamic response of the masonry vault shows that taking into account the high strain-rates phenomena at the material level is secondary for the investigated systems.

The results obtained in this Chapter can be useful for improving our understanding on the dynamic behavior of masonry structures under blast actions, for which the scientific literature is quite limited. Moreover, as presented in Chapter 5, they give useful insight and can be used with validation purposes in order to select appropriate numerical methods based on continuum mechanics (upscaling/homogenization) in the investigation of large masonry structures of non-standard geometry for which the DEM is prohibitive due to the high computational cost.

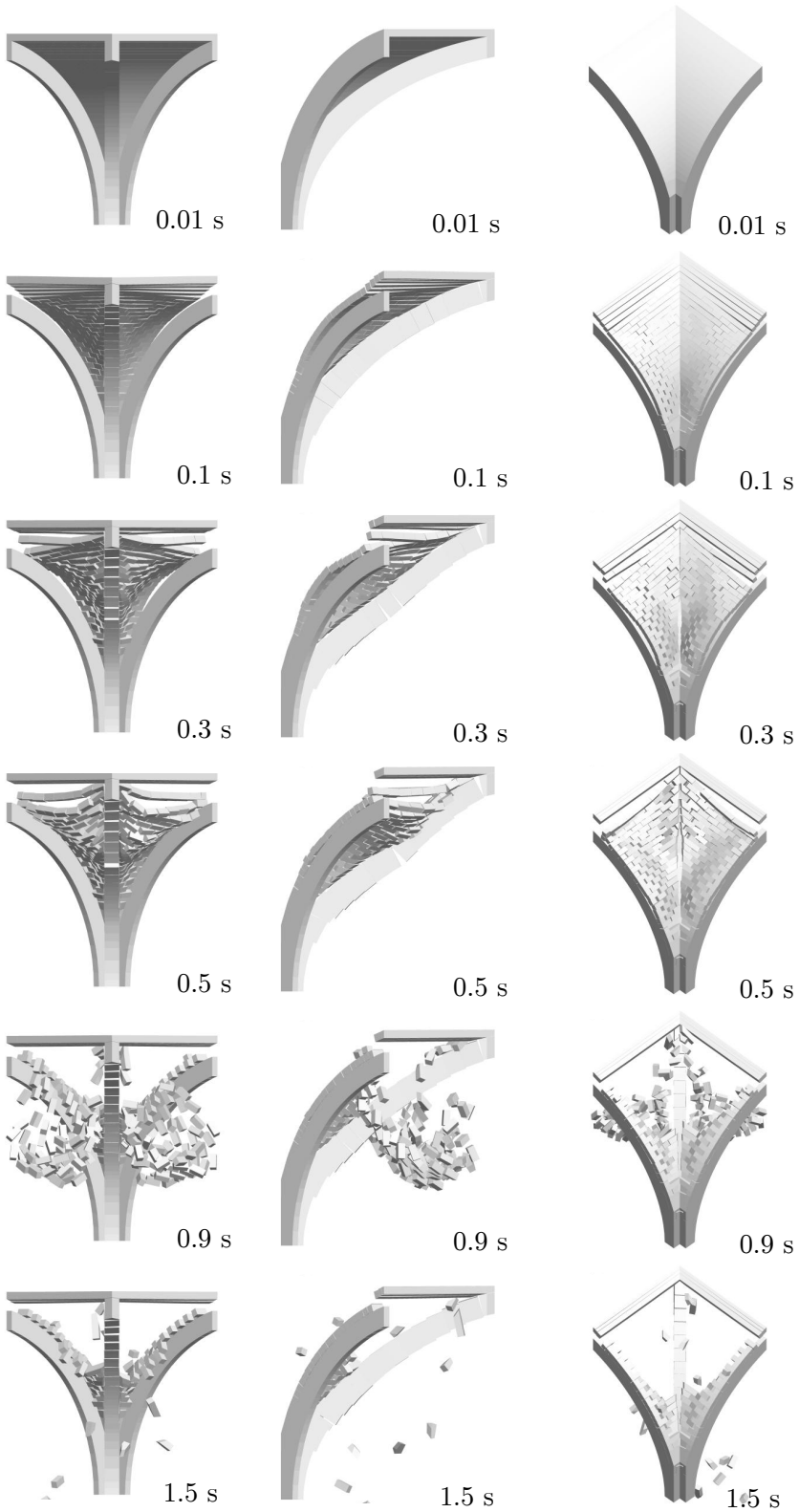

(a) bottom view (b) side view (c) top view

Figure 4.43 – Dynamic response of a cross vault, with half the blocks dimensions, subjected to 18 kg.

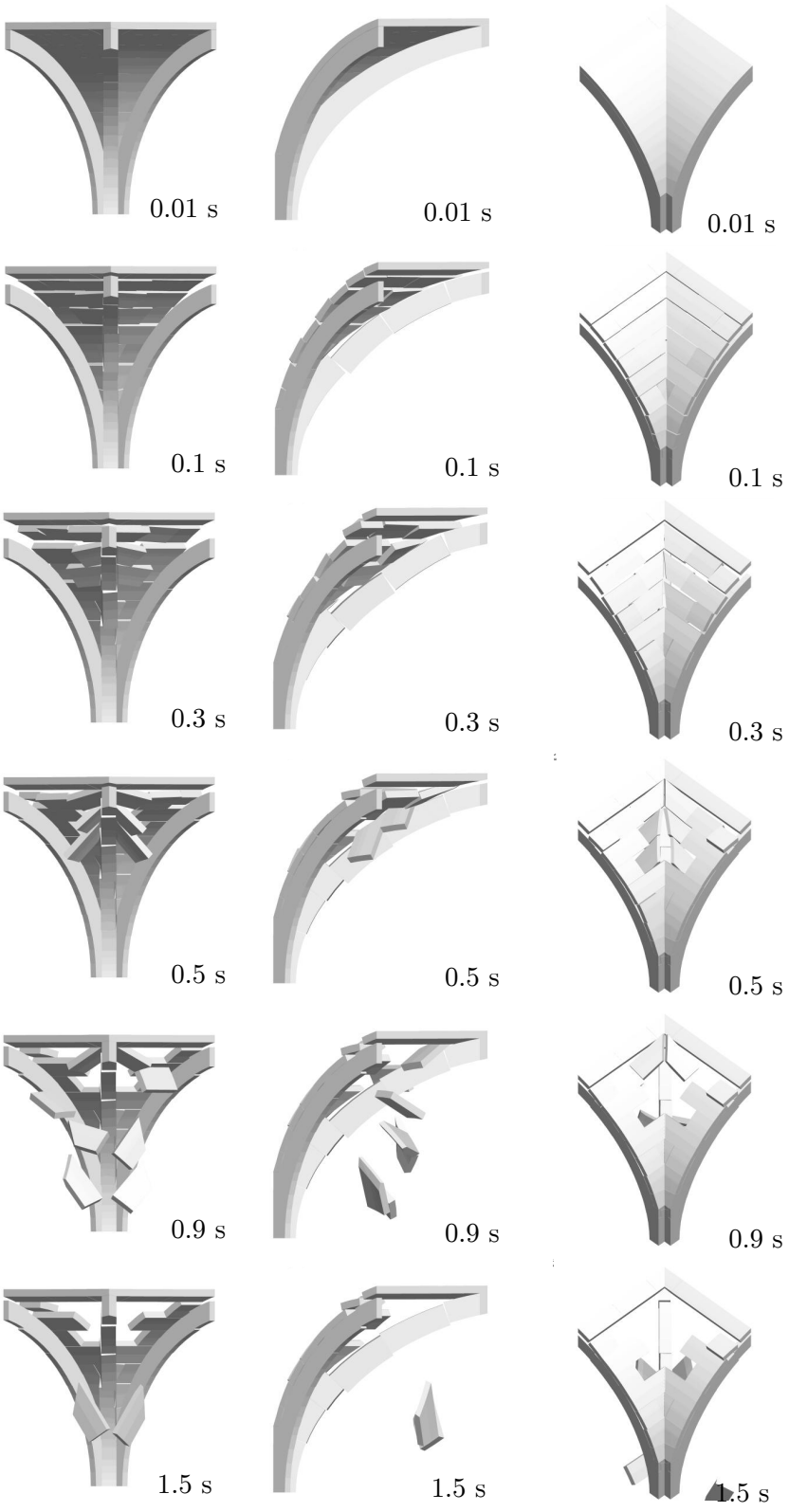

(a) bottom view (b) side view (c) top view

Figure 4.44 – Dynamic response of a cross vault, with twice the blocks dimensions, subjected to 18 kg.

Chapter 5

Simplified macro-scale modeling of masonry structures subjected to blast loads

Abstract. *Whilst meso-scale approaches allow detailed modeling of the behavior of masonry structures, their computational cost is prohibitive for modeling whole structures. Here we present a simplified macro-scale modeling approach.*
Beside its strong assumptions, the proposed model allows to mimic the meso-scale behavior in large Finite Element simulations, accounting for variations in the specific parameters which characterize the masonry, such as the building blocks dimensions, the elastic parameters of the constituents, as well as the material strength and softening behavior.
Our Finite Element results are corroborated with existing experimental tests and Discrete Element simulations involving regular and non-standard masonry structures subjected to explosions. Despite its limitations, our approach allows good estimations of the blast resistance and represents a satisfactory compromise between accuracy and associated computational cost.
We show the performance of such an approach by investigating the response of a non-standard historical building in a blast scenario.

Contents

5.1 Introduction

Meso-scale, and in particular the DEM, approaches offer high degree of accuracy in studying the behavior of masonry structures (cf. Chapter 4). Nevertheless, because of the difficulty in determining the exact mechanical parameters at the meso-level and the considerable computational cost of discrete type approaches, continuum macroscopic models attract wide scientific interest. The main reason for using continuum models is that they offer a certain degree of abstraction and allow to upscale the meso-mechanical characteristics to the macro-scale [1]. In particular, macro-models represent a computational efficient way to model large structures, which can hardly be modeled with meso-scale approaches, e.g. DEM.

Macro-models, typically based on the Finite Element Method (FEM), regard the masonry material as a homogeneous isotropic or anisotropic continuum. Either a classical Cauchy continuum formulation (Heyman, 1995; Page, 1978; Alpa and Monetto, 1994; Pande et al., 1989; Cecchi and Sab, 2002; Zucchini and Lourenço, 2002, 2007; Milani et al., 2006; Pelà et al., 2013; Petracca et al., 2017) is followed or micromorphic continua (Sulem and Mühlhaus, 1997; Masiani and Trovalusci, 1996; Stefanou et al., 2008, 2010; Godio et al., 2017; Trovalusci and Pau, 2014) are used, in order to take into account internal lengths related to the size of the masonry units (Lourenço, PhD Thesis, 1997; Lourenço et al., 1998; Pelà et al., 2013; Rafsanjani et al., 2015). The formulation of macroscopic constitutive laws is still a challenging task (Pelà et al., 2013; Stefanou et al., 2015a; Godio et al., 2017).

Asymptotic homogenization techniques (Bakhvalov and Panasenko, 1989) have been widely used to provide closed-form solutions of the material parameters at the macro-level. Most of the available continuum models describe the elastic behavior. Only few works studied the inelastic behavior of masonry through non-linear homogenization approaches that in most of the cases are based on extensive numerical simulations (see e.g. Lourenço et al., 2007; Stefanou et al., 2015a; Godio et al., 2017). For a comprehensive review of various continuum models we refer to Lourenço et al. (2007).

As discussed in Section 2.5.2, in the past decades, increasing scientific interest has been shown to multi-scale approaches. Multi-scale models allow to capture the effects of the micro-/meso-scales and upscale the mechanical response, providing a more complete macro-scale description then simplified, ad-hoc models for masonry. Nevertheless, in most of the cases, the computational cost becomes prohibitive for studying large masonry structures. However their cost could be considerably reduced by using Machine Learning as shown in Chapter 6.

However, simplified models will always be needed for engineering applications at large scale. For that reason, the aim of this Chapter is to develop a simplified and fast material model for masonry, which can be used to obtain preliminary estimates of the resistance and failure modes of large masonry structures subjected to blast actions. In particular, we develop a macro-model based on the FEM, whose macroscopic overall properties can mimic, in a certain extent, the meso-scale behavior (cf. Chapter 4) and account for variations in the specific parameters which characterize the masonry, such as the

1. For the definition of the meso- and macro-scales used in this Thesis we refer to Section 2.5

building blocks dimensions, the elastic parameters of the constituents, as well as the material strength and softening behavior.
This is accomplished by a two-step strategy. Elastic and inelastic material behaviors are derived through distinct upscaling and averaging procedures, based on energetic equivalence. First, relying on the developments of Cecchi and Sab (2002) (asymptotic homogenization), the macroscopic elastic material properties are derived. A simplified isotropic material formulation is proposed on an energetic basis. Then, the softening behavior is considered relying on the smeared cracking model (also known as cohesive crack model, Bazant and Planas, 1997), first developed by Hillerborg et al. (1976). Through an energy-based upscaling procedure, we propose a macroscopic smeared cracking model for mode I fracture of the masonry. These simplifying assumptions are, with no doubt, very strong, but can allow the direct use of existing commercial codes such as ABAQUS and LS-DYNA, which are accessible by practitioners. Notice that more complete and advanced macroscopic models, based on upscaling and homogenization, exist in the current literature (Zucchini and Lourenço, 2002; Brasile et al., 2007; Massart et al., 2007; Zucchini and Lourenço, 2009; Marfia and Sacco, 2012; Stefanou et al., 2015a; Petracca, 2016; Bertolesi et al., 2018; D'Altri et al., 2019).

The Chapter is structured as follows. We develop the macroscopic FE model in Section 5.2. Section 5.3 presents the comparison of the proposed model with the experimental tests of a masonry wall performed by Michaloudis and Gebbeken (2019). Then, the macro-FE model is compared with our DEM results for a wide range of non-standard, curvilinear masonry structures, subjected to explosions. Finally, we present in Section 5.4 an application to a representative large, non-standard masonry structure. The performance and limitations of this simplified approach are presented and discussed in Section 5.2.

5.2 Macro-modeling of masonry structures subjected to explosions: upscaling procedure

We present in this Section the simplified upscaling procedure we use to derive the macroscopic overall properties of masonry. The upscaling process consists in replacing a heterogeneous medium by an equivalent homogeneous one. The quasi-periodic geometrical pattern of blocks and mortar joints makes it possible to assume that the heterogeneous masonry material is comparable to a composite one with a periodic micro-structure. Such a medium is defined by a characteristic elementary pattern−or representative elementary volume (REV)−whose repetition represents the whole structure, see Figure 5.1. Once the macroscopic parameters of the representative volume element are computed, we assume that every material point of the equivalent homogeneous medium has the same behavior with the characteristic element. This assumption is a good approximation if the ratio of the characteristic length of the representative volume (or internal length), ℓ^*, over the characteristic length of the structure, ℓ, over is small enough, namely if

$$\epsilon = \frac{\ell^*}{\ell} \ll 1.$$

5.2. Macro-modeling of masonry structures subjected to explosions: upscaling procedure

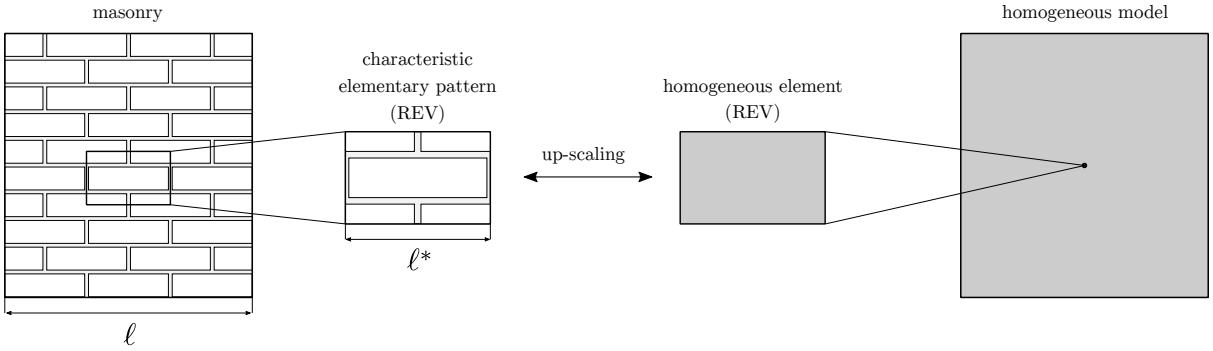

Figure 5.1 – Upscaling procedure.

A two-step strategy, based on an energetic equivalence, is followed to derive the elastic and inelastic macroscopic behavior. We consider only the case of masonry with mortar joints. The proposed, simplified model assumes isotropic behavior. This is usually not the case for masonry, which displays, in most of the cases, an orthotropic behavior. Several more detailed numerical models exist to well capture the anisotropic response of the masonry (see the references in the Section 5.1). Nevertheless, for real, large, non-standard masonry structures such as monuments and historical building, detailed documentations and architectural surveys are needed to adequately consider the masonry pattern in each part of the investigated building. In most cases, three-dimensional laser scanning techniques are the only available tool to map the brickwork pattern across such structures, but still the internal fill of masonry is hard to investigate throughout the structure. No detailed information is, in general, available for historical masonry buildings, therefore the assumption of considering a simplified isotropic macroscopic description of the material allows to have first, design-estimates of the dynamic response of the whole structure. This preliminary estimate can be sufficient for some engineering applications.

5.2.1 Elastic response

Cecchi and Sab (2002) performed asymptotic homogenization of the stack and running bond [2] masonry pattern (see Fig. 5.2). Masonry blocks and mortar are assumed isotropic with a linear elastic behavior. Due to the geometric distribution in space of the masonry, the derived homogenized constitutive model is transversely isotropic.

According to Cecchi and Sab (2002), the macroscopic elastic parameters are functions of two main parameters: a geometric parameter, $\mathsf{b} = \frac{h_m}{h_b}$, defining the relationship between the thickness of the mortar joint and the size of the bricks, and a deformability parameter, $\mathsf{a} = \frac{E_m}{E_b}$, defining the ratio of the mortar stiffness, E_m, to the block stiffness, E_b. The model gives very good approximation of the elastic macroscopic parameters only for relatively small values of a and b (Cecchi and Sab, 2002). A third additional geometric parameter, $\mathsf{c} = \frac{l_m}{l_b}$, is also considered to account for the case where mortar bed and head

2. In masonry construction, the stack bond is the pattern of installation of masonry units one of the top of another. The running bond is the pattern and sequence of installation of masonry units in a running fashion with each course, either 1/3 , 1/2 or 1/4 further than the adjacent course.

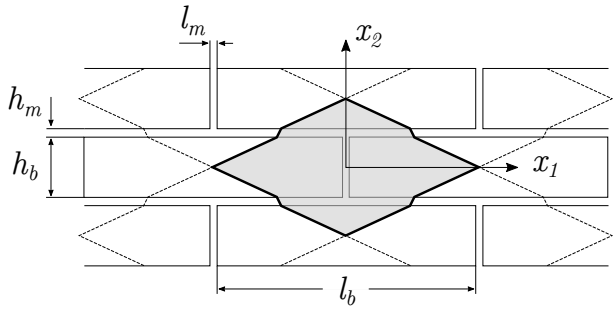

Figure 5.2 – Characteristic elementary pattern for a 1/2 running masonry bond, from (Cecchi and Sab, 2002).

joints have different thickness.
For the case of running bond masonry, with the same mortar thickness, h_m, for the head and bed joints, Cecchi and Sab (2002) derived an analytical expression of the homogenized compliance tensor $\mathbb{A}^H$. In particular, we have:

$$\mathbb{A}^H_{1111} = \mathsf{b}\,\frac{\left(\mathbb{A}^b_{1111}K' + \mathsf{b}B\right)\left(4K' + \mathsf{c}^{-1}K''\right)}{4\,\mathsf{cb}^3B + \mathsf{b}C\mathbb{A}^b_{1111} + K'D}, \tag{5.1a}$$

$$\mathbb{A}^H_{2222} = K'\,\frac{\mathsf{cb}B + K'\mathbb{A}^b_{1111}}{\mathsf{cb}^2B + (1+\mathsf{c})\mathsf{b}\mathbb{A}^b_{1111} + K'^2}, \tag{5.1b}$$

$$\mathbb{A}^H_{1122} = \mathsf{b}K'\,\frac{\mathbb{A}^b_{1122}\left(4K' + \mathsf{c}^{-1}K''\right)}{4\mathsf{cb}^3B + \mathsf{b}C\mathbb{A}^b_{1111} + K'\mathrm{D}}, \tag{5.1c}$$

$$\mathbb{A}^H_{1212} = \mathsf{b}K''\,\frac{\mathsf{c}\mathbb{A}^b_{1212}\left(K' + 4\mathsf{c}K''\right)}{\mathsf{b}F\mathbb{A}^b_{1212} + K''G}, \tag{5.1d}$$

where

$$K' = \left(1 + \frac{\nu_m}{1-\nu_m}\right)\frac{E_m}{1+\nu_m} \quad \text{and} \quad K'' = \frac{E_m}{2(1+\nu_m)}, \tag{5.2}$$

$$B = (\mathbb{A}^b_{1111})^2 - (\mathbb{A}^b_{1122})^2, \tag{5.3a}$$
$$C = 4(1+\mathsf{c})\mathsf{b}K' + \mathsf{bc}^{-1}K'', \tag{5.3b}$$
$$D = 4\mathsf{b}K' + \mathsf{bc}^{-1}K'', \tag{5.3c}$$
$$F = \mathsf{cb}K' + 4\mathsf{c}^2\mathsf{b}(1+\mathsf{c})K'', \tag{5.3d}$$
$$G = \mathsf{cb}K' + 4\mathsf{c}^2\mathsf{b}K'', \tag{5.3e}$$

and

$$\mathbb{A}^b_{1111} = \frac{E_b}{1-\nu_b^2}, \tag{5.4a}$$

$$\mathbb{A}^b_{1122} = \frac{\nu_b E_b}{1-\nu_b^2}, \tag{5.4b}$$

$$\mathbb{A}^b_{1212} = \frac{1-\nu_b}{2}\frac{E_b}{1-\nu_b^2}. \tag{5.4c}$$

Equivalently, Cecchi and Sab (2002) derived the homogenized elastic constants for the case of stack bond masonry. The following expressions refer to the case of constant mortar thickness h_m and plane stress conditions:

$$\mathbb{A}^H_{1111} = K' \frac{\mathbb{A}^b_{1111}K' + \mathsf{b}B}{\mathsf{cb}^2B + (1+\mathsf{c})\mathsf{b}K'\mathbb{A}^b_{1111} + K'^2}, \tag{5.5a}$$

$$\mathbb{A}^H_{2222} = K' \frac{\mathsf{cb}B + K'\mathbb{A}^b_{1111}}{\mathsf{cb}^2B + (1+\mathsf{c})\mathsf{b}K'\mathbb{A}^b_{1111} + K'^2}, \tag{5.5b}$$

$$\mathbb{A}^H_{1122} = \frac{K'^2\mathbb{A}^b_{1122}}{\mathsf{cb}^2B + (1+\mathsf{c})\mathsf{b}K'\mathbb{A}^b_{1111} + K'^2}, \tag{5.5c}$$

$$\mathbb{A}^H_{1212} = \frac{K''\mathbb{A}^b_{1212}}{(1+\mathsf{c})\mathsf{b}\mathbb{A}^b_{1111} + K''}. \tag{5.5d}$$

From the knowledge of the geometric and elastic parameters of the masonry blocks (i.e., E_b, ν_b, h_b, and l_b) and mortar joints (i.e., E_m, ν_m, and h_m), it is straightforward to compute, from the expression of the elastic constants (Eq.s (5.1a)-(5.1d), for running bond, or Eq.s (5.5a)-(5.5d), for stack bond), the equivalent macroscopic Young's moduli along the horizontal and vertical directions, E^H_{11} and E^H_{22}, respectively; the shear modulus, G^H_{12}; and the Poisson's coefficient ν^H_{12}.
Whilst the derivation in (Cecchi and Sab, 2002) gives a homogenized orthotropic material in two-dimensions (in-plane), we stress that a three-dimensional formulation can be obtained by further assuming $E^H_{33} = E_b$, $G^H_{13} = G^H_{23} = G_b$, and $\nu^H_{23} = \nu^H_{13} = \nu_b$. This is a strong assumption [3] (compared to rigorous theories, see e.g. Vannucci, 2018), which will be tested and motivated by comparisons with DEM simulations (see Section 5.3).

Isotropic simplification

Following the work of Cecchi and Sab (2002) and the above developments, the homogenized macroscopic medium displays an orthotropic behavior. Nevertheless, due to the difficulty in determining the orientation of the masonry pattern in real, historical masonry buildings, a simplified isotropic macroscopic material is here preferred. In particular, we consider a fictitious isotropic medium with Young's and shear moduli equal to

$$E^M = \max\left(E^H_{11}, E^H_{22}\right), \qquad G^M = G^H_{12}. \tag{5.6a}$$

This choice stems from energetic arguments. Indeed, choosing $E^M = \max\left(E^H_{11}, E^H_{22}\right)$ gives conservative estimations of the (specific) total work (i.e., the elastic energy density $1/2f_t^2/E^M$) that has to be done to reach the ultimate strength of the material, f_t. Notice that the Poisson 's coefficient of the fictitious isotropic medium is computed on the basis of E^M and G^M, i.e., $\nu^M = E^M/2G^M - 1$.

3. Notice that, for all cases here considered, the thermodynamic restrictions on the elastic coefficients are verified.

5.2.2 Inelastic response

The inelastic material response is modeled using the basic assumption that damage only takes place at the masonry joints/interfaces, while the blocks are considered to be linearly elastic, see Chapter 4 for more details. Strain-rate effects are neglected (cf. Sect. 2.3). The inelastic material behavior is here modeled relying on the smeared cracking model, originally developed for concrete Hillerborg et al. (1976). From the identification of the characteristic parameters to describe the fracture mode I of masonry joints, we develop an energy-based upscaling procedure to obtain the failure parameters of the material, at the macroscopic scale.

Notice that we neglect, in our simplified model, plastic deformations, internal friction, and fracture mode II. This simplifying assumption is strong, but it allows direct use of existing material models implemented in commercial softwares such as ABAQUS and LS-DYNA. The important limitations of neglecting plastic deformations and sliding will become apparent later on, or shown already in Chapter 4.

Smeared cracking model

The basic assumption of the smeared cracking model is the formation, as an extension of the real crack, of a fictitious crack, referred to as the process zone (Carpinteri, 2012) with finite thickness l_{ch}, where the material, albeit damaged, is still able to transfer stresses, see Figure 5.3. The process zone represents the area in which energy dissipation takes place. Damage starts to form when the principal tensile stress reaches the material tensile strength, f_t, in the direction perpendicular to the direction of the principal stress (Rankine criterion). According to the smeared cracking model, once the onset of failure is met, the stress transferred by the material is (monotonically decreasing) function of the separation w (called also the opening displacement):

$$\sigma = \tilde{\sigma}(w).$$

In the uncracked zone the behaviour of the material is linear elastic. By definition, $\tilde{\sigma}(0) = f_t$. The terminal point of the softening curve $\tilde{\sigma}(w)$ is denoted as w_f, $\tilde{\sigma}(w_f) = 0$. The area under the entire softening stress-separation curve, $\tilde{\sigma}(w)$, represents the total energy dissipated by the fracture process per unit of the crack surface area−that is, the fracture energy G_F (in J/m^2).
The smeared cracking model assumes the existence of a fracture characteristic length, l_{ch}, see Figure 5.4. Indeed, in materials exhibiting strain-softening, the strain localizes into a narrow zone of finite thickness (Van der Pluijm, 1999) where energy is dissipated. In the smeared cracking, this narrow zone is smeared over a finite volume V, with cross section A and length l_{ch}. Accordingly, the softening law depends on both the material fracture energy per unit of crack surface area, G_F, and the characteristic length l_{ch}, in such a way that the following relation holds:

$$G_F = \frac{W}{A} = \frac{W}{V} l_{ch} = g_F l_{ch}, \tag{5.7}$$

where W is the total energy dissipated by the fracture process, $A = ht$ is the crack surface area, g_F is the fracture energy per unit of volume, which is a material parameter, and

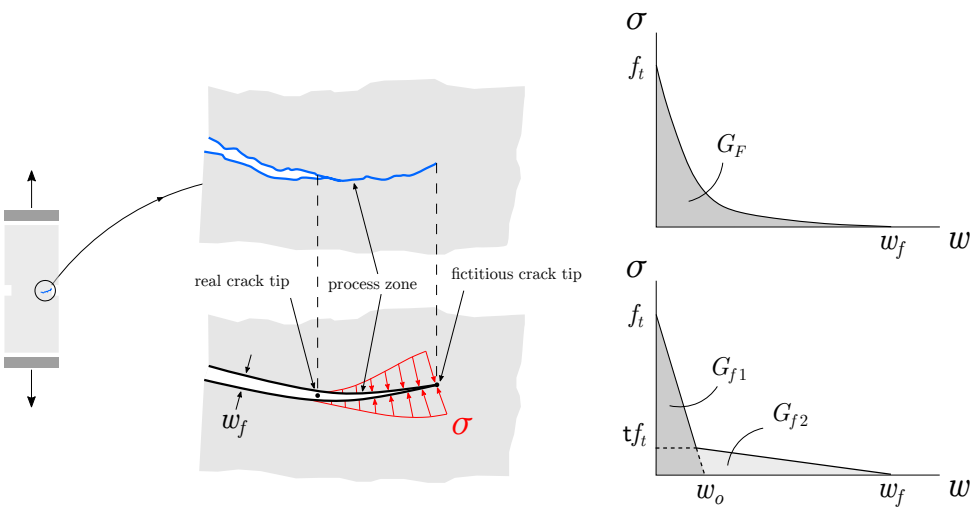

Figure 5.3 – The basic assumption of the smeared cracking model is to consider, as an extension of the real crack, of a fictitious crack, referred to as the process zone (Carpinteri, 2012) with finite thickness l_{ch}, where the material, albeit damaged, is still able to transfer stresses.

$V = htl_{ch}$ is the volume of the dissipative zone (see Fig 5.4).
Notice that in the classical Cauchy continuum, which has no internal lengths, strain localization takes place on a mathematical plane, of zero-thickness, which is an artifact when experimental evidence is taken into account. Consequently, in Finite Element Method (FEM) simulations, Cauchy continuum models lead to strain localization bands whose thickness is 1 to 2 Finite Elements. As a result, dissipation is mesh dependent and regularization techniques are needed to overcome this issue (Stefanou and Gerolymatou, 2019). In the smeared cracking model, the characteristic length l_{ch} is selected so that it allows to regularize the aforementioned mesh dependency (l_{ch} depends on the material and mesh discretization, see Petracca et al., 2016).

The tail of the softening branch, $\tilde{\sigma}(w)$, is usually very long, which poses practical problems for the experimental measurement of the fracture energy G_F (Van der Pluijm, 1997). In the initial work of Hillerborg et al. (1976), $\tilde{\sigma}(w)$ is described as a decaying exponential with a horizontal asymptote below axis w. Later, from the work of Petersson (1981), a simple bi-linear form has been generally adopted, see Figure 5.3. Function $\tilde{\sigma}(w)$ first descends very steeply and then, at $\sigma = \mathtt{t}f_t$, the descent becomes slower.
In the light of this bi-linear approximation, the fracture energy is written as follows:

$$G_F = \int_0^{w_f} \tilde{\sigma}(w)\,\mathrm{d}w = G_{f1} + G_{f2}, \tag{5.8a}$$

$$G_{f1} = \frac{f_t w_o}{2} = \frac{f_t^2}{2E'} l_{ch}, \tag{5.8b}$$

$$G_{f2} = \frac{\mathtt{t}f_t\,[w_f - (\mathtt{t}-1)w_o]}{2}, \tag{5.8c}$$

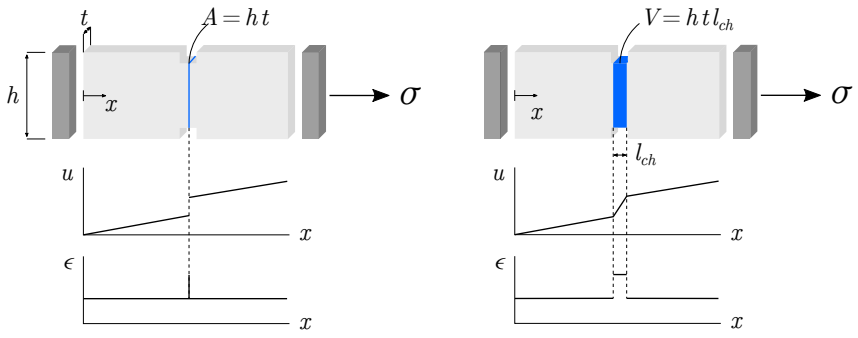

Figure 5.4 – Representation of displacement and strain fields in mode I fracture: localization of strains in classical Cauchy continuum into a mathematical plane (left) and regularized smeared discontinuity−smeared cracking model (right).

where G_{f1} corresponds to the area beneath the initial tangent of slope E' (cf. Fig. 5.3). According to Planas et al. (1992), only G_{f1} controls the maximum load (resistance) of structures.
Assuming the slope change occurs at stress $\mathsf{t}t_f$, we have

$$G_F = \mathsf{r} G_{f1}, \quad \text{with} \quad \mathsf{r} = 1 + \mathsf{t}\left(\frac{w_f}{w_o} - 1\right), \tag{5.9a}$$

$$w_f = \left(\frac{\mathsf{r}-1}{\mathsf{t}} + 1\right) w_o. \tag{5.9b}$$

According to investigations of Wittmann et al. (1988); Rokugo et al. (1989); Bazant and Planas (1997) for concrete-like materials, $\mathsf{t} \approx 1/4$. Several works (Planas et al., 1992; Guinea et al., 1994; Bažant and Becq-Giraudon, 2002) suggest $\mathsf{r} = 2.5$. However for masonry structures different values for r and t may hold. This is investigated in the next paragraph. In particular, we present a calibration of these material parameters for mortar joints.

Bi-linear approximation of the softening behavior of mortar joints

Relying on the bi-linear approximation of the softening branch, $\tilde{\sigma}(w)$, we aim at providing estimates of the dimensionless parameters r and t for the case of mortar joints. Notice that the same values are used to characterize the macroscopic material. We refer here to the extensive experimental campaign performed by Van der Pluijm (1997) and, in particular, to the tensile tests (33, in number) on masonry prisms with wire cut Joosten clay bricks and 1:1:6 (cement:lime:sand) mortar.
In all tests, failure of the masonry joints is reported, with high scatter of the tensile bond strength and of the fracture energy. The mean values of the mortar Young's modulus, tensile strength, fracture energy were

$$E_m = 1.2 \text{ GPa}, \quad f_t = 0.4 \text{ MPa}, \quad G_F = 5.5 \text{ N/m}.$$

These values are considered for deriving the parameters r and t.The first contribute to the fracture energy of the masonry joints, G_{f1}, is assumed such that the initial tangent

slope E' is equal to the mortar Young's modulus [4], E_m. Furthermore, we assume that the characteristic fracture length is equal to the mortar thickness, i.e., $l_{ch} = h_m$ (with $h_m = 14$ mm in (Van der Pluijm, 1997)), so that

$$w_o = \frac{f_t}{E_m} h_m.$$

Notice that this latter assumption stems from imposing that the volume of the dissipative zone during the fracture process coincides with the mortar. From the best-fitting of the bi-linear softening curve,

$$\sigma = \tilde{\sigma}(w) = \begin{cases} f_t \left(1 - \frac{w}{w_o}\right) & 0 \le w \le w_*, \\ \mathsf{t} f_t \left(1 - \frac{w/w_* - 1}{w_f/w_* - 1}\right) & w_* \le w \le w_f, \end{cases} \tag{5.10}$$

where $w_* = (\mathsf{t} - 1)w_o$, with the experimental results we obtain

$$\mathsf{t} = 0.2 \quad \text{and} \quad \mathsf{r} = 5.$$

Notice that these values are close to the aforementioned values for concrete-like materials ($\mathsf{t} \approx 1/4$ and $\mathsf{r} = 2.5$). Figure 5.5 displays some of the experimental stress-elongation curves from (Van der Pluijm, 1997), the average bi-linear approximation herein proposed, and, for completeness, the average exponential approximation proposed in (Lourenco et al., 1995).

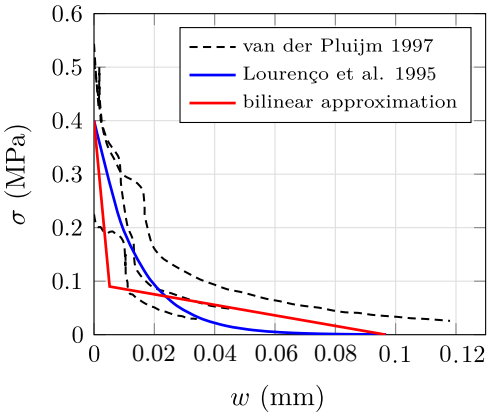

Figure 5.5 – Comparison of the stress-elongation curves from (Van der Pluijm, 1997) with the average exponential approximation from (Lourenco et al., 1995) and the average bi-linear approximation proposed, with $\mathsf{t} = 0.2$ and $\mathsf{r} = 5$.

In the following, we shall assume that the softening behavior of the mortar joints can be, in first approximation, described through the bi-linear curve, Eq. (5.10), with $\mathsf{t} = 0.2$ and $\mathsf{r} = 5$.

4. Imposing $E' = E_m$ is equivalent to assuming that the first contribute of the fracture energy per unit of volume coincides with the elastic energy per unit of volume, namely, $f_t^2/(2E_m)$.

Energy-based upscaling of the smeared cracking model for masonry

Once the characteristic smeared cracking parameters for mortar joints have been derived, we introduce an energy-based upscaling procedure to derive the macroscopic material constitutive description. Similarly to the work of Petracca et al. (2016), we introduce a macroscopic fracture energy by imposing the equivalence of the energy dissipated by material fracture.

Derivation of the macro-scale fracture energy. Consider the REV with dimensions $l^\mu \times h^\mu \times t^\mu$, composed of masonry units and mortar joints (meso-scale). We assume, as in Chapter 4, that damage only takes place at the masonry joints (see Fig. 5.6). The total energy, dissipated by the fracture process involving volume V_D^μ (i.e., the volume of the mortar), is given by:

$$W_D^\mu = \frac{G_F^\mu}{l_{ch}^\mu} V_D^\mu = G_F^\mu h^\mu t^\mu, \tag{5.11}$$

where G_F^μ is the fracture energy per unit of crack surface of the mortar material and l_{ch}^μ is the characteristic length of the mortar joints, assumed equal to the mortar thickness, i.e., energy dissipation due to fracture occurs over the entire thickness of the mortar, $l_{ch}^\mu = h_m$

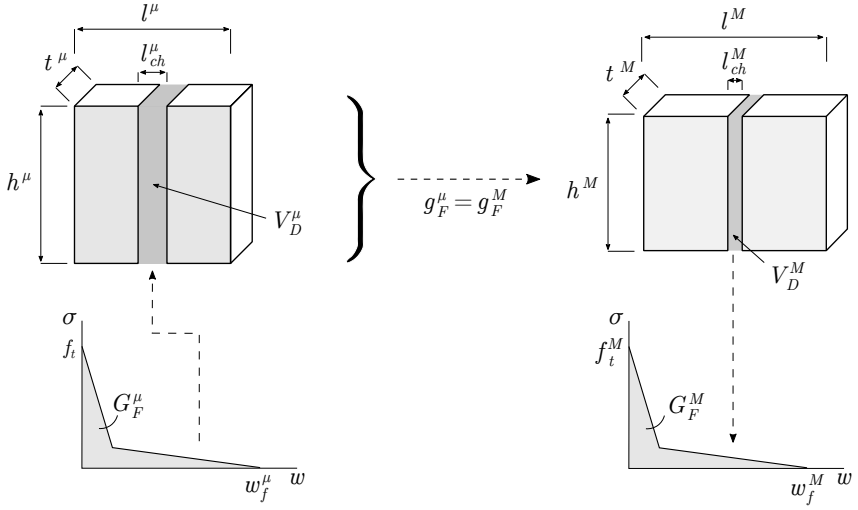

Figure 5.6 – Fracture energy based upscaling.

Following the work of Petracca et al. (2016), the dissipated energy can be distributed over the entire volume of the REV, by definition of a specific fracture energy g_F^μ as

$$g_F^\mu = \frac{W_D^\mu}{V^\mu} = \frac{W_D^\mu}{l^\mu h^\mu t^\mu} = \frac{G_F^\mu}{l^\mu}. \tag{5.12}$$

At the macro-scale, by assuming the existence of a macroscopic fracture energy G_F^M, the whole dissipated energy is given by

$$W_D^M = \frac{G_F^M}{l_{ch}^M} V_D^M = G_F^M h^M t^M, \tag{5.13}$$

where l_{ch}^M represents the characteristic length of the crack at macro-scale, and h^M, t^M are the height and width of the FE discretizing the macro-domain. As previously done for the REV, we consider the macro-scale dissipated energy smeared over the entire volume of a single FE, $V^M = l^M h^M t^M$, by introduction of a macroscopic specific fracture energy g_F^M, namely

$$g_F^M = \frac{W_D}{V^M} = \frac{G_F^M}{l^M}. \tag{5.14}$$

By requiring that the smeared dissipated energy of the REV is equal to the smeared dissipated energy of the FE, i.e., $g_F^\mu = g_F^M$, we obtain the following definition of the fracture energy which will be used for the FE analyses

$$G_F^M = \mathsf{L} G_F^\mu, \quad \text{with} \quad \mathsf{L} = \frac{l^M}{l^\mu}. \tag{5.15}$$

From Eq. (5.15) it can be seen that the macro-scale fracture energy should be multiplied by a scaling factor L, which is the ratio between the length of FE and the length of the REV. We stress that, in the case of regular masonry as it is the case here, the value of the scaling factor L depends on the direction along which is computed, see Figure 5.7. In order to obtain an isotropic damage formulation, we select the scaling factor to be the smallest over the two directions: horizontal and vertical. This gives the smallest (over the two directions) value of L, which hence allows to have a conservative value of the macroscopic fracture energy, G_F^M. Furthermore, we stress that the direction along which L takes the smallest value represents the privileged direction for tensile failure in a masonry panel, subjected to out-of-plane loading. For instance, if one considers $l_b > h_b$ (and equal head and bed joints thickness, h_m), then the scaling factor is

$$\mathsf{L} = \min\left(\mathsf{L}_{\text{bed}}, \mathsf{L}_{\text{head}}\right) = \min\left(\frac{l^M}{h_b + h_m}, \frac{l^M}{l_b + l_m}\right) = \frac{l^M}{l_b + l_m}.$$

Definition of the softening behavior at the macro-scale. To define the softening behavior of the macroscopic material, we assume the bi-linear approximation of the stress with respect to the separation w. From the smearing assumption introduced in paragraph 5.2.2, i.e., $l_{ch}^\mu = h_m$, we have

$$G_{f1}^\mu = \frac{f_t^2}{2E_m} h_m, \tag{5.16}$$

with $w_o^\mu = f_t h_m / E_m$. Using Eq. (5.15) and further imposing that the tensile strength of the material at the macro-level is equal to the tensile strength of the masonry joints (i.e., $f_t^M = f_t$), and that $\mathsf{r}^M = \mathsf{r}^\mu$ and $\mathsf{t}^M = \mathsf{t}^\mu$, we obtain

$$G_{f1}^M = \mathsf{L} \frac{f_t^2}{2E_m} h_m, \tag{5.17a}$$

$$G_F^M = \mathsf{r} G_{f1}^M, \tag{5.17b}$$

$$w_o^M = \mathsf{L} \frac{f_t}{E_m} h_m, \tag{5.17c}$$

$$w_f^M = \left(\frac{\mathsf{r} - 1}{\mathsf{t}} + 1\right) w_o^M. \tag{5.17d}$$

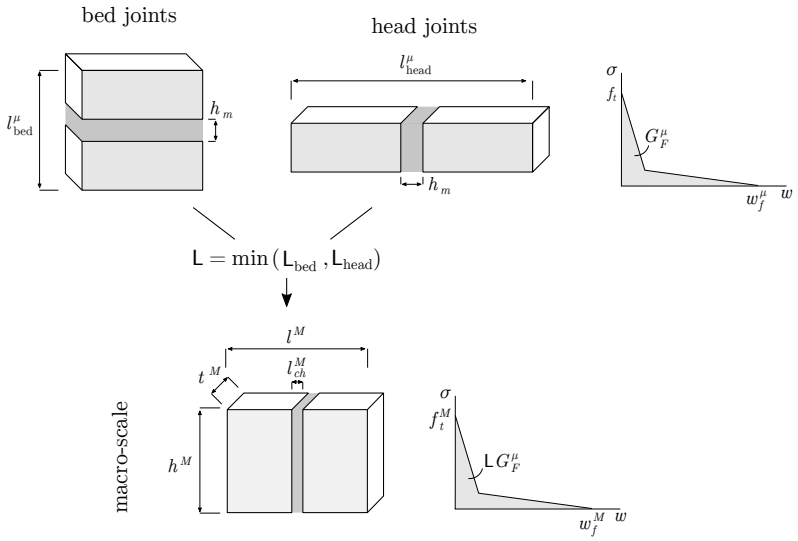

Figure 5.7 – The scaling factor L depends on the considered direction: vertical (bed joints), L_{bed}, or horizontal (head joints) L_{head}. The selected scaling factor is the minimum between the two values.

It is worth stressing that the proposed model only accounts for mode I fracture. Sliding and bending (mode II and III) fracture modes are neglected in our simplified model. More detailed models already exist in the current literature (e.g. Rafsanjani et al., 2015; Carpinteri et al., 2003; Reyes et al., 2008; Gálvez et al., 2013). Nevertheless, our aim is to propose a model which can describe the main features of the structural behavior of masonry elements under blast actions, and to keep the corresponding computational cost as small as possible. Moreover we aim at a model which is accessible to practitioners and can be directly use in commercial FE codes (ABAQUS, LS-DYNA, etc.).
Notice that, for dry joints, the tensile strength is zero, G_F as well—see Eq. (5.17). Consequently, the use of this approach can lead to numerical problems. In this case, we suggest the use of a small value of the tensile strength, thus of the fracture energy.

5.3 Macro-model at comparison with the DEM and experiments

We investigate herein the performance of the proposed simplified macro-modeling strategy. The detailed DE simulations presented in Chapter 4 and the experimental results of Michaloudis and Gebbeken (2019) are considered as reference for evaluating the FE approximate model.

5.3.1 Comparison with experimental tests

As in Section 4.3, we consider the experimental tests conducted by Michaloudis and Gebbeken (2019). We use the same material properties used in the DE model, which have been selected from the literature, see e.g. (Stefanou et al., 2015a; Wild et al., 1997; Petry and Beyer, 2015b). Table 5.1 presents the material parameters of the masonry blocks and mortar joints, as well as the fracture energy of the joints. The boundary conditions

used in the DE model are kept the same for the FE model.
Numerical FE simulations are performed using ABAQUS/Explicit software (ABAQUS, 2018). A small amount of artificial bulk viscosity is used in all analyses to prevent elements from collapsing under extremely high velocity gradients (extreme distortion). No material damping is considered. Blast actions are applied using ConWep model, which is already implemented in ABAQUS.
From mesh sensitivity analyses, a FE discretization consisting of linear tetrahedral elements with average dimension of 30 mm is selected. Before performing the numerical simulation of two experimental tests, we investigate the simplified isotropic approximation of the elastic constants, as discussed in paragraph 5.2.1, for a quantity of equivalent TNT $W = 500$ kg, located at a stand-off distance $R = 20$ m.

Table 5.1 – Material parameters of the macro-model.

Blocks properties			Joints properties					
density(kg/m^3)		2470	E_m	(MPa)	500	f_t	(kPa)	100
E_b	(MPa)	5000	G_m	(MPa)	208	G_f	(N/m)	0.021
G_b	(MPa)	2083				G_F,	(N/m)	0.50
						w_f	(mm)	0.042

5.3.1.1 Elastic response

Relying on the homogenization method proposed by Cecchi and Sab (2002) (cf. par. 5.2.1), considering plane stress conditions and running bond, the following elastic parameters are obtained:

$$E_{11}^H = 4111 \text{ MPa}, \quad E_{22}^H = 2689 \text{ MPa}, \quad G_{12}^H = 1077 \text{ MPa}, \quad \nu_{12}^H = 0.16,$$
$$E_{33}^H = 5000 \text{ MPa}, \quad G_{23}^H = G_{13}^H = 2083 \text{ MPa}, \quad \nu_{23}^H = \nu_{13}^H = 0.2.$$

Figure 5.8 shows the deflection, at different locations, of the wall obtained using DEM and a FE model, considering a three-dimensional orthotropic material behavior. The macro-model, as expected, agrees very well with the discrete one.

In order to obtain an isotropic medium, with Young's modulus E^M and shear modulus G^M, whose response is relatively close to the more exact orthotropic one we selected, we consider a macro-FE model with $E^M = \max(E_{11}^H, E_{22}^H) = 4111$ MPa and $G^M = 1077$ MPa. Figure 5.9 displays the comparison between the DEM and the isotropic macro-FE model. As expected, the approximate, isotropic case gives smaller deflections compared to those obtained with the DEM. Nevertheless, it allows to obtain reasonable estimates of the structural resistance, which can be used in engineering applications.

5.3.1.2 Non-linear response

According to the upscaling procedure presented in paragraph 5.2.2, the following macro-material parameters are obtained: fracture energy $G_F^M = 0.062$ N/m and ultimate opening $w_f^M = 0.005$ mm, with $\mathsf{L} = 0.125$.

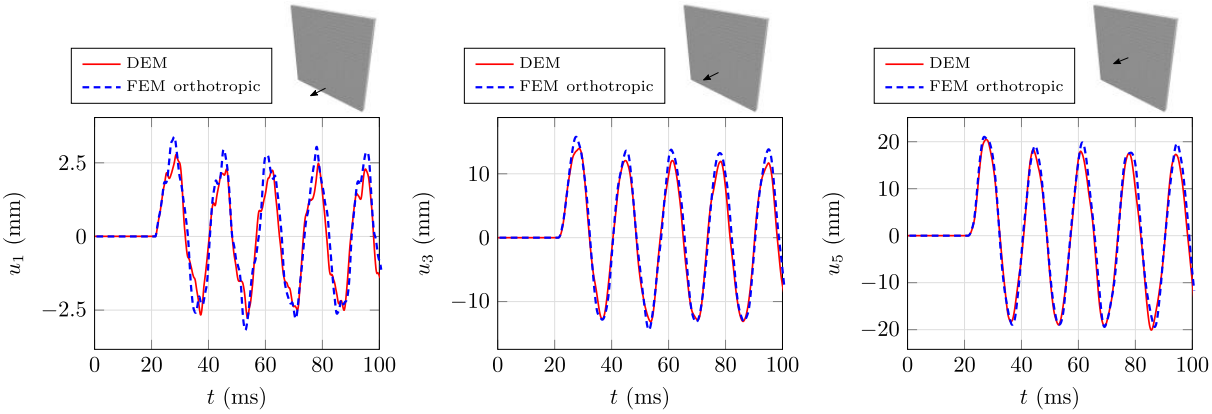

Figure 5.8 – Comparison of the deflection (in elastic regime) of the wall computed by the DE model and as a result of a macro-FE model, with a three-dimensional orthotropic material.

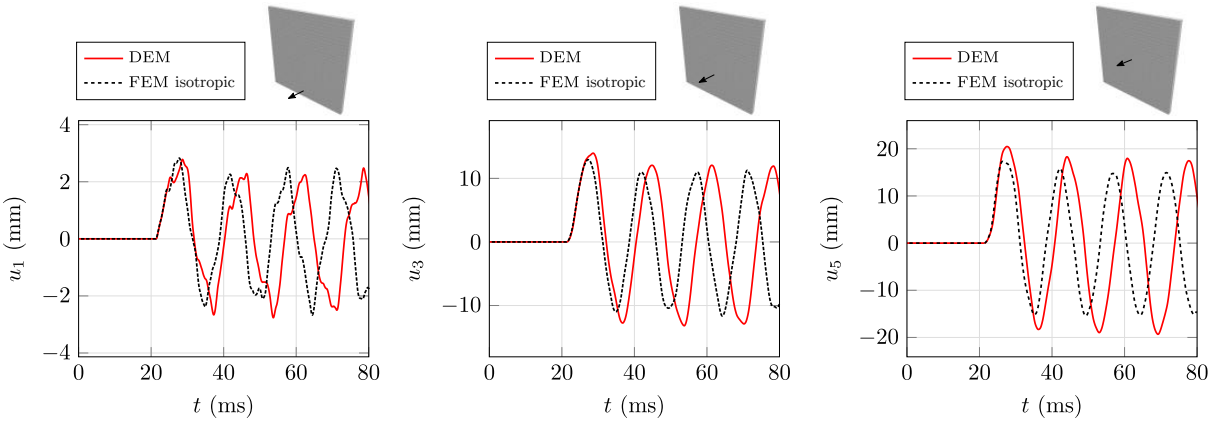

Figure 5.9 – Comparison of the deflection (in elastic regime) of the wall computed by the DE model and as a result of a macro-FE model, with isotropic behavior.

We compare in Table 5.2 the numerical results obtained with the FE model with those of the DEM and the experimental data (Michaloudis and Gebbeken, 2019) for Test 1 ($W_1 = 810$ kg, $R = 37$ m). The approximate macro-model predicts outward and inward deflections with relative error within 7.23% the experimental values. We present in Figure 5.10a the time evolution of the numerically measured deflection at the center of the wall. Whilst the peak outward and inward deflections predicted by the FE model agree with the experiment (and the DE model), the evolution of the free-oscillating response of the macro-model strongly differs from the DE one.
This is due to the fact that the approximate FE model lacks several physical mechanisms (e.g. friction, plasticity, fracture II mode, internal length) that would allow to dissipate the energy in a more realistic way. Indeed, if a small amount of mass-proportional damping is considered, the comparison of the free-oscillating deflection is more satisfactory, see Figure 5.10b. This is an apparent limitation of our simplified macro-model. Nevertheless, the aim is to develop a time-efficient macroscopic approach that gives first estimates of

the resistance of masonry structures. This is achieved, for the problem at hand (cf. Test 1), by satisfactorily predicting the out-of-plane maximum displacements.

Table 5.2 – Comparison between experimental results, DEM, and isotropic FEM of the maximum outward and inward deflection at the centre of the wall for Test 1.

Maximum deflection	Experiment	DEM	FEM
Outward (mm)	77.0	78.2	82.57
Inward (mm)	37.0	38.2	37.97

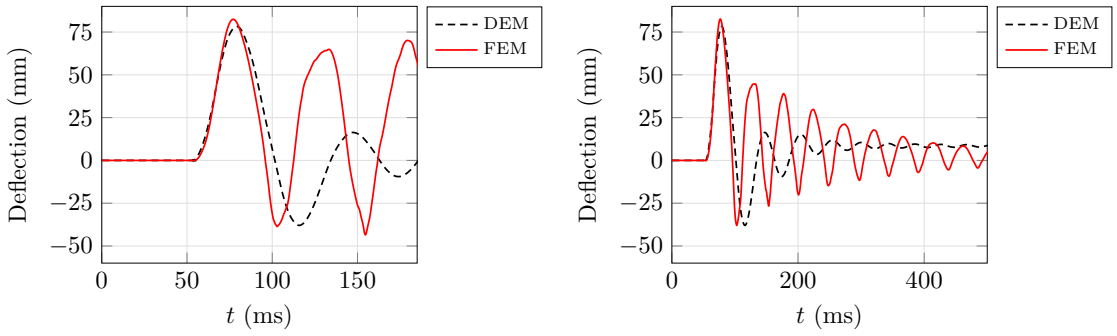

Figure 5.10 – Time evolution of the deflection at the center of the wall from the numerical FE and DE simulations of Test 1 ($W_1 = 810$ kg, $R = 37$ m): (a) no material damping and (b) small amount of material damping to dissipate free-oscillations.

For Test 2 ($W_2 = 1150$ kg, $R = 37$ m), we present in Figure 5.11 the out-of-plane response and the consequent formation of the breach, using the macro-FE model. Figure 5.12 compares the breach dimensions of the numerical simulations with the experimental evidence and the DEM results. The FE macro-model is found to capture overall the location of the breach [5]. Nevertheless, the dimensions of the breach differ both in width and height. This is, once more, due to the fact that only mode I fracture is accounted for and the reduced physics on which the simplified FE model is based.

Moreover, besides some differences between the experimental tests and the numerical results obtained with the DEM, the simplified macro-FE model is found to give first approximations that can be satisfactory for engineering applications. For instance, it leads to a failure mechanism similar to the that of the experiment (and DEM). The size of the breach predicted by the approximate FE model is not that different: the maximum height and width of the (FE) predicted breach are 0.95 and 1.05 the maximum height and width in the experimental test, respectively. Finally, we point out that the

5. According to (ABAQUS, 2018), finite elements undergoing complete loss of strength (computed at the integration points) are assigned zero mass and are removed from the mesh.

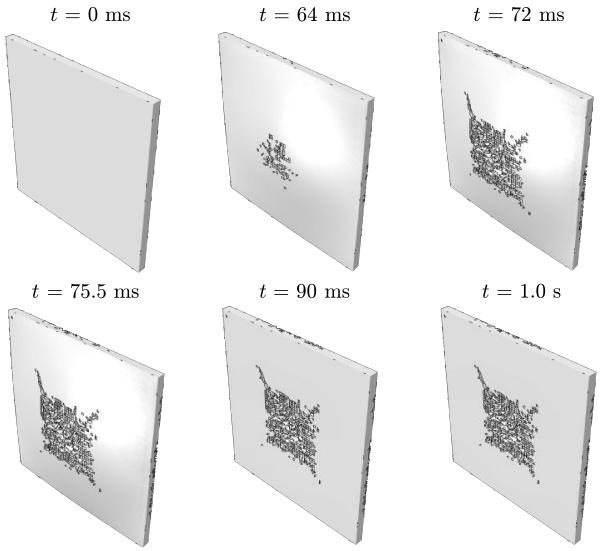

Figure 5.11 – Response of the FE model for Test 2 ($W_2 = 1150$ kg, $R = 37$ m).

computational time[6] of the FE simulations, involving softening behavior, is less than 0.03 times the time for simulating the same problem using DE (namely, ≈ 15 minutes for FEM versus ≈ 550 minutes for DEM). This is a significant advantage of the simplified approach for performing preliminary dynamic analyses in engineering problems.

5.3.2 Comparison with the detailed DEM analyses

In this paragraph we investigate the performance of our simplified macro-FE model in predicting the dynamic response and strength of non-standard, curvilinear masonry structures against explosions. In the lack of experimental tests for such structures (cf. Chapter 2), we use, as a reference, the DEM results presented in Chapter 4. In particular, we only consider simulations involving joints with zero dilantancy, which we often met in real masonry structures.
A small amount of artificial bulk viscosity is used in all analyses to prevent elements from collapsing under extremely high velocity gradients. No material damping is considered.

5.3.2.1 Planar arches

We aim at investigating, through the FEM, the critical explosive quantity of a planar semi-circular arch (cf. par. 4.4.1). The considered arch has thickness $w = 0.2$ m and slenderness ratio $\eta = w/r = 0.13$, with mean radius $r = 1.5$ m the mean radius. The total number of masonry blocks is 21, with mean radial dimension equal to $h_b = 214$ mm and mortar joints thickness $h_m = 10$ mm. Notice that the arch contain a small number of blocks. Therefore, we are at the limits for describing this system with a continuum model as the approximate macro-FE model presented herein. From the material properties of the masonry blocks and mortar joints (cf. par. 4.4.1), we obtain the macro-material parameters shown in Table 5.3. Discretization is selected upon mesh

6. in a 24-cores workstation.

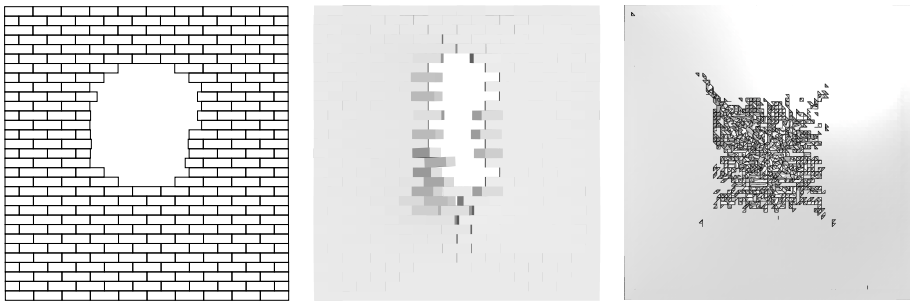

Figure 5.12 – Comparison between the experiment (left), the numerical DEM (center) and FEM (right) results for Test 2 ($W_2 = 1150$ kg, $R = 37$ m). The experimental breach extension is schematically represented by the black dashed line.

converge analyses and consists of linear tetrahedrons with average dimension equal to 40 mm. Boundary conditions in the macro-FE model consists in constraining horizontal and vertical displacement at the base of the arch.

Table 5.3 – Material parameters of the macro-model of a planar semi-circular arch.

Elastic parameters			Inelastic parameters		
density	(kg/m^3)	2000	G_F^M	(N/m)	0.047
E^M	(MPa)	7133	w_f^M	(mm)	0.0039
G^M	(MPa)	3302			

The DEM predicts a critical stand-off distance $W^* = 1500$ g, while the macro-FE model predicts $W^* = 1300$ kg. Whilst the difference in the predicted values, the macroscopic model seems to provide a safe estimate of the structural resistance. Furthermore in both FEM and DEM results, the structural collapse consists of failure under self-weight, after the end of the blast loading.

5.3.2.2 Barrel vault

We investigate the macro-FE modeling of a barrel vault (cf. Sect. 4.5). The FE model is discretized into linear tetrahedral elements with average length equal to 30 mm. The boundary conditions of the macroscopic model of the barrel vault are shown in Figure 5.13. Contrary to the DE model (Fig. 5.13b), there is no need to model explicitly the fixed supports. On the contrary, the FE model is constrained by simply fixing the extremities of the vault.

First, we study the dynamic response due to a surface blast of 5 kg of TNT equivalent, located at the center of the structure, assuming a linear elastic material—as previously done for the case of a simple flat wall (cf. 5.3.1.1). The structure is first subjected to

gravitational acceleration, through a static analysis. The obtained configuration is then used for the subsequent blast simulation. The results of the DEM model are compared with the macro-FE model [7]. The elastic constants (considering either a three-dimensional orthotropic material formulation or an isotropic one) are derived using the developments in Cecchi and Sab (2002) and Eq. (5.6), see Table 5.4. Figure 5.14 displays the out-of-plane displacements at different locations of the barrel vault. The orthotropic macroscopic model satisfactorily predicts the first peak outward deflections. Nevertheless, we observe that the time evolution predicted by the continuum (ortho- and isotropic) approaches differs from the discrete model results. The discrepancy is more important for the masonry blocks next to the fixed supports (u_4 and, in particular, u_2). The reason lies on the fact that the size of the blocks is quite important to the overall size of the structure and the wavelength developed during the wave propagation inside the structure—only 10 blocks along the longitudinal direction—see Stefanou et al. (2008) for a discussion on the topic. Moreover, the boundary conditions between the FE and DE models cannot be exactly the same due to software limitations.

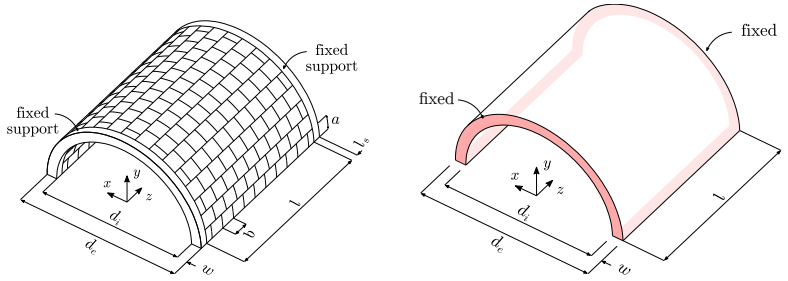

(a) DE model. (b) macro-FE model.

Figure 5.13 – Boundary conditions of a barrel vault: (a) DE model and (b) macro-FE model.

Table 5.4 – Material parameters of the macro-model of a barrel vault.

Elastic parameters			Inelastic parameters		
density	(kg/m^3)	2000	G_F^M	(N/m)	0.037
E^M	(MPa)	11464	w_f^M	(mm)	0.0027
G^M	(MPa)	3906			

Next, the approximate macro-FE model is used to predict the response of the barrel vault subjected to 10 and 20 kg of TNT, accounting for the inelastic material behavior.

7. Notice that the deformed shape under self-weight slightly differs between the FE and DE models. In the proximity of the fixed supports, the FE is found to underestimate the deflection due to the assumed boundary conditions.

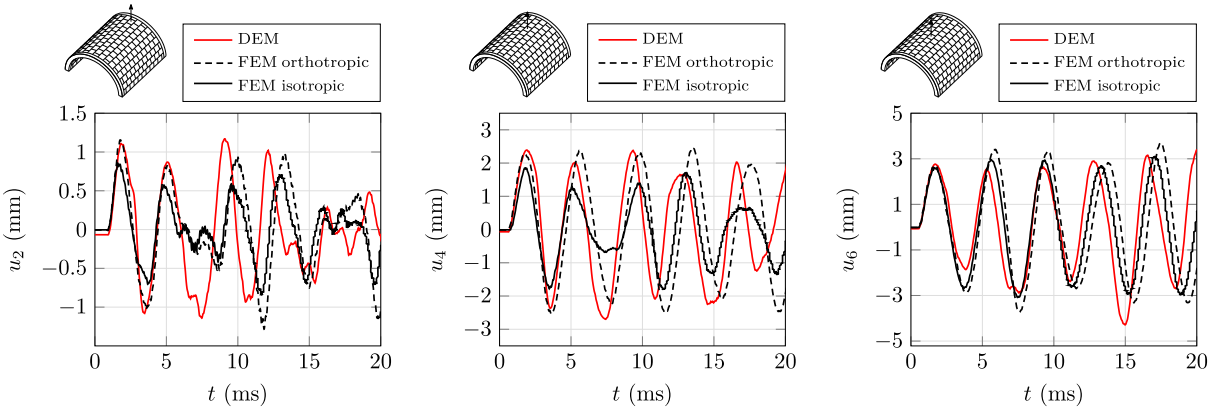

Figure 5.14 – Comparison of the deflection (in elastic regime) of the barrel vault computed by the DE model and by the macro-FE model, either using a three-dimensional orthotropic material formulation or a simplified isotropic one.

According to the parametric analyses[8] in paragraph 4.5.4, we consider masonry joints with tensile strength $f_t = 100$ kPa and zero dilatant sliding behavior, $\psi = 0°$, with friction angle $\varphi = 35°$. Table 5.4 shows the inelastic macro-material parameters used in the approximate FE model.
Figures 5.15 and 5.16 display the deflections at different locations due to a surface blast of 10 and 20 kg of TNT, respectively. The macro-FE model is found to predict well the shape of the time-history variation, at least for blocks sufficiently far from the fixed supports (i.e., u_4 and u_6). Nevertheless, the maximum deflections observed in the approximate model are almost 45% smaller than those predicted by the DE model in the case of 10 kg of TNT. The main reasons of this difference are: (1) the low quality approximation of the upscaling approach as the size of the blocks is comparable with the dimensions of the structures; (2) the difference in the applied boundary conditions; and (3) the lacking of mode II fracture and elasticity mechanisms in the FE model. In particular, it is worth stressing that, in the proximity of the fixed supports, the DE model predicts failure due to shear stresses and consequent slippage of the blocks (see Fig. 5.15, left). This phenomenon is not accounted in our simplified macroscopic approach. Therefore the failure mechanisms are different and, as expected, the FE model is less realistic.
Despite of the aforementioned discrepancies, the FE model gives at least safe estimates of the overall resistance. Indeed, the structural damage predicted by the model is larger than the one obtained with the more detailed DEM, see Figures 5.17 and 5.18.
We stress, once again, that our simplified model accounts only for the most predominant parameters (elasticity of the constituents, strength of the joints, blocks size, etc.) in order to keep the computational time as small as possible and predict, in a safe manner, the resistance of masonry structures under explosions.
Notice that the computational time to run the aforementioned FEM simulations was

8. The numerical DEM simulations showed that the first peak response, in term of out-of-lane displacements, is almost independent from the tensile strength of the masonry joints for the variations considered in paragraph 4.5.4.

overall 5% of the one required to run the corresponding DEM analyses.

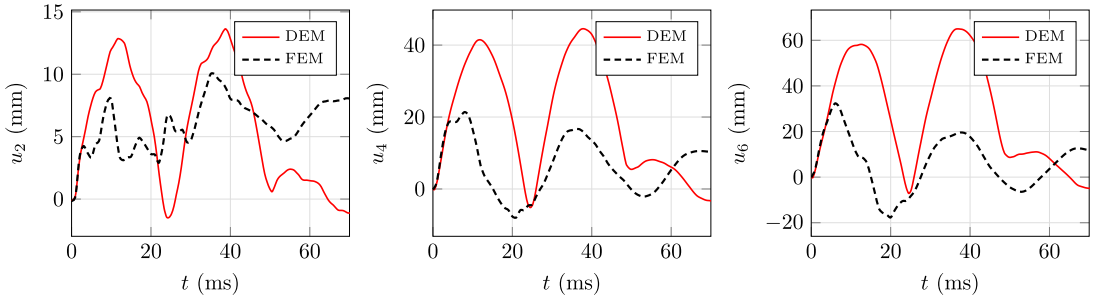

Figure 5.15 – Comparison of the deflections of the barrel vault computed by the DE model and by the macro-FE model, for a TNT equivalent weight $W = 10$ kg (the different locations are identified in Fig. 5.14).

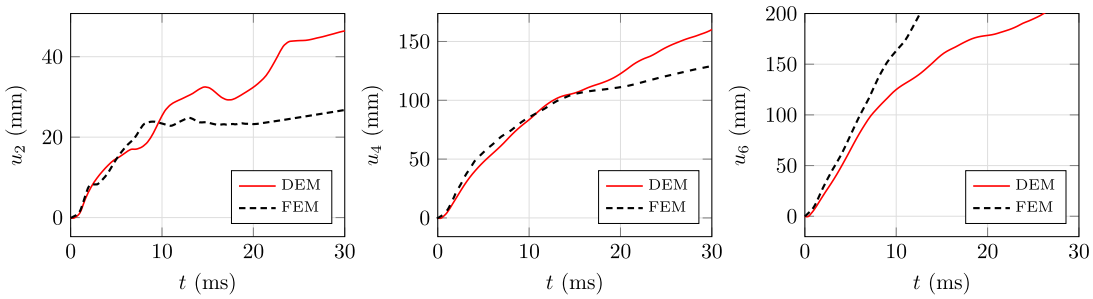

Figure 5.16 – Comparison of the deflections of the barrel vault computed by the DE model and by the macro-FE model, for a TNT equivalent weight $W = 20$ kg (the different locations are identified in Fig. 5.14).

Building blocks size effects. The capability of the macroscopic model to simulate the building blocks size effects is here demonstrated through comparison with the numerical simulations presented in paragraph 4.5.5. In particular, we select masonry blocks with half and twice the reference size. The elastic and inelastic material properties of the FE model are accordingly changed [9].

We show in Figure 5.19 the deflection of the center of the vault's key as predicted by the macro-model. It is worth noticing that the FE model underestimates the maximum peak deflection (overall by a factor of 2). This discrepancy is due to the above mentioned reasons. However, the simplified model is able to predict the same dependency with respect to the blocks size to that observed with the DEM, depicted in Figure 4.30. The smaller the blocks are, the larger the out-of-plane displacements becomes.

The overall damage for the different configurations is shown in Figure 5.20. For larger building blocks, the macro-FE model predicts larger amounts of damage. This is due

9. Notice that the thickness of the mortar joints is kept the same, $h_m = 10$ mm. This results in a change of the elastic parameters due to changes of the geometric parameter, b, see Eq.s (5.1a-5.1d). The inelastic parameters changes according to changes of the parameter scaling parameter, L, see Eq. (5.17).

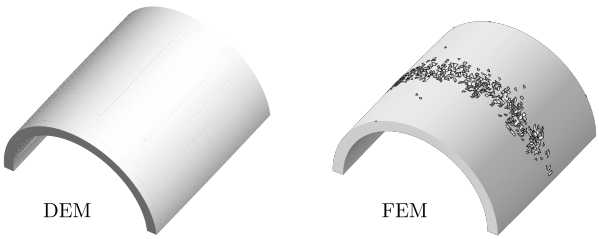

Figure 5.17 – Damage of the barrel vault computed by the DE model and by the macro-FE model, for a TNT equivalent weight $W = 10$ kg, at 100 ms after detonation.

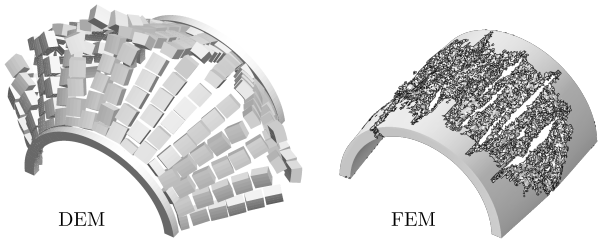

Figure 5.18 – Damage of the barrel vault computed by the DE model and by the macro-FE model, for a TNT equivalent weight $W = 20$ kg, at 300 ms after detonation. Notice that both models predicts failure of the entire structure.

to the dependency of the macroscopic material model on the blocks size. As the blocks dimensions increase, the brittleness of the material increases (L decreases). Accordingly, the fracture energy for the model with half and twice blocks size are $G_F = 0.0476$ N/m and $G_F = 0.0174$ N/m, respectively.

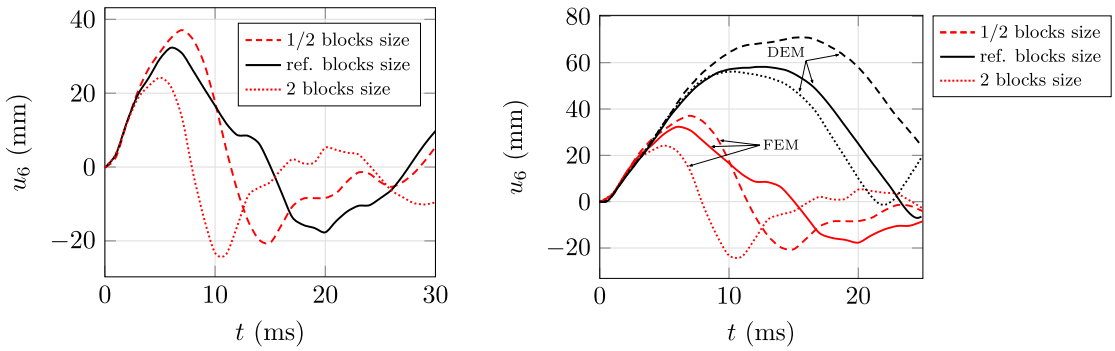

Figure 5.19 – Comparison of the response of the FE model of the barrel vault in terms of deflection at the center of the vault's key for different size of the building blocks (left) and comparison with the DEM (right).

5.3.2.3 Cross vault

Relying on the numerical simulations in Section 4.6, we study the resistance of a cross vault subjected to a centered surface blast. The material parameters of the macro model are shown in Table 5.5. We distinguish between the masonry of vault's skin and the one

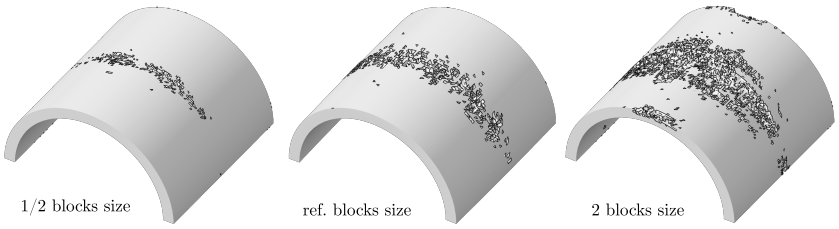

Figure 5.20 – Comparison of the damage of the barrel vault computed by the FE model representing different blocks sizes, for a TNT equivalent weight $W = 10$ kg, at 100 ms after detonation.

constituting the ribs. We select a tensile strength of the joints equal to $f_t = 100$ kPa.

Table 5.5 – Material parameters of the macro-model of the cross vault.

Masonry skin					
Elastic parameters			Inelastic parameters		
density	(kg/m^3)	2000	G_F^M	(N/m)	0.0105
E^M	(MPa)	9010	w_o^M	(mm)	4.2×10^{-5}
G^M	(MPa)	4697	w_f^M	(mm)	8.8×10^{-4}

Masonry ribs					
Elastic parameters			Inelastic parameters		
density	(kg/m^3)	2000	G_F^M	(N/m)	0.0092
E^M	(MPa)	7428	w_o^M	(mm)	3.7×10^{-5}
G^M	(MPa)	3989	w_f^M	(mm)	7.7×10^{-4}

Figure 5.21 shows the vertical out-of-plane displacements at different points along the diagonal ribs (cf. Fig. 4.36). Similarly to what observed for the barrel vault, the macro-FE model predicts smaller displacements with respect to the DEM. The reason lies on the fact that: (1) the dimensions of the blocks constituting the ribs are comparable with the dimensions of the structure and (2) mode II fracture and frictional mechanisms are neglected. Nevertheless, once more, the FE model provides safe estimates of the structural resistance. According to the macroscopic model, the structure fails under the action of 18 kg of TNT. While the DE model predicts collapse at 20 kg. Most of the damage, within the macroscopic model, takes place at the ribs (diagonal and lateral ones), as shown in Figure 5.22. Such results is only in partial agreement with the DEM predictions. The approximate FE model shows different failure modes. Indeed, the discrete model shows large amount of slippage and opening of the masonry joints at the bottom blocks of the ribs. Nevertheless, partial collapse of the masonry skin is also observed in the DE

simulations. This discrepancy is mainly caused by the approximation introduced in the simplified approach of smearing the contact interfaces between the masonry skin and the load-carrying ribs into a continuum medium.
Notice that the computational time to run the aforementioned FEM simulations was overall 2% of the one required to run the corresponding DEM analyses.

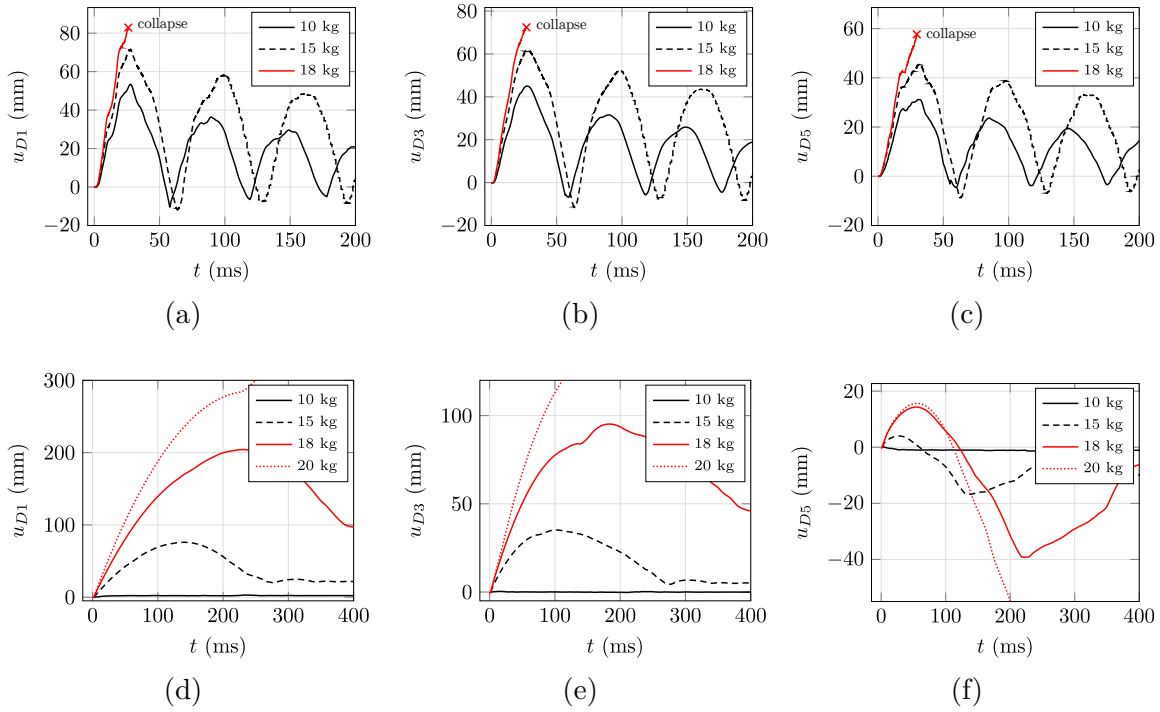

Figure 5.21 – Comparison of the deflection, at different locations (cf. Fig. 4.36), of a cross vault subjected to various explosive weights. Figures (a-c) represents the predictions of the macro-FE model, Figures (d-f) those of the DE model. The FE model predicts collapse for 18 kg, while the DE model for 20 kg.

Considerations about the geometric model. The considered geometric model of the cross vault, as mentioned in Section 4.6, is a simplified configuration of a realistic cross vault, realized by intersecting two pointed vaults (see Fig. 4.35). Such a simplification has been introduced due to the complexity of discretizing non-ruled surfaces in 3DEC, hence of discretizing the exact CAD model. However, in ABAQUS Finite Element Software, the realistic model can be used without any constraint. This is why, herein, after having compared the DEM and the FEM for the simplified geometric model, we investigate the differences that might come from the geometric simplifications introduced. Namely, we compare the stress state and dynamic response of the simplified cross vault and the exact geometric model, i.e., that shown in Figure 4.34. Finite elements size, boundary conditions, and material properties are kept the same, as mentioned above.
Notice that the FE model can give us only qualitative results regarding the influence of the exact geometry of the cross vault on the dynamic response of the system.

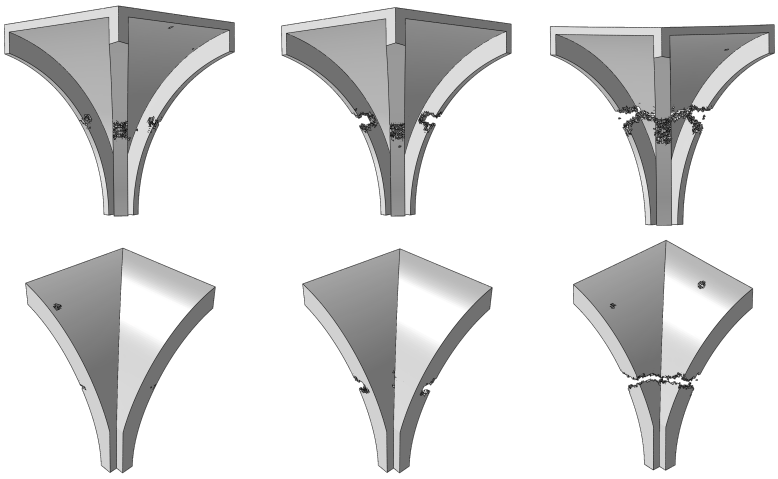

(a) 10 kg. (b) 15 kg. (c) 18 kg.

Figure 5.22 – Comparison of the material damage, according to the macro-FE model, at varying of the explosive weight.

Figure 5.23 displays the maximum principal stress induced by gravity in both models. We notice that the exact geometry is such that the vast majority of the structure is actually in a compressive state [10].

We show in Figure 5.24 the vertical out-of-plane displacement evolution for different quantities of explosive weight, at the vault's key. The exact geometric model undergoes much larger displacements and total collapse conditions are met for an explosive quantity as small as 15 kg (the simplified model fails under 18 kg). Figure 5.25 shows the material damage within the exact geometric model (cf. Fig. 5.22). The smaller resistance of the exact geometry stems from the different spatial evolution of the overpressure, within the impinged surface of the structure. This is represented in Figure 5.26, where we can clearly see how the different shape of the vaults gives rise to different pressure profiles. Such a result highlights the importance of the geometry when dealing with blast actions, especially for the case of quasi-brittle materials, such as masonry. A small variation of the shape of an architectural element changes, of course, the stress distribution within the structure, but it may also significantly affect the blast loading. Nevertheless, we would like to recall that the empirical model here used to assess the loads arising from an explosion (Hyde, 1991) may be not extremely representative of the reality, as focalization and confinement of shock waves may play an important role (cf. Sect. 1.6).

10. For the sake of clarity, the total mass of both models is approximately the same, with the simplified geometric model being 0.1% lighter than the exact one.

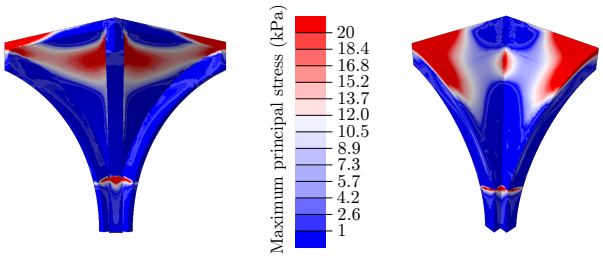

(a) Simplified geometry.

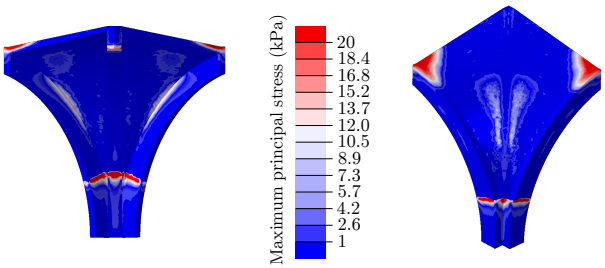

(b) Exact geometry.

Figure 5.23 – Stress state of the cross vault, under self-weight: comparison between the simplified geometric model (a) and the exact one (b).

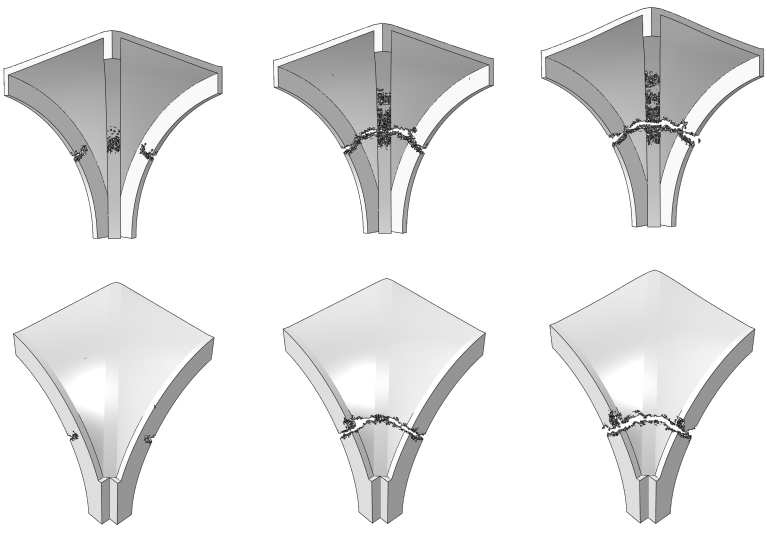

(a) 10 kg. (b) 15 kg. (c) 18 kg.

Figure 5.24 – Comparison of the material damage, for the exact geometric FE model of the cross vault, at varying of the explosive weight (cf. Fig. 5.22).

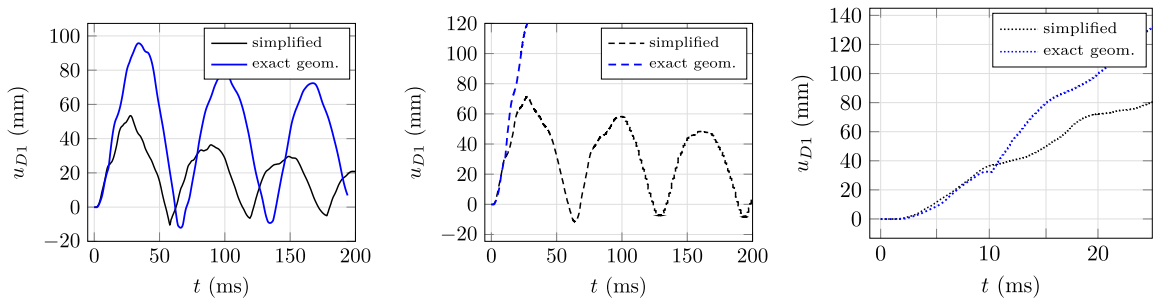

(a) 10 kg. (b) 15 kg. (c) 18 kg.

Figure 5.25 – Comparison of the vertical displacement evolution, at the vault's key, between the simplified and the exact geometric model of a cross vault subjected to (a) 10 kg, (b) 15 kg, and (c) 18 kg of TNT.

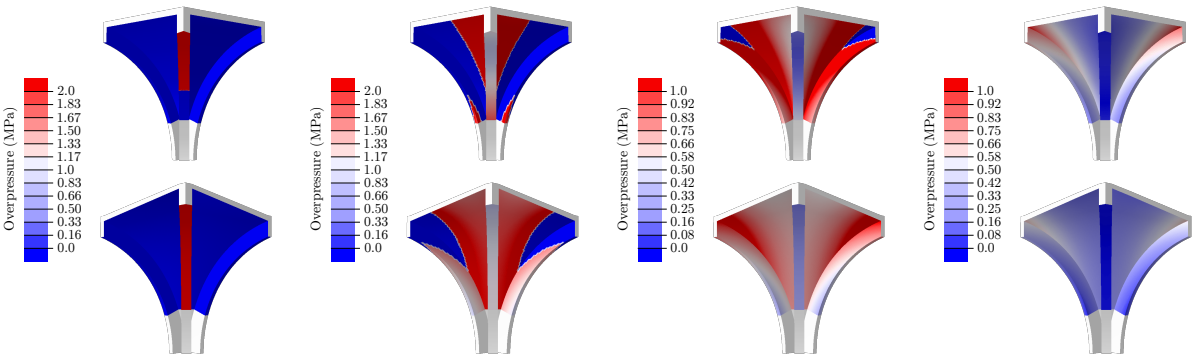

(a) $t = 2$ ms. (b) $t = 2.5$ ms. (c) $t = 3$ ms. (d) $t = 3.5$ ms.

Figure 5.26 – Evolution of the overpressure field (computed by ConWep Hyde (1991)) due to a centered explosion of 15 kg of TNT: simplified geometric model (top) and exact geometry (bottom).

5.4 A case study of a large, non-standard structure subjected to blast actions

We investigate the overall resistance and collapse modes of a representative historical building, as a direct application of the proposed macroscopic simplified modeling approach. It is worth emphasizing that the approximate FE model gave moderate results when compared with specific structural elements of typical masonry buildings of standard and non-standard geometry. However, this does not mean that its use can lead to unrealistic failure mechanisms at the level of a large structure, like the one used in this Section. To the author's knowledge, experimental data on the dynamic behavior and failure due to explosions of large structures are absent in the current literature. Moreover large DEM analyses at that scale are impossible to perform nowadays due to the prohibitive calculation cost. Therefore, it is impossible to assess the validity of the simplified model used herein. More detailed comparisons are expected to be performed in the future using in-scale laboratory tests (see Chapter 7).

For the aims of this study, we model only a transversal unit of the whole structure, see Figure 5.27. Notice that the structure is selected to by representative of non-standard geometry masonry buildings and any resemblance to real buildings is purely coincidental. Due to the complexity of typical historical buildings, we make some geometric simplifications. In particular, all the parts with merely decorative purposes are not accounted for−e.g. windows, traceries and pinnacles. The vaults are modeled carefully, considering additional fillings between 0° and 30°, of the angle swept from the arches' center.
Whilst the roof of the building is here neglected in the evaluation of the geometric model, its weight is modeled, in the following simulations, as a dead linear load (2×10^3 kg/m). Additionally, the building's floor, with thickness equal to 50 cm, as well as, the ground floor, with total thickness of 1.5 m, are also modeled.

The material parameters for the masonry are derived using the simplified macroscopic model (cf. Sect. 5.2) and are presented in Table 5.6. The inelastic material parameters are derived using a characteristic FE size of 15 cm (linear tetrahedrons, selected upon mesh convergence analyses). The same properties are assumed for the building's floor. For the materials composing the additional fillings of the vaults and the ground floor, we consider the parameters shown in Table 5.7.

5.4.1 Numerical simulations

The numerical simulations are performed using only a quarter of the geometric model − imposing appropriate symmetry boundary conditions, see Figure 5.28. Additionally, the bottom face of the ground floor is fixed. First, we perform a static analysis, considering the solely roof's load and gravitational load. Figure 5.29 depicts the maximum principal stresses due to self-weight. The obtained configuration is then used in a dynamic (explicit) analysis where blast actions, due to a certain amount of explosive weight, are modeled using ConWep (Hyde, 1991), cf. Sect. 1.6. The explosive location is assumed to be at the center of the unit, at 1 m from the floor, see Fig. 5.28a. In particular, we investigate the response to $W = W^{\dagger}$ and $W = 2W^{\dagger}$.
A small amount of artificial bulk viscosity is used in all analyses to prevent elements

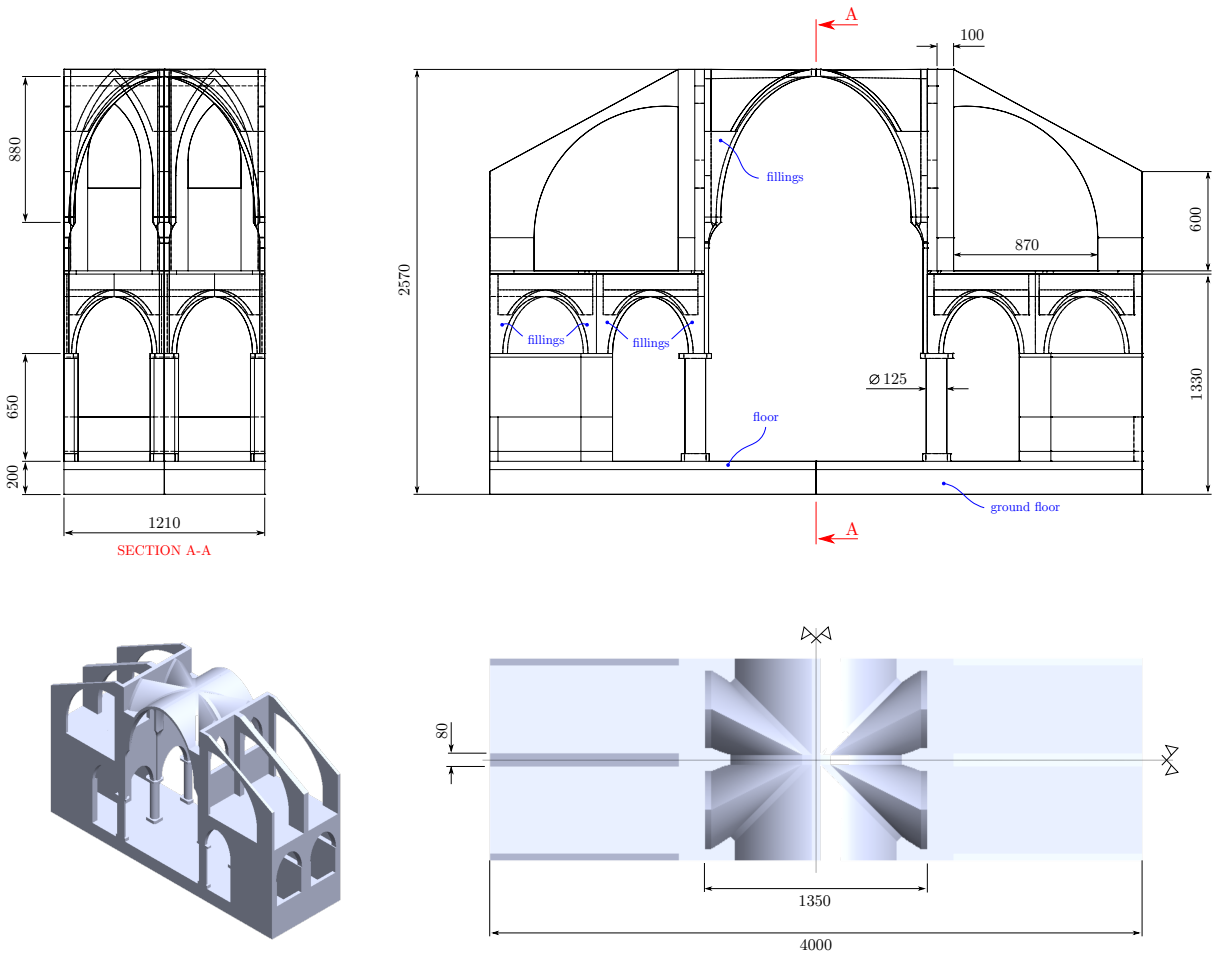

Figure 5.27 – Geometric model of a typical historical building. Dimensions are in centimeters.

from collapsing under extremely high velocity gradients (extreme distortion). No material damping is considered.
The simulations are performed using a 24-cores workstation. Each dynamic (non-linear) analysis took around 60 hours.

Figures 5.30 and 5.31 display the evolution of the overpressure and structural response for $W = W^{\dagger}$ and $W = 2W^{\dagger}$, respectively. In both cases, the evolution of damage is identified in terms of a damage variable, which assumes a unit value for elements experiencing complete loss of strength. For the smaller explosive weight, blast loads result in damage of the structure in the proximity of the charge (formation of a crater within the floor), flying buttresses, and of the main vault. Whilst partial collapse of masonry elements is not observed in the numerical simulations, the load-bearing capacity of the structure is extremely compromised by the explosion. For an explosive weight $W = 2W^{\dagger}$, the structure is severely damaged. The dimensions of the crater become larger and cracks spread all over the building. In particular, the flying buttresses and the main vault are largely destroyed and undergo collapse. Figure 5.32 depicts the structural

Table 5.6 – Material parameters of the macro-model of the masonry material of the historical building. We assume a thickness of the mortar joints equal to 10 mm and blocks with dimensions $160 \times 80 \times 20$ mm. The Young's and shear moduli of the masonry joints are 2500 MPa and 1042 MPa, respectively. While for the masonry blocks we consider Young's and shear moduli equal to 15000 MPa and 6250 MPa.

Elastic parameters			Inelastic parameters		
density	(kg/m^3)	2000	G_F^M	(N/m)	0.72
E^M	(MPa)	12210	f_t	(kPa)	300
G^M	(MPa)	5250	w_f^M	(mm)	0.030

Table 5.7 – Material parameters of the macro-model of the ground floor and additional filling of the vaults. Both materials are assumed linear elastic.

Ground floor			Fillings		
density	(kg/m^3)	1600	density	(kg/m^3)	1600
E^M	(MPa)	3000	E^M	(MPa)	100
G^M	(MPa)	1485	G^M	(MPa)	50

damage at 1 second after the detonation for the two different explosive quantities.

We stress that analogies can be drawn for both loading scenarios. Indeed, the surface blast causes the partial (or complete) damage of structural elements far away from the explosive source, and hence not exposed to overpressures as high as those acting on elements closer to the explosive. This is for instance the case of the main vault, and in particular of the flying buttresses, which are only indirectly exposed to the blast loading. The reason stems from the strong coupling between adjacent elements in the overall response of the structure. The propagation of shock waves is such that flying buttresses undergo important flexural deformations, which ultimately result in tensile damage. Due to the importance of the flying buttresses for the structural stability of the building (Vannucci et al., 2017b; Vannucci, 2020), the collapse of the vault is eminent.
The same can be observed for the sexpartite vault, which is exposed, in the current simulations, to blast loads relatively smaller than those acting on the cross vaults of the aisle. The numerical simulations allow us to highlight the importance of the overall structural response of non-standard geometry assets in their resistance and behavior to blast loads.

Nevertheless, we shall notice that, in a real blast scenario, complex fluid-structure interaction phenomena, as discussed in Chapter 1, may take place. According the case-study in Section 1.6, the empirical blast load model here used, ConWep (Hyde, 1991), underestimates the blast overpressure by a factor of 4. Assuming that the same

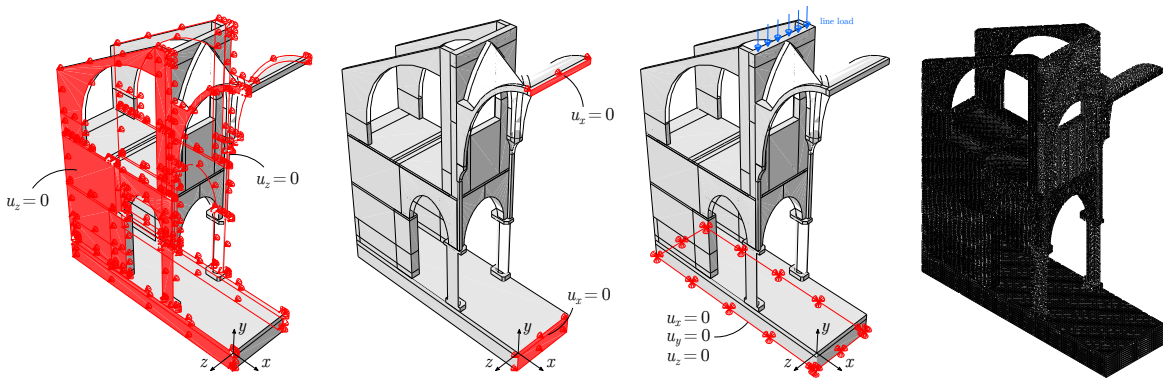

(a) boundary conditions. (b) FE model.

Figure 5.28 – Boundary conditions (a) and FE mesh discretization (b) of the analyzed unit.

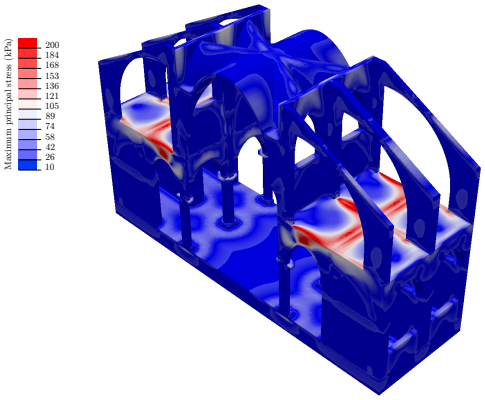

Figure 5.29 – Maximum principal stress due to gravitational acceleration and roof's weight.

amplification, due to shock waves focalization, takes also place in the structure here analyzed, the sexpartite vault would be subjected to higher pressure loads. Qualitatively, we can account for such phenomena by multiplying with a factor of 4 the empirical predictions of the overpressure computed by ConWep model for the exposed surfaces of the sexpartite vault. Figure 5.33 shows the structural response and damage evolution for the loading scenario $W = W^{\dagger}$, with such a modification. In this case, the main vault fails under the flexural deformations induced by the overpressure peak. The consequent collapse of the vault results in the tensile solicitation of the flying buttresses and, eventually, in their failure. Nevertheless, we shall notice that more detailed numerical simulations, accounting for the coupling of shock waves with the structure, are mandatory to draw quantitative conclusions. This is possible when considering real case structures−such as a precedent study carried out on the Pantheon, in Rome (Masi et al., 2018b)−for which material and geometric data are available.

We shall notice that the above results highlighted the role played by the overall

mechanical behavior of structures, and not only of load-bearing elements, in the resistance to blast loads. This is crucial to evaluate the vulnerability of such kind of structures against deliberate explosions. Mitigation techniques and passive protective devices can be designed considering the full structural behavior of masonry assets. In this case, the numerical results suggest that retrofitting using reinforced polymers or polyurea (Lantz et al., 2016), applied to the upper part of the main, sexpartite vault and the flying buttresses, may be a viable and appropriate protection. Modeling such reinforcing measures is straightforward in our FE model but extents the scope of this work.

5.5 Additional remarks

An approximate, engineering oriented macroscopic material model for masonry, based on the Finite Element Method and relying on a simplified upscaling technique based on the developments in Cecchi and Sab (2002) and the smeared cracking model (Hillerborg et al., 1976), was proposed. The approach allows considering in a certain extent the influence of several mechanical parameters, such as the building blocks dimensions and the strain softening behavior.
The domain of validity and the limitations of the proposed approach were explored based on available experimental tests of masonry walls subjected to explosions and detailed DEM analyses (benchmarks) of masonry structural elements (arches, barrel and cross vaults). Finally, the simplified modeling procedure was used to investigate the response of a representative large, non-standard masonry structure.

From an engineering point of view, the proposed model leads to acceptable estimations both of the dynamic response and failure of masonry structures. Furthermore, it provides safe estimates of the structural resistance, which is of primary importance when dealing with the preservation of existing ancient masonry buildings and the design of new ones. Our analyses are dynamic and non-linear, which already approximate better the physical reality, compared to static analyses or limit analysis calculations (see Section 2.5 for a discussion). Despite the dynamic and non-linear character of our analyses, the calculation cost was relatively low, i.e., some couple of hours for single structural masonry elements to less than a day for a large masonry structure. This can allow preliminary studies for assessing the dynamic response and resistance of existing masonry buildings and the design of new ones. However it is worth listing the limitations of the present approach:

- the material is modeled as an approximate isotropic medium in both elastic and inelastic deformation regimes;

- only mode I fracture (due to tensile stress) is accounted for. Mode II fracture and plastic/frictional mechanisms, which can play an important role (depending on the structural geometry, boundary conditions, and local stress configuration), are neglected.

- the homogeneous material model has no internal length, which can result in poor quality modeling, under some circumstances (Stefanou et al., 2008).

We intend to address this limitations by resorting to physics-based multiscale analyses

that exploit Machine Learning techniques for minimizing the calculation cost. Some first steps towards this kind of approaches are presented in the next Chapter. We intend also to verify/falsify our results on the basis of reduced-scaled laboratory experiments following the scaling laws presented in Chapter 7.

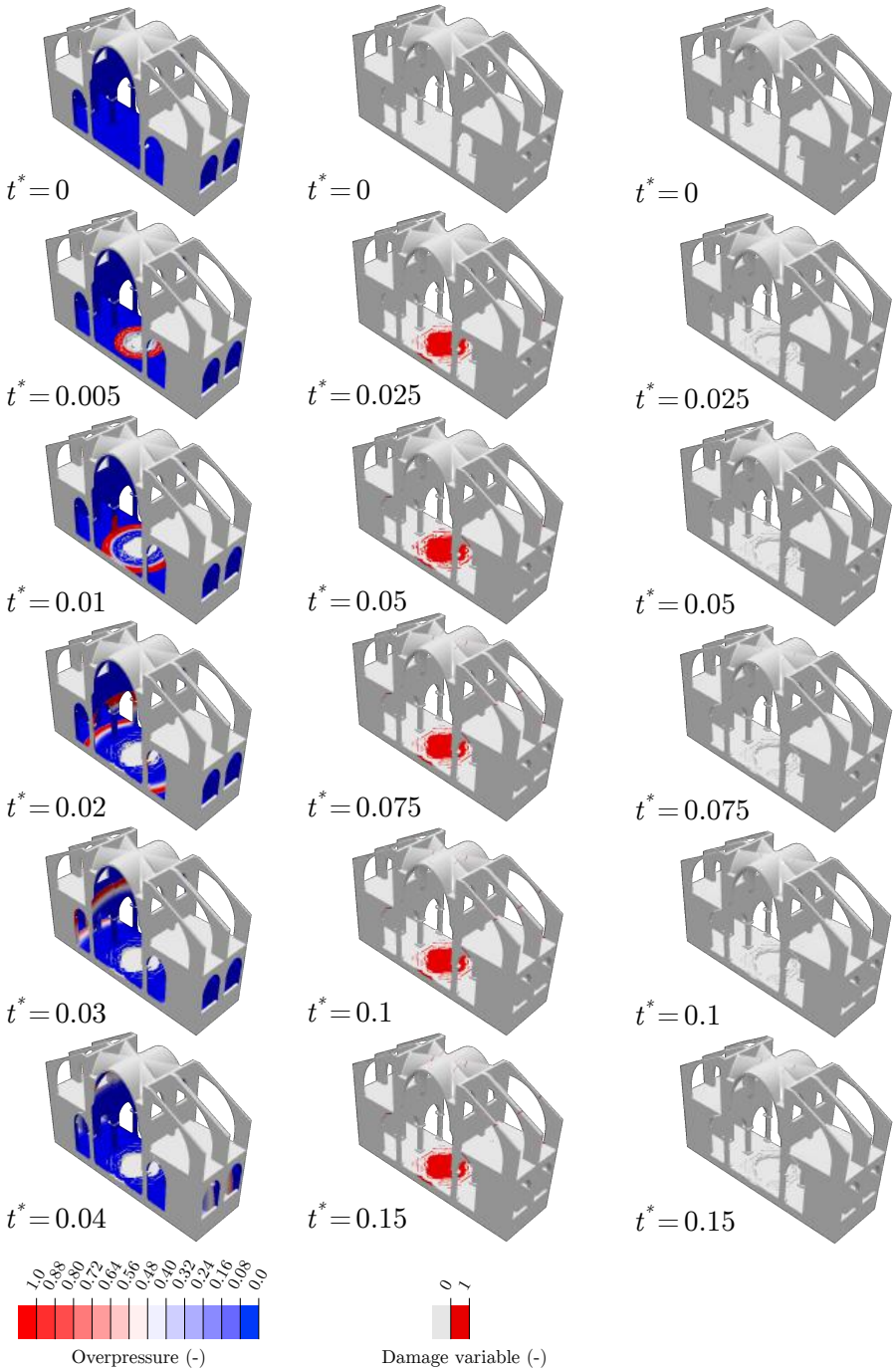

Figure 5.30 – Evolution of the normalized overpressure (left) and of the structural response in terms of the damage variable (center) and accounting for element deletion (right), due to a TNT weight $W = W^{\dagger}$ (the time scale is here normalized). Finite elements undergoing complete loss of strength (at their integration point) correspond to a unit damage variable. Displacements are increased by a factor equal to 100 to display purposes.

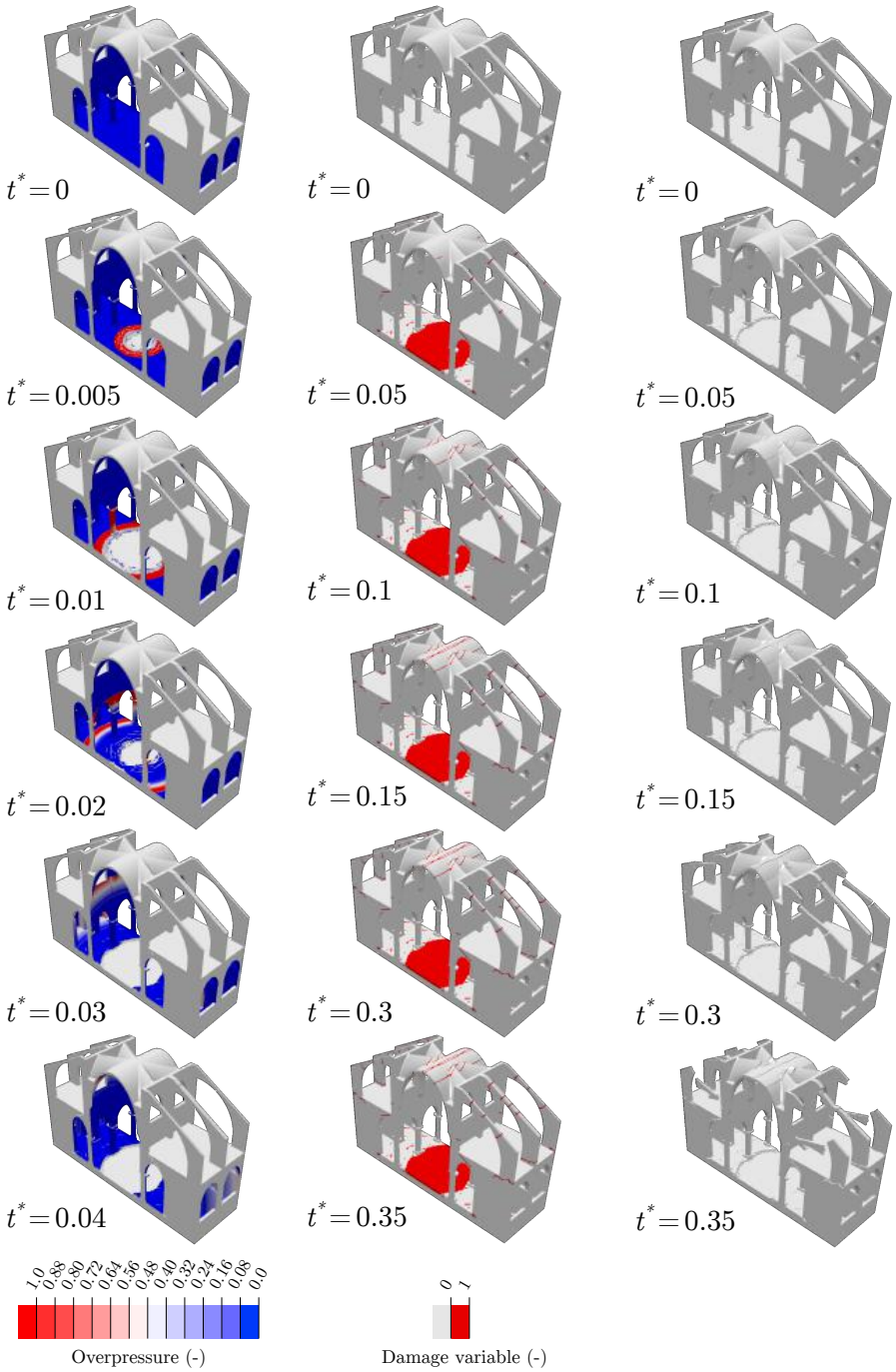

Figure 5.31 – Evolution of the normalized overpressure (left) and of the structural response in terms of the damage variable (center) and accounting for element deletion (right), due to a TNT weight $W = 2W^{\dagger}$ (the time scale is here normalized). Finite elements undergoing complete loss of strength (at their integration point) correspond to a unit damage variable. Displacements are increased by a factor equal to 100 to display purposes.

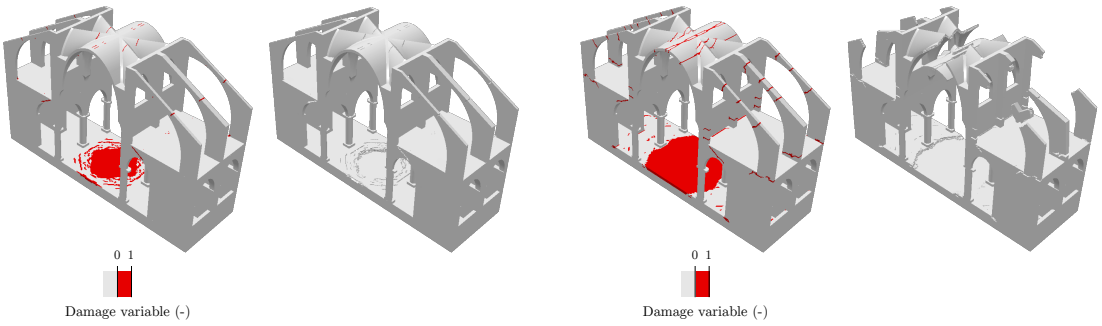

(a) $W = W^{\dagger}$. (b) $W = 2W^{\dagger}$.

Figure 5.32 – Damage at 1 s after detonation, for explosive weight equal to $W^{\dagger}$ (a) and $2W^{\dagger}$ (b), accounting for the damage variable (left) and element deletion (right).

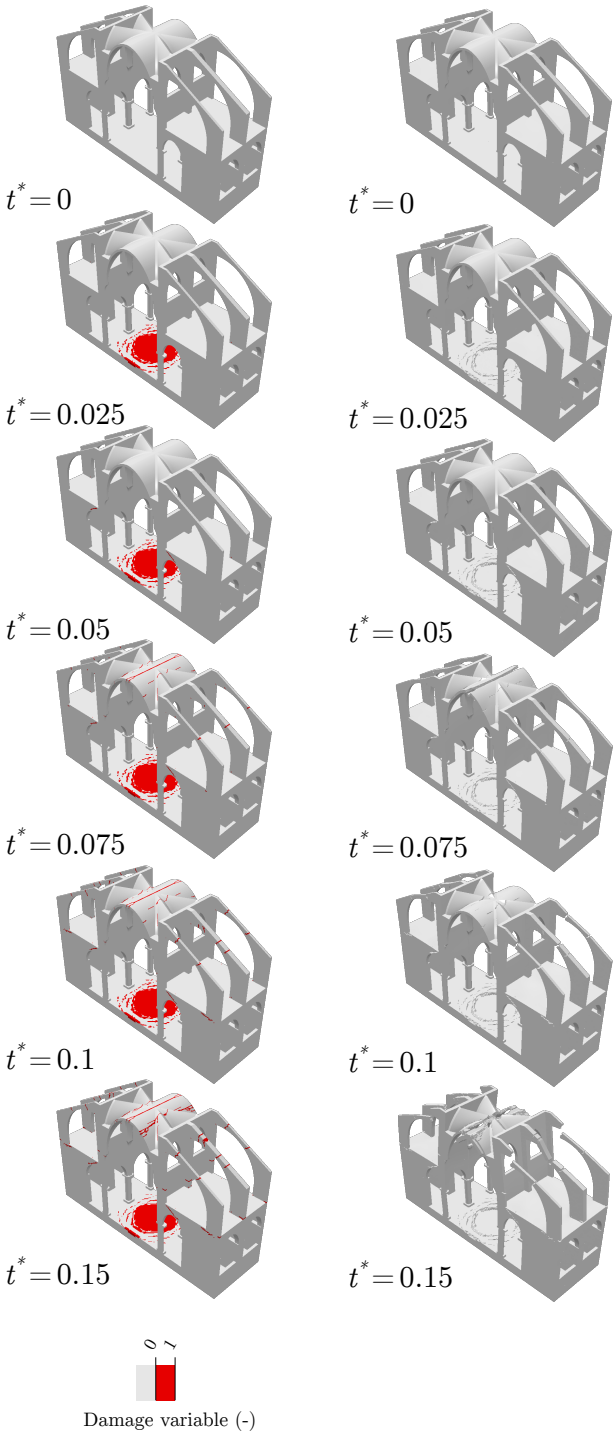

Figure 5.33 – Evolution of the structural response in terms of the damage variable (left) and accounting for element deletion (right), due to a TNT weight $W = W^{\dagger}$ and qualitatively accounting for shock waves focalization at the sexpartite vault. Finite elements undergoing complete loss of strength (at their integration point) correspond to a unit damage variable. Displacements are increased by a factor equal to 100 to display purposes.

Chapter 6

Macro-scale modeling via Machine Learning: a preliminary investigation using Thermodynamics-based Artificial Neural Network

Abstract. *In the view of multiscale modeling strategies, which offer high degree of accuracy and a more detailed material description than the simplified, engineering oriented macro-scale model proposed in the previous Chapter, Machine Learning methods and, in particular, Artificial Neural Networks (ANNs) have demonstrated promising capabilities in material constitutive modeling (Ghaboussi et al., 1991; Lefik and Schrefler, 2003; Ghaboussi and Sidarta, 1998; Jung and Ghaboussi, 2006; Heider et al., 2020; Settgast et al., 2019; Ghavamian and Simone, 2019; Lu et al., 2019; Xu et al., 2020; Huang et al., 2020; Mozaffar et al., 2019). However, one of the main drawbacks of such approaches is the lack of a rigorous frame based on the laws of physics. This may render physically inconsistent the predictions of a trained network, which can be dangerous for real applications. Here we propose a new class of data-driven, physics-based, neural networks for constitutive modeling of strain-rate independent processes at the material point level, which we define as Thermodynamics-based Artificial Neural Networks (TANNs). The two basic principles of thermodynamics are encoded in the network's architecture by taking advantage of automatic differentiation to compute the numerical derivatives of a network with respect to its inputs. In this way, derivatives of the free-energy, the dissipation rate and their relation with the stress and internal state variables are hardwired in the network. Consequently, our network does not have to identify the underlying pattern of thermodynamic laws during training, reducing the need of large data-sets. Moreover the training is more efficient and robust, and the predictions more accurate. Finally and more important, the predictions are always thermodynamically consistent, even for unseen data. Based on these features, TANNs are a starting point for data-driven, physics-based constitutive modeling with neural networks.*

We demonstrate the wide applicability of TANNs in modeling elasto-plastic materials, with strain hardening and strain softening. Detailed comparisons show that the predictions of TANNs outperform those of standard ANNs. This Chapter presents preliminary investigations using Machine Learning to represent the constitutive behavior of materials. Further developments and applications for masonry materials, using experimental or numerical

data, is the following step.

Contents

Chapter 5 demonstrated the applicability of macroscopic modeling techniques to predict the behavior and overall resistance of masonry structures subjected to explosions. This was accomplished by developing a simplified engineering up-scaling procedure for masonry. Further improvements can be achieved by relying on a more detailed description of the macroscopic constitutive behavior of the masonry.

Existing constitutive laws can account for phenomena taking place in various length scales. This is achieved either through heuristic approaches and assumptions or through asymptotic approximations and averaging (see Chapter 2 and e.g. Lloberas Valls et al., 2019; Nitka et al., 2011; Feyel, 2003; Bakhvalov and Panasenko, 1989). However, it is likely that the existing constitutive models might not be sufficient for describing complex material behaviors emerging from the microstructure in inelasticity. Moreover, calibration (parameter fitting) of known constitutive descriptors might be insufficient for representing the full space of material response. A remedy for the above limitations could be the execution of sophisticated micro-mechanical simulations and the application of multiscale numerical methods such as the FE^2 (Feyel, 2003; Eijnden et al., 2016; Lloberas Valls et al., 2019) or FEM×DEM (Nitka et al., 2011; Guo and Zhao, 2014; Claramunt, 2016; Liu et al., 2017; Argilaga et al., 2018). Nevertheless, the calculation cost of the latter methods is prohibitive for real applications.

A promising solution to this issue seems to be *Machine Learning*. According to Géron (2019), "Machine Learning is the science (and art) of programming computers so they can learn from data". In the context of computer programming, learning is defined by E. Tom Mitchell (Mitchell et al., 1997) as follows: "A computer program is said to learn from experience E with respect to some task T and some performance measure P, if its performance on T, as measured by P, improves with experience". In the frame of constitutive modeling, a Machine Learning program can learn the stress-strain behavior of a material, given examples of stress-strain increments, which are either determined experimentally or through detailed micro-/meso-mechanical simulations. The data that the system uses to learn are called the training data-set and each training example is called a training instance (or sample). In our case, the task T, for instance, can be the prediction of the stress for a given increment and internal state of the material. The experience E is the training data-set and the performance measure P can be the prediction error. Machine Learning is a general term to describe a large spectrum of numerical methods. Some of them offer very rich interpolation spaces, which, in theory, could be used for approximating complicated functions belonging to uncommon spaces. Here we focus on the method of Artificial Neural Networks (ANNs), which is considered to be a sub-class of Machine Learning methods. According to Chen and Chen (1995) and Cybenko (1989), ANNs have proved to be universal approximators, due to their rich interpolation space. Therefore, they seem to be a useful and promising tool for data-driven constitutive modeling of many materials (e.g. sand, seismic faults, masonry, concrete, alloys, ceramics, polymers, composites etc.).

Recognizing this potential, there is an increasing amount of new literature employing ANNs in constitutive modeling. Starting form the seminal work of Ghaboussi et al. (1991) and without being exhaustive, we refer to Lefik and Schrefler (2003); Ghaboussi and Sidarta (1998); Jung and Ghaboussi (2006); Heider et al. (2020); Settgast et al.

(2019); Ghavamian and Simone (2019); Liu and Wu (2019); Lu et al. (2019); Xu et al. (2020); Huang et al. (2020); Mozaffar et al. (2019); Frankel et al. (2019); Liu and Wu (2019); Gajek et al. (2020) and references therein. The main idea in these works is to appropriately train ANNs, feeding them with material data, and predict the material response at the material point level. In this sense, ANNs can be seen as rich interpolation spaces, able to represent complex material behavior. The Boundary Value Problem (BVP), set to determine the behavior of a solid under mechanical and/or multiphysics couplings, is then solved by replacing the standard constitutive equations or algorithms by the trained ANN. This replacement is straightforward and non-intrusive in Finite Element codes. It is worth emphasizing that the aforementioned data-driven approaches are different from another promising data-driven method (i.e., data driven computing (Kirchdoerfer and Ortiz, 2016)) in which the BVP is solved directly from experimental material data (measurements), bypassing the empirical material modeling step, involving the calibration of constitutive parameters Kirchdoerfer and Ortiz (2016); Ibañez et al. (2017); Kirchdoerfer and Ortiz (2018); Ibanez et al. (2018); Eggersmann et al. (2019); Reese et al. (2019); Carrara et al. (2020). While data-driven computing can be extremely powerful in many applications Eggersmann et al. (2019); Carrara et al. (2020), the first class of the aforementioned methods (based on the constitutive behavior at the material point level) can be advantageous when modeling complex and abstract constitutive behaviors, which are not a priori known. Moreover, they can be used even if the boundary value problem (BVP) does not have a unique solution due to important non-linearities and bifurcation phenomena (e.g. loss of uniqueness, strain localization at the length of interest, runway instabilities, ill-poseness etc.).

Nevertheless, until now ANNs for constitutive modeling are mainly used as a 'black-box' mathematical operator, which once trained on available data-sets, does not embody the basic laws of thermodynamics. As a result, vast amount of high quality data (e.g. with reduced noise and free of outliers) are needed to enable ANNs to identify and learn the underlying thermodynamic laws. Moreover, nothing guarantees that the predictions of trained ANNs will be thermodynamically consistent, especially for unseen data.

In this Chapter, we provide preliminary results in constitutive modeling through Artificial Neural Networks, using relative simple applications. In particular, we encode in the ANN architecture the two basic laws of thermodynamics. This assures thermodynamically consistent predictions, even for unseen data (i.e., data which can exceed the range of training data-sets). Moreover, our network does not have to identify/learn the underlying pattern of thermodynamic laws. Consequently, smaller data-sets are needed, in principle, the training is more efficient and the accuracy of the predictions higher. The price to pay, in comparison with existing approaches, is the need of two additional scalar functions (outputs) in the training data-set. These are the free-energy and the dissipation rate. However, these quantities are easily accessible in micro-mechanical simulations (e.g. Nitka et al., 2011; Eijnden et al., 2016; Feyel, 2003) and can also be obtained experimentally in some cases (Kahirdeh and Khonsari, 2015; Gavrilov et al., 2017). Then, based on classical derivations in thermodynamics (e.g. Houlsby and Puzrin, 2007; Einav, 2012) specific interconnections are programmed inside our ANN architecture to impose the necessary thermodynamic restrictions. These thermodynamic restrictions concern

the stresses and internal state variables and their relation with the free-energy and the dissipation rate. Our approach is inspired by the so-called Physics-Informed Neural Networks (PINNs) (Raissi et al., 2019), in which *reverse-mode autodiff* (Baydin et al., 2017) is used, allowing the numerical calculation of the derivative of an ANN with respect to its inputs.

The calculation of these derivatives, imposes some numerical requirements regarding the mathematical class of the activation functions to be used. More specifically, the internal ANN restrictions, derived from the first law of thermodynamics, require activation functions whose second gradient does not vanish. Otherwise, the problem of *second-order vanishing gradients*, as it is called here (cf. classical *vanishing gradients* problem in ANNs (e.g. Géron, 2019)), can inhibit back-propagation and make training to fail. This new problem and its remedy is extensively explored and discussed herein.

For the sake of simplicity and for distinguishing our approach from existing ones, we call the proposed ANN architecture *Thermodynamics-based Artificial Neural Networks* (TANNs). In our opinion TANN should be the starting point for data-driven and physics-based constitutive modeling at the material point level. For the implementation of TANNs, we leverage Tensorflow v2.0, an open-source symbolic tensor manipulation software library (Abadi et al., 2016). Other libraries/packages can be used as well.

The Chapter is structured as follows. Section 6.1 presents a brief summary of the theoretical background of thermodynamics. In Section 6.2 an overview of the methodology proposed and architecture of TANN is given. The main differences with classical, standard ANNs for material constitutive modeling are also discussed. Particular attention is given to the choice of activation functions and the new-discovered issue of second-order vanishing gradient is investigated in detail. Generation of material data-sets, with which the training of ANNs is performed, is presented in Section 6.3. Some applications of TANN for uni and three-dimensional elasto-plastic material models are presented in Section 6.4. Extensive comparisons with standard ANNs which are not based on thermodynamics are also presented.

6.1 Thermodynamics principles: energy conservation and dissipation inequality

6.1.1 Energy conservation

A convenient way to express the (local) energy conservation is

$$\rho \dot{\mathsf{e}} = \sigma \cdot \mathrm{D}^{\mathrm{Sym}}\mathrm{v} - \mathrm{div} q + \rho h, \tag{6.1}$$

with ρ being the material density; e the specific internal energy (per unit mass); σ the Cauchy stress tensor; $\mathrm{D}^{\mathrm{Sym}}\mathrm{v}$ the symmetric part of the spatial velocity gradient tensor; q the rate of heat flux per unit area; h the specific energy source (supply) per unit mass, and "$\cdot$" denotes contraction of adjacent indices.

6.1.2 Second principle

The second law of thermodynamics can be formulated in terms of the local Clausius-Duhem inequality

$$\rho \dot{\mathsf{s}} \geq \frac{\rho h}{\theta} - \mathrm{div}\left(\frac{q \cdot n}{\theta}\right), \tag{6.2}$$

with s being the specific (per unit mass) entropy; h/θ and $-(q\cdot n)/\theta$ the rate of entropy supply and flux, respectively; and div denotes the divergence operator. By removing the heat supply h between the energy equation (6.1) and the entropy inequality (6.2) leads to

$$\rho\left(\theta\dot{\mathsf{s}}-\dot{\mathsf{e}}\right)+\sigma\cdot\mathrm{D}^{\mathrm{Sym}}\mathrm{v}-\frac{q\cdot\mathrm{D}\theta}{\theta}\geq 0, \tag{6.3}$$

where the first two terms represent the rate of mechanical dissipation $\mathsf{D}=\rho\left(\theta\dot{\mathsf{s}}-\dot{\mathsf{e}}\right)+\sigma\cdot\mathrm{D}^{\mathrm{Sym}}\mathrm{v}$ and the latter the thermal dissipation rate, i.e., $\mathsf{D}^{th}=-\frac{q\cdot\mathrm{D}\theta}{\theta}$. We assume that the mechanical dissipation rate must itself be non-negative (point-wise), i.e., $\mathsf{D}\geq 0$. The reason is that the thermal dissipation is non-negative because heat only flows from regions of higher temperature to lower temperature−that is, the heat flux q is always in the direction of the negative thermal gradient.

6.1.3 Dissipation function

Using the definition of the mechanical dissipation rate D, Eq. (6.1) becomes

$$\rho\dot{\mathsf{e}}=\rho\theta\dot{\mathsf{s}}+\sigma\cdot\mathrm{D}^{\mathrm{Sym}}\mathrm{v}-\mathsf{D}. \tag{6.4}$$

Let define the specific (per unit volume) internal energy $\mathsf{E}=\rho\mathsf{e}$ and entropy $\mathsf{S}=\rho\mathsf{s}$ and further assume constant material density, i.e., $\frac{\mathrm{d}}{\mathrm{d}t}\rho=0$−that is, $\dot{\mathsf{E}}=\rho\dot{\mathsf{e}}$ and $\dot{\mathsf{S}}=\rho\dot{\mathsf{s}}$. This assumption is reasonable for many materials in solid mechanics. However, it can be easily removed. We shall assume a small strain regime, i.e., $\mathrm{D}u\ll 1$, with $\varepsilon:=\mathrm{D}^{\mathrm{Sym}}u$ the infinitesimal strain tensor, where u is the displacement vector field, and $\dot{\varepsilon}:=\mathrm{D}^{\mathrm{Sym}}\mathrm{v}$ its rate of change. Equation (6.4) hence becomes

$$\dot{\mathsf{E}}=\theta\dot{\mathsf{S}}+\sigma\cdot\dot{\varepsilon}-\mathsf{D}. \tag{6.5}$$

Let assume a strain-rate independent material such that the free energy is

$$\mathsf{E}:=\widetilde{\mathsf{E}}\left(\mathsf{S},\varepsilon,\mathcal{Z}\right), \tag{6.6}$$

and the mechanical dissipation rate is

$$\mathsf{D}:=\widetilde{\mathsf{D}}\left(\mathsf{S},\varepsilon,\mathcal{Z},\dot{\mathcal{Z}}\right), \tag{6.7}$$

where $\mathcal{Z}=(\zeta_i,\ldots,\zeta_N)$ denotes a set of N (additional) internal state variables, ζ_i, $i=1,\ldots,N$, and $:=$ denotes an assignment/definition. We define here (thermodynamic) state variables those macroscopic quantities characterizing the state of a system, see e.g. (Maugin and Muschik, 1994). The physical representation of ζ_i is not *a priori* prescribed. For instance, in the case of isotropic damage, ζ is a scalar; in anistotropic damage, a tensor; in the case of elasto-plasticity, a second order tensor, etc. The generalization to a finite-strain formulation can be achieved by considering the deformation gradient, F, and the first Piola-Kirchhoff tensor, P, as strain and stress measures, respectively (see e.g. (Mariano and Galano, 2015) and (Anand et al., 2012)). Nevertheless, as it would presented in Section 6.2, an incremental formulation of the material response is herein adopted. Therefore, the hypothesis of a small strain regime is usually realistic, at least

for a large class of materials and an updated Lagrangian integration scheme.
Time differentiation of the internal energy gives

$$\dot{\mathsf{E}} = \frac{\partial \mathsf{E}}{\partial \mathsf{S}} \cdot \dot{\mathsf{S}} + \frac{\partial \mathsf{E}}{\partial \varepsilon} \cdot \dot{\varepsilon} + \sum_{i=1}^{N} \frac{\partial \mathsf{E}}{\partial \zeta_i} \cdot \dot{\zeta}_i, \tag{6.8}$$

which is equal to (6.5) and, by collecting terms, it leads to

$$\left(\frac{\partial \mathsf{E}}{\partial \mathsf{S}} - \theta\right) \dot{\mathsf{S}} + \left(\frac{\partial \mathsf{E}}{\partial \varepsilon} - \sigma\right) \cdot \dot{\varepsilon} - \left(\sum_{i=1}^{N} \frac{\partial \mathsf{E}}{\partial \zeta_i} \cdot \dot{\zeta}_i + \mathsf{D}\right) = 0. \tag{6.9}$$

The arbitrariness of $\dot{\mathsf{S}}$, $\dot{\varepsilon}$, and $\dot{\zeta}$, and the indeendence of D from $\dot{\mathsf{S}}$ and $\dot{\varepsilon}$ lead to the following relations

$$\theta = \frac{\partial \mathsf{E}}{\partial \mathsf{S}}, \tag{6.10a}$$

$$\sigma = \frac{\partial \mathsf{E}}{\partial \varepsilon}, \tag{6.10b}$$

$$\sum_{i=1}^{N} \frac{\partial \mathsf{E}}{\partial \zeta_i} \cdot \dot{\zeta}_i + \mathsf{D} = 0. \tag{6.10c}$$

Further introducing the thermodynamic stress, conjugate to ζ_i, $\mathcal{X} = (\chi_1, \ldots, \chi_N)$, with

$$\chi_i := -\frac{\partial \mathsf{E}}{\partial \zeta_i} \qquad \forall\, i \in [1, N]\,, \tag{6.11}$$

we obtain the following, alternative form of the dissipation

$$\mathsf{D} = \sum_{i=1}^{N} \chi_i \cdot \dot{\zeta}_i \tag{6.12}$$

6.1.4 Isothermal processes

In the case of isothermal process, the (specific) Helmholtz free-energy, $\mathsf{F} := \mathsf{E} - \mathsf{S}\theta = \widetilde{\mathsf{F}}(\theta, \varepsilon, \mathcal{Z})$, which is the Legendre transform conjugate of e, is preferable. In this case, the dissipation rate is such that $\mathsf{D} := \widetilde{\mathsf{D}}(\theta, \varepsilon, \mathcal{Z}, \dot{\mathcal{Z}})$. The equations presented above (6.9-6.24) still hold (by replacing E with F)

$$\mathsf{S} = -\frac{\partial \mathsf{F}}{\partial \theta}, \quad \sigma = \frac{\partial \mathsf{F}}{\partial \varepsilon}, \quad \mathsf{D} = -\sum_{i} \frac{\partial \mathsf{F}}{\partial \zeta_i} \cdot \dot{\zeta}_i = \sum_{i} \chi_i \cdot \dot{\zeta}_i. \tag{6.13}$$

6.2 Standard ANNs and Thermodynamics-based Artificial Neural Networks

Within the framework of standard ANN material models, we can distinguish two main classes. The first consists of direct, so-called "black-box" (Raissi et al., 2019), approaches, where the information flow passes through the machine learning tool (usually feed-forward

or recurrent artificial neural networks), which functions as a mere regression operator, see e.g. (Ghaboussi et al., 1991; Lefik and Schrefler, 2003). The second class coincides with ANN models incorporating some knowledge in an informed, guided graph, see e.g. (Heider et al., 2020). In this case, the stress increments are predicted, following an ad-hoc information flow, where intermediate outputs of the network represent some measurable quantities [1] (such as the elastic and plastic strain). Both classes, however, are affected by the lack of physics, being the predictions not always compatible with thermodynamic principles (at least). Figure 7.7a depicts the direct approach (BB), in which ANNs,

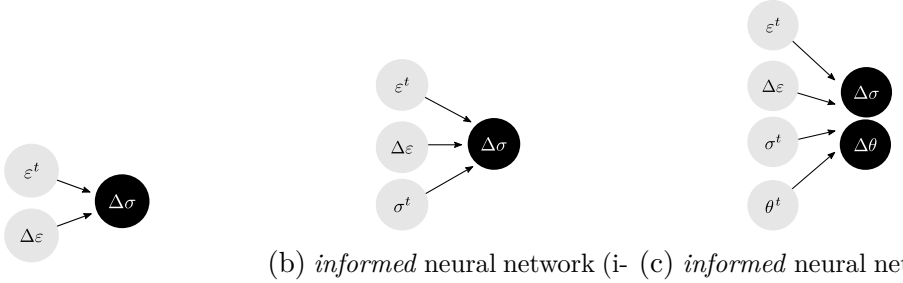

(a) black-box (BB) network.

(b) *informed* neural network (i-NN1).

(c) *informed* neural network (i-NN1).

Figure 6.1 – Examples of direct, black-box (BB) (left) and informed (right) neural networks for material laws modeling. Inputs are highlighted in gray (●), outputs in black (●).

either forward fed or recurrent, are used to predict the stress increment, (output, $\mathcal{O}$) $\mathcal{O} = \Delta\sigma = \sigma^{t+\Delta t} - \sigma^t$, from the input $\mathcal{I} = (\varepsilon^t, \Delta\varepsilon)$, being ε^t the precedent strain state and $\Delta\varepsilon$ its increment. In concise form, we write $\mathcal{O} = \mathsf{BB}@\mathcal{I}$. In this scheme, ε^t and $\Delta\varepsilon$ can be regarded as the state variables, namely the *ANN state variables* (not necessarily coinciding with those introduced in Sect. 6.1), on which the updated material stress depends on. Two examples of guided, informed ANNs are illustrated in Figures 7.7b and 7.7c. In both cases, the ANN intrinsically accounts for path-dependency, see e.g. (Heider et al., 2020), making sequence of predictions of the main output. The network i-NN1 makes use of the last predicted output, i.e., σ^t, to make predictions of the next output, $\mathcal{O} = \Delta\sigma$. The inputs are hence $\mathcal{I} = (\varepsilon^t, \Delta\varepsilon, \sigma^t)$. We shall notice that, differently from BB, the stress at the precedent state, σ^t, is also considered to be an ANN state variable. Other alternatives exist in the selection of the ANN variables of state.
In the case of temperature-dependent material response, the second case (i-NN2) allows to make predictions that depend on the precedent temperature state, θ^t, namely $\mathcal{O} =$ i-NN2$@\mathcal{I}$, with $\mathcal{I} = (\varepsilon^t, \Delta\varepsilon, \sigma^t, \theta^t)$ and $\mathcal{O} = (\Delta\sigma, \Delta\theta)$.

The main aim of this work is to change the classical paradigm of data-driven ANN material modeling into physics-based ANN material modeling. By exploiting the theoretical background presented in Section 6.1, we propose neural networks which, by definition,

1. For a complete discuss, about measurable quantities and thermodynamic state variables, we refer to Maugin and Muschik (1994).

respect the thermodynamic principles, holding true for any class of material [2]. In this framework, TANN posses the special feature that the entire constitutive response of a material can be derived from definition of only two potential functions: an energy potential and a dissipation (pseudo-) potential (Houlsby and Puzrin, 2007). TANNs are fed with thermodynamics "information" by relying on the automatic differentiation technique (Baydin et al., 2017) to differentiate neural networks outputs with respect to their inputs.

The model relies on an incremental formulation and can be directly used in existing Finite Element formulations (among others), see e.g. (Lefik and Schrefler, 2003). Figure 6.2 illustrates the scheme of TANN. The model inputs are the strain increment, the previous material state at time t, which is identified herein through the material stress, σ^t, temperature, θ^t, and the internal state variables, ζ_i^t, as well as the time increment Δt, namely $\mathcal{I} = (\varepsilon^t, \Delta\varepsilon, \sigma^t, \theta^t, \zeta_i^t, \Delta t)$. The *primary* outputs, $\mathcal{O}_1$, are internal variables increment, $\Delta\zeta_i$, the temperature increment, $\Delta\theta$, and the energy potential at time $t+\Delta t$, $\mathsf{F}^{t+\Delta t}$, i.e. $\mathcal{O}_1 = (\Delta\zeta_i, \Delta\theta, \mathsf{F}^{t+\Delta t})$. *Secondary* outputs, $\mathcal{O}_2$−that is, outputs computed by differentiation of the neural network with respect to the inputs−are the stress increment, $\Delta\sigma$, and the dissipation rate, $\mathsf{D}^{t+\Delta t}$, which we denote as $\mathcal{O}_2 = \nabla_{\mathcal{I}}\mathcal{O}_1 = (\Delta\sigma, \mathsf{D}^{t+\Delta t})$.

The class of neural network we propose differs from the previous ones by the fact that the quantity of main interest, i.e., the stress increment, is obtained as a derived one, which intrinsically satisfies the first principle of thermodynamics (and, as we shall see, the second principle, as well). In the following, we briefly recall the basic concepts of artificial neural networks (paragraph 6.2.1), we then focus on the issue of the second-order vanishing gradients that may afflict the training and the performance of an ANN model (paragraph 6.2.2). Finally, we present in detail the architecture of our model (paragraph 6.2.3).

6.2.1 Overview of Artificial neural networks method

We give herein a brief overview of the basic concepts of artificial neural networks [3] (ANNs). ANNs are non-linear operators, consisting of an assembly of mutually connected processing units−nodes−, which take an input signal $\mathcal{I}$ and return the output $\mathcal{O}$, namely

$$\mathcal{O} = \mathsf{ANN}@\mathcal{I}. \tag{6.14}$$

ANNs consist of at least three types of layers: input, output and hidden layers. Figure 6.3 depicts an examle of a network containing one hidden layer, with 3 nodes, an input layer with 2 inputs, and an output layer with 1 node. When an ANN has two or more hidden layers, it is called a deep neural network (Géron, 2019). Denoting the input array with $\mathcal{I} = (i_m)$, with $m = 1, 2 \ldots, n_{\mathcal{I}}$ ($n_{\mathcal{I}}$ is the number of inputs), and the outputs with

2. Here we limit our approach to strain-rate independent materials. However, our approach can be extended, following the developments in (Houlsby and Puzrin, 2000), to materials showing viscosity and strain-rate dependency, but this will be presented in a future work.

3. For more details, we refer to (Hu and Hwang, 2002; Géron, 2019)

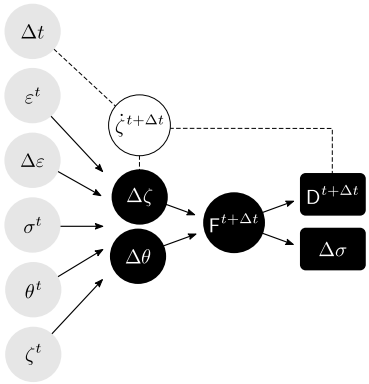

Figure 6.2 – Schematic architecture of TANN. Inputs are highlighted in gray (●); outputs in black, (●) and (▬); and intermediate quantities in white (○). Dashed lines represent definitions, while arrows are used to denote ANN.

$\mathcal{O} = (o_j)$, with $j = 1, 2 \ldots, n_{\mathcal{O}}$ ($n_{\mathcal{O}}$ is the number of outputs), the signal flows from layer $(l-1)$ to layer (l) according to

$$p_k^{(l)} = \mathcal{A}^{(l)}\left(z_k^{(l)}\right), \quad \text{with} \quad z_k^{(l)} = \sum_s^{n_{\mathcal{N}}^{(l-1)}} \left(w_{ks}^{(l)} p_s^{(l-1)}\right) + b_k^{(l)}, \tag{6.15}$$

where $p_k^{(l)}$ is the output of node k, at layer (l); $\mathcal{A}^{(l)}$ is the activation function of layer (l); $n_{\mathcal{N}}^{(l-1)}$ is the number of neurons in layer $(l-1)$; $w_{ks}^{(l)}$ is the *weight* between the s-th node in layer $(l-1)$ and the k-th node in layer (l); and $b_k^{(l)}$ are the *biases* of layer (l). With reference to Figure 6.3, the output is given by

$$\begin{aligned} \mathcal{O} = &\quad \mathcal{A}^{(\mathrm{o})}\left(z^{(\mathrm{o})}\right) \quad \text{with} \quad z^{(\mathrm{o})} = \textstyle\sum_r w_r^{(2)} p_r^{(1)} + b^{(2)} \\ p_r^{(1)} = &\quad \mathcal{A}^{(1)}\left(z_r^{(1)}\right) \quad \text{with} \quad z_r^{(1)} = \textstyle\sum_t w_{rt}^{(1)} i_t + b_r^{(1)}, \end{aligned}$$

where the activation function of the output layer, $\mathcal{A}^{(\mathrm{out})}$, in a regression problem, is a linear function, in the most part of applications. The weights and biases of interconnections are adjusted, in an iterative process (gradient descent algorithm, Géron, 2019), to minimize the error between the benchmark, $\overline{\mathcal{O}}$, and prediction, $\mathcal{O}$, that is measured by a *loss function*, $\mathcal{L}$. In the following, the Mean (over a set of N samples) Absolute Error is used as loss function, i.e.,

$$\mathcal{L} = \frac{\sum_{i=1}^{N} |\overline{\mathcal{O}}_i - \mathcal{O}_i|}{N}, \tag{6.16}$$

where $i = 1, 2, \ldots N$, but other could be used as well (e.g., the Mean Square Error). The errors related to each node of the output layer are hence back-propagated to the nodes in the hidden layers and used to calculate the gradient of the loss function, namely

$$\frac{\partial \mathcal{L}}{\partial w_{ks}^{(l)}} = \frac{\partial \mathcal{L}}{\partial o_j} \frac{\partial o_j}{\partial z_r^{(l+m)}} \frac{\partial z_r^{(l+m)}}{\partial p_r^{(l+m-1)}} \cdots \frac{\partial z_k^{(l+1)}}{\partial p_k^{(l)}} \frac{\partial p_k^{(l)}}{\partial w_{ks}^{(l)}}, \tag{6.17}$$

which is also used to update weights and biases, and force the minimization of the loss function values, according to

$$w_{ks}^{(l)-\text{new}} := w_{ks}^{(l)} - \varpi \frac{\partial \mathcal{L}}{\partial w_{ks}^{(l)}}, \tag{6.18}$$

where ϖ is the so-called *learning rate*. The weights and biases updating, the so-called

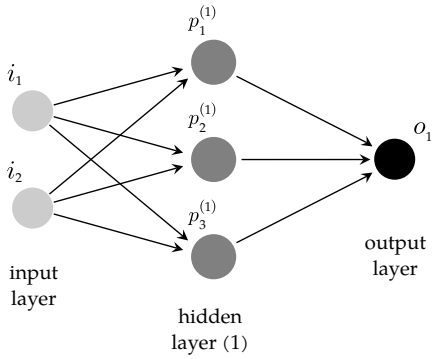

Figure 6.3 – Graph illustration of an ANN structure with two inputs, one output, and one hidden layer with three nodes.

training process, is performed on a subset of the input-output data-set, defined as training set, known from experimental tests or numerical simulations of the phenomenon investigated. The ANN is *trained* by performing iteration and updating the weights and biases, according to Eq. (6.18). The training process is stopped when the loss function is below a specific tolerance. Then a test set, a subset of the input-output data-set different to the training set, is used to check the error of the network predictions. Once the ANN is trained, it is used in recall mode, namely to make predictions from new combinations of input data. In ANNs, the choice of hyper-parameters, such as the number of neurons, the network topology, the weights, etc. are problem-dependent and determined by the application at hand (Chen and Chen, 1995; Cybenko, 1989). The same stands for the activation functions, which may be chosen to have some desirable properties of non-linearity, differentiation, monotonicity, etc. Most of these properties mostly stem from issues related to the gradient descent algorithm and the so-called (first-order) vanishing gradient problem. In the following, we briefly present this well-known problem and we present also the second-order vanishing gradient problem which appeared in our TANN approach.

6.2.2 First- and second-order vanishing gradients

During the training process, if the gradient of the loss function with respect to a certain weight is zero or close to zero—that is, see Eq. (6.18), when $\mathcal{A}'^{(l)} = \partial p_j^{(l)} / \partial z_j^{(l)} \approx 0$ (with $\mathcal{A}'$ the first-derivative of the activation function with respect to its arguments)—the update operation fails, and the weight and biases values cannot be updated. In this case, we have the so-called *first-order* vanishing gradient (Géron, 2019). Figure 6.4 displays some of the most common activation functions and their derivatives. More specifically, we present the logistic (sigmoid) function, the hyperbolic tangent, the Rectified Linear

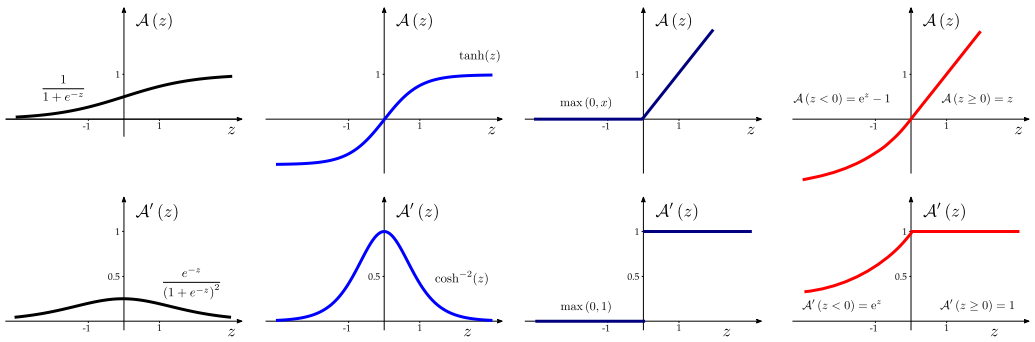

Figure 6.4 – Some of the most common activation functions and their first-order gradient. From left to right: the logistic (sigmoid) function, the hyperbolic tangent, the Rectified Linear Unit (ReLU), and the Exponential Linear Unit (ELU).

Unit (ReLU), and the Exponential Linear Unit (ELU) and their derivatives. The sigmoid function is S-shaped, continuous, differentiable, its output values range from 0 to 1, and its first-order gradient (derivative) takes values much smaller than 1. When inputs become large (negative or positive), the function saturates at 0 or 1, with a derivative extremely close to 0. Thus during backpropagation, the gradient is almost zero and training is impossible. The hyperbolic tangent activation function is very similar to the sigmoid, but it is centered at zero allowing to maintain the output values within a normalized range (between -1 and 1). Nevertheless, it suffers from saturated gradients (for input value z, such that $z = 0$, $z << -1$, or $z >> 1$), meaning that the gradient remains practically the same, for $z << -1$ or $z >> 1$, obstructing the minimization process. ReLU is continuous but not differentiable at $z = 0$. Nevertheless it is an unsaturated activation function for positive values of z (its gradient has no maximum) and, therefore, it allows to avoid vanishing gradient issues for $z > 0$. Nevertheless, it suffers from a problem known as the *dying ReLUs*: during training, some neurons are effectively deactivated, meaning they stop outputting anything other than zero (for $z < 0$). To this purpose many variants exist. The ELU activation, for instance, takes negative values when $z < 0$, which allows the unit to have an average output closer to 0. This helps alleviate the vanishing gradient problem, as discussed earlier. Moreover, it has a nonzero gradient for $z < 0$, which avoids the dying units issue. Finally, the function is smooth everywhere, including z = 0, which helps speed up gradient descent.

When dealing with TANN, *second-order* vanishing gradients can appear. This is a new concept and, in order to illustrate it, we will use a simple example. Assume an ANN which takes as input some $\mathcal{I} = x$ and returns (a) $\mathcal{O}_1 = x^2$ and (b) its derivative with respect to the input, i.e., $\mathcal{O}_2 = \nabla_{\mathcal{I}}\mathcal{O}_1 = 2x$ (see Figure 6.5). Let consider one hidden layer, with activation function $\mathcal{A}$ and N_n nodes. The activation function of the single output layer, which returns x^2, is assumed to be linear. In this case, the output (a) is

given by

$$\begin{aligned}\mathcal{O}_1 &= p^{(\mathrm{o})} = \mathcal{A}^{(\mathrm{o})}\left(z_k^{(\mathrm{o})}\right)\\ \mathcal{O}_1 &= \sum_j w_j^{(\mathrm{o})} p_j^{(1)} + b^{(\mathrm{o})}\\ \mathcal{O}_1 &= \sum_j w_j^{(\mathrm{o})} \mathcal{A}\left(w_j^{(1)} i + b_j^{(1)}\right) + b^{(\mathrm{o})}.\end{aligned} \tag{6.19}$$

The derivatives of the outputs with respect to the inputs can be easily computed, in this simple example, by taking advantage of the automatic (numerical) differentiation (Baydin et al., 2017). Output (b) is hence computed by the ANN as

$$\begin{aligned}\mathcal{O}_2 = \nabla_{\mathcal{I}}\mathcal{O}_1 = \frac{\partial \mathcal{O}_1}{\partial \mathcal{I}} &= \sum_j \frac{\partial p^{(\mathrm{o})}}{\partial z^{(\mathrm{o})}} \frac{\partial z^{(\mathrm{o})}}{\partial p_j^{(1)}} \frac{\partial p_j^{(1)}}{\partial z_j^{(1)}} \frac{\partial z_j^{(1)}}{\partial \mathcal{I}}\\ \frac{\partial \mathcal{O}_1}{\partial \mathcal{I}} &= \sum_j w_j^{(\mathrm{o})} w_j^{(1)} \mathcal{A}'\left(z_j^{(1)}\right).\end{aligned} \tag{6.20}$$

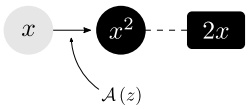

Figure 6.5 – ANN which takes as input x and returns (a) $\mathcal{O} = x^2$ and (b) its derivative with respect to the input, i.e., $\nabla_{\mathcal{I}}\mathcal{O} = 2x$, with one hidden layer whose activation function is $\mathcal{A}$.

Consider the following loss function

$$\mathcal{L} = \mathsf{w}_o \mathcal{L}_o + \mathsf{w}_{\nabla_{\mathcal{I}}\mathcal{O}} \mathcal{L}_{\nabla_{\mathcal{I}}\mathcal{O}},$$

where $\mathcal{L}_o$ and $\mathcal{L}_{\nabla_{\mathcal{I}}\mathcal{O}}$ are the loss functions corresponding to output $\mathcal{O}$ and $\nabla_{\mathcal{I}}\mathcal{O}$, respectively. Regularized weights, w_o and $\mathsf{w}_{\nabla_{\mathcal{I}}}$, can be used to obtain comparable order of magnitude of the two loss functions. During training, weights and biases are updated according to Eq. (6.18) where the computed gradients are

$$\frac{\partial \mathcal{L}}{\partial w_j^{(\mathrm{o})}} = \mathcal{A}\mathcal{L}_o' + w_j^{(1)} \mathcal{A}' \mathcal{L}_{\nabla_{\mathcal{I}}\mathcal{O}}' \tag{6.21a}$$

$$\frac{\partial \mathcal{L}}{\partial w_j^{(1)}} = i w_j^{(\mathrm{o})} \mathcal{A}' \mathcal{L}_o' + \left(w_j^{(\mathrm{o})} \mathcal{A}' + i w_j^{(1)} \mathcal{A}''\right) \mathcal{L}_{\nabla_{\mathcal{I}}\mathcal{O}}' \tag{6.21b}$$

$$\frac{\partial \mathcal{L}}{\partial b^{(\mathrm{o})}} = \mathcal{L}_o' \tag{6.21c}$$

$$\frac{\partial \mathcal{L}}{\partial b_j^{(1)}} = w_j^{(\mathrm{o})} \mathcal{A}' \mathcal{L}_o' + w_j^{(\mathrm{o})} w_j^{(1)} \mathcal{A}'' \mathcal{L}_{\nabla_{\mathcal{I}}\mathcal{O}}'. \tag{6.21d}$$

It follows, from relations (6.21b) and (6.21d), that the gradient descent algorithm needs the computation of both first- and second-order gradients of the activation function $\mathcal{A}$. This particular result is a direct consequence of the minimization of the error between the gradient of the outputs with respect to the inputs, i.e. $\mathcal{O}_2 = \nabla_{\mathcal{I}}\mathcal{O}_1$, and the corresponding benchmark values, $2x$. This is what we call second-order vanishing gradient problem. It is similar to the first-order variant, but it involves the second derivatives (and not only the first) of the activation functions in an ANN. With reference to Figure 6.4, none of the depicted, classical activation functions is suitable for such class of problems. Consequently, care must be taken in selecting activation functions that do not have second-order vanishing gradients, when derivatives of the outputs are also used in the architecture of the neural network, as in the case of TANNs.

In the following, we investigate the performance and influence of different activation functions on the computational time to train an ANN with input $\mathcal{I}$, *primary* output $\mathcal{O}_1$, and *secondary* output $\mathcal{O}_2 = \nabla_{\mathcal{I}}\mathcal{O}_1$. Consider the above discussed example with $\mathcal{I} = x$, $\mathcal{O}_1 = x^2$, and $\mathcal{O}_2 = 2x$. The ANN has one hidden layer, with $N_n = 6$ nodes, and activation functions as reported in Table 6.1. The output layer has linear activation and null bias. The absolute error is selected as loss function for both $\mathcal{O}_1$ and $\mathcal{O}_2$. Training is performed on 1000 samples, normalized between -1 and 1. A very small fixed value for the learning rate is selected, i.e., $\varpi = 10^{-5}$ in order to facilitate the gradient descent algorithm in reaching small values of the loss function. We use *early-stopping*. In other words, training is stopped as the error of a validation set (500 samples) starts to increase while the learning error still decreases (Géron, 2019). The validation set and early-stopping are used to avoid over-fitting of the training data.

Table 6.1 – Set of activation functions considered for investigating the performance of the network with outputs $\mathcal{O} = x^2$ and $\nabla_{\mathcal{I}}\mathcal{O} = 2x$, with $\mathcal{I} = x$, in the framework of first- and second-order vanishing gradients.

Function	z range	$\mathcal{A}(z)$	$\mathcal{A}'(z)$	$\mathcal{A}''(z)$
	$z < 0$	0	0	0
	$z \geq 0$	z	1	0
	$z < 0$	0	0	0
	$z \geq 0$	$0.5z^2 + z$	$z + 1$	1
	$z < 0$	0	0	0
	$z \geq 0$	z^2	$2z$	2
ELU_e	$\forall z$	$\text{e}^z - 1$	e^z	e^z
	$z < 0$	$\text{e}^z - 1$	e^z	e^z
	$z \geq 0$	z	1	0
	$z < 0$	$\text{e}^z - 1$	e^z	e^z
	$z \geq 0$	$0.5z^2 + z$	$z + 1$	1
	$z < 0$	$\text{e}^z - 1$	e^z	e^z
	$z \geq 0$	z^2	$2z$	2
	$z < 0$	$\text{e}^z - 1$	e^z	e^z
	$z \geq 0$	z^4	$4z^3$	$12z^2$
	$z < 0$	$\text{e}^z - 1$	e^z	e^z
	$z \geq 0$	$z^4 + 0.5z^2 + z$	$4z^3 + z + 1$	$12z^2 + 1$

6.2. Standard ANNs and Thermodynamics-based Artificial Neural Networks

For each tested activation function, Table 6.2 shows the Mean Absolute Error (MAE) calculated using a set of new, unseen data (500 samples) of input-output predictions for x^2 and $2x$. The advancement of training is quantified herein as the number of *epochs*, i.e., the number of optimization iterations to train the network on the training data-set (Géron, 2019). Activation functions with quadratic terms, or of higher degree, perform very well, compared to their linear equivalents. RELU_{z^2}, ELU_{z^2} outperform as their shape is very similar to the input-output regression they are trained to learn. Nevertheless, it is worth noticing that training fails when activation functions with vanishing second gradient are used (e.g. RELU_z and ELU_z). Figure 6.6 compares the ANN predictions for a selection of activation functions with the analytical (exact) results. Whilst RELU_z is clearly inadequate, ELU_z predictions overall agree with the analytical values. This is due to the fact that the ANN takes advantage of the exponential term, for negative z and thus successfully manages to satisfy both $\mathcal{O}$ and $\nabla_{\mathcal{I}}\mathcal{O}$. Notice that additional hidden layers are expected to improve the performance of the network. It can be further noticed that activation functions of high degree, e.g. $\mathrm{ELU}_{\mathrm{e}}$, ELU_{z^4}, and $\mathrm{ELU}_{z^4+0.5z^2+z}$, even if successful, would require a larger number of epochs, depending on the functional space of the functions to be interpolated.

Table 6.2 – Activation functions and performance with unseen data.

Activation function $\mathcal{A}$	$\mathcal{L}$ (10^{-4})	$\mathcal{L}_{\mathcal{O}}$ (10^{-4})	$\mathcal{L}_{\nabla_{\mathcal{I}}\mathcal{O}}$ (10^{-4})	no. epochs (-)
ReLU_z	1521.2	205.98	1315.18	920
$\mathrm{ReLU}_{0.5z^2+z}$	762.4	93.58	668.85	8054
ReLU_{z^2}	0.061	0.0241	0.0371	148
$\mathrm{ELU}_{\mathrm{e}}$	127.2	26.83	100.38	19477
ELU_z	108.56	12.12	96.44	17280
$\mathrm{ELU}_{0.5z^2+z}$	65.5	10.91	54.63	12178
ELU_{z^2}	0.13	0.067	0.067	88
ELU_{z^4}	65.36	33.75	31.61	20051
$\mathrm{ELU}_{z^4+0.5z^2+z}$	12.94	1.81	11.13	9683

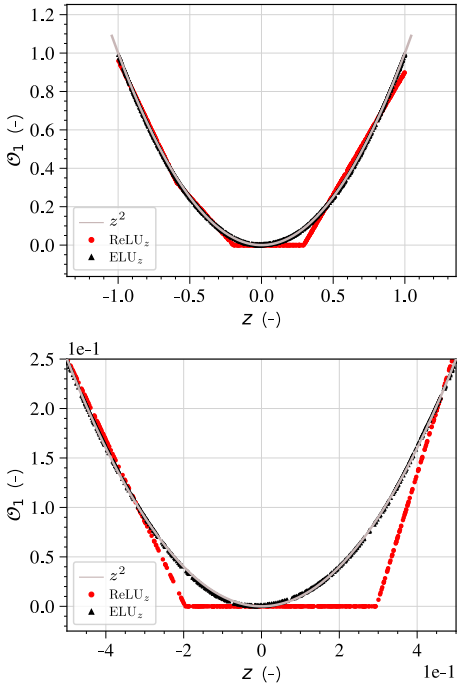

(a) x^2 predictions, $\mathcal{O}_1$, using ReLU and ELU$_z$.

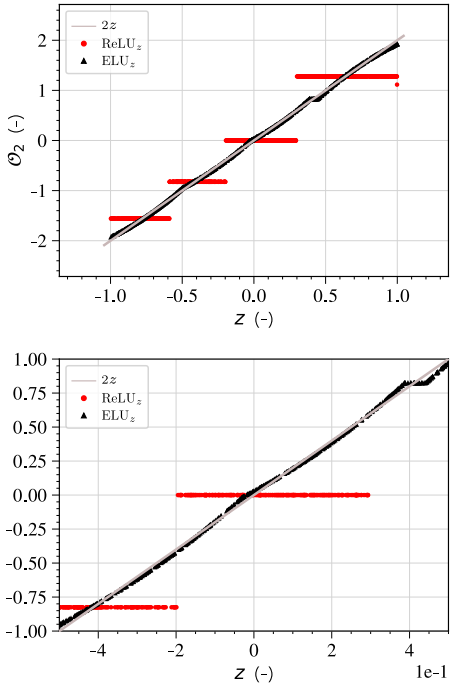

(b) $2x$ predictions, $\mathcal{O}_2$, using ReLU and ELU$_z$.

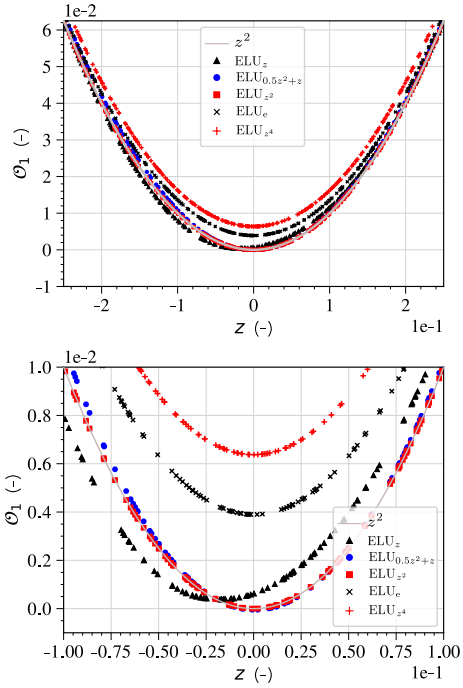

(c) x^2 predictions, $\mathcal{O}_1$, using ELU$_z$, ELU$_{0.5z^2+z}$, ELU$_{z^2}$, ELU$_e$, and ELU$_{z^4}$.

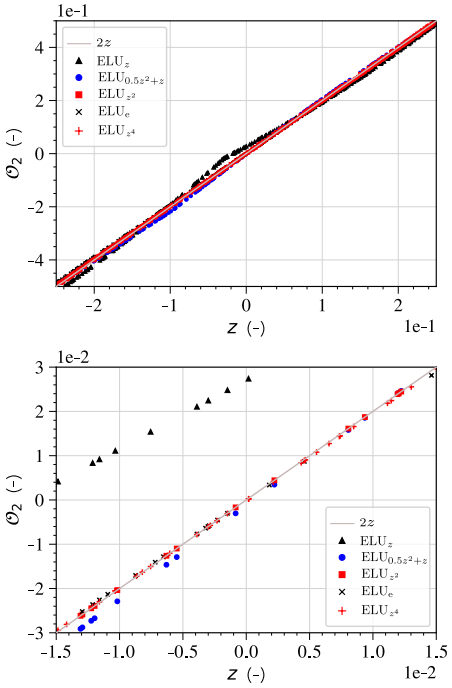

(d) $2x$ predictions, $\mathcal{O}_2$, using ELU$_z$, ELU$_{0.5z^2+z}$, ELU$_{z^2}$, ELU$_e$, and ELU$_{z^4}$.

Figure 6.6 – Comparison of different activation functions for the prediction of the primary output, x^2 (a), and secondary output, $2x$ (b). From top to bottom the range of z decreases from larger to smaller values, to observe the behavior at $z \approx 0$.

6.2.3 Architecture of Thermodynamics-based ANN

The architecture of TANNs is detailed in Figure 6.7. The input vector is $\mathcal{I} = (\varepsilon^t, \Delta\varepsilon, \sigma^t, \theta^t, \zeta_i^t, \Delta t)$, the primary and secondary outputs are $\mathcal{O} = (\Delta\zeta_i, \Delta\theta, \mathsf{F}^{t+\Delta t})$ and $\nabla_{\mathcal{I}}\mathcal{O} = (\Delta\sigma, \mathsf{D}^{t+\Delta t})$, respectively. TANNs involve the following steps:

1. computation of the updated strain (definition): $\varepsilon^{t+\Delta t} := \varepsilon^t + \Delta\varepsilon$
2. prediction of the kinematic variables (not necesssarily thermodynamic state variables) and temperature increments with two sub-ANNs:

$$\Delta\zeta = \mathsf{sNN}_\zeta@\left(\varepsilon^{t+\Delta t}, \Delta\varepsilon^t, \sigma^t, \theta^t, \zeta^t\right)$$

and

$$\Delta\theta = \mathsf{sNN}_\theta@\left(\varepsilon^{t+\Delta t}, \Delta\varepsilon, \sigma^t, \theta^t, \zeta^t\right)$$

3. computation of
   (a) the updated kinematic variables rates (backward finite difference approximation): $\dot{\zeta}^{t+1} \approx \frac{\Delta\zeta}{\Delta t}$
   (b) the updated kinematic variables (definition): $\zeta^{t+1} := \zeta^t + \Delta\zeta^t$
   (c) the updated temperature (definition): $\theta^{t+1} := \theta^t + \Delta\theta$
4. prediction of the updated energy potential:

$$\mathsf{F}^{t+\Delta t} = \mathsf{sNN}_\mathsf{F}@\{\varepsilon^{t+\Delta t} \quad \zeta^{t+\Delta t} \quad \theta^{t+\Delta t}\}$$

5. computation of the updated dissipation (definition, Eq. (6.13)): $\mathsf{D}^{t+\Delta t} := -\frac{\partial \mathsf{F}^{t+\Delta t}}{\partial \zeta^{t+\Delta t}} \cdot \dot{\zeta}^{t+\Delta t}$
6. computation of
   (a) the updated stress (definition, Eq. (6.13)): $\sigma^{t+\Delta t} := \frac{\partial \mathsf{F}^{t+\Delta t}}{\partial \varepsilon^{t+\Delta t}}$
   (b) the stress increment (definition): $\Delta\sigma := \sigma^{t+\Delta t} - \sigma^t$

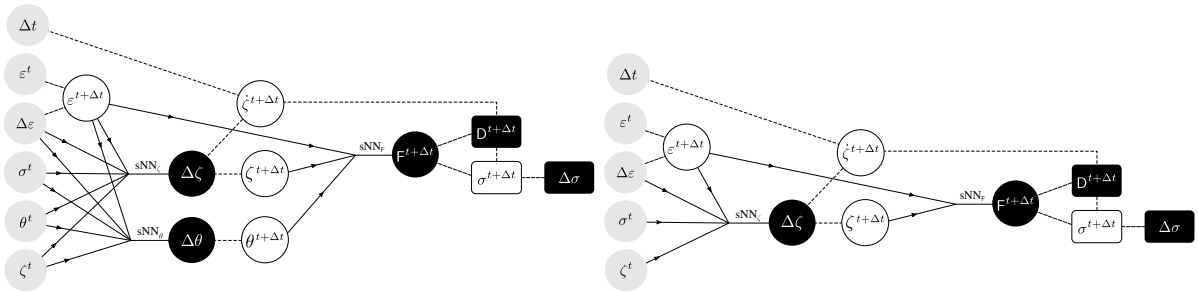

(a) non-isothermal processes.

(b) isothermal processes.

Figure 6.7 – Architecture of TANN: general case (a) and for isothermal processes (b). Inputs are highlighted in gray (●); outputs in black, (■) for direct ANN predictions and (■) for derived outputs; and intermediate quantities (definitions) are in white (○) and (▭). Relationships obtained from definitions are represented with dashed lines, while arrows denote ANNs.

TANN is thus composed of three sub-ANNs; sNN_ζ predicts the internal variables increment, sNN_θ predicts the temperature increment (note that in the case of isothermal

conditions, this component is removed from the architecture, see Fig. 6.7b), and $\mathsf{sNN_F}$ predicts the Helmholtz free-energy. The main output, the increment in stress, is computed according to expression (6.13), which stems from thermodynamic requirements. By virtue of the fact that the entire constitutive response of a material can be derived from definition of only two potential functions, the model is able to predict the stress increment from the knowledge of the energy potential (and the internal variables ζ_i). It is worth noticing that, differently from common approaches (cf. Sect. 6.2), the sub-network $\mathsf{sNN_F}$ is required to learn a scalar quantity−that is, the Helmholtz free-energy potential. This offers compelling advantages. For example, passing from a uni-dimensional (1D) problem to a three-dimensional one increases the number of variables the ANN needs to learn. This increase of the dimensions results in an important increase of the computational cost ('curse of dimensions', Bessa et al., 2017). Nevertheless, TANN is, in principle, less affected by this issue as the two potentials, on which the entire set of predictions relies on, are scalar functions.

The computation of dissipation, from expression (6.13), plays a double role. First, it assures thermodynamic consistency of the predictions of TANN (first law). Second, it brings the information to distinguish between reversible and irreversible processes, e.g. elasticity from plasticity/damage, etc., and it is trained to be positive or zero (second law).

6.3 Generation of data

We present the procedure used to generate material data TANN is trained with. Herein, data are obtained by numerical integration of an incremental form of the constitutive relations. To this purpose, we assume the Ziegler's orthogonality condition (see paragraph 6.3.1 and (Ziegler, 2012; Houlsby and Puzrin, 2000, 2007)), which, in general, it is not a strict requirement. Nevertheless, it is worth emphasizing that this restriction applies only on the generated data, and not on the ANN class here proposed. More precisely, TANN architecture still holds even for materials for which the Ziegler's normality condition does not apply. We shall recall that the aim is to demonstrate the advantages of thermodynamics-based neural networks with respect to classical approaches. Hence the restrictions, imposed by the orthogonality hypothesis for the generation of data, are expected not to affect the comparisons presented in Section 6.4.

6.3.1 Incremental formulation

Following the hyperplasticity framework proposed in (Einav et al., 2007), the thermo-mechanical, non-linear, incremental constitutive relation for strain-rate independent materials, undergoing infinitesimal strains, is here derived in the framework of isothermal processes (θ = constant). By differentiating the energy expressions (6.13) and rearranging the terms, we obtain the following non-linear incremental relations

$$\dot{\sigma} = \partial_{\varepsilon\varepsilon}\mathsf{F} \cdot \varepsilon + \sum_k \partial_{\varepsilon\zeta_k}\mathsf{F} \cdot \dot{\zeta}_k, \tag{6.22a}$$

$$-\dot{\chi}_i = \partial_{\zeta_i\varepsilon}\mathsf{F} \cdot \varepsilon + \sum_k \partial_{\zeta_i\zeta_k}\mathsf{F} \cdot \dot{\zeta}_k. \tag{6.22b}$$

where the following notation is adopted

$$\partial_{\varepsilon\varepsilon}\mathsf{F} = \frac{\partial^2 \mathsf{F}}{\partial \varepsilon_{ij} \partial \varepsilon_{kl}}, \quad \partial_{\varepsilon\zeta_k}\mathsf{F} = \frac{\partial^2 \mathsf{F}}{\partial \varepsilon_{ij} \partial \zeta_k}, \quad \partial_{\zeta_i\zeta_k}\mathsf{F} = \frac{\partial^2 \mathsf{F}}{\partial \zeta_i \partial \zeta_k}.$$

We introduce the thermodynamic dissipative stresses $\mathcal{X}^\dagger = (X_1, \ldots, X_N)$ with

$$X_i := \frac{\partial \mathsf{D}}{\partial \dot{\zeta}_i} \qquad \forall\, i \in [1, N]. \tag{6.23}$$

For a rate-independent material, the dissipation is a first-order homogeneous function in the internal variable rates $\dot{\zeta}_i$ (Houlsby and Puzrin, 2007). This homogeneity can be expressed by the Euler's relation

$$\mathsf{D} = \sum_{i=1}^{N} \frac{\partial \mathsf{D}}{\partial \dot{\zeta}_i} \cdot \dot{\zeta}_i = \sum_i X_i \cdot \dot{\zeta}_i, \tag{6.24}$$

which, together with (6.11), implies

$$\sum_{i=1}^{N} (X_i - \chi_i) \cdot \dot{\zeta}_i = 0 \tag{6.25}$$

Ziegler's orthogonality condition Ziegler (2012) is further assumed, i.e., $X_i = \chi_i \,\forall\, i \in [1, N]$.
As D is first-order homogeneous function in $\dot{\zeta}_i$, the Legendre transform, conjugate to X_i, is degenerate. In particular, the Legendre transform is equal to zero and represents the yield function $y = \tilde{y}(\varepsilon, \mathcal{Z}, \mathcal{X}^\dagger)$, i.e.

$$\lambda y = \sum_i X_i \cdot \dot{\zeta}_i - \mathsf{D} = 0, \tag{6.26}$$

where λ is a non-negative multiplier ($\lambda > 0$). From the properties of Legendre transform, the following flow rules must hold

$$\dot{\zeta}_i = \lambda \frac{\partial y}{\partial X_i} \quad \forall\, i \in [1, N]. \tag{6.27}$$

Since $\lambda > 0$ and $\lambda y = 0$, $y \leq 0$. If $y = 0$, the following consistency equation is met

$$\dot{y} = \frac{\partial y}{\partial \varepsilon} \cdot \dot{\varepsilon} + \sum_{i=1}^{N} \frac{\partial y}{\partial \zeta_i} \cdot \dot{\zeta}_i + \sum_{i=1}^{N} \frac{\partial y}{\partial X_i} \cdot \dot{X}_i = 0. \tag{6.28}$$

By further using the flow rules (6.27) and Ziegler's normality condition, we obtain

$$\lambda = -\frac{\mathcal{C}_\varepsilon}{B} \cdot \dot{\varepsilon}, \tag{6.29}$$

with

$$\mathcal{C}_\varepsilon = \frac{\partial y}{\partial \varepsilon} - \sum_{i=1}^{N} \frac{\partial y}{\partial X_i} \cdot \partial_{\zeta_i \varepsilon} \mathsf{F},$$

and

$$B = \sum_{i=1}^{N} \frac{\partial y}{\partial \zeta_i} \cdot \frac{\partial y}{\partial X_i} - \sum_{i=1}^{N} \frac{\partial y}{\partial X_i} \left(\sum_{k=1}^{N} \partial_{\zeta_k \varepsilon} \mathsf{F} \cdot \frac{\partial y}{\partial X_k} \right).$$

Finally, we arrive to the following, incremental non-linear formulation, for $y = 0$,

$$\dot{\Xi} = \mathcal{M}|_{y=0}\, \dot{\xi}, \quad \text{with} \quad \dot{\Xi} = \begin{bmatrix} \dot{\sigma} \\ -\dot{X}_i \\ \dot{\zeta}_i \\ \lambda \end{bmatrix}, \quad \dot{\xi} = \begin{bmatrix} \dot{\varepsilon} \\ \dot{\theta} \end{bmatrix}, \quad \mathcal{M}|_{y=0} = \begin{bmatrix} \mathsf{M}_{\varepsilon\varepsilon} \\ \mathsf{M}_{\zeta\varepsilon} \\ -\dfrac{\mathcal{C}_\varepsilon}{B} \cdot \frac{\partial y}{\partial X_i} \\ -\dfrac{\mathcal{C}_\varepsilon}{B} \end{bmatrix}, \tag{6.30}$$

and

$$\begin{aligned} \mathsf{M}_{\varepsilon\varepsilon} = &\ \partial_{\varepsilon\varepsilon}\mathsf{F} - \textstyle\sum_k \partial_{\varepsilon\zeta_k}\mathsf{F} \cdot \left(\frac{\mathcal{C}_\varepsilon}{B} \cdot \frac{\partial y}{\partial X_k} \right), \\ \mathsf{M}_{\zeta\varepsilon} = &\ \partial_{\zeta_i\varepsilon}\mathsf{F} - \textstyle\sum_k \partial_{\zeta_i\zeta_k}\mathsf{F} \cdot \left(\frac{\mathcal{C}_\varepsilon}{B} \cdot \frac{\partial y}{\partial X_k} \right). \end{aligned}$$

In case of $y < 0$, relation (6.30) becomes

$$\dot{\Xi} = \mathcal{M}|_{y<0}\, \dot{\xi}, \quad \text{with} \quad \mathcal{M}|_{y<0} = \begin{bmatrix} \partial_{\varepsilon\varepsilon}\mathsf{F} \\ \partial_{\zeta_i\varepsilon}\mathsf{F} \\ \emptyset \\ \emptyset \end{bmatrix}, \tag{6.31}$$

where $\emptyset$ denotes a quantity (scalar or tensorial, depending on the dimensionality of the internal variable set) equal to zero.

6.3.2 Data generation

Data are generated in a Python environment (McKinney et al., 2011), where SymPy (Meurer et al., 2017) and SciPy (Virtanen et al., 2020) libraries are used for symbolic calculations and numerical integration. Data are generated by identifying an initial state for the material at time t,

$$\text{state at time } t: \qquad \Xi^t = \begin{bmatrix} \sigma^t \\ -X_i^t \\ \zeta_i^t \\ 0 \end{bmatrix} \quad \text{and} \quad \varepsilon^t,$$

and a given strain increment $\dot{\varepsilon}^t$, assuming, without loss of generality, constant and unitary time increment $\Delta t = 1$ ($\dot{\varepsilon}^t = \Delta\varepsilon^t$). Numerical integration of the above ordinary

differential equations is performed with an explicit solver, Runge-Kutta method (Bogacki and Shampine, 1989), to obtain the state at the new time $t + \Delta t$, i.e.,

$$\text{state at time } t + \Delta t : \qquad \Xi^{t+\Delta t} = \begin{bmatrix} \sigma^{t+\Delta t} \\ -X_i^{t+\Delta t} \\ \zeta_i^{t+\Delta t} \\ \lambda^{t+\Delta t} \end{bmatrix}$$

The training data play a crucial role for both the accuracy of the predictions and the generalization with respect to the ANN state variables, e.g., strain increments. The *generalization* capability of a network is here defined as the ability to make predictions for loading paths different from those used in the training operation. Nevertheless, a significant dependency on the ANN state variables is usually observed. This may result in a poor network generalization. In Lefik and Schrefler (2003), an improvement of the generalization capability of the ANN was proposed. Artificial sub-sets of data, with zero strain increments, were added in the set of training data to force the network in learning that zero output increments correspond to zero input increments.
In the available literature, strain-stress loading paths are commonly used in training. When recursive neural networks are used, feeding them with history variables (loading paths) is the only possible solution (see e.g. Mozaffar et al., 2019). Nevertheless, ANNs do not necessary need the data-sets to be (history) paths.

Herein, we generate data randomly, and without following prescribed loading paths. This allows us (1) to improve the representativeness of the material data and (2) to improve the generalization of the network on the strain increments. The initial state, Ξ^t and ε^t, and the strain increment, $\Delta\varepsilon^t$, are randomly generated from standard distributions with mean value equal to zero and standard deviation equal to $\Xi_{\max}$, $\varepsilon^t_{\max}$, and $\Delta\varepsilon^t_{\max}$, respectively. The Cauchy and thermodynamic stresses, σ^t and X_i^t, as well as the internal variables ζ_i^t are then calculated to satisfy the constraint $y^t \leq 0$. This incremental procedure is repeated for N_{samples}, resulting in a set of N_{samples} ordered pairs $\{\Xi^t, \varepsilon^t, \Delta\varepsilon^t; \Xi^{t+\Delta t}\}$, from which the corresponding energy potential and dissipation rate at time $t + \Delta t$ are evaluated.
The choice of the standard deviations $\Xi^t_{\max}$, $\varepsilon^t_{\max}$, and $\Delta\varepsilon^t_{\max}$ depends on the investigated problem. In the following, they are selected in a way such that $50 \div 60\%$ of the data samples lie on the yield surface, i.e., $y^t = 0$. Figure 6.8 depicts the sampling for one of the investigated applications.

6.4 Applications to elasto-plasticity

Herein we use TANNs for the modeling of multi-dimensional elasto-plastic materials and demonstrate their wide applicability and effectiveness. It is worth noticing that, even though the examples presented involve only elasto-plasticity, the proposed class of ANN can be successfully applied (without any modification) to materials with different or more complex behavior, accounting for instance damage and/or other non-linearities, in the framework of strain-rate independent processes. In paragraph 6.4.1, a one-dimensional example is given. Then, the more general cases of three-dimensional elasto-plastic materials (paragraph 6.4.2), accounting for perfect-plasticity, hardening and softening behaviors,

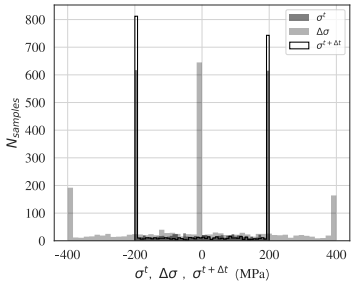

(a) Cauchy stress, σ^t, $\sigma^{t+\Delta t}$, and increment $\Delta\sigma$.

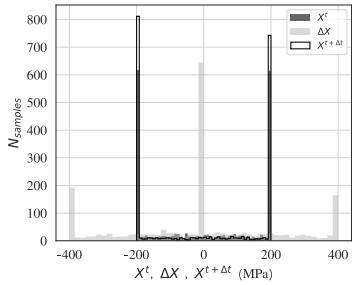

(b) thermodynamic stress, X^t, $X^{t+\Delta t}$, and increment ΔX.

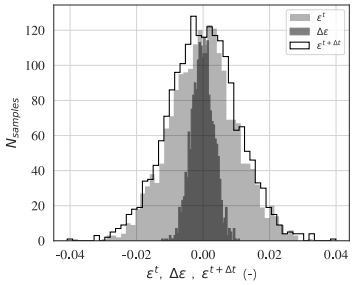

(c) total strain, ε^t, $\varepsilon^{t+\Delta t}$, and increment $\Delta\varepsilon$.

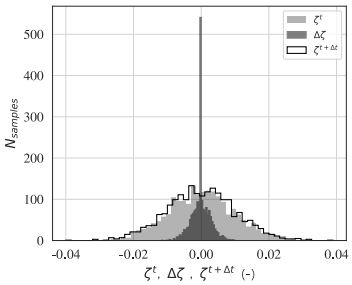

(d) internal variable (inelastic strain), ζ^t, $\zeta^{t+\Delta t}$, and increment $\Delta\zeta$.

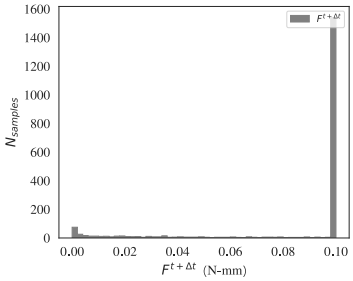

(e) Helmholtz free-energy $F^{t+\Delta t}$.

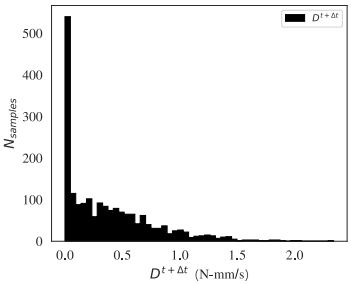

(f) dissipation rate $D^{t+\Delta t}$.

Figure 6.8 – Sampling for one of the studied applications (paragraph 6.4.1). 1D elasto-plastic material with Young's modulus $E = 200$ GPa and yield strength $\sigma_y = 200$ MPa. Standard deviations $\sigma^t_{\max} = X^t_{\max} = 2\sigma_y$, $\varepsilon^t_{\max} = \zeta^t_{\max} = 10^{-2}$, and $\Delta\varepsilon^t_{\max} = 10^{-3}$.

are presented.
The hyper-parameters of the networks (i.e., number of hidden layers, neurons, activation functions, etc.) of the networks are selected to give the best predictions, while requiring minimum number of hidden layers and nodes per layer. This is accomplished by trial-and-error. In each training process, we use the commonly used technique of early-stopping: the iterative update of weights and biases is stopped as the test error starts to increase while the learning error still decreases, which indicates over-fitting.
Throughout this Section relatively simple deep feed-forward neural networks architectures are used (with, at maximum, two hidden layers) and no additional regularization techniques are employed (e.g., L1/L2 penalties, dropout, etc.). Each numerical example is accompanied with a detailed discussion about the network architecture.

6.4.1 1D elasto-plasticity with kinematic hardening

The Helmholtz free-energy potential, dissipation rate, and yield function that define the elasto-plastic 1D model with kinematic hardening (1D spring-slider, Houlsby and

Puzrin (2007)) are:

$$\begin{aligned} \mathsf{F} =& \frac{E}{2}(\varepsilon-\zeta)^2+\frac{H}{2}\zeta^2, \quad \mathsf{D}=k|\dot{\zeta}|, \\ \text{and} \quad y =& \frac{|\sigma-H\zeta|}{k}-1\leq 0, \end{aligned} \tag{6.32}$$

with H being the kinematic hardening/softening-parameter and k being the yield strength (slider threshold). The internal variable, ζ, represents herein the plastic deformation. Table 6.3 displays the choice of the material parameters, selected to represent a steel-like material with either (1) perfect-plastic, (2) hardening, or (3) softening behavior.

Table 6.3 – Material parameters for 1D elasto-plastic materials.

case	E (GPa)	k (MPa)	H (GPa)
1D-A	200	200	0
1D-B	200	200	10
1D-C	200	200	-10

6.4.1.1 Training

According to the procedure detailed in Section 6.3, 2000 data (random increments at random states) are generated, for each (material) case, with the procedure detailed in Section 6.3. Training is performed with 50 % of them (i.e., 1000). A validation set of 500 samples (validation data) is used for avoiding over-fitting. The performance of the predictions, at the end of the training, is evaluated on a set of 500 samples (test data). The sampling for material case 1D-A is shown in Figure 6.8, while the samples distribution for cases 1D-B and 1D-C are presented in D.1 and D.2 (in Appendix D). Adam optimizer with Nesterov's acceleration gradient (Dozat, 2016) is selected for the training algorithm and a batch size of 10 samples is used. We use the Mean Absolute Error (MAE) as loss functions for each output in order to assure the same precision between data of low and high numerical values (cf. Mean Square Error). Regularized weights are used to have consistent order of magnitude of different quantities involved in the loss functions. The architecture of TANN for all 1D cases consists of one hidden layer with 6 neurons (and leaky ReLU activation function) for the predictions of $\Delta\zeta$ and one hidden layer with 9 neurons (activation ELU_{z^2}) to predict $\mathsf{F}^{t+\Delta t}$. The output layers for both sub-networks have linear activation functions and biases are set to zero. The corresponding number of degrees of freedom, i.e., the number of the hyper-parameters, is 72. Higher number of hidden layers could be used as well, but this was not necessary. Figure 6.9 displays the loss functions of each output as the training is performed, i.e., in number of epochs. The early stopping rule assures convergence with MAEs of the same order of magnitude for the 4 outputs, $\Delta\zeta$, $\mathsf{F}^{t+\Delta t}$, $\Delta\sigma$, and $\mathsf{D}^{t+\Delta t}$. Figure D.3 shows the comparison between the predictions of the neural network and the set of test data, for (material) case 1D-A (cf. Table 6.3). Similar behaviors in training and performance with

respect to the set of test data are also found for cases 1D-B and 1D-C. For this reason, they are not presented herein.

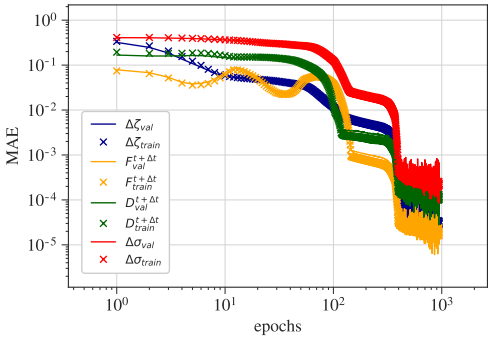

Figure 6.9 – Errors of the predictions of TANN (loss functions), as the training is being performed, evaluated with respect to the training (train) and validation (val) sets. Weights and biases update are computed only on the training set.

6.4.1.2 Predictions in recall mode

Once the neural networks have been trained, we use them in recall mode to predict the stress increment for a given strain, strain increment, and possibly other variables. We then compare the predictions with the corresponding targets. The results of the numerical integration scheme, presented in Section 6.3, are considered as the exact solution of the material response. In particular, starting from an initial configuration, we make cyclic (or random) increments of the strain, $\Delta\varepsilon$. TANN hence predicts the corresponding increments, $\{\Delta\zeta, \Delta\sigma\}$, which will be transformed into the inputs in the successive call, as well as the energy and dissipation rates, $\{\mathsf{F}^{t+\Delta t}, \mathsf{D}^{t+\Delta t}\}$. This procedure is applied recursively. The neural network is so self-fed. Figures 6.10a, 6.10b, and 6.10c illustrate—for cases 1D-A, 1D-B, and 1D-C, respectively—the predictions of TANN for cyclic paths with strain increments $\Delta\varepsilon^n = \Delta\varepsilon \operatorname{sgn}\left(\cos\frac{n\pi}{2N}\right)$, where $n = 1, 2, \ldots$, $N = \varepsilon_{\max}/\Delta\varepsilon$, $\varepsilon_{\max} = 2\times10^{-3}$, and $\Delta\varepsilon = 10^{-4}$. TANN is found to successfully predict all quantities of interest. Moreover, and most important, the architecture and the training of the network allows to obtain thermodynamically consistent results. The first law of thermodynamics is automatically satisfied as a result of the structure of TANN and the predicted dissipation rate is always positive. Indeed, even if the second principle of thermodynamics is not explicitly assured by the TANN architecture, the fact that the training has been performed with consistent material data (i.e., positive dissipation rate) results automatically in the fulfillment of the second principle. Moreover, the linear dependency of dissipation with respect to $\dot{\zeta}$, property that stems from the strain-rate independent material formulation, is also automatically satisfied by TANN.

6.4.1.3 Generalization

We investigate the generalization capability of TANN (i.e., the ability to make predictions for loading paths different from those used in the training operation). This is achieved by feeding the trained network with input values that not necessarily belong to the

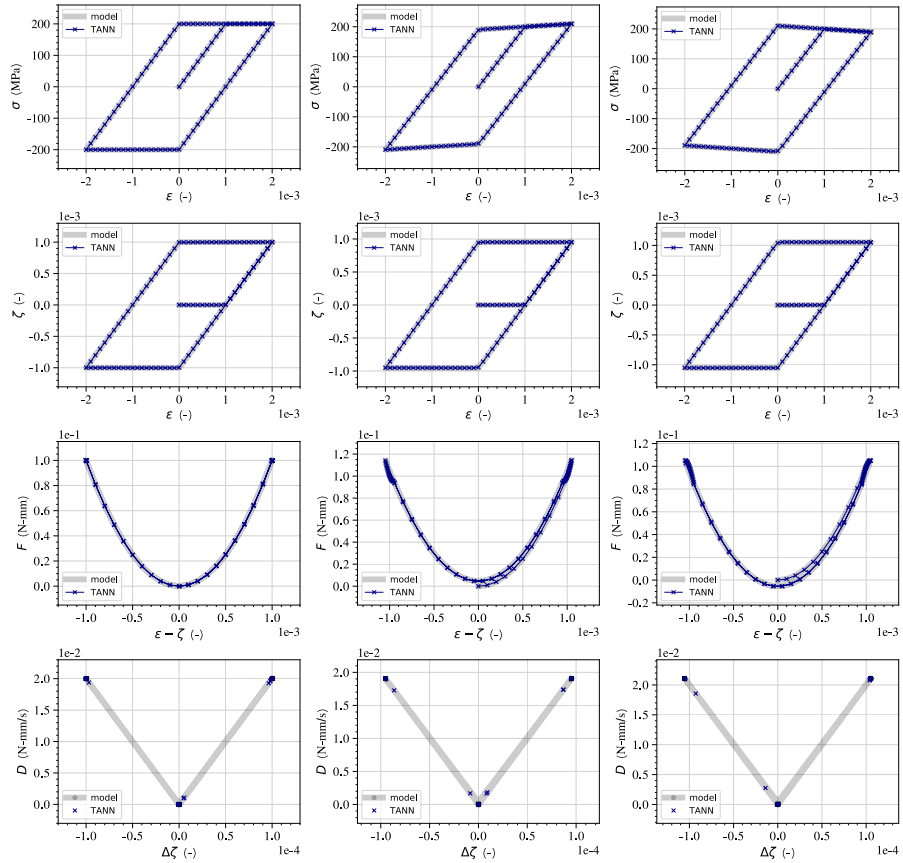

(a) material case 1D-A. (b) material case 1D-B. (c) material case 1D-C.

Figure 6.10 – Predictions of TANN due to cyclic loading, compared with the target constitutive model for cases (a) 1D-A, (b) 1D-B, and (c) 1D-C (see Tab. 6.3), with strain increments $\Delta\varepsilon = 10^{-4}$.

training range (Table 6.4). Figure 6.11 displays the predictions for a cycling loading path $\Delta\varepsilon^n = \Delta\varepsilon \operatorname{sgn}\left(\cos\frac{n\pi}{2N}\right)$ −with $\Delta\varepsilon \in (10^{-5}, 1)$. We clearly see that for input variables outside the training range, the predictions of the network become less accurate. We shall notice that a possible treatment, as suggested by Lefik and Schrefler (2003), exist to extrapolate predictions at strain increments smaller than those belonging to the training data set. However, the same is to possible, within a rigorous framework, for larger strain increments. This is way, as discussed below, we focus attention on predictions of the network at strain increments larger than those contained in the training set.
Furthermore, TANN makes predictions which are always thermodynamically consistent. Moreover, the quantities of primary interest, such as the stress, the internal state variable, and the energy are in extremely good agreement with the reference model. The same stands also for the dissipation rate. We notice, once more, that its values are always positive, even when the network is used for predictions beyond the training range. Figures 6.12 and 6.13 (in Appendix D) presents the predictions for the plastic hardening and softening behaviors, respectively.

Table 6.4 – Range of the value of inputs used for training, for material cases 1D-A, 1D-B, and 1D-C.

case	$\max \lvert\varepsilon^t\rvert$, $\min \lvert\varepsilon^t\rvert$ (-)	$\max \lvert\Delta\varepsilon\rvert$, $\min \lvert\Delta\varepsilon\rvert$ (-)	$\max \lvert\zeta^t\rvert$, $\min \lvert\zeta^t\rvert$ (-)	$\max \lvert\sigma^t\rvert$, $\min \lvert\sigma^t\rvert$ (MPa)
1D-A	0.04, 1×10^{-7}	0.014, 1×10^{-7}	0.04, 6×10^{-6}	200, 0.168
1D-B	0.04, $4. \times 10^{-6}$	0.012, 1×10^{-7}	0.036, 6×10^{-7}	495, 0.300
1D-C	0.04, 1×10^{-7}	0.014, 1×10^{-7}	0.035, 6×10^{-6}	505, 0.060

It is worth noticing that in all the cases, even for very large strain increments−for which the predictions of the network in terms of dissipation rate, energy potential, and (for some values) stress and internal variable differ from the target values−, TANN successfully predicts the Jacobian, i.e., $\frac{\partial \sigma}{\partial \epsilon}$, in very good agreement with the reference model. This is true even when the error in the stress prediction is not negligible (Fig.s 6.12 and 6.13, with $\Delta\varepsilon = 1 \times 10^{-1}$). This is of particular importance for numerical simulations with implicit algorithms. Therefore, TANN seems to be able to successfully replace complicated constitutive models or multiscale approaches, by considerably and safely decreasing the calculation cost, even when the requested increments are outside the training range.

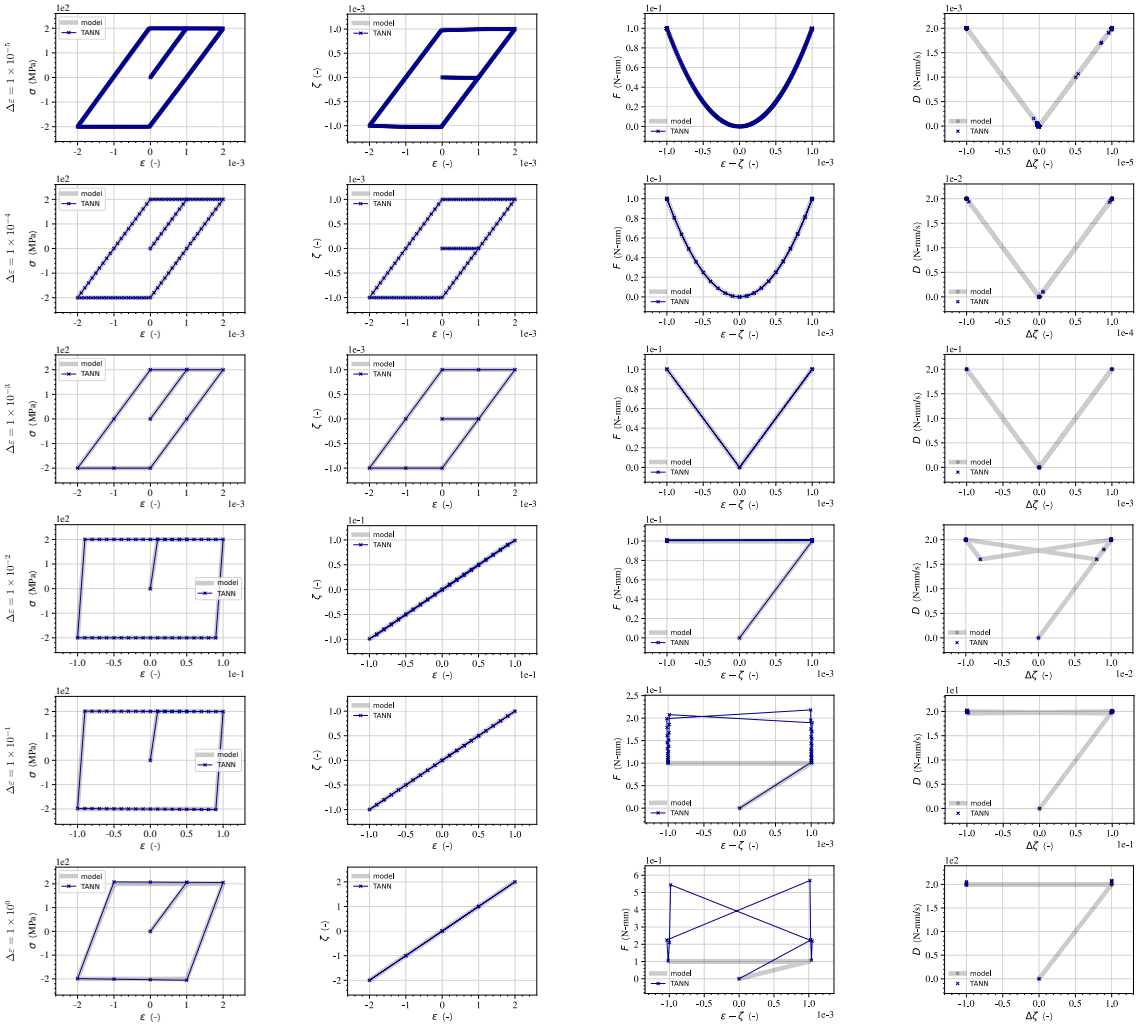

(a) σ prediction. (b) ζ prediction. (c) F prediction. (d) D prediction.

Figure 6.11 – Sensitivity on the inputs for material case 1D-A, with strain increments $\Delta\varepsilon = \Delta\varepsilon \operatorname{sgn}\left(\cos\frac{n\pi}{2N}\right)$ −with $N = \varepsilon_{\max}/\Delta\varepsilon$, $\varepsilon_{\max} = 2 \times 10^{-3} \div 2$, and $\Delta\varepsilon$ varying from $\times 10^{-5}$ (top) to 1 (bottom). Each column displays the response (from left to right) in term of $\Delta\sigma$ (a), $\Delta\zeta$ (b), $\mathsf{F}^{t+\Delta t}$ (c), and $\mathsf{D}^{t+\Delta t}$ (d). Each row represents the prediction at different $\Delta\varepsilon$.

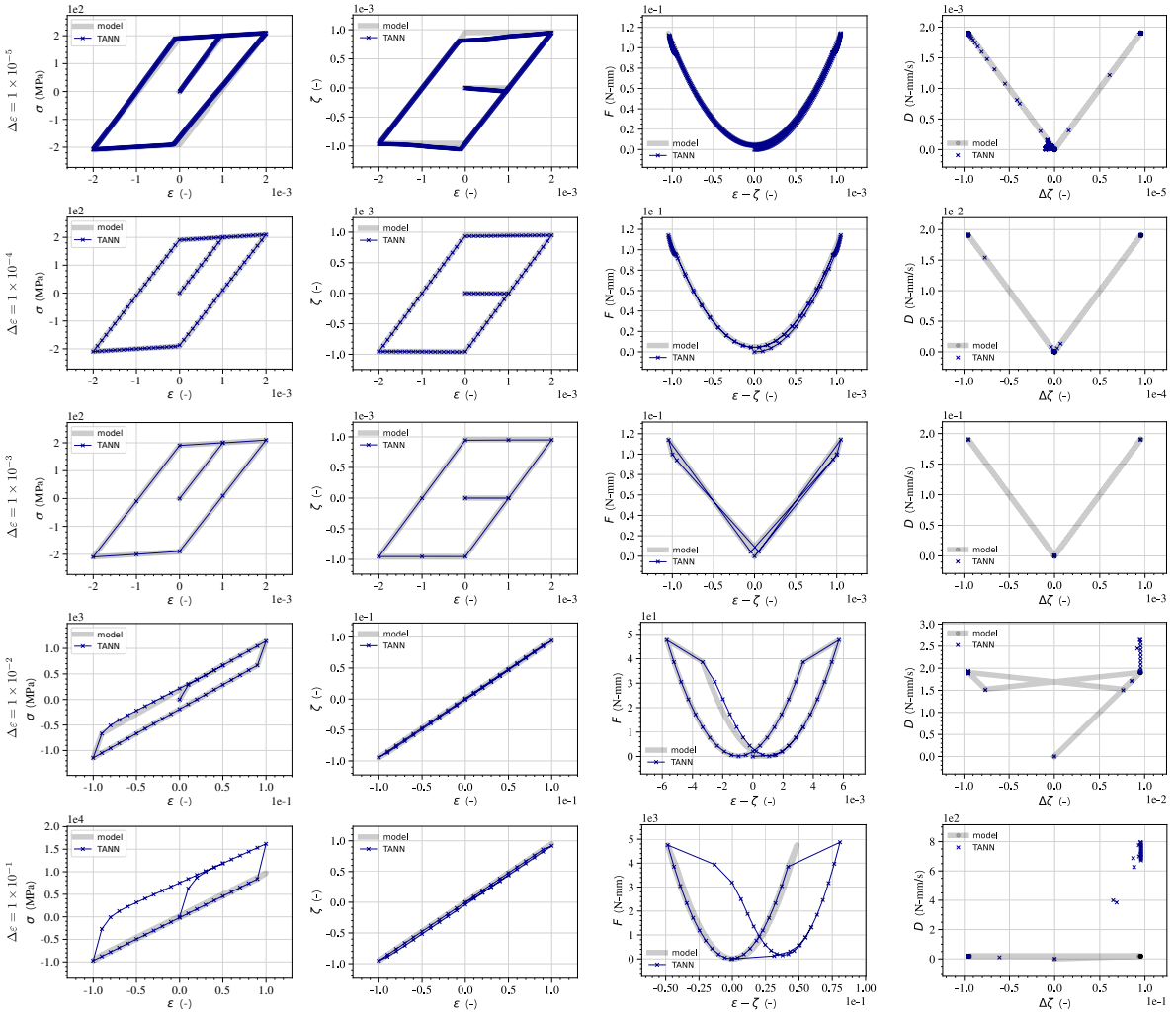

(a) σ prediction. (b) ζ prediction. (c) F prediction. (d) D prediction.

Figure 6.12 – Sensitivity on the inputs for material case 1D-B, with strain increments $\Delta\varepsilon = \Delta\varepsilon \operatorname{sgn}\left(\cos\frac{n\pi}{2N}\right)$ −with $N = \varepsilon_{\max}/\Delta\varepsilon$, $\varepsilon_{\max} = 2 \times 10^{-3} \div 2$, and $\Delta\varepsilon$ varying from $\times 10^{-5}$ (top) to 1×10^{-1} (bottom). Each column displays the response (from left to right) in term of $\Delta\sigma$ (a), $\Delta\zeta$ (b), $\mathsf{F}^{t+\Delta t}$ (c), and $\mathsf{D}^{t+\Delta t}$ (d). Each row represents the prediction at different $\Delta\varepsilon$.

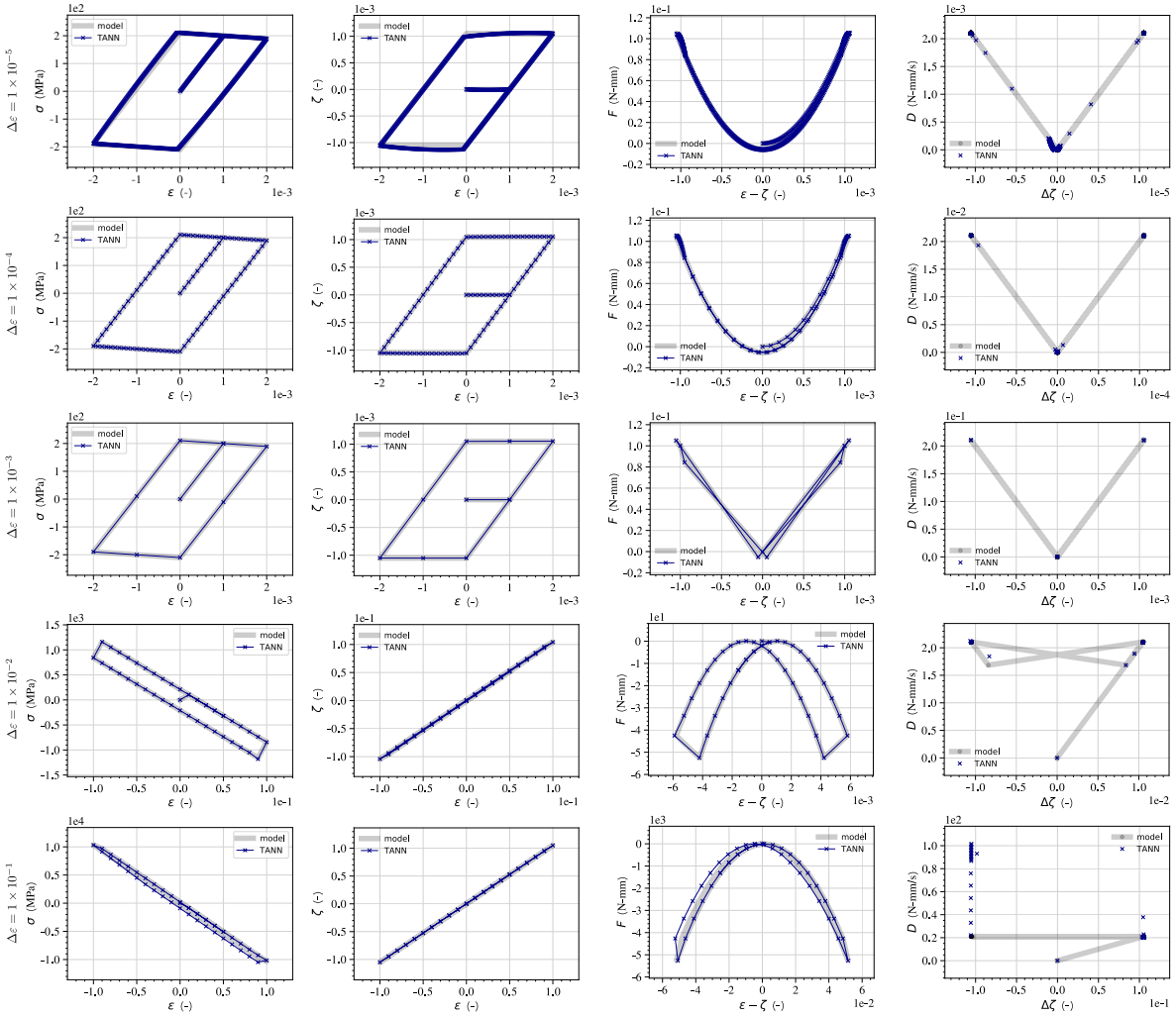

(a) σ prediction. (b) ζ prediction. (c) F prediction. (d) D prediction.

Figure 6.13 – Sensitivity on the inputs for material case 1D-C, with strain increments $\Delta\varepsilon = \Delta\varepsilon \operatorname{sgn}\left(\cos\frac{n\pi}{2N}\right)$ –with $N = \varepsilon_{\max}/\Delta\varepsilon$, $\varepsilon_{\max} = 2 \times 10^{-3} \div 2$, and $\Delta\varepsilon$ varying from $\times 10^{-6}$ (top) to 1×10^{-1} (bottom). Each column displays the response (from left to right) in term of $\Delta\sigma$ (a), $\Delta\zeta$ (b), $\mathsf{F}^{t+\Delta t}$ (c), and $\mathsf{D}^{t+\Delta t}$ (d). Each row represents the prediction at different $\Delta\varepsilon$.

6.4.1.4 TANN vs standard ANN

We compare herein the performance, in recall mode, of TANN with respect to the classical approach of ANN for constitutive modeling (see for example Ghaboussi et al., 1991; Lefik and Schrefler, 2003). Figure 6.14 displays the architecture of the network, ANN, with inputs $\mathcal{I} = (\varepsilon^t, \Delta\varepsilon, \sigma^t, \zeta^t)$ and output $\mathcal{O} = (\Delta\zeta, \Delta\sigma)$. As for TANN, the stress increment is derived by assuming ANN state variables (see Sect. 6.2) such that they coincide with the thermodynamic state variables, i.e., ε^t and ζ^t, and their increments, i.e., $\Delta\varepsilon$ and $\Delta\zeta$, as in Lee (2018); Yu and Carrillo (2019). ANN is thus composed of two sub-ANNs; aNN_ζ predicts the internal variables increment and sNN_σ predicts the stress increment, i.e., $\Delta\sigma = \mathsf{aNN}_\sigma(\varepsilon^{t+\Delta}, \Delta\varepsilon, \zeta^{t+\Delta t}, \Delta\zeta)$. The architecture of the standard ANN network is selected to give the best performance while assuring the same amount of degrees of freedom, hyper-parameters, with those of TANN, for allowing fair comparisons. Both sub-networks, aNN_ζ and aNN_σ, consist of one hidden layer, with 6 neurons each and leaky ReLU activation functions. Same with TANN, the output layers have linear activation function and zero bias. Training is performed on the same set of samples that are used for the thermodynamics-based network. Figure 6.15 displays the error of the predictions of ANN, as training is performed, and compares it with TANN.

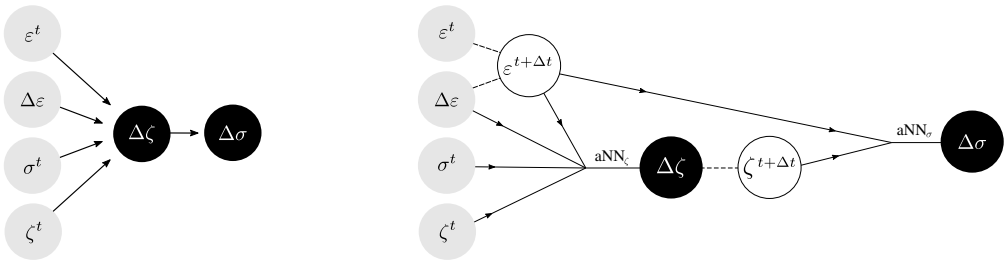

(a) ANN scheme. (b) ANN architecture.

Figure 6.14 – Schematic (a) and full architecture (b) of the network, not based on thermodynamics, ANN. Inputs are highlighted in gray (●), outputs in black (●).

We present in Figures 6.16, 6.17, and 6.18 the comparisons between the predictions of TANN and ANN, in terms of stress, for a cycling loading path $\Delta\varepsilon^n = \Delta\varepsilon \operatorname{sgn}\left(\cos\frac{n\pi}{2N}\right)$. TANN is clearly superior in terms of (a) accuracy of the prediction and (b) generalization with respect to the inputs. Moreover, ANN predictions do not fulfill the principles of thermodynamics, even though the training of the network has been performed on thermodynamically consistent material data. This is clearly shown by computing from the predictions of ANN the increment of the Helmholtz free-energy and dissipation rate using the corresponding definitions, Eq. (6.32). Figures 6.16c and 6.16d display the computed quantities, F and D, for material case 1D-A. The predictions of the standard ANN clearly do not respect the principles of thermodynamics.

Figure 6.19 displays the predictions of both TANN and standard ANN for a random loading path, for a perfectly plastic behavior (Fig. 6.19a), hardening (Fig. 6.19b), and softening (Fig. 6.19c). Once more, the performance of the thermodynamics-based network, as well as its generalization capabilities, are significantly better than those of the

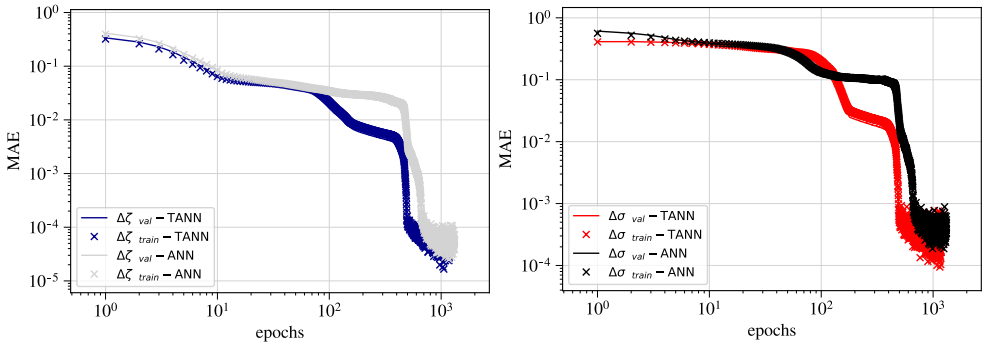

(a) mean absolute error of $\Delta\zeta$ prediction (b) mean absolute error of $\Delta\sigma_i$ prediction

Figure 6.15 – Training of ANN compared with TANN evaluated with respect to the training (train) and validation (val) sets.

standard ANN. One could, of course, increase the number of layers and neurons in order to assure better predictions for the standard ANN, but still there would be no guarantee that the predictions of standard ANN would be thermodynamically consistent.

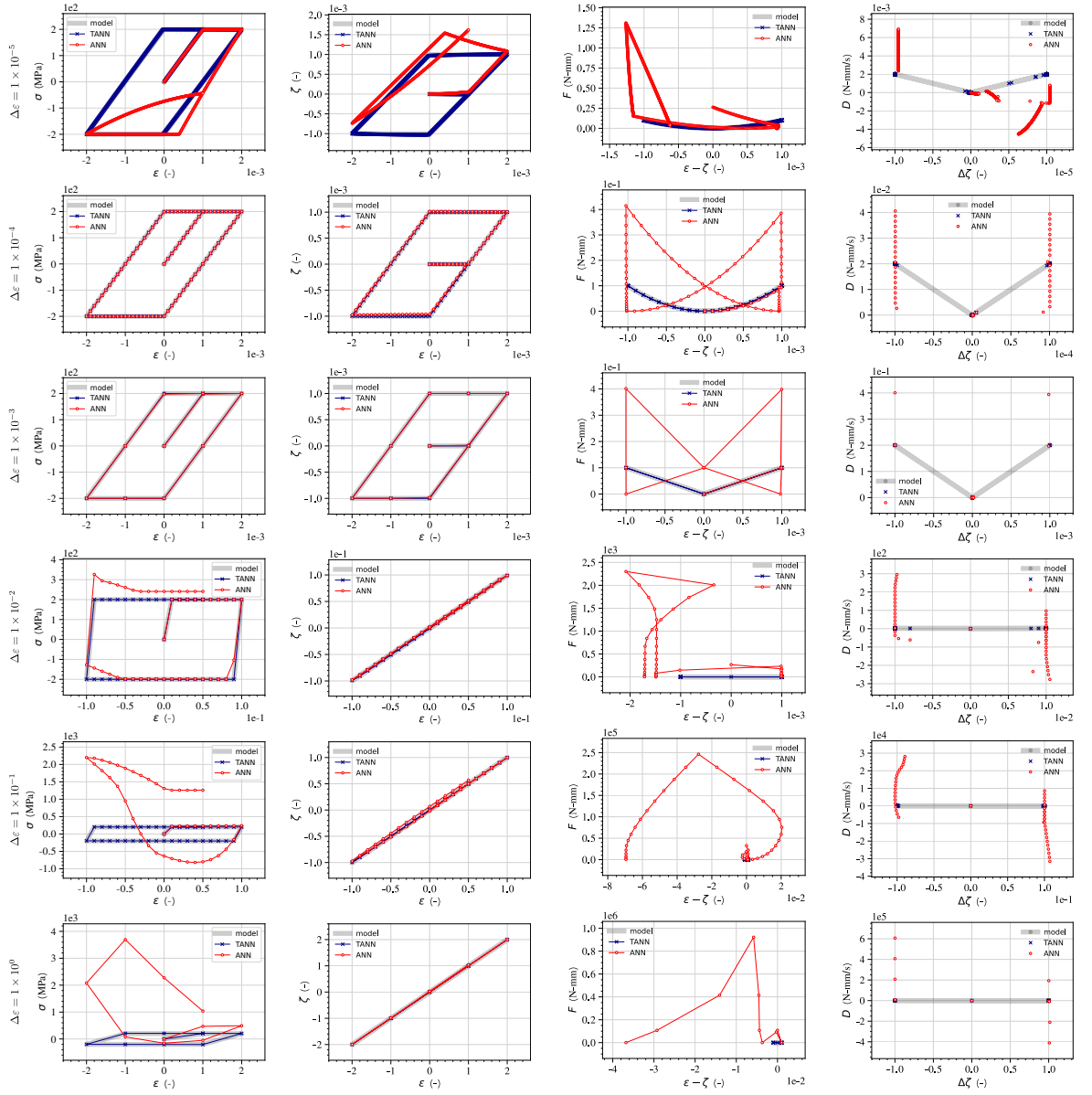

(a) σ prediction. (b) ζ prediction. (c) F prediction (TANN), Eq. (6.32) (ANN). (d) D prediction (TANN), Eq. (6.32) (ANN).

Figure 6.16 – Comparison of the predictions of TANN and those of standard ANN, for material case 1D-A (perfect plasticity). Each row represents the prediction at different $\Delta\varepsilon$.

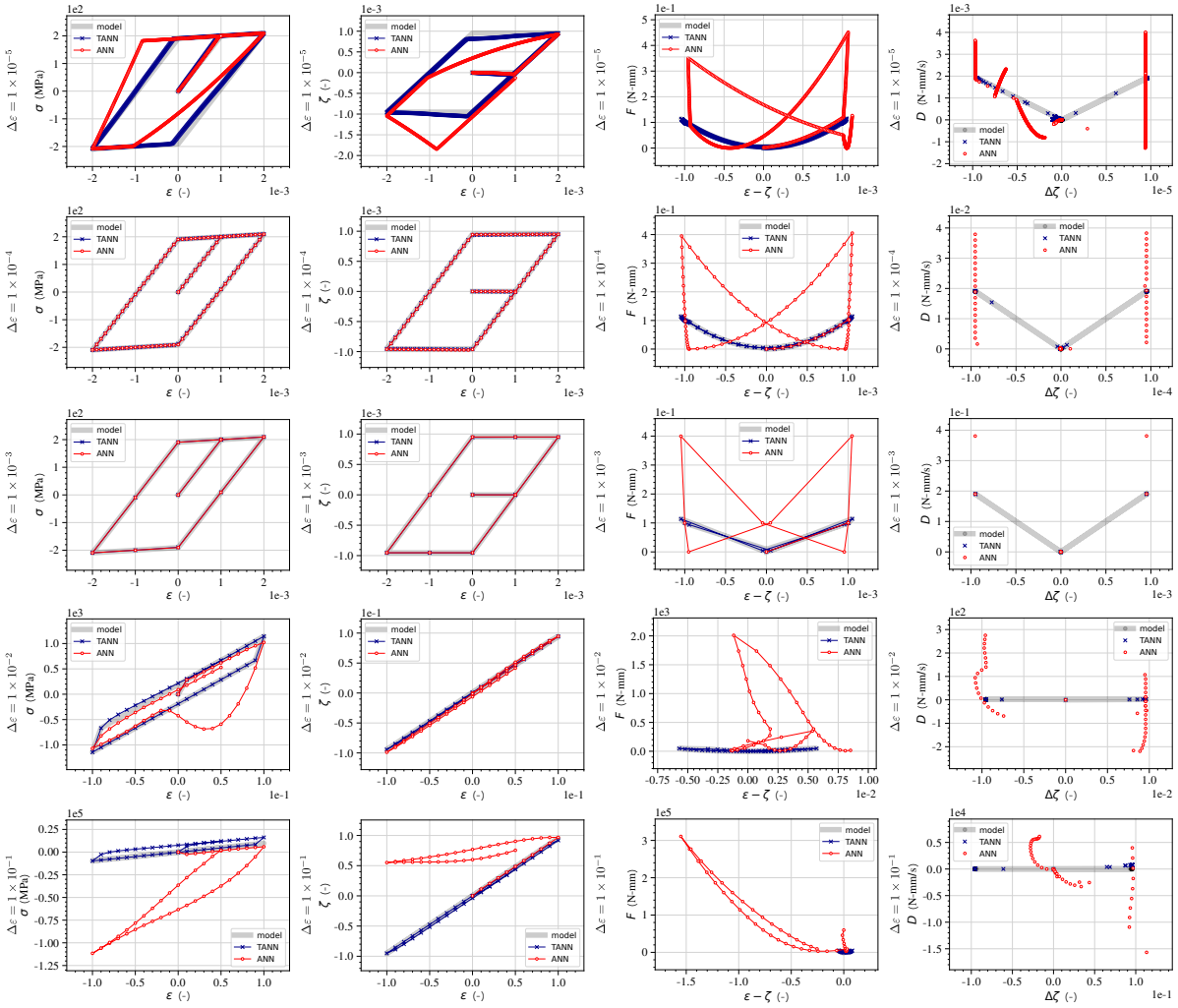

(a) σ prediction (b) ζ prediction (c) F, def. (6.32) (d) D, def. (6.32)

Figure 6.17 – Comparison of the predictions of TANN and those of standard ANN, for material case 1D-B (hardening). Each row represents the prediction at different $\Delta\varepsilon$.

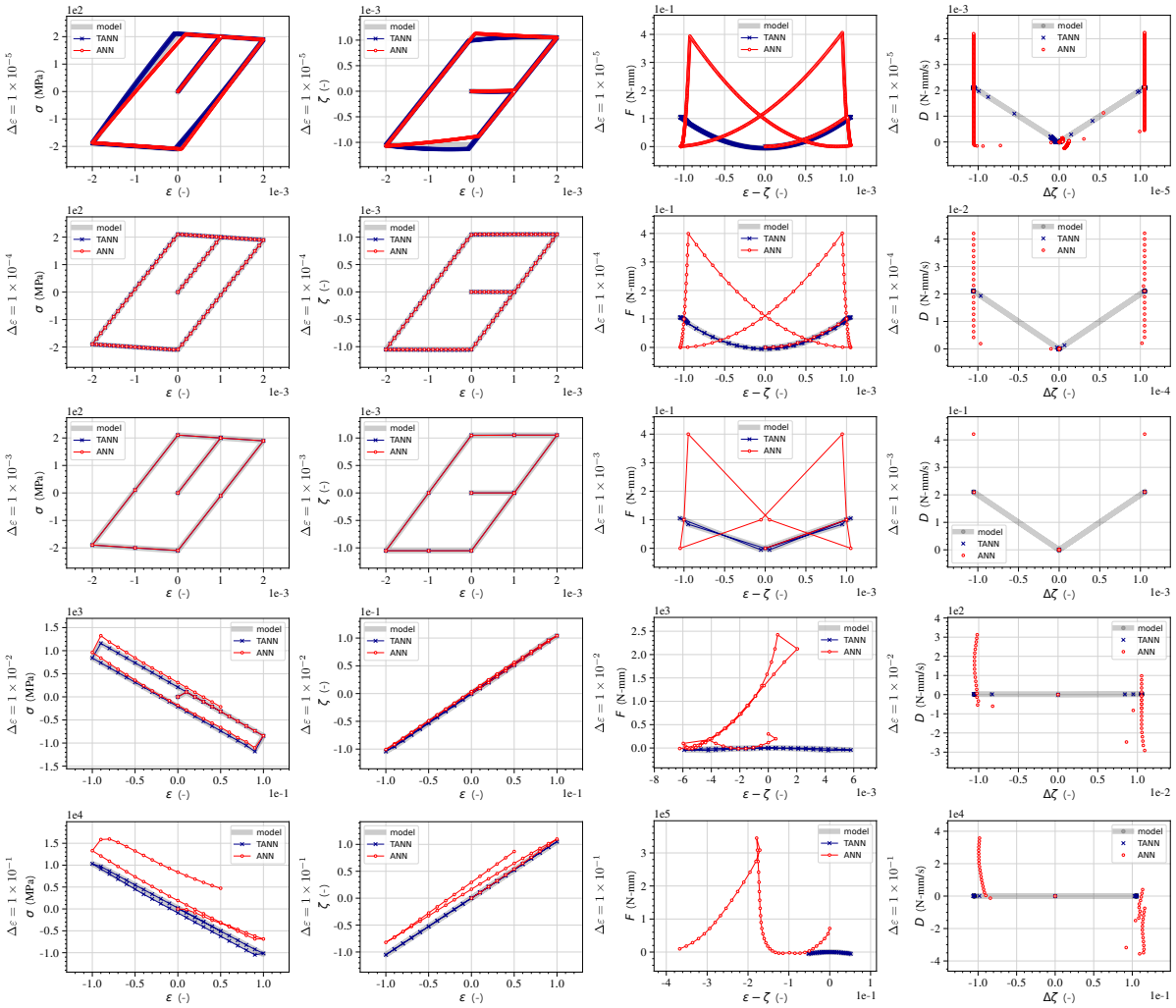

(a) σ prediction (b) ζ prediction (c) F, def. (6.32) (d) D, def. (6.32)

Figure 6.18 – Comparison of the predictions of TANN and those of standard ANN, for material case 1D-C (softening). Each row represents the prediction at different $\Delta\varepsilon$.

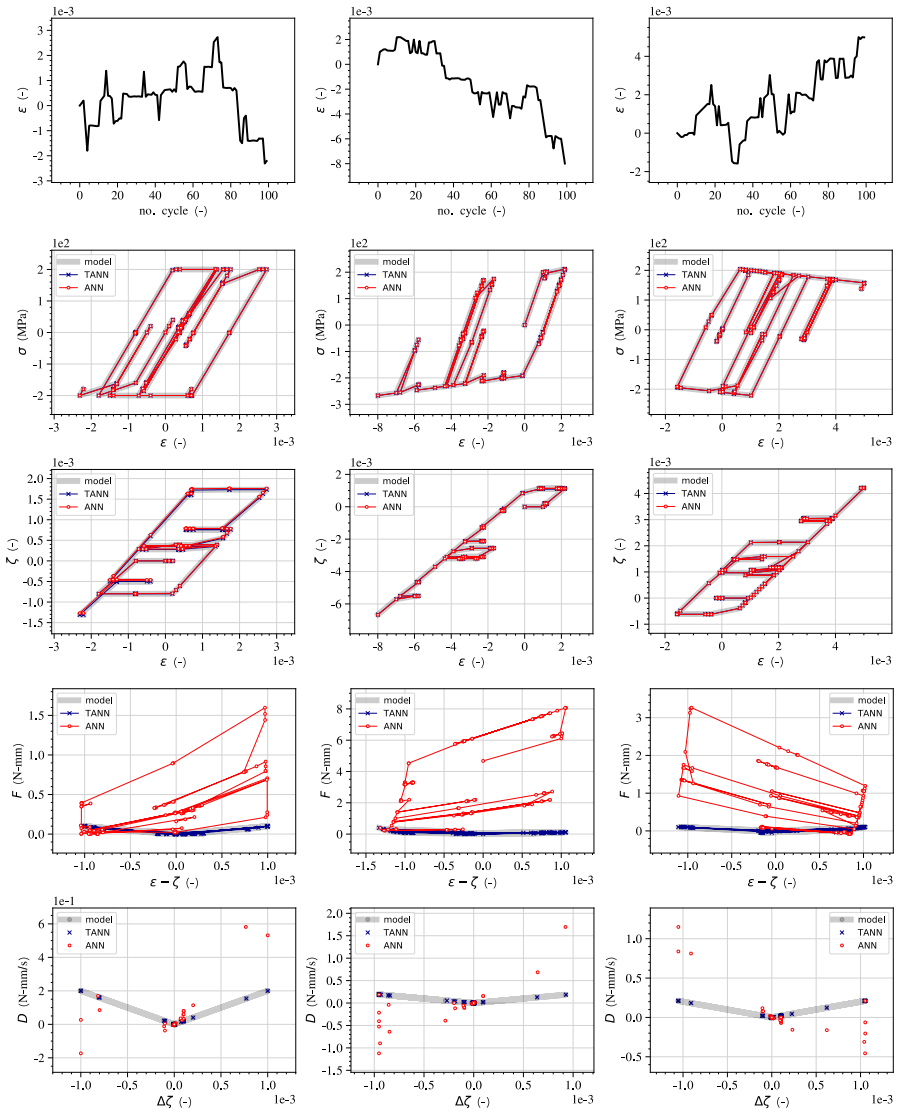

(a) material case 1D-A (b) material case 1D-B (c) material case 1D-C

Figure 6.19 – Comparison of the predictions of TANN and standard ANN for a random loading path, for material cases 1D-A, perfect plasticity (a), 1D-B, hardening (b), and 1D-C, softening (c). The loading path is displayed at the first row, in each case.

6.4.2 3D elasto-plasticity

In order to illustrate the performance of TANN in three-dimensional elasto-plasticity, we use the simple von Mises elasto-plastic model with kinematic softening (and hardening). The model can be derived from the following expressions of the energy potential and dissipation rate

$$\begin{aligned} \mathsf{F} =& \frac{9K}{2}\left(\varepsilon_p - \zeta_p\right)\cdot\left(\varepsilon_p - \zeta_p\right) + \\ &+ G\left(e - z\right)\cdot\left(e - z\right) + \frac{H}{2} z\cdot z, \\ \mathsf{D} =& k\sqrt{2}\sqrt{\dot{z}\cdot\dot{z}}, \end{aligned} \tag{6.33}$$

where k represents the elastic limit in simple shear; K and G are the bulk and shear moduli, respectively; ε_p and ζ_p are, respectively, the mean total and plastic deformation; and e and z are, respectively, the total and plastic deviatoric strain tensors. The yield surface can be derived as shown in paragraph 6.3.1 (see also Houlsby and Puzrin, 2007) and is written as

$$y = D - X'\cdot z = \sqrt{X'\cdot X'} - \sqrt{2}k \leq 0, \tag{6.34}$$

with $X'_{ij} = 2G\left(e_{ij} - z_{ij}\right) + Hz_{ij}$.

Table 6.5 – Material parameters for three-dimensional elasto-plastic von Mises material.

case	K (GPa)	G (GPa)	k (MPa)	H (GPa)
3D-A	167	77	140	0
3D-B	167	77	140	10
3D-C	167	77	140	-10

6.4.2.1 Training

Data are generated as detailed in Section 6.3. A total of 6000 data with random increments of deformation are generated. In order to improve the performance of the network in recall mode, additional sampling with random uni-axial and bi-axial loading paths are also used. The samples are split into training (50%), validation (25%), and test (25%) sets.

The network architecture is adapted to the size of the inputs and outputs, with respect to the mono-dimensional case. In particular, the sub-network sNN_ζ consists of two hidden layers, with 48 neurons (leaky ReLU activation functions), and three output layers, one per each (principal) component of (increment of) ζ. The sub-network $\mathsf{s\text{-}NN}_\mathsf{F}$ has one hidden layer with 36 neurons (activations ELU_{z^2}). The output layers for both sub-networks have linear activation functions and biases set to zero. The resulting number of hyper-parameters is approximately 3000. Figure 6.20 displays the loss functions of each output as the training is performed.

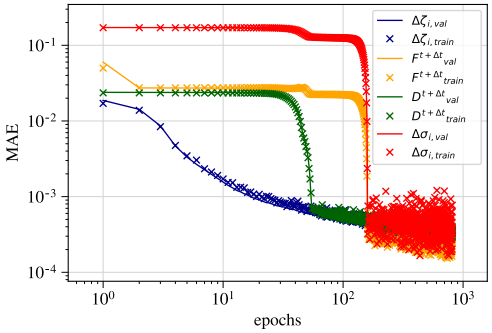

Figure 6.20 – Errors of the predictions of TANN (loss functions), as the training is being performed, evaluated with respect to the training (train) and validation (val) sets. Weights and biases update is computed only on the training set.

6.4.2.2 Predictions in recall mode

Once the network has been trained, it is used, in recall mode, to make predictions. We briefly present the performance of TANNs in predicting the material response for a cyclic loading path. Figure 6.21 depicts the comparison with the target material model for the material case 3D-A. The predictions for the same loading path with the material cases 3D-B and 3D-C are presented in Figures 6.22 and 6.23. In all the cases, the network shows good performance.
Similarly with the 1D case, the generalization capabilities of the network are presented together with the comparison of the thermodynamics-based network with the standard ANN approach.

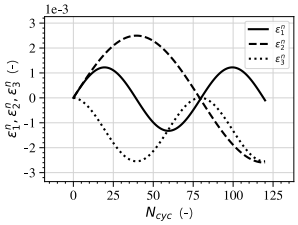

(a) loading path.

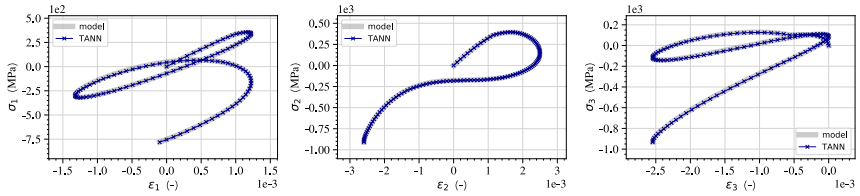

(b) σ_i prediction.

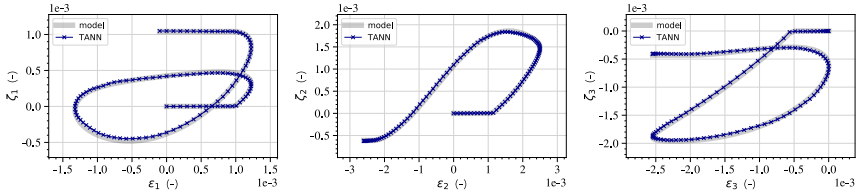

(c) ζ_i prediction.

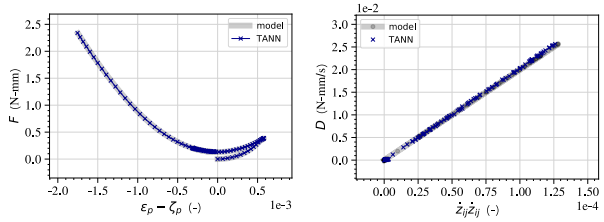

(d) energy (left) and dissipation rate (right) predictions.

Figure 6.21 – Predictions of TANN due to cyclic loading, compared with the target constitutive model, case 3D-A, perfect plasticity: loading path (6.21a), in terms of principal deformations; principal stress predictions $(\sigma_1, \sigma_2, \sigma_3)$ (6.21b); plastic deformation predictions $(\zeta_1, \zeta_2, \zeta_3)$ (6.21c); energy (F) and dissipation rate predictions (D) (6.21d).

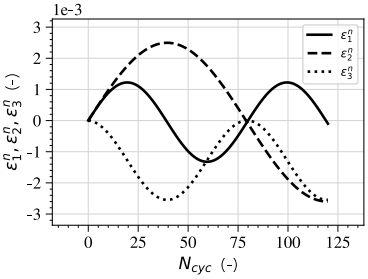

(a) loading path.

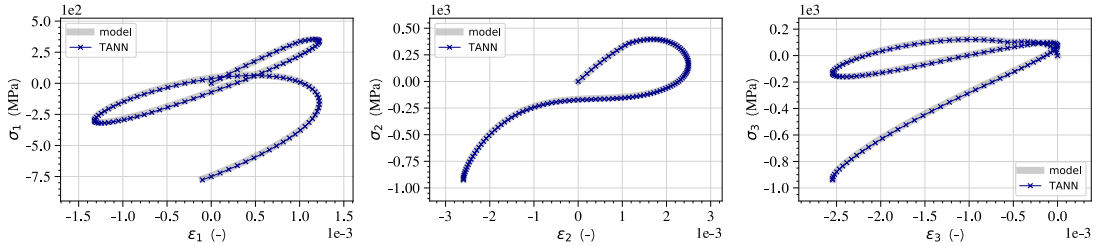

(b) σ_i prediction.

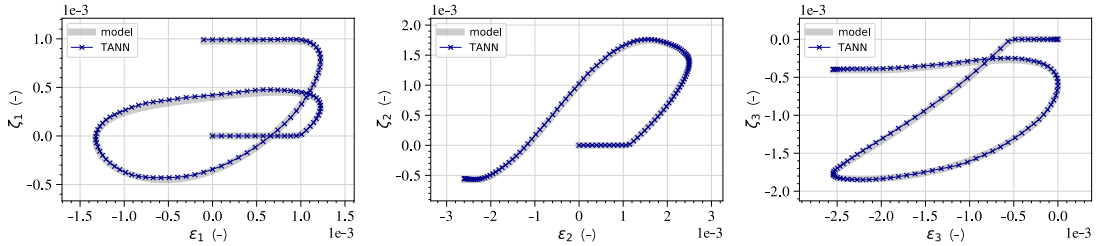

(c) ζ_i prediction.

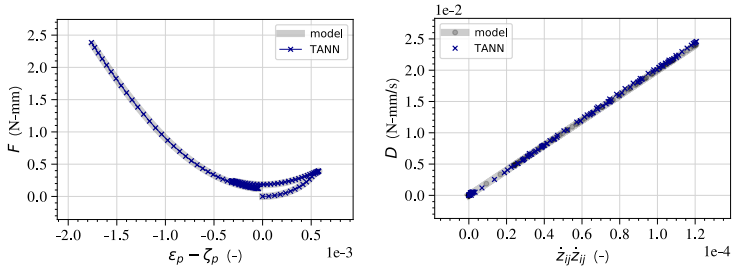

(d) energy (left) and dissipation rate (right) predictions.

Figure 6.22 – Predictions of TANN due to cyclic loading, compared with the target constitutive model, case 3D-B, hardening: (a) loading path, in terms of principal deformations; (b) principal stress predictions $(\sigma_1, \sigma_2, \sigma_3)$; (c) plastic deformation predictions $(\zeta_1, \zeta_2, \zeta_3)$; (d) energy (F) and dissipation rate predictions (D).

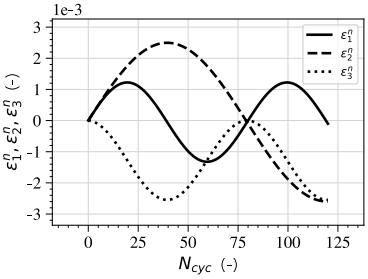

(a) loading path.

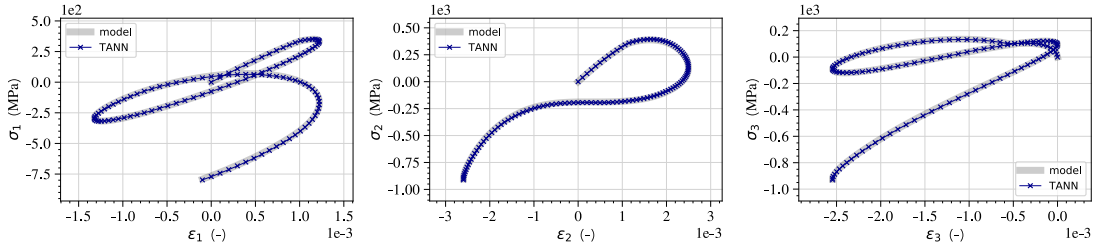

(b) σ_i prediction.

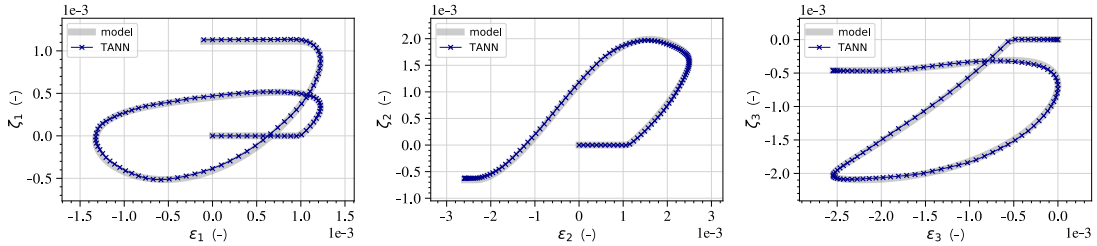

(c) ζ_i prediction.

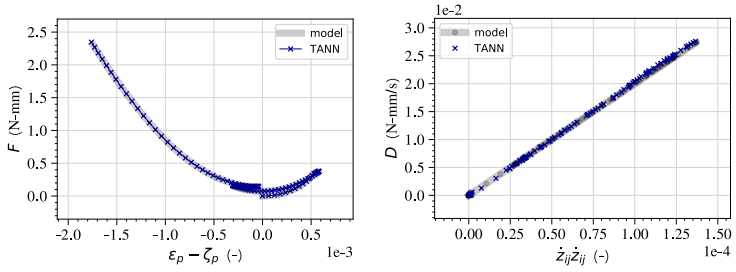

(d) energy (left) and dissipation rate (right) predictions.

Figure 6.23 – Predictions of TANN due to cyclic loading, compared with the target constitutive model, case 3D-C, softening: (a) loading path, in terms of principal deformations; (b) principal stress predictions $(\sigma_1, \sigma_2, \sigma_3)$; (c) plastic deformation predictions $(\zeta_1, \zeta_2, \zeta_3)$; (d) energy (F) and dissipation rate predictions (D).

TANN vs standard ANN. Generalization of the network

Herein we investigate the performance of TANN with respect to the classical approach of ANN (see Ghaboussi et al., 1991; Lefik and Schrefler, 2003), as well as the sensitivity with respect to the input variables range, i.e., the generalization capability. Similarly to the comparisons in paragraph 6.4.1.4, we select a network with inputs $\mathcal{I} = (\varepsilon_i^t, \Delta\varepsilon_i, \sigma_i^t, \zeta_i^t)$ and output $\mathcal{O} = (\Delta\zeta_i, \Delta\sigma_i)$, with $i = 1, 2, 3$ denoting the principal components. The architecture of the network is selected to give the best performance while assuring the same amount of degrees of freedom, hyper-parameters, of TANN. The two sub-networks, aNN_ζ and aNN_σ, has two hidden layers, with leaky ReLU activation functions, and number of neurons per layer equal to 48. As for sNN_ζ and sNN_σ, in aNN_ζ and aNN_σ three output layers (1 neuron each) are used, with linear activation functions and zero biases. In Figure 6.24 we present the comparison of the MAE of the network predictions with respect to the target values (training and validation data-sets).

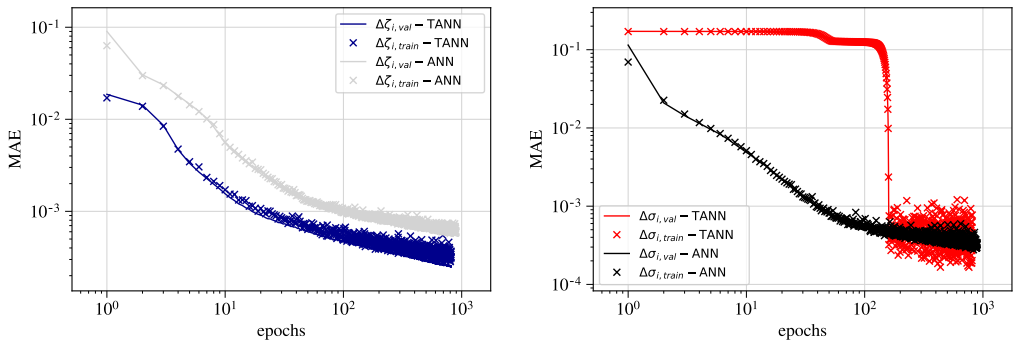

(a) mean absolute error of $\Delta\zeta$ prediction (b) mean absolute error of $\Delta\sigma_i$ prediction

Figure 6.24 – Errors of the predictions of ANN (loss function), as the training is being performed, compared to that of TANN.

We first compare the performance of both networks, TANN and standard ANN, in predicting the material response for cyclic isotropic loading paths (material case 3D-A, cf. Table 6.5). For this loading path, a linear elastic material response is expected and it is indeed retrieved. Figure 6.25 displays the stress predictions of TANN and ANN, compared with the target values, for different strain increments. It is worth mentioning that the standard approach of ANN does not succeed in accurately predicting the elastic deformation range. Moreover, contrary to TANN, the stress predictions of standard ANN, depend strongly on the cyclic loading. As the network is used recursively, in recall mode, the stress predictions rapidly become less and less precise, due to error accumulation in the standard ANN.

The performance of both networks is further compared for the following three loading

paths

$$\begin{aligned}
\text{uni-axial:} \quad & \Delta\varepsilon_1^n = \Delta\varepsilon \ \text{sgn}\left(\cos\frac{n\pi}{2N}\right), \quad \Delta\varepsilon_2^n = \Delta\varepsilon_3^n = 0; \\
\text{bi-axial:} \quad & \Delta\varepsilon_1^n = \Delta\varepsilon \ \text{sgn}\left(\cos\frac{n\pi}{2N}\right), \quad \Delta\varepsilon_2^n = -\Delta\varepsilon \ \text{sgn}\left(\cos\frac{n\pi}{4N}\right), \quad \Delta\varepsilon_3^n = 0; \\
\text{tri-axial:} \quad & \Delta\varepsilon_1^n = \Delta\varepsilon \ \text{sgn}\left(\cos\frac{n\pi}{2N}\right), \quad \Delta\varepsilon_2^n = \Delta\varepsilon_3^n = \Delta\varepsilon \ \text{sgn}\left(\sin\frac{n\pi}{2N}\right),
\end{aligned} \tag{6.35}$$

with $N = \frac{\varepsilon_{\max}}{\Delta\varepsilon}$, $\varepsilon_{\max} = 2 \times 10^{-3} \div 2$, and $\Delta\varepsilon = 10^{-4} \div 1$.

In Figures 6.26 and 6.27 the results obtained for a uni-axial loading scheme are presented, for different values of the strain increment for the material case 3D-C, softening (cf. Table 6.5). Figures 6.26a and 6.26b display the material response in terms of the principal stress, σ_1, and inelastic strain, ζ_1, over the principal strain, ε_1. Figures 6.26c and 6.26d compare the energy and dissipation rate predicted by TANN with those computed, with standard ANN, directly using the corresponding definitions for the free-energy and dissipation rate, Eq. (6.33). The predictions of TANN are in good agreement with the constitutive model, independently from the strain increment, which exceeds considerably the training range. Nevertheless, the performance of ANN is found to be strongly affected by the values of $\Delta\varepsilon$. Standard ANN performs poorly for strain increments smaller and larger than the ones at which it was trained ($\Delta\varepsilon = 1 \times 10^3$). Furthermore, standard ANN predicts again thermodynamically inconsistent outputs.
We emphasize that, even though for relatively large strain increments TANN predictions are less accurate (see e.g. Fig. 6.26d), predictions remain thermodynamically consistent. Moreover, the network successfully predicts the Jacobian, $\frac{\partial\sigma}{\partial\varepsilon}$, contrary to standard ANN. Figure 6.27 illustrates the stress predictions, but in terms of the mean and deviatoric stress (computed from the principal stress predictions).

Figures 6.28 to 6.30 present the predictions of TANN and standard ANN for the bi-axial cyclic path (Eq. (6.35)), in terms of the principal, mean, and deviatoric stresses, for the material case (c), softening (cf. Table 6.5). Similarly, Figures 6.31 to 6.34 show the predictions for the tri-axial loading path. The predictions obtained for the same loading path but for the material cases 3D-A, perfect plasticity, and 3D-B, hardening, are presented in Figures D.4-D.21, in Appendix D. As mentioned above, TANN capabilities of generalizing the predictions with respect to the values assumed by the input variables are remarkably good. Standard ANN succeeds in correctly predicting the stress increments only in a reduced range of the strain increment values, close to the range of its training data. It is worth pointing out that in the computation of the mean and deviatoric stress, from the principal stress components, TANN gives relatively high errors, but still much lower when compared with those of ANN). The performance of TANN in predicting p and q can be further improved by small modifications to include these invariants as outputs. However, this kind of optimization is unnecessary for the scope of the current investigations.

Finally, it should be stressed that the performance of TANN and standard ANN can be improved by increasing the dimension of the training data-set, the number of the hyperparameters (e.g. numbers of hidden layers, etc.). Nevertheless, the fundamental gap between the two approaches in terms of accuracy and in assuring thermodynamically consistent results is striking.

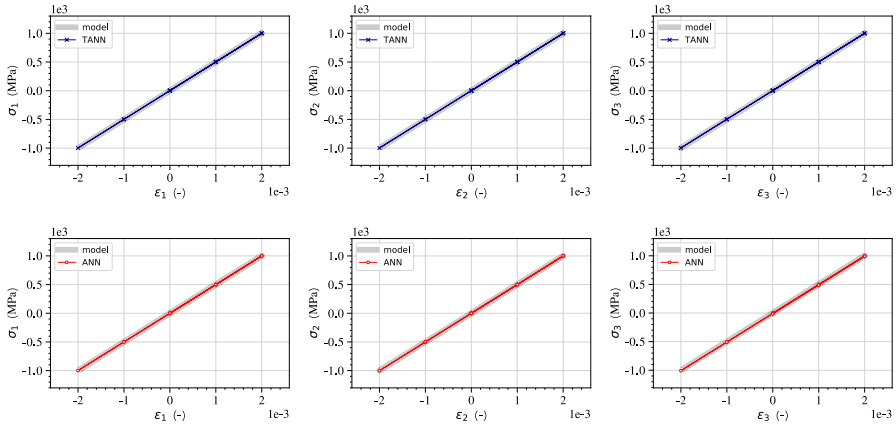

(a) strain increment $\Delta\varepsilon = 1 \times 10^{-3}$.

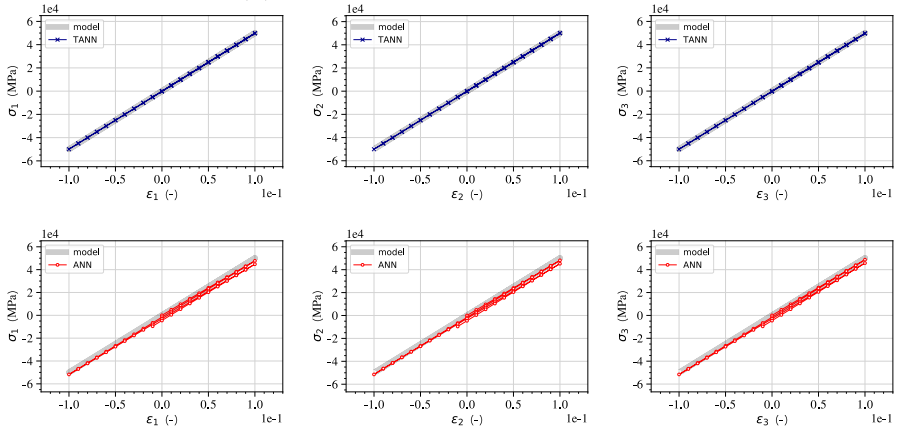

(b) strain increment $\Delta\varepsilon = 1 \times 10^{-2}$.

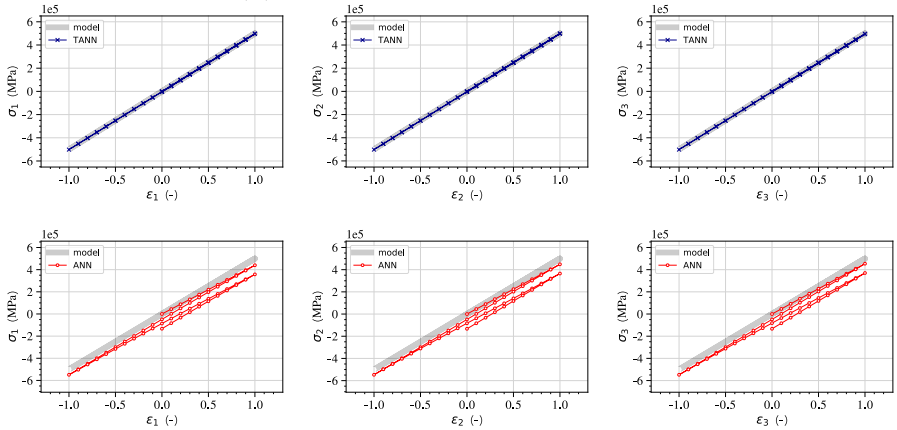

(c) strain increment $\Delta\varepsilon = 1 \times 10^{-1}$.

Figure 6.25 – Comparison of the stress predictions of TANN and standard ANN with respect to the target values, for the cyclic, isotropic loading path $\Delta\varepsilon_1^n = \Delta\varepsilon_2^n = \Delta\varepsilon_3^n = \Delta\varepsilon \text{ sgn}\left(\cos\frac{n\pi}{2N}\right)$ –with $N = \varepsilon_{\max}/\Delta\varepsilon$, $\varepsilon_{\max} = 2{\times}10^{-3}$ (a), $\varepsilon_{\max} = {\times}10^{-1}$ (b), and $\varepsilon_{\max} = 1$ (c), for material case 3D-A, perfect plasticity. Each row represents the prediction at different $\Delta\varepsilon$ increments.

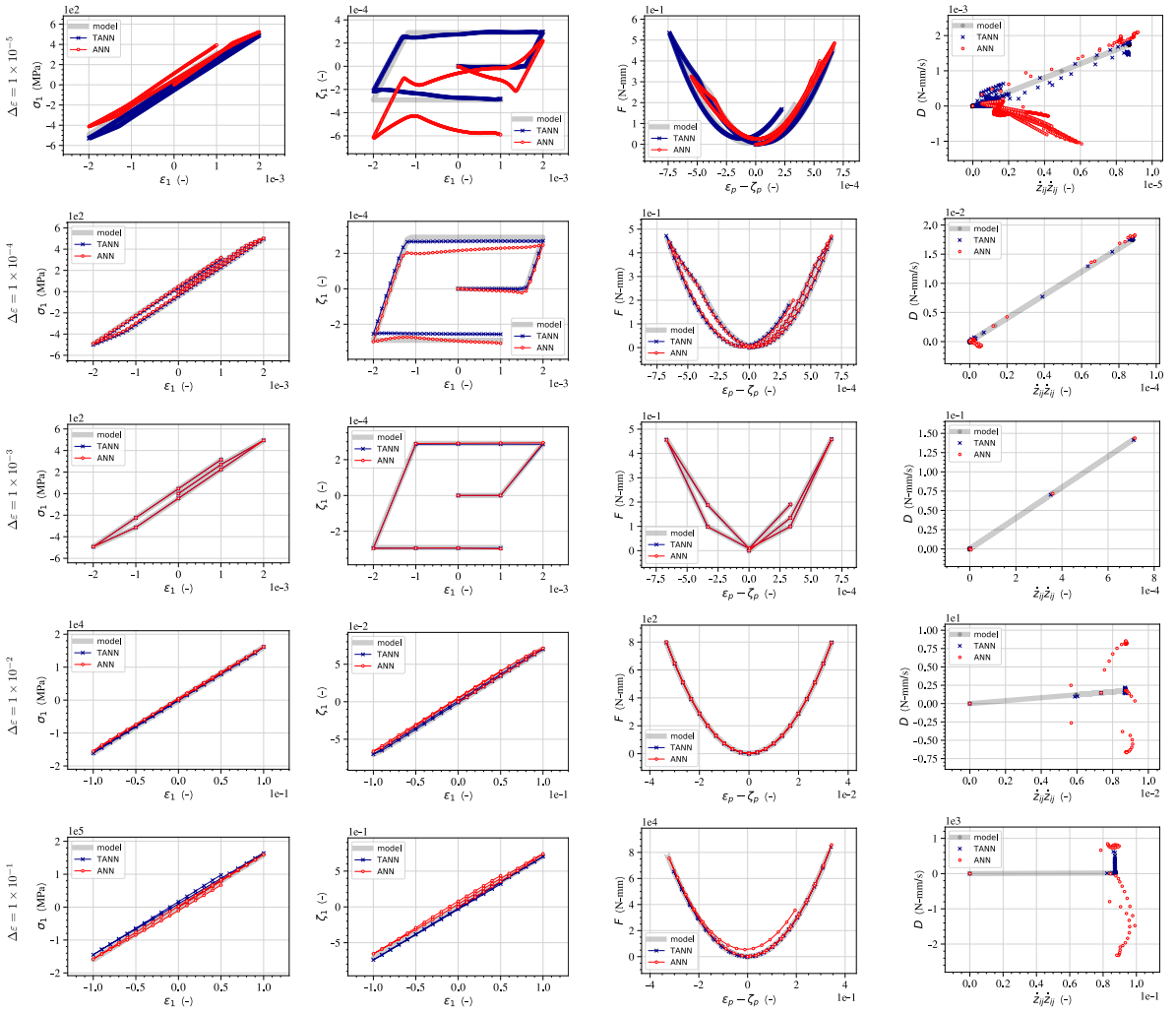

(a) σ prediction (b) ζ prediction (c) F prediction (TANN), Eq. (26) (ANN). (d) D prediction (TANN), Eq. (26) (ANN).

Figure 6.26 – Comparison of the predictions of TANN and standard ANN with respect to the target values, for the uni-axial cyclic loading path, Eq. (6.35), for material case 3D-C, softening. Each row represents the prediction at different $\Delta\varepsilon$ increments.

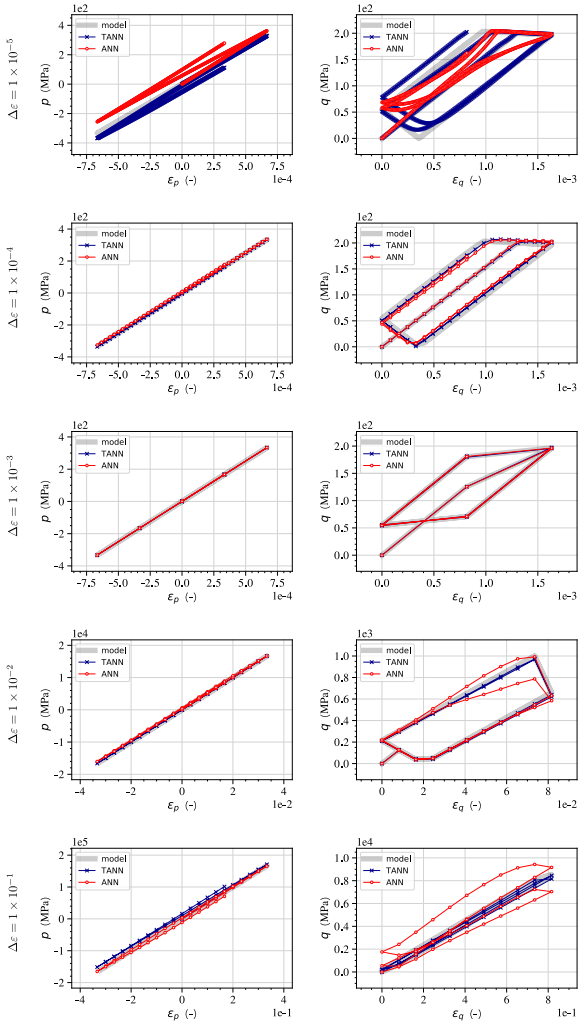

(a) p computation. (b) q computation.

Figure 6.27 – Comparison of the stress predictions of TANN and ANN in terms of mean and deviatoric stress, p (left) and q (right), for the uni-axial loading path in Figure D.13 and material case 3D-C, softening. Each row represents the prediction at different $\Delta\varepsilon$ increments.

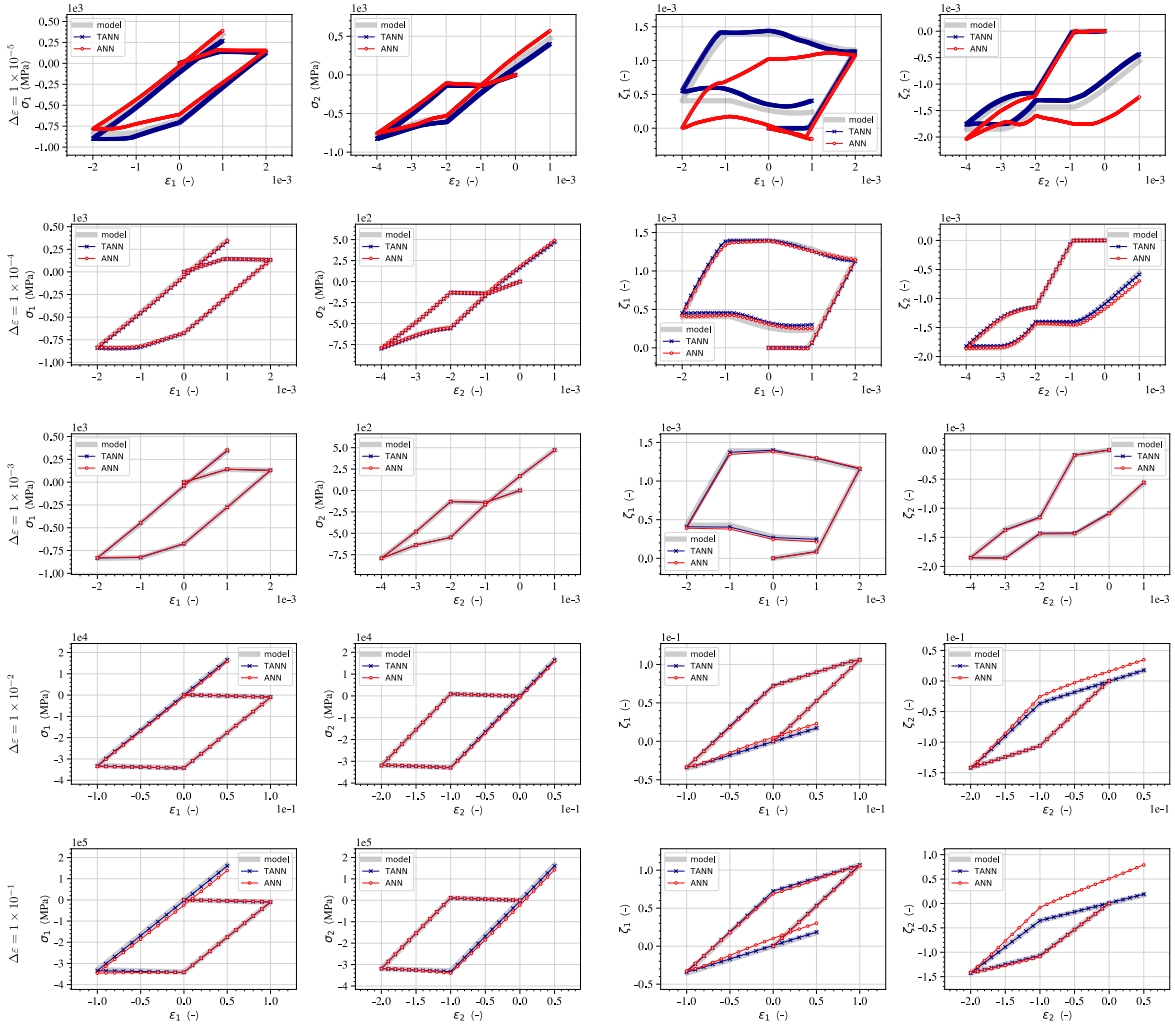

(a) σ prediction. (b) ζ prediction.

Figure 6.28 – Comparison of the stress and internal variable predictions of TANN and standard ANN with respect to the target values, for the bi-axial cyclic loading path, Eq. (6.35), for material case 3D-C, softening. Each row represents the prediction at different $\Delta\varepsilon$ increments.

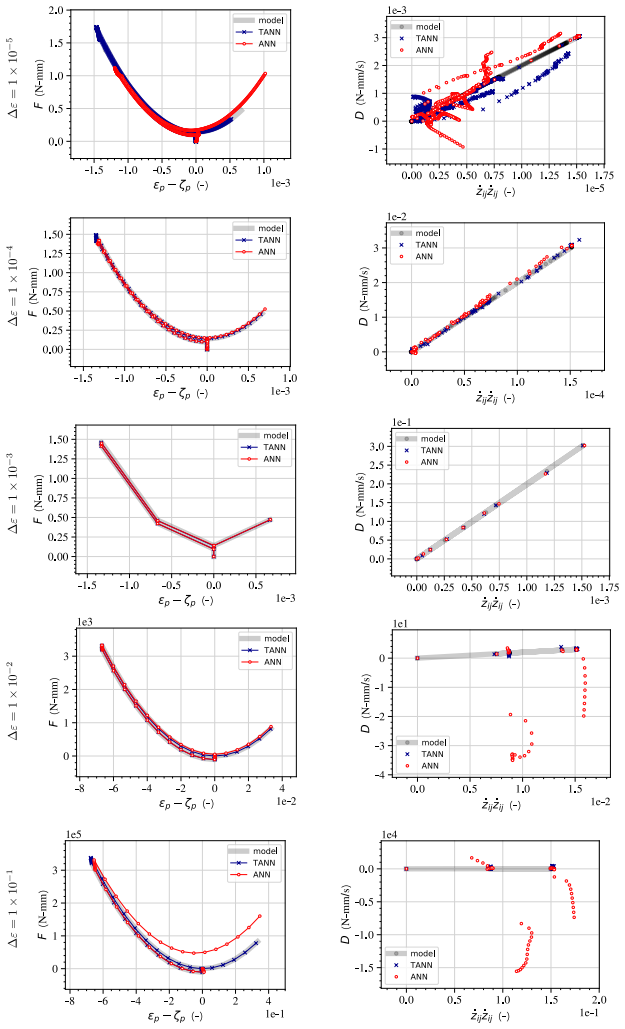

(a) F prediction (TANN), Eq. (6.33) (ANN).

(b) D prediction (TANN), Eq. (6.33) (ANN).

Figure 6.29 – Comparison of the energy and dissipation rate predictions of TANN and computation according to Eq. (6.33) for standard ANN with respect to the target values, for the bi-axial cyclic loading path, Eq. (6.35), for material case , case 3D-C, softening. Each row represents the prediction at different $\Delta\varepsilon$ increments.

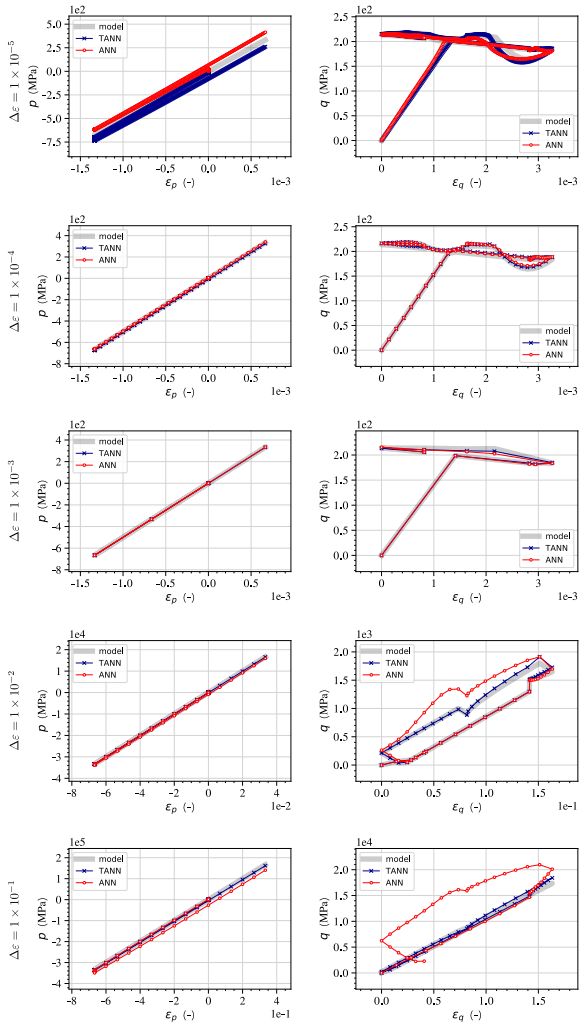

(a) p computation. (b) q computation.

Figure 6.30 – Comparison of the stress predictions of TANN and standard ANN in terms of mean and deviatoric stress, p and q, for the bi-axial loading path in Figures 6.28 and 6.29, case 3D-C, softening. Each row represents the prediction at different $\Delta\varepsilon$ increments.

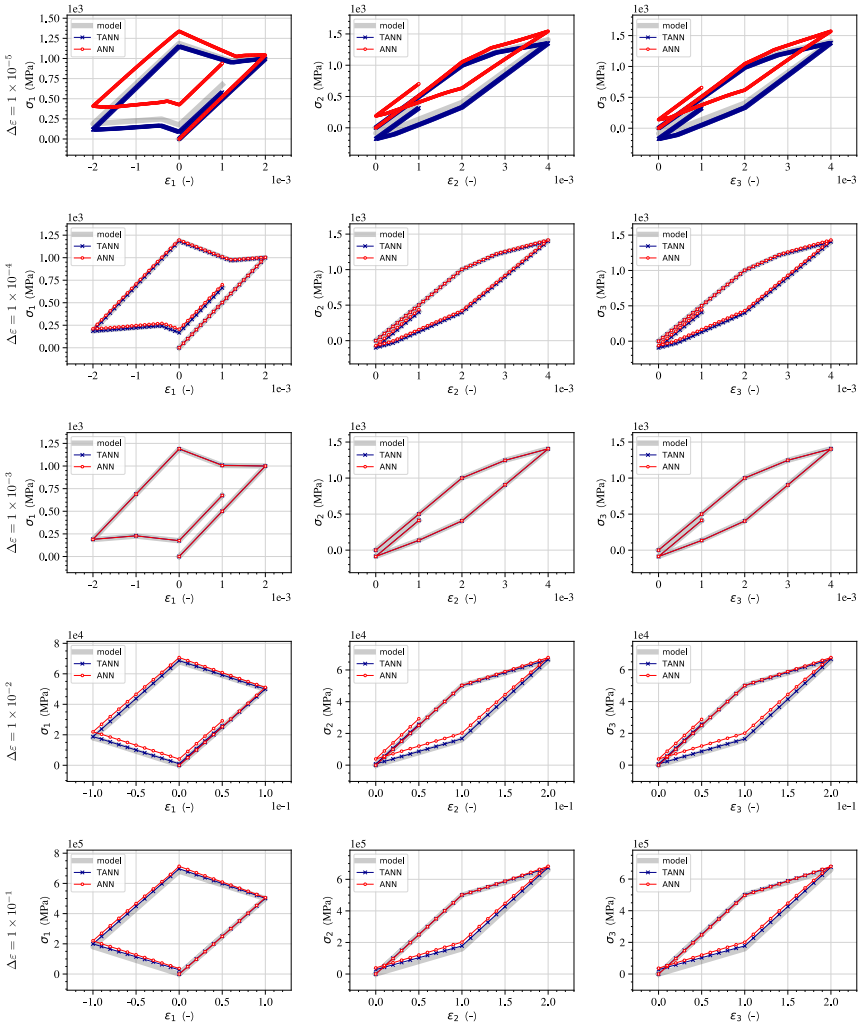

Figure 6.31 – Comparison of the stress predictions of TANN and standard ANN with respect to the target values, for the tri-axial cyclic loading path, Eq. (6.33), for material case 3D-C, softening. Each row represents the prediction at different $\Delta\varepsilon$ increments.

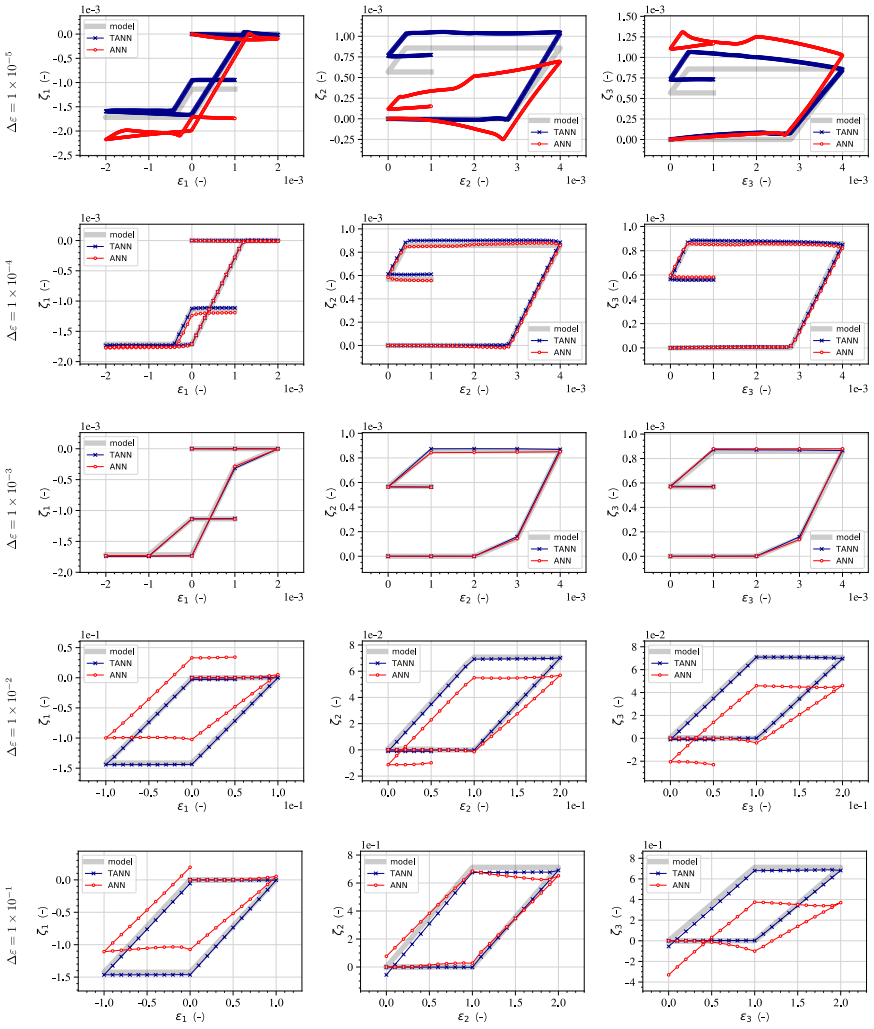

Figure 6.32 – Comparison of the internal variable predictions of TANN and standard ANN with respect to the target values, for the tri-axial cyclic loading path, Eq. (6.35), for material case 3D-C, softening. Each row represents the prediction at different $\Delta\varepsilon$ increments.

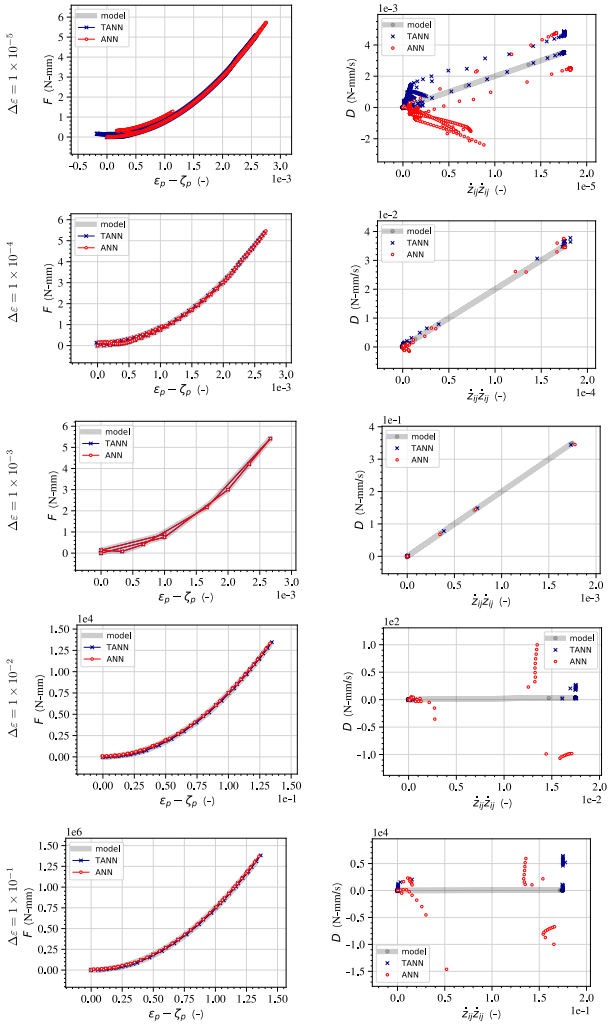

(a) F prediction (TANN), Eq. (6.33) (ANN).

(b) D prediction (TANN), Eq. (6.33) (ANN).

Figure 6.33 – Comparison of the energy and dissipation rate predictions of TANN and computation according to Eq. (6.33) for standard ANN with respect to the target values, for the tri-axial cyclic loading path, Eq. (6.35), for material case 3D-C, softening. Each row represents the prediction at different $\Delta\varepsilon$ increments.

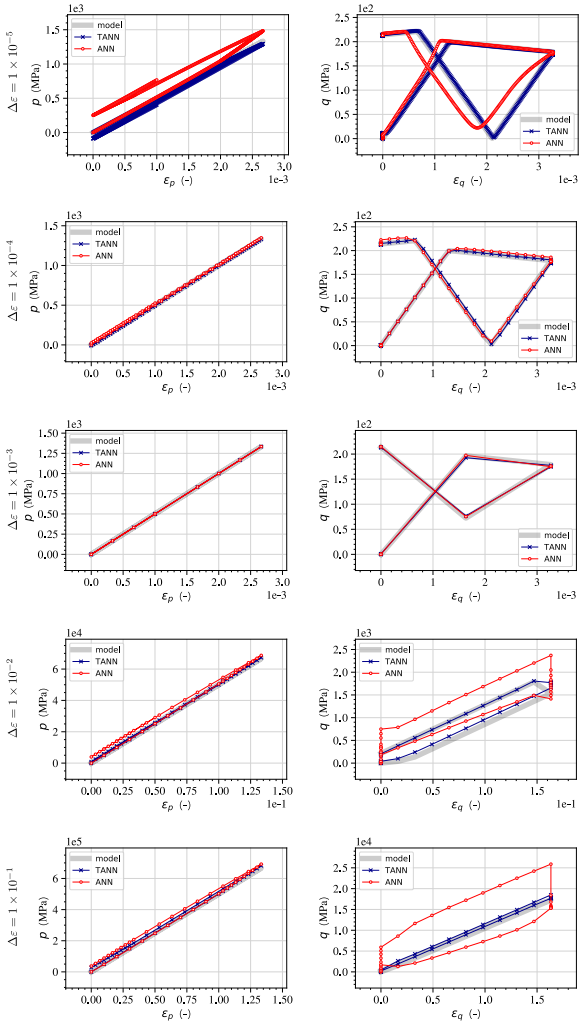

(a) p computation. (b) q computation.

Figure 6.34 – Comparison of the stress predictions of TANN and standard ANN in terms of mean and deviatoric stress, p and q, for the tri-axial loading path in Figures 6.31, 6.32, and 6.33 (softening), Eq. (6.35). Each row represents the prediction at different $\Delta\varepsilon$ increments.

6.5 Additional remarks

A new class of artificial neural networks models to replace constitutive laws and predict the material response at the material point level was proposed. The two basic laws of thermodynamics were directly encoded in the architecture of the model, which we refer to as Thermodynamics-based Neural Network (TANN). Our approach was inspired by the so-called Physics-Informed Neural Networks (PINNs) (Raissi et al., 2019), where the automatic differentiation was used to perform the numerical calculation of the derivative of a neural network with respect to its inputs.

The numerical requirements regarding the mathematical class of appropriate activation functions to be used together with automatic differentiation were investigated. More specifically, the internal restrictions, derived from the first law of thermodynamics, require activation functions whose second gradient does not vanish. This new problem and its remedy was extensively explored and discussed in this Chapter.

In TANN, the entire constitutive response of a material can be derived from definition of only two scalar functions: the free-energy and the dissipation rate, which are learned. This assures thermodynamically consistent predictions both for seen and unseen data. Contrary to the standard ANN approaches, TANN does not have to identify, through learning, the underlying thermodynamic laws. Indeed, predictions of standard ANNs are often thermodynamically inconsistent, even though the training of the network has been performed on consistent material data. Being aware of the underlying physics, TANNs are found to be a robust approach. Moreover, if the training data-sets are not thermodynamically consistent, the training operation of the network would be unsuccessful, contrary to the standard ANN approach (see Fig. D.22). This is reassuring for applications in continuum mechanics and engineering.

For the cases here investigated, we showed that TANNs are characterized by high accuracy of the predictions, higher than those of standard approaches. The integration of thermodynamic principles inside the network renders TANN's ability of generalization remarkably good (i.e., make predictions for loading paths different from those used in the training operation). Consequently, TANN promises to be an excellent candidate for replacing constitutive calculations at Finite Element incremental formulations.
In the case of masonry, we record the successful applications of standard ANNs by Plevris and Asteris (2014); Mishra et al. (2019); Friaa et al. (2020). Relying on the developments here presented for TANNs, further applications involving masonry are of significant interest. Indeed, thanks to the implementation of the free-energy in TANN predictions and its thermodynamic relation with the stresses, the jacobian $\frac{\partial \Delta\sigma}{\Delta\varepsilon}$ at the material point level is better predicted even for increments far outside the training data-set range. As a result quadratic convergence in implicit formulations can be preserved, reducing the calculation cost. More importantly, training TANNs using detailed micro-scale analyses can significantly reduce the calculation cost in solving large boundary value problems by assuring, at the same time, the thermodynamic consistency of the results. As a consequence, large-scale applications on masonry structures could be performed (see also Perspectives).

Part III

Towards experimental validation

Chapter 7

Scaling laws for masonry structures subjected to blast loads

Abstract. *The response of masonry structures to explosions can be hardly investigated relying only on numerical and analytical tools. Experimental campaigns are of paramount importance to improve the current understanding and validate existing models. Nevertheless, experimental tests are, at present, partial and limited in number, compared to tests under different dynamic conditions, such as earthquakes. The reason lies on the fact that full-scale blast experiments present many difficulties, mainly due to the nature of the loading action. Experiments in reduced-scale offer instead greater flexibility in testing. Nevertheless, appropriate scaling laws for the response of masonry structures under blast excitations are needed before performing such tests.*
In this Chapter, we derive scaling laws for the dynamic response and failure modes of masonry structures under blast loads. The proposed scaling laws assure similarity in terms of the material (elastic and/or inelastic) response and the rigid body response, which occurs after material failure. We corroborate the derived scaling laws against detailed numerical simulations accounting for combined rocking, up-lifting and sliding mechanisms. Then, the application to multi-drum stone columns is considered. In particular, we show that, whilst the presence of complex behaviors, such as wobbling (point-sliding) and impacts, similarity is assured. The developments demonstrate their applicability in the design of reduced-scale experiments of masonry structures.

Contents

7.1 Introduction

In Chapters 3, 4, and 5, we demonstrated that analytical and numerical tools are of great interest to understand the dynamic behavior of masonry structures subjected to explosions. Nevertheless, experimental testing and validation represents a major and necessary step before using these models in practice.

As we discussed in Chapter 2, experimental campaigns have focused attention, at present, only on regular geometries, such as walls. Moreover, they are quite limited. This is due to the fact that blast testing of masonry structures is particularly challenging. Furthermore, the complexity stemming from non-standard geometry structures adds non-trivial difficulties into the design of experimental tests. Some important in-situ tests of masonry exist (summarizing we refer to Gabrielsen et al., 1975; Varma et al., 1997; Abou-Zeid et al., 2011; Keys and Clubley, 2017; Gilbert et al., 2002; Li et al., 2017; Michaloudis and Gebbeken, 2019, and Chapter 2). These tests provided some information but reproducting the same conditions is highly demanding due to associated high cost, safety issues, reduced repeatability, technical complications, etc. (Draganić et al., 2018). For instance, explosive charge weights need to be as small as possible. Moreover, specialized personnel is required to built masonry and the execution of repeated, in-situ experiments is hardly possible. It is needless to mention that performing real-scale tests in proper laboratory conditions is impossible unless large investments are made. Investments of that size may exist but they are probably military with all the advantages and disadvantages regarding repeatability and falsifiability of the results.

Conversely, reduced-scale tests (e.g. Wang et al., 2012) offer many advantages, such as reduced cost, reduced hazard and risk associated to the safety of the testing environment and of the personnel. Nevertheless, the design of small-scale tests requires appropriate scaling laws in order to guarantee similarity. Similitude theory provides the conditions to design a scaled model of a prototype (full-scale structure) and to predict the structural response of the prototype from the scaled results. Similarity of the blast wave propagation and load need to be assured between the scaled model/system and the prototype. The same holds true for the specimen where scaling laws for the dynamic structural response have to be derived to assure similarity between the model and the prototype. Notice, though, that deriving adequate scaling laws for both the blast load and the structure is not trivial due to the different underlying physics.
As for it concerns blast loads, the Hopkinson-Cranz scaling law (Hopkinson, 1915; Cranz, 1925) is widely used. This scaling law assumes similarity at constant scaled distances, $Z = R/W^{1/3}$, with W the TNT equivalent explosive weight and R the stand-off distance between the charge and the target. Accordingly, the scaled distance in the model needs to be equal to the scaled distance in the prototype. As a result, the overpressure peak, originated by the explosion, remains the same in the prototype and the small-scale system. The Hopkinson-Cranz scaling law has been successfully applied in numerous applications. For more details, we refer to the work of Baker et al. (1991). Nevertheless, it is worth emphasizing that a scaling preserving the overpressure peak is disadvantageous

and inadequate for performing reduced-scale tests in a laboratory environment. Indeed, most of the benefits of reduced-scale testing with respect to full-scale testing are lost, as the intensity of the explosive load is un-scaled. As a result, the scaling laws available in the current literature are not a viable mean to design safe, laboratory tests of whole masonry structures.

The main goal of this Chapter is to provide a new set of scaling laws for masonry structures subjected to explosions and guide towards experimental testing of non-standard assets, such as those analyzed in Chapters 4 and 5.

In particular, based on developments of Chapter 3, we derive here scaling laws for masonry structures in a blast event. This is done considering both the material (elastic and inelastic) response and the rigid body response, occurring after material failure. Indeed, under the action of the impulsive loading arising from an explosion, local failure of the joints and blocks results, in most cases, in failure modes which can be described, depending on the kinematics of the failure mode, as a rigid body motion (cf. Chapter 2). Nevertheless, both the rigid body and the material responses can be scaled according to the approach here proposed.

This Chapter is structured as follows. Section 7.2 presents an overview of common blast load sources which can be used in experimental testing. Particular attention is given to methodologies whose use is more likely in reduced-scale experiments. We state the problem under investigation in Section 7.3. Then, scaling laws for the rigid body response and material response are derived in Sections 7.4 and 7.5.
With particular attention to rigid body failure mechanisms, we validate the proposed scaling laws with numerical cases of monolithic (rigid) prototypes and models and through three-dimensional Finite Element simulations, Section 7.6.
Finally, we show that the derived scaling laws hold true for deformable blocky-structures, by investigating the response of multi-drum columns−typical examples of key load-carrying elements in ancient masonry structures and monuments−in Section 7.7.
It should be mentioned that this work is a first step towards the design of reduced-scale experiments of masonry structures, providing for the the first time appropriate scaling laws assuring the similarity of both blast loading and structural dynamic response. Further investigations accounting for more detailed characterization of blast wave propagation and secondary effects as well as different masonry assets are needed.

7.2 Common blast load sources for experimental testing

Most of the blast load sources in testing can be classified into (1) TNT (or any other high-explosive such as ANFO, RDX, or C4), (2) shock tubes, (3) blast simulators, and (4) blast chambers−according to Draganić et al. (2018).

TNT. Often used in field tests, TNT and other high-explosives are undoubtedly the most effective representation of a blast source and scenario (Gabrielsen et al., 1975; Varma et al., 1997; Abou-Zeid et al., 2011; Li et al., 2017; Michaloudis and Gebbeken, 2019; Badshah et al., 2020). Nevertheless, high-explosive sources are frequently used in

full-scale tests, which are characterized by high costs and usually involve large amount of explosives.

Shock tubes. Shock tubes consist of two major sections: a driven section and an expansion section, separated by one or multiple diaphragms. The test starts by filling the driver chamber with compressed air. When the diaphragms fails due to pressure in the driver section, shock waves generate and travel down the expansion section and load the specimen, located at the end of the tube (usually in a target vessel), see Figure 7.1.
Conceiving the initial pressure and the length of the high-pressure section of the shock tube allows to load the specimen with a precise time-history.
Shock tubes can be successfully used for full- and small-scale tests. Nevertheless, only isolated structural elements can be tested with this method, such as columns, slabs and masonry walls (Lloyd et al., 2011; Keys and Clubley, 2017; Schneider et al., 2020). The reason is that the loading is rather directional then (hemi-)spherical.

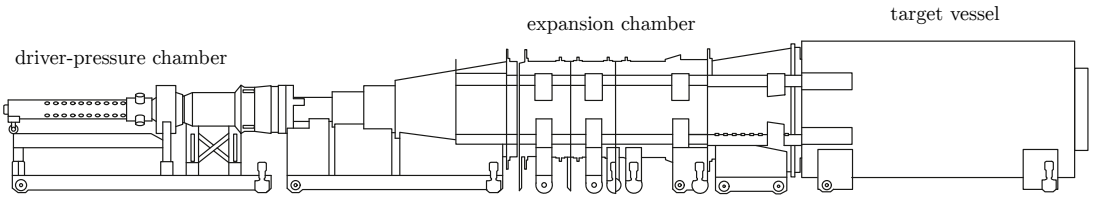

Figure 7.1 – Schematic representation of a shock tube, from (Draganić et al., 2018).

Acoustic systems. Acoustic systems, with appropriate amplification, can be used, in principle, to recreate blast loading. This alternative has been investigated in a previous work Aboagye (2020) (co-supervised by the author). Nevertheless, even in reduced-scale experiments, high values of sound amplitude are required, which can reach 200 dB. For existing speakers and amplifiers, available in the market, such values are impossible to reach. Nevertheless, recent technological developments (see e.g. Mackenzie, 1997; François, 2020) may allow in the future such high levels of sound amplitudes and, hence, be used to recreate blast loading.

Blast simulators. Blast simulators are apparatus able to provide blast-like loading conditions on structures in a controlled laboratory environment. Among others, we refer to the hydraulic blast simulator at the University of California, (Stewart et al., 2014), and the underwater blast wave generator (Pereira et al., 2015), see Figure 7.2.
The hydraulic blast simulator (Stewart et al., 2014) is a hydraulically driven, computer-controlled impulse generator, designed to produce an impulse by impacting the specimen with a mass in a controlled manner. The simulator is able to reproduce quantitative and qualitative blast loading and ensures repeatability of experiments eliminating blast wave and fireball interference with measuring instruments.
The underwater blast wave generator (Pereira et al., 2015) consists of water containers, in which an explosive charge is detonated. After the detonation, the detonation products expand generating shock waves in water. The specimen is attached to the water containers and thus experiences an equivalent impulsive loading. The underwater blast wave generator

allows further to avoid generation of high velocity fragments.
Nevertheless, as for the above-mentioned testing procedure, blast simulators can only used to investigate the response of single structural elements (and not structures/buildings).

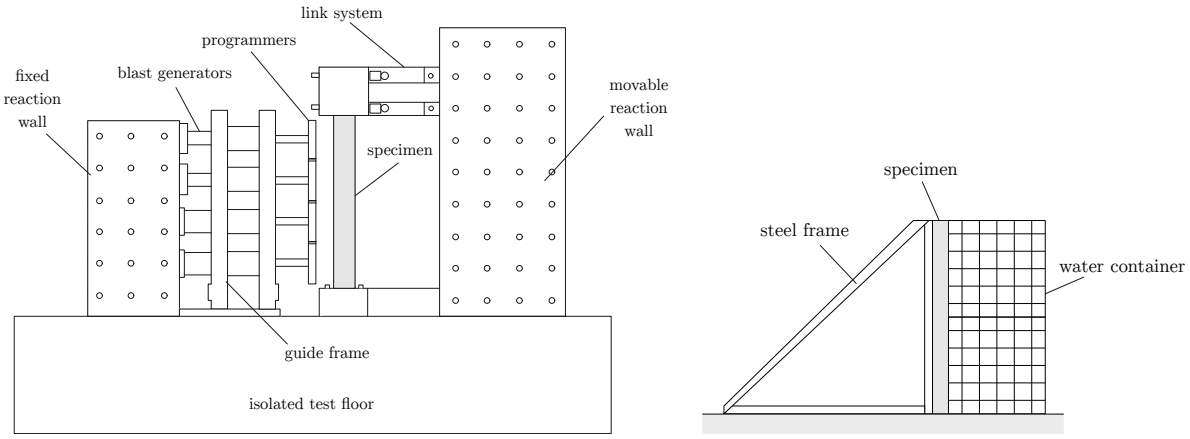

(a) hydraulic blast simulator, from (Stewart et al., 2014).

(b) underwater blast wave generator, from (Pereira et al., 2015).

Figure 7.2 – Schematic representation of blast simulators.

Blast chambers. Blast chambers are structures used to fully or partially contain the effects of high explosions (Snyman et al., 2016). The chamber, of compact size (centimetric size), with spherical, cylindrical, or rectangular shape, is designed to withstand the load arising from the internal detonation of a certain amount of explosive weight. Blast chambers are mainly used to investigate blast waves phenomena (Zyskowski et al., 2004; Sauvan et al., 2012; Gault et al., 2020), such as multiple reflections and confinement effects, and the response of structural elements, usually in reduced scale (Wu et al., 2007).
Blast chambers offer the possibility of testing both full- and small-scale structures. In particular, differently from the above techniques, the set-up of blast chambers is extremely advantageous to design scaled tests of entire buildings, and not only of few structural elements. Of course, this can be accomplished only if appropriate scaling laws for the blast loading and the dynamic response of the target are used−which is not the case for masonry structures, at present.
In the case of small-scale experiments, several ways exist to recreate realistic blast loading. The use of small solid explosive charges, in a reduced-scale environment, may not be the best choice due to undesired secondary effects, which can affect the repeatability of the experimental test (for more, we refer to Kim et al., 2008). A better alternative is the compressed balloon analogue, first introduced by the seminal work of Brode (1955). The idea of the balloon method is to use a region (balloon) with compressed gas. Boyer (1960) performed scaling experiments based on glass spheres, with a diameter of 5 cm, filled with either air or helium, at an initial pressure of around 2 MPa. The recent experimental work of Courtiaud et al. (2019) investigated the after-burning (secondary combustion) phenomenon using glass sphere filled with compressed air, in reduced scale, see Figure

7.3. Further developments using latex balloons were conducted by Skinner et al. (2020), with the design of the so-called Hydrogen Unconfined Combustion Test Apparatus. The balloons are ignited with an electric spark, located at the center.
Alternatively, the work of Zyskowski et al. (2004) suggests that equivalent blast loading can be recreated by the ignition, through an electric discharge, of an explosive gaseous (hydrogen and oxygen) mixture, confined in a hemispherical soap bubble.

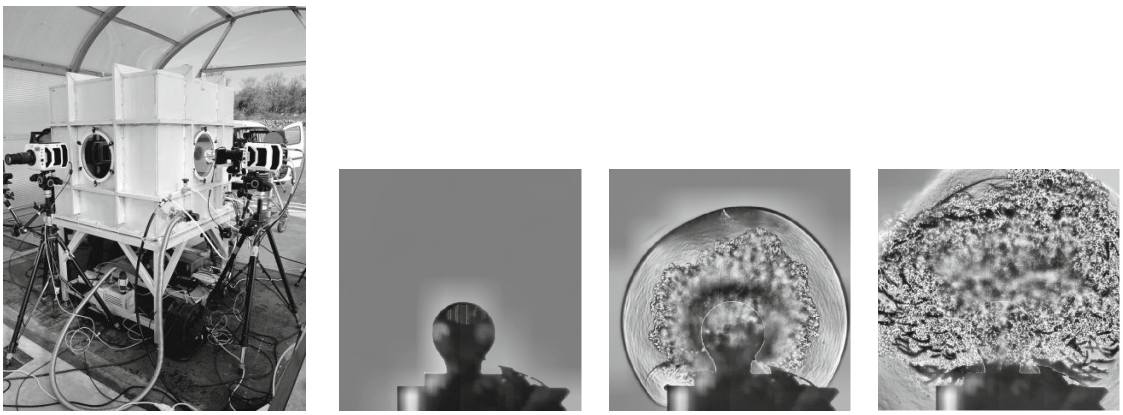

(a) Blast chamber and high-speed cameras instrumentation.

(b) schlieren image of the pressurized glass sphere.

(c) schlieren image of the primary shock wave.

(d) schlieren image of the secondary shock wave.

Figure 7.3 – Experimental set-up (a) and schlieren images of the test (b-d), from (Courtiaud et al., 2019).

Considering the advantages and disadvantages of the above methods, adequate scaling laws will determine the most appropriate strategy to be used for a given reduced-scale experiment.

7.3 Problem statement

Let us consider a masonry structure, of arbitrary shape, composed of masonry units, interacting one with the other through interfaces. The structure is subjected to the load of an explosion and undergoes a combination of material (elastic and/or inelastic) deformations and, after the material failure, depending on the kinematics of the failure mode, rigid body motion, see Figure 7.4. We further assume a strain-rate independent constitutive material response. The loading force is characterized by its maximum specific thrust $\mathcal{P}$ and the maximum specific impulse $\mathcal{I}$. For targets small enough to assume that the blast wave acts simultaneously and uniformly on the impinged surfaces, the maximum specific thrust and impulse can be computed as the overpressure peak and impulse of an equivalent blast load, acting on the centroid of the structure. Following the developments in Masi et al. (2019a) and Chapter 3, we shall consider only the pressure load applied on the front surface S (incident surface, Figure 7.4) of the target. We further assume that the blast wave impinges all points of S at the same time (simultaneously) and with the same magnitude (uniformly). The limitations of these assumptions are discussed in Section 7.7 and in Appendix E. Moreover, we account only for the positive phase of the

blast load. The negative phase is expected to have a stabilizing effect. Therefore, it can be neglected to have safe estimates of the system response, as shown in Masi et al. (2019a).

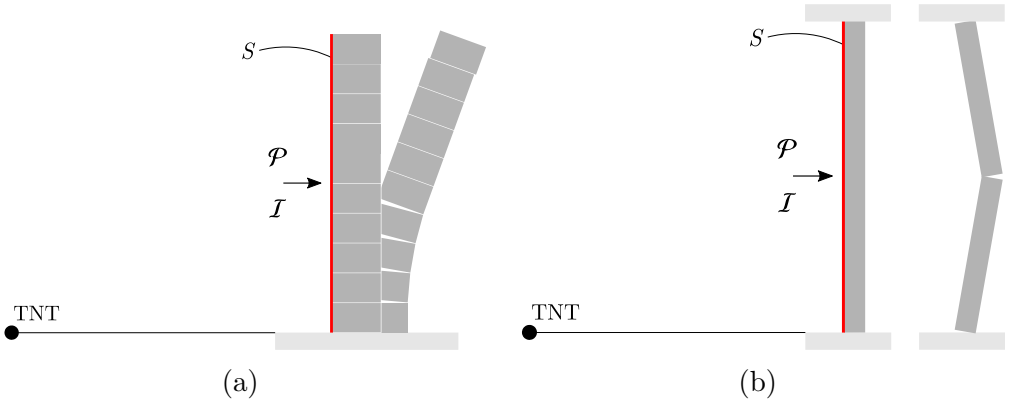

Figure 7.4 – Representative scheme of the problem, e.g. a multidrum column (a) or a one-way spanning wall (b) under blast loading.

We denote the geometry of the structure by (i) a characteristic length l (e.g., the height of the structure in Figure 7.4), (ii) dimensionless length ratios l_i, which relate all other length to the characteristic one, and (iii) generalized angles α_i. The structure is further characterized by mass m, mass moment of inertia J about some specific axis, and non-dimensional mass moments of inertia ratios J_i, which relate all other components of the rotational inertia tensor to the characteristic mass moment of inertia. We denote the gravitational acceleration with g and the friction coefficient at the interface (with the base) with $\mu = \tan\varphi$, where φ is the angle of friction. Coulomb friction is adopted. The material has density ρ. Material strain and stress are denoted with ε_j and σ_j, where $j = 1, 2, 3$ denotes a certain material principal axis. We further introduce the material stiffness parameters [1], along axis j, denoted with $C_j = \partial\sigma_j/\partial\varepsilon_j$. In the case of an elastic material, C_j represent the material elastic constants. For each block constituing the structure, we identify the sliding distance, x, the linear velocity and acceleration, $\dot{x}$ and $\ddot{x}$, the rocking angle, θ, and the angular velocity and acceleration, $\dot{\theta}$ and $\ddot{\theta}$ of the blocks.

From the π Theorem (Bertrand, 1878) and following Baker et al. (1991), we identify the following terms for the material response:

$$\pi_{a,01} = \varepsilon_j, \quad \pi_{a,02} = l_i, \quad \pi_{a,03} = \alpha_i \tag{7.1a}$$

$$\pi_{a,11} = \frac{C_j}{\sigma_j}, \tag{7.1b}$$

$$\pi_{a,21} = \frac{\mathcal{P}}{C_j}, \quad \pi_{a,22} = \frac{\mathcal{I}}{l\sqrt{\rho C_j}}, \tag{7.1c}$$

1. Notice that C_j correspond to the elements lying on the diagonal of the Jacobian matrix.

Terms $\pi_{a,01} - \pi_{a,03}$ represent the geometric similarity and term $\pi_{a,11}$ assures constitutive similarity. The last two terms, $\pi_{a,21}$ and $\pi_{a,22}$, correspond to the loading similarity.

After material failure, we assume a rigid body response of the blocks and an additional set of π terms is identified:

$$\pi_{b,01} = J_i, \quad \pi_{b,02} = \frac{x}{l}, \quad \pi_{b,03} = \theta, \tag{7.2a}$$

$$\pi_{b,11} = \ddot{\theta}\frac{l}{g}, \quad \pi_{b,12} = \dot{\theta}\sqrt{\frac{l}{g}}, \tag{7.2b}$$

$$\pi_{b,13} = \frac{\ddot{x}}{g}, \quad \pi_{b,14} = \frac{\dot{x}}{\sqrt{lg}}, \tag{7.2c}$$

$$\pi_{b,15} = t\sqrt{\frac{g}{L}}, \tag{7.2d}$$

$$\pi_{b,21} = \mu, \quad \pi_{b,22} = \frac{J}{ml^2}, \tag{7.2e}$$

$$\pi_{b,23} = \frac{\mathcal{P}l^2}{mg}, \quad \pi_{b,24} = \frac{\mathcal{I}}{m}\sqrt{\frac{l^3}{g}} \tag{7.2f}$$

Terms $\pi_{b,01} - \pi_{b,03}$, together with $\pi_{a,02}$ and $\pi_{a,03}$, represent the geometric similarity and terms $\pi_{b,11} - \pi_{b,15}$ identify the kinematic similarity, i.e., the response of the system in terms of linear and angular displacements, velocities, and accelerations. The remaining four terms $\pi_{b,21} - \pi_{b,24}$ determine the dynamic similarity in terms of rigid body motion. For further details, we refer to (Baker et al., 1991).

By imposing the equivalence of the above π terms, one can investigate and predict the response of a full-scale system (namely, a prototype) by studying the response of a reduced scale system (i.e., a model), satisfying the similarity statements of the material response and rigid body motion.

Let us suppose that both prototype and model consist of blocks with a uniformly distributed mass, $\tilde{m}$ and m, respectively. The geometric scaling performed on the model is determined by the ratio of the characteristic lengths of the two systems, i.e.,

$$\lambda = \frac{\tilde{l}}{l},$$

with superscript $\sim$ denoting model's quantities. We further consider the ratio of the model to prototype material constants as

$$\mathsf{k}_j = \frac{\tilde{C}_j}{C_j}.$$

In the following, we shall assume that the ratios of material stiffness parameters are equal along any principal direction—that is, $\mathsf{k}_j = \mathsf{k}$. Further consider that both prototype and

model are subjected to the gravitational fields g and $\tilde{g}$, respectively; we quantity their ratio through the gravitational scale factor,

$$\varsigma = \frac{\tilde{g}}{g}.$$

The density scale factor is identified by

$$\gamma = \frac{\tilde{\rho}}{\rho}.$$

The friction coefficients are assumed to be equal in both systems−that is, $\lambda_\mu = \tilde{\mu}/\mu = 1$. Notice that this assumption is made to simplify the following developments, but it is not stricly necessary.

Following the similarity statements determined by the π terms, we can determine how, derived quantities are scaled in the model, upon the definition of the scaling factors λ, ς, and γ. The scaling factor of a quantity 'f' is identified as $\lambda_f = \tilde{f}/f$. The scaling laws for the material response require that

$$\frac{\tilde{\varepsilon}_j}{\varepsilon_j} = \frac{\tilde{l}_i}{l_i} = \frac{\tilde{\alpha}_i}{\alpha_i} = 1 \tag{7.3a}$$

$$\lambda_{\sigma_j} = \mathsf{k} \tag{7.3b}$$

$$\lambda_{\mathcal{P}} = \mathsf{k}, \quad \lambda_{\mathcal{I}} = \lambda\sqrt{\gamma\mathsf{k}}. \tag{7.3c}$$

The scaling laws for the rigid body motion additionally require that

$$\frac{\tilde{J}_i}{J_i} = 1 \tag{7.4a}$$

$$\lambda_x = \lambda, \quad \lambda_\theta = 1, \tag{7.4b}$$

$$\lambda_{\ddot{\theta}} = \frac{\varsigma}{\lambda}, \quad \lambda_{\dot{\theta}} = \sqrt{\frac{\varsigma}{\lambda}}, \tag{7.4c}$$

$$\lambda_{\ddot{x}} = \varsigma, \quad \lambda_{\dot{x}} = \sqrt{\varsigma\lambda}, \tag{7.4d}$$

$$\lambda_t = \sqrt{\varsigma\lambda}, \tag{7.4e}$$

$$\lambda_\mu = 1, \quad \lambda_J = \gamma\lambda^5, \tag{7.4f}$$

$$\lambda_{\mathcal{P}} = \gamma\varsigma\lambda, \quad \lambda_{\mathcal{I}} = \gamma\sqrt{\varsigma\lambda^3}. \tag{7.4g}$$

We observe that if similarity of the material response and of rigid body motion hold simultaneously, then the material constants ratio, k, needs to be such that $\mathsf{k} = \gamma\varsigma\lambda$. This means that the scaling laws for the material response can be directly identified from the scaling laws used for the rigid body response, by providing that the above-mentioned relation holds. This is why, as it follows, we will first focus on the rigid body motion

similarity.

Nevertheless, we emphasize that, if a geometric scaling is imposed, only two parameters, $\lambda_{\mathcal{P}}$ and $\lambda_{\mathcal{I}}$, need to specified (see also Baker et al., 1991). The independent scaling factors are three, i.e., λ, ς, and γ, but only two equations ($\lambda_{\mathcal{P}} = \gamma\varsigma\lambda$ and $\lambda_{\mathcal{I}} = \gamma\sqrt{\varsigma\lambda^3}$) need to be satisfied in defining the model [2]. The system is thus over-determined, as the three scaling factors cannot independently satisfy the expression of $\lambda_{\mathcal{P}}$ and $\lambda_{\mathcal{I}}$.

7.4 Scaling laws for the rigid body motion

We consider the rigid body response of masonry structure, after material failure. We assume that both the model and the prototype share the same gravitational field, so that $\varsigma = 1$. Two parameters have to be selected: the geometric scaling, λ, and the density scaling factor, γ.
As detailed in Section 1.4, both the duration time, the pressure peaks, and the impulse are functions of the stand-off distance, R, and the explosive quantity, W. In particular, $P_{ro} = \hat{P}_{ro}(Z)$ is function of the scaled distance, Z, while t_o and i_{ro} are functions of both Z and W, i.e., $t_o = W^{1/3}\hat{t}_{ow}(Z)$ and $i_{ro} = W^{1/3}\hat{i}_{row}(Z)$. The above functions are presented in Appendix A.
By definition of the scaled distance $Z = R/W^{1/3}$, the explosive quantity scaling factor reads $\lambda_W = (\lambda/\lambda_Z)^3$. The scaling factors for i_{ro}, t_o, and P_{ro} are hence:

$$\lambda_{i_{ro}} = \frac{\hat{i}_{row}(\bar{Z})}{\hat{i}_{row}(Z)}\lambda_w^{\frac{1}{3}}, \tag{7.5a}$$

$$\lambda_{t_o} = \frac{\hat{t}_{ow}(\bar{Z})}{\hat{t}_{ow}(Z)}\lambda_w^{\frac{1}{3}}, \tag{7.5b}$$

$$\lambda_{P_{ro}} = \frac{\hat{P}_{ro}(\bar{Z})}{\hat{P}_{ro}(Z)}. \tag{7.5c}$$

The selection of λ_Z—that is, λ_W, as the geometric scaling for the stand-off distance is imposed to be equal to λ—needs to be such that the following identities are verified

$$\lambda_{i_{ro}} = \lambda_{\mathcal{I}} = \gamma\sqrt{\lambda^3}, \tag{7.6a}$$

$$\lambda_{t_o} = \lambda_t = \sqrt{\lambda}, \tag{7.6b}$$

$$\lambda_{P_{ro}} = \lambda_{\mathcal{P}} = \gamma\lambda. \tag{7.6c}$$

It can be proven that no possible solution exists for λ_Z such that all the similarity statements are verified simultaneously (see Baker et al., 1991). Nevertheless, the system can be relaxed if one considers that the blast load is fast enough, compared to the characteristic time of the structure. In this case the blast load is considered as an impulsive load. This approximation is usually true in a wide range of applications, nevertheless it requires to be a posteriori verified.

For impulsive loads, $\pi_{b,23}$ vanishes and any difference between λ_{t_o} and λ_t is negligible as the time-history of the load is no more a main parameter (impulsive loading hypothesis).

2. Or equivalently: $\lambda_{\mathcal{P}} = \mathsf{k}$ and $\lambda_{\mathcal{I}} = \lambda\sqrt{\gamma\mathsf{k}}$.

Therefore, from the three initial equations, only one needs to be verified−that is, $\lambda_{i_{ro}} = \lambda_{\mathcal{I}}$. Due to the high non-linearity of the function $i_{row}(Z)$, an analytical solution does not exists. The scaling factor for the scaled distance can be found by solving the following non-linear equation [3]:

$$\text{find } \lambda_Z \text{ such that} \qquad \frac{1}{\lambda_Z}\frac{\hat{i}_{row}(Z\lambda_Z)}{\hat{i}_{row}(Z)} = \gamma\sqrt{\lambda^5}. \tag{7.7}$$

The above equation is non-linear due to the form of the function $\hat{i}_{row}(Z)$, see Appendix A. It is worth mentioning that there exists a particular case of scaling laws for which $\lambda_Z = \hat{Z}/Z = 1$. This is the Hopkinson-Cranz similarity law (Hopkinson, 1915; Cranz, 1925). In this case, the scaling factor for the explosive quantity is $\lambda_W = \lambda^3$. Nevertheless, differently from the proposed scaling, the Hopkinson-Cranz similarity law prescribes the density scaling factor: $\gamma = 1/\sqrt{\lambda}$.
The general scaling law, Eq. (7.7), does not have restrictions neither on the geometric scaling, λ, nor on the density (or mass) scaling, γ. For the particular (Hopkinson-Cranz) case, the mass of the model, instead, is directly identified as $\tilde{m} = m\lambda^{5/2}$. In order to obtain such values, either the model material should have much higher density than that of the prototype material or masses should be added for assuring the proper equivalent density, by respecting the mass moment inertia similarity. Nevertheless, in this second scenario, the scaled distance in the model would equal the scaled distance in the prototype, which means that in both systems the pressure P_{ro} would have to be the same. This usually represents a disadvantageous scaling, as one of the main objectives of conducting in-scale experimental tests is the reduction of the intensity of the explosive load.
The proposed scaling laws and the case of Hopkinson-Cranz similarity are schematized in Table 7.1 and 7.2, respectively.

Table 7.1 – Relations for model and prototype variables, for general case.

Variable	Scaling factor	Variable	Scaling factor	Variable	Scaling factor
Length, l	λ	Angle, θ	1	Mass, m	$\gamma\lambda^3$
Material density, ρ	γ	Angular velocity, $\dot{\theta}$	$\lambda^{-1/2}$	Mass moment of inertia, J	$\gamma\lambda^5$
Linear displacement, x	λ	Angular acceleration, $\ddot{\theta}$	1	Blast impulse	$\gamma\lambda^{3/2}$
Linear velocity, $\dot{x}$	$\lambda^{1/2}$	Time, t	$\lambda^{1/2}$	TNT equivalent, W	see Eq. (7.7)
Linear acceleration, $\ddot{x}$	λ^{-1}				

7.5 Scaling laws for the material response

In Section 7.3, we have seen that in order to assure similarity of both the material response and the rigid body response, after material failure, the value of material constant

3. Or equivalently, in terms of λ_W:

$$\text{find } \lambda_W \text{ such that} \qquad \lambda_W^{1/3}\frac{\hat{i}_{row}\left(\frac{\lambda R}{\lambda_W^{1/3}W^{1/3}}\right)}{\hat{i}_{row}\left(\frac{R}{W^{1/3}}\right)} = \gamma\sqrt{\lambda^7}.$$

Table 7.2 – Relations for model and prototype variables, respecting Hopkinson-Cranz similarity.

Variable	Scaling factor	Variable	Scaling factor	Variable	Scaling factor
Length, l	λ	Angle, θ	1	Mass, m	$\lambda^{5/2}$
Material density, ρ	$\lambda^{-1/2}$	Angular velocity, $\dot{\theta}$	$\lambda^{-1/2}$	Mass moment of inertia, J	$\lambda^{9/2}$
Linear displacement, x	λ	Angular acceleration, $\ddot{\theta}$	1	Blast impulse	λ
Linear velocity, $\dot{x}$	$\lambda^{1/2}$	Time, t	$\lambda^{1/2}$	TNT equivalent, W	λ^3
Linear acceleration, $\ddot{x}$	λ^{-1}				

ratio, k, is prescribed by the value of the geometric, density, and gravitational scaling factors. Following the aforementioned developments, i.e., considering the blast load as an impulsive load, the term $\pi_{a,21}$ vanishes. So that, for model and prototype sharing the same gravitational field (i.e., $\varsigma = 1$), the only condition to be met, in order to assure the scaling of the material response, is:

$$\lambda_{i_{ro}} = \lambda_{\mathcal{I}} = \lambda\sqrt{\gamma\mathsf{k}}. \tag{7.8}$$

By selecting $\mathsf{k} = \gamma\lambda$, we retrieve the same scaling law found for the rigid body response. From the scaling relations identified in Table 7.1, we have additionally that principal stresses σ_j and material constants C_j are scaled by $\gamma\lambda$.

7.6 Validation of the scaling laws for the rigid body motion

In the case of masonry structures subjected to explosive loads, the material deformations are, in most of the cases, limited respect with rigid body mechanisms (sliding, opening, etc.) that may appear after material failure and depending on the kinematics of the failure mode (see Chapter 2). For this reason, we investigate only the validity of the scaling laws for masonry structures displaying rigid body motion, after material failure. First, we compare the prototype and model responses obtained by numerical integration of the non-linear equations of rocking motion (see Chapter 3), paragraph 7.6.1. Then, the validation is performed relying on three-dimensional Finite Element (FE) simulations, paragraph 7.6.2. Only the blast positive phase is considered (safety side) and the first-order approximation (see paragraph 1.5.1.3), of the Friedlander equation is used.

The target consists of a rectangular (rigid) block with uniformly distributed mass m. The dimensions of the block are $2b \times 2h \times 2w$ and the radial distance from the rocking pivot point O from the center of gravity is $r = h/\cos\alpha$, with α being the slenderness angle. As presented in Chapter 3, the equations of motion for a rocking response mechanism are

$$\mathscr{J}_o\ddot{\theta} + mgr\sin\left[\alpha\ \mathrm{sgn}\left(\theta\right) - \theta\right] = SrP_r(t)\cos\left[\alpha\ \mathrm{sgn}\left(\theta\right) - \theta\right], \tag{7.9}$$

where $\mathscr{J}_o = \frac{4}{3}mr^2$ is the moment of inertia with respect to the pivot point, and $\theta = \theta(t)$ is the inclination angle.
In order to validate the general scaling law, schematized in Table 7.1, which is different from the Hopkinson-Cranz scaling (Table 7.2), we consider several case studies. First,

the similarity between prototype and models is tested considering similar materials, i.e., equal density, $\gamma = 1$. Then, the case of different materials (i.e., $\gamma \neq 1$).

Finally, the validation is performed through three-dimensional numerical FE simulations (paragraph 7.6.2). The validity of the scaling law is thus verified with the effects of combined sliding, rocking, and uplift (flight mode). We consider Coulomb friction at the interface of the block with the rigid base, with an angle of friction equal to 35°, which is common for many geomaterials (concrete, marble, stone etc.). Blast loads are applied as in paragraph 1.5.1.3, relying on the best-fit interpolations in Appendix A. ABAQUS commercial software is used for the computations. A hard contact formulation is used, i.e., no penetration is allowed at the contact of the rocking block with the base. The rigid base is fixed and the rigid block is free to translate and rotate along all directions (see Figure 7.13).

7.6.1 Equations of motions

7.6.1.1 Same material modeling

We consider a prototype block, with density $\rho_p = 2000$ kg m$^{-1/3}$, height $2h_p = 10$ m, slenderness angle $\alpha_p = 15°$, and arbitrary depth $2w_p$, subjected to the loading of the detonation of a given explosive quantity, W_p, at a stand-off distance $R_p = 2$ m. Two different geometric scales are considered; $\lambda_1 = 1/20$ and $\lambda_2 = 1/200$, see Figure 7.5. Table 7.3 displays the geometry parameters for the prototype and the two models. For both models, we assume a unit density scaling factor, i.e., $\gamma = 1$. Three different quantities of TNT equivalent are considered: (a) $W_{pa} = 50$ kg, (b) $W_{pb} = 100$ kg, and (c) $W_{pc} = 79.8$ kg. For case (a), according to the analytical developments in Masi et al. (2019a), and by numerical integration of Eq. (7.9), the prototype block rocks, without overturning. Overturning is instead expected for case (b). In case (c) $W_{pc} = 79.8$ kg, which represents the critical quantity of explosive at the stand-off distance $R_p = 2$ m, i.e., the maximum quantity of explosive for which toppling does not happen.

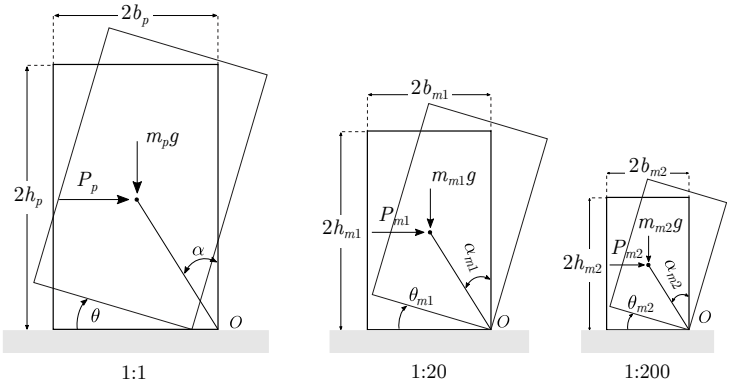

Figure 7.5 – Prototype system (left) and models with geometric scaling $\lambda_1 = 1/20$ (center) and $\lambda_2 = 1/200$ (right).

By numerically solving Eq. (7.6b) for λ_Z and for each loading case scenario (a-c),

we obtain the quantities of explosive (and scaled distances) for the models, as shown in Table 7.4.

Table 7.3 – Geometry parameters for the prototype and the two models, shown in Figure 7.5.

Prototype			Model 1			Model 2		
Height, $2h_p$	10	m	h_{m1}	50	cm	h_{m2}	5	cm
Width, $2b_p$	2.68	m	$2b_{m1}$	13.40	cm	$2b_{m2}$	1.34	cm
Slenderness angle, α_p	15	°	α_{m1}	15	°	α_{m2}	15	°
Stand-off distance, R_p	2	m	R_{m1}	10	cm	R_{m2}	1	cm

Table 7.4 – Geometry parameters for the prototype and the two models, shown in Figure 7.5.

case	Prototype			Model 1			Model 2		
a	TNT, W_{pa}	50	kg	W_{m1}	1.0	mg	W_{m2}	0.233	μg
	Scaled distance, Z_{pa}	0.54	$\mathrm{m}\sqrt[3]{\mathrm{kg}}$	Z_{m1}	0.99	$\mathrm{m}\sqrt[3]{\mathrm{kg}}$	Z_{m2}	1.62	$\mathrm{m}\sqrt[3]{\mathrm{kg}}$
b	TNT, W_{pb}	100	kg	W_{m1}	2.06	mg	W_{m2}	0.492	μg
	Scaled distance, Z_{pb}	0.43	$\mathrm{m}\sqrt[3]{\mathrm{kg}}$	Z_{m1}	0.78	$\mathrm{m}\sqrt[3]{\mathrm{kg}}$	Z_{m2}	1.26	$\mathrm{m}\sqrt[3]{\mathrm{kg}}$
c	TNT, W_{pc}	79.8	kg	W_{m1}	1.635	mg	W_{m2}	0.386	μg
	Scaled distance, Z_{pc}	0.46	$\mathrm{m}\sqrt[3]{\mathrm{kg}}$	Z_{m1}	0.85	$\mathrm{m}\sqrt[3]{\mathrm{kg}}$	Z_{m2}	1.37	$\mathrm{m}\sqrt[3]{\mathrm{kg}}$

We can notice that for scaling factors $\lambda < 1$, the calculated scaled distance of the model is higher than that one of the prototype. This is a favorable feature of the proposed scaling, since the intensity of the blast in the model is smaller than that in the prototype. The overpressure peak and impulse have thus smaller intensities in the model. This is not the case for Hopkinson-Cranz scaling law. Figure 7.6 displays the dependency of the scaling factors on overpressure (7.6a), scaled distance (7.6b), and impulse (7.6c) with respect to the geometric scaling. The Hopkinson-Cranza scaling is shown by dashed lines.
For scaling factor $\lambda = 1/200$, the overpressure peak is only $5 \div 8\%$ the value for the prototype. The impulse in the model is found to be only 0.3% the impulse in the prototype. Instead, if the Hopkison-Cranz law is used, the model overpressure peak equals the prototype value and the impulse is 5% the value in the prototype, which is high. In Figure 7.7 we present the (dimensional) overpressure peak, scaled distance, and impulse for the same scaling.

From numerical integration of (non-linear) Eq. (7.9), we compare the response of the prototype with the response of model 2, which has $\lambda = 1/200$. Figure 7.8 displays the evolution of the rocking angle, the angular velocity, and the blast load for the prototype system and the three quantities of explosive. Figure 7.9 shows the response of the model.

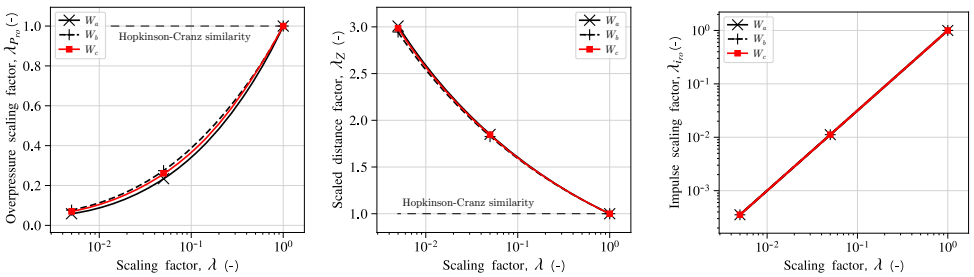

(a) overpressure. (b) scaled distance. (c) impulse.

Figure 7.6 – Scaling factors of overpressure (a), scaled distance (b), and impulse (c), at varying of the geometric scaling factor, λ (see Table 7.3). The scaling law permits overpressure and impulse reduction, differently from the Hopkinson-Cranz similarity law (see Table 7.2).

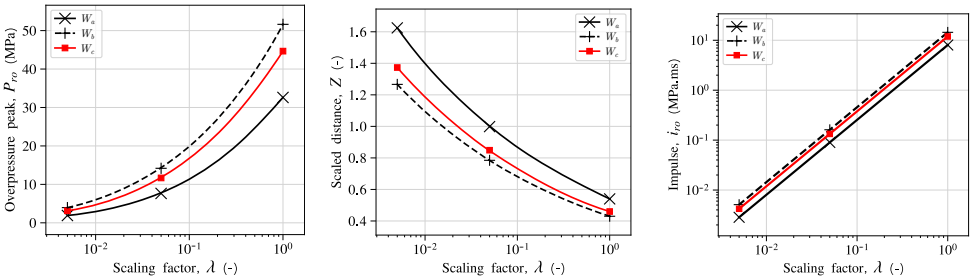

(a) overpressure. (b) scaled distance. (c) impulse.

Figure 7.7 – Overpressure (a), scaled distance (b), and impulse (c), at varying of the geometric scaling factor, λ (see Table 7.3).

The scaled model agrees with the prototype in terms of the final state of the block. For W_{pa}, both systems rock (without toppling); for W_{pb}, both systems undergo overturning; while W_{pc} and its scaled counterpart represent the critical explosive quantity of both systems.

Figure 7.10 compares the prototype response with that of the model, upscaled, i.e., all quantities are multiplied by the inverse of the scaling factor (cf. Table 7.3). The curves of the systems coincide which confirms the derived scaling laws. For the critical explosive quantity, W_{pc}, a negligible offset between model and prototype exists. This is a special, critical case, as it refers to the critical explosive quantity to avoid overturning. In this case numerical errors can determine overturning or not. Nevertheless, the scaling law is found to correctly capture the dynamics of the prototype when the phase space is examined.

7.6.1.2 Different material modeling

We consider here the scaling laws in the frame of different material modeling. This may be advantageous in experimental tests, as it allows to reduce the intensity of the blast load (cf. Table 7.1). More specifically, a material model with density lower

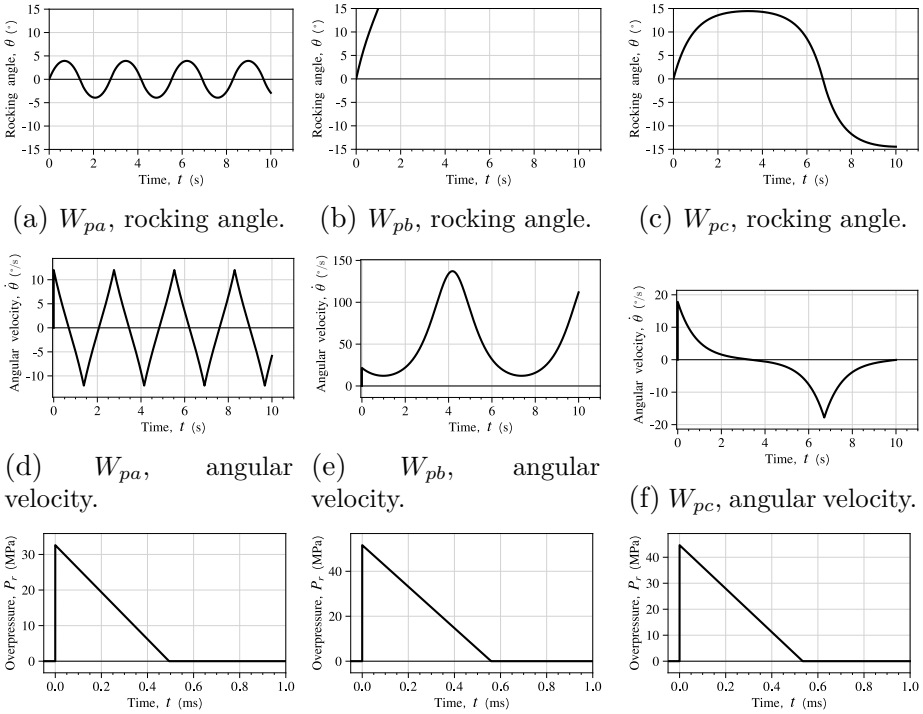

(a) W_{pa}, rocking angle. (b) W_{pb}, rocking angle. (c) W_{pc}, rocking angle.

(d) W_{pa}, angular velocity. (e) W_{pb}, angular velocity. (f) W_{pc}, angular velocity.

(g) W_{pa}, blast load. (h) W_{pb}, blast load. (i) W_{pc}, blast load.

Figure 7.8 – Response of the prototype for $W_{pa} = 50$ kg, $W_{pb} = 100$ kg, and $W_{pc} = 79.8$ kg, in terms of rocking angle θ (a-c), angular velocity $\dot{\theta}$ (d-f), and overpressure P_r (g-i).

than that of the prototype material allows reducing both the model pressure peak and impulse. In Figure 7.11 we show how the overpressure, scaled distance, and impulse scaling factors vary for a given geometric scaling. For instance, assuming $\lambda = 1/200$, the model overpressure peak equals 5.8% the prototype peak, with a density scaling factor $\gamma = 1$. For the same scaling, but with a dissimilar material such that $\gamma = 0.05$, the model overpressure peak reduces to 0.18%.

As previously done for the similar material modeling, we validate, through the numerical integration of the equation of motion (7.9), the scaling laws for materials with different densities. A light material as balsa (average density equal to 140 kg m$^{-1/3}$) is considered for the model system. The density scaling factor is thus $\gamma = 0.07$. In Figure 7.12 the response of the prototype is compared with the up-scaled results of the model. The comparison gives the same results with the case of same materials between model and prototype.

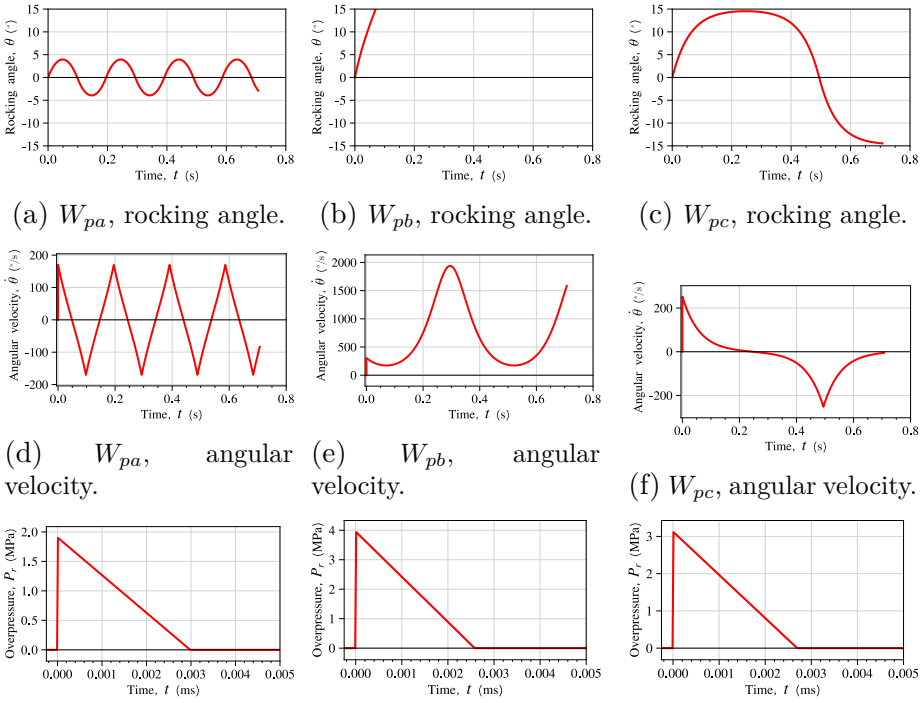

(a) W_{pa}, rocking angle. (b) W_{pb}, rocking angle. (c) W_{pc}, rocking angle.

(d) W_{pa}, angular velocity. (e) W_{pb}, angular velocity. (f) W_{pc}, angular velocity.

(g) W_{pa}, blast load. (h) W_{pb}, blast load. (i) W_{pc}, blast load.

Figure 7.9 – Response of the model for prototype explosive charges $W_{pa} = 50$ kg, $W_{pb} = 100$ kg, and $W_{pc} = 79.8$ kg, in terms of rocking angle θ (a-c), angular velocity $\dot{\theta}$ (d-f), and overpressure P_r (g-i).

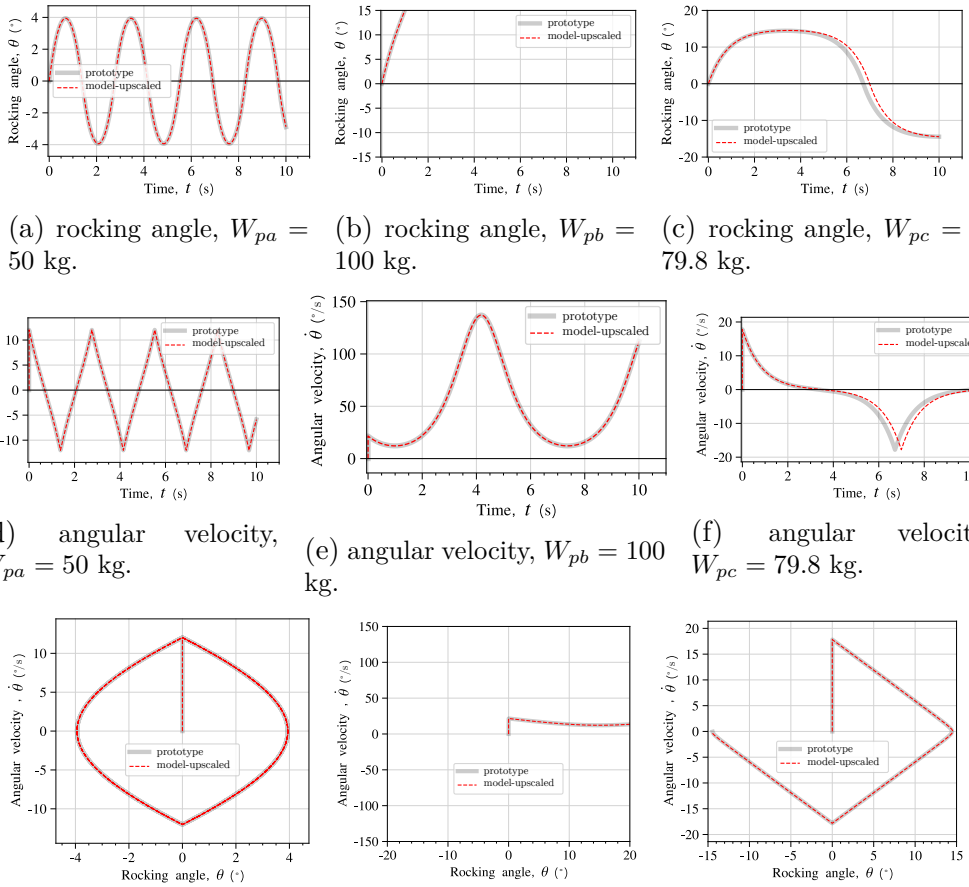

(a) rocking angle, $W_{pa} = 50$ kg. (b) rocking angle, $W_{pb} = 100$ kg. (c) rocking angle, $W_{pc} = 79.8$ kg.

(d) angular velocity, $W_{pa} = 50$ kg. (e) angular velocity, $W_{pb} = 100$ kg. (f) angular velocity, $W_{pc} = 79.8$ kg.

(g) phase portrait, $W_{pa} = 50$ kg. (h) phase portrait, $W_{pb} = 100$ kg. (i) phase portrait, $W_{pc} = 79.8$ kg.

Figure 7.10 – Comparison between the prototype response and the model response ($\lambda = 1/200$). The model is upscaled, i.e., all quantities are multiplied by the inverse of the scaling factor (cf. Table 7.3). Columns represent the three different quantities of explosive: W_{pa} (left), W_{pb} (center), and W_{pc} (right).

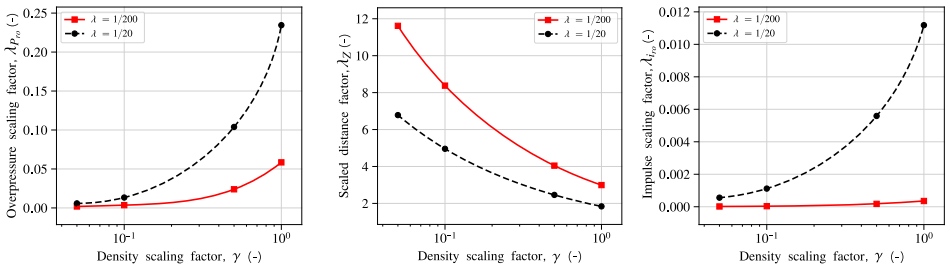

(a) scaling factor. (b) scaled distance. (c) impulse.

Figure 7.11 – Scaling factors of overpressure (a), scaled distance (b), and impulse (c), at varying of the density scaling factor, γ (see Table 7.3), and for two geometric scaling factors and prototype explosive quantity 50 kg.

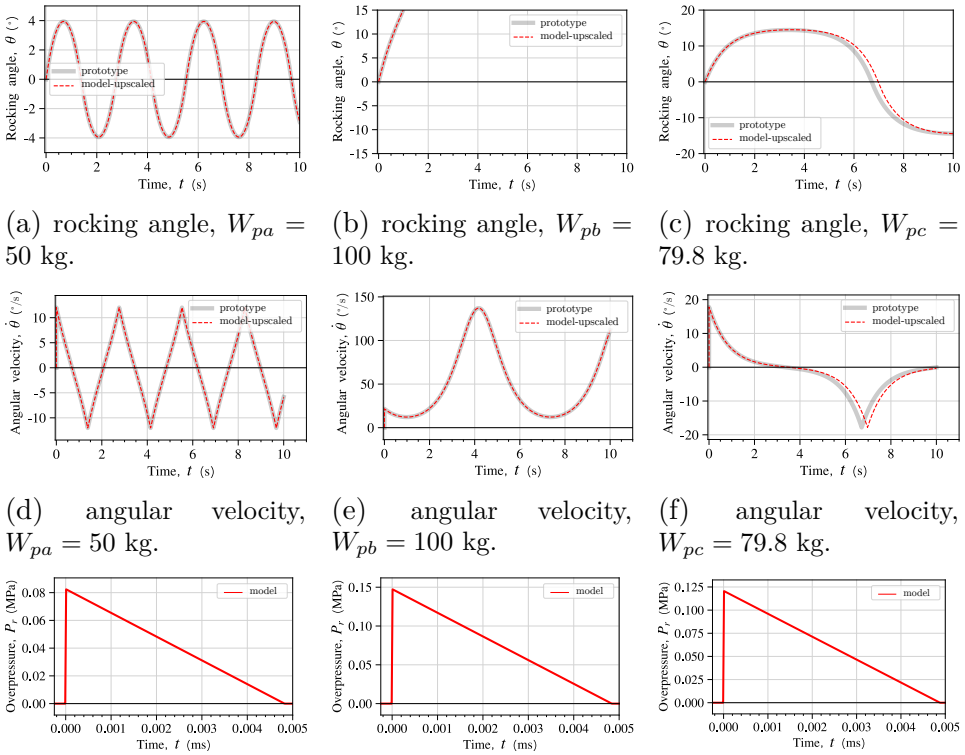

(a) rocking angle, $W_{pa} = 50$ kg. (b) rocking angle, $W_{pb} = 100$ kg. (c) rocking angle, $W_{pc} = 79.8$ kg.

(d) angular velocity, $W_{pa} = 50$ kg. (e) angular velocity, $W_{pb} = 100$ kg. (f) angular velocity, $W_{pc} = 79.8$ kg.

(g) model loading, $W_{pa} = 50$ kg. (h) model loading, $W_{pb} = 100$ kg. (i) model loading, $W_{pc} = 79.8$ kg.

Figure 7.12 – Comparison between the prototype response and the model response ($\lambda = 1/200$) and dissimilar materials ($\gamma = 0.07$). The model is upscaled, i.e., all quantities are multiplied by the inverse of the scaling factor (cf. Table 7.3). Columns represent the three different quantities of explosive: W_{pa} (left), W_{pb} (center), and W_{pc} (right).

7.6.2 FEM simulations

After validation of the proposed scaling laws for rocking response mechanisms, we consider the more realistic scenario of a masonry structure undergoing rocking, sliding, and up-lifting. This is investigated through three-dimensional FE simulations of a rigid block standing on a rigid base, see Figure 7.13. First, slender blocks, with geometric dimensions as in Table 7.3, are considered. Then, non-slender blocks are also investigated.

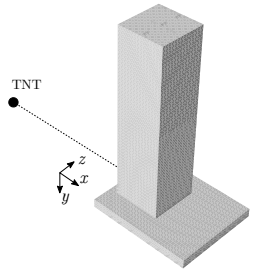

Figure 7.13 – Geometric and mesh discretization of the rigid block subjected to a TNT explosion.

In the case of slender blocks, two quantities of explosive are considered: $W_{pa} = 50$ kg and $W_{pb} = 100$ kg (prototype values). The evolution of the rigid body motion is displayed in Figure 7.14. It is worth noticing that rocking prevails over the other mechanisms.
In the case of non-slender blocks, one quantity of explosive is only considered, i.e., 2500 kg. Even if such a large quantity of TNT may cause damage to the target (instead of a rigid body response), this choice is only made to validate the scaling laws for mechanisms where sliding is dominant.

7.6.2.1 Slender blocks

By applying the scaling laws for a geometric scaling factor $\lambda = \lambda_2 = 1/200$, two different models are investigated. First, we consider a model made of the same material with the prototype. Then, a different material modeling is investigated. The block dimensions are those in Table 7.3 (Prototype and Model 2).

Figure 7.15 displays the FE results of the prototype and of the model, with the same material. The prototype and model responses coincide. It is worth noticing that, for both systems, the FE results agree remarkably well with the numerical solution of Eq. (7.9). Indeed, whilst rocking, sliding and up-lifting happen together, the former prevails for slender blocks. Nevertheless, a shift in the rocking angle between the FE results and the rocking equation of motion appears after the first impact with the ground (at 1.3 ms from the arrival time). This is mainly due to repeated impacts with the ground base. Figure 7.16 displays the horizontal and vertical displacement and velocities obtained with FE simulations and compared them with the rocking model. Repeated impacts at the ground (7.16a and 7.16d) alter the motion when the rocking angle changes sign.

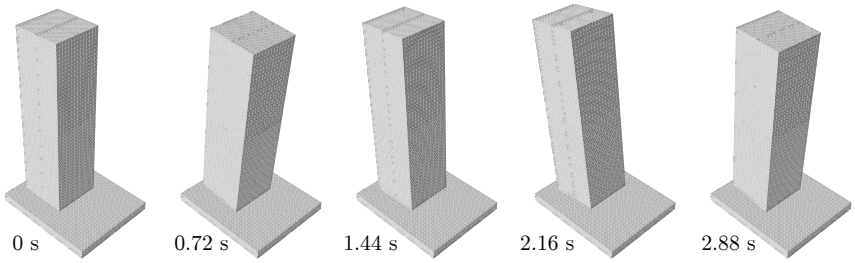

(a) $W_{pa} = 50$ kg.

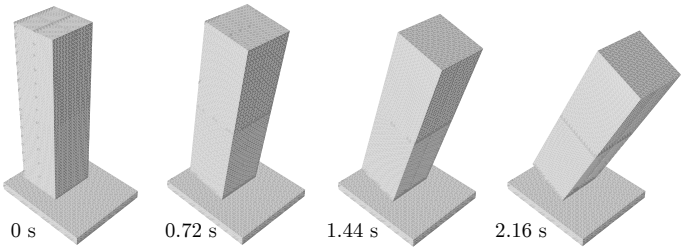

(b) $W_{pb} = 100$ kg.

Figure 7.14 – Dynamic evolution of a rigid block subjected to (a) $W_{pa} = 50$ kg and (b) $W_{pb} = 100$ kg, according to the FE simulations.

Even if a model made of lighter material, such as balsa (cf. paragraph 7.6.1.2), is used, the scaling laws still assure similarity with the prototype. The results of the FE simulations are shown in Figure 7.17 for quantities $W_{pa} = 50$ kg and $W_{pb} = 100$ kg. Once more, the model response is similar to the prototype one. By up-scaling the reduced scale quantities, the rocking angle and velocity perfectly coincide with the prototype.

7.6.2.2 Non-slender blocks

Sliding predominant responses are now investigated. We assume a non-slender prototype block, with height $2h_p = 10$ m, slenderness angle $\alpha = 35°$, and depth and width $2w_p = 2b_p = 3.5$ m. The prototype model is subjected to an explosion of 2500 kg of TNT, at 3 m.
The model is characterized by a geometric scaling factor $\lambda_2 = 1/200$ and unit density scaling factor. According to the scaling (Tab. 7.1), we compute a similar explosive quantity equal to 14.26 mg. The numerical results of the prototype and model systems are presented in Figure 7.18, while the dynamic evolution of the prototype is displayed in Figure 7.19. The systems response perfectly coincide up to 0.8 s after the arrival of the shock wave. At this moment, the block is almost at rest (after sliding for a distance of approximately 1 m), and a series of impacts with the ground base take place. Due to the successive impacts, the response of the model is found to differ from the one of the prototype. This might also be due to minor numerical issues related to contact calculations. Nevertheless, the scaling laws assure similarity of the predominant quantity (sliding distance and velocity).

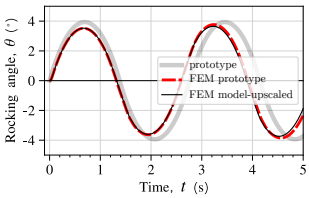

(a) rocking angle, $W_{pa} = 50$ kg.

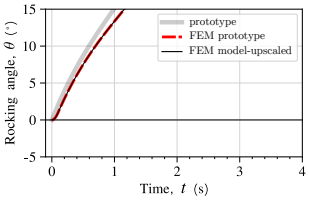

(b) rocking angle, $W_{pb} = 100$ kg.

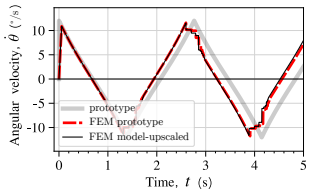

(c) angular velocity, $W_{pa} = 50$ kg.

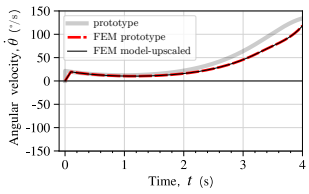

(d) angular velocity, $W_{pb} = 100$ kg.

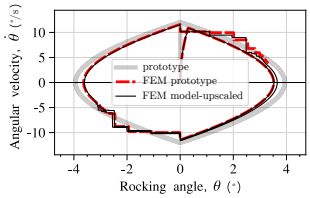

(e) phase portrait, $W_{pa} = 50$ kg.

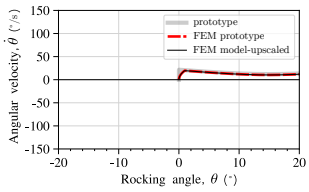

(f) phase portrait, $W_{pb} = 100$ kg.

Figure 7.15 – FE simulations of prototype and model responses ($\lambda = 1/200$) and comparison with the solution of Eq. (7.9). Both prototype and model are made of the same material. Left column refers to $W_{pa} = 50$ kg and right column to $W_{pb} = 100$ kg.

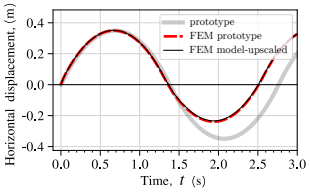

(a) horizontal displacement.

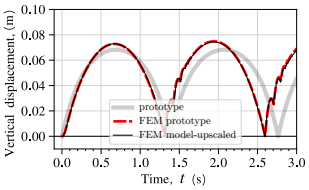

(b) vertical displacement.

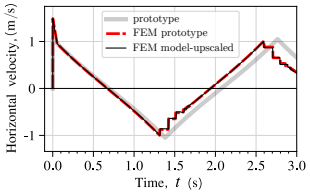

(c) horizontal velocity.

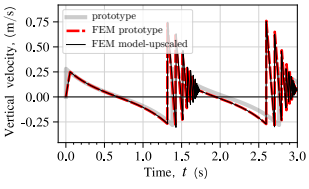

(d) vertical velocity.

Figure 7.16 – FE simulations of prototype and model responses ($\lambda = 1/200$) and comparison with the solution of Eq. (7.9). The results refer to an explosive quantity $W_{pa} = 50$ kg.

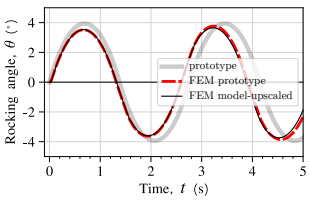

(a) rocking angle, $W_{pa} = 50$ kg.

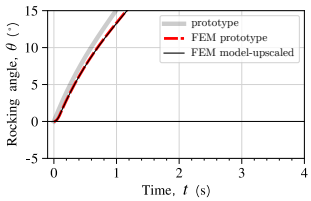

(b) rocking angle, $W_{pb} = 100$ kg.

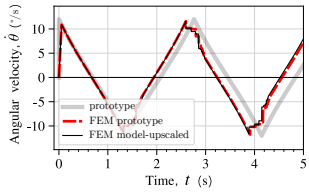

(c) angular velocity, $W_{pa} = 50$ kg.

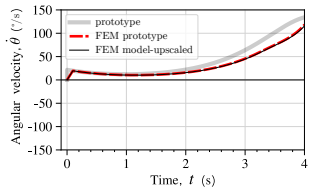

(d) angular velocity, $W_{pb} = 100$ kg.

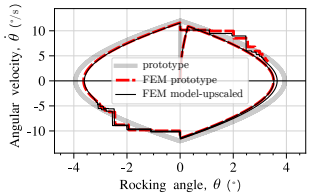

(e) phase portrait, $W_{pa} = 50$ kg.

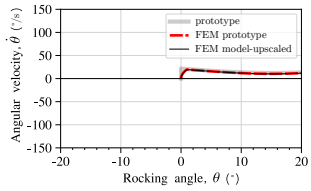

(f) phase portrait, $W_{pb} = 100$ kg.

Figure 7.17 – FE simulations of prototype and model responses ($\lambda = 1/200$) and comparison with the solution of Eq. (7.9). The density scaling factor is $\gamma = 0.07$. Left column refers to $W_{pa} = 50$ kg and right column to $W_{pb} = 100$ kg.

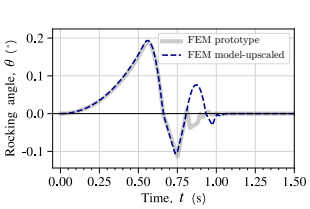

(a) rocking angle.

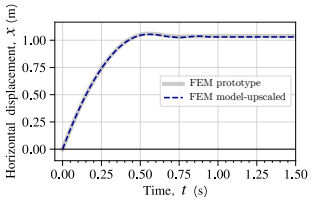

(b) horizontal (linear) displacement.

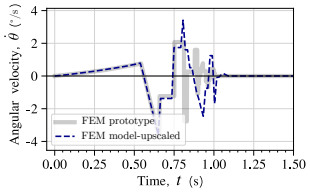

(c) angular velocity

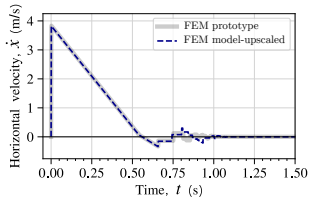

(d) horizontal (linear) velocity.

Figure 7.18 – FE simulations of prototype and model responses ($\lambda = 1/200$) for non-slender blocks ($\alpha = 35°$) subjected to a prototype explosive charge of 2500 kg at 3 m. The prototype and model are made of the same material.

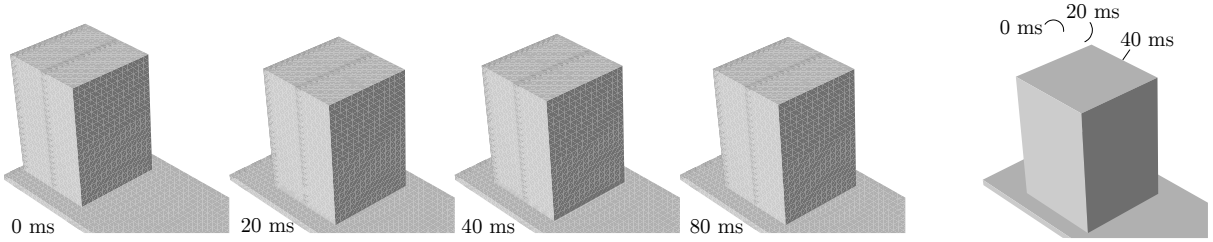

Figure 7.19 – Dynamic evolution of a non-slender rigid block subjected to 2500 kg, at a stand-off distance of 3 m, according to the FE simulations.

7.7 Application to multi-drum masonry columns

We consider multi-drum columns, made of fitted stone drums, placed on top of each other, avoiding the use of cement (mortar), see Figure 7.20. These structures show rich dynamics (Psycharis et al., 2000; Konstantinidis and N., 2005; Stefanou et al., 2011b; Makris and Vassiliou, 2013b; Drosos and Anastasopoulos, 2014; Sarhosis et al., 2016a; Fragiadakis et al., 2016) and therefore they are a very interesting benchmark for the derived scaling laws.

Columns of two different sections are considered: one with a square section (Fig. 7.20-a) and one of a circular one (Fig. 7.20-b). The multi-drum columns are 10 m high and are composed of ten 1 m high drums. The length of the square section and the diameter of the circular section vary from 1.65, at the base, to 1.28 m, at the top. The geometry is inspired by the external, Doric columns of the Parthenon (Neils, 2005).

We stress that the scaling laws have been derived for masonry structures undergoing rigid body motion. In Section 7.6, only monolithic masonry blocks were investigated. The following application shall show that the validity of the proposed scaling laws are also valid for multi-blocks structures.

Contrary to Section 7.6, we account for the deformability of the blocks. However, the scaling laws for the material response are not considered. Each drum is made of marble, which is considered to be (homogeneous) linearly elastic (with bulk and shear moduli equal to 50 and 27 GPa, respectively). For all numerical calculations, stresses are always found to be below the strength of the material. Deformations of the drums are, for all considered cases, negligible. This shows that, for multi-block structures, as those studied here, a rigid body response is predominant. We consider a Coulomb friction, with an angle of friction equal to 35°, at the interface of each drum. A hard contact formulation (ABAQUS, 2018) is used.

Blast loads are applied only on the front surfaces considering two different methods:

(a) Method A. Blast loads are applied as in Section 7.6 (cf. paragraph 1.5.1.3), relying on the best-fit interpolations shown in Appendix A, assuming simultaneity and uniformity of the pressure load.

(b) Method B. We account for the non-simultaneity of the load, the effects of surface rotation of the blocks, incident angle (Mach stem), and the relative distance between explosive and blocks. Following the approach in Vannucci et al. (2017a); Masi et al. (2020a) the position and the angle of incident of the center of the front surface of blocks are used to compute the blast loads.

In Appendix E, a third, more realistic blast load model is considered. In particular, we account for all exposed surfaces (front, side, and rear ones) in the blast load calculation. We consider a model with same material as the prototype and a geometric scaling $\lambda = 1/100$.

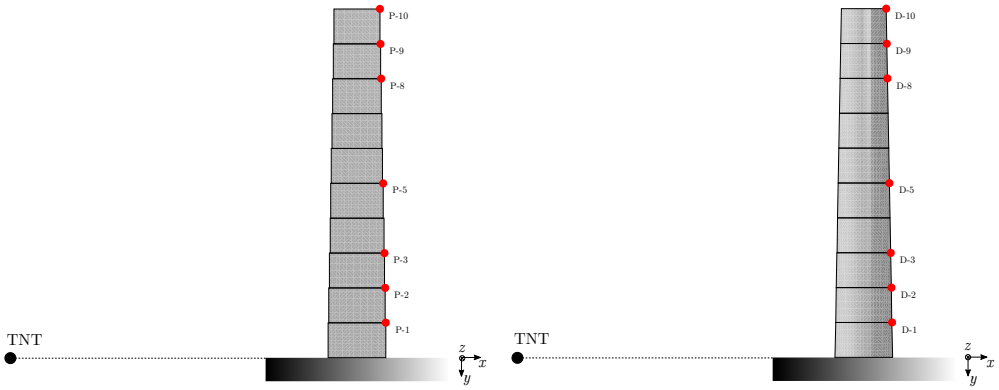

(a) Multi-drum column with rectangular section.

(b) Multi-drum column with circular section.

Figure 7.20 – Geometric and mesh discretization of the multi-drum columns with (a) square and (b) circular cross-section. Monitoring points are highlighted.

7.7.1 Multi-drum column with square cross-section

The (prototype) columns are subjected to the loading arising from the denotation of (a) 250 kg and (b) 500 kg at a stand-off distance of 10 m. A schematic representation of the response mechanism to the two quantities of explosive is shown in Figure 7.21.

7.7.1.1 Method A

By relying on the simplified approach of considering a planar shock wave impinging only the front surface of the structure, we investigate the dynamic response and the validity of the proposed scaling laws for deformable multi-block masonry structures. Figure 7.22 displays the horizontal displacement and velocity (along x-axis, see Fig. 7.20) at different monitoring points, for the column with square cross-section, subjected to an explosive quantity of 250 kg at 10 m away. The responses of both the prototype and the model (up-scaled) are plotted. Figure 7.23 refers instead to an explosive quantity of 500 kg. In both cases, we can see that the overall response of the prototype is well captured by the model. This is particularly true for the response of the blocks at the top (i.e., P-5 to P-10, cf. Fig. 7.20).

Differences, between the prototype and the model, are visible at the lower blocks (P-1 and P-3). This is mainly due to numerical errors and discrepancies related to the contact algorithm used. Furthermore, we only considered the scaling laws for the rigid body motion. As a result, similarity for elastic deformation mechanisms is not guaranteed. The repeated impacts (exciting the elastic response of the interfaces) are the main cause of the differences between the two systems. It is worth noticing that the same issue is found also for single rigid blocks. Nevertheless, the comparisons in paragraph 7.6.2 proved that the elastic deformation at the interfaces has very small influence on the dynamic response. The deformations of the drums may, as well, have some minor influence on the differences between the model and the prototype.

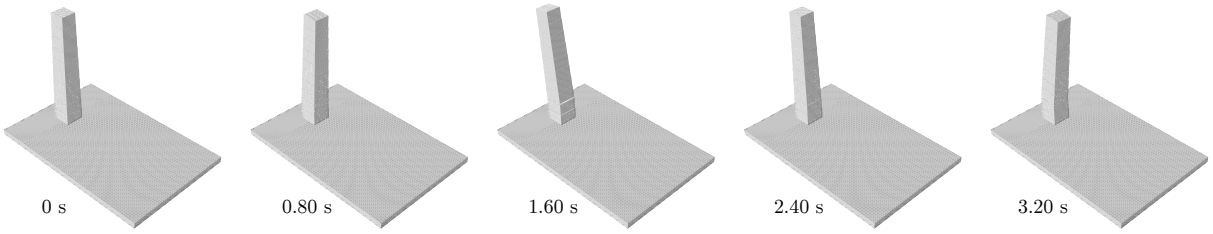

(a) response mechanism under 250 kg at 10 m.

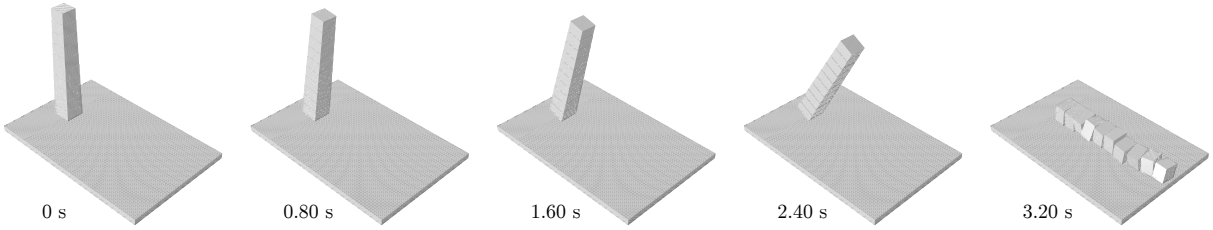

(b) response mechanism under 500 kg at 10 m.

Figure 7.21 – Response mechanisms for a multi-drum column, with square cross-section, subjected to 250 kg (a) and 500 kg, at a stand-off distance of 10 m. The time scale refers to the prototype system.

7.7.1.2 Method B

The more detailed characterization of blast loads is here adopted and the scaling laws are tested. In particular, we consider the spatial and temporal effects of an hemispherical shock wave. More complex phenomena than those considered in deriving the similarity laws are thus accounted for. In particular, the shock wave velocity (or, equivalently, the fact that the blast wave does not impinge all the front surface simultaneously) represents a main parameter.
Figures 7.24 and 7.25 show the response of the prototype and (upscaled) model against 250 and 500 kg prototype explosive charges, respectively. It is worth noticing that the main response of the system is well predicted by the model. Nevertheless, some differences exist. This is particularly true for the bottom blocks. The reason relies on the fact that the shock wave velocity, i.e., the shifting of the arrival time for each surface, is not taken into account by the proposed scaling laws. This results to minor differences between the two systems.

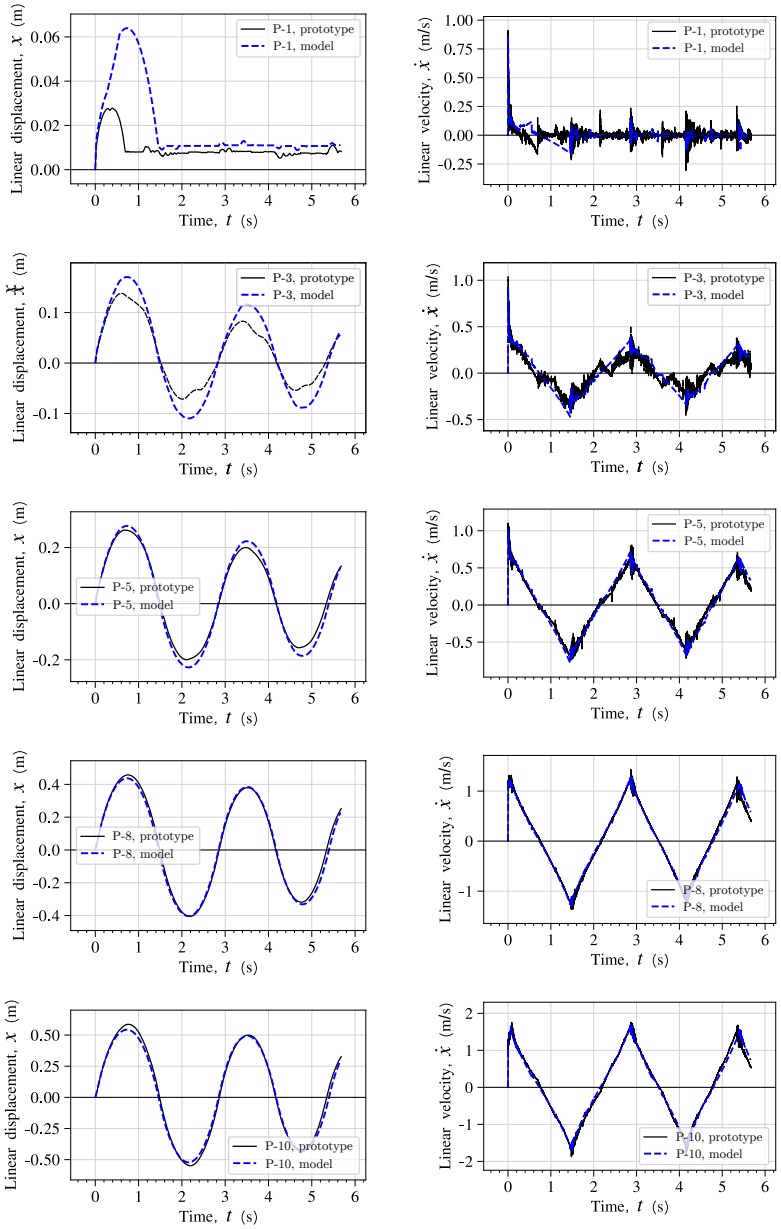

(a) horizontal displacement.

(b) horizontal velocity.

Figure 7.22 – Comparison between the prototype response and the model response ($\lambda = 1/100$), for a multi-drum column with square cross-section subjected to 250 kg at 10 m (Method A). Displacements and velocities of various monitoring points (cf. Fig. 7.20) are represented in (a) and (b), respectively.

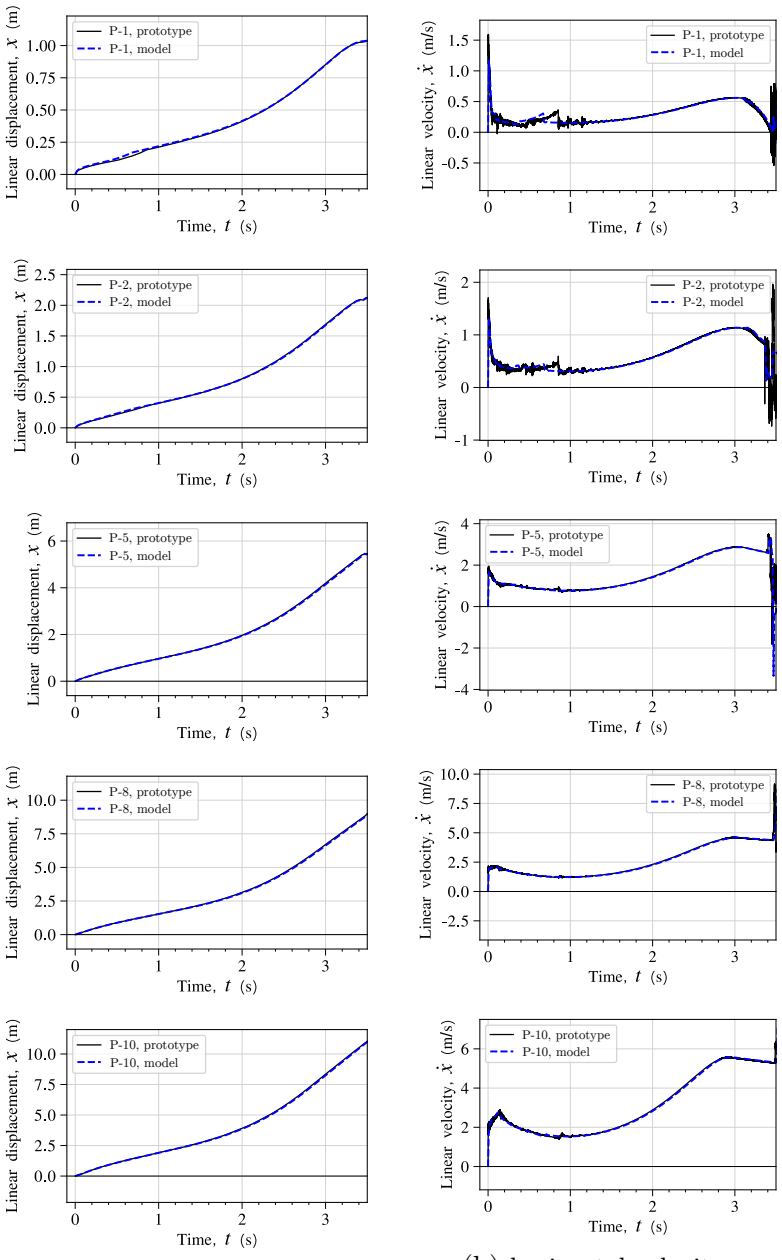

(a) horizontal displacement.

(b) horizontal velocity.

Figure 7.23 – Comparison between the prototype response and the model response ($\lambda = 1/100$), for a multi-drum column with cross-square section subjected to 500 kg at 10 m (Method A). Displacements and velocities of various monitoring points (cf. Fig. 7.20) are represented in (a) and (b), respectively.

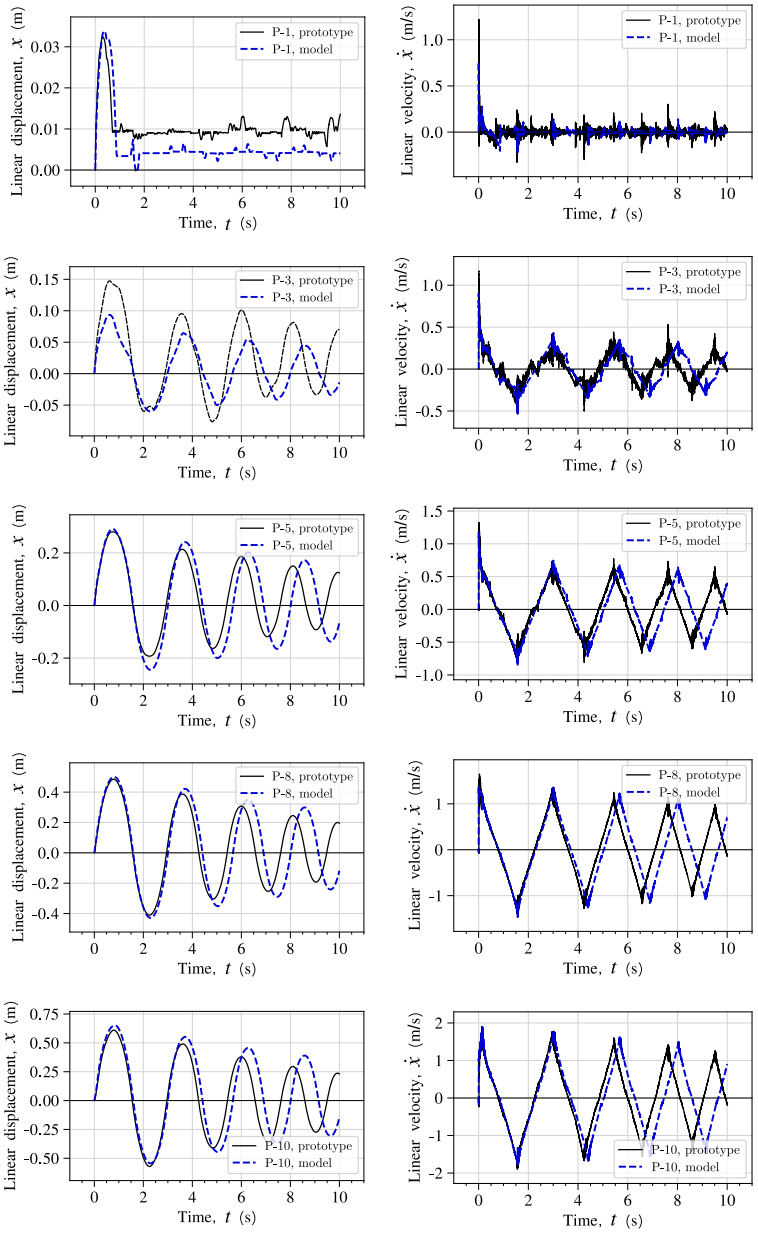

(a) horizontal displacement. (b) horizontal velocity.

Figure 7.24 – Comparison between the prototype response and the model response ($\lambda = 1/100$), for a multi-drum column with cross-square section subjected to 250 kg at 10 m (Method B). Displacements and velocities of various monitoring points (cf. Fig. 7.20) are represented in (a) and (b), respectively.

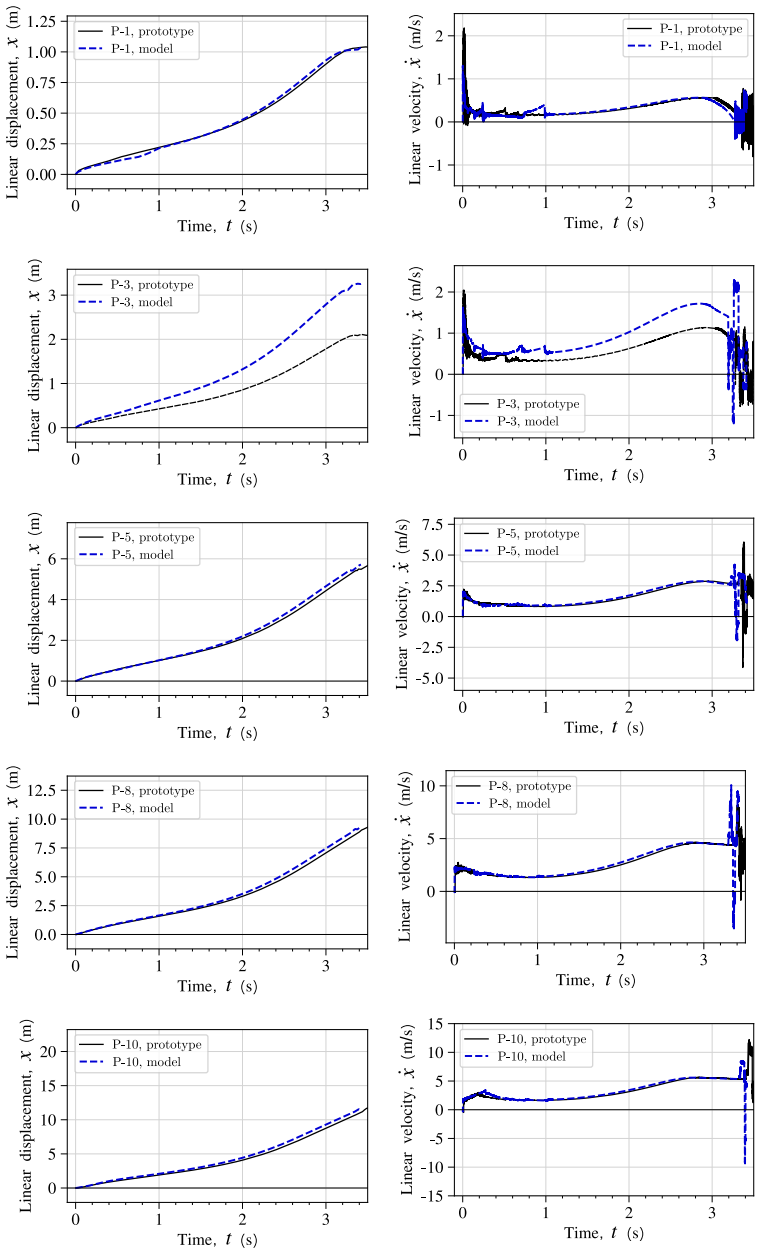

(a) horizontal displacement. (b) horizontal velocity.

Figure 7.25 – Comparison between the prototype response and the model response ($\lambda = 1/100$), for a multi-drum column with cross-square section subjected to 500 kg at 10 m (Method B). Displacements and velocities of various monitoring points (cf. Fig. 7.20) are represented in (a) and (b), respectively.

7.7.2 Multi-drum column with circular cross-section

The (prototype) columns are subjected to the loading arising from the detonation of (a) 200 kg and (b) 400 kg at a stand-off distance of 10 m. A schematic representation of the response mechanism under the two quantities of explosive is shown in Figure 7.26.

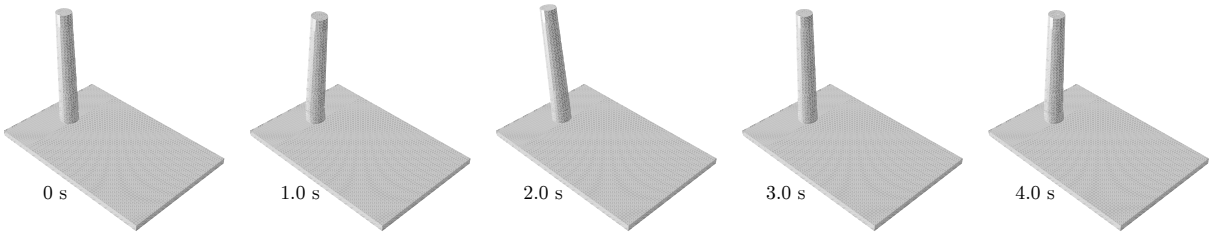

(a) response mechanism under 200 kg at 10 m.

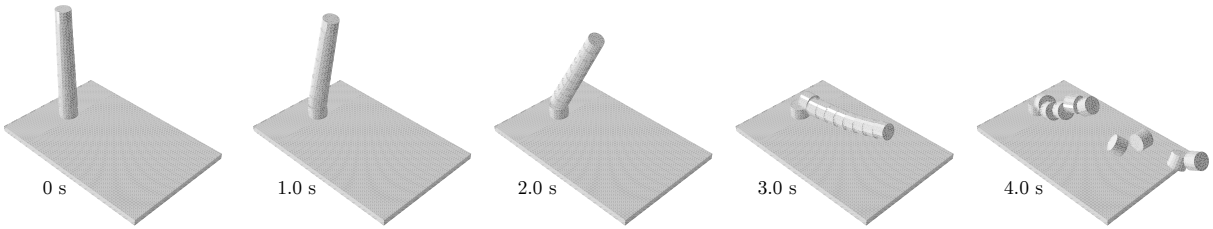

(b) response mechanism under 400 kg at 10 m.

Figure 7.26 – Response mechanisms for a multi-drum column, with circular cross-section, subjected to 200 kg (a) and 400 kg, at a stand-off distance of 10 m.

7.7.2.1 Method A

Assuming a planar shock wave impinging the front surfaces at the same time, we study the response of a multi-drum column with a circular cross-section. Figure 7.27 and 7.28 display the displacement and velocity, at several monitoring points, of a column with circular cross-section under 200 kg and 400 kg of TNT equivalent, respectively. Once more, the first peak response is extremely well captured by the model. Nevertheless, after the first impact (≈ 1.5 s), the response predicted by the model is found to diverge from that of the prototype. The reason relies on the complex response of the system, characterized by repeated impacts, wobbling motion, stick-slips, and rocking, see e.g. Stefanou et al. (2011b). Examining carefully the results, we observe that the model does not capture exactly the period of the movement. By considering the full equation of motion for wobbling (Stefanou et al., 2011b) one can derive the required, exact scaling laws for columns of circular cross-section. However, this exceeds the scope of this Thesis. Notice that this is not the case, for instance, of a square column, for which wobbling does not take place.
Nevertheless, even for the case of circular columns, the scaling laws give satisfactory results and accurately predict the first peak response, as well as the main response mechanism (collapse against 400 kg of TNT).
In Figure 7.26 we present the evolution of the response of the structure due to the two quantities of explosive.

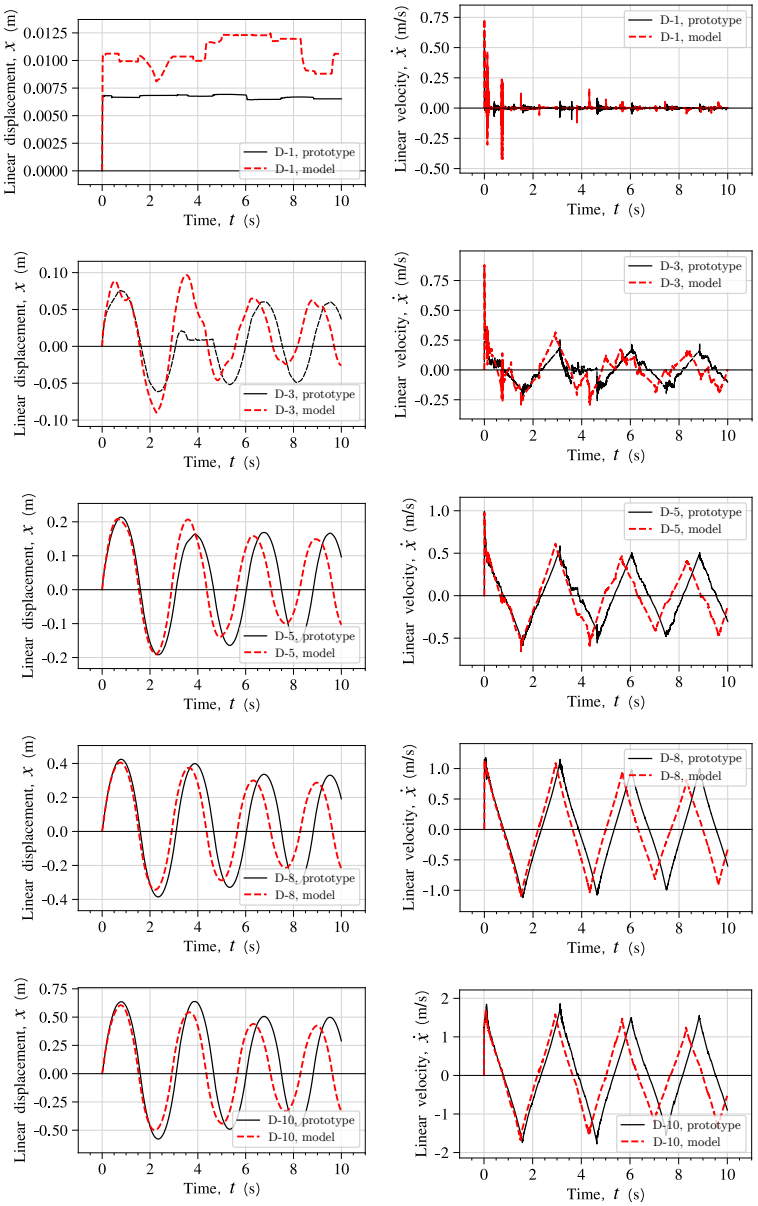

(a) horizontal displacement. (b) horizontal velocity.

Figure 7.27 – Comparison between the prototype response and the model response ($\lambda = 1/100$), for a multi-drum column with circular cross-section subjected to 200 kg at 10 m (Method A). Displacements and velocities of various monitoring points (cf. Fig. 7.20) are represented in (a) and (b), respectively.

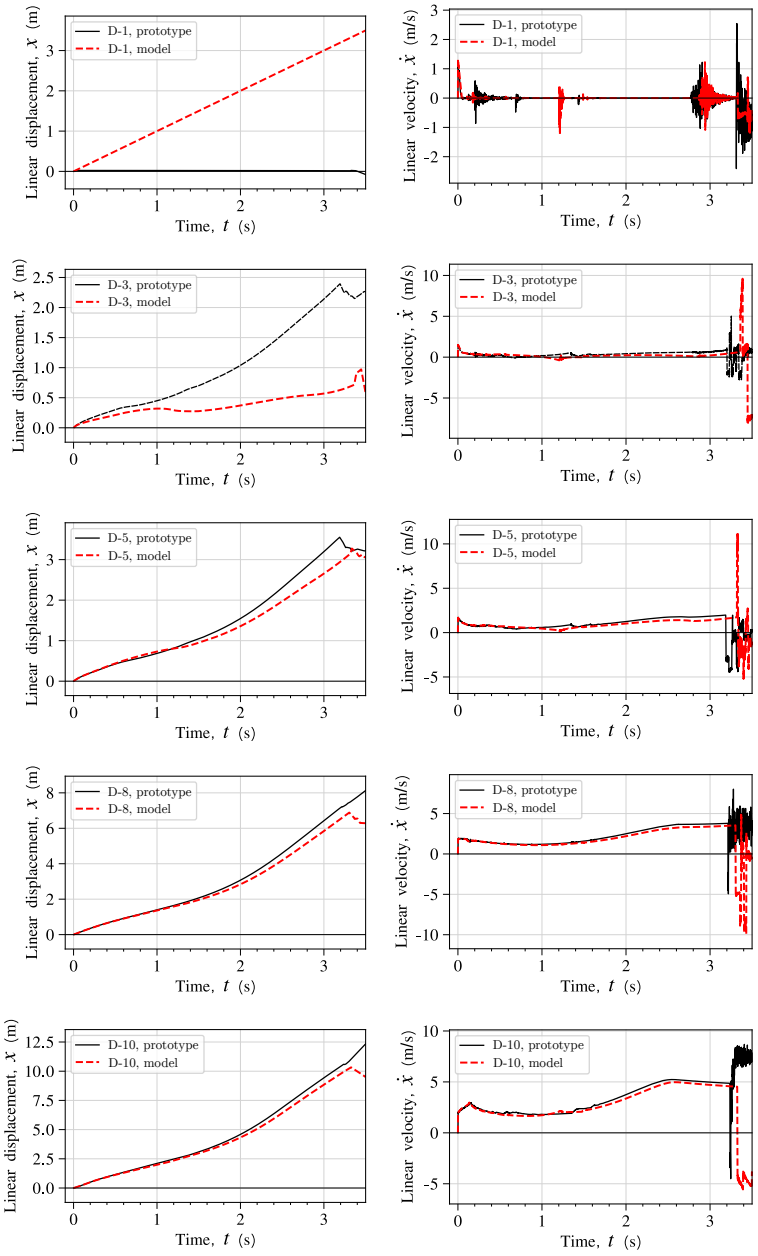

(a) horizontal displacement. (b) horizontal velocity.

Figure 7.28 – Comparison between the prototype response and the model response ($\lambda = 1/100$), for a multi-drum column with circular cross-section subjected to 400 kg at 10 m (Method A). Displacements and velocities of various monitoring points (cf. Fig. 7.20) are represented in (a) and (b), respectively.

7.7.2.2 Method B

We consider here the response of a circular cross-section column by using the more detailed description of the blast load. Contrary to the case of the column with square section, the responses of the prototype and the model differ significantly for the load scenario of 200 kg. Figure 7.29 displays the horizontal displacement and velocities at several monitoring points. The very first instants after the shock arrival (≈ 1 s) are well captured by the model. Nevertheless, the model overturns while the prototype does not.

The difference relies on the complex dynamics of wobbling which, enhanced by the effect of dissimilar shock wave velocity (between prototype and model), causes important differences. Further investigations and developments to include the effects of differing shock wave arrival time are needed. Nevertheless, it is worth noticing that for the detonation of 400 kg, the model perfectly predicts the prototype response as overturning takes place. Indeed, under such quantity of explosive, the shock wave velocity is far higher (Vannucci et al., 2017a). Consequently the shifting of the arrival time of the shock front on the impinged surfaces has minor effects.

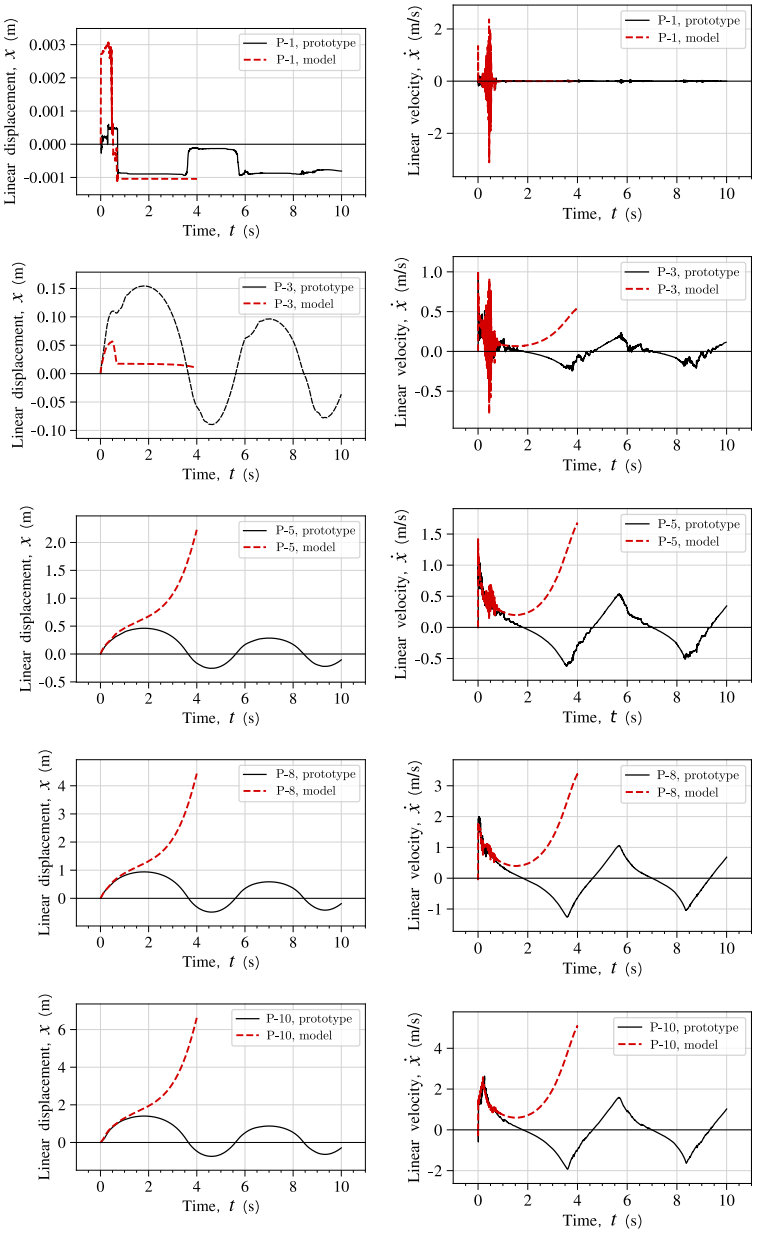

(a) horizontal displacement.

(b) horizontal velocity.

Figure 7.29 – Comparison between the prototype response and the model response ($\lambda = 1/100$), for a multi-drum column with circular cross-section subjected to 200 kg at 10 m (Method B). Displacements and velocities of various monitoring points (cf. Fig. 7.20) are represented in (a) and (b), respectively.

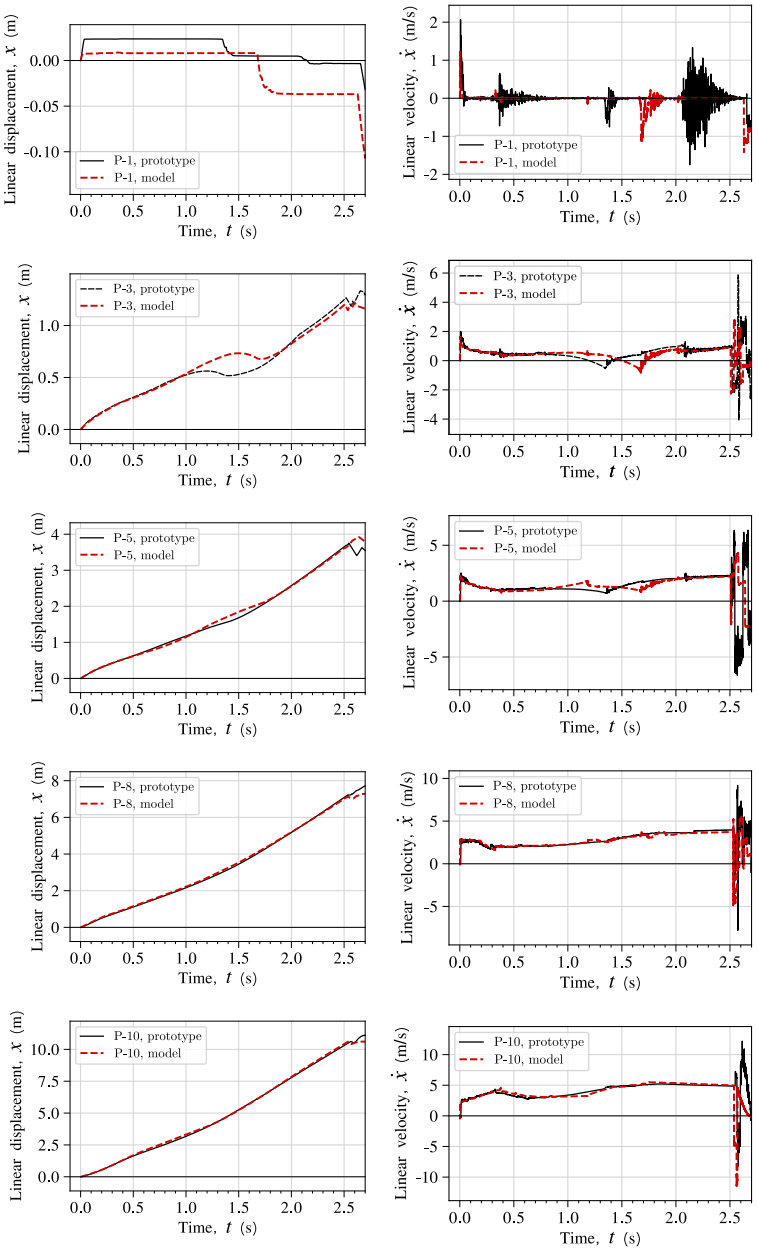

(a) horizontal displacement.

(b) horizontal velocity.

Figure 7.30 – Comparison between the prototype response and the model response ($\lambda = 1/100$), for a multi-drum column with circular cross-section subjected to 400 kg at 10 m (Method B). Displacements and velocities of various monitoring points (cf. Fig. 7.20) are represented in (a) and (b), respectively.

7.8 Additional remarks

Experiments of masonry structures under blast loads are rare in the available literature. This is an obstacle for designing appropriate protective devices to preserve masonry structures against blasts. Indeed, experimental testing of this kind of elements is particularly challenging due to the complex structural dynamic response of masonry. Furthermore, field testing shows several limitations related to cost, environmental hazards, safety risks, and repeatability. In addition, one of main restrictions to full-scale field testing stems from the explosive charge weight, which cannot exceed safety values (for the personnel and the monitoring equipment). Field testing of reduced scales prototype is thus necessary. In order to perform and accurately design scaled tests, scaling laws for both the blast loads and the specimens are mandatory.

We aim at providing scaling laws for masonry structures subjected to explosions. Based on previous works (Masi et al., 2019a, 2020b), we derived similarity laws for the rigid-body motion and the material response of structures, considering empirical models for the blast actions. In contrast with the well-known Hopkinson-Cranz scaling laws (Hopkinson, 1915; Cranz, 1925), the proposed scaling laws allow to design experiments by reducing the blast intensity, which is compelling for safe experiments.

With particular attention to the rigid body response, scaling laws were validated against numerical cases of monolithic prototypes and models and through three-dimensional Finite Element simulations. Finally, multi-drum columns, typical examples of key load-carrying elements in ancient masonry structures and monuments, were investigated. In particular, we showed that the scaling laws are valid for multi-block, deformable structures.

We give first insights of how reduced-scale experiments of ancient and modern masonry structures can be designed. Further investigations including richer dynamics, such as the wobbling motion, and the consideration of the blast wave front propagation along the structure are needed. Nevertheless, the derived scaling laws can be directly used for the design of preliminary experiments of masonry structures.

Conclusions and future work

Concluding remarks

The main objectives of this Thesis were:

1. Extend the current understanding/knowledge on the dynamic response and failure of masonry structures of standard and non-standard geometry subjected to explosions.
2. Develop modeling approaches/strategies to study the behavior of existing buildings and to design new ones.
3. Set the basis for designing new experimental tests for validating/falsifying the derived models and theoretical assumptions.

In this work, several methodologies and modeling strategies were developed. In particular, we analyzed the dominant mechanical parameters of the dynamic behavior and failure modes of masonry structures subjected to blast loads. On the basis of an extensive literature review, we detailed modeling and theoretical assumptions for the problems here considered (e.g., neglect material strain-rate dependency), see Chapters 1 and 2.

We investigated the response of masonry structures displaying monolithic behavior through simplified tools, developing new analytical predictions for the rocking and overturning response (objective 1). The analytical findings were compared with existing experimental tests and detailed numerical simulations accounting for the complex fluid-structure interaction phenomena, see Chapter 3.

We studied the behavior of standard and non-standard masonry structures using detailed numerical simulations, accounting for the discrete nature of the masonry (meso-scale) and using the Discrete Element Method (objective 1). The numerical simulations and the theoretical assumptions were validated with existing experimental tests. Then several structural elements were analyzed: walls, planar arches, and vaults. Furthermore, we addressed and studied in detail the influence of several (micro-) mechanical parameters of the masonry on the structural behavior, see Chapter 4.

We proposed a simplified, engineering-oriented macroscopic model, using the Finite Element Method, to be used in the study of large existing masonry structures and in the design of new ones (objective 2). The model was compared with existing experimental tests and the aforementioned detailed Discrete Element simulations, see Chapter 5. The limitations of the simplified model were highlighted together with its advantages for engineering applications.

With the aim of deriving in the future detailed and more sophisticated multiscale descriptions of the masonry material, we proposed a new class of Artificial Neural Networks (ANNs)

which respect the basic laws of thermodynamics. We called this new class of ANNs, *Thermodynamics-based Artificial Neural Networks* (TANNs). The next ste will be to use TANNs to reduce the computational cost of multiscale analyses and make them a viable strategy to analyze large masonry buildings (objective 2), see Chapter 6.

Finally, we derived new scaling laws for the blast loading and the response of masonry structures (objective 3). These findings are the first step towards designing and defining an experimental methodology for validating/falsifying, in the near future, the derived models and theoretical assumptions, based on reduced-scale laboratory experiments, see Chapter 7.

For the sake of clarity, we detail, in the form of a list, the principal and secondary findings and developments of our study:

- Due to the mechanical excitations arising in a blast scenario, the structural response of masonry structures involves either monolithic behavior or deformation regimes characterized by a strong coupling of the in-plane and out-of-plane motion (see Sect. 2.4).

- In the case of a monolithic response, we demonstrated that overturning is the predominant failure mechanism, over sliding, up-lifting, and direct material damage (see Chapter 3).

- In the case of a monolithic behavior or after material damage and depending on the kinematics of the failure modes, we proposed a new analytical model that allows us to study the dynamic response. This model was validated using comparisons with existing experimental tests and detailed numerical simulations (see Sect. 3.5).

- The detailed Discrete Element numerical simulations shed light on the influence of several mechanical parameters of the masonry as well as the resistance and behavior of different structural masonry elements (see Chapter 4).

- The numerical simulations demonstrated that for masonry structures with joints of low strength, the dynamic response and failure is governed by the masonry joints, and that the damage of blocks and stones is very limited (see Sect.s 4.3-4.6).

- The detailed simulations showed that, for all considered cases, the strain-rate effects are limited and, consequently, that the dynamic increase factor is low. Neglecting such effects equals, in the worst case scenario, to consider a factor of safety for the material strength that is equal to 2 (see Sect. 2.3 and Chapter 4).

- For the quantities of explosive and material parameters considered, we found that semi-circular arches are more vulnerable to blast loads than other non semi-circular ones (see Sect. 4.4).

- We showed that the response of a barrel vault restrained to fixed supports is similar

to that of a planar wall subjected to out-of-plane loads, confined with supports that prevent outward movement. Under the action of blast loads, membrane compressive forces develop and the longitudinal layers of bricks bend, giving rise to an arching mechanism (see Sect. 4.5).

- The numerical simulations highlighted the important role played by the (non-) associativity of the sliding behavior of the masonry joints. Masonry joints with zero dilatancy (non-associative plastic behavior) lead to reduced transmitted forces between blocks and to an increase in out-of-plane deflections of the structure. Zero dilatancy of the joints results in a reduction of the strength of the masonry (see Sect.s 4.3 and 4.5).

- Due to the strain-softening behavior and the importance of non-associativity of the masonry joints, limit analysis approaches could lead to important overestimations of the strength and therefore their application for engineering applications in masonry is questioned (see Sect.s 4.3 and 4.5).

- The cohesion and tensile strength of the masonry joints was found to have reduced influence on the overall structural response, at least for the investigated elements and blast scenarios (see Sect.s 4.5 and 4.6).

- By investigating the influence of the size of the building blocks, we found that under blast loads the larger the blocks are, the larger the resistance of the masonry is (see Sect.s 4.5, 4.6).

- The Discrete Element numerical simulations demonstrated the importance of setting up an appropriate methodology for reliable results. Otherwise inaccurate results and numerical artifacts can appear (see Chapter 4 and Appendix C).

- The simplified macroscopic approach we proposed, using the Finite Element Method, demonstrated to be a practical tool for preliminary analyses of the dynamic response and resistance of masonry buildings subjected to blast loading (see Chapter 5).

- Our engineering-oriented simplified model usually provided safe estimates of the resistance of structures. Moreover, the calculation cost of the simplified macroscopic model was relatively low, i.e., some couple of hours for single structural masonry elements to less than a day for a large masonry structure (see Sect.s 5.3 and 5.4).

- However, it presents many significant limitations that were emphasized in the manuscript (see Sect. 5.3). In these cases, more sophisticated models of masonry are of paramount importance. In particular, other constitutive models or physics-based multiscale analyses are needed, but their calculation cost may be prohibitive (see Sect. 2.5).

- We proposed a theoretical development of standard Artificial Neural Networks (ANNs), called here Thermodynamics-based Artificial Neural Networks (TANNs),

to be used for the constitutive modeling in the frame of multiscale analyses and for minimizing the calculation cost (see Chapter 6).

- TANNs demonstrated their superiority with respect to standard ANNs in terms of accuracy of the predictions and "generalization" of the network. Moreover, TANNs assured the thermodynamic consistency of the outputs, unconditionally (see Sect. 6.4).

- The calculations performed by TANNs required the resolution of the vanishing gradients problem for higher order derivatives. In particular, we revealed the new problem of second-order vanishing gradients, as it was called here, that can inhibit back-propagation and make training of the network to fail. Remedies to this issue were extensively explored and discussed. These developments can have a large spectrum of applications (see Sect 6.2).

- Through several applications, we showed that Thermodynamics-based Artificial Neural Networks go beyond and surpass the standard framework of Machine Learning methods used for constitutive modeling, as far it concerns the thermodynamic requirements (see Sect. 6.4).

- Experimental tests of masonry structures subjected to blast loads are, at present, partial and very limited in number. The reason lies on the fact that full-scale blast experiments present many difficulties, e.g. high cost, safety issues, and reduced repeatability. Experiments in reduced-scaled offer instead great flexibility. Nevertheless, they need appropriate scaling laws to assure the similarity at the reduced-scale (see Chapter 7).

- We proposed new scaling laws for both the dynamic response and failure of masonry structures and the blast loads (see Sect.s 7.4 and 7.5).

- In contrast with the well-known Hopkinson-Cranz scaling laws (see Sect 1.1), the proposed scaling laws allow to design experiments by reducing the blast intensity, which is compelling for safe experiments, in a laboratory environment (see Sect. 7.6).

- The proposed scaling laws were validated with numerical simulations and further applied to the modeling of multi-drum masonry columns, whose dynamics is rich and challenging for reduced-scale models (see Sect. 7.7).

- Further investigations including richer dynamics, such as the wobbling motion, and the consideration of the blast wave front propagation along the structure are needed (see Sect. 7.7).

The above findings and developments have a direct link with the specific objectives of the Thesis.

Practical and theoretical implications

- Our analytical model for the rocking and overturning response of masonry structures subjected to blast loads can be used in several applications. In this Thesis, we presented, in the form of design charts, the critical stand-off distance—i.e., the minimum distance between the explosive and the target to prevent overturning—for different dimensions of targets. Such charts can be helpful in several applications, such as the the construction and positioning of blast walls and barriers to protect existing buildings and assets.

- The Discrete Element simulations allowed for the first time to investigate in detail the response to blast loads of non-standard and standard masonry structures. The methodology allows to foresee applications to different structural elements (domes, buttresses, columns, etc.) under fast-dynamic excitations.

- We analyzed the significant role played by the dilatancy of the masonry joints. Dilatancy is related to two competing mechanisms, one that enhances failure due to sliding at the joints, when dilatancy is low, and another that enhances brick failure when dilatancy is high. These competing effects give rise to the possibility of designing mortars that provide the optimal dilatancy for a given structural system.

- Our detailed discrete simulations showed the failure mechanisms of typical non-standard masonry elements. Based on these studies, passive protective devices, such as retrofitting using reinforced polymers or polyurea, can be designed ad-hoc to improve the blast performance of structural elements.

- Through the integration of such passive protections into a macroscopic continuum model, optimization studies can be conducted with the aim of providing appropriate strategies to prevent the collapse of existing masonry buildings, and design solutions in the construction of new ones.

- Our simplified macroscopic model, using the Finite Element Method, is a engineering-oriented practical tool to investigate, with reduced calculation cost, the resistance of existing, large masonry buildings and to design new ones. The model relies on simplifying assumptions which are, with no doubt, very strong, but they result in the direct use of existing commercial codes such as ABAQUS and LS-DYNA, which are accessible by practitioners.

- Furthermore, on the basis of our simplified macroscopic model, we addressed and quantify the limitations of engineering approaches for modeling masonry structures with simplistic assumptions (e.g., isotropic behavior, mode I fracture, and neglect plastic deformations and mechanisms).

- The new scaling laws will allows us to reduce the high cost associated with blast experiments and design new laboratory tests in reduced-scale.

The findings and developments of the Thesis foresee implications and applications to many disciplines, not exclusively concerning masonry structures. In particular

– Our analytical model for the rocking response of monolithic structures can be used in museums, for determining the minimum perimeter around statues of high historical and aesthetic value, as we presented in Appendix B. The presented model can be used as well for devising energy absorbing systems based on rocking motion.

– In a more theoretical context, the new class of Thermodynamics-based Artificial Neural Networks can be used in several domains of solid mechanics. In particular, due to the general thermodynamic framework on which our model relies, our network can be used for modeling materials displaying more complex behavior than masonry, with different characteristic material lengths and multiphysic couplings.

Perspectives

Further investigations and developments of the presented work can be pursued. The perspectives are the following:

- Our simulations exclusively account for the mechanical effects of a blast, in a rather simplified way. Nevertheless, during detonation, thermal shocks producing high-temperatures are also released, provided that these phenomena are proved to be important for the dynamic behavior of masonry. Furthermore, depending on the geometry, focalization of the blast waves and other fluid-structure phenomena may take place (see a previous study of the author, Masi et al., 2018b).

- The proposed class of Thermodynamics-based Artificial Neural Networks can be used to model the masonry material in multiscale analyses and further integrate the trained network into Finite Element codes. This can be achieved without any changes to the proposed architecture. Furthermore, they can be used for multiscale analyses of other materials too (e.g. sand, geomaterials, concrete, earthquake faults).

- The proposed scaling laws will be used to perform laboratory tests (at reduced scale). The experimental results will validate or falsify the results presented in this work. Consequently, at a later stage, the experiments will allow us to investigate the performance of possible protective devices and improve our understanding of the physical phenomena taking place in a blast scenario involving non-standard masonry structures.

The aforementioned steps will be directly implemented in the frame of BLAST (Blast LoAds on STructures, http://blastructures.eu/)−Connect Talent project, funded by Pays de la Loire and Nantes Metropole−and CoQuake (Controlling earthQuakes, http://coquake.eu/)−ERC project.

References

M. Abadi, P. Barham, J. Chen, Z. Chen, A. Davis, J. Dean, M. Devin, S. Ghemawat, G. Irving, M. Isard, et al. Tensorflow: A system for large-scale machine learning. In *12th USENIX Symposium on Operating Systems Design and Implementation*, pages 265–283, 2016. 177

ABAQUS. Abaqus analysis user's guide. Technical Report Abaqus 6.14 Documentation, Simulia Corp., 2018. 23, 24, 26, 78, 86, 149, 151, 253

B. Aboagye. *Design of reduced scale experiments of masonry structures subjected to blast loads*. PhD thesis, École Centrale de Nantes, 2020. 232

B. M. Abou-Zeid, W. W. El-Dakhakhni, A. G. Razaqpur, and S. Foo. Response of Arching Unreinforced Concrete Masonry Walls to Blast Loading. *Journal of Structural Engineering*, 137(10):1205–1214, 2011. 48, 99, 230, 231

E. Çakt, Özden Saygl, J. V. Lemos, and C. S. Oliveira. Discrete element modeling of a scaled masonry structure and its validation. *Engineering Structures*, 126:224 – 236, 2016. ISSN 0141-0296. 100, 317

C. Alessandri, M. Garutti, V. Mallardo, and G. Milani. Crack patterns induced by foundation settlements: Integrated analysis on a renaissance masonry palace in italy. *International Journal of Architectural Heritage*, 9(2):111–129, 2015. 55

H. Alexakis and N. Makris. Minimum thickness of elliptical masonry arches. *Acta Mechanica*, 224(12):2977–2991, 2013. 104

G. Alpa and I. Monetto. Microstructural model for dry block masonry walls with in-plane loading. *Journal of the Mechanics and Physics of Solids*, 42(7):1159–1175, 1994. 137

L. Anand, O. Aslan, and S. A. Chester. A large-deformation gradient theory for elasticplastic materials: Strain softening and regularization of shear bands. *International Journal of Plasticity*, 30-31:116 – 143, 2012. ISSN 0749-6419. 178

A. Argilaga, J. Desrues, S. Dal Pont, G. Combe, and D. Caillerie. Femxdem multiscale modeling: Model performance enhancement from newton strategy to element loop parallelization. *International Journal for Numerical Methods in Engineering*, 114(1): 47–65, 2018. 56, 175

D. Asprone, E. Cadoni, A. Prota, and G. Manfredi. Dynamic behavior of a mediterranean natural stone under tensile loading. *International Journal of Rock Mechanics and Mining Sciences*, 46(3):514–520, 2009. 1, 37, 39

J. Bachmann, M. Strand, M. Vassiliou, M. Broccardo, and B. Stojadinović. Is rocking motion predictable? *Earthquake Engineering & Structural Dynamics*, 47(2):535–552, 2018. 65

E. Badshah, A. Naseer, M. Ashraf, and T. Ahmad. Response of masonry systems against blast loading. *Defence Technology*, 2020. 231

W. E. Baker, J. J. Kulesz, R. E. Ricker, R. L. Bessey, P. S. Westine, V. B. Parr, and G. A. Oldham. Workbook for predicting pressure wave and fragment effects of exploding propellant tanks and gas storage vessels. 19760012208. Technical report, NASA, United States, 1975. 66

W. E. Baker, P. S. Westine, and F. T. Dodge. Simulating rigid body motion. In *Similarity Methods in Engineering Dynamics*, volume 12 of *Fundamental Studies in Engineering*, pages 73 – 95. Elsevier, 1991. 81, 230, 235, 236, 238

N. Bakhvalov and G. Panasenko. Homogenisation: Averaging Processes in Periodic Media: Mathematical Problems in the Mechanics of Composite Materials, 1989. 2, 54, 137, 175

D. Baraldi and A. Cecchi. A full 3d rigid block model for the collapse behaviour of masonry walls. *European Journal of Mechanics-A/Solids*, 64:11–28, 2017. 55

A. G. Baydin, B. A. Pearlmutter, A. A. Radul, and J. M. Siskind. Automatic differentiation in machine learning: a survey. *The Journal of Machine Learning Research*, 18(1):5595–5637, 2017. 177, 181, 185

Z. P. Bažant and E. Becq-Giraudon. Statistical prediction of fracture parameters of concrete and implications for choice of testing standard. *Cement and concrete research*, 32(4):529–556, 2002. 144

Z. P. Bazant and J. Planas. *Fracture and size effect in concrete and other quasibrittle materials*, volume 16. CRC press, 1997. 138, 144

D. J. Benson. Computational methods in lagrangian and eulerian hydrocodes. *Computer methods in Applied mechanics and Engineering*, 99(2-3):235–394, 1992. 24

D. J. Benson and S. Okazawa. Contact in a multi-material eulerian finite element formulation. *Computer methods in applied mechanics and engineering*, 193(39-41): 4277–4298, 2004. 25

E. Bertolesi, G. Milani, and S. Casolo. Homogenization towards a mechanistic rigid body and spring model (hrbsm) for the non-linear dynamic analysis of 3d masonry structures. *Meccanica*, 53(7):1819–1855, 2018. 138

J. Bertrand. Sur l'homogénéité dans les formules de physique. *Cahiers de recherche de l'Academie de Sciences*, 86:916–920, 1878. 235

M. Bessa, R. Bostanabad, Z. Liu, A. Hu, D. W. Apley, C. Brinson, W. Chen, and W. K. Liu. A framework for data-driven analysis of materials under uncertainty: Countering the curse of dimensionality. *Computer Methods in Applied Mechanics and Engineering*, 320:633–667, 2017. 190

L. Blanc, S. Santana Herrera, and J. L. Hanus. Simulating the blast wave from detonation of a charge using a balloon of compressed air. *Shock Waves*, 28(4):641–652, 2018. 25, 66, 79

P. Block, T. Ciblac, and J. Ochsendorf. Real-time limit analysis of vaulted masonry buildings. *Computers & structures*, 84(29-30):1841–1852, 2006. 43

P. C. V. Block. *Thrust network analysis: exploring three-dimensional equilibrium*. PhD thesis, Massachusetts Institute of Technology, 2009. 56

P. Bogacki and L. F. Shampine. A 3 (2) pair of Runge-Kutta formulas. *Applied Mathematics Letters*, 2(4):321–325, 1989. 193

D. Bogosian, J. Ferritto, and Y. Shi. Measuring uncertainty and conservatism in simplified blast models. In *30th Explosives Safety Seminar. Atlanta, GA, USA*, pages 1–26, 2002. 23

D. Boyer. An experimental study of the explosion generated by a pressurized sphere. *Journal of Fluid Mechanics*, 9(3):401–429, 1960. 233

S. Brasile, R. Casciaro, and G. Formica. Multilevel approach for brick masonry walls–part i: A numerical strategy for the nonlinear analysis. *Computer Methods in Applied Mechanics and Engineering*, 196(49-52):4934–4951, 2007. 138

M. Brocato. *Un modèle thermo-mécanique de polycristal pour l'étude des bandes de cisaillement*. PhD thesis, 1994. 123

M. Brocato. *Statique. De la géométrie à la conception des structures*, volume 9782859784904. Presses de Ponts, 2016. 104

M. Brocato. Conception des structures. In *Génie Civil et Construction*. Champs-sur-Marne, France, 2020. Course. 104

M. Brocato and G. Capriz. Gyrocontinua. *International journal of solids and structures*, 38(6-7):1089–1103, 2001. 123

M. Brocato, A. De Domenico, and F. Zanghi. Feedback control of a masonry vault. *WIT Transactions on The Built Environment*, 55, 2001. 44

H. L. Brode. Numerical solutions of spherical blast waves. *Journal of Applied Physics*, 26(6):766–775, 1955. 25, 233

R. S. Browning, J. A. Sherburn, and L. E. Schwer. Predicting blast loads using ls-dyna and cth. In *Proceedings of 2013 ASCE Structures Congress, Pittsburgh*, 2013. 19

T. Bui and A. Limam. Masonry walls under membrane or bending loading cases : experiments and Discrete Element analysis. *Proceedings of the 11th International Conference on Computational Structures Technology, Dubrovnik, Croatia, 47 September*, 2012. 317

T.-T. Bui, A. Limam, and V. Sarhosis. Failure analysis of masonry wall panels subjected to in-plane and out-of-plane loading using the discrete element method. *European Journal of Environmental and Civil Engineering*, 2019. 95, 96

S. Burnett, M. Gilbert, T. Molyneaux, A. Tyas, B. Hobbs, and G. Beattie. The response of masonry joints to dynamic tensile loading. *Materials and structures*, 40(5):517–527, 2007. 34, 38, 39

A. Carpinteri. *Nonlinear crack models for nonmetallic materials*, volume 71. Springer Science & Business Media, 2012. 142, 143

A. Carpinteri, P. Cornetti, F. Barpi, and S. Valente. Cohesive crack model description of ductile to brittle size-scale transition: dimensional analysis vs. renormalization group theory. *Engineering fracture mechanics*, 70(14):1809–1839, 2003. 148

P. Carrara, L. De Lorenzis, L. Stainier, and M. Ortiz. Data-driven fracture mechanics. *arXiv preprint arXiv:2006.03133*, 2020. 59, 176

C. Casapulla, L. Giresini, and P. B. Lourenço. Rocking and kinematic approaches for rigid block analysis of masonry walls: state of the art and recent developments. *Buildings*, 7(3):69, 2017. 67, 310

L. Cascini, R. Gagliardo, and F. Portioli. Lialock_3d: a software tool for collapse mechanism analysis of historic masonry structures. *International Journal of Architectural Heritage*, pages 1–20, 2018. 55, 56, 95

CEB-FIP (Comité Euro-International du Beton Fédération International de la Précontrainte). Model code 2010 - final draft. *Thomas Thelford Publications, Lausanne, Switzerland.*, 2010. 37, 38

A. Cecchi and K. Sab. A multi-parameter homogenization study for modeling elastic masonry. *European Journal of Mechanics-A/Solids*, 21(2):249–268, 2002. 54, 96, 137, 138, 139, 140, 141, 149, 154, 167

D. L. Chapman. On the rate of explosion in gases. *The London, Edinburgh, and Dublin Philosophical Magazine and Journal of Science*, 47(284):90–104, 1899. 18

T. Chen and H. Chen. Universal approximation to nonlinear operators by neural networks with arbitrary activation functions and its application to dynamical systems. *IEEE Transactions on Neural Networks*, 6(4):911–917, 1995. 175, 183

X. Chen, S. Wu, and J. Zhou. Experimental study on dynamic tensile strength of cement mortar using split hopkinson pressure bar technique. *Journal of materials in civil engineering*, 26(6):04014005, 2014. 1, 38, 39

A. A. Claramunt. *FEMxDEM double scale approach with second gradient regularization applied to granular materials modelization*. PhD thesis, 2016. 56, 175

N. A. Collins-Craft, I. Stefanou, J. Sulem, and I. Einav. A cosserat breakage mechanics model for brittle granular media. *Journal of the Mechanics and Physics of Solids*, page 103975, 2020. ISSN 0022-5096. 53, 58

M. Como. *Statics of historic masonry constructions*. Springer Verlag, Berlin, Germany, 2013. 55

E. Cosserat and F. Cosserat. *Théorie des corps déformables*. A. Hermann et fils, 1909. 123

S. Courtiaud, N. Lecysyn, G. Damamme, T. Poinsot, and L. Selle. Analysis of mixing in high-explosive fireballs using small-scale pressurised spheres. *Shock Waves*, 29(2): 339–353, 2019. 233, 234

C. Cranz. Lehrbuch der ballistik. *Julius Springer, Berlin*, 27, 1925. 12, 230, 239, 266

P. A. Cundall and O. D. Strack. A discrete numerical model for granular assemblies. *geotechnique*, 29(1):47–65, 1979. 96

G. H. Custard and J. R. Thayer. Target response to explosive blast. ad0715475. Technical report, Falcon Research and Development. U.S. Department of Defense, 1970. 66

G. Cybenko. Approximation by superpositions of a sigmoidal function. *Mathematics of control, signals and systems*, 2(4):303–314, 1989. 175, 183

A. M. D'Altri, S. de Miranda, G. Castellazzi, and V. Sarhosis. A 3d detailed micro-model for the in-plane and out-of-plane numerical analysis of masonry panels. *Computers & Structures*, 206:18–30, 2018. 54

A. M. DAltri, S. De Miranda, G. Castellazzi, V. Sarhosis, J. Hudson, and D. Theodossopoulos. Historic barrel vaults undergoing differential settlements. *International Journal of Architectural Heritage*, pages 1–14, 2019. 54

A. M. D'Altri, F. Messali, J. Rots, G. Castellazzi, and S. de Miranda. A damaging block-based model for the analysis of the cyclic behaviour of full-scale masonry structures. *Engineering Fracture Mechanics*, 209:423–448, 2019. 138

A. M. DAltri, V. Sarhosis, G. Milani, J. Rots, S. Cattari, S. Lagomarsino, E. Sacco, A. Tralli, G. Castellazzi, and S. de Miranda. Modeling strategies for the computational analysis of unreinforced masonry structures: review and classification. *Archives of Computational Methods in Engineering*, pages 1–33, 2019. 52

R. O. Davis and A. P. Selvadurai. *Plasticity and geomechanics*. Cambridge university press, 2005. 33, 34, 40, 56

W. C. Davis. Shock waves; rarefaction waves; equations of state. In *Explosive effects and applications*, pages 47–113. Springer, 1998. 14

D. D'Ayala and E. Speranza. Definition of collapse mechanisms and seismic vulnerability of historic masonry buildings. *Earthquake Spectra*, 19(3):479–509, 2003. 55

M. J. DeJong. *Seismic assessment strategies for masonry structures*. PhD thesis, Massachusetts Institute of Technology, 2009. 40, 43

M. J. DeJong, L. De Lorenzis, S. Adams, and J. A. Ochsendorf. Rocking stability of masonry arches in seismic regions. *Earthquake Spectra*, 24(4):847–865, 2008. 45, 47, 55, 104

G. Del Piero. Limit analysis and no-tension materials. *International Journal of Plasticity*, 14(1-3):259–271, 1998. 55

M. Del Prete, F. Guadagno, and G. Scarascia-Mugnozza. Earthquake induced damage in an historic area: the september–october 1997 seismic sequence which affected assisi, central italy. *Bulletin of Engineering Geology and the Environment*, 57(1):101–109, 1998. 47

J. M. Dewey. *Measurement of the Physical Properties of Blast Waves*, pages 53–86. Springer International Publishing, Cham, 2016. 9, 15, 22

M. Dhanasekar, P. W. Kleeman, and A. W. Page. Biaxial stress-strain relations for brick masonry. *Journal of structural Engineering*, 111(5):1085–1100, 1985. 33

J. S. Diaz. Explosion analysis from images: Trinity and beirut, 2020. 12

E. G. Dimitrakopoulos and M. J. DeJong. Revisiting the rocking block: closed-form solutions and similarity laws. *Proceedings of the Royal Society of London A: Mathematical, Physical and Engineering Sciences*, 468(2144):2294–2318, 2012. 55, 65

T. Dozat. Incorporating Nesterov momentum into Adam. 2016. 195

H. Draganić, D. Varevac, and S. Lukić. An overview of methods for blast load testing and devices for pressure measurement. *Advances in Civil Engineering*, 2018, 2018. 1, 230, 231, 232

V. Drosos and I. Anastasopoulos. Shaking table testing of multidrum columns and portals. *Earthquake Engineering & Structural Dynamics*, 43(11):1703–1723, 2014. 253

A. Drougkas, L. Pelà, and P. Roca. Numerical modelling of masonry shear walls failure mechanisms. In *Proceedings of 9th International Masonry Conference, Guimarães, Portugal*, 2014. 54

R. Eggersmann, T. Kirchdoerfer, S. Reese, L. Stainier, and M. Ortiz. Model-free data-driven inelasticity. *Computer Methods in Applied Mechanics and Engineering*, 350: 81–99, 2019. 59, 176

A. P. V. D. Eijnden, P. Bésuelle, F. Collin, R. Chambon, and J. Desrues. Modeling the strain localization around an underground gallery with a hydro-mechanical double scale model ; effect of anisotropy. *Computers and Geotechnics*, 2016. ISSN 0266-352X. 56, 58, 175, 176

I. Einav. The unification of hypo-plastic and elasto-plastic theories. *International Journal of Solids and Structures*, 49(11-12):1305–1315, 2012. 176

I. Einav, G. Houlsby, and G. Nguyen. Coupled damage and plasticity models derived from energy and dissipation potentials. *International Journal of Solids and Structures*, 44(7-8):2487–2508, 2007. 190

European Committee for Standardization. Eurocode 6: Design of masonry structures. 2010. 40

M. Fantin, T. Ciblac, and M. Brocato. Resistance of flat vaults taking their stereotomy into account. *Journal of Mechanics of Materials and Structures*, 13(5):657–677, 2019. 43, 103

V. R. Feldgun, Y. S. Karinski, I. Edri, and D. Z. Yankelevsky. Prediction of the quasi-static pressure in confined and partially confined explosions and its application to blast response simulation of flexible structures. *International Journal of Impact Engineering*, 90:46–60, 2016. 10

F. Feyel. A multilevel finite element method (FE2) to describe the response of highly non-linear structures using generalized continua. *Computer Methods in applied Mechanics and engineering*, 192(28-30):3233–3244, 2003. ISSN 00457825. 54, 56, 57, 58, 175, 176

T. Forgács, V. Sarhosis, and K. Bagi. Minimum thickness of semi-circular skewed masonry arches. *Engineering Structures*, 140:317–336, 2017. 104, 108

M. Fragiadakis, I. Stefanou, and I. N. Psycharis. Vulnerability assessment of damaged classical multidrum columns. In *Computational Modeling of Masonry Structures Using the Discrete Element Method*, pages 235–253. IGI Global, 2016. 253

A. L. Frankel, R. E. Jones, C. Alleman, and J. A. Templeton. Predicting the mechanical response of oligocrystals with deep learning. *Computational Materials Science*, 169: 109099, 2019. 58, 176

C. François. TEDxRennes2020. Faire du froid avec du son à partir de la chaleur, 2020. URL `https://www.tedxrennes.com/`. https://www.equium.fr/. 232

L. Freund. Crack propagation in an elastic solid subjected to general loading-I. Constant rate of extension. *Journal of the Mechanics and Physics of Solids*, 20(3):129 – 140, 1972a. ISSN 0022-5096. 37

L. Freund. Crack propagation in an elastic solid subjected to general loading-II. Non-uniform rate of extension. *Journal of the Mechanics and Physics of Solids*, 20(3):141 – 152, 1972b. ISSN 0022-5096. 37

H. Friaa, M. L. Hellara, I. Stefanou, K. Sab, and A. Dogui. Artificial neural networks prediction of in-plane and out-of-plane homogenized coefficients of hollow blocks masonry wall. *Meccanica*, 55:525–545, 2020. 54, 58, 226

F. G. Friedlander. The diffraction of sound pulses. i. diffraction by a semi-infinite plate. *Proceedings of the Royal Society of London A*, (186):322 – 344, 1946. 22

B. Gabrielsen, C. Wilton, and K. Kaplan. Response of arching walls and debris from interior walls caused by blast loading. Technical report, URS Reasearch Company, San Mateo. CA, 1975. 1, 48, 115, 230, 231

S. Gajek, M. Schneider, and T. Böhlke. On the micromechanics of deep material networks. *Journal of the Mechanics and Physics of Solids*, page 103984, 2020. 58, 176

J. Gálvez, J. Planas, J. Sancho, E. Reyes, D. Cendón, and M. Casati. An embedded cohesive crack model for finite element analysis of quasi-brittle materials. *Engineering Fracture Mechanics*, 109:369–386, 2013. 148

K. Gault, I. Sochet, L. Hakenholz, and A. Collignon. Influence of the explosion center on shock wave propagation in a confined room. *Shock Waves*, 30:473–481, 2020. 233

M. Gavrilov, R. Chétrite, and J. Bechhoefer. Direct measurement of weakly nonequilibrium system entropy is consistent with gibbs–shannon form. *Proceedings of the National Academy of Sciences*, 114(42):11097–11102, 2017. 176

E. E. Gdoutos. *Fracture mechanics: an introduction*, volume 263. Springer Nature, 2020. 33, 40

N. Gebbeken, T. Linse, and T. Araújo. Masonry under dynamic actionsexperimental investigations, material modeling and numerical simulations. *Advances in Protective Structures Research*, 1:131, 2012. 39

M. Geers, V. G. Kouznetsova, and W. Brekelmans. Multiscale first-order and second-order computational homogenization of microstructures towards continua. *International Journal for Multiscale Computational Engineering*, 1(4), 2003. 57

M. G. Geers, V. G. Kouznetsova, and W. Brekelmans. Multi-scale computational homogenization: Trends and challenges. *Journal of computational and applied mathematics*, 234(7):2175–2182, 2010. 57

P. Germain. The method of virtual power in continuum mechanics. part 2: Microstructure. *SIAM Journal on Applied Mathematics*, 25(3):556–575, 1973a. 123

P. Germain. La méthode des puissances virtuelles en mécanique des milieux continus, premiere partie: théorie du second gradient. *Journal de mécanique*, 12(2):235–274, 1973b. 123

A. Géron. *Hands-On Machine Learning with Scikit-Learn, Keras, and TensorFlow: Concepts, Tools, and Techniques to Build Intelligent Systems*. O'Reilly Media, 2019. 175, 177, 181, 182, 183, 186, 187

J. Ghaboussi and D. Sidarta. New nested adaptive neural networks (NANN) for constitutive modeling. *Computers and Geotechnics*, 22(1):29–52, 1998. 58, 173, 175

J. Ghaboussi, J. H. Garrett, and X. Wu. Knowledge-based modeling of material behavior with neural networks. *Journal of Engineering Mechanics*, 117(1):132–153, 1991. 58, 173, 175, 180, 202, 213

F. Ghavamian and A. Simone. Accelerating multiscale finite element simulations of history-dependent materials using a recurrent neural network. *Computer Methods in Applied Mechanics and Engineering*, 357:112594, 2019. 58, 173, 176

G. Giambanco, S. Rizzo, and R. Spallino. Numerical analysis of masonry structures via interface models. *Computer methods in applied mechanics and engineering*, 190(49-50): 6493–6511, 2001. 54

M. Gilbert, B. Hobbs, and T. Molyneaux. The performance of unreinforced masonry walls subjected to low-velocity impacts: experiments. *International Journal of Impact Engineering*, 27(3):231–251, 2002. 43, 44, 48, 230

M. Godio, I. Stefanou, K. Sab, J. Sulem, and S. Sakji. A limit analysis approach based on cosserat continuum for the evaluation of the in-plane strength of discrete media: Application to masonry. *European Journal of Mechanics - A/Solids*, 66:168 – 192, 2017. ISSN 0997-7538. 53, 95, 96, 123, 137

M. Godio, I. Stefanou, and K. Sab. Effects of the dilatancy of joints and of the size of the building blocks on the mechanical behavior of masonry structures. *Meccanica*, 53 (7):1629–1643, May 2018. 54, 56, 95, 96, 97, 100, 103, 116, 120, 132, 317

S. A. Granström. Loading characteristics of air blasts from detonating charges. Technical Report 100, Transactions of the Royal Institute of Technology, Stockholm, 1956. 22, 23

X. Gu, Q. Zhang, D. Huang, and Y. Yv. Wave dispersion analysis and simulation method for concrete shpb test in peridynamics. *Engineering Fracture Mechanics*, 160:124 – 137, 2016. ISSN 0013-7944. 86

G. Guinea, J. Planas, and M. Elices. A general bilinear fit for the softening curve of concrete. *Materials and structures*, 27(2):99–105, 1994. 144

N. Guo and J. Zhao. A coupled FEM/DEM approach for hierarchical multiscale modelling of granular media. *International Journal for Numerical Methods in Engineering*, 99(11): 789–818, 2014. 56, 175

H. Hao and B. Tarasov. Experimental study of dynamic material properties of clay brick and mortar at different strain rates. *Australian Journal of Structural Engineering*, 8 (2):117–132, 2008. 38, 39

H. Hao and Y. Zhou. Dynamic response of rigid blocks to simultaneous horizontal and vertical ground shock. *Advances in Structural Engineering*, 15(7):1069–1082, 2012. 65, 66, 67, 78

S. Harsh, Z. Shen, and D. Darwin. Strain-rate sensitive behavior of cemet paste and mortar in compression. American Concrete Institute, 1990. 38, 39

Y. Heider, K. Wang, and W. Sun. SO(3)-invariance of informed-graph-based deep neural network for anisotropic elastoplastic materials. *Computer Methods in Applied Mechanics and Engineering*, 363:112875, 2020. ISSN 0045-7825. 58, 173, 175, 180

A. W. Hendry. *Structural masonry*. Macmillan International Higher Education, 1998. 34

J. Heyman. *The Mansonry Arch*. 1982. 104

J. Heyman. *The stone skeleton*. Cambridge University Press, Cambridge, UK, 1995. 56, 137

A. Hillerborg. The theoretical basis of a method to determine the fracture energy g_f of concrete. *Materials and structures*, 18(4):291–296, 1985. 36, 37

A. Hillerborg, M. Modéer, and P. E. Petersson. Analysis of crack formation and crack growth in concrete by means of fracture mechanics and finite elements. *Cement and Concrete Resistance*, 6:773–782, 1976. 3, 86, 138, 142, 143, 167

G. Hoffinann and P. Schubert. Compressive strength of masonry parallel to the bed joints. 1994. 33

B. Hopkinson. British ordinance board minutes 13565. *The National Archives, Kew, UK*, 11, 1915. 12, 230, 239, 266

G. Houlsby and A. Puzrin. A thermomechanical framework for constitutive models for rate-independent dissipative materials. *International journal of Plasticity*, 16(9):1017–1047, 2000. 181, 190

G. T. Houlsby and A. M. Puzrin. *Principles of hyperplasticity: an approach to plasticity theory based on thermodynamic principles*. Springer Science & Business Media, 2007. 176, 181, 190, 191, 194, 208

G. W. Housner. The behavior of inverted pendulum structures during earthquakes. *Bulletin of the seismological society of America*, 53(2):403–417, 1963. 65, 71

Y. H. Hu and J.-N. Hwang. Handbook of neural network signal processing, 2002. 181

D. Z. Huang, K. Xu, C. Farhat, and E. Darve. Learning constitutive relations from indirect observations using deep neural networks. *Journal of Computational Physics*, page 109491, 2020. 58, 173, 176

H. Hugoniot. Mémoire sur la propagation du mouvement dans les corps et spécialement dans les gaz parfaits, 1e partie. *Journal de l'École Polytechnique (Paris)*, 57:3–97, 1887. 15

H. Hugoniot. Mémoire sur la propagation du mouvement dans les corps et spécialement dans les gaz parfaits, 2e partie. *Journal de l'École Polytechnique (Paris)*, 58:1–125, 1889. 15

D. Hyde. ConWep: Conventional weapons effects program. *US Army Engineer Waterways Experiment Station, USA*, 1991. 23, 86, 160, 162, 163, 165

R. Ibañez, D. Borzacchiello, J. V. Aguado, E. Abisset-Chavanne, E. Cueto, P. Ladevèze, and F. Chinesta. Data-driven non-linear elasticity: constitutive manifold construction and problem discretization. *Computational Mechanics*, 60(5):813–826, 2017. 59, 176

R. Ibanez, E. Abisset-Chavanne, J. V. Aguado, D. Gonzalez, E. Cueto, and F. Chinesta. A manifold learning approach to data-driven computational elasticity and inelasticity. *Archives of Computational Methods in Engineering*, 25(1):47–57, 2018. 59, 176

Itasca Consulting Group, Inc. *3DEC 5.0* . Minneapolis, MN 55401, 2018. 54, 96, 97, 98

X. Jin, C. Hou, X. Fan, C. Lu, H. Yang, X. Shu, and Z. Wang. Quasi-static and dynamic experimental studies on the tensile strength and failure pattern of concrete and mortar discs. *Scientific reports*, 7(1):1–15, 2017. 1, 38, 39

H. Jones and A. R. Miller. The detonation of solid explosives. *Proc. Royal Soc. A*, 194: 480, 1948. 18, 25

E. Jouguet. On the propagation of chemical reactions in gases. *Journal de Mathematiques Pures et Appliquees*, 1(347–425):2, 1905. 18

S. Jung and J. Ghaboussi. Neural network constitutive model for rate-dependent materials. *Computers & Structures*, 84(15-16):955–963, 2006. 58, 173, 175

A. Kahirdeh and M. Khonsari. Energy dissipation in the course of the fatigue degradation: Mathematical derivation and experimental quantification. *International Journal of Solids and Structures*, 77:74–85, 2015. 176

V. Karlos and G. Solomos. Calculation of Blast Loads for Application to Structural Components. Technical report, Joint Research Center of the European Commission, 2013. 14, 19, 21

R. A. Keys and S. K. Clubley. Experimental analysis of debris distribution of masonry panels subjected to long duration blast loading. *Engineering Structures*, 130:229 – 241, 2017. 1, 48, 49, 50, 99, 230, 232

C.-K. Kim, J. G. Moon, M.-C. Lai, and K.-S. IM. Afterburning of tnt explosive products in air with aluminum particles. In *46th AIAA Aerospace Sciences Meeting and Exhibit*, page 1029, 2008. 233

C. N. Kingery and G. Bulmash. Technical report ARBRL-TR-02555: Air blast parameters from TNT spherical air burst and hemispherical burst. Technical report, U.S. Army Ballistic Research Laboratory, 1984. 12, 19, 21, 22, 86, 113

T. Kirchdoerfer and M. Ortiz. Data-driven computational mechanics. *Computer Methods in Applied Mechanics and Engineering*, 304:81–101, 2016. 59, 176

T. Kirchdoerfer and M. Ortiz. Data-driven computing in dynamics. *International Journal for Numerical Methods in Engineering*, 113(11):1697–1710, 2018. 59, 176

D. Konstantinidis and N. Makris. Experimental and analytical studies on the response of 1/4-scale models of freestanding laboratory equipment subjected to strong earthquake shaking. *Bulletin of Earthquake Engineering*, 8(6):1457–1477, Dec 2010. ISSN 1573-1456. 55, 65

D. Konstantinidis and M. N. Seismic response analysis of multidrum classical columns. *Earthquake Engineering & Structural Dynamics*, 34(10):1243–1270, 2005. 253

S. L. Kramer et al. *Geotechnical earthquake engineering*. Pearson Education India, 1996. 56

T. Krauthammer and A. Altenberg. Negative phase blast effects on glass panels. *International Journal of Impact Engineering*, 24(1):1 – 17, 2000. 23, 28

L. Lantz, J. Maynez, W. Cook, and C. M. D. Wilson. Blast protection of unreinforced masonry walls: a state-of-the-art review. *Advances in Civil Engineering*, 2016, 2016. 167

B. Larbi, W. Dridi, P. Dangla, and P. Le Bescop. Link between microstructure and tritiated water diffusivity in mortars: Impact of aggregates. *Cement and Concrete Research*, 82:92–99, 2016. 52

M. Larcher and F. Casadei. Explosions in Complex Geometries A Comparison of Several Approaches. *International Journal of Protective Structures*, 1(2):169–195, 2010. 25

S. Lawrence, H. Sugo, and A. Page. Masonry bond strength and the effects of supplementary cementitious materials. *Australian Journal of Structural Engineering*, 8(2):101–115, 2008. 33

E. L. Lee, H. C. Hornig, and J. W. Kury. *Adiabatic Expansion Of High Explosive Detonation Products*. 5 1968. 18, 25

J. Lee. Analysis methodology of inelastic constitutive parameter using state space method and neural network. *International Journal of Engineering & Technology*, 7(3.34), 2018. 202

M. Lefik and B. A. Schrefler. Artificial neural network as an incremental non-linear constitutive model for a finite element code. *Computer methods in applied mechanics and engineering*, 192(28-30):3265–3283, 2003. 58, 173, 175, 180, 181, 193, 197, 202, 213

P. Legrand, S. Kerampran, and M. Arrigoni. Replacing detonation by compressed balloon approaches in finite element models. *Advances in Civil Engineering*, 2020, 2020. 25

J. Lemos. Numerical issues in the representation of masonry structural dynamics with Discrete Elements. *Proceedings of the 1st ECCOMAS Thematic Conference on Computational Methods in Structural Dynamics and Earthquake Engineering (COMPDYN 2019), Papadrakakis, Fraiadakis (eds), Crete, Greece, 1315 June*, page 1126, 2007a. 317

J. Lemos. Contact representation in rigid block models of masonry. *International Journal of Masonry Research and Innovation*, 2:321–334, 2017. 317, 318

J. Lemos. Discrete Element Modeling of the Seismic Behavior of Masonry Construction. *Buildings*, 9(43), 2019. 95, 96

J. V. Lemos. Discrete element modeling of masonry structures. *International Journal of Architectural Heritage*, 1(2):190–213, 2007b. 54

C. Lesté-Lasserre. Scientists are leading Notre Dames restoration-and probing mysteries laid bare by its devastating fire. *American Association for the advancement of science*, 2020. 47

Z. Li, L. Chen, Q. Fang, H. Hao, Y. Zhang, H. Xiang, W. Chen, S. Yang, and Q. Bao. Experimental and numerical study of unreinforced clay brick masonry walls subjected to vented gas explosions. *International Journal of Impact Engineering*, 104:107 – 126, 2017. 1, 48, 230, 231

V. I. Lishak, V. I. Yagust, and D. Z. Yankelevsky. 2-d orthotropic failure criteria for masonry. *Engineering structures*, 36:360–371, 2012. 41, 42

C. Liu, Q. Sun, and Y. Yang. Multi-scale modelling of granular pile collapse by using material point method and discrete element method. *Procedia Engineering*, 175:29–35, 2017. 56, 175

Z. Liu and C. Wu. Exploring the 3d architectures of deep material network in data-driven multiscale mechanics. *Journal of the Mechanics and Physics of Solids*, 127:20–46, 2019. 58, 176

O. Lloberas-Valls, F. Everdij, D. Rixen, A. Simone, and B. Sluys. Concurrent multiscale analysis of heterogeneous materials. *Delft University of Technology*, 2, 2012. 57

O. Lloberas Valls, M. Raschi Schaw, A. E. Huespe, and X. Oliver Olivella. Reduced finite element square techniques (rfe2): towards industrial multiscale fe software. In *COMPLAS 2019: XV International Conference on Computational Plasticity: Fundamentals and Applications*, pages 157–169. International Centre for Numerical Methods in Engineering (CIMNE), 2019. 54, 56, 58, 175

A. Lloyd, E. Jacques, M. Saatcioglu, D. Palermo, I. Nistor, and T. Tikka. Capabilities of a shock tube to simulate blast loading on structures. *Special Publication*, 281:1–20, 2011. 232

H. R. Lotfi and P. B. Shing. Interface model applied to fracture of masonry structures. *Journal of structural engineering*, 120(1):63–80, 1994. 54

P. Lourenco, J. G. Rots, and J. Blaauwendraad. Two approaches for the analysis of masonry structures: micro and macro-modeling. *HERON, 40 (4), 1995*, 1995. 145

P. B. Lourenço. Computational strategies for masonry structures. *TU Delft, The Netherlands*, PhD Thesis, 1997. 36, 53, 95, 137

P. B. Lourenço, J. G. Rots, and J. Blaauwendraad. Continuum model for masonry: parameter estimation and validation. *Journal of structural engineering*, 124(6):642–652, 1998. 53, 137

P. B. Lourenço, G. Milani, A. Tralli, and A. Zucchini. Analysis of masonry structures: review of and recent trends in homogenization techniques. *Canadian Journal of Civil Engineering*, 34(11):1443–1457, 2007. 2, 54, 137

P. B. Lourenço and L. F. Ramos. Characterization of cyclic behavior of dry masonry joints. *Journal of Structural Engineering*, 130(5):779–786, 2004. 35, 97, 102

X. Lu, D. G. Giovanis, J. Yvonnet, V. Papadopoulos, F. Detrez, and J. Bai. A data-driven computational homogenization method based on neural networks for the nonlinear anisotropic electrical response of graphene/polymer nanocomposites. *Computational Mechanics*, 64(2):307–321, 2019. 58, 173, 176

D. Mackenzie. Cool sounds at 200 decibels. *Science*, 278(5346):2060–2060, 1997. 232

N. Makris and D. Konstantinidis. The rocking spectrum and the limitations of practical design methodologies. *Earthquake Engineering & Structural Dynamics*, 32(2):265–289, feb 2003. ISSN 0098-8847. 65

N. Makris and M. F. Vassiliou. Planar rocking response and stability analysis of an array of free-standing columns capped with a freely supported rigid beam. *Earthquake Engineering & Structural Dynamics*, 42(3):431–449, mar 2013a. ISSN 00988847. 91

N. Makris and M. F. Vassiliou. Planar rocking response and stability analysis of an array of free-standing columns capped with a freely supported rigid beam. *Earthquake Engineering & Structural Dynamics*, 42(3):431–449, 2013b. 253

D. Malomo, M. J. DeJong, and A. Penna. Distinct element modelling of the in-plane cyclic response of urm walls subjected to shear-compression. *Earthquake Engineering & Structural Dynamics*, 2019. 97, 318

S. Marfia and E. Sacco. Multiscale damage contact-friction model for periodic masonry walls. *Computer Methods in Applied Mechanics and Engineering*, 205:189–203, 2012. 138

P. M. Mariano. Configurational forces in continua with microstructure. *Zeitschrift für angewandte Mathematik und Physik ZAMP*, 51(5):752–791, 2000. 123

P. M. Mariano and L. Galano. *Fundamentals of the Mechanics of Solids*. Springer, 2015. 178

F. Masi, P. M. Mariano, and P. Vannucci. Blast actions in aircrafts: an integrated methodology for designing protection devices. *Engineering Structures*, 175:895–911, 2018a. ISSN 0141-0296. 24

F. Masi, I. Stefanou, and P. Vannucci. A study on the effects of an explosion in the Pantheon of Rome. *Engineering Structures*, 164:259–273, 2018b. ISSN 0141-0296. 14, 25, 26, 27, 79, 166, 272, 312

F. Masi, I. Stefanou, P. Vannucci, and V. Maffi-Berthier. Rocking response of inverted pendulum structures under blast loading. *International Journal of Mechanical Sciences*, 157-158:833 – 848, 2019a. ISSN 0020-7403. 20, 120, 132, 234, 235, 241, 266, 305, 345

F. Masi, I. Stefanou, P. Vannucci, and V. Maffi-Berthier. A discrete element method approach for the preservation of the architectural heritage against explosions. *Proceedings of the 12th International Congress on Mechanics Thessaloniki (HSTAM), Thessaloniki, Greece, 22-25 September*, 2019b. 56, 96, 97, 98, 100, 317

F. Masi, I. Stefanou, V. Maffi-Berthier, and P. Vannucci. A discrete element method based-approach for arched masonry structures under blast loads. *Engineering Structures*, 216:110721, 2020a. ISSN 0141-0296. 24, 56, 253, 345

F. Masi, I. Stefanou, P. Vannucci, and V. Maffi-Berthier. Resistance of museum artefacts against blast loading. *Journal of Cultural Heritage*, 2020b. 266

R. Masiani and P. Trovalusci. Cosserat and cauchy materials as continuum models of brick masonry. *Meccanica*, 31(4):421–432, 1996. 123, 137

T. Massart, R. Peerlings, and M. Geers. An enhanced multi-scale approach for masonry wall computations with localization of damage. *International journal for numerical methods in engineering*, 69(5):1022–1059, 2007. 138

G. A. Maugin and W. Muschik. Thermodynamics with internal variables. Part I. General concepts, 1994. 178, 180

W. M. C. McKenzie. *Design of Structural Masonry*. Red Globe Press, 2001. 43

W. McKinney et al. Pandas: a foundational Python library for data analysis and statistics. *Python for High Performance and Scientific Computing*, 14(9), 2011. 192

D. Merkle, M. Rochefort, and C. Tuan. Equipment shock tolerance. Technical Report F08635-88-C-0067, U. S. Air Force Civil Engineering Support Agency. Tyndall Air Force Base, Albuquerque, NM, 1993. 65, 66

A. Meurer, C. P. Smith, M. Paprocki, O. Čertík, S. B. Kirpichev, M. Rocklin, A. Kumar, S. Ivanov, J. K. Moore, S. Singh, et al. SymPy: symbolic computing in Python. *PeerJ Computer Science*, 3:e103, 2017. 192

M. A. Meyers. *Dynamic behavior of materials*. John wiley & sons, 1994. 86

G. Michaloudis and N. Gebbeken. Modeling masonry walls under far-field and contact detonations. *International Journal of Impact Engineering*, 123:84 – 97, 2019. ISSN 0734-743X. 1, 48, 50, 95, 99, 100, 101, 138, 148, 150, 230, 231

G. Milani, P. B. Lourenço, and A. Tralli. Homogenised limit analysis of masonry walls, part i: Failure surfaces. *Computers & structures*, 84(3-4):166–180, 2006. 137

M. Milankovitch. Theorie der druckkurven. *Zeitschrift für Mathematik und Physik*, 55: 1–27, 1907. 56, 104, 105

M. Mishra, A. Bhatia, and D. A. Maity. A comparative study of regression, neural network and neuro-fuzzy inference system for determining the compressive strength of brickmortar masonry by fusing nondestructive testing data. *Engineering with Computers*, 2019. 54, 58, 226

MIT. Circ. N. 617 of 2/2/2009: Istruzioni per l'applicazione delle nuove norme tecniche per le costruzioni di cui al Decreto Ministeriale 14 Gennaio 2008. Technical report, Ministry of Infrastructures and Transportation, Italy, 2009. 34

T. M. Mitchell et al. Machine learning. 1997. *Burr Ridge, IL: McGraw Hill*, 45(37): 870–877, 1997. 175

H. Moseley. The mechanical principles of engineering and architecture, eds, 1853. 56, 104

M. Mozaffar, R. Bostanabad, W. Chen, K. Ehmann, J. Cao, and M. Bessa. Deep learning predicts path-dependent plasticity. *Proceedings of the National Academy of Sciences*, 116(52):26414–26420, 2019. 58, 173, 176, 193

MyMiniFactory. *Scan The World*. 5 Sycamore Street, London, UK. 312, 313

C. E. Needham. Ideal high explosive detonation waves. In *Blast Waves*, pages 41–71. Springer, 2018. 15, 16, 18, 23

J. Neils. *The Parthenon: from antiquity to the present*. Cambridge University Press, 2005. 253

V. P. Nguyen, M. Stroeven, and L. J. Sluys. Multiscale continuous and discontinuous modeling of heterogeneous materials: a review on recent developments. *Journal of Multiscale Modelling*, 3(04):229–270, 2011. 56, 57

M. Nitka, G. Combe, C. Dascalu, and J. Desrues. Two-scale modeling of granular materials: a DEM-FEM approach. *Granular Matter*, 13(3):277–281, mar 2011. ISSN 1434-5021. 54, 56, 58, 175, 176

M. A. Nuggehally, M. S. Shephard, C. Picu, and J. Fish. Adaptive model selection procedure for concurrent multiscale problems. *International Journal for Multiscale Computational Engineering*, 5(5), 2007. 57

J. A. Ochsendorf. *Collapse of masonry structures*. PhD thesis, University of Cambridge, 2002. 56

A. Oishi and G. Yagawa. Computational mechanics enhanced by deep learning. *Computer Methods in Applied Mechanics and Engineering*, 327:327–351, 2017. 58

F. Omori. Seismic experiments on the fracturing and overturning of columns. *Publications of the Earthquake Investigation Committe in Foreign Language*, 4:69–141, 1900. 65

F. Omori. On the overturning and sliding of columns. *Publications of the Earthquake Investigation Committe in Foreign Language*, 12:8–27, 1902. 65

A. Orduña. Block users manual. *Guimarães: University of Minho*, 2004. 56

J. Ožbolt, A. Sharma, B. İrhan, and E. Sola. Tensile behavior of concrete under high loading rates. *International Journal of Impact Engineering*, 69:55–68, 2014. 36, 37

A. Page. The biaxial compressive strength of brick masonry. *Proceedings of the Institution of Civil Engineers*, 71(3):893–906, 1981. 1, 33, 34, 35

A. Page. The strength of brick masonry under biaxial tension-compression. *International journal of masonry construction*, 3(1):26–31, 1983. 1, 33, 34, 35

A. W. Page. Finite element model for masonry. *Journal of the Structural Division*, 104 (8):1267–1285, 1978. 137

G. Pande, J. Liang, and J. Middleton. Equivalent elastic moduli for brick masonry. *Computers and Geotechnics*, 8(3):243–265, 1989. 137

B. Pantò, F. Cannizzaro, S. Caddemi, and I. Caliò. 3d macro-element modelling approach for seismic assessment of historical masonry churches. *Advances in Engineering Software*, 97:40–59, 2016. 55

C. Papadopoulos, E. Basanou, I. Vardoulakis, M. Boulon, and G. Armand. Mechanical behaviour of Dionysos marble smooth joints under cyclic loading: II constitutive modelling. In *Proceedings of the international conference on mechanics of jointed and faulted rock*, Vienna, Austria, 1998. 68

R. Pape, K. R. Mniszewski, and A. Longinow. Explosion phenomena and effects of explosions on structures. i: Phenomena and effects. *Practice Periodical on Structural Design and Construction*, 15(2):135–140, 2010. 9, 15

F. Parisi, C. Balestrieri, and D. Asprone. Blast resistance of tuff stone masonry walls. *Engineering Structures*, 113:233 – 244, 2016. ISSN 0141-0296. 317

F. Peña, F. Prieto, P. B. Lourenço, A. Campos Costa, and J. V. Lemos. On the dynamics of rocking motion of single rigidblock structures. *Earthquake Engineering & Structural Dynamics*, 36(15):2383–2399, 2007. 55, 65

L. Pelà, M. Cervera, and P. Roca. An orthotropic damage model for the analysis of masonry structures. *Construction and Building Materials*, 41:957–967, 2013. 53, 137

R. J.-M. Pellenq, A. Kushima, R. Shahsavari, K. J. Van Vliet, M. J. Buehler, S. Yip, and F.-J. Ulm. A realistic molecular model of cement hydrates. *Proceedings of the National Academy of Sciences*, 106(38):16102–16107, 2009. 53

G. C. Peng, M. Alber, A. B. Tepole, W. R. Cannon, S. De, S. Dura-Bernal, K. Garikipati, G. Karniadakis, W. W. Lytton, P. Perdikaris, et al. Multiscale modeling meets machine learning: What can we learn? *Archives of Computational Methods in Engineering*, pages 1–21, 2020. 58

A. Penna, S. Lagomarsino, and A. Galasco. A nonlinear macroelement model for the seismic analysis of masonry buildings. *Earthquake Engineering & Structural Dynamics*, 43(2):159–179, 2014. 55

A. D. Penwarden, P. F. Grigg, and R. Rayment. Measurements of wind drag on people standing in a wind tunnel. *Building and environment*, 13(2):75–84, 1978. 310

J. M. Pereira and P. B. Lourenço. Experimental characterization of masonry and masonry components at high strain rates. *Journal of Materials in Civil Engineering*, 29(2): 04016223, 2017. 1, 38, 39

J. M. Pereira, J. Campos, and P. B. Lourenço. Masonry infill walls under blast loading using confined underwater blast wave generators (wbwg). *Engineering Structures*, 92: 69–83, 2015. 1, 232, 233

P.-E. Petersson. Crack growth and development of fracture zones in plain concrete and similar materials. 1981. 143

M. Petracca. Computational multiscale analysis of masonry structures. 2016. 54, 138

M. Petracca, L. Pelà, R. Rossi, S. Oller, G. Camata, and E. Spacone. Regularization of first order computational homogenization for multiscale analysis of masonry structures. *Computational mechanics*, 57(2):257–276, 2016. 143, 146

M. Petracca, L. Pelà, R. Rossi, S. Zaghi, G. Camata, and E. Spacone. Micro-scale continuous and discrete numerical models for nonlinear analysis of masonry shear walls. *Construction and Building Materials*, 149:296–314, 2017. 53, 137

S. Petry and K. Beyer. Scaling unreinforced masonry for reduced-scale seismic testing. *Bulletin of earthquake engineering*, 12(6):2557–2581, 2014. 95, 101, 120, 132

S. Petry and K. Beyer. Cyclic test data of six unreinforced masonry walls with different boundary conditions. *Earthquake Spectra*, 31(4):2459–2484, 2015a. 101

S. Petry and K. Beyer. Cyclic test data of six unreinforced masonry walls with different boundary conditions. *Earthquake Spectra*, 31(4):2459–2484, 2015b. 40, 95, 99, 148

J. Planas, M. Elices, and G. Guinea. Measurement of the fracture energy using three-point bend tests: Part 2influence of bulk energy dissipation. *Materials and Structures*, 25(5):305–312, 1992. 144

V. Plevris and P. G. Asteris. Modeling of masonry failure surface under biaxial compressive stress using neural networks. *Construction and Building Materials*, 55: 447 – 461, 2014. ISSN 0950-0618. 54, 58, 226

F. Portioli, C. Casapulla, M. Gilbert, and L. Cascini. Limit analysis of 3d masonry block structures with non-associative frictional joints using cone programming. *Computers & Structures*, 143:108–121, 2014. 56

I. Psycharis, D. Y. Papastamatiou, and A. P. Alexandris. Parametric investigation of the stability of classical columns under harmonic and earthquake excitations. *Earthquake Engineering and Structural Dynamics*, 29:1093–1109, 2000. 253

I. N. Psycharis, M. Fragiadakis, and I. Stefanou. Seismic reliability assessment of classical columns subjected to near-fault ground motions. *Earthquake Engineering & Structural Dynamics*, 42(14):2061–2079, jun 2013. ISSN 00988847. 91

A. Quinonez, J. Zessin, A. Nutzel, and J. Ochsendorf. Small-scale models for testing masonry structures. In *Advanced Materials Research*, volume 133, pages 497–502. Trans Tech Publ, 2010. 44, 46

D. Radenkovic. Théorie des charges limites. Extension a la mécanique du sol. In *J. Mandel (ed.), Séminaire de Plasticité*, pages 129–141. Ecole Polytechnique 1961, Magasin C.T.O., 1962. 56

M. L. Raffa, F. Lebon, E. Sacco, and H. Welemane. A multi-level interface model for damaged masonry. 2013. 54

S. H. Rafsanjani, P. B. Lourenço, and N. Peixinho. Implementation and validation of a strain rate dependent anisotropic continuum model for masonry. *International Journal of Mechanical Sciences*, 104:24–43, 2015. 1, 53, 137, 148

M. Raissi, P. Perdikaris, and G. E. Karniadakis. Physics-informed neural networks: A deep learning framework for solving forward and inverse problems involving nonlinear partial differential equations. *Journal of Computational Physics*, 378:686–707, 2019. 59, 177, 179, 226

W. J. Rankine. On the thermodynamic theory of waves of finite longitudinal disturbance. *Philosophical Transactions of the Royal Society of London*, 160:277–288, 1870. 15

H. Rattez, I. Stefanou, and J. Sulem. The importance of Thermo-Hydro-Mechanical couplings and microstructure to strain localization in 3D continua with application to seismic faults. Part I: Theory and linear stability analysis. *Journal of the Mechanics and Physics of Solids*, 115:54–76, 2018a. ISSN 0022-5096. 58

H. Rattez, I. Stefanou, J. Sulem, M. Veveakis, and T. Poulet. The importance of Thermo-Hydro-Mechanical couplings and microstructure to strain localization in 3D continua with application to seismic faults. Part II: Numerical implementation and post-bifurcation analysis. *Journal of the Mechanics and Physics of Solids*, 115:1 – 29, 2018b. ISSN 0022-5096. 58

J. W. S. L. Rayleigh. The problem of the whispering gallery. *Philosophical Magazine, Series 6*, 20:1001–1004, 1910. 27

J. W. S. L. Rayleigh. Further applications of bessels functions of high order to the whispering gallery and allied problems. *Philosophical Magazine, Series 6*, 27:100–109, 1914. 27

S. Reese, R. Eggersmann, T. Kirchdoerfer, L. Stainier, and M. Ortiz. Data-driven mechanics-an alternative to constitutive modeling? In *Book of Abstracts*, page 31, 2019. 59, 176

J.-F. Remacle, J. Lambrechts, B. Seny, E. Marchandise, A. Johnen, and C. Geuzainet. Blossom-quad: A non-uniform quadrilateral mesh generator using a minimum-cost perfect-matching algorithm. *International journal for numerical methods in engineering*, 89(9):1102–1119, 2012. 56, 57

A. M. Remennikov. A review of methods for predicting bomb blast effects on buildings. *Journal of Battlefield Technology*, 6:5–10, 2003. 22

E. Reyes, M. Casati, and J. Gálvez. Cohesive crack model for mixed mode fracture of brick masonry. *International Journal of Fracture*, 151(1):29, 2008. 148

R. Rezakhani and G. Cusatis. Asymptotic expansion homogenization of discrete fine-scale models with rotational degrees of freedom for the simulation of quasi-brittle materials. *Journal of the Mechanics and Physics of Solids*, 88:320–345, 2016. 57

S. Rigby, T. Lodge, S. Alotaibi, A. Barr, S. Clarke, G. Langdon, and A. Tyas. Preliminary yield estimation of the 2020 beirut explosion using video footage from social media. *Shock Waves*, 2020. 12

S. E. Rigby. *Blast Wave Clearing Effects on Finite-Sized Targets Subjected to Explosive Loads*. PhD thesis, University of Sheffield, Sheffield, UK, 2014. 23, 27

S. E. Rigby, A. Tyas, T. Bennett, S. D. Clarke, and S. D. Fay. The negative phase of the blast load. *International Journal of Protective Structures*, 5(1):1–19, 2014. 23, 28

P. Roca, M. Cervera, G. Gariup, et al. Structural analysis of masonry historical constructions. classical and advanced approaches. *Archives of computational methods in engineering*, 17(3):299–325, 2010. 40, 54

P. Roca, P. B. Lourenco, and A. Gaetani. *Historic Construction and Conservation: Materials, Systems and Damage*. Routledge, 2019. 45, 95

I. B. C. M. Rocha, P. Kerfriden, and F. P. van der Meer. On-the-fly construction of surrogate constitutive models for concurrent multiscale mechanical analysis through probabilistic machine learning, 2020. 58

K. Rokugo, M. Iwasa, T. Suzuki, and W. Koyanagi. Testing to determine tensile strain softening curve and fracture energy of concrete. In *International workshop on fracture toughness and fracture energy*, pages 153–163, 1989. 144

C. A. Ross, J. Tedesco, et al. Split-hopkinson pressure-bar tests on concrete and mortar in tension and compression. *Materials Journal*, 86(5):475–481, 1989. 36, 37

M. Rossi, C. Calderini, and S. Lagomarsino. Experimental testing of the seismic in-plane displacement capacity of masonry cross vaults through a scale model. *Bulletin of Earthquake Engineering*, 14(1):261–281, 2016. 44, 46

M. Rossi, C. C. Barentin, T. Van Mele, and P. Block. Experimental study on the behaviour of masonry pavilion vaults on spreading supports. In *Structures*, volume 11, pages 110–120. Elsevier, 2017. 44, 46

J. G. Rots. *Structural masonry: an experimental/numerical basis for practical design rules*. AA Balkema, 1997. 33, 34

E. Sacco. Micro, multiscale and macro models for masonry structures. In *Mechanics of Masonry Structures*, pages 241–291. Springer, 2014. 52

R. G. Sachs. The dependence of blast on ambient pressure and temperature. Technical report, Army Ballistic Research Lab 466, 1944. 13

J. Salençon. Théorie des charges limites. In *Séminaire de Plasticité et Viscoplasticité*, pages 205–229. Ecole Polytechnique 1972, Ediscience, 1974. 56

V. Sarhosis and J. Lemos. A detailed micro-modelling approach for the structural analysis of masonry assemblages. *Computers & Structures*, 206:66–81, 2018. 52, 54

V. Sarhosis, P. Asteris, T. Wang, W. Hu, and Y. Han. On the stability of colonnade structural systems under static and dynamic loading conditions. *Bulletin of Earthquake Engineering*, 14(4):1131–1152, 2016a. 253

V. Sarhosis, K. Bagi, J. V. Lemos, and G. Milani. *Computational modeling of masonry structures using the discrete element method*. IGI Global, 2016b. 54, 97, 318

V. Sarhosis, S. De Santis, and G. de Felice. A review of experimental investigations and assessment methods for masonry arch bridges. *Structure and Infrastructure Engineering*, 12(11):1439–1464, 2016c. 44, 45

P. Sauvan, I. Sochet, and S. Trelat. Analysis of reflected blast wave pressure profiles in a confined room. *Shock Waves*, 22(3):253–264, 2012. 233

K. Scherbatiuk and N. Rattanawangcharoen. Experimental testing and numerical modeling of soil-filled concertainer walls. *Engineering Structures*, 30(12):3545 – 3554, 2008. ISSN 0141-0296. 66, 67, 78

K. Scherbatiuk, N. Rattanawangcharoen, D. Pope, and J. Fowler. Generation of a pressure–impulse diagram for a temporary soil wall using an analytical rigid-body rotation model. *International journal of impact engineering*, 35(6):530–539, 2008. 66

K. D. Scherbatiuk. *Analytical models for calculating the response of temporary soil-filled walls subjected to blast loading*. PhD thesis, Department of Civil Engineering - University of Manitoba, Winnipeg, Manitoba, 2010. 66, 74, 78, 80, 82, 83, 84, 85

J. Schneider, M. von Ramin, A. Stottmeister, and A. Stolz. Characterization of debris throw from masonry wall sections subjected to blast. *Engineering Structures*, 203: 109729, 2020. 232

P. Schubert. Influence of mortar on the strength of masonry. *Brick and Block Masonry(8 th IBMAC) London, Elsevier Applied Science,*, 1:162–174, 1988. 33

C. Settgast, M. Abendroth, and M. Kuna. Constitutive modeling of plastic deformation behavior of open-cell foam structures using neural networks. *Mechanics of Materials*, 131:1–10, 2019. 58, 173, 175

E. E. Shapiro. *Collapse mechanisms of small-scale unreinforced masonry vaults*. PhD thesis, Massachusetts Institute of Technology, 2012. 43, 44, 45

J. Shin, A. S. Whittaker, and D. Cormie. Incident and normally reflected overpressure and impulse for detonations of spherical high explosives in free air. *Journal of Structural Engineering*, 141(12):04015057–13, 2015. 19

L. C. Silva, P. B. Lourenço, and G. Milani. Rigid block and spring homogenized model (hrbsm) for masonry subjected to impact and blast loading. *International journal of impact engineering*, 109:14–28, 2017. 1, 55

T. Skinner, M. Hargather, J. Blackwood, M. Hays, and M. Bangham. An apparatus for producing tunable, repeatable, hydrogen–oxygen-deflagrative blast waves. *Shock Waves*, 30(3):315–323, 2020. 234

I. Snyman, F. Mostert, and W. Grundling. Design and commissioning of a semi-confined blast chamber. *Defence technology*, 12(2):147–158, 2016. 233

I. Sochet. Blast effects of external explosions. 2010. 12, 15

W. G. Soper. Modeling laws related to target vulnerability. Technical Report T-9/67 (Classified), U. S. Naval Weapons Lab, Dahlgren, Virginia, 1967. 66, 78, 80, 84

O. Stamati, E. Roubin, E. Andò, and Y. Malecot. Tensile failure of micro-concrete: from mechanical tests to fe meso-model with the help of x-ray tomography. *Meccanica*, 54 (4-5):707–722, 2019. 53

I. Stefanou and E. Gerolymatou. Strain localization in geomaterials and regularization: rate-dependency, higher order continuum theories and multi-physics. In *30th ALERT Geomaterials Doctoral School*. 2019. 57, 143

I. Stefanou, J. Sulem, and I. Vardoulakis. Three-dimensional cosserat homogenization of masonry structures: elasticity. *Acta Geotechnica*, 3(1):71–83, 2008. 53, 123, 137, 154, 167

I. Stefanou, J. Sulem, and I. Vardoulakis. Homogenization of interlocking masonry structures using a generalized differential expansion technique. *International Journal of Solids and Structures*, 47(11-12):1522–1536, 2010. 137

I. Stefanou, I. Psycharis, and I.-O. Georgopoulos. Dynamic response of reinforced masonry columns in classical monuments. *Construction and Building Materials*, 25 (12):4325 – 4337, 2011a. 34, 95

I. Stefanou, I. Vardoulakis, and A. Mavraganis. Dynamic motion of a conical frustum over a rough horizontal plane. *International Journal of Non-Linear Mechanics*, 46(1): 114–124, 2011b. 67, 253, 260

I. Stefanou, K. Sab, and J.-V. Heck. Three dimensional homogenization of masonry structures with building blocks of finite strength: A closed form strength domain. *International Journal of Solids and Structures*, 54:258 – 270, 2015a. ISSN 0020-7683. 53, 137, 138, 148

I. Stefanou, K. Sab, and J.-V. Heck. Three dimensional homogenization of masonry structures with building blocks of finite strength: A closed form strength domain. *International Journal of Solids and Structures*, 54:258–270, 2015b. 95, 96, 99, 317

Stefanou, I. and Psycharis, I. and Georgopoulos, I.-O. Dynamic response of reinforced masonry columns in classical monuments. *Construction and Building Materials*, 25 (12):4325–4337, 2011. 310

L. Stewart, A. Freidenberg, T. Rodriguez-Nikl, M. Oesterle, J. Wolfson, B. Durant, K. Arnett, R. Asaro, and G. Hegemier. Methodology and validation for blast and shock testing of structures using high-speed hydraulic actuators. *Engineering Structures*, 70: 168–180, 2014. 232, 233

J. Sulem and H.-B. Mühlhaus. A continuum model for periodic two-dimensional block structures. *Mechanics of Cohesive-frictional Materials: An International Journal on Experiments, Modelling and Computation of Materials and Structures*, 2(1):31–46, 1997. 137

M. M. Swisdak Jr. Simplified kingery airblast calculations. Technical report, Naval Surface Warfare Center Indian Head Division MD, 1994. 19

G. I. Taylor. The formation of a blast wave by a very intense explosion i. theoretical discussion. *Proceedings of the Royal Society of London. Series A. Mathematical and Physical Sciences*, 201(1065):159–174, 1950. 12

A. Tengattini, E. Andò, G. D. Nguyen, G. Viggiani, and I. Einav. Double-scale assessment of micro-mechanics based constitutive models for granular materials undergoing mechanical degradation. In *International Workshop on Bifurcation and Degradation in Geomaterials*, pages 175–180. Springer, 2014. 53

P. Trovalusci and A. Pau. Derivation of microstructured continua from lattice systems via principle of virtual works: the case of masonry-like materials as micropolar, second gradient and classical continua. *Acta Mechanica*, 225(1):157–177, 2014. 137

USACE. TM 5-1300: Structures to Resist the Effects of Accidental Explosions. Technical report, U.S. Army, 1990. 19

USACE. UFC 3-340-02: Structures to Resist the Effects of Accidental Explosions. Technical report, U.S. Army, 2008. 10, 12, 14, 23, 37

F. Vales, S. Moravka, R. Brepta, and J. Cerv. Wave propagation in a thick cylindrical bar due to longitudinal impact. *JSME international journal. Ser. A, Mechanics and material engineering*, 39(1):60–70, 1996. 86

R. Van der Pluijm. Deformation controlled shear tests on masonry. *Rep. BI-92*, 104, 1992. 36

R. Van der Pluijm. Non-linear behaviour of masonry under tension. *Heron*, 42:25–54, 1997. 34, 35, 36, 38, 143, 144, 145

R. Van der Pluijm. *Out-of-Plane bending of Masonry. Behavior and Strength*. Technische Universiteit Eindhoven, 1999. 1, 33, 34, 36, 95, 97, 142

T. Van Mele, J. McInerney, M. J. DeJong, and P. Block. Physical and computational discrete modeling of masonry vault collapse. In *Structural analysis of historical constructions: proceedings of the 8th International Conference on Structural Analysis of Historical Constructions, SAHC 2012, 15-17 October, Wroclaw, Poland*, pages 2252–2560. DWE, 2012. 54

P. Vannucci. *Anisotropic elasticity*. Springer, 2018. 33, 141

P. Vannucci. Structural study of the notre-dame ancient charpente. *arXiv preprint arXiv:2005.12584*, 2020. 165

P. Vannucci, F. Masi, and I. Stefanou. A comparative study on the effects of blast actions on a monumental structure. 2017a. 20, 23, 24, 25, 27, 28, 253, 263, 305, 345

P. Vannucci, I. Stefanou, and F. Masi. Report of the project "Cathédrales durables". Technical report, CNRS, Paris, France, 2017b. 26, 165

R. K. Varma, C. P. S. Tomar, S. Parkash, and V. S. Sethi. Damage to brick masonry panel walls under high explosive detonations. *Pressure vessels and piping division. ASME*, 351:207 – 216, 1997. 48, 230, 231

P. Virtanen, R. Gommers, T. E. Oliphant, M. Haberland, T. Reddy, D. Cournapeau, E. Burovski, P. Peterson, W. Weckesser, J. Bright, et al. SciPy 1.0: fundamental algorithms for scientific computing in Python. *Nature methods*, 17(3):261–272, 2020. 192

L. F. R. Vélez, G. Magenes, and M. C. Griffith. Dry stone masonry walls in bendingpart i: Static tests. *International Journal of Architectural Heritage*, 8(1):1–28, 2014. 97

E. Voyagaki, I. N. Psycharis, and G. Mylonakis. Rocking response and overturning criteria for free standing rigid blocks to singlelobe pulses. *Soil Dynamics and Earthquake Engineering*, 46:85–95, 2013. 55, 65, 71

M. Wang, H. Hao, Y. Ding, and Z.-X. Li. Prediction of fragment size and ejection distance of masonry wall under blast load using homogenized masonry material properties. *International Journal of Impact Engineering*, 36(6):808 – 820, 2009. ISSN 0734-743X. 1

W. Wang, D. Zhang, F. Lu, S.-C. Wang, and F. Tang. Experimental study on scaling the explosion resistance of a one-way square reinforced concrete slab under a close-in blast loading. *International Journal of Impact Engineering*, 49:158–164, 2012. 230

Y. Wang, S. W. Cheung, E. T. Chung, Y. Efendiev, and M. Wang. Deep multiscale model learning. *Journal of Computational Physics*, 406:109071, 2020. 58

J. Weerheijm. *Concrete under impact tensile loading and lateral compression*. PhD thesis, TU Delft, Delft University of Technology, 1992. 37

X. Wei and H. Hao. Numerical derivation of homogenized dynamic masonry material properties with strain rate effects. *International Journal of Impact Engineering*, 36(3): 522–536, 2009. 86

X. Wei and M. G. Stewart. Model validation and parametric study on the blast response of unreinforced brick masonry walls. *International Journal of Impact Engineering*, 37 (11):1150 – 1159, 2010. ISSN 0734-743X. 1

S. Wild, A. Gailius, H. Hansen, L. Pederson, and J. Szwabowski. Pozzolanic properties of a variety of European clay bricks. *Building Research & Information*, 25(3):170–175, 1997. 99, 148

M. L. Wilkins, B. Squier, and B. Halperin. The equation of state of PBX 9404 and LX-04-01. In *Tenth Symposium (International) on Combustion*, pages 769–778. (The Combustion Institute), 1965. 18, 25

F. Wittmann, K. okugo, E. Brühwiler, H. Mihashi, and P. Simonin. Fracture energy and strain softening of concrete as determined by means of compact tension specimens. *Materials and Structures*, 21(1):21–32, 1988. 144

L. N. Y. Wong, C. Zou, and Y. Cheng. Fracturing and failure behavior of carrara marble in quasistatic and dynamic brazilian disc tests. *Rock Mechanics and Rock Engineering*, 47(4):1117–1133, 2014. 86

C. Wu, D. J. Oehlers, J. Wachl, C. Glynn, A. Spencer, M. Merrigan, and I. Day. Blast testing of rc slabs retrofitted with nsm cfrp plates. *Advances in Structural Engineering*, 10(4):397–414, 2007. 233

W. Xiao, M. Andrae, and N. Gebbeken. Air blast tnt equivalence concept for blast-resistant design. *International Journal of Mechanical Sciences*, page 105871, 2020. 12

L. Xiong, M. Wei, and Z. Xu. Effects of strain rate, temperature and freeze–thaw cycle on the mechanical properties of cement mortar composite specimen. *Structural Concrete*. 39, 40

K. Xu, D. Z. Huang, and E. Darve. Learning constitutive relations using symmetric positive definite neural networks. *arXiv preprint arXiv:2004.00265*, 2020. 58, 173, 176

S. Xu, Y. Zhao, and Z. Wu. Study on the average fracture energy for crack propagation in concrete. *Journal of materials in civil engineering*, 18(6):817–824, 2006. 37

W. Yu and D. Carrillo. Chapter 1 - hierarchical dynamic neural networks for cascade system modeling with application to wastewater treatment. In A. Y. Alanis, N. Arana-Daniel, and C. López-Franco, editors, *Artificial Neural Networks for Engineering Applications*, pages 1 – 8. Academic Press, 2019. ISBN 978-0-12-818247-5. 202

J. Zhang and N. Makris. Rocking response of free-standing blocks under cycloidal pulses. *Journal of Engineering Mechanics*, 127(5):473–483, 2001. 55, 65

J. Zhou and X. Chen. Stress-strain behavior and statistical continuous damage model of cement mortar under high strain rates. *Journal of materials in civil engineering*, 25 (1):120–130, 2013. 39, 40

H. Ziegler. *An introduction to thermomechanics*. Elsevier, 2012. 190, 191

A. Zucchini and P. B. Lourenço. A micro-mechanical model for the homogenisation of masonry. *International Journal of Solids and Structures*, 39(12):3233–3255, 2002. 137, 138

A. Zucchini and P. B. Lourenço. Mechanics of masonry in compression: Results from a homogenisation approach. *Computers & structures*, 85(3-4):193–204, 2007. 137

A. Zucchini and P. B. Lourenço. A micro-mechanical homogenisation model for masonry: Application to shear walls. *International Journal of Solids and Structures*, 46(3-4): 871–886, 2009. 138

A. Zyskowski, I. Sochet, G. Mavrot, P. Bailly, and J. Renard. Study of the explosion process in a small scale experiment–structural loading. *Journal of Loss Prevention in the Process Industries*, 17(4):291–299, 2004. 233, 234

List of publications

Journal papers

(1) F. Masi, I. Stefanou, P. Vannucci, V. Maffi-Berthier (2020). Similarity laws for the rigid-body response of masonry structures subjected to blast loads. *Submitted to the special issue Recent Advances on the Mechanics of Masonry Structures*, *Journal of Engineering Mechanics*.

(2) F. Masi, I. Stefanou, P. Vannucci, V. Maffi-Berthier (2020). Thermodynamics-based Artificial Neural Networks for constitutive modeling. *Journal of the Mechanics and Physics of Solids*, 104277 (in press). doi: 10.1016/j.jmps.2020.104277

(3) F. Masi, I. Stefanou, V. Maffi-Berthier, P. Vannucci (2020). A Discrete Element Method based-approach for arched masonry structures under blast loads, *Engineering Structures* 216, 110721. doi: 10.1016/j.engstruct.2020.110721

(4) F. Masi, I. Stefanou, P. Vannucci, V. Maffi-Berthier (2020). Resistance of museum artefacts against blast loading. *Journal of Cultural Heritage* 44, 163-173. doi: 10.1016/j.culher.2020.01.015

(5) F. Masi, I. Stefanou, P. Vannucci, V. Maffi-Berthier (2019). Rocking response of inverted pendulum structures under blast loading, *International Journal of Mechanical Sciences* 157158, 833-848. doi: 10.1016/j.ijmecsci.2019.05.024

(6) P. Vannucci, F. Masi, I. Stefanou (2019). A nonlinear approach to the wind strength of Gothic Cathedrals: the case of Notre Dame of Paris, *Engineering Structures* 183, 860-873. doi: 10.1016/j.engstruct.2019.01.030

(7) F. Masi, P. M. Mariano, P. Vannucci (2018). Blast actions in aircrafts: an integrated methodology for designing protection devices, *Engineering Structures* 175, 895-911. doi: 10.1016/j.engstruct.2018.08.082

(8) F. Masi, I. Stefanou, P. Vannucci (2018). On the origin of the cracks in the dome of the Pantheon in Rome, *Engineering Failure Analysis* 92, 587-596. doi: doi.org/10.1016/j.engfailanal.2018.06.013

(9) F. Masi, I. Stefanou, P. Vannucci (2018). A study on the effects of an explosion in the Pantheon of Rome, *Engineering Structures* 164, 259-273. doi: 10.1016/j.engstruct.2018.02.082

Technical reports

(*i*) P. Vannucci, F. Masi, I. Stefanou, V. Maffi-Berthier (2019). Structural integrity of Notre Dame Cathedral after the fire of April 15th, 2019.

(*ii*) P. Vannucci, F. Masi, I. Stefanou (2017). A study on the simulation of blast actions on a monument structure.

(*iii*) P Vannucci, I Stefanou, F Masi (2017). Report of the project Cathédrales Durables. Technical report (Confidential). CNRS, Paris, France.

Conference proceedings

(a) F. Masi, I. Stefanou, P. Vannucci, V. Maffi-Berthier (2020). Material modeling via Thermodynamics-based Artificial Neural Networks, École de Physique des Houches, Joint Structures and Common Foundations of Statistical Physics, Information Geometry and Inference for Learning. Les Houches, France, 26-31 July.

(b) F. Masi, I. Stefanou, P. Vannucci, V. Maffi-Berthier (2019). Michelangelos David or Aphrodite of Milos: who is more resistant to blast loads?, Proceedings of the 12th HSTAM International Congress on Mechanics. Thessaloniki, Greece, 22-25 September.

(c) F. Masi, I. Stefanou, P. Vannucci, V. Maffi-Berthier (2019). A Discrete Element Method approach for the preservation of the architectural heritage against explosions, Proceedings of the 12th HSTAM International Congress on Mechanics. Thessaloniki, Greece, 22-25 September.

(d) F. Masi, I. Stefanou, P. Vannucci, V. Maffi-Berthier (2019). Rocking response and overturning of museum artefacts due to explosions, Proceedings of the 7th International Conference on Computational Methods in Structural Dynamics and Earthquake Engineering. Crete, Greece, 24-26 June.

(e) F. Masi, I. Stefanou, P. Vannucci, V. Maffi-Berthier (2019). Masonry vaults under explosive loads, Proceedings of the 7th International Conference on Computational Methods in Structural Dynamics and Earthquake Engineering. Crete, Greece, 24-26 June.

(f) F. Masi, I. Stefanou, P. Vannucci, V. Maffi-Berthier (2019). Response of monumental buildings to internal explosions, Proceedings of the 7th International Conference on Computational Methods in Structural Dynamics and Earthquake Engineering. Crete, Greece, 24-26 June.

(g) F. Masi, I. Stefanou, P. Vannucci (2018). V. Maffi-Berthier. Simulations of blast effects in monumental structures, Proceedings of the 13th World Congress on Computational Mechanics / 2nd Pan American Congress on Computational Mechanics. New York City, USA, 22-27 July.

(h) F. Masi, I. Stefanou, P. Vannucci (2018). Étude de la réponse structurale de structures à géométrie complexe aux explosions : le cas du Panthéon de Rome, Proceedings of the 2ème Édition des Journées Nationales Maçonnerie, IFSTTAR. Marne- la-Vallée, France, March.

(i) F. Masi, I. Stefanou, P. Vannucci (2018). Une approche non-linéaire pour l'étude de la résistance au vent d'une cathédrale gothique : Notre Dame de Paris, Proceedings of the 2ème Édition des Journées Nationales Maçonnerie, IFSTTAR. Marne- la-Vallée, France, March.

Appendix A

Interpolations of the surface-blast parameters

The expressions for the air-blast parameters for a surface burst are given below and presented in Figure A.1. For more details we refer to Vannucci et al. (2017a); Masi et al. (2019a).

– normal incident pressure peak P_{so}:

$$\begin{aligned} P_{so}(Z) = \; & \left(1+\frac{1}{2e^{10Z}}\right)\exp\Big[0.26473 - 1.5168\ln Z \\ & -0.079822\ln^2 Z - 0.57802\sin(\ln Z) - 0.228409\sin^2(\ln Z)\Big] \end{aligned}$$

– normal reflected pressure peak P_{ro}:

$$\begin{aligned} P_{ro}(Z) \; = \; & \left(1+\frac{1}{2e^{10Z}}\right)\exp\Big[2.0304 - 1.8036\ln Z \\ & -0.09293\ln^2 Z - 0.8779\sin(\ln Z) - 0.3603\sin^2(\ln Z)\Big] \end{aligned}$$

– scaled and effective positive reflected impulse i_{rw}, i_r:

$$\begin{aligned} i_{rw}(Z,W) &= \exp\Big[-0.110157 - 1.40609\ln Z + 0.0847358\ln^2 Z\Big], \\ i_r(Z) &= W^{\frac{1}{3}} i_{rw}(Z,W) \end{aligned}$$

– scaled and effective arrival time t_{Aw}, t_A:

$$\begin{aligned} t_{Aw}(Z,W) &= \begin{cases} \exp\Big[-0.6847 + 1.4288\ln Z + 0.0290\ln^2 Z \\ \qquad +0.4108\sin(\ln Z)\Big] & \text{if } Z \geq 0.18 \text{ m/kg}^{1/3}, \\ 0.0315495 & \text{if } Z < 0.18 \text{ m/kg}^{1/3}, \end{cases} \\ t_A(Z) &= W^{\frac{1}{3}} t_{Aw}(Z,W) \end{aligned}$$

– scaled and effective positive duration time t_{ow}, t_o:

$$t_{ow}(Z,W) = \begin{cases} \exp\Big[0.592 + 2.913\ln Z - 1.287\ln^2 Z - 1.788\ln^3 Z \\ \quad + 1.151\ln^4 Z + 0.325\ln^5 Z - 0.383\ln^6 Z \\ \quad + 0.090\ln^7 Z - 0.004\ln^8 Z - 0.0004\ln^9 Z \\ \quad + 0.537\cos^7\Big[1.032\,(\ln Z - 0.859)\Big] \\ \quad\quad \sinh\Big[1.088\,(\ln Z - 2.023)\Big]\Big] & \text{if } Z \geq 0.18 \text{ m/kg}^{1/3}, \\ 0.251703 & \text{if } Z < 0.18 \text{ m/kg}^{1/3}, \end{cases}$$

$$t_o(Z) = W^{\frac{1}{3}} t_{ow}(Z,W)$$

– reflected negative pressure peak P_{ro-}:

$$P_{ro-}(Z) = \Big(0.0415 + \frac{1}{2e^{0.1449Z}}\Big)\exp\Big[-1.7850 - 0.1213\ln Z \\ -0.0514\ln^2 Z - 0.4083\sin(\ln Z) - 0.3824\sin^2(\ln Z)\Big]$$

– scaled and effective negative duration time t_{ow-}, t_{o-}:

$$t_{ow-}(Z,W) = \exp\Big[2.4052 + 0.1177\ln Z + 0.0312\ln^2 Z \\ -0.0107\ln^3 Z + 0.1092\cos(\ln Z)\Big],$$

$$t_{ow-}(Z) = W^{\frac{1}{3}} t_{ow-}(Z,W)$$

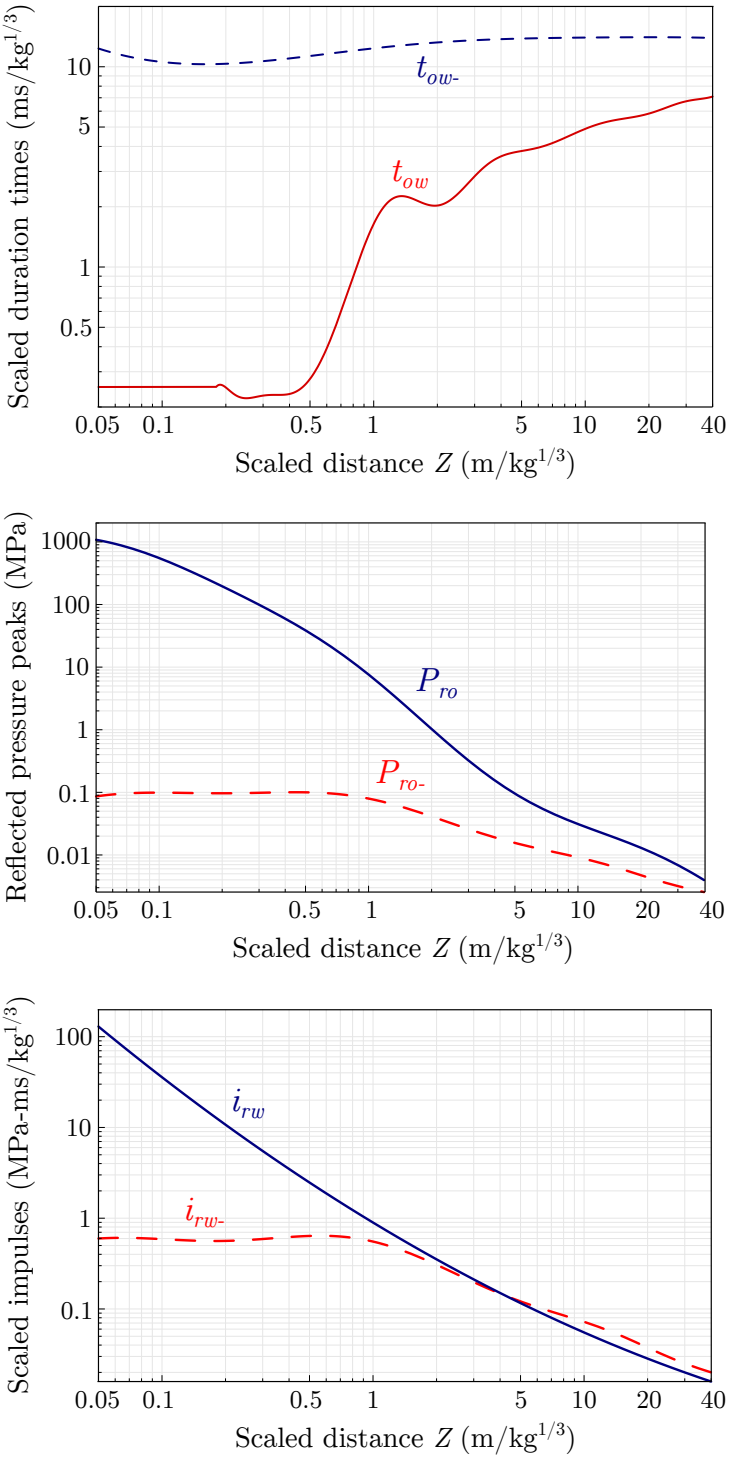

Figure A.1 – Analytical interpolations for blast loading: scaled duration times (top), reflected pressure (center) and impulses (bottom) as functions of the scaled distance, Z.

Appendix B

Resistance of museum artifacts to blast loading

The dynamics of museum artifacts and statues under fast-dynamic excitations arising from explosions is investigated. The study focuses on the most predominant failure mechanisms, namely overturning and fracture due to the tensile stresses developed by the impact of shock waves.

Attention is then focused on the response of existing museum artifacts to blast loading. We assess the overturning domain of some emblematic statues of high aesthetic and cultural value, and namely: Michelangelo's David, Farnese Hercules, Aphrodite of Milos, Athena Giustiniani, Laocoön and His Sons, and Belvedere Torso. The proposed analytical model is adopted by defining appropriate correction parameters to consider the real geometry of the museum objects in contrast to the simplified case of a rectangular rocking block.

Finally, direct damage due to the high tensile stresses is investigated for one case-study.

B.1 Introduction

The resistance of un-anchored museum artifacts against fast-dynamic excitations arising from explosions is studied herein. In particular, attention is focused on the evaluation of the vulnerability of emblematic artifacts and their preservation against deliberate blasts. The response and failure of (slender) blocks subjected to blast actions is found to be governed by two main mechanisms: rocking/toppling and (direct) material damage due to shock waves.

The main goal here is the preservation of un-anchored equipment and museum (slender) artifacts from overturning, such as statues. In particular, we consider some of the most emblematic statues of the world cultural heritage and namely: Michelangelo's *David* (Gallery of the Academy of Florence, Florence), *Farnese Hercules* (Archaeological National Museum, Naples), *Aphrodite of Milos* (Louvre Museum, Paris), *Athena Giustiniani*, *Laocoön and His Sons*, and *Belvedere Torso* (Vatican Museums, Vatican City) These objects belong to the world cultural heritage and their protection has raised important issues throughout history. We refer e.g. to the lost and/or destroyed artefacts of Athena Parthenos, Colossus of Rhodes, the statue of Zeus at Olympia, and more recently the Buddhas statue of Bamiyan. The proposed analytical model can further be used in

the engineering design framework, for securing historical buildings made of monolithic columns from collapse (e.g. classical Greek and Roman temples Stefanou, I. and Psycharis, I. and Georgopoulos, I.-O. (2011); Casapulla et al. (2017)).

In the following, we investigate the design of protective barriers around museum artifacts against explosions and some examples involving emblematic statues are presented. The study relies on the analytical model derived in Chapter 3. Then, we focus attention on the vulnerability to direct damage induce by shock wave. In particular, we compare the critical stand-off distance to avoid damage with one to prevent toppling for one emblematic museum statue, *Aphrodite of Milos*.

B.2 Overturning of museum artifacts

We are interested in the identification of the minimum perimeter around artifacts for protection against explosions.
The artifact is modeled as a rigid block, with front surface S equal to the front surface of the artefact and moment of inertia around the pivot point O equal to the one of the artifact, $\mathscr{I}_o^\sharp$. With reference to Figure B.1, the center of gravity is located at distance r from the pivot point, at a height $h_g = r\cos\alpha$ from the ground and horizontal distance $b = r\sin\alpha$. The centroid of the front surface, impinged by the blast wave (simultaneously and uniformly), is at height h_c from the ground (see Fig. B.1).

Blast loads are modeled as in Section 3.3 (cf. Sect. 3.2, (*iii*)). The drag coefficient C_D is supposed to be equal to 2 (C_D of a rectangular target) for front surfaces of any shape. We use the empirical predictions of P_{ro} (Appendix A), which are valid for rectangular objects. This assumption is on the safety side. For instance, a human body-like shaped target has a drag coefficient $C_D \approx 0.97 - 1.43$ (Penwarden et al., 1978).

Assuming small slenderness angles α and a unilateral rocking response, the dimensionless equation of motion (3.9) holds. The dimensionless rocking moment and normalized time are corrected to consider the real geometry of the artifact as follows

$$\chi \to \chi\,(1+\delta)\,, \tag{B.1}$$

$$\tau \to \frac{\tau}{\sqrt{\kappa}}\,, \tag{B.2}$$

$$\tau_o \to \frac{\tau_o}{\sqrt{\kappa}}\,, \tag{B.3}$$

$$\text{with} \quad \kappa = \frac{\mathscr{I}_o^\sharp}{\mathscr{I}_o}, \quad \delta = \frac{h_c - h_g}{r} \tag{B.4}$$

where κ is the ratio of the moment of inertia of the artifact $\mathscr{I}_o^\sharp$ and of the rectangular block $\mathscr{I}_o$ and δ is the dimensionless contribution to the rocking moment due to the misalignment of the surface's center and the center of gravity.

Accordingly, the linearized overturning condition (3.13) remains the same, $2\chi I \geq 1$. The above mentioned inequality allows to compute the minimum stand-off distance R^*, between a given artifact and a selected explosive quantity, to avoid overturning. This parameter can be used to design barriers to prevent visitors from getting closer than the critical overturning distance.

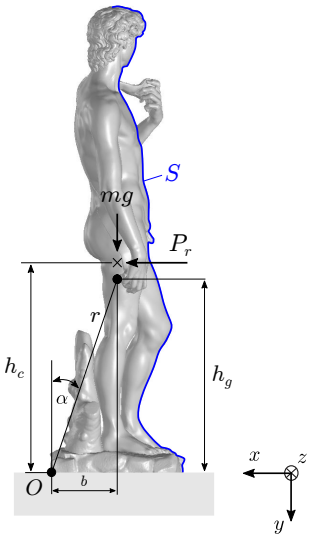

Figure B.1 – Configuration considered for the rocking problem of museum artifacts: an arbitrarily shaped rigid block with rectangular base, resting on a horizontal plane with uniformly distributed mass (center of gravity at h_g), subjected to a uniform blast pressure applied to surface S (blue), with center at h_c). The arrival of the blast wave at surface S is assumed to be same for each point.

We consider herein some emblematic museum statues belonging to the world cultural heritage as case studies for the assessment of protective barriers, see Figure B.2. For each statue, we consider the worst case scenario: a blast wave with a direction such that the statue rocking resistance is the smallest one.
Table B.1 shows the overturning domain for each artifact as function of the explosive weight, W. The case of Michelangelo's *David* is particularly interesting. A large height and a high slenderness angle confer to the statue an excellent resistance to rocking, hence to overturning. Notice that the protective barrier around the statue of Michelangelo's *David* at the Gallery of the Academy of Florence is such that it is impossible to approach the statue closer than ≈ 1.50 m, meaning that the artifact is safe for explosive weights as high as 30 kg and greater. The same holds for the statues of *Farnese Hercules* and *Aphrodite of Milos*. Diversely, the other statues do not fulfill the standards of a safe design to prevent overturning under explosive loads. For instance, *Laocoön and His Sons* does not have any protective barrier and this might cause its loss for explosive weights as small as 10 kg.

B.3 Damage vs. overturning vulnerability of the statue of *Aphrodite of Milos*

We focus attention herein on the damage vulnerability (worst case scenario) of the statue of *Aphrodite of Milos*. The material behavior is modeled as described in Section 3.6 and contact at the interface between the statue and the base is considered as in paragraph 3.5.1. We present in Figure B.4 a detail of the geometry and of the numerical model used, consisting of 4-node linear tetrahedra elements of $0.7 \times 0.7 \times 0.7$ cm^3 size (≈ 5.2 millions of FE). ConWep model is used to apply the blast load on all exposed surfaces of the statue

Table B.1 – Rocking and overturning parameters for the considered artefacts, recovered from the platform Scan The World MyMiniFactory.

Museum artefact	m [kg]	$\mathscr{I}_o^\sharp$ [kg m^2 $\times 10^3$]	h_g [m]	h_c [m]	α [ř]	b [m]	S [m^2]
Michelangelo's David	5800	1650	2.28	2.35	17.6	0.70	5.02
Farnese Hercules	4380	390	1.26	1.41	19.3	0.44	3.39
Athena Giustiniani	765	26.7	0.91	0.92	13.8	0.22	1.39
Laocoön and His Sons	1328	13.6	0.61	0.79	27.1	0.32	1.83
Aphrodite of Milos	565	16.4	0.86	0.87	18.4	0.28	0.83
Belvedere Torso	760	16.5	0.67	0.8	18.7	0.23	0.84

(front, rear, lateral sides, and top). We stress that such blast load model allows to take into account the inclination of the shock front direction of propagation with the normal to the impinged surface (at a local level, i.e., finite elements), the non-simultaneity and non-uniformity of the blast pressure over the target surfaces. Clearing, lift, and drag effects, as well as multiple reflections are neglected, but, as discussed above, their influence is minor when failure due to material damage is under investigation.

Figure B.5 displays the time evolution of the dimensionless stress ς due to 10 kg of TNT at a stand-off distance $R = 2$ m. The non-standard geometry of the target gives rise to strong stress localization. At time $t = 300$ after the shock arrival, damage appears in the lower part of the body and propagates within. As the stress waves travel through the material, a strong localization at the level of the neck takes place and causes its breakage ($t = 950$). Figure B.6 displays the damage evolution throughout the body of the statue.

The particular geometry of the statue renders it extremely vulnerable to damage. This is due to the focalisation of the refracted stress waves within the upper part of the statue, a phenomenon similar to what observed for blast waves in confined and internal explosions (cf. Masi et al. (2018b)). Table B.2 shows the value of Γ_{crit} to avoid damage of the artifact and compares the critical distances for material failure and overturning. Even if the statue is found to be safe against overturning, the existing protective perimeter around *Aphrodite of Milos*, at Louvre Museum (Paris), is insufficient for the preservation of the artifact against explosions produced by a TNT quantity as great as 10 kg or more.

The purpose of our analysis is to derive reliable decision making tools in the design of protective devices to preserve the historical heritage. We focused attention to the use of the analytical model for the preservation of museum objects, for determining the minimum perimeter around statues of high historical and aesthetic value. A rather strong vulnerability of such artifacts to explosive threats was found, at least for the considered objects, either due to overturning or direct material damage. Our results can be directly used for re-evaluating the existing perimeter in the museums of the investigated statues.

Table B.2 – *Aphrodite of Milos* subjected to 10, 20, and 50 kg of TNT. Values of Γ_{crit} to avoid damage of the artifact and comparison between the critical distances for material failure, R^*_{dam}, (critical in this case) and overturning, R^*.

W [kg]	Γ_{crit}	R^*_{dam} [m]	R^* [m]
10	5.87	2.12	0.7
20	5.87	2.67	1.0
50	4.85	3.37	1.66

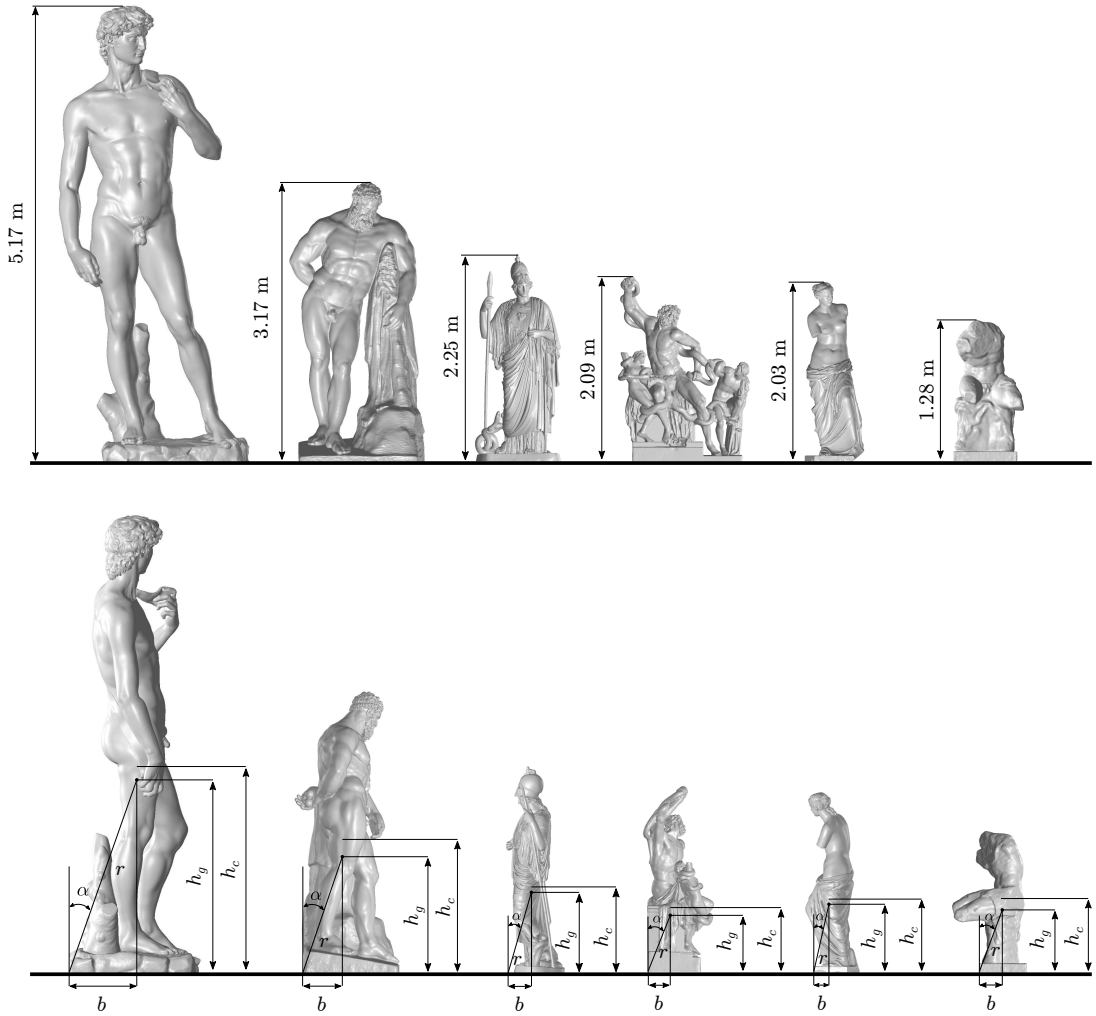

Figure B.2 – Different museum artefacts considered. From left to right: Michelangelo's *David* (Gallery of the Academy of Florence, Florence), *Farnese Hercules* (Archaeological National Museum, Naples), *Athena Giustiniani* (Vatican Museums, Vatican City), *Laocoön and His Sons* (Vatican Museums, Vatican City), *Aphrodite of Milos* (Louvre Museum, Paris), and *Belvedere Torso* (Vatican Museums, Vatican City). The three-dimensional models are recovered from the platform Scan The World MyMiniFactory.

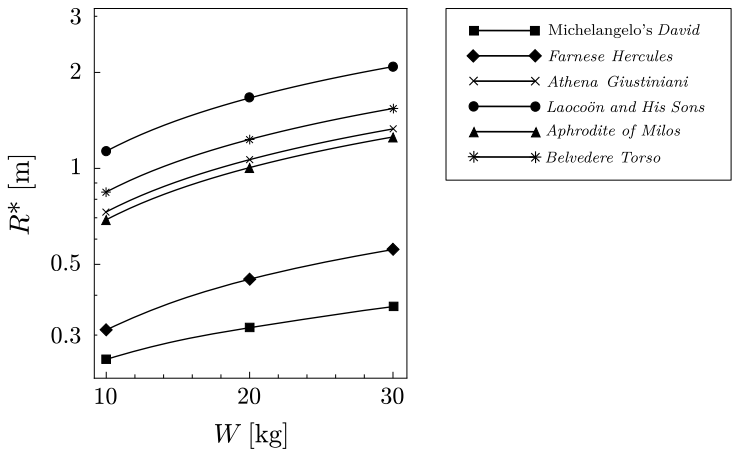

Figure B.3 – Critical stand-off distance R^* for the considered museum artifacts, as function of the explosive weight W.

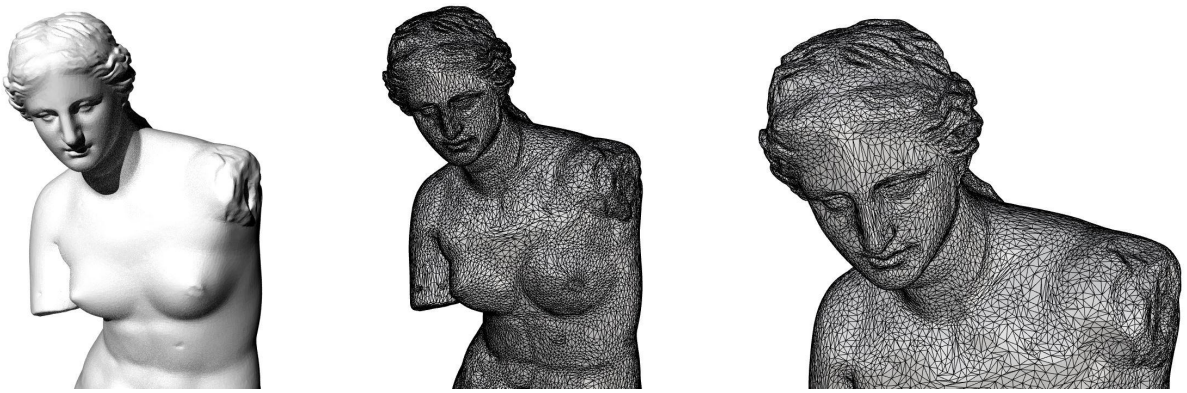

Figure B.4 – Model used for the statue of *Aphrodite of Milos*. Details of the geometry (left) and of the Finite Element mesh (right).

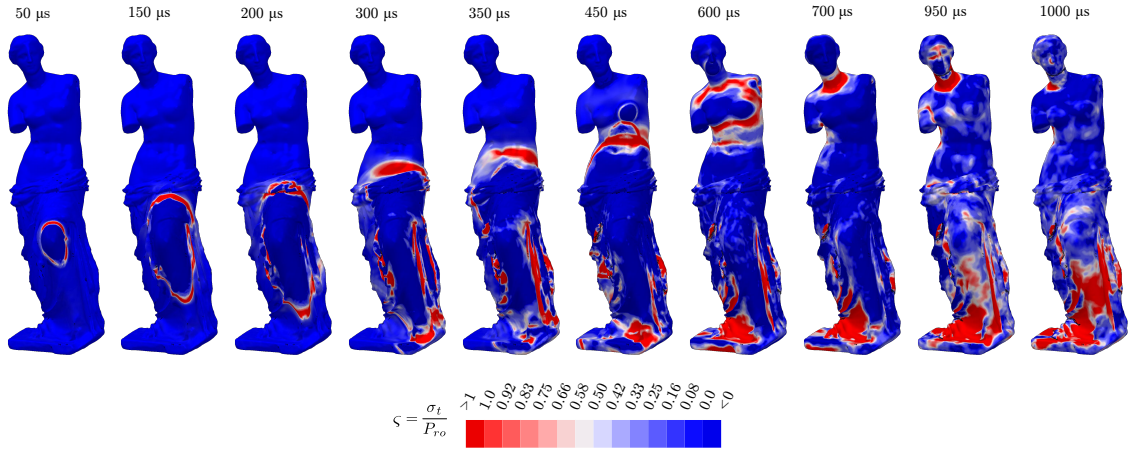

Figure B.5 – Time evolution of the dimensionless stress $\varsigma = \sigma_t / P_{ro}$ for the statue of *Aphrodite of Milos* due to 10 kg of TNT at a stand-off distance $R = 2$ m.

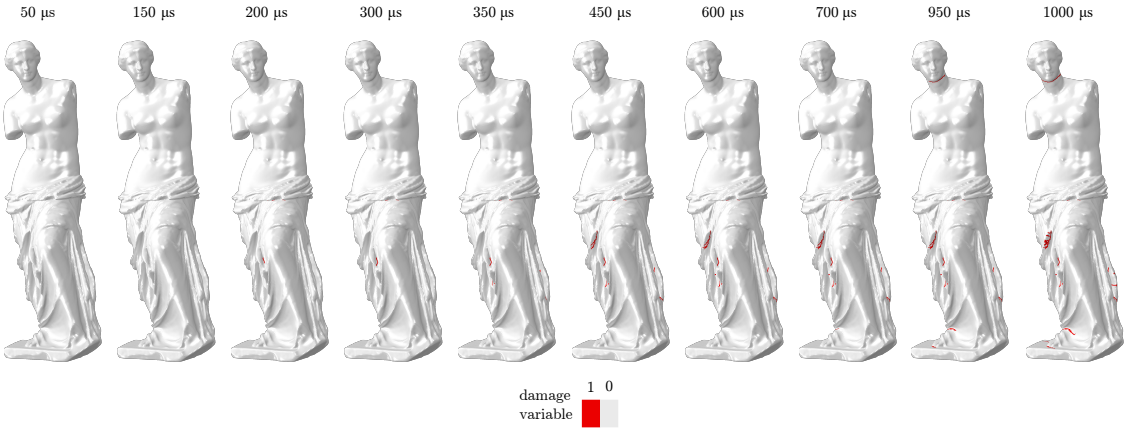

Figure B.6 – Evolution of damage for the statue of *Aphrodite of Milos* due to 10 kg of TNT at a stand-off distance $R = 2$ m. Finite elements undergoing damage correspond to a unit damage variable.

Appendix C

Rigid vs deformable Discrete Elements

A common strategy in DEM analyses for reducing this cost is to consider rigid blocks instead of deformable ones. However, such an assumption may affect the predicted structural response when a certain degree of confinement and out-of-plane deformations take place, which is also our case. This is why the assumption of infinitely rigid blocks is also investigated by comparing the numerical results obtained using deformable blocks. For the applications and geometry herein considered, the rigid blocks model underperforms compared to the deformable one. The inferior performance of the rigid blocks is due to the particular cases herein studied which involved out-of-plane loading of confined, shell-like structures. In particular, the rigid block model shows very high stiffness in bending, affecting the deformation modes and therefore the static and dynamic response of the system for both associative and non-associative frictional interfaces. This artificial high bending stiffness is defined here as rotational locking as it is the result of the relative rotations of the building blocks.

C.1 Is a rigid blocks assumption always appropriate?

Herein we investigate the simplified modelling assumption of infinitely rigid blocks which is often preferred in the literature, see e.g. Bui and Limam (2012); Çakt et al. (2016); Godio et al. (2018), because of its reduced computational cost with respect to the more detailed model with deformable blocks we are using herein. Under in-plane conditions, the rigid blocks assumption is usually reasonable under relatively low compressive loads, where the deformation is principally concentrated at the interfaces Stefanou et al. (2015b). Nevertheless, for masonry structures subjected to out-of-plane loading, like those due to a blast, a rigid blocks model may give unrealistic results, see e.g. Parisi et al. (2016); Masi et al. (2019b).

Here we provide comparisons between rigid and deformable blocks models of the arched geometry previously investigated.

As mentioned in Section 4.5, several contact points through the thickness of the masonry structure undergoing out-of-plane displacement are required both for rigid and deformable blocks models (see also Lemos (2007a, 2017); Godio et al. (2018); Masi et al. (2019b)). However, in a rigid block model, the stress distribution at the interfaces is linear. Consequently, an accurate discretization of contacts is fundamental. For instance, it has been proved that in the frame of the DEM code herein used, 3DEC, at least 3 contact points along the thickness are required to obtain a satisfactory representation of

the bending stiffness Lemos (2017).

With rigid blocks, the normal and tangential stiffness (k_n and k_t, respectively) of the interfaces are modified with respect to the expressions previously derived (see Sect. 4.2) to account for the deformability of the blocks in the real structure (see also Malomo et al. (2019)):

$$k_n = \frac{E_b E_m}{E_b h_m + E_m h_b}, \tag{C.1}$$

$$k_t = \frac{G_b G_m}{G_b h_m + G_m h_b}. \tag{C.2}$$

The elasticity lumping formulae (C.1) and (C.2) are derived for in-plane loading of planar structures Sarhosis et al. (2016b). For head joints, the block thickness h_b represents the brick length, while for bed joints, h_b is the brick height.
Table C.1 displays the material elastic parameters used for the model with rigid blocks, derived from those given in Table 4.7 (for deformable DE) and considering the non-deformability of the blocks, see Eq.s (C.1, C.2). The material parameters that define the plasticity behavior and the corresponding softening remain unchanged, see Sect. 4.2. The fineness of the contacts discretization is investigated following the same approach used for deformable blocks (see Sect. 4.5, paragraph 4.5.1). The selected discretization consists of 5×4 (thickness $\times$ width) contact points at each masonry joint.

Table C.1 – Material parameters used in the numerical simulations of the masonry barrel vault using a rigid block model. Superscripts b and h refer to bed and head masonry joints, respectively.

Blocks properties		Joints properties					
density(kg/m^3)	2000	k_n^b	(GPa/m)	36.0	k_n^h	(GPa/m)	32.0
		k_t^b	(GPa/m)	15.0	k_n^h	(GPa/m)	13.4

C.2 Rigid vs deformable blocks under quasi-static conditions

A constant uniform pressure equal to 100 kPa is applied to a central layer of the barrel vault (see Fig. 4.19). We assume a linear elastic behavior of the interfaces for both models as in the case with deformable blocks (par. 4.5.1). Mass proportional damping is used (in this paragraph) to dissipate oscillations and reach equilibrium fast.
Figure C.1 displays the deformed shape obtained at the equilibrium, using rigid and deformable blocks, respectively.

The models with rigid and deformable blocks display different deformation modes and stiffness. In particular, the rigid blocks model shows a very high bending stiffness. This is due to the fact that the rigid discrete elements have infinite bending stiffness (i.e., non-deformable), as illustrated in Figure C.2. As a result, a pure shear mode of deformation is observed. The rigid model is affected by what we define here as *rotational locking*; an artifact that can be quite important under out-of-plane loads leading to artificially high

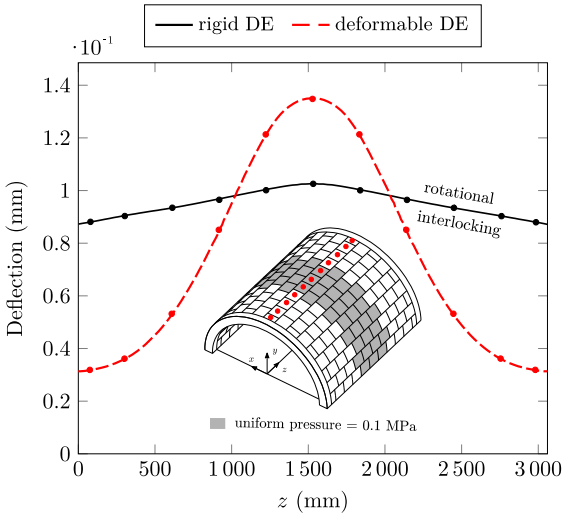

Figure C.1 – Comparison of the discrete element model with deformable and rigid blocks under a constant pressure 100 kPa applied to the region highlighted in grey. An elastic behavior is assumed for the masonry joints.

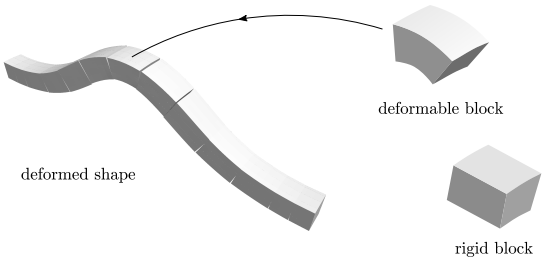

Figure C.2 – Out-of-plane deformation mode of blocky structure, modeled with deformable blocks (left). Block bending modes (right) with deformable (top) and rigid (bottom) blocks.

bending stiffness, as shear locking does in the Finite Element method.
We emphasize that the rotational locking is not a related to the lumping of elasticity at the interfaces, as performed in the rigid blocks model. Indeed, using building blocks that are half and twice their original size (refer to Fig. 4.29, paragraph 4.5.5), for both rigid and deformable block models, we obtain results comparable to those showed in Figure C.1.

C.3 Rigid vs deformable blocks under blast actions

We explore here the adequacy of a rigid blocks assumption under blast actions. In particular, we are interested in analyzing the effects of rotational locking on bending non-linear eigenmodes, accounting for the shear- and tensile-failure at the masonry interfaces. No damping is considered.

We assume zero cohesion and tensile strength, $f_t = c = 0$ MPa, constant angle of friction of the joints, $\varphi^b = \varphi^h = 35°$, and either an associative sliding behavior ($\psi^b = \psi^h = \varphi^b = \varphi^h$) or zero dilatancy joints, $\psi^b = \psi^h = 0°$.

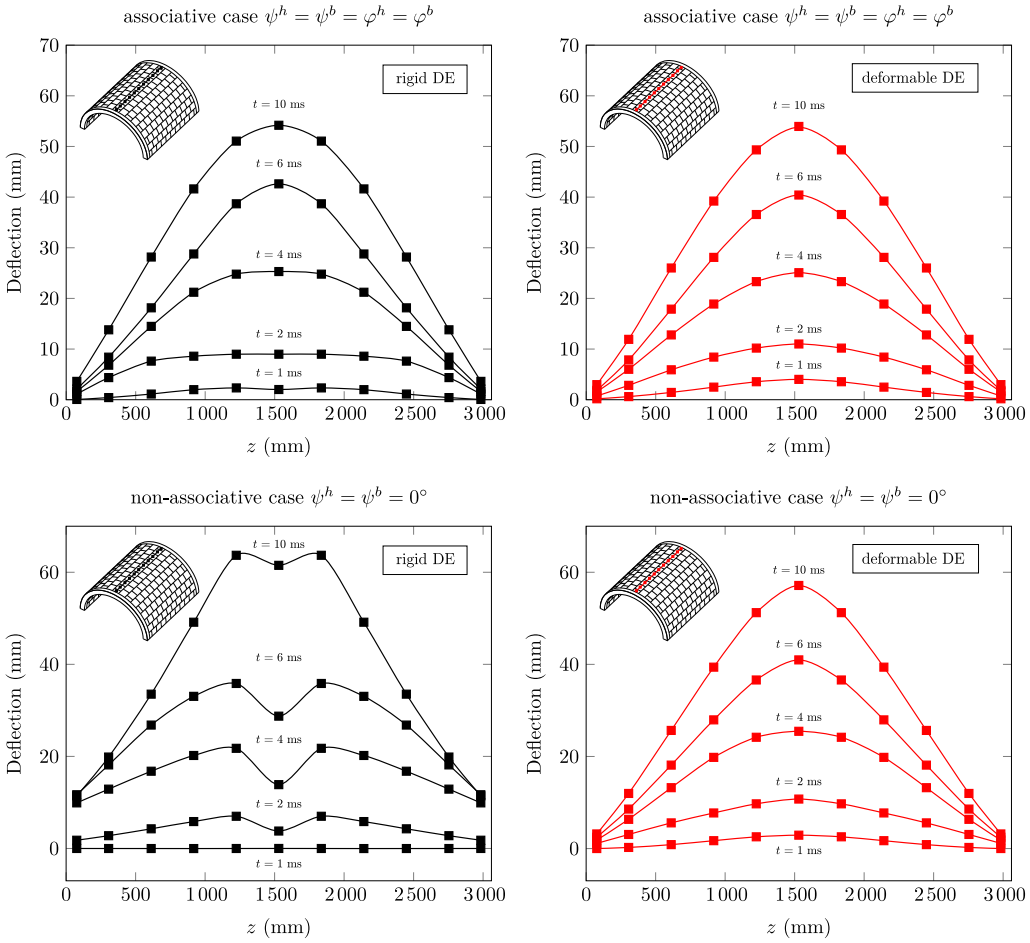

Figure C.3 – Evolution of the deformed shape, along the longitudinal direction, at the key's vault of the masonry vault subjected to 10 kg of TNT, obtained with rigid blocks (left) and deformable ones (right).

In Figure C.3 we compare the evolution of the deformed shape for both rigid and deformable blocks models subjected to 10 kg of TNT. When an associative behavior of the interfaces is assumed, the overall response predicted by rigid DE is tantamount to the one obtained with deformable ones. The relative error is smaller than 2.7%, see Table C.2. The dilatant behavior of the interfaces increases the local contact pressure which results in increase bending stiffness (for both models).

For zero dilatancy masonry joints, the rigid blocks model response is found to highly differ from the one predicted by the deformable DE model. Rotational locking (infinite bending stiffness) is at the origin. The rigid blocks model displays shear failure of the interfaces of the central (rigid) block and at the boundaries (see Fig. C.3). The central block presents a time-lag in deflection compared to its adjacent blocks from the very beginning. This ultimately leads to the loss of any arching mechanism (differently to what observed with deformable blocks). Figure C.4 depicts the different deformed shapes

obtained with the rigid and deformable models. For the non-associative case, the rigid blocks predict a maximum deflection which is approximately 30% larger.

Table C.2 – Maximum deflection observed in the masonry vault at varying of φ^h and ψ^b ($\varphi^b = 35°$, $\psi^h = 0°$, and $f_t = c = 0$ MPa). Comparison between the numerical results obtained with infinitely rigid blocks and deformable ones.

sliding behavior	$\varphi^b = \varphi^h$ (°)	$\psi^b = \psi^h$ (°)	Maximum deflection deformable blocks (mm)	rigid blocks (mm)	rigid to def. blocks error (%)
associative	35	35	55.80	57.29	2.67
non-associative	35	0	65.04	84.43	29.8

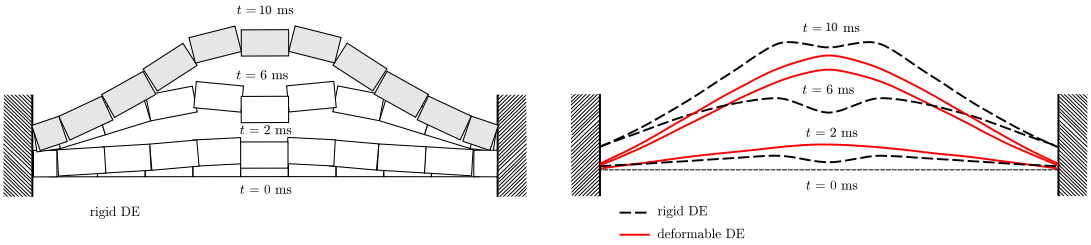

Figure C.4 – Representative scheme of the rotational locking displayed by infinitely rigid blocks (left) and comparison of the resulting deformed shaped with a deformable blocks model (right), for the non-associative case.

C.3.1 Influence of the building blocks size

We explore the effects of rotational locking at varying of the building blocks size. Table C.3 presents the maximum deflection measured within the structure for friction angle $\varphi^b = \varphi^h = 35°$. The results obtained with infinitely rigid blocks and their relative error are also shown.

We find that the rotational locking phenomenon influences the rigid blocks model, independently from the size of the building blocks. Nevertheless, major differences between deformable and rigid blocks are found for bricks of twice the original size. The associativity or not of the sliding behavior of the masonry joints is, once again, found to affect the rigid model predictions, even if to a smaller extent with respect to the reference block size.

The simplified assumption of rigid blocks for blocky confined structures undergoing out-of-plane deformation is thus found to perform poorly under both quasi-static and fast-dynamic loads (independently from the size of building blocks), for the scenarios here considered.

Table C.3 – Maximum deflection observed in the masonry vault at varying of the building blocks size. Comparison between deformable and rigid blocks models, and corresponding relative error, between parentheses. The results are for $c = f_t = 0$ MPa.

sliding behavior	blocks	$\varphi^b = \varphi^h$ (°)	$\psi^b = \psi^h$ (°)	Maximum deflection 1/2 bocks size (mm)	reference blocks size (mm)	2 blocks size (mm)
associative	deformable	35	35	64.55	55.80	52.08
	rigid			72.25	57.29	69.82
				(11.93 %)	(2.67 %)	(34.06 %)
non-associative	deformable	35	0	70.95	65.04	59.29
	rigid			89.52	84.43	98.98
				(26.17 %)	(29.80 %)	(66.94 %)

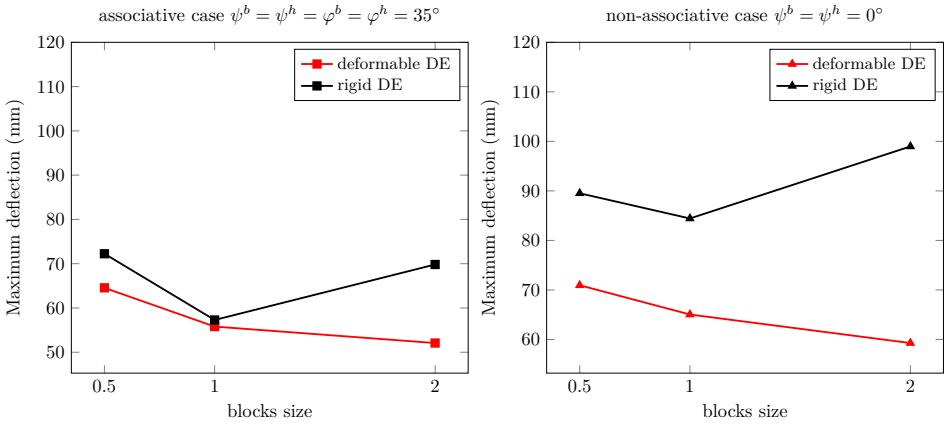

Figure C.5 – Comparison of the response of the masonry vault in terms of deflection in the proximity of fixed supports (left) and at the center of the vault's key (right) for different size of the building blocks. The results are for $\varphi^h = 10°$, $\psi^b = 0°$, and $c = f_t = 0$ MPa.

Appendix D

Supplementary material for Thermodynamics-based Artificial Neural Networks

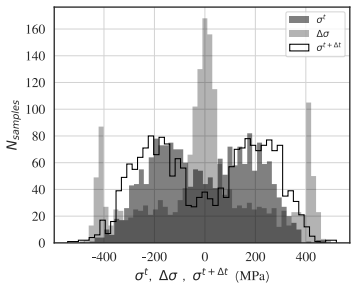

(a) Cauchy stress, σ^t, $\sigma^{t+\Delta t}$, and increment $\Delta\sigma$.

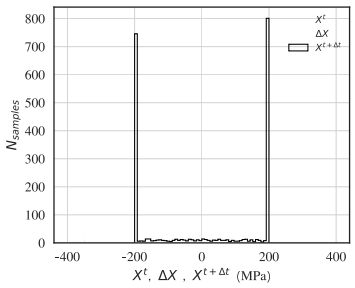

(b) thermodynamic stress, X^t, $X^{t+\Delta t}$, and increment ΔX.

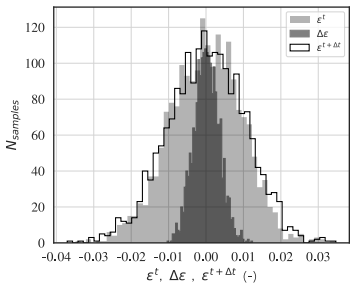

(c) total strain, ε^t, $\varepsilon^{t+\Delta t}$, and increment $\Delta\varepsilon$.

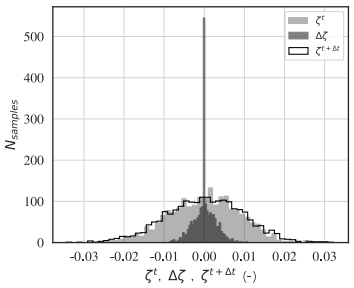

(d) internal variable (inelastic strain), ζ^t, $\zeta^{t+\Delta t}$, and increment $\Delta\zeta$.

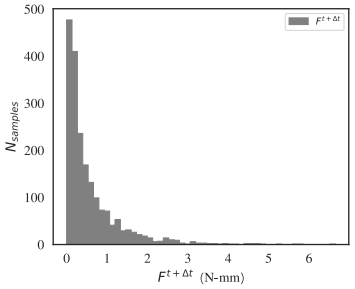

(e) Helmholtz free-energy $F^{t+\Delta t}$.

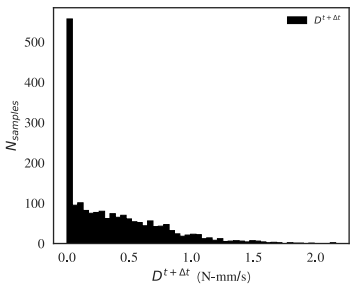

(f) dissipation rate $D^{t+\Delta t}$.

Figure D.1 – Sampling for material case 1D-B (hardening), see Fig. 6.8.

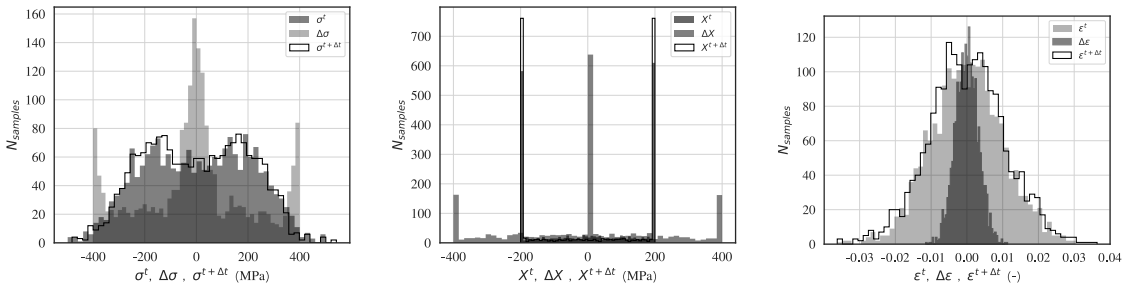

(a) Cauchy stress, σ^t, $\sigma^{t+\Delta t}$, and increment $\Delta\sigma$.

(b) thermodynamic stress, X^t, $X^{t+\Delta t}$, and increment ΔX.

(c) total strain, ε^t, $\varepsilon^{t+\Delta t}$, and increment $\Delta\varepsilon$.

(d) internal variable (inelastic strain), ζ^t, $\zeta^{t+\Delta t}$, and increment $\Delta\zeta$.

(e) Helmholtz free-energy $F^{t+\Delta t}$.

(f) dissipation rate $D^{t+\Delta t}$.

Figure D.2 – Sampling for material case 1D-C (softening), see Fig. 6.8.

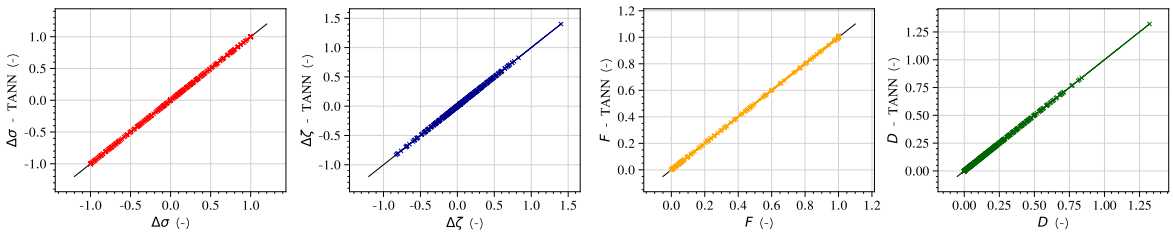

Figure D.3 – Predictions, after training, of TANN compared with the test data.

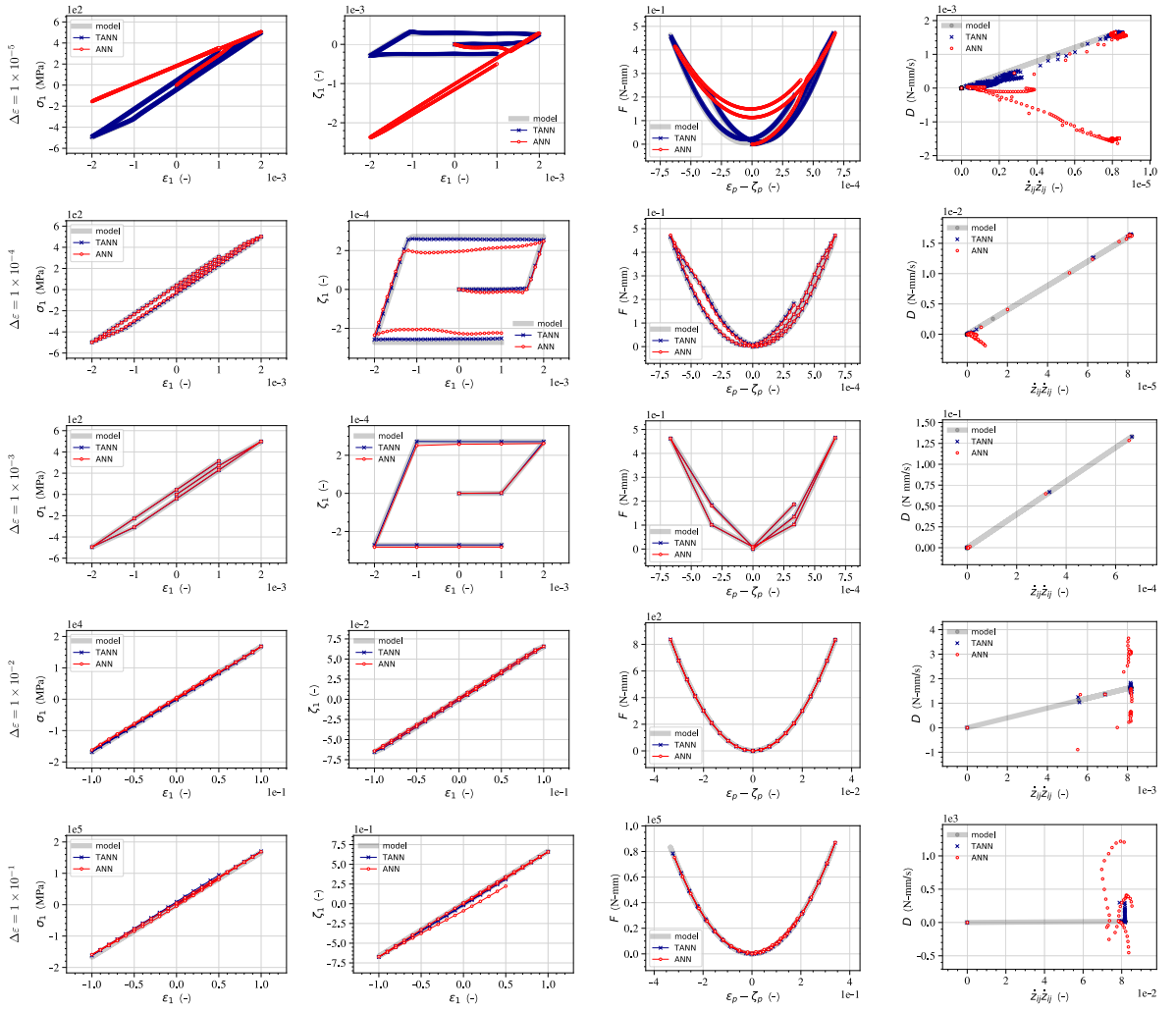

(a) σ prediction (b) ζ prediction (c) F prediction (TANN), Eq. (6.33) (ANN). (d) D prediction (TANN), Eq. (6.33) (ANN).

Figure D.4 – Comparison of the predictions of TANN and standard ANN with respect to the target values, for the uni-axial cyclic loading path, Eq. (6.35), for material case 3D-A, perfect plasticity. Each row represents the prediction at different $\Delta\varepsilon$ increments.

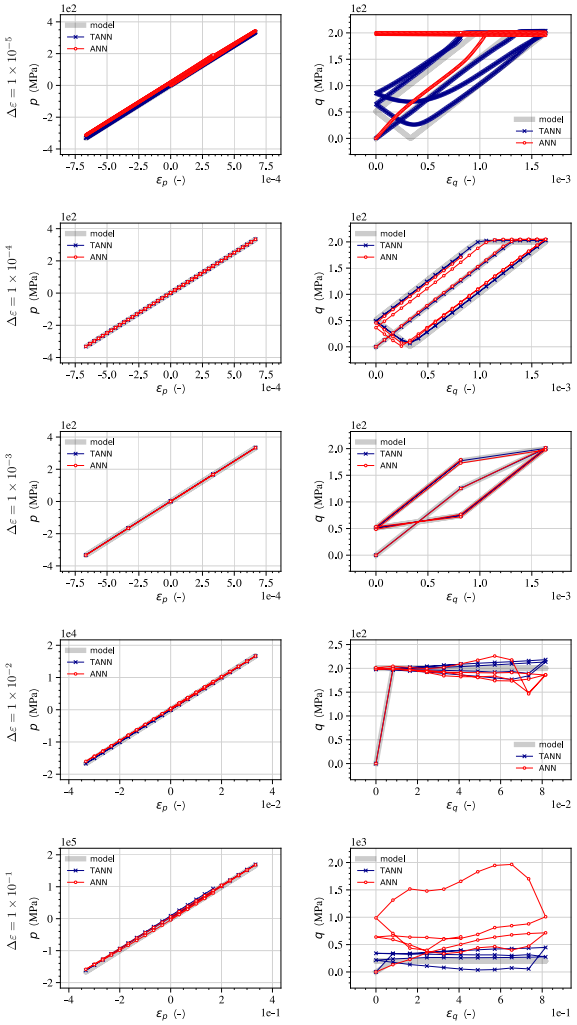

(a) p computation. (b) q computation.

Figure D.5 – Comparison of the stress predictions of TANN and ANN in terms of mean and deviatoric stress, p (left) and q (right), for the uni-axial loading path in Figure D.4, Eq. (6.35), for material case 3D-A, perfect plasticity. Each row represents the prediction at different $\Delta\varepsilon$ increments.

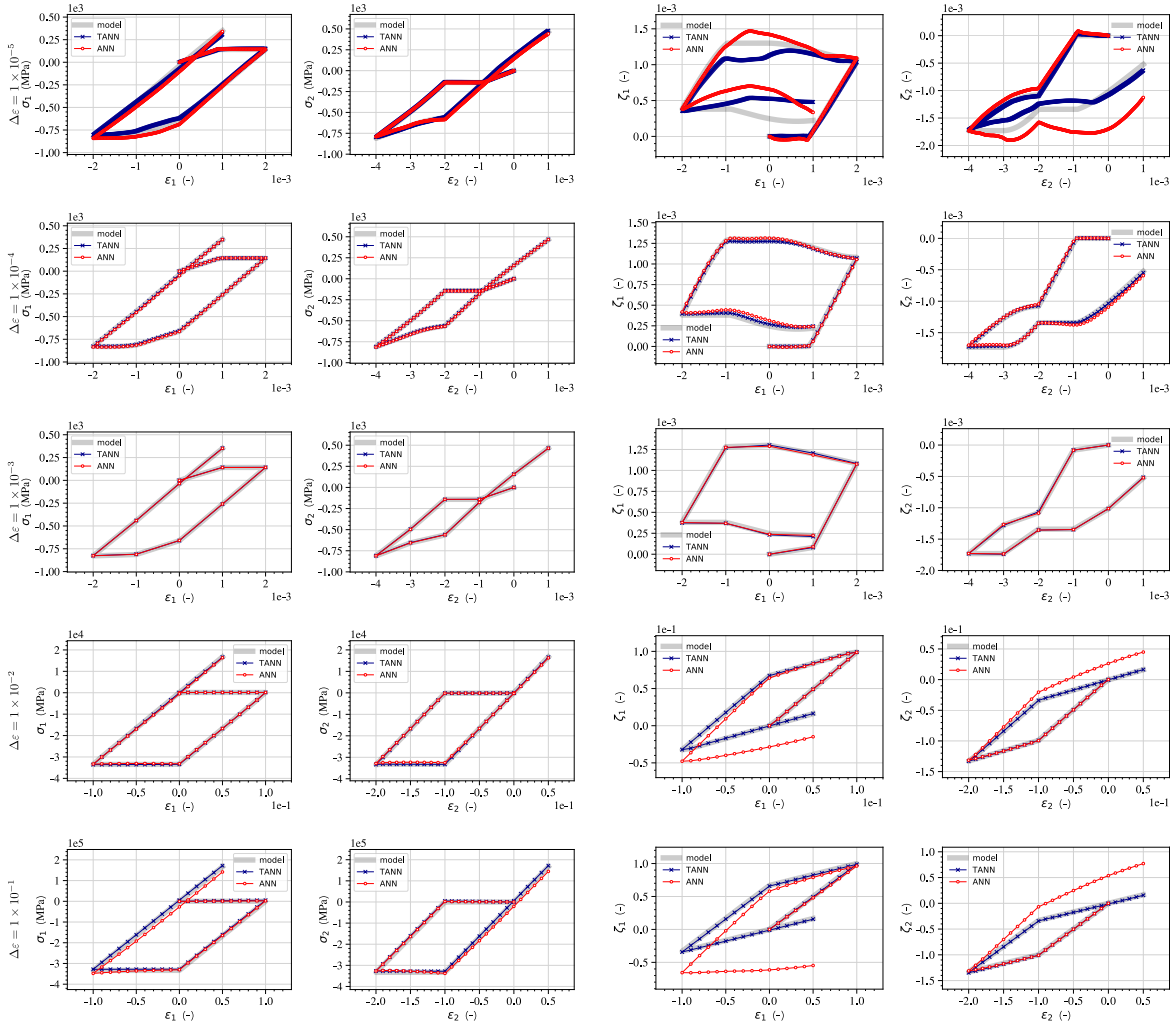

(a) σ prediction. (b) ζ prediction.

Figure D.6 – Comparison of the stress and internal variable predictions of TANN and standard ANN with respect to the target values, for the bi-axial cyclic loading path, Eq. (6.35), for material case 3D-A, perfect plasticity. Each row represents the prediction at different $\Delta\varepsilon$ increments.

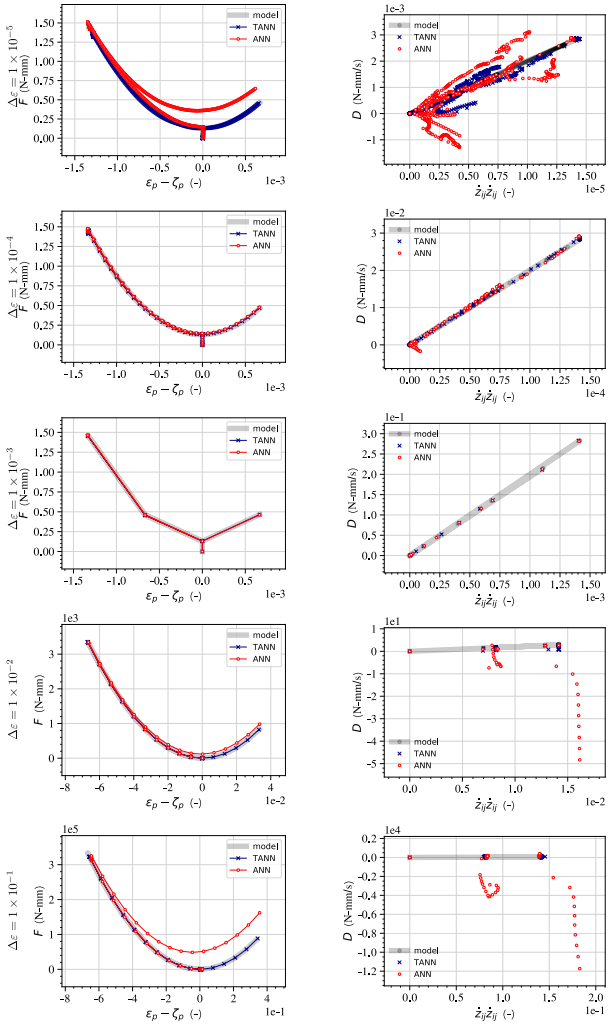

(a) F prediction (TANN), Eq. (6.33) (ANN).

(b) D prediction (TANN), Eq. (6.33) (ANN).

Figure D.7 – Comparison of the energy and dissipation rate predictions of TANN and computation according to Eq. (6.33) for standard ANN with respect to the target values, for the bi-axial cyclic loading path, Eq. (6.35), for material case 3D-A, perfect plasticity. Each row represents the prediction at different $\Delta\varepsilon$ increments.

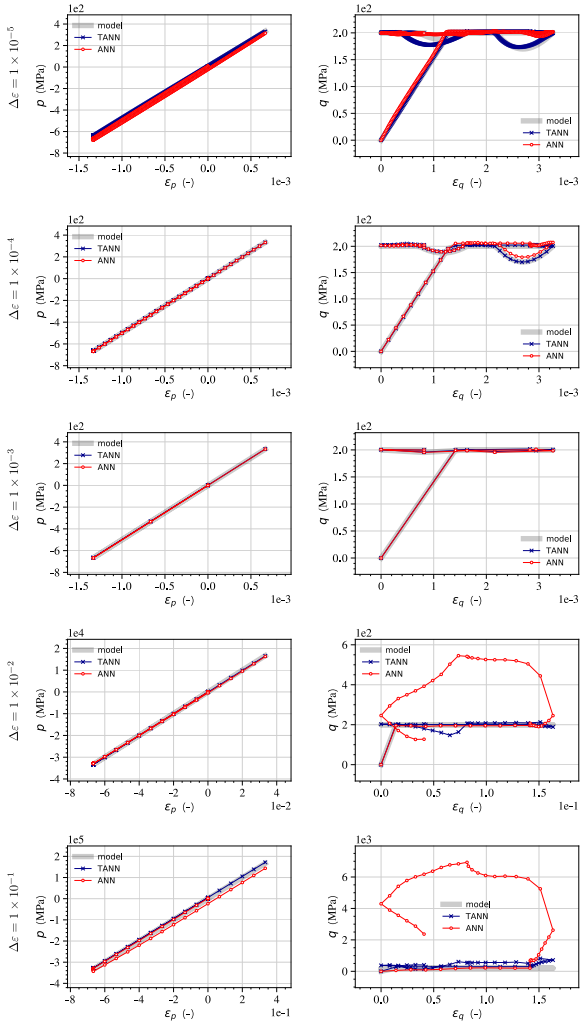

(a) p computation. (b) q computation.

Figure D.8 – Comparison of the stress predictions of TANN and standard ANN in terms of mean and deviatoric stress, p and q, for the bi-axial loading path in Figures D.6 and D.7 (perfect plasticity), Eq. (6.35). Each row represents the prediction at different $\Delta\varepsilon$ increments.

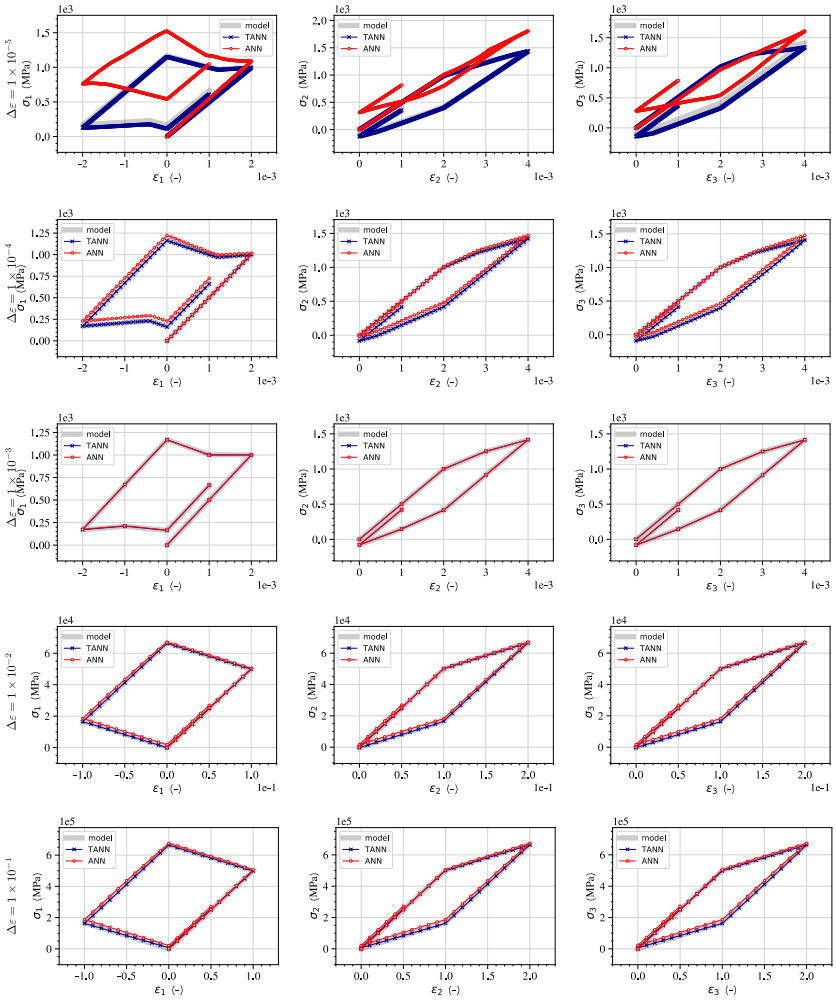

Figure D.9 – Comparison of the stress predictions of TANN and standard ANN with respect to the target values, for the tri-axial cyclic loading path, Eq. (6.35), for material case 3D-A, perfect plasticity. Each row represents the prediction at different $\Delta\varepsilon$ increments.

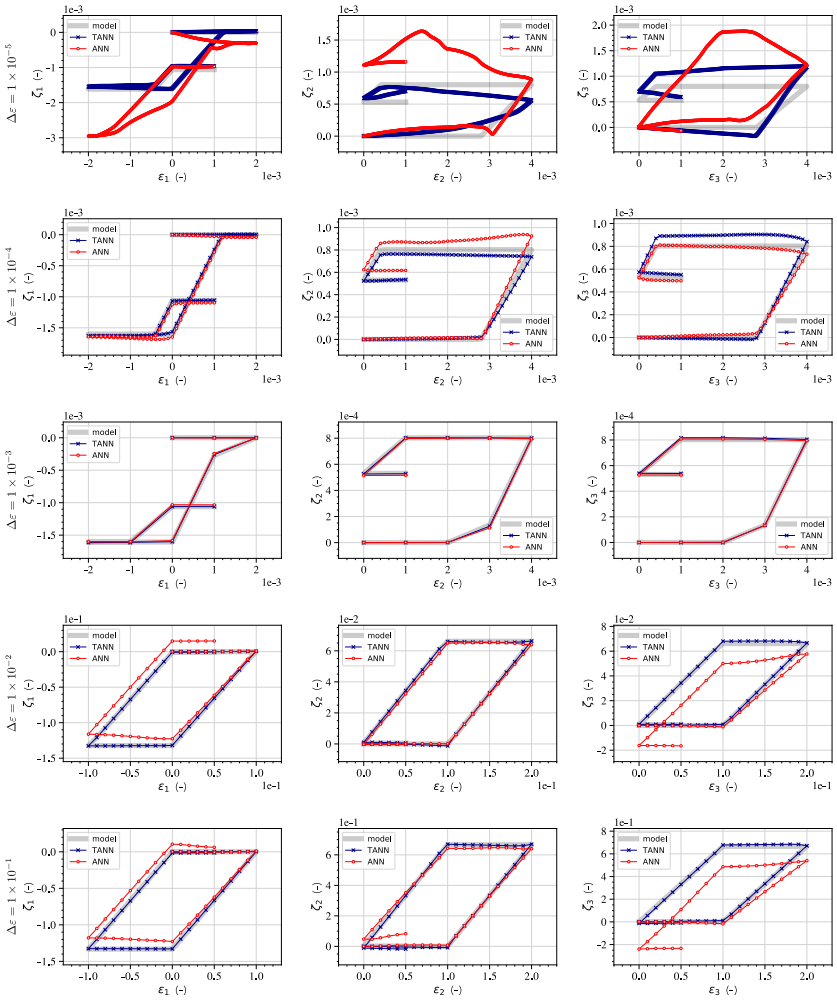

Figure D.10 – Comparison of the internal variable predictions of TANN and standard ANN with respect to the target values, for the tri-axial cyclic loading path, Eq. (6.35), for material case 3D-A, perfect plasticity. Each row represents the prediction at different $\Delta\varepsilon$ increments.

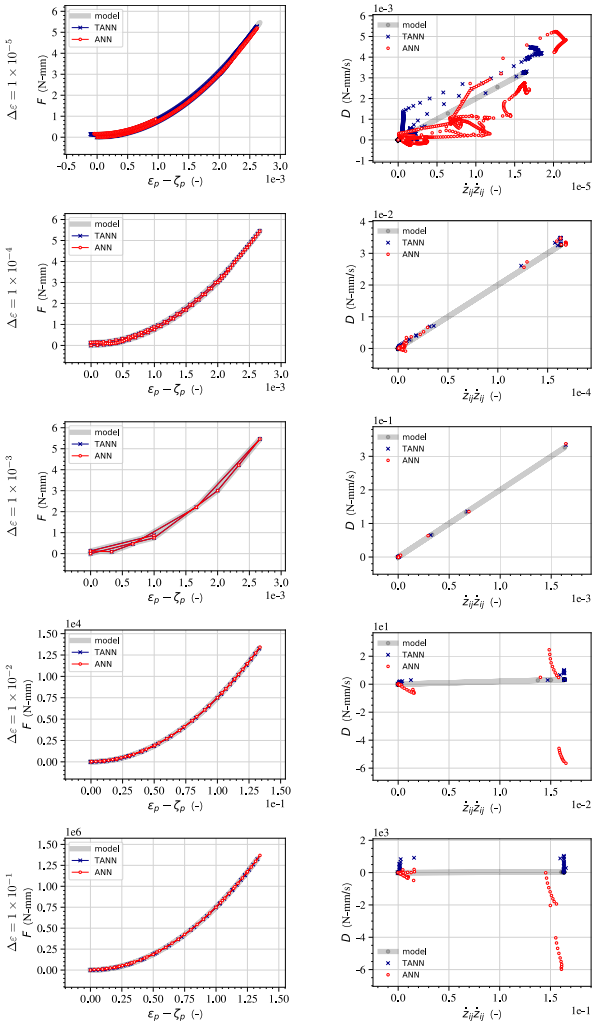

(a) F prediction (TANN), Eq. (6.33) (ANN).

(b) D prediction (TANN), Eq. (6.33) (ANN).

Figure D.11 – Comparison of the energy and dissipation rate predictions of TANN and computation according to Eq. (6.33) for standard ANN with respect to the target values, for the tri-axial cyclic loading path, Eq. (6.35), for material case 3D-A, perfect plasticity. Each row represents the prediction at different $\Delta\varepsilon$ increments.

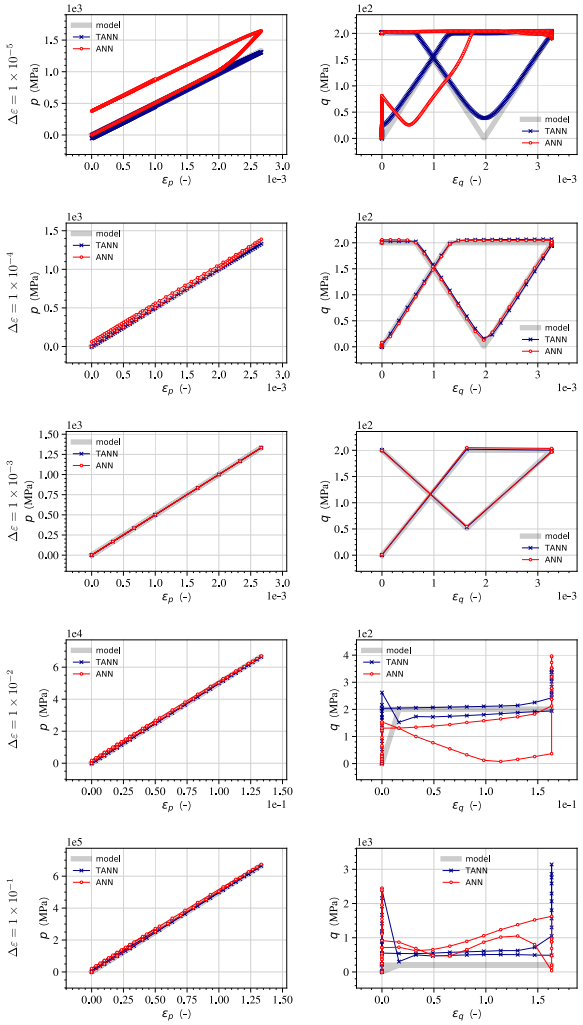

(a) p computation. (b) q computation.

Figure D.12 – Comparison of the stress predictions of TANN and standard ANN in terms of mean and deviatoric stress, p and q, for the tri-axial loading path in Figures D.9, D.10, and D.11 (perfect plasticity), Eq. (6.35). Each row represents the prediction at different $\Delta\varepsilon$ increments.

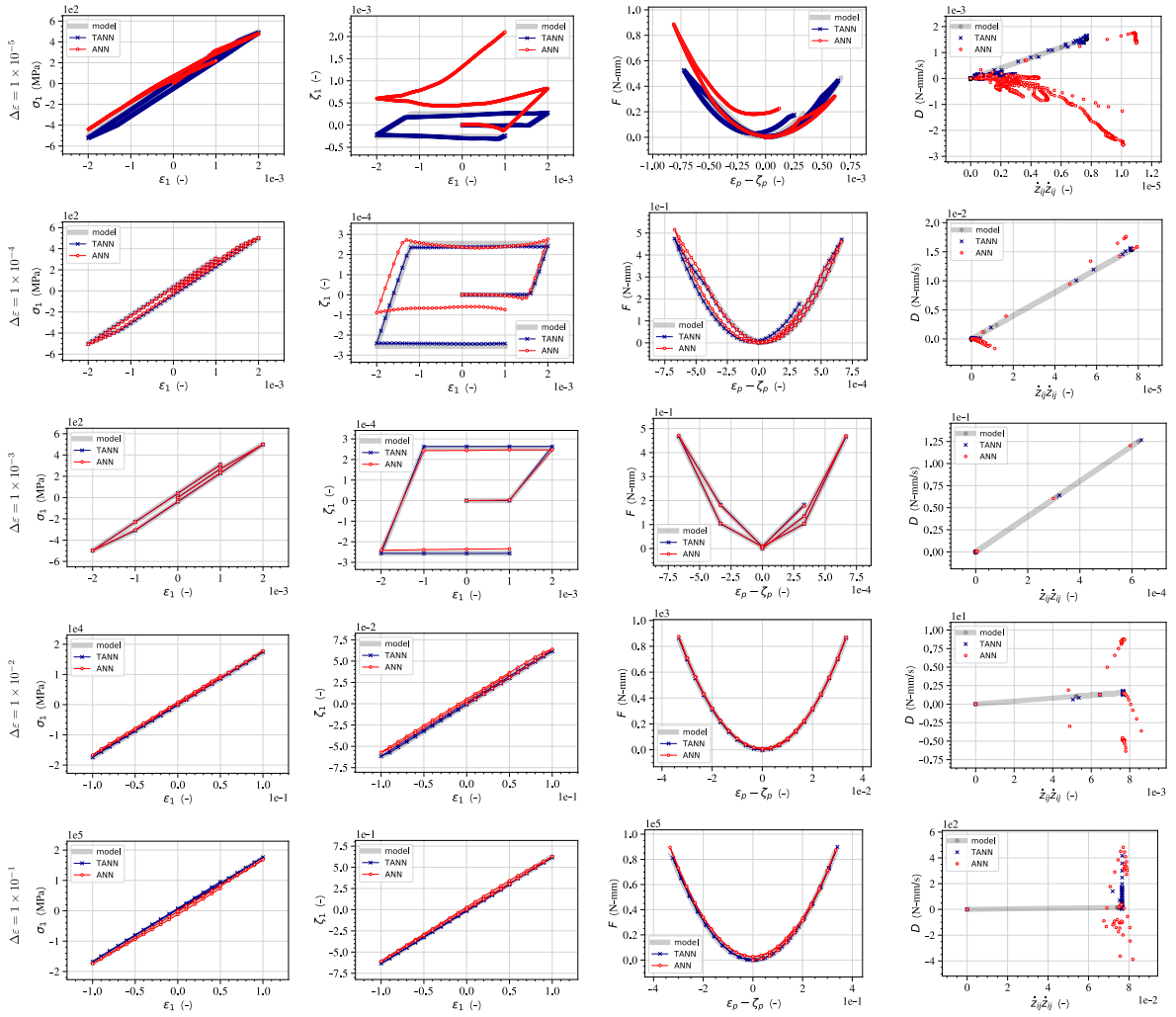

(a) σ prediction (b) ζ prediction (c) F prediction (TANN), Eq. (26) (ANN). (d) D prediction (TANN), Eq. (26) (ANN).

Figure D.13 – Comparison of the predictions of TANN and standard ANN with respect to the target values, for the uni-axial cyclic loading path, Eq. (6.35), for material case 3D-B, hardening. Each row represents the prediction at different $\Delta\varepsilon$ increments.

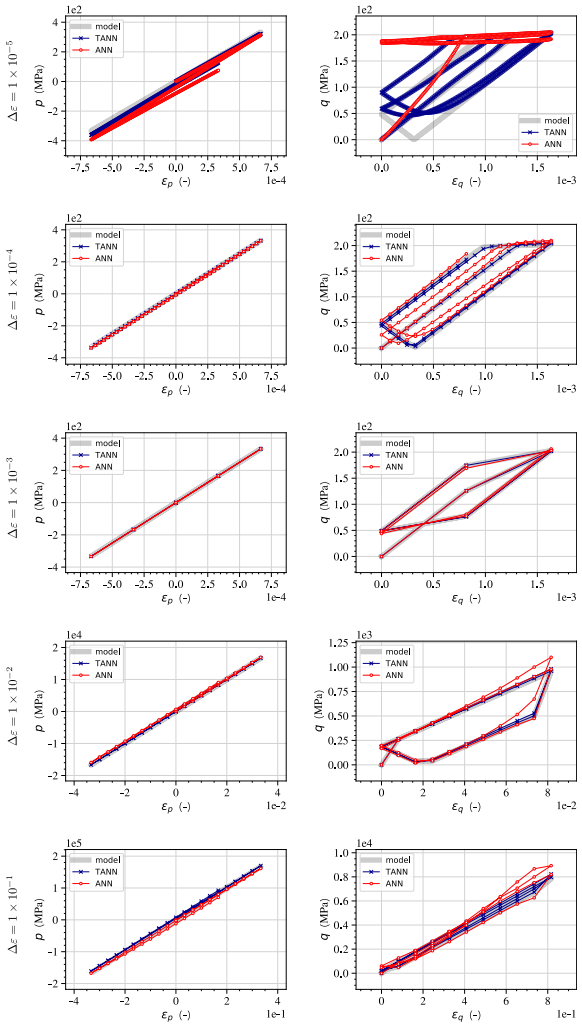

(a) p computation. (b) q computation.

Figure D.14 – Comparison of the stress predictions of TANN and ANN in terms of mean and deviatoric stress, p (left) and q (right), for the uni-axial loading path in Figure D.13 (hardening), Eq. (6.35). Each row represents the prediction at different $\Delta\varepsilon$ increments.

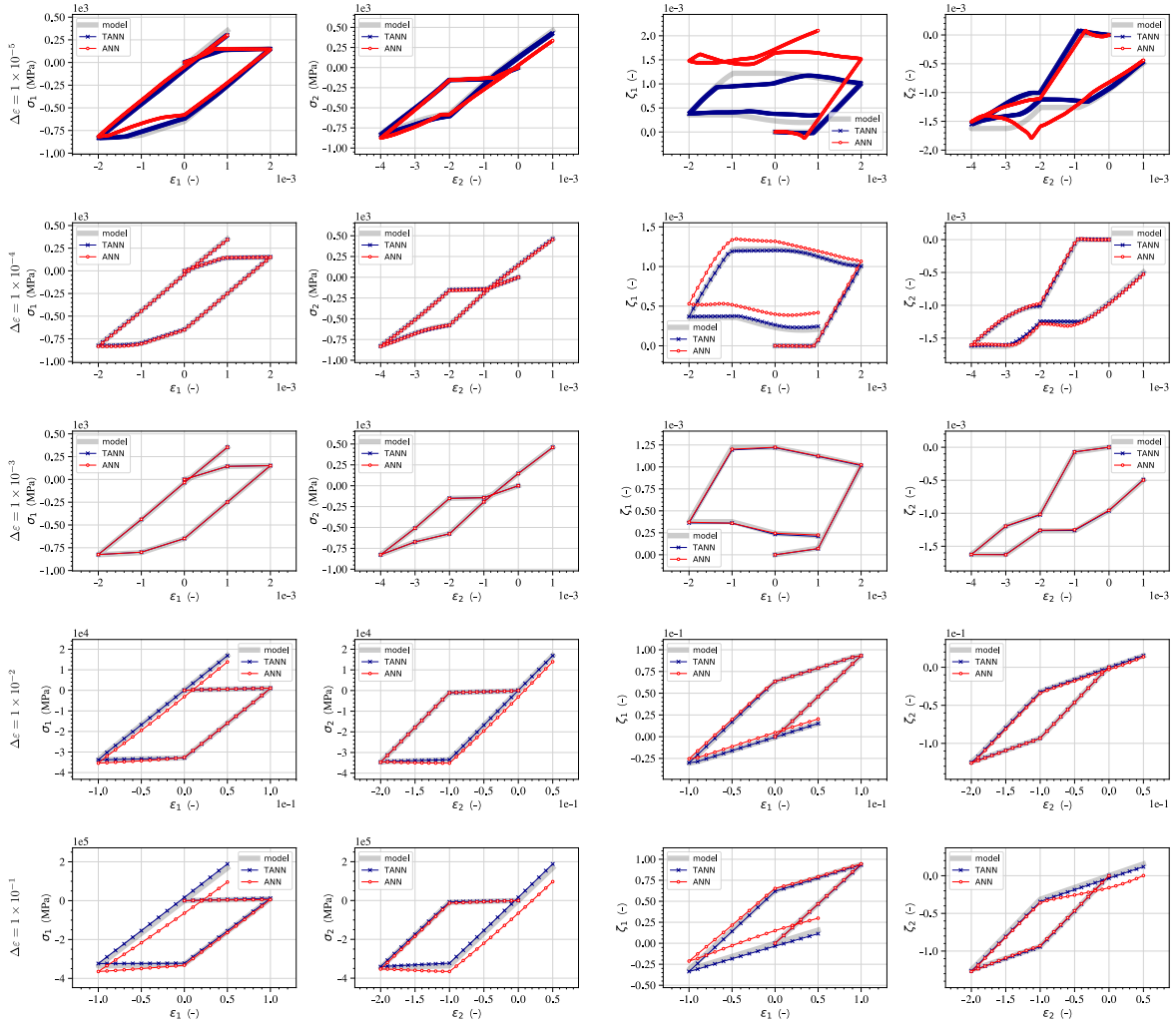

(a) σ prediction. (b) ζ prediction.

Figure D.15 – Comparison of the stress and internal variable predictions of TANN and standard ANN with respect to the target values, for the bi-axial cyclic loading path, Eq. (6.35), for material case 3D-B, hardening. Each row represents the prediction at different $\Delta\varepsilon$ increments.

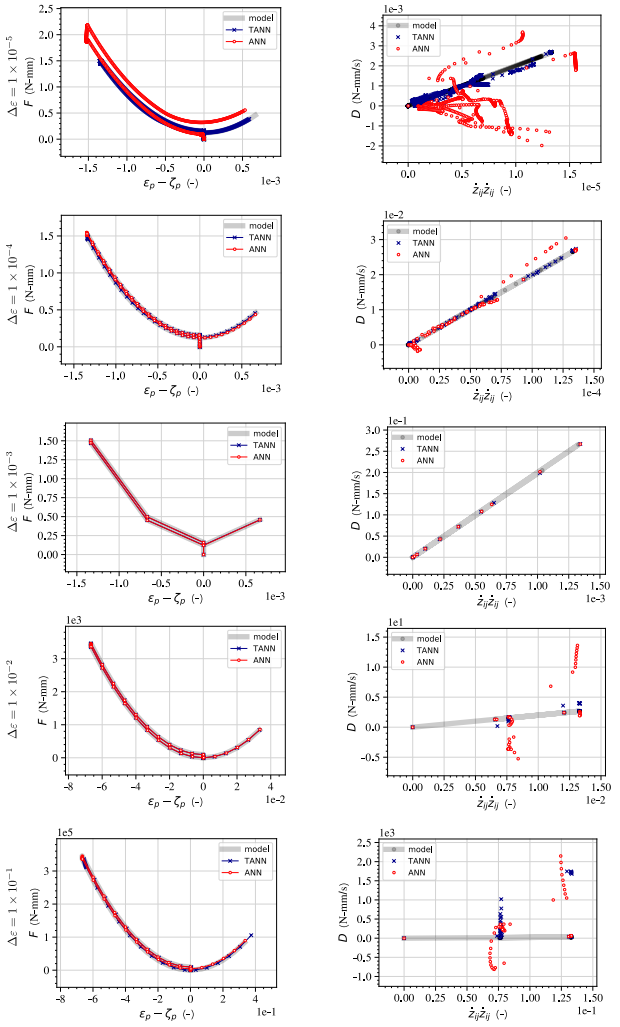

(a) F prediction (TANN), Eq. (6.33) (ANN).

(b) D prediction (TANN), Eq. (6.33) (ANN).

Figure D.16 – Comparison of the energy and dissipation rate predictions of TANN and computation according to Eq. (6.33) for standard ANN with respect to the target values, for the bi-axial cyclic loading path, Eq. (6.35), for material case 3D-B, hardening. Each row represents the prediction at different $\Delta\varepsilon$ increments.

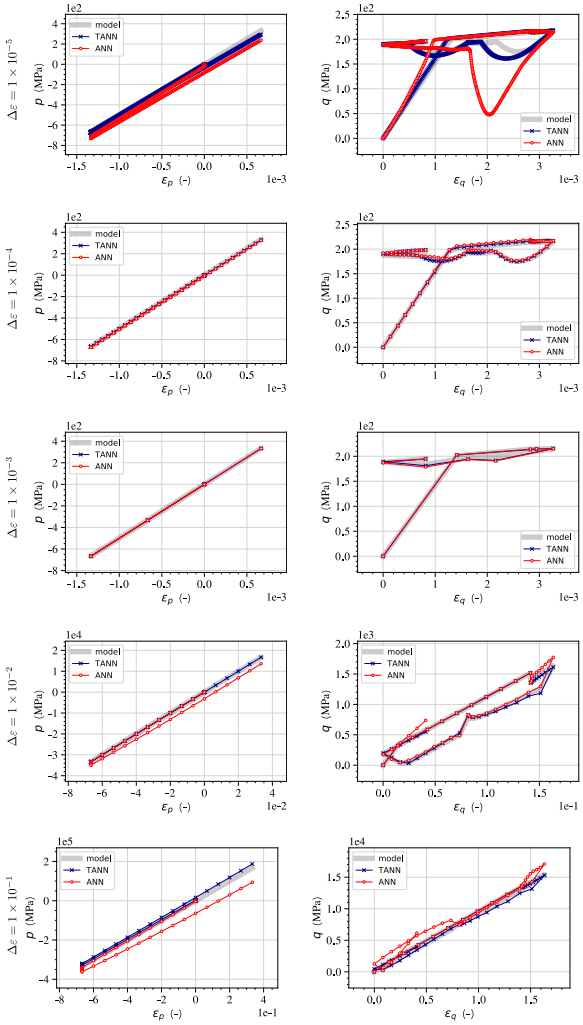

(a) p computation. (b) q computation.

Figure D.17 – Comparison of the stress predictions of TANN and standard ANN in terms of mean and deviatoric stress, p and q, for the bi-axial loading path in Figures D.15 and D.16 (hardening), Eq. (6.35). Each row represents the prediction at different $\Delta\varepsilon$ increments.

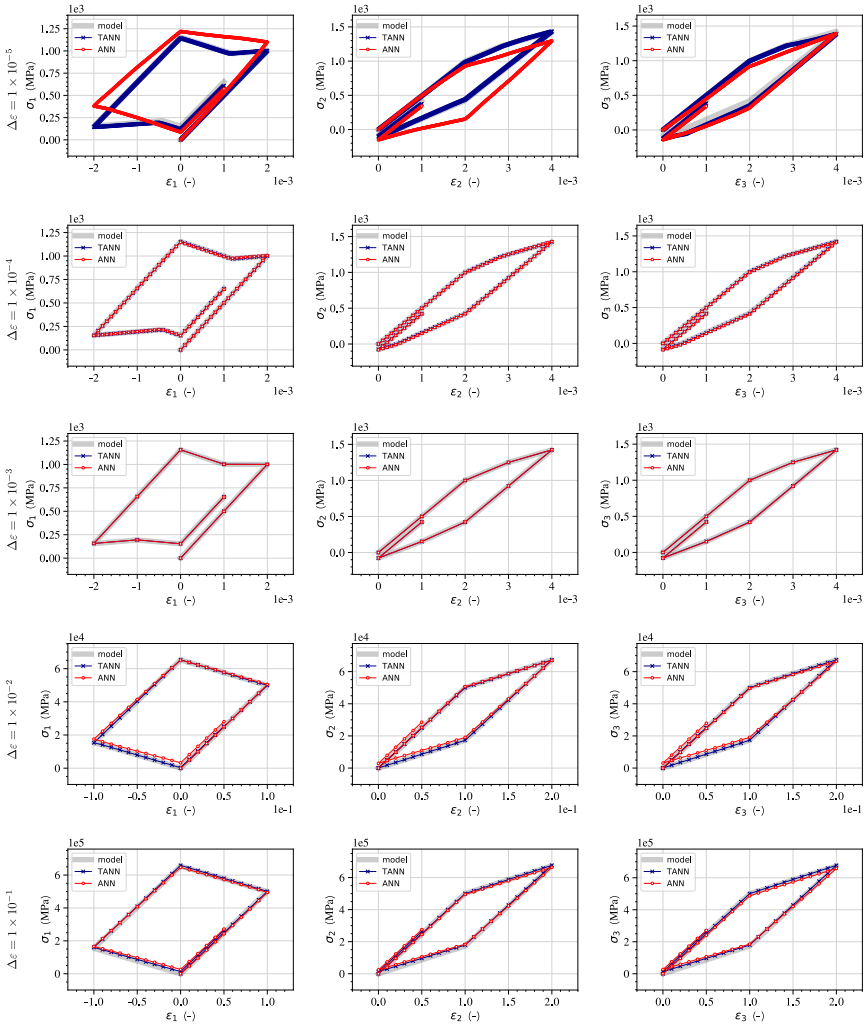

Figure D.18 – Comparison of the stress predictions of TANN and standard ANN with respect to the target values, for the tri-axial cyclic loading path, Eq. (6.33), for material case 3D-B (hardening). Each row represents the prediction at different $\Delta\varepsilon$ increments.

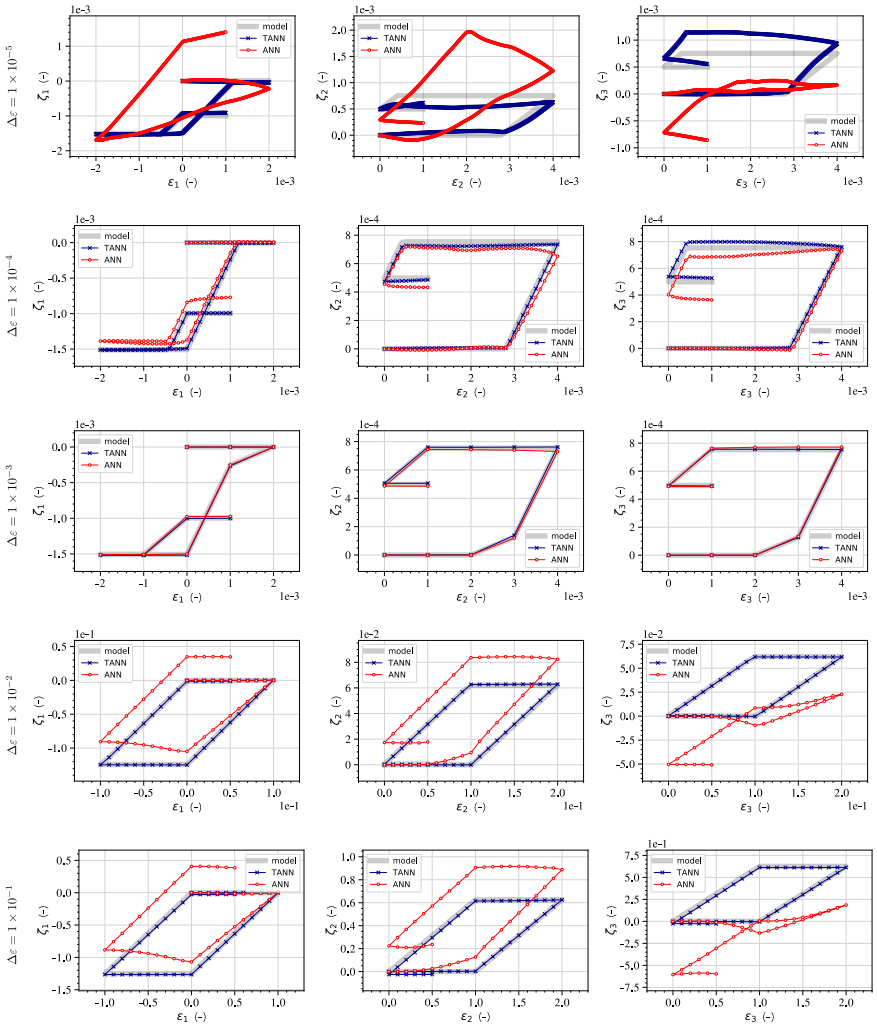

Figure D.19 – Comparison of the internal variable predictions of TANN and standard ANN with respect to the target values, for the tri-axial cyclic loading path, Eq. (6.35), for material case 3D-B, hardening. Each row represents the prediction at different $\Delta\varepsilon$ increments.

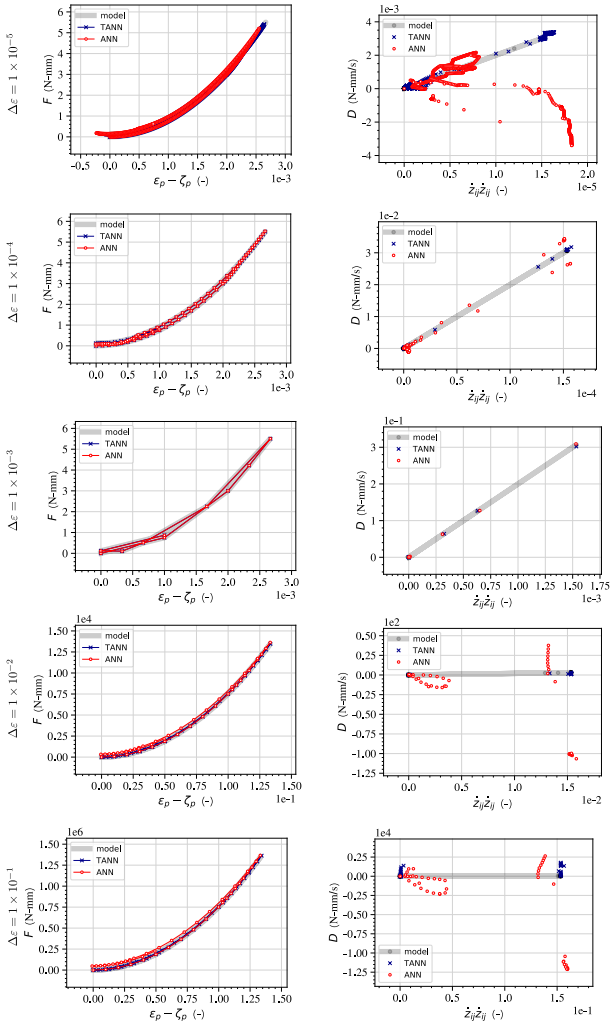

(a) F prediction (TANN), Eq. (6.33) (ANN).

(b) D prediction (TANN), Eq. (6.33) (ANN).

Figure D.20 – Comparison of the energy and dissipation rate predictions of TANN and computation according to Eq. (6.33) for standard ANN with respect to the target values, for the tri-axial cyclic loading path, Eq. (6.35), for material case 3D-B, hardening. Each row represents the prediction at different $\Delta\varepsilon$ increments.

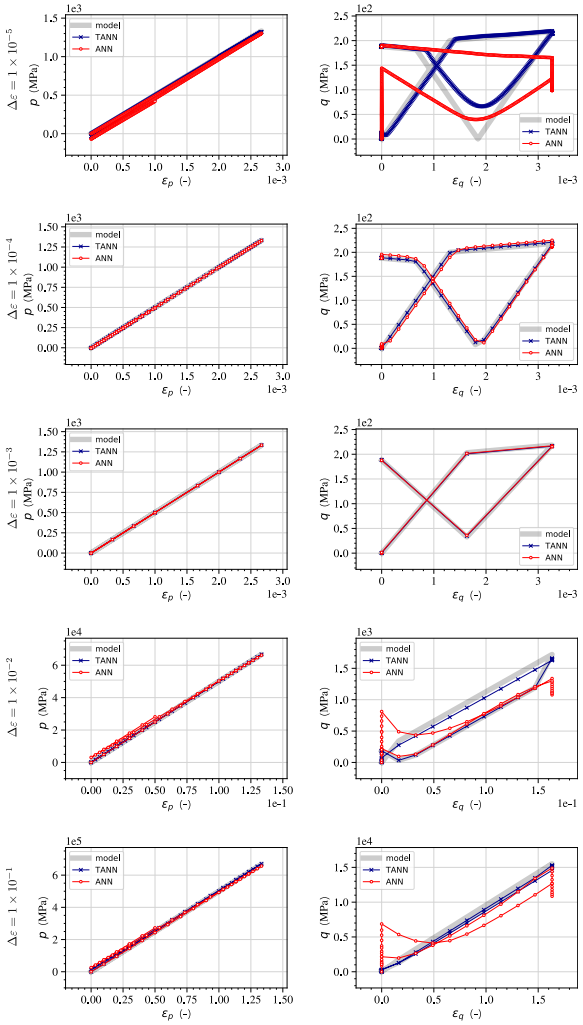

(a) p computation. (b) q computation.

Figure D.21 – Comparison of the stress predictions of TANN and standard ANN in terms of mean and deviatoric stress, p and q, for the tri-axial loading path in Figures D.18, D.19, and D.20 (hardening), Eq. (6.35). Each row represents the prediction at different $\Delta\varepsilon$ increments.

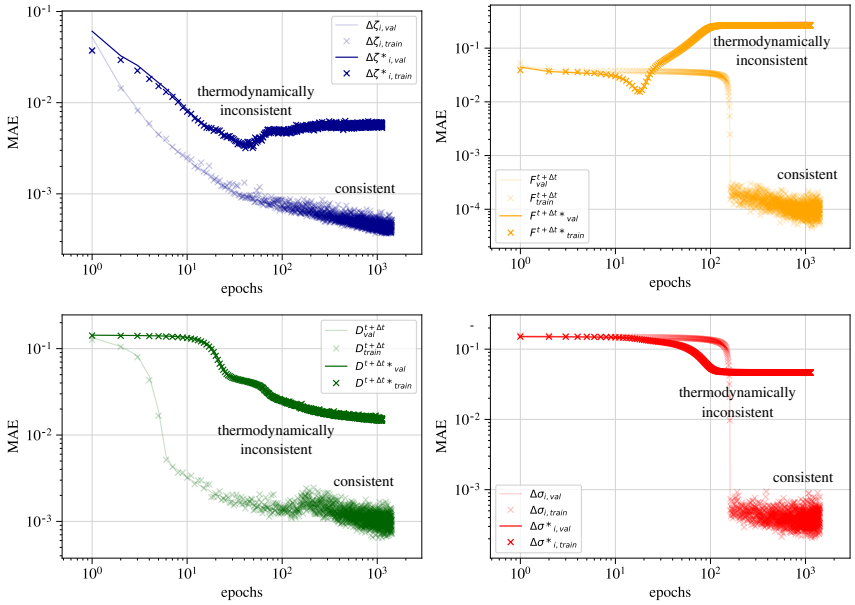

(a) MAE of TANN for thermodynamically unconsistent and consistent data.

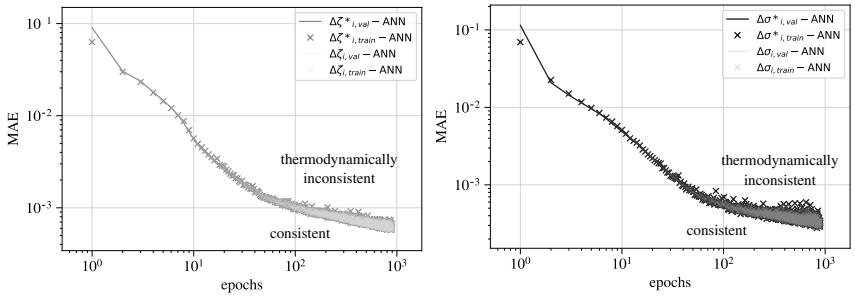

(b) MAE of ANN for thermodynamically unconsistent and consistent data.

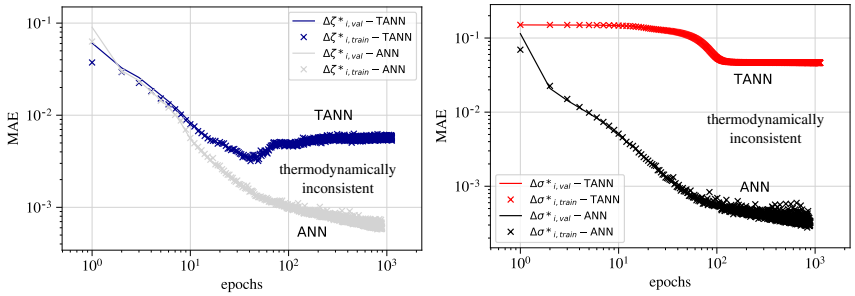

(c) MAE of ANN vs TANN.

Figure D.22 – Errors of the predictions of TANN (a) and standard ANN (b), as the training is being performed, with consistent and unconsistent datasets (denoted with superscript $*$). Unconsistency in the training dataset make the training procedure of TANN unsuccessful, while ANN, lacking of a frame based on thermodynamics, learns the unconsistent data (and relationship between them).

Appendix E

Scaling laws considering the effects of the angle of incidence

The scaling laws for a (deformable) multi-drum column, with square cross-section, are investigated by considering a more realistic characterization of the blast loading (cf. 7.7). In particular, we consider here all the exposed surfaces of the structure (front, top, lateral, and rear), and not only the front surface (cf. Figure 7.4). For each surface, we account for the non-simultaneity of the load, the effects of surface rotation of the blocks, incident angle (Mach stem), and the relative distance between explosive and blocks, as in Section 7.7 (Method B). Following the approach in Vannucci et al. (2017a); Masi et al. (2020a) the position and the angle of incident of the front surface of blocks are used to computed the blast loads.

The prototype is subjected to several explosive quantities: 250, 500, 750, and 1000 kg. Differently from the results in paragraph par:nonplanar, the overturning happens for a quantity of 1000 kg. Indeed, the effects of the pressure acting on rear surfaces are stabilizing Masi et al. (2019a).

We present in Figures E.1-E.4 the prototype and (upscaled) model responses. For an explosive charge of 250 kg of TNT equivalent, the model predictions strongly differ from those of the prototype. While, for larger explosive weights, the predictions agree remarkably well, especially for first peak response. It is worth noticing that the scaling laws do not account for differing arrival times of the shock wave at different points of the structure. As a result the equivalent impulse acting on the prototype structure is, in principle, not similar with that of the model. Nevertheless, for large (enough) charge weights, the similarity is preserved. Indeed, in these cases, the shock wave velocity is fast enough to have minor effects in the dynamic response of both the prototype and the model. The shifting in the shock arrival time can hence be approximately neglected. This is true for the case herein considered. Further investigations are necessary.

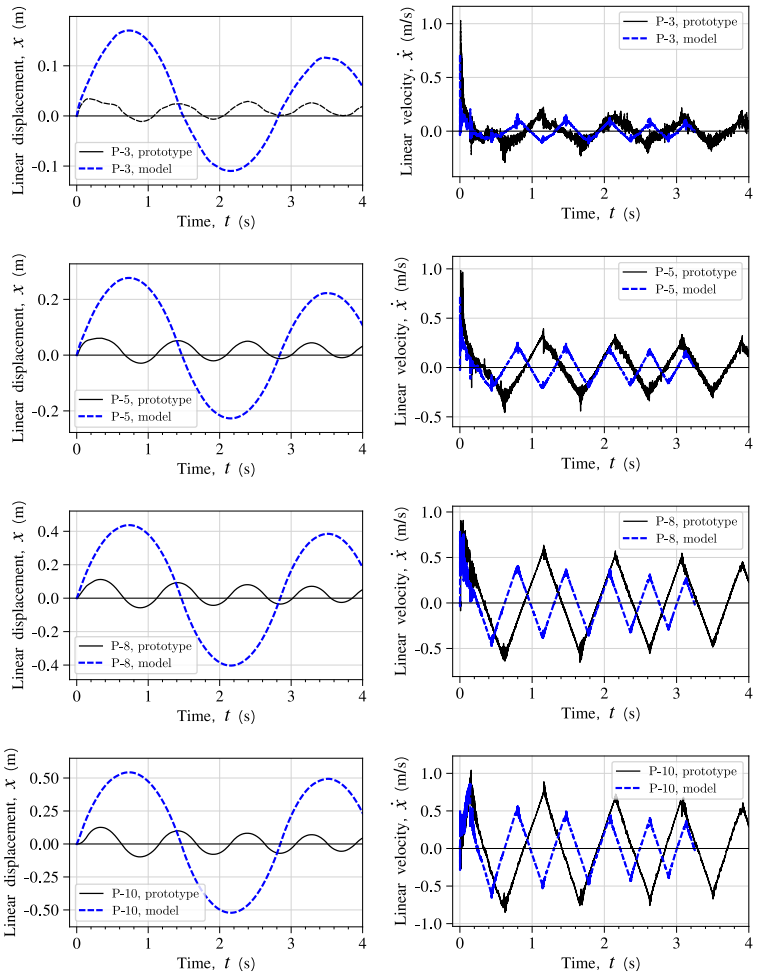

(a) horizontal displacement. (b) horizontal velocity.

Figure E.1 – Comparison between the prototype response and the model response ($\lambda = 1/100$), for a multi-drum column with cross-square section subjected to 250 kg at 10 m (Method C). Displacements and velocities of various monitoring points (cf. Fig. 7.20) are represented in (a) and (b), respectively.

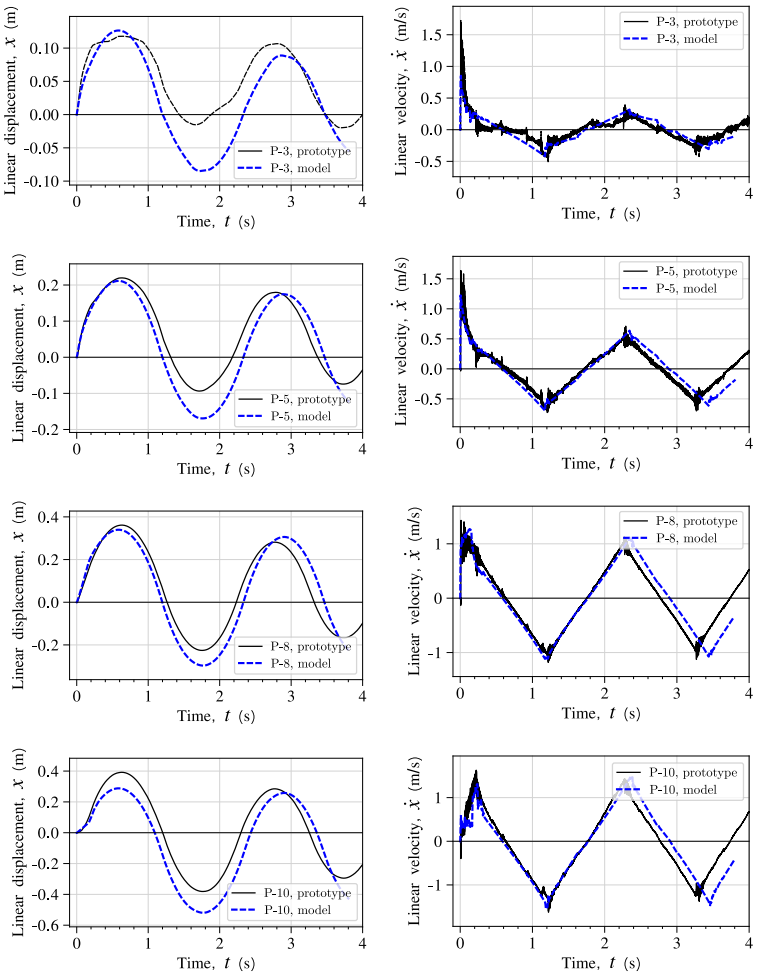

(a) horizontal displacement. (b) horizontal velocity.

Figure E.2 – Comparison between the prototype response and the model response ($\lambda = 1/100$), for a multi-drum column with cross-square section subjected to 500 kg at 10 m (Method C). Displacements and velocities of various monitoring points (cf. Fig. 7.20) are represented in (a) and (b), respectively.

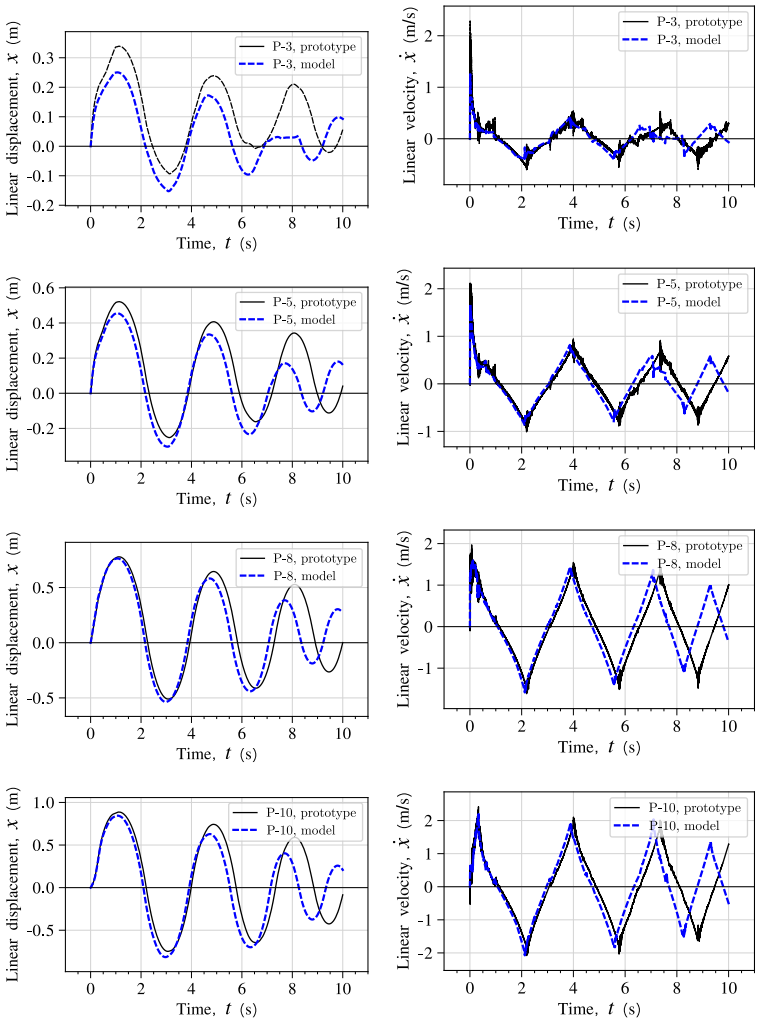

(a) horizontal displacement. (b) horizontal velocity.

Figure E.3 – Comparison between the prototype response and the model response ($\lambda = 1/100$), for a multi-drum column with cross-square section subjected to 750 kg at 10 m (Method C). Displacements and velocities of various monitoring points (cf. Fig. 7.20) are represented in (a) and (b), respectively.

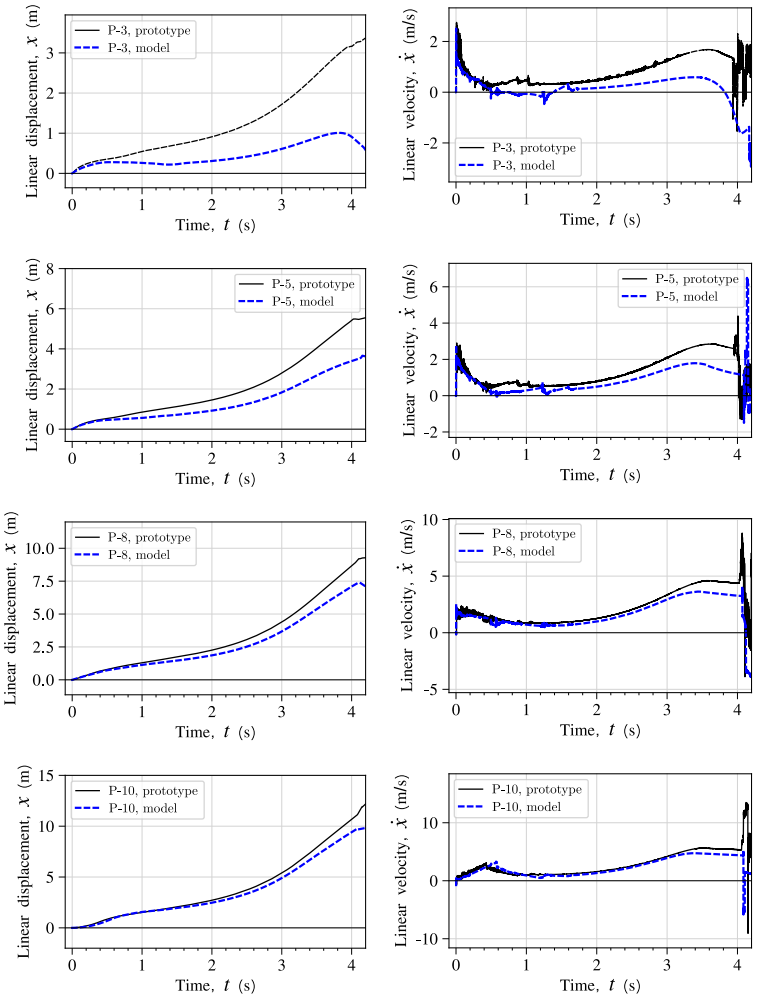

(a) horizontal displacement. (b) horizontal velocity.

Figure E.4 – Comparison between the prototype response and the model response ($\lambda = 1/100$), for a multi-drum column with cross-square section subjected to 1000 kg at 10 m (Method C). Displacements and velocities of various monitoring points (cf. Fig. 7.20) are represented in (a) and (b), respectively.

Titre : Analyse du comportement et de la rupture des structures en maçonnerie de géométrie non-standard en dynamique rapide

Mots clés : Maçonnerie ; Explosions; Méthode aux Éléments Discrets ; Méthode aux Éléments Finis ; Réseaux des neurones artificiels ; Lois de similitude.

Résumé : Les bâtiments en maçonnerie ont souvent une géométrie non-standard, caractérisée par des arcs, des voûtes et des dômes. C'est également le cas des structures du patrimoine bâti historique, qui sont souvent des cibles symboliques et privilégiées des actions violentes, telles que des explosions. L'objectif principal de ce travail est de mettre en lumière le comportement dynamique et les modes de ruine des structures maçonnées avec soit un comportement monolithique soit une géométrie non-standard, vis-à-vis d'explosions. Ceci est d'abord accompli grâce à des outils analytiques simplifiés et à des simulations numériques détaillées reposant sur la Méthode aux Éléments Discrets (ED). Ensuite, une approche de modélisation macroscopique simplifiée, utilisant la Méthode aux Éléments Finis (EF), est introduite comme un outil d'ingénieur pour étudier de grands bâtiments en maçonnerie, tels que des monuments. En particulier, de nouvelles solutions analytiques pour la réponse en basculement des structures élancées et monolithiques sont dérivées et validées par rapport à des expériences existantes et à des simulations numériques détaillées. La Méthode aux ED est utilisée pour étudier la réponse des structures maçonnées non-standard, telles que des arcs et des voûtes, et l'influence de divers paramètres mécaniques.

En nous appuyant sur les résultats numériques ED, nous développons une approche de modélisation aux EF macroscopique, basée sur des techniques simplifiées de upscaling et un modèle de fissuration étalé, afin de prédire la réponse d'éléments structuraux en maçonnerie à grande échelle. Le modèle proposé prévoit un comportement isotrope et permet de prendre en compte le phénomène d'adoucissement, qui affecte fortement la réponse du matériau. Dans le but de développer des modèles de matériaux plus précis et détaillés de l'approche mentionnée ci-dessus, une nouvelle classe de réseaux de neurones artificiels (ANNs) est également proposée comme un outil robuste, basé sur la thermodynamique, pour dériver des modèles constitutifs, au niveau du point matériel, dans le cadre d'analyses physiques multi-échelle. Les réseaux de neurones artificiels basés sur la thermodynamique (TANNs) sont appliqués - et leur supériorité par rapport aux approches ANNs classiques est prouvée - pour le cas des matériaux présentant un comportement d'adoucissement.
Enfin, nous proposons de nouvelles lois de similitude pour la réponse des structures en maçonnerie soumises à des explosions. Notre objectif est de concevoir de futurs essais expérimentaux à échelle réduite, qui sont d'une importance capitale pour améliorer la connaissance actuelle et corroborer les modèles proposés.

Title : Fast-dynamic response and failure of masonry structures of non-standard geometry subjected to blast loads

Keywords : Masonry; Blast loads; Discrete Element Method; Finite Element Method; Artificial Neural Networks; Scaling laws.

Abstract : Masonry structures are often characterized by non-standard geometries, consisting of arches, vaults, and domes. This is also the case for historical and monumental structures, which are often primary targets of accidental and deliberate explosions. The main goal of this work is to shed light on the dynamic behavior and failure modes of monolithic and non-standard, curvilinear masonry geometries subjected to blast loading. This is, first, accomplished through simplified analytical tools and advanced numerical simulations relying on the Discrete Element Method (DEM). Then, a simplified macroscopic modeling approach, using the Finite Element Method (FEM), is presented as an engineering tool to be used in the investigation of complex, large masonry buildings, such as monuments. In particular, new analytical, closed-form solutions for the rocking response and the overturning domain of slender, monolithic structures are derived and validated against existing experiments and detailed numerical simulations. DEM is used to investigate the response of non-standard masonry structures and the influence of various mechanical parameters.

Relying on DEM numerical results, we develop a macroscopic FEM modeling approach, based on simplified upscaling techniques and the smeared cracking model, to make preliminary predictions of the structural response of masonry assets at large scale. With the aim of developing more accurate and detailed material models of the afore-mentioned simplified approach, a new class of Artificial Neural Networks (ANNs) is also proposed as a robust, thermodynamics-based, tool to derive constitutive models, at the material point level, in the framework of physics-based multiscale analyses. Thermodynamics-based Artificial Neural Networks (TANNs) are applied-and their superiority with the respect to classical ANNs approaches is proved-for the case of materials displaying softening behavior.
Finally, we propose new scaling laws for the response of masonry structures subjected to explosions. Our aim is to design future experimental, reduced-scale experiments, which are of paramount importance to further improve current understanding and corroborate the proposed models.